Study of the optical properties of X-ray selected galaxy clusters : multi-wavelengths analysis and implications for the future large surveys

Marina Ricci

UNIVERSITÉ CÔTE D'AZUR

ÉCOLE DOCTORALE
SCIENCES FONDAMENTALES ET APPLIQUÉES

THÈSE DE DOCTORAT

ÉTUDE DES PROPRIÉTÉS OPTIQUES D'AMAS DE GALAXIES DÉTECTÉS EN RAYONS X: ANALYSE MULTI-LONGUEURS D'ONDE ET IMPLICATIONS POUR LES GRANDS RELEVÉS DU FUTUR

Marina RICCI

Laboratoire J-L. Lagrange - Observatoire de la Côte d'Azur

Présentée en vue de l'obtention du grade de docteur en Sciences de la Planète et de l'Univers de l'Université Côte d'Azur
Dirigée par : Sophie Maurogordato
Co-encadrée par : Christophe Benoist
Soutenue le : 03 octobre 2018

Devant le jury, composé de :
Monique ARNAUD, DR CEA, CEA Saclay
Stéphane ARNOUTS, CR CNRS, Université Aix-Marseille
Christophe BENOIST, Astronome Adjoint, OCA
Andrea BIVIANO, Chercheur, Observatoire de Trieste (Italie)
Chiara FERRARI, Astronome, OCA
Emmanuel GANGLER, DR CNRS, Université Clermont-Auvergne
Sophie MAUROGORDATO, DR CNRS, UCA
Marguerite PIERRE, DR CEA, CEA Saclay

Étude des propriétés optiques d'amas de galaxies détectés en rayons X: analyse multi-longueurs d'onde et implications pour les grands relevés du futur

Jury :

Présidente du jury :

Mme Chiara FERRARI, Astronome, Observatoire de la Côte d'Azur

Rapporteurs :

Mme. Monique ARNAUD, Directrice de Recherches CEA, CEA Saclay
M. Andrea BIVIANO, Chercheur, Observatoire de Trieste (Italie)

Examinateurs :

M. Stéphane ARNOUTS, Chargé de Recherche CNRS, Université Aix-Marseille
M. Emmanuel GANGLER, Directeur de Recherches CNRS, Université Clermont-Auvergne
Mme. Marguerite PIERRE, Directrice de Recherches CEA, CEA Saclay

Étude des propriétés optiques d'amas de galaxies détectés en rayons X: analyse multi-longueurs d'onde et implications pour les grands relevés du futur

Résumé :

Répondre aux questions fondamentales concernant notre compréhension de l'Univers, comme la cause de son expansion accélérée ou la nature de la matière noire, requiert de confronter les théories aux observations. Dans ce contexte, les amas de galaxies peuvent être utilisés comme de puissantes sondes observationnelles. Cependant, à l'heure actuelle, leur utilisation est limitée par des incertitudes et des effets systématiques, qui affectent notamment la mesure de leur masse, que l'on présume dominée par la matière noire.

Les amas de galaxies peuvent être étudiés à différentes longueurs d'onde : le gaz chaud qui compose le milieu intra-amas (ICM en anglais) émet des rayons X et est observable dans le domaine millimétrique via l'effet Sunyaev-Zel'dovich (SZ), alors que les galaxies rayonnent principalement en optique et infrarouge. Combiner et comparer ces observables permet de réduire les incertitudes et les effets systématiques des contraintes cosmologiques issues des amas. Dans ce contexte, cette thèse a pour but de préparer les grands relevés observationnels du futur comme Euclid et le Large Synoptic Survey Telescope (LSST). Elle présente les analyses multi-longueurs d'onde d'un échantillon d'amas détectés en X dans le relevé XXL, couvrant une large gamme de masses et de redshifts. La première partie de cette thèse introduit le contexte cosmologique et présente les propriétés observationnelles des galaxies et amas de galaxies, ainsi que les ingrédients pour construire des échantillons cosmologiques d'amas.

La deuxième partie traite de la caractérisation optique des amas XXL et des propriétés de leurs galaxies membres. Nous commençons par la présentation de XXL et du Canada-France-Hawaii Telescope Legacy Survey (CFHTLS), un relevé optique associé. Ensuite, nous nous concentrons sur la caractérisation de la qualité des redshifts photométriques du CFHTLS et sur leur utilisation pour construire les fonctions de luminosité (LF en anglais) optiques des galaxies d'amas XXL. Il apparaît que la LF des galaxies satellites dépend légèrement de la richesse des amas, le principal proxy de masse en optique, mais ne montre pas d'évolution significative avec le redshift. Ensuite, nous entreprenons l'étude de la couleur et de la fraction de galaxies à noyaux actifs (AGN en anglais) dans les galaxies d'amas XXL et montrons que la masse joue un rôle clé dans la régulation de l'activité de formation stellaire dans les amas. Pour finir, l'algorithme de détection d'amas WaZP est utilisé pour étudier la contrepartie optique des amas XXL.

La troisième partie de cette thèse est consacrée au projet observationnel dédié à la cartographie du signal SZ de trois amas XXL distants, avec la camera à haute résolution angulaire NIKA2. La préparation du projet est discutée, en se servant des données optiques et X afin de prédire le signal SZ attendu. Ensuite, nous présentons la procédure d'observation au télescope et la réduction des données, dédiée à la production des cartes SZ étalonnées. Le projet est en cours et un amas, XLSSC102, à z = 0.97, a été observé partiellement. Nous développons ensuite une méthode de détection en aveugle des potentielles galaxies qui peuvent contaminer le signal SZ, permettant la découverte fortuite de galaxies poussiéreuses à haut taux de formation stellaire dans le champ de XLSSC102. La morphologie et l'état dynamique de XLSSC102 sont ensuite caractérisés grâce à la combinaison des données optiques, SZ et X et les profils radiaux de masse et de propriétés thermodynamiques de l'ICM sont mesurés en associant les données X et SZ. Cela permet de montrer que XLSSC102 est un amas en coalescence avec une masse de $\sim 3 \times 10^{14}$ $M_{\odot}$, et est compatible avec le scénario d'évolution standard de la formation des amas.

Mots clé: Cosmologie observationnelle; Amas de galaxies; Galaxies; Observations multi-longueurs d'onde

Study of the optical properties of X-ray selected galaxy clusters: multi-wavelength analysis and implications for the future large surveys

Abstract :

Addressing fundamental questions regarding our understanding of the Universe, such as the cause of its accelerated expansion or the nature of dark matter, requires to confront theories and observations. In this context, galaxy clusters can be used as powerful observational probes. However, their current utilisation is limited by uncertainties and systematic effects, notably affecting the measurement of their mass, which is presumably dominated by dark matter.

Galaxy clusters can be studied at different wavelengths: the hot gas composing the Intra Cluster Medium (ICM) shines in X-ray and is observable at millimetre wavelengths via the Sunyaev-Zel'dovich (SZ) effect, whereas galaxies emit principally in the optical and infrared. Combining and comparing these observables allows us to reduce the uncertainties and systematics in the cosmological constraints obtained from clusters. In this context, this thesis aims at paving the way of future large surveys such as *Euclid* and the Large Synoptic Survey Telescope. It presents the multi-wavelength analyses of a sample of clusters detected in X-ray in the XXL survey, spanning a wide range of masses and redshifts. The first part of the thesis introduces the cosmological context and presents the observational properties of galaxies and clusters, and the ingredients to build cosmological cluster samples.

The second part concentrates on the optical characterisation of XXL clusters and the properties of their member galaxies. It starts by presenting XXL and the Canada-France-Hawaii Telescope Legacy Survey (CFHTLS), an optical counterpart survey. Then, it focuses on the characterisation of the CFHTLS photometric redshifts quality and their use to construct the optical galaxy luminosity functions (LF) of XXL clusters. The LF of satellite galaxies is found to slightly depend on cluster richness, the main optical mass proxy, but no significant redshift evolution is observed. Then, the study of the colour and active galactic nuclei (AGN) fraction in XXL cluster galaxies is performed, finding that the mass plays a key role in shaping AGN and star formation activity in clusters. Finally, the WAZP optical cluster finder algorithm is used to investigate the optical counterparts of XXL clusters.

The third part of this thesis is dedicated to the observational project dedicated to the mapping of the SZ signal in three distant XXL clusters, with the high angular resolution NIKA2 camera. The preparation of the project is discussed, making use of the X-ray and optical data to predict the expected SZ signal. Then, the observation procedure at the telescope and the data reduction, dedicated to produce calibrated SZ maps, are presented. The project is still ongoing and one cluster, XLSSC102, at $z = 0.97$, has been partially observed. The development of the blind detection of galaxies potentially contaminating the SZ signal is developed, allowing for the serendipitous discovery of dusty star forming galaxies in the field of XLSSC102. The morphology and dynamical state of XLSSC102 are then characterised using optical, SZ and X-ray data and the radial ICM thermodynamics and mass profiles are measured combining SZ and X-ray data. This allows us to show that XLSSC102 is a merging cluster with a mass $\sim 3 \times 10^{14}$ $M_{\odot}$, and is compatible with the standard evolution scenario of cluster formation.

Keywords: Observational cosmology; Clusters of galaxies; Galaxies; Multi-wavelength observations

Remerciements :

Et voilà le dernier point de la thèse à finaliser... Et ce n'est pas facile ! Comment résumer trois années en quelques lignes et n'oublier personne ? Beaucoup de pression !

Bon, je me lance.

Tout d'abord, je tiens à remercier chacun des membres de mon jury pour avoir accepté mon invitation et avoir été présent à ma soutenance: Stéphane Arnouts, Emmanuel Gangler, Marguerite Pierre et en particulier mes rapporteurs Monique Arnaud et Andrea Biviano, qui ont évalué mon manuscrit avec beaucoup d'attention et Chiara Ferrari, qui a accepté d'en être la présidente. Ensuite, merci à mes directeurs de thèse, Sophie Maurogordato et Christophe Benoist, qui m'ont accompagnée durant ces trois années à travers la longue aventure qu'est le doctorat.

Le travail présenté dans ce manuscrit s'est enrichi de diverses collaborations et je tiens à remercier particulièrement : Rémi Adam, qui m'a introduite au domaine SZ et avec qui j'ai construit le projet d'observation auquel une partie entière de ma thèse est consacrée ; Elias Koulouridis avec qui j'ai étudié l'activité AGN dans les amas XXL, ce qui m'a permis d'élargir mon domaine de recherche ; Dominique Eckert, pour sa contribution à l'analyse combinée X+SZ de XLSSC102 et son expertise sur le sujet ; les membres de la collaboration XXL avec qui j'ai pu échanger et qui ont contribué à l'amélioration du travail présenté ici ; la collaboration NIKA2, qui a développé les outils utilisés dans l'analyse des données SZ ; le staff de l'IRAM qui s'occupe des observations au 30m ; Matthieu Bethermin, avec qui j'ai discuté de SMGs lorsque la météo nous empêchait d'observer au 30m, ce qui a conduit à une des analyses développée dans ce manuscrit ; Oliver Hahn, qui a mis à ma disposition ses simulations hydrodynamiques d'amas de galaxies ; enfin la collaboration Euclid qui m'a permis d'insérer dans ma thèse des travaux non publiés.

Je remercie également mes collègues au sein de l'équipe Galaxie et Cosmologie du Laboratoire Lagrange. Un mot particulier pour Mathias, qui s'est toujours montré à l'écoute, Vanessa, pour ses commentaires constructifs avant la soutenance, Oliver, pour ses discussions très intéressantes lors des "journals clubs" et "ExtraGalactic meetings", Rémi pour ses conseils, son altruisme et son dynamisme, Chiara, pour son support tout au long de mes études malgré son emploi du temps très chargé, Alvaro, pour son aide, son soutien et ses "scientific life hacks".

Merci à Gilles Niccolini qui a été mon maître Jedi de l'enseignement et qui m'a suivi depuis la licence. Merci aussi aux étudiants et étudiantes que j'ai pu avoir en TD et TP, j'espère que je ne vous ai pas trop traumatisé-e-s et que vous avez pu comprendre un peu mieux la Thermo. Ce n'est pas facile d'enseigner en fin de thèse ! J'en profite aussi pour remercier le système éducatif public français, duquel je suis un pur "produit".

Merci aux services "techniques" du labo et notamment à Jean-Philippe Ghibaudo pour sa gentillesse et sa rapidité à résoudre mes problèmes informatiques, ainsi que Sylvie Goletto pour sa flexibilité et sa bienveillance, malgré mes retours de mission toujours tardifs...

Merci à toute l'équipe du restaurant (qui nous manque lorsque l'on quitte l'observatoire), pour leur bonhomie et leur super cuisine. Et merci à Khaled de m'avoir fait rire et permis de me resservir plusieurs fois !

Merci à mes collègues doctorants, post-doctorants et autres, puisque que chacun a participé à la bonne ambiance que j'ai ressenti à l'Observatoire. Merci pour (en vrac) les sorties au bar, au restau, à la plage ou à la montagne, les concerts des Wathermelons, les "Ach So!" cafés, les parties de ping-pong ("high energy meetings"), les soirées à Tandoori Flame, les breaks de 17h, et les discussions à la cantine.

Durant ces trois années j'ai rencontré beaucoup de personnes (la plupart actuellement à l'autre bout du monde) qui m'ont marquée chacune à leur manière. Par ordre approximatif d'apparence dans ma vie j'aimerais saluer chaleureusement et remercier: Alvaro, Gerardo, Srivatsan, Alkis, Kateryna, Pierre, The Captain, Nanda, Hendrick, Clément, Steeve, Govind, Nastia,

Rémi, Michael H., Edouard, Michael B., Francesco, Emma.

Enfin merci à mes amis de longue date et à ma famille pour leur soutien tout au long de mes études et pour m'avoir permis de déconnecter parfois. Pour finir merci à mon amoureux pour ses encouragements, son réconfort, son temps et son aide indéfectible, durant ces moments parfois difficiles.

Enfin merci à toi qui me lis, et bon courage si tu es en train d'écrire ta thèse!

Contents

Introduction

> Notre univers porte les marques de la jeunesse et nous pouvons espérer reconstituer son histoire. Les documents dont nous disposons ne sont pas enfouis dans les ampilement de briques poinçonnées des Babyloniens, notre bibliothèque ne risque pas d'être détuite dans quelque incendie ; c'est l'espace admirablement vide où se conservent les ondes lumineuses mieux que le son sur la cire des phonographes.
>
> Georges Lemaître, L'expansion de l'espace, 1931

Our understanding of the content of the Universe and its evolution has drastically improved during the last hundred years, as a result of major theoretical and observational breakthroughs. These have set the bricks of our current cosmological paradigm, the extended Lambda Cold Dark Matter (ΛCDM) model. The ΛCDM model accounts for many independent observables, over a wide range of scales and across a large fraction of the Universe history. It is based on general relativity to describe gravity, and assumes that the Universe is homogeneous an isotropic on large scales. This model was able to predict observational features and is unchallenged so far, despite being phenomenological, rather than physically, motivated.

The ΛCDM cosmological model is relatively simple as it can be described by a set of six parameters only. Nowadays, almost all are constrained to a level of a few percents. Nevertheless, the model raises some fundamental questions. First, it needs to be extended to include the inflation theory, in order to explain both the homogeneity and isotropy of the Universe on large scales, and the origin of the fluctuations that eventually led to the matter distribution that we observe today. While being largely accepted, this paradigm is not yet confirmed directly by observations. Secondly and more puzzlingly, the ΛCDM model requires the introduction of either a cosmological constant or a mysterious form of energy, to counterbalance gravity and cause the accelerated expansion of the Universe that we observe today. The nature of this so called *dark energy*, or cosmological constant, remains unknown, but it is believed to dominate the current cosmic energetic budget. Lastly, the ΛCDM model relies on the existence of dark matter as the main constituent of the Universe. The presence of an invisible form of matter was supposed as early as in the 1930s to account for the dynamics of stars and galaxies, but its physical nature is still unknown. The understanding of dark energy and dark matter are among the main challenges of modern cosmology. It requires constraining cosmological models with high precision by combining various observational probes, related to the geometry, content and evolution of the Universe.

According to the inflation paradigm, the large-scale structures of the Universe arise from primordial quantum fluctuations, which evolved and caused inhomogeneities in the matter density field. These seeds of matter grew by gravitational collapse in a hierarchical fashion: small structures (galaxies) formed first, and then aggregated to constitute the larger ones. Gravitation instabilities shaped the large scale matter density field, which shows a web-like structure containing voids, filaments, sheets and nodes. Galaxy clusters reside in the latter and are the more massive gravitationally bound objects in the Universe.

Galaxy clusters are made of dark matter, hot gas (the intra cluster medium, ICM) and galaxies that interact with each other. They are key environments to study the co-evolution of dark and baryonic matter. This is important not only for cluster studies, but also for other large scale structure probes, which can be affected by baryonic feedbacks on small scales. The number density of galaxy clusters as a function of their mass and redshift is sensitive to the expansion and the growth history of the Universe. It is thus a promising probe to constrain the nature of dark energy. Moreover, comparison with early Universe probes, such as the cosmic microwave background (CMB) allows us to trace the evolution of density perturbations through time. Achieving

precision cosmology with galaxy clusters requires the accurate estimation of their masses and redshifts and the control of any bias related to their formation and evolution.

Clusters are objects that can be studied at different wavelengths, as their galaxies principally emit in the optical and infrared and the ICM shines in X-ray and leaves an imprint in the CMB, known as the Sunyaev-Zel'dovich (SZ) effect, observable at millimetre wavelengths. In surveys, the cluster total mass can be inferred from those observables, through the use of scaling relations, arising from the fact that clusters are nearly self-similar objects since their formation is driven by gravitational collapse. However, strong deviations from these relations may arise when baryonic feedbacks become important, particularly in low mass and high redshift clusters. The correct modelling of the scaling relations and survey selection functions is the primary challenge of cluster cosmology.

Tensions arose recently from the comparison of cosmological constraints inferred from clusters and from the CMB. In order to reconcile the two, a large bias in the mass measurements of clusters has been invoked. However, it is at odds with other cluster observations and simulations. This is either a sign of a breakdown of ΛCDM and a need for new physics, or, the consequence of a profound misunderstanding of the physical properties of galaxy clusters.

Being dense and massive objects, clusters are indeed the place of complex astrophysical processes, arising from the interplay between their different components. Clusters are thus unique laboratories to study the connection between the galaxies, gas and dark matter. For instance, galaxies in clusters are known to be affected by the ICM and the strong gravitational potential, and they display specific properties. Analysing those phenomena as a function of cosmic time and cluster global properties allows us to put strong constraints on galaxy formation and evolution scenarios. It is also highly valuable for a better characterization and detection of galaxy clusters.

Several surveys have been conducted at different wavelengths, allowing us to build complementary cluster catalogues and infer cosmological constraints. However, the analyses have been limited so far to massive clusters up to intermediate redshifts, whereas distant clusters have higher cosmological constraining power and low mass clusters are by far more numerous. In the coming years, many surveys will be undertaken with new instruments such as eROSITA in the X-ray or *Euclid* and the Large Synoptic Survey Telescope (LSST) in the optical and near infrared. They will lead to the detection of hundreds of thousands of clusters over an unprecedented range of masses and up to high redshift, with precise mass measurements and associated multi-wavelength observations. This will allow us to study galaxies and cluster physics in regimes unexplored or limited to low number statistics so far. The exquisite data quality will bring cluster cosmology to a new era and, likely, will provide us with the tools to shed light on the current tensions.

My thesis work takes place in the general frame of observational cosmology and the specific context of galaxy cluster analyses aiming to pave the way to future large surveys, such as *Euclid* and LSST in the optical/near infrared. This thesis manuscript is organised in three parts. In Part I, I introduce the general context:

- I present the cosmological framework and how galaxy clusters can be used as cosmological probes in Chapter 1;
- I discuss the observational properties of galaxies and galaxy clusters, and I explain the different steps needed to construct a cosmological cluster sample in Chapter 2.

In Part II, I conduct the optical characterisation of a statistical sample of X-ray detected clusters from the XXL survey, covering a wide range of masses and redshifts. The goal is to investigate the properties of cluster galaxies and derive a reference parametrisation for cluster modelling and detection.

- I introduce the XXL survey and its optical counterpart, the Canada-France-Hawaii Telescope Legacy Survey (CFHTLS) in Chapter 3;
- I analyse the quality of the photometric redshifts in the CFHTLS in Chapter 4, in order to define an unbiased way to select galaxies for later studies;
- The luminosity function (LF) is a key statistical tool to describe galaxies. In Chapter 5, I construct the optical LFs in XXL clusters and I identify and quantify associated systematics;
- I perform the analyses of the XXL cluster galaxies LFs in Chapter 6, and I study their dependences with redshift and richness, used as a mass proxy;
- I then examine the activity of XXL cluster galaxies trough their AGN fraction and their colour in Chapter 7, and I discuss its impact on the detection and characterisation of clusters;
- Comparing catalogues detected at different wavelengths allows for the validation of cluster surveys selection functions. Thereby, in Chapter 8, I present the WaZP optical cluster finder, its application to the CFHTLS W1 field and the matching statistics between the XXL and WaZP cluster samples .

In Part III, I present the motivations and preparatory analyses of the observational project I am leading, aiming at mapping three distant ($z \sim 1$) X-ray XXL detected clusters in SZ, with the NIKA2 camera at the IRAM 30m telescope. The aim is to achieve a multi-wavelength characterisation of those systems and to test if they deviate from the expectations of standard evolution of clusters. The observations are ongoing, and I present the preliminary results obtained for one of our clusters.

- I describe the project motivations and the analyses performed to prepare the observations in Chapter 9;
- In Chapter 10, I present the NIKA2 instruments and the procedures from the data acquisition at the telescope to the data reduction and map-making;
- Serendipitous sub-millimetre galaxies are present in the field of XLSSC102, the only cluster that was observed so far. I develop the tools to detect and analyse them in Chapter 11;
- In Chapter 12, I present the preliminary analysis of the morphology, radial physical properties and global properties of our observed cluster and compare them to standard evolution expectations.

Lastly, I give my general conclusions in Part Closing remarks and perspectives. I also show the analyses that I performed for the preparation of the *Euclid* mission in Appendix A and B.

Part I

General context

Table of Contents

Chapter 1

The Universe at large scale

Contents

Abstract: In this Chapter, we introduce the cosmological framework in which this thesis takes place. After a brief historical review, we describe the main observational probes and present the current concordance cosmological model and the fundamental questions that it raises. We then discuss how the matter distribution in the Universe evolves across cosmic time, leading to the formation of clusters and galaxies as we see them today. Finally, we focus on the use of galaxy clusters as cosmological probes and how they compare to other probes.

1.1 Cosmological context

1.1.1 A bit of history

Physical cosmology is the science of the Universe as a whole: its origin, content and evolution. The modern vision of cosmology emerged from two main breakthroughs at the beginning of the XIX$^{\text{th}}$ century. The first discovery was that the Milky Way is not unique, but one over many galaxies. This was put in evidence, notably, by the measurements of the distance of the Andromeda galaxy by Vesto Slipher (Slipher 1913), Heber Curtis (Curtis 1917), Ernst Opik (Opik 1922) and Edwin Hubble (Hubble 1925). The second breakthrough was the application, by Albert Einstein, of its newly discovered theory of general relativity to the whole Universe (Einstein 1917). Alexander Friedmann showed latter that the static model found by Einstein was

unstable and that the Universe itself could be a dynamical object (Friedmann 1922). Georges Lemaître worked independently on this problem and proposed that the Universe was expanding (Lemaître 1927). Using a list of nebulae[1] observed by Gustaf Strömberg (Stromberg 1925) and Edwin Hubble (Hubble 1926), he estimated, for the first time, the value of the now called *Hubble constant*[2]. A few years latter Lemaître came up with the concept of "primeval atom", better known nowadays as the "Big Bang" theory (Lemaitre 1931; Lemaître 1931). This model was largely debated and it is only with the measurements of the cosmic microwave background (CMB) (see Penzias and Wilson 1965, and Dicke et al. 1965, but also Naselsky et al. 2006 for a list of earlier detections), interpreted as a radiation from the early Universe, and the measurement of the abundance of the light elements from the primordial nucleosynthesis (Alpher et al. 1948), that it became generally accepted.

The Big Bang theory sets the framework of our current cosmological concordance model. Major theoretical progresses were made at the beginning of the 80's to account for apparent problems related to the initial conditions of the Universe and to the fact that the Universe is very homogeneous on large scales but presents tiny fluctuations, from which the large scale structures formed along cosmic evolution. Those advances led to the inflation paradigm (Starobinsky 1980; Guth 1981; Linde 1982), which is now largely accepted as part of the standard cosmological model. At the same period, the existence of an invisible form of matter, called the dark matter, postulated in the 20-30's (see e.g. Zwicky 1933), reached a quasi consensus and the current Cold Dark Matter scenario was accepted (see Einasto 2011, for an historical review). In the late 90's, analyses of galaxy clusters led to growing evidence for a low matter density Universe (see e.g. Bahcall and Fan 1998). Around the same time, two teams that used supernovae as *standard candles* measured that the expansion of space was accelerating with high confidence (Riess et al. 1998; Perlmutter et al. 1999). This was followed by the measurement of the first acoustic peak in the CMB power spectrum, which showed that the Universe was nearly flat (De Bernardis et al. 2000; Lange et al. 2001), and an accurate estimation of the Hubble constant (Freedman et al. 2001). These studies set the bricks for the ΛCDM model, our current cosmological concordance model. A few years latter, the first results from the observations of the CMB by the Wilkinson Microwave Anisotropy Probe (WMAP) satellite confirmed the model and refined its parameters (Spergel et al. 2003). In the last decade, many experiments going from CMB observations to surveys of the more local Universe, allowed us to enter the era of precision cosmology, reaching percent error measurements on the parameters describing our model.

The progresses achieved in the understanding of our Universe were made possible by the advances of telescopes and the development of detectors and computers technology. The creation of X-ray and radio telescopes, in the second part of the XIX$^{\text{th}}$ century, led to the advent of the "multi-wavelength astronomy", particularly fruitful for galaxy clusters studies. More recently, the detections of the first gravitational wave (Abbott et al. 2017) and the first extragalactic neutrino (The IceCube collaboration et al. 2018) that were later associated to electromagnetic signal, marked the beginning of the promising "multi-messenger astronomy" era.

1.1.2 Theoretical framework

In the following we introduce the main theoretical concepts and equations that are necessary to describe the dynamics and the geometry of the Universe. This is done within the framework of general relativity. More details can be found in e.g. Weinberg (1972) and Hogg (1999).

[1] Originally, the term nebula was designating diffuse astronomical object, including galaxies beyond the Milky Way.

[2] See Way (2013) for an historical review and a discussion about the Hubble legacy.

1.1.2.1 Dynamics of the Universe

In a Universe following the cosmological principal, i.e. that is homogeneous and isotropic, which is a very good approximation on large scales (as we will see in the following sections), an exact solution of the equations of general relativity is given by the *Friedmann equations* (Friedmann 1922, 1924). They describe the dynamics of the Universe, parametrised by the scale factor $a(t)$, and are given by[3]:

$$\left(\frac{\dot{a}}{a}\right)^2 = H^2(a) = \frac{8\pi G}{3}\rho - \frac{k}{a^2} + \frac{\Lambda}{3} \tag{1.1}$$

and

$$\frac{\ddot{a}}{a} = -\frac{4\pi G}{3}(\rho + 3P) + \frac{\Lambda}{3}. \tag{1.2}$$

The scale factor provides the evolution of the expansion of space, H is the Hubble parameter, G is the gravitation constant, k is the space curvature, ρ and P are the sum of all contributions to the energy density and pressure in the Universe, respectively, and Λ is the cosmological constant. The cosmological constant was introduced, and then discarded, by Einstein, but was found latter to be necessary to account for the accelerated expansion of the Universe at late time ($\ddot{a} > 0$). Note that alternatively, one could postulate the existence of a component with negative pressure, called the dark energy. The current value of the Hubble parameter, H_0, is called the Hubble constant, and is often express, in an adimensional form, as $h = H_0/100$ km s^{-1} Mpc^{-1}. The space curvature can be either $k = -1, 0$ or $+1$, depending if the Universe is open, flat, or closed.

The total energy density of the Universe can be written as:

$$\rho_{\rm tot} = \rho_{\rm r} + \rho_{\rm m} + \rho_\Lambda, \tag{1.3}$$

where $\rho_{\rm r}$, $\rho_{\rm m}$, and $\rho_\Lambda \equiv \frac{\Lambda}{8\pi G}$ are the contributions from ultra-relativistic particles (radiation), non-relativistic matter, and the cosmological constant (or dark energy), respectively. The term describing the matter can be itself decomposed between the baryonic ("normal") component and the dark matter component as $\rho_{\rm m} = \rho_{\rm b} + \rho_{\rm c}$. Each component can be parametrised by an equation of state of the form:

$$P_i = w_i \times \rho_i, \tag{1.4}$$

where i stands for the different components. For the radiation $w_r = 1/3$, for the matter $w_m = 0$ (no pressure, either for the baryonic or the dark matter) and for the cosmological constant, $w_\Lambda = -1$. In the case of dark energy, deviations from $w_{\rm DE} = -1$ are possible in the limit $w_{\rm DE} < -1/3$. In the following we will adopt this notation either for dark energy or for a cosmological constant.

Equations 1.1 and 1.2 can be combined to give:

$$\dot{\rho} = -3H(\rho + P), \tag{1.5}$$

so that if $w = P/\rho$ is constant through times, we can solve Equation 1.5, for each component, with:

$$\dot{\rho_i} = \rho_{i,0} \times \left(\frac{a}{a_0}\right)^{-3(1+w_i)}. \tag{1.6}$$

By setting the normalised density Ω_i such that:

$$\Omega_i = \rho_i/\rho_{\rm crit}, \tag{1.7}$$

[3] In the following we adopted the unit system in which the speed of light is set to $c \equiv 1$. We note $\dot{x}$ for the time derivative of x and use the indices x_0 to refer to the value of x at the present time.

with $\rho_{\rm crit} = \frac{3H^2}{8\pi G}$ the critical density, i.e., the density that the Universe would have if it was flat ($k = 0$), we can rewrite Equation 1.1 as:

$$\left(\frac{\dot{a}}{a}\right)^2 = H(a)^2 = H_0^2 \times \left[\Omega_{r,0}\left(\frac{a}{a_0}\right)^{-4} + \Omega_{m,0}\left(\frac{a}{a_0}\right)^{-3} + \Omega_{k,0}\left(\frac{a}{a_0}\right)^{-2} + \Omega_{\Lambda,0}\left(\frac{a}{a_0}\right)^{-3(1+w_{\rm DE})}\right] \tag{1.8}$$

where $\Omega_{k,0} = -\frac{k}{a_0^2 H_0^2}$ gives a measure of the space curvature at the present time and $\Omega_{\Lambda,0}$ is equivalent to $\frac{\Lambda}{3H_0}$ for $w_{\rm DE} = -1$ and can be generalised to non-constant $w_{\rm DE}$. This equation describes the evolution of the content of the Universe.

1.1.2.2 Measurement of cosmological distances

In cosmology, the definition of distances is essential to connect models to observations and they will be used along this thesis. Lets first introduce the notion of *redshift* z, which quantifies the change in the wavelength of the light emitted by an object and seen by an observer, resulting from its radial motion or gravitational effects:

$$1 + z = \frac{\lambda_{\rm obs}}{\lambda_{\rm emit}} \tag{1.9}$$

with $\lambda_{\rm obs}$ and $\lambda_{\rm emit}$ the observed and emitted wavelengths, respectively. In this definition, the redshift contribution related to the radial motion arises from the sum of the peculiar velocity of an object and its cosmological recession velocity (contribution called the *cosmological redshift*, $z_{\rm cosmo}$). If the peculiar velocity and the gravitational redshift can be neglected, which is a very good approximation beyond the local Universe, it follows:

$$1 + z \approx 1 + z_{\rm cosmo} = \frac{a_0}{a}. \tag{1.10}$$

Under this hypothesis we can rewrite Equation 1.8 as:

$$H(z)^2 = H_0^2 E(z)^2 \tag{1.11}$$

with:

$$E(z) = \sqrt{\Omega_{r,0}\,(1+z)^4 + \Omega_{m,0}\,(1+z)^3 + \Omega_{k,0}\,(1+z)^2 + \Omega_{\Lambda,0}\,(1+z)^{3(1+w)}}. \tag{1.12}$$

We can now define:

– the *comoving distance* D_c, which is a measure of the line-of-sight distance that is invariant to the Universe dynamics:

$$D_{\rm C} = \int_0^z \frac{dz'}{H(z')} = \frac{1}{H_0}\int_0^z \frac{dz'}{E(z')}; \tag{1.13}$$

– the *transverse comoving distance* D_M, which is a measure of the comoving distances between two events at same redshift z, separated by an angle $\delta\theta$ on the sky:

$$D_{\rm M} = \delta\theta \times \begin{cases} \frac{1}{H_0}\frac{1}{\sqrt{\Omega_k}}\sinh\left[\sqrt{\Omega_k}\,D_{\rm C}\,H_0\right] & \text{for } \Omega_k > 0 \\ D_{\rm C} & \text{for } \Omega_k = 0 \\ \frac{1}{H_0}\frac{1}{\sqrt{|\Omega_k|}}\sin\left[\sqrt{|\Omega_k|}\,D_{\rm C}\,H_0\right] & \text{for } \Omega_k < 0 \end{cases} \tag{1.14}$$

– the *proper distance* $d(t)$, which is a measure of line-of-sight distance that changes with time because of the Universe expansion (or contraction):

$$d(t) = aD_c. \tag{1.15}$$

Similarly, we can define the *transverse proper distance* as $d_M(t) = aD_M$. For a gravitationally bound object, d_M gives a measure of the physical size;

– the *angular diameter distance* $D_{\rm A}$, which gives the ratio between the physical size and the observed angular size of an object:

$$D_{\rm A} = \frac{D_{\rm M}}{1+z} \tag{1.16}$$

– the *luminosity distance* $D_{\rm L}$, which is related to the intrinsic bolometric luminosity L of an object and its bolometric flux ϕ as $D_{\rm L} \equiv \sqrt{\frac{L}{4\pi\phi}}$, and is given by:

$$D_{\rm L} = (1+z)\, D_{\rm M} = (1+z)^2\, D_{\rm A} \tag{1.17}$$

The association of Equations 1.16 and 1.17 shows that the bolometric observed surface brightness $S_{\rm bol,\ obs}$ of an object is related to its intrinsic bolometric surface brightness $S_{\rm bol,\ intr}$ by :

$$S_{\rm bol,\ obs} = \left(\frac{D_{\rm A}}{D_{\rm L}}\right)^2 S_{\rm bol,\ intr} = \frac{S_{\rm bol,\ intr}}{(1+z)^4} \tag{1.18}$$

– the *comoving volume element* $dV_{\rm C}$, which is associated to the comoving volume $V_{\rm C}$. Expressed in solid angle $d\Omega$ and redshift interval dz it is given by:

$$dV_{\rm C} = \frac{(1+z)^2\, D_{\rm A}^2}{H_0\, E(z)}\, d\Omega\, dz = \frac{D_{\rm M}^2}{H(z)}\, d\Omega\, dz. \tag{1.19}$$

1.1.3 The main cosmological probes

Constraining cosmological models requires observations that are sensitive to the parameters that describe them, and that can be used to constrain their values (they are therefore called *cosmological probes*). These probes are based on observations at different redshifts and thus, provide cosmological tests at various epochs of the history of the Universe, from the primordial era to the current time. Combining different probes is a powerful way to disentangle degeneracies on parameters and to compare the systematics, which affect each of them differently. In the following we give a non exhaustive overview of the main observational cosmological probes to date. More details can be found in e.g. Weinberg et al. (2013).

The cosmic microwave background (CMB) The CMB is a fossil radiation that emanates from the early Universe plasma, when protons and electrons combined and photons were able to stream freely, leading to the last scattering surface. This process occurred at $z \sim 1100$, when the plasma was at a temperature of ~ 3000 K. The CMB has a nearly perfect blackbody spectrum, which corresponds, today, after redshift evolution, to a temperature $T_{CMB,0} = 2.7255 \pm 0.0006$ K (Fixsen 2009). Note that later, in the more recent Universe, the intergalactic gas get reionised due to the energy released by the formation of the first stars, and the CMB photons are affected by scattering once more, leaving an imprint in the CMB fluctuations. The CMB is close to be homogeneous, but presents small anisotropies in temperature and polarisation, which carry information about the matter distribution in the early Universe. The power spectra of these anisotropies can be used to constrain cosmological parameters (see Planck Collaboration et al. 2018a, for a review of the latest measurements).

Supernovae (SNe) SNe are bright transient events arising from the last evolutionary stages of a certain type of stars. In particular, SNe of type Ia are created by the explosion of white dwarfs in binary systems and have a characteristic light curve, from which their intrinsic luminosity can be inferred. They can thus be used as *standard candles*: by comparing observed and intrinsic luminosities, one can derive their luminosity distance (see Equation 1.17). By combining it to their redshift, one can then infer cosmological parameters. This method allowed for the

discovery of the cosmic accelerated expansion (see Section 1.1.1). SNe Ia are sensitive to $D_{\rm L}$ (see Equation 1.17) and are particularly constraining at high redshift. The relation between their light curve and total luminosity is usually calibrated at low redshift using *cepheids*, a certain type of stars that can also be used as standard candle (Leavitt and Pickering 1912). Local calibrators also allows to directly measure H_0, as $E(z) \sim 1$ in Equation 1.13 (see e.g. Riess et al. 2018, for recent measurements).

Gravitational waves (GW) Provided that the redshift of their host galaxies can be measured, the recently discovered GW caused by merging black holes can be used as *standard sirens*. This constitutes a direct and independent way to measure H_0 (Abbott et al. 2017). Moreover, GW are also useful to test general relativity (see Abbott et al. 2016, and e.g. Yunes and Siemens 2013 for a review).

Baryon acoustic oscillations (BAO) Counteracting forces of gravity and pressure created by the small overdensities in the early Universe plasma led to acoustic oscillations. After the decoupling of photons that resulted in the CMB radiation, the oscillations froze and left an imprint in the baryon density field around overdensity regions, with a characteristic radius corresponding to the sound horizon at this time. When the large scale structures formed under the action of gravity, they organised preferentially on the sound horizon scale. The BAO are thus detectable in the CMB power spectrum (see De Bernardis et al. 2000, for their first detection), but also in the galaxy distribution, via the measurement of the two point correlation function (see Eisenstein et al. 2005, for their first detection). As the BAO comoving scale r_s does not change with time, it can be seen as a *standard ruler* and can be used to infer cosmological parameters. Indeed, the radial scale of the BAO is related to $H(z)$ and r_s, while the angular scale is related to $D_{\rm A}$ and r_s (see e.g. Sánchez et al. 2013).

Weak lensing (WL) The distortion of the shapes of distant galaxies, induced by the gravitational lensing of foreground structures, allows us to probe the total matter distribution and geometry of the Universe (see e.g. Kilbinger 2015; Bartelmann and Maturi 2017, for reviews). As this cosmic shear signal is usually weak, it is assessed statistically, through the analysis of the correlation of the shapes of galaxies (see e.g. Bacon et al. 2000; Kaiser et al. 2000; Van Waerbeke et al. 2000; Wittman et al. 2000, for the first detections). The dependence of WL statistics on cosmological parameters is non trivial, but WL is mainly sensitive to a combination of matter density and amplitude of the matter fluctuations (Ω_m and σ_8, see Section 1.2). The gravitational distortions do not affect only the shapes of distant galaxies. They can be studied at higher redshifts using, for instance, the CMB as the light source (see e.g. Lewis and Challinor 2006).

Galaxy clusters Clusters are important probes for cosmology. As for WL, they are sensitive to both the geometry of the Universe and the growth rate of structures. Their utilisation will be detailed in Section 1.3.

1.1.4 The current cosmological paradigm

Over the last decades, the use of the cosmological probes discussed in Section 1.1.3 allowed us to converge to the current cosmological paradigm. This cosmological concordance model is based on the Big-Bang theory, according to which the Universe is expanding, and was much hotter and denser in the past than it is today. It supposes, in agreement with observations, that the Universe is homogeneous and isotropic on large scales and that general relativity holds true (thus the equations derived in Section 1.1.2 apply). More generally, it assumes that the laws of physics are the same at every points in the Universe. The model accounts for the

acceleration of the expansion of the Universe, assuming that it is caused by a property of space, and that it can be described by a cosmological constant Λ in Equations 1.1 and 1.2. In the cosmological concordance model, the matter is dominated by a form of cold (non relativistic) dark matter, which is non-baryonic, pressureless ($w_m = 0$ in Equation 1.4), dissipationless and collisionless. Moreover, as shown by observations, the spacial curvature is very small ($\Omega_k \sim 0$) and the Universe is generally assumed to be flat. The concordance model parametrisation is called the ΛCDM model (for Λ dominated Cold Dark Matter). The assumptions on which it is based derive either from observational evidence or from postulates that are comforted by several probes (see e.g. Planck Collaboration et al. 2018b, for a review).

The ΛCDM model is relatively simple as it is based on 6 independent parameters only, but explains many observables at different scales and cosmic times. The base parameters are related to the matter content of the Universe via the normalised baryon and cold dark matter energy density parameters, $\Omega_b h^2$ and $\Omega_c h^2$ and the late time ionisation state of the Universe through the value of the optical depth to reionisation, parametrised by τ. Additionally, the model depends on the amplitude and the tilt of the primordial scalar fluctuations power spectrum (see equation 1.20), A_s and n_s, and the angular scale of sound horizon at recombination, encoded in the parameter $\theta_{\rm MC}$. The list of the main cosmological parameters, estimated from CMB and BAO measurements, is presented in Table 1.1. While only 6 parameters are independent, several other parameters are part of the base ΛCDM model (see Tabel 1.1).

In addition to the base model, the inflation paradigm, which presumes a phase of exponential expansion of space right after the Big Bang, is often accepted as an extension of ΛCDM to explain the origin of the fluctuations and the large scale homogeneity of the Universe. If it happened, the inflation is expected to produce tensor perturbations that would be detectable in the CMB polarisation, in addition to the scalar perturbations, and which are encoded in the tensor-to-scalar ratio parameter, r. Several other parameters can also be released to extend the ΛCDM model, such as the spatial curvature Ω_k, the sum of the mass of the neutrinos Σm_ν (which affects the formation of structures), the number of extra relativistic degrees of freedom $N_{\rm eff}$, and the dark energy equation of state parameter $w_{\rm DE}$.

According to the values of the parameters given in Table 1.1, baryons account for only a small fraction of the matter content of the Universe while dark matter is preponderant. We live in a Universe dominated by a form of dark energy (which could be the manifestation of the cosmological constant) responsible for its accelerated expansion. This has not always been the case, and we can derive from Equation 1.11 that radiation was dominating the energy density of the Universe before $z \sim 3600$, and matter dominated afterwards, until $z \sim 0.4$. So far, no clear departure from the ΛCDM model have been observed.

1.1.5 Fundamental unanswered questions in modern cosmology

Although the concordance model accounts for many independent observations, it raises fundamental questions. The first one is the physical origin of the accelerated expansion of the Universe: does it come from an intrinsic property of space, is it related to the presence of a dark energy, or is it a manifestation of the breakdown of general relativity on cosmic scales (see e.g. Weinberg et al. 2013)? This issue has profound implications for fundamental physics as it is connected to the nature of the vacuum, and thus related to the quantum description of the standard model of particle physics. The second main question regards the nature of dark matter, which has important consequences for our understanding of particles physics. Again, it could also be a sign that our theory of gravitation is incomplete. Finally, while the concordance model predicts well the statistical properties of the matter in the Universe, it is insufficient to fully explain the evolution of the structures and reproduce all the observations. In particular, at galaxy scale, several observations seem to challenge the predictions from the ΛCDM model (see e.g. Bullock and Boylan-Kolchin 2017, for a review). It is till unclear if this is related to an incorrect modelling of baryon or dark matter physics.

Table 1.1: Main cosmological parameters constrained from CMB and BAO measurements (Planck Collaboration et al. 2018a). The first block gives 6 independent parameters from the ΛCDM model, the second block gives the main additional ΛCDM parameters and the third block gives the main parameters from the extended ΛCDM model. The density parameters are evaluated at $z = 0$.

$\Omega_{\rm b}h^2$	0.02242 ± 0.00014	Normalised baryon density
$\Omega_{\rm c}h^2$	0.11933 ± 0.00091	Normalised dark matter density
$100\theta_{\rm MC}$	1.04101 ± 0.00029	$100 \times r_*/D_A$, with D_A the angular diameter distance at z_*
$\ln(10^{10}A_{\rm s})$	3.047 ± 0.014	Primordial power spectrum at $k_0 = 0.05$ Mpc^{-1}
$n_{\rm s}$	0.9665 ± 0.0038	Spectral index of the primordial power spectrum
τ	0.0561 ± 0.0071	Thomson interaction optical depth due to reionisation
$\Omega_{\rm m}$	0.3111 ± 0.0056	Normalised matter density
$\Omega_{\rm r}$	$< 10^{-4}$	Normalised radiation density
Ω_Λ	0.6889 ± 0.0056	Normalised dark energy density
H_0	67.66 ± 0.42	Hubble constant (km s^{-1} Mpc^{-1})
Age	13.787 ± 0.020	Age of the Universe (Gyr)
z_*	1089.80 ± 0.21	Redshift for which the optical depth is 1
r_*	144.57 ± 0.22	Comoving length of sound horizon at z_* (Mpc)
$z_{\rm re}$	7.82 ± 0.71	Redshift at which half of the Universe is reionise
σ_8	0.8102 ± 0.0060	Standard deviation of the matter distribution at 8 Mpc/h
Ω_k	0.0007 ± 0.0019	Spatial curvature density
Σm_ν	< 0.120 (95% C.L.)	Sum of the neutrino mass (eV)
$N_{\rm eff}$	$2.99^{+0.34}_{-0.33}$	Number of effective extra relativistic degrees of freedom
$w_{\rm DE}$ $^{(\dagger)}$	-1.028 ± 0.032	Dark energy equation of state parameter
r	< 0.106 (95% C.L.)	Tensor-to-scalar ratio

Note: $^{(\dagger)}$ Measured in combinaison with type Ia supernovae.

1.2 The distribution of matter in the Universe

In Section 1.1.2, we presented the equations governing the dynamics of the Universe under the hypotheses of homogeneity and isotropy. This is true on large scales, as can be seen for instance in the CMB temperature map (overall homogeneous with tiny fluctuations). However this approach is not sufficient to account for the cosmic structures, and, in fact, does not hold on small scales. In this section we introduce the theory of structure formation, and present how initial quantum fluctuations led to the galaxies and clusters of galaxies that we see today (more detailed information can be found in e.g. Bernardeau et al. 2002, and the following lecture notes[4] [5] [6]).

1.2.1 The growth of structures

According to the inflation paradigm, cosmic structures formed from quantum fluctuations that expand during the inflationary phase, leading to small inhomogeneities in the density field. The power spectrum of these primordial scalar fluctuations can be expressed as:

$$P_{\rm prim}(k) = A_s k^{n_{\rm s}-1}, \tag{1.20}$$

[4] http://www.damtp.cam.ac.uk/user/db275/Cosmology/Lectures.pdf,
[5] https://www.astro.rug.nl/~weygaert/tim1publication/lss2009/lss2009.linperturb.pdf,
[6] https://cosmologist.info/teaching/EU/ADC_Structure_formation2.pdf

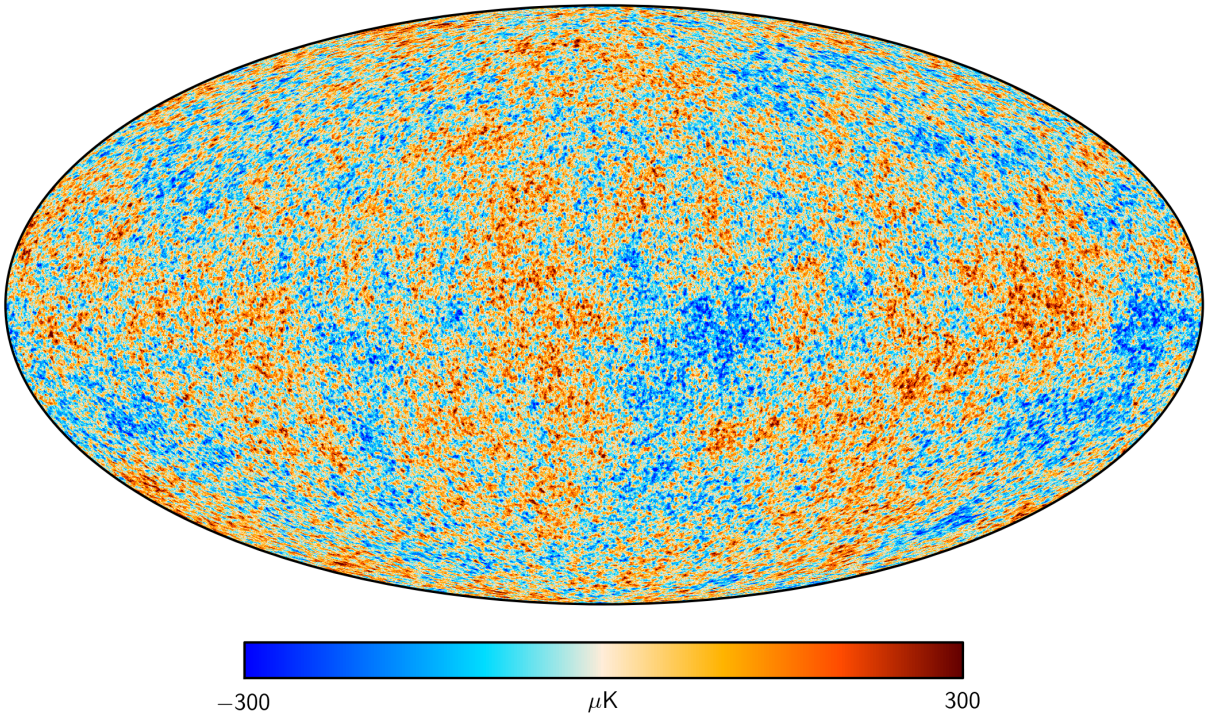

Figure 1.1: CMB temperature map as observed by the Planck satellite (Planck Collaboration et al. 2016a).

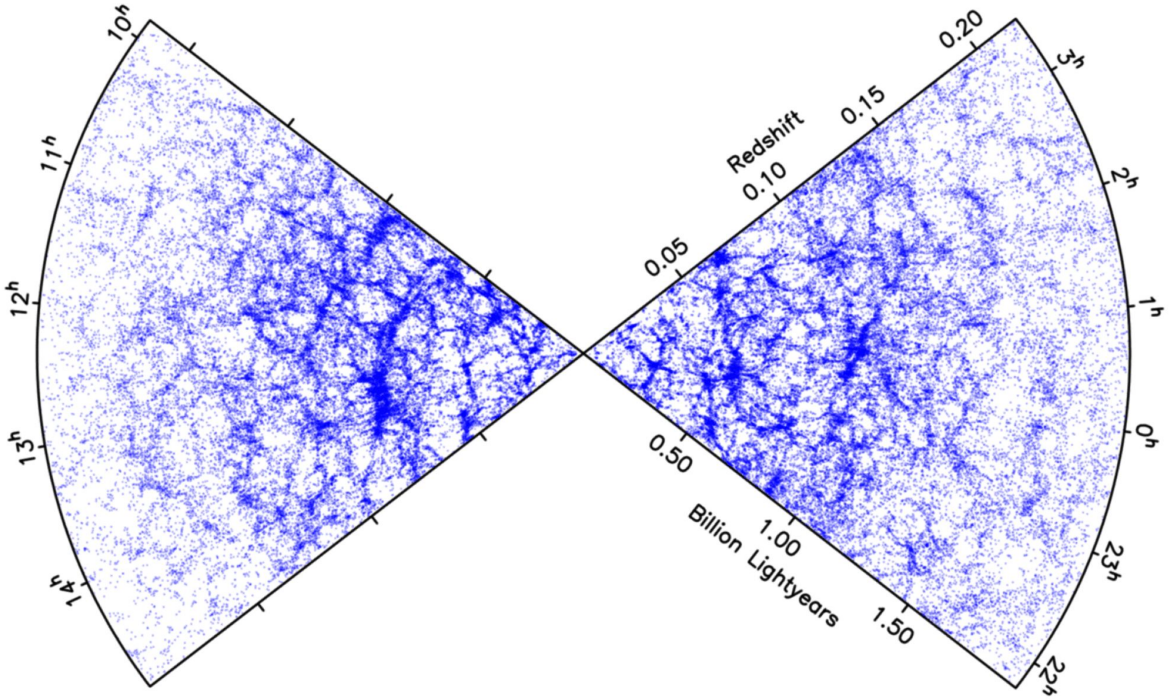

Figure 1.2: Positions of the galaxies observed by the 2dF Galaxy Redshift Survey. Credits: http://magnum.anu.edu.au/~TDFgg/.

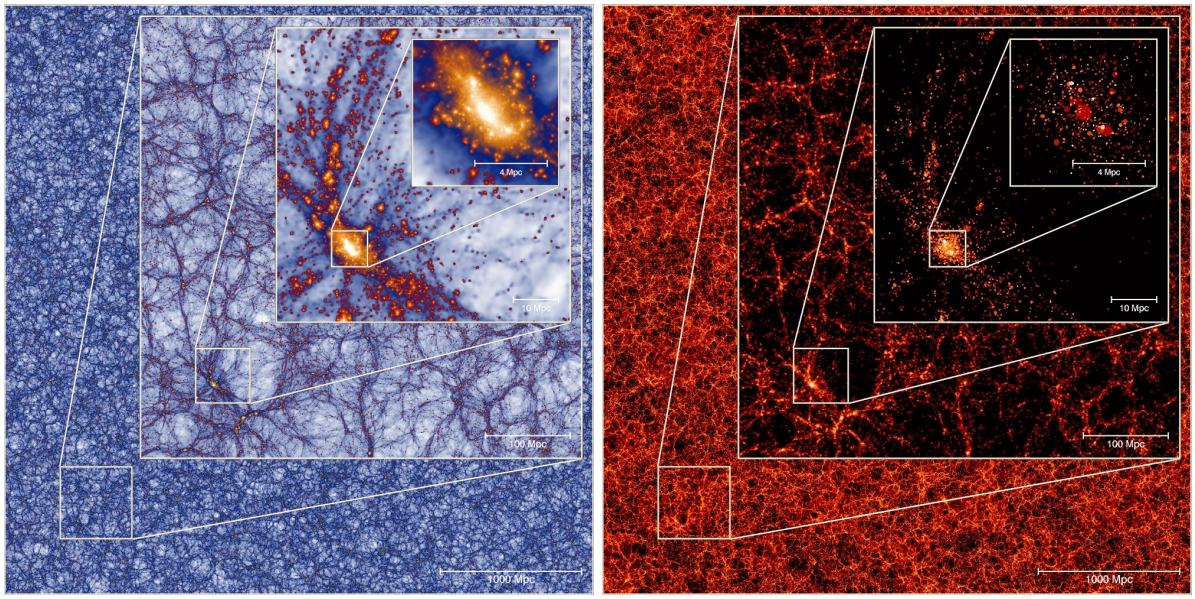

Figure 1.3: Dark matter (*left panel*) and galaxy (*right panel*) distributions in a $z = 0$ slice of the XXL-Millenium simulation. The images show the cosmic web and a zoom towards a galaxy cluster. Credits: https://wwwmpa.mpa-garching.mpg.de/mpa/research/current_research/hl2011-9/hl2011-9-en.html.

A_s and n_s being ΛCDM parameters (see Table 1.1). As $n_s \sim 1$, the primordial power spectrum (Equation 1.20) is nearly scale invariant. The density fluctuations, which follow a quasi Gaussian distribution, can be expressed by their density contrast $\delta(x)$ as:

$$\delta(x) = \frac{\rho(x) - \bar{\rho}}{\bar{\rho}}, \tag{1.21}$$

with x a comoving location and $\bar{\rho}$ the mean density of the Universe.

As can be seen in Figure 1.1, the primordial fluctuations left their imprint in the CMB as temperature anisotropies, the coldest spots tracing the densest regions. After the decoupling of photons, baryons follow the gravitational potential of the dark matter that is already structured and the initial fluctuations grow via the action of gravitation. Voids get emptier and overdensities get denser, and the distribution of matter becomes log-normal. Voids, walls, filament and clusters start to emerge, creating the *cosmic web*. As shown in Figure 1.2, this foam-like structure can be observed in the distribution of galaxies, and is also evident in cosmological simulations (see Figure 1.3).

In the linear regime, the matter density power spectrum evolves with redshift as:

$$P_{\mathrm{m}}(k, z) = D^2(z)T^2(k)P_{\mathrm{prim}}(k). \tag{1.22}$$

with $T(k)$ the transfer function of the perturbations up to $z \sim 1000$, and $D(z)$ the linear growth factor, controlling the development of structures. Both quantities depends on cosmological parameters. The variance of the amplitude of density fluctuations at a characteristic mass scale M can be calculated as:

$$\sigma(M, a)^2 = \int \frac{d^3k}{(2\pi)^3} W(kR) P_{\mathrm{m}}(k, a), \tag{1.23}$$

with $W(kR) = 3\left(\frac{\sin(kR)}{(kR)^3} - \frac{\cos(kR)}{(kR)^2}\right)$ the 3D window function associated to a sphere or radius R. For historical reasons, $\sigma(M, a)$ is often evaluated at a scale of 8 Mpc h^{-1} for $a = 1$ ($z = 0$). In this form, the parameter is written σ_8 (see Table 1.1).

Following the Press and Schechter formalism (Press and Schechter 1974), we can derive that a sphere of matter will collapse under its own gravity, thus decoupling from expansion, when it reaches a density contrast $\delta(c) \sim 1.686$. The collapse is stabilised when an equilibrium is reached, and the structure becomes *virialised*[7]. It can be shown that the characteristic time required for an object to collapse is an increasing function of its mass (see e.g. Mo et al. 2010). Therefore, low mass structures, as dwarfs galaxies, formed before massive objects like galaxy clusters.

1.2.2 The formation of galaxies

After a structure collapsed, the gas that it contains may be dense enough for initiating radiative cooling. If this process is short and effective, the gas does not reach hydrostatic equilibrium, but accretes in the centre, forming a proto-galaxy. This results in a clear segregation between the dark and the baryonic matter, the latter residing at the centre of the dark matter diffuse halo. Eventually, the gas collapses under its own gravity, making the cooling even more effective and triggering a runaway collapse process. Finally, the gas cloud fragments into high density proto-stellar regions and the galaxy eventually light up and build its stellar mass (see e.g Mo et al. 2010; Benson 2010, for reviews on galaxy formation).

The fraction of stellar mass is not constant in every galaxy, but depends on the halo mass (see e.g. Behroozi et al. 2013a; Kravtsov et al. 2018). The most efficient galaxies to form stars have halo masses of the order of $\sim 10^{12}$ $M_\odot$, limit that barely changes with redshift. This behaviour is associated to baryonic feedback processes at play in low and high mass haloes. Those effects may forbid or cease the star formation activity by, either removing their gas supply, or heating it and preventing it to condensate. Effects from stellar photo-ionisation and supernovae are at play in low mass galaxies, while at the group and cluster scales, feedback from active galactic nuclei (AGN) and starburst events are suspected to affect the star formation of the central galaxies (see e.g. Dekel and Birnboim 2006; Erb 2015).

1.2.3 The formation of galaxy clusters

As discussed in Section 1.2.1, galaxy clusters are the last, and the most massive, structures to collapse. Their number as a function of mass and redshift can be assessed through the halo mass function (HMF). An approximation of the HMF can be derived analytically, (see Press and Schechter 1974, for the formalism), but more precise estimations require to use cosmological simulations. The form of the HMF is usually given by:

$$\frac{dN}{d\ln M}(M,z) = f(\sigma)\frac{\rho_{c,0}}{M}\frac{d\ln\sigma}{d\ln M}, \tag{1.24}$$

with σ computed from Equation 1.23, $\rho_{c,0}$ the current value of the critical density, M the mass defined as $M = \frac{4\pi}{3}\rho_{c,0}R^3$, and $f(\sigma)$ the fitting function that depends on the analyses (see Murray et al. 2013, for a review). As shown in Figure 1.4, the number of haloes decreases with increasing mass, following a power law and an exponential cut-off at high mass. The distinction between cosmological parameters is clearer at high mass and at higher redshift. This is why massive galaxy clusters at high redshift are the most constraining for cosmology, besides their rarity.

As we will see in Chapter 2, the gas in galaxy clusters is heated to temperatures of $\sim 10^{7-8}$ K, and thus inefficient to form stars (see e.g. Voit 2005). Therefore, as we will see in Chapter 2, the stellar content of clusters is sub-dominant. As shown in Figure 1.3, clusters are embedded in the cosmic web and grow by accretion of matter, either continuously from the filaments or through mergers with other massive haloes.

[7]Meaning that the virial theorem, linking the potential (E_p) and kinetic (E_k) energy, as $2E_k = -E_p$, applies.

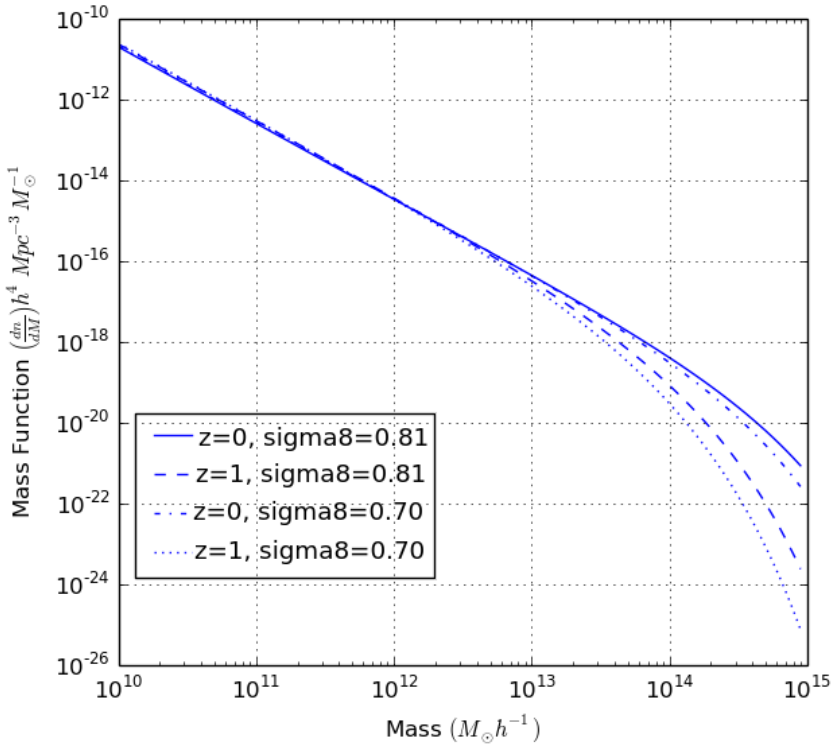

Figure 1.4: Example of halo mass functions for different redshifts and values of the σ_8 parameter, evaluated for $M \equiv M_{500}$. The cosmological parameters used to compute it are the one obtained in Planck Collaboration et al. (2014a), except for σ_8, as indicated in the legend. The fitting function, $f(\sigma)$, is taken from Angulo et al. (2012). This figure was created using the `HMFcalc` calculator: `http://hmf.icrar.org/`, (Murray et al. 2013).

The edges of clusters are not well defined and we usually use overdensity contrasts $\Delta = \bar{\rho_R}/\rho_c(z)$, as a limit. The radius within which the cluster is virialised corresponds to $\Delta \sim 180$, and R_{500} or R_{200} are the scale radii that are the most commonly used.

1.3 Galaxy clusters as cosmological probes

Being the most massive collapsed structures in the Universe, galaxy clusters trace the highest peaks of the cosmological density field. Their evolution is thus closely connected to that of the Universe as a whole. Moreover, they are key laboratories to understand the co-evolution of baryonic and dark matter.

Galaxy clusters are a historical cosmological probe (see e.g. Allen et al. 2011). Notably, they provided one of the first evidence for the presence of a dark form of matter (Zwicky 1933; Smith 1936), for a sub-critical value of the matter density in the Universe (Gott et al. 1974), and one of the first observational hint for the accelerated expansion of the Universe (Hoessel et al. 1980). Nowadays, they constitute promising tools to constrain the origin of the cosmic accelerated expansion (see e.g. Albrecht et al. 2006; Weinberg et al. 2013; Huterer et al. 2015).

1.3.1 Galaxy cluster counts

One of the most powerful way of using clusters as cosmological probes is to measure their abundance as a function of redshift and mass (see, for example, Allen et al. 2011, for a review).

Comparing observations to theoretical models Given a set of cosmological parameters, the expected observed number of clusters N per unit of redshift z and solid angle Ω can be written as:

$$\frac{dN}{dzd\Omega} = \frac{dV_{\rm C}}{dzd\Omega}(z) \int \hat{\chi}(\mathcal{O}, z, \vec{u}) d\mathcal{O} \int P(\mathcal{O}|M, z) \frac{dn(M, z)}{dM} dM. \tag{1.25}$$

In this expression, $\frac{dV_{\rm C}}{dzd\Omega}(z)$ is the comoving volume element at redshift z, as defined in equation 1.19. The cluster sample selection function is given by $\hat{\chi}(\mathcal{O}, z, \vec{n})$, which depends on an observable $\mathcal{O}$, the redshift, and possibly the position on the sky $\vec{u}$. The quantity $P(\mathcal{O}|M, z)$ describes the mass observable-relation, i.e. the probability that a halo of mass M at redshift z is observed as a cluster with observable property $\mathcal{O}$ (see Section 2.3 for more details). Finally, $\frac{dn(M,z)}{dM}$ is the halo mass function as given by equation 1.24.

The sensitivity on cosmological parameters arises from the comoving volume element (see equation 1.19) and the mass function (see equation 1.24). Thereby, clusters probe both the background geometry of the Universe and the growth rate of cosmic structures. Cluster counts are thus especially powerful to constrain σ_8 and Ω_m, but also $w_{\rm DE}$ and $D(z)$. We note that the detection of only one extreme cluster can challenge a given cosmological model. However, large homogeneous samples detected from surveys are usually used. On the observational side, obtaining precise cosmological constraints from cluster counts requires to detect large number of clusters in order to increase the statistical power, to construct a well defined selection function, to avoid any selection bias, and to accurately measure masses and redshifts (as discussed further in Section 2.3). On the modeling side, cluster counts require to compare observations to a well calibrated halo mass function. To date, the main uncertainties arise from the mass and selection function estimations (see Section 1.3.3).

Mass-observable relation and selection function The detection of galaxy clusters can be performed at various wavelengths (see Section 2.3). In all cases, a primary observable is related to the mass of the cluster via mass – observable scaling relations, $P(\mathcal{O}|M, z)$, that need to be calibrated. Since the mass obtained from the scaling relation will be compared to that of the HMF, cluster counts require that the detected clusters are representative of the true underlying cluster population. This is non-trivial as the detection of clusters may depend on their physical properties (in addition to their masses and redshift), with different dependences at different wavelengths. Intuitively, one can see from equation 1.25 that a lower scatter in the scaling relation will lead to lower uncertainties in the derived cosmological constraints, and thus, not all mass proxies are equivalent (see also Section 2.3 for further discussions). The survey selection function $\hat{\chi}(\mathcal{O}, z, \vec{u})$, determines the fraction of detected clusters as a function of the observable, redshift and possibly position on the sky, and is thus crucial to connect observations to theoretical models. As can be seen in equation 1.25, improvements in the cosmological power of a survey can be reached, via improvements in the selection function, by increasing the completeness and the purity as much as possible, i.e., maximising the number of detected clusters while minimising the number of false positive. The measurement of the purity and the completeness can be achieved either by comparing cluster catalogues obtained from different observations (e.g. calibration of the selection function of a wide, but shallow survey, with observations from a small, but deep survey, possibly at different wavelength), or by using numerical simulations.

1.3.2 Other ways of using clusters

Besides their number counts, several other properties of galaxy clusters can be used to constrain cosmological models and test fundamental physics. In the following we review the most used or most promising alternative ways of using clusters.

1.3.2.1 Cluster clustering

Dark matter haloes are biased tracers of the underlying matter density distribution (Kaiser 1987). In particular, galaxy clusters are more clustered than galaxies (see e.g. Veropalumbo et al. 2014; Marulli et al. 2018). The halo power spectrum at a given mass M, P_{hh}, can be related to the matter power spectrum, $P(k, z)$, through:

$$P_{hh} = b(M, z)^2 \times P(k, z), \tag{1.26}$$

with $b(M, z)$ the bias factor, that depends on the cluster masses and redshifts. The halo power spectrum, or, similarly, its associated correlation function can thus be used to constraints cosmological parameters (see e.g. Moscardini et al. 2001; Veropalumbo et al. 2016). While currently cluster clustering alone is not competitive with respect to other probes, it can be combined to cluster number counts, in a self-calibration manner, to break degeneracies and obtain tighter constraints on cosmology (see e.g. Majumdar and Mohr 2004; Mana et al. 2013; Sartoris et al. 2016).

1.3.2.2 Baryon fraction

The ratio of the gas mass to the total mass in clusters (the $f_{\rm gas}$ parameter), as can be inferred from X-ray observations, is sensitive to the baryon fraction. By assuming that galaxy clusters are representative of the cosmic baryon budget, these measurement can be used to constrain the cosmological parameters (see, e.g., for the method and results, Ettori et al. 2009). This probe has been used historically to measure Ω_m (White et al. 1993), and more recently to constrain the dark energy equation of state (Allen et al. 2008; Mantz et al. 2014). While this method provides a complementary and independent constraint on dark energy, astrophysical systematic effects are limiting the measurement (see Ettori et al. 2009, for further discussions).

1.3.2.3 Testing the nature of dark matter

As they result from strong concentration of matter, galaxy clusters can serve as fundamental physics laboratories. In particular, the properties of dark matter have strong effects on the formation of clusters and their internal structures, so that clusters can be used to constrain the nature of dark matter (see e.g. Spergel and Steinhardt 2000; Peter et al. 2010). Comparing the cluster mass profiles measured from galaxy velocities and from gravitational lensing can also inform us about the dark matter equation of state (Serra and Domínguez Romero 2011; Sartoris et al. 2014) and the nature of gravitation (Pizzuti et al. 2016). Alternatively, galaxy cluster mergers can be used to test the properties of dark matter (see e.g. Kahlhoefer et al. 2014). For instance, the detection and multi-wavelength analysis of the Bullet cluster, an extreme merging system, was claimed to provide a direct empirical proof of the existence of dark matter (Clowe et al. 2006), and was used to constrain its self-interaction cross section (see e.g. Markevitch et al. 2004).

1.3.2.4 Cluster peculiar velocity

The peculiar velocity of galaxy clusters can be used to constrain cosmological models (see e.g. Bhattacharya and Kosowsky 2007, 2008). This can be achieved in a statistical manner (see e.g. Hand et al. 2012), or using extreme merging clusters (Springel and Farrar 2007; Bouillot et al. 2015). The recent detections of the kinetic Sunyaev-Zel'dovich (kSZ, see also Chapter 2) effect induced by the moving gas (Hand et al. 2012; Mroczkowski et al. 2012; Sayers et al. 2013c; Adam et al. 2017; De Bernardis et al. 2017) offers a unique way to measure clusters' velocity with respect to that of the CMB (Haehnelt and Tegmark 1996). Studying the peculiar velocities of clusters is therefore a promising way to constrain cosmological models.

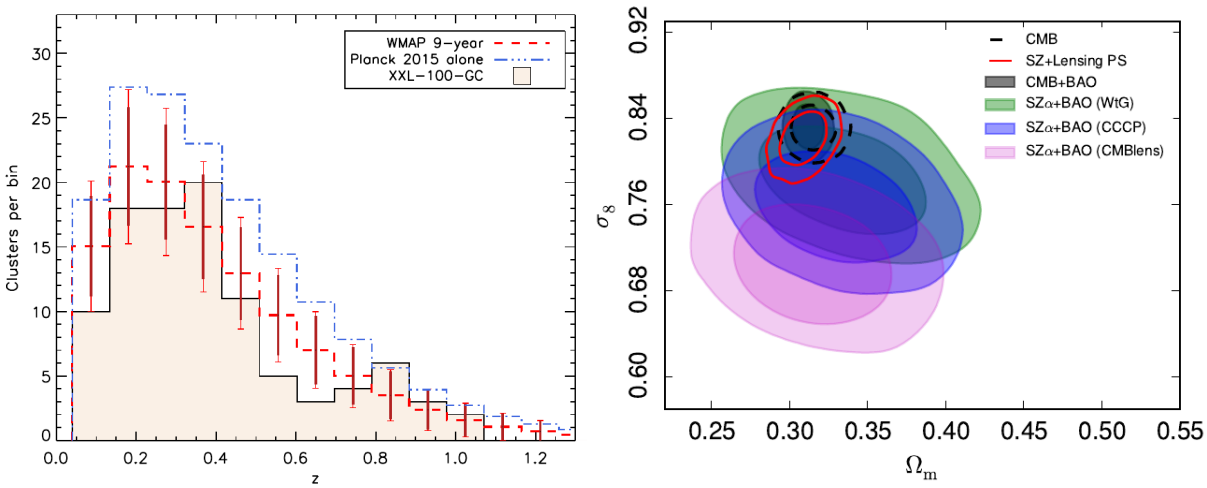

Figure 1.5: *Left:* redshift distribution of the bright sample of XXL X-ray detected clusters, compared to cosmic microwave background (CMB) expectations. We observe a deficit of clusters with respect to predictions from the cosmological model constrained by the Planck CMB measurement. Figure from Pacaud et al. (2016). *Right:* comparison of the constraints on σ_8 and Ω_m obtained by Planck using the CMB (black dashed circle), and cluster counts with different mass modelling (green, blue and pink shaded regions). Depending on the mass model used, we remark a tension between the two observables, depending on the mass calibration that is used. Figure from Planck Collaboration et al. (2016d).

1.3.3 Tensions with other probes

As galaxy clusters constitute a low redshift, late Universe cosmological probe, it is interesting to compare their constraints on parameters to that of high redshift, early Universe probes, such as the primary anisotropies of the CMB. By doing so, various analyses reported a deficit of clusters when compared to prediction from the ΛCDM cosmological model constrained by the CMB (see e.g. Planck Collaboration et al. 2014b, 2016d; Pacaud et al. 2016, and the left panel of Figure 1.5). As shown in the right panel of Figure 1.5, this deficit in the observed number of clusters translates into a tension between the σ_8 and Ω_m cosmological parameters inferred from the CMB and from cluster counts. The strength of this tension depends of the mass modelling employed, in particular it is alleviated by assuming that the cluster masses, estimated based on the hot gas physics, are biased low by a factor $\sim 40\%$. However, such a high bias value is at odds with gas fraction measurements in clusters (see e.g. Eckert et al. 2015) and is not expected from cosmological hydrodynamical simulations (e.g. Biffi et al. 2016). Interestingly, some other late Universe probes show similar tensions with the CMB cosmology (e.g. Hildebrandt et al. 2017; Riess et al. 2018), which could be a sign for physics beyond ΛCDM. Disentangling the effects of cluster mismodelling from that of a potential failure of the concordance cosmological model requires the in depth understanding of cluster physics, and is now becoming a major topic in modern cosmology.

Chapter 2

Observational properties of galaxies and galaxy clusters

Contents

Abstract: In this Chapter, we present the observational properties of galaxies, focussing on the ones that are pertinent for galaxy cluster studies. We then review the multi-wavelength observational properties of galaxy clusters components, and describe the processes needed to extract cosmological constraints from cluster surveys. Finally, we give an overview of the main current and future cluster surveys.

2.1 Observational properties of galaxies

The characterisation of the physical properties of galaxies essentially relies on the observations of their electromagnetic radiation at different wavelengths. In the following, we present the origin of the galaxies light emission and review the history of their star formation. We then focus on their colour and star formation properties and discuss their variation with mass and environment. Lastly, we introduce the processes that affect galaxies in clusters. This section is inspired from the review of Mo et al. (2010) about galaxy formation and evolution.

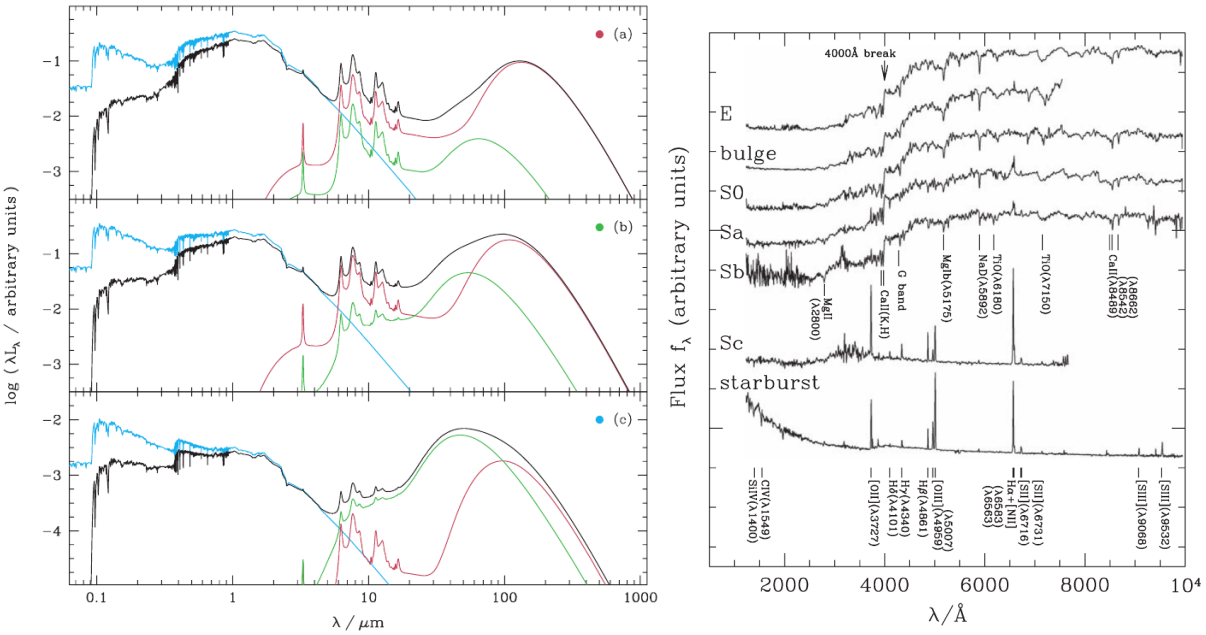

Figure 2.1: *Left:* Example of ultra-violet (UV) to far-infrared simulated spectral energy distributions (SED) of a quiescent star forming galaxy (a) ; a normal star forming galaxy (b) ; and a starburst galaxy (c). The blue lines show the unattenuated stellar spectra ; the green and red lines show the dust emission from stellar birth clouds and from the ambient inter stellar medium, respectively ; and the black line shows the total dust attenuated SED. Figure from da Cunha et al. (2008). *Right:* Example of UV to near-infrared spectra for different types of galaxy, from early to late type ($\sim$ passive to starburst) from top to bottom. The main spectral features are indicated in the figure. Figure from Mo et al. (2010).

2.1.1 Light emission from galaxies

The baryonic content of galaxies is made of gas and dust (the inter stellar medium, ISM) and stars. The gas is mainly atomic and is composed of a mix of hot and cold phases. The emission of normal galaxies (i.e. the non active galaxies) extends from the ultra-violet (UV) to the far-infrared (FIR) rest-frame wavelengths and mainly originates (directly or indirectly) from the stellar light. As can be seen in the left panel of Figure 2.1, part of the stellar emission, mainly at short wavelengths, is absorbed by the ISM and re-emitted thermally by the dust at longer wavelengths. The direct stellar emission dominates the spectral energy distribution (SED) from the UV to the near-infrared (NIR), while the thermal emission from dust takes over in the mid-infrared (MIR) to FIR wavelengths range. At radio wavelengths, relativistic electrons moving in the magnetic fields embedded in the ISM also emit synchrotron radiation. Additionally, ionised hydrogen clouds (HII regions) are responsible for *free-free* emission induced by electrons scattering off ions.

The SED of galaxies can be reconstructed from multi-band photometry. However, as shown in the right panel of Figure 2.1, galaxies also present emission and absorption lines, which can be measured from spectroscopy. Emission lines arise from the ionisation of the interstellar medium by hot young stars, while the majority of absorption lines occurs in the atmosphere of old stars. Emission lines arising from cold molecular gas (e.g. CO) also show up at radio wavelengths. The SED and spectra of galaxies encode information on their star formation history. Emission lines testify of recent star formation, while absorption lines provide information mainly on the old stellar population. Also, the amount of star formation is proportional to the rest frame UV-to-NIR and FIR-to-NIR flux ratios. The colour of galaxies, i.e the ratio of their luminosity in two photometric passbands, is thus related to their star formation history. For

instance, in optical bands, star forming galaxies will appear as blue, while galaxies that stopped forming stars will be red. However, colours do not vary only with the galaxies stellar age but also with their metallicities (i.e. the amount of chemical elements heavier than helium) and dust content: dusty and metal rich galaxies appear redder at optical wavelengths.

The star formation of galaxies is also related to their morphology. At low redshifts, the morphology of galaxies can be crudely separated between disk-like or spheroid-like, which correspond to, respectively, late and early type classification in the Hubble diagram (see e.g. Conselice 2014, for a review on the structural properties of galaxies). As shown in the right panel of Figure 2.1, the stellar emission from early type and elliptical galaxies is dominated by old stars and host little or no star formation, while late type galaxies have a high star formation rate (SFR) and are dominated by young stars.

Stars are driving the emission of light in normal galaxies. However, a small fraction of galaxies also shine at X-ray and are very bright at radio wavelengths. They are referred to as *active galaxies*. Their emission results from the accretion of matter onto their central super-massive black holes and is confined in a very small region, the active galaxy nuclei (AGN[1]). AGN are powerful sources: their luminosity can exceed that of their host galaxies by a factor of 10^3 and they can induce energy feedback, which have an important impact on galaxy evolution. The masses of the super massive black holes are positively correlated to the stellar mass of their host galaxies, which imply that AGN and star formation are connected.

For historical reasons, the brightness of galaxies is often expressed in magnitude units. The apparent (observed) magnitude m of an object in a spectral band x is related to its observed flux density in the same spectral band f_x by:

$$m_x \propto -2.5 \log\left(f_x\right). \tag{2.1}$$

The exact calibration of this relation depends on the magnitude system used (see Conventions used in this thesis for the one used in this thesis). The difference of magnitudes of the same object in two different bands gives a measure of its colour. The absolute (intrinsic) magnitude of an object in a rest frame band y is related to its apparent magnitude observed in a spectral band x by:

$$M_y = m_x - \mu - K_{\rm corr}, \tag{2.2}$$

where μ is the distance modulus defined as:

$$\mu = -5\left(\log\left(\frac{D_{\rm L}}{10}\right) - 1\right), \tag{2.3}$$

with $D_{\rm L}$ the luminosity distance expressed in parsec (see equation 1.17). $K_{\rm corr}$ is the K-correction, a correction factor needed to convert from the observed band x to the rest-frame band y. It depends on the source spectra and the x filter transmission (see e.g. Poggianti 1997; Hogg et al. 2002, for its derivation). For certain combinations of spectra, filters, and redshifts, the K-correction can be negative and compensate the dimming of the apparent magnitude with redshift, which allows us to detect distant objects (for instance, it is the case for dusty galaxies at $z > 1$ observed at sub-millimetre wavelengths).

2.1.2 Star formation history

The SFR in galaxies can be inferred from their UV or FIR rest frame emission, although it relies on some assumptions. By observing galaxies in the rest-frame UV and FIR ranges at different redshifts, it is thus possible to estimate the cosmic SFR as a function of time since the Big-Bang (see Madau and Dickinson 2014, for a review). The current picture of the cosmic star

[1]The term AGN is often used to refer to their host active galaxies and we will use that convention in the following sections.

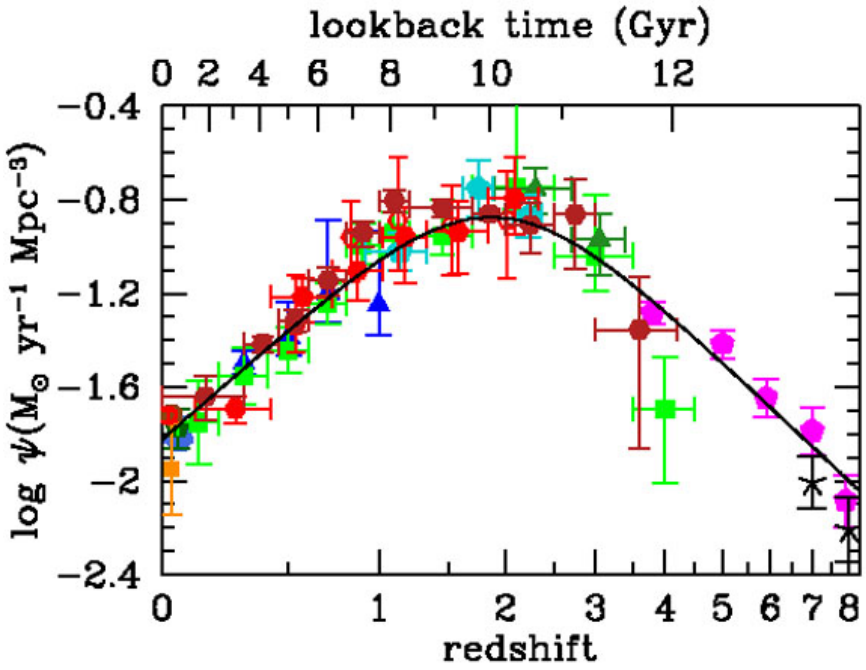

Figure 2.2: Evolution of the star formation rate density with redshift. The data points indicate measurements at rest frame ultraviolet and far-infrared wavelengths, the black line shows the best fit model. Figure from Madau and Dickinson (2014).

formation history is shown in Figure 2.2. The SFR density increases along with the formation of structures and galaxies from $z \sim 8$ to $z \sim 2$, where the peak of star formation is reached, and then gradually declines to the present day: the value that is reached at $z = 0$ is similar to that at $z \sim 7$. This also implies that half of the stellar mass seen today was formed at $z > 1.3$. The exact processes responsible for the evolution of the cosmic star formation history are still poorly known. One of the main question about galaxy evolution is to understand why the SFR started to decrease ~ 10 Gyr ago.

2.1.3 Galaxy bi-modality

In the local Universe, galaxies are known to harbour bi-modal colour distributions, with a clear distinction between blue and red galaxies (see e.g. Strateva et al. 2001; Blanton et al. 2003; Baldry et al. 2004; Kauffmann et al. 2003), this trend is visible up to at least $z \sim 1$ (e.g., Bell et al. 2004; Willmer et al. 2006; Cooper et al. 2007). As shown in the left panel of Figure 2.3, galaxies are distributed in two main regions in the $U - B$ versus B colour magnitude diagram, referred to as the red sequence and blue cloud: red galaxies follow a tight linear relation with a slight positive slope with luminosity, while blue galaxies are more scattered. This is related to the fact that red galaxies host stellar populations of similar ages whereas the stellar age distribution in blue galaxies is wider. As can be seen from the left panel of Figure 2.3, the ratio of red galaxies increases with luminosity. As discussed in Section 2.1.1, galaxy colours are related to their star formation and the ratio of red galaxies has often been used as a proxy for the ratio of galaxies with quenched star formation (see e.g. Peng et al. 2010, 2012). However,

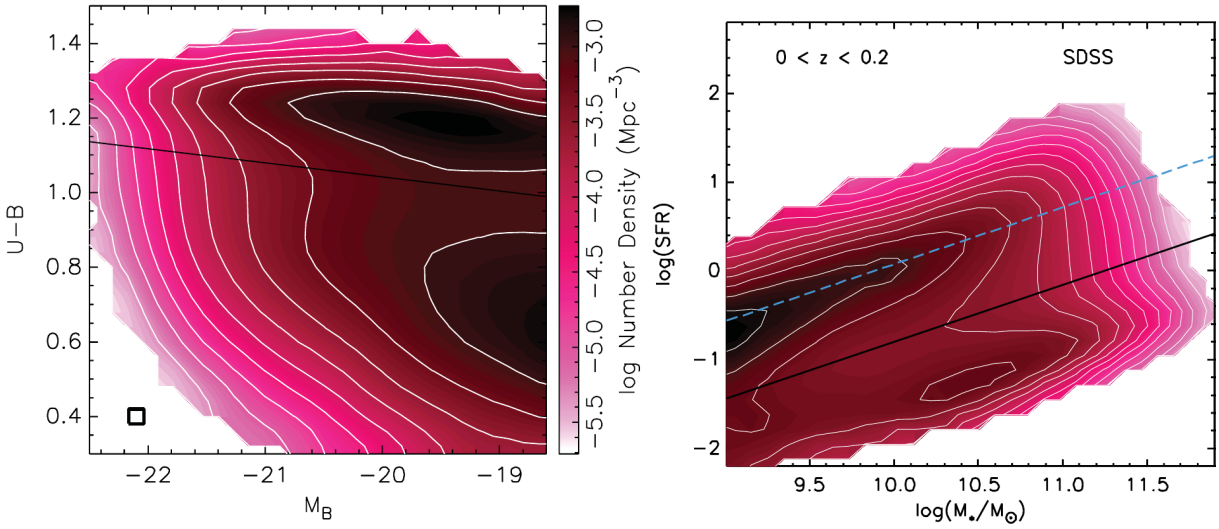

Figure 2.3: *Left:* colour magnitude relation for SDSS galaxies at $z < 0.2$: colours get redder from bottom to top and luminosity increases from right to left. The line divides the colour bimodality. *Right:* star formation rate as a function of stellar mass for SDSS galaxies at $z < 0.2$. The black line separates the sample between star forming and passive galaxies and the blue line is a fit to the star formation main sequence. Figures from Woo et al. (2013)

colours are an imperfect surrogate for star formation quenching (see e.g. Woo et al. 2013). The latter study found that 30% of red sequence galaxies are not quenched and show star formation, but are reddened by dust.

As shown in the right panel of Figure 2.3, the SFR of galaxies increases with their stellar mass (see Brinchmann et al. 2004; Noeske et al. 2007; Salim et al. 2007; Gilbank et al. 2010, for example). The relation followed by star forming galaxies is called the main sequence. Starburst galaxies lie above the main sequence and the passive, quenched, galaxies lie below. Because of the low number of starburst galaxies, the SFR-stellar mass diagrams present a bimodal distribution between star forming and passive galaxies. At low stellar mass, the fraction of quenched galaxies is low, but at high mass, quenched galaxies are the most numerous (see e.g. Wetzel et al. 2012; Woo et al. 2013). One of the most pressing question of galaxy evolution is to understand when, how, and why galaxies get quenched.

2.1.4 Star formation as a function of mass and environment

The reasons of the star formation quenching are still unclear. Both internal (mass related) and external (environment related) processes are believed to play a role (see e.g. Peng et al. 2010, 2012; Wetzel et al. 2012; Woo et al. 2013, but also e.g. Aragon-Calvo et al. 2016 for effects related to the cosmic web). As many properties of galaxies are related (e.g. more massive galaxies are also predominantly found in dense environments), answering that question necessitate to distinguish the different effects at play.

2.1.4.1 Central and satellite distinction

When studying the statistical properties of galaxies it is convenient to separate them according to their evolutionary processes. One method to do so is to use the *central/satellite* galaxy classification inherited from halo occupation distribution formalism (see e.g. Kravtsov et al. 2004). Central galaxies are the most massive galaxies in a dark matter halo and reside at the bottom of the potential well. Other galaxies inside the halo are satellite galaxies. Depending on the number of satellite galaxies associated to it, a central galaxy can be either an isolated field galaxy or

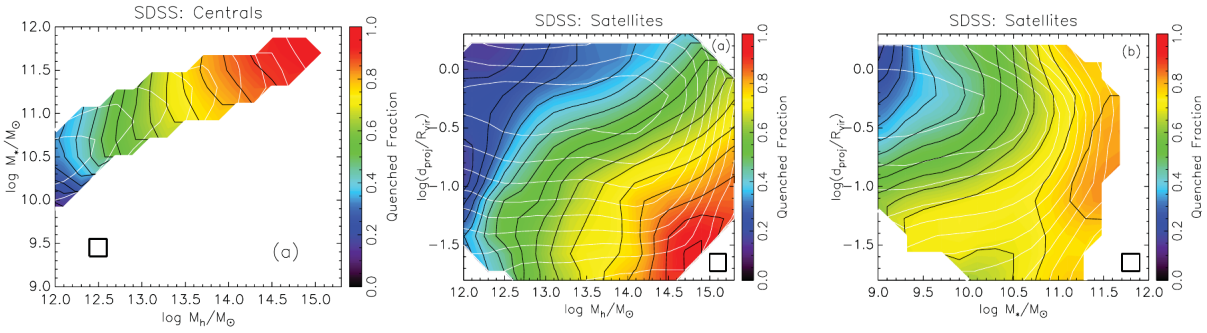

Figure 2.4: Quenched fraction for central and satellites SDSS galaxies at $z < 0.2$, as a function of different parameters. *Left:* quenched fraction of central galaxies as a function of stellar and halo mass. *Middle:* quenched fraction of satellite galaxies as a function of projected distance from the group centre (in virial radius units) and halo mass. *Right:* same as in the middle panel, but as a function of stellar mass instead of halo mass. The black contours indicate quenching fraction steps of 0.05 and the white contours indicate levels of number density spaced by 0.5 dex. Figures from Woo et al. (2013).

the central galaxy of a cluster. On an observational point of view, the central galaxies are often the brightest cluster galaxies, and can be identified as such.

2.1.4.2 The nature versus nurture debate

Because of the entanglement of the properties of galaxies, a complete census of the mechanisms responsible for galaxy quenching has not been reached yet. This problem is often related to a *nature versus nurture* debate (see, e.g., De Lucia 2007; De Lucia et al. 2012): does quenching originates from intrinsic, internal, phenomena or from external effects? On one hand, galaxy stellar mass can play a role. Indeed, more massive galaxies appear to be more quenched than low mass ones. This can be due to stellar and AGN feedbacks suppressing the star formation by removing the gas and/or preventing it to condensate (e.g., Cicone et al. 2014; Carniani et al. 2016; Baron et al. 2018). On the other hand, environmental effects affect galaxies and may cease their star formation: cluster galaxies are more quenched than field galaxies. In order to disentangles between internal and external effects, one must measure the quenching fraction as a function of both processes simultaneously. Moreover, these effects may be different for central and satellites galaxies and vary with redshift.

The global picture that appears to emerge is that environmental effects are dominant at $z \lesssim 1$ and internal (stellar mass related) effects are dominant at $z \gtrsim 1$ (see e.g. Darvish et al. 2016). At low redshifts, the quenched fraction of central galaxies increases predominantly with halo mass (see e.g. Wetzel et al. 2012; Woo et al. 2013, and left panel of Figure 2.4). The fraction of passive satellites increases both with halo mass and proximity to the centres of their host groups or clusters (see middle panel of Figure 2.4). The stellar mass only plays a role at large distance from the centres, where more massive satellites are more often quenched (see Woo et al. 2013, and right panel of Figure 2.4). As discussed in Section 2.1.1, the colours of galaxies are not entirely driven by the star formation rate: in fact Woo et al. (2013) found that the fraction of red galaxies strongly correlates with the stellar mass, in opposition to what is found for the fraction of quenched galaxies.

2.1.4.3 Processes affecting galaxies in clusters

Galaxies in dense environment (groups and clusters) display different properties than those in the field. They present more spheroid-like morphologies, redder colours, and higher quenched fraction. This is due to different processes, which result from interactions with other galaxies

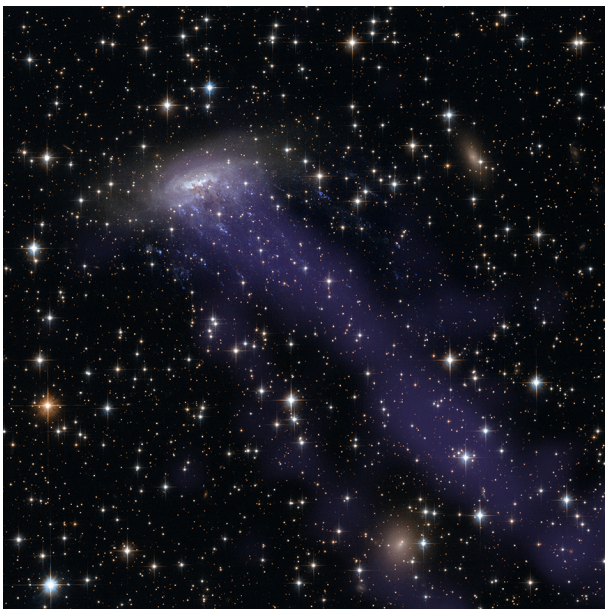

Figure 2.5: Composite image of the spiral star forming galaxy ESO 137-001, infalling in the rich, nearby cluster, A3627. The X-ray emission is overplotted in purple on a composite optical image. Ram pressure stripping causes a 70 kpc tail visible in X-ray, where signs of star formation have been spotted (Sun et al. 2007). Credits: X-ray: NASA/CXC/UAH/Sun et al. (2006); Optical: NASA, ESA, & the Hubble Heritage Team (STScI/AURA); see http://chandra.harvard.edu/photo/2014/eso137/.

and/or with the Intra Cluster Medium (ICM). They are usually referred to as: *galaxy harassment*, *ram pressure stripping*, *starvation* and *galactic cannibalism* (see e.g. Mo et al. 2010; Biviano 2008, for reviews) and affect satellite galaxies.

- *The galaxy harassment* is caused by the high speed encounters between galaxies. Those tend to change galaxies' morphologies from disk to spheroid like. Galaxies loose mass and get heated in the process.
- *The ram pressure stripping* phenomena arises from the motion of galaxies in the ICM, that causes the stripping of their gas. Its effect on star formation is not clear yet. While the removal of the gas may quench the galaxies, shock compressions in the ISM, induced by tidal forces, can also trigger bursts of star formation. See Figure 2.5 for an illustration of ram pressure stripping at play in a galaxy.
- *The starvation* process refers to the stripping of the warm gas halo around galaxies. With no gas reservoir left, galaxies slowly run out of star formation fuel and get gradually quenched.
- *The galactic cannibalism* is an environmental process that describes the phenomena during which the satellite galaxies, which sink towards the clusters potential well, get accreted by the central galaxies.

All these processes affect the observational properties of cluster galaxies. They are thus important for the deep understanding of the astrophysics of clusters as well as their use as cosmological probes. They also highlight the complex interactions at play between the different component of clusters, which we discuss in Section 2.2.

2.2 The components of galaxy clusters and their observational signatures

Galaxy clusters are mainly composed of dark matter ($\sim$ 80%), which is not directly observable. The other two components are the hot gas constituting the ICM ($\sim$ 15%) and the galaxies ($\sim$ 5%), both observable from radio to X-ray wavelengths. In this section, we review the observational signatures of the components of galaxy clusters. We use the cluster Abell 209 for illustration, as shown in Figure 2.6, as it is one of the few clusters for which public multi-wavelength data are available from radio to X-ray (see the following footnotes to retrieve the data [2,3,4,5,6]). Abell 209 is a typical massive ($M_{500} = 9.64 \pm 1.97 \times 10^{14}$ M$_\odot$, Umetsu et al. 2016) merging cluster at relatively low redshift ($z = 0.206$).

2.2.1 Cluster galaxies

As their name suggest, galaxy clusters were first detected as regroupments of *nebulae* (Biviano 2000). Nowadays, galaxies are used to detect and characterise clusters, either by imaging or spectroscopy. As discussed in Section 2.1.4, environmental effects affect the galaxies in-falling into clusters. This results in cluster galaxies displaying a common set of properties, over a large redshift range. In the following we portray the typical image of cluster galaxies (see e.g Biviano 2008, for a review). However, as we will see in this thesis, these properties may vary, for instance, with cluster mass, redshift, and dynamical state.

Because of the physical processes affecting galaxies in clusters (see Section 2.1.4.3), clusters host preferentially lenticular and elliptical galaxies (e.g. Wetzel et al. 2012; Kormendy and Bender 2012) and contain a central galaxy, often the BCG, near their centre. At optical and NIR wavelengths, the fractions of both red and luminous galaxies is higher in clusters than in the field and increases towards the clusters centre. The fraction of red galaxies is also a function of the redshift and more distant clusters host bluer galaxies than their local counterparts (this effect is known as the Butcher–Oemler effect, Butcher and Oemler 1978). At high redshifts (z$\sim$1.5), the situation seems to reverse and star formation occurs preferentially in cluster centres (see e.g. Brodwin et al. 2013). The optical properties of clusters will be studied in depth in Chapters 5, 6,7 and 8.

When observing clusters at FIR (or sub-millimetre) wavelengths, the emission is dominated by sub-millimetre galaxies (SMG). At these wavelengths, the flux-redshift relations is expected to be flat for distant dusty star-forming galaxies, because of negative K-correction. Therefore, very distant SMGs are easily found in cluster fields, where they can be gravitationally lensed (see e.g. Blain 1997; Smail et al. 1997; Wilson et al. 2008). Magnification factors of $\sim 2-4$ are common in cluster core regions, and can reach up to 30 or more. The sub-millimetre galaxies present in a cluster field will be studied in Chapter 11.

Clusters can also host AGNs, especially in their BCGs. Those AGNs may appear as X-ray and/or radio sources. The frequency of X-ray AGNs in cluster galaxies (BCG excluded) will be studied in Chapter 7.

An example of a cluster (Abell 209) observed at sub-millimetre (250 μm) and optical wavelengths is given in the middle left and right panels of Figure 2.6, respectively. Cluster galaxies are easily distinguishable in the optical by their yellowish colour and elliptical shape. A clear BCG is present in the centre. The majority of the sub-millimetre galaxies do not seem to belong to the cluster and have faint optical counterparts, and we note that these observations were performed to search for distant galaxies lensed by the cluster (Egami et al. 2010). The upper

[2]TGSS: http://tgssadr.strw.leidenuniv.nl/doku.php
[3]BOLOCAM: http://irsa.ipac.caltech.edu/data/Planck/release_2/ancillary-data/bolocam/
[4]Herschel: https://irsa.ipac.caltech.edu/applications/Herschel/
[5]CLASH (Subaru data and lensing model): https://archive.stsci.edu/prepds/clash/
[6]Chandra: http://cda.harvard.edu/pop/mainEntry.do;jsessionid=B5EkH+jrMBbec00B5j3-vSXe

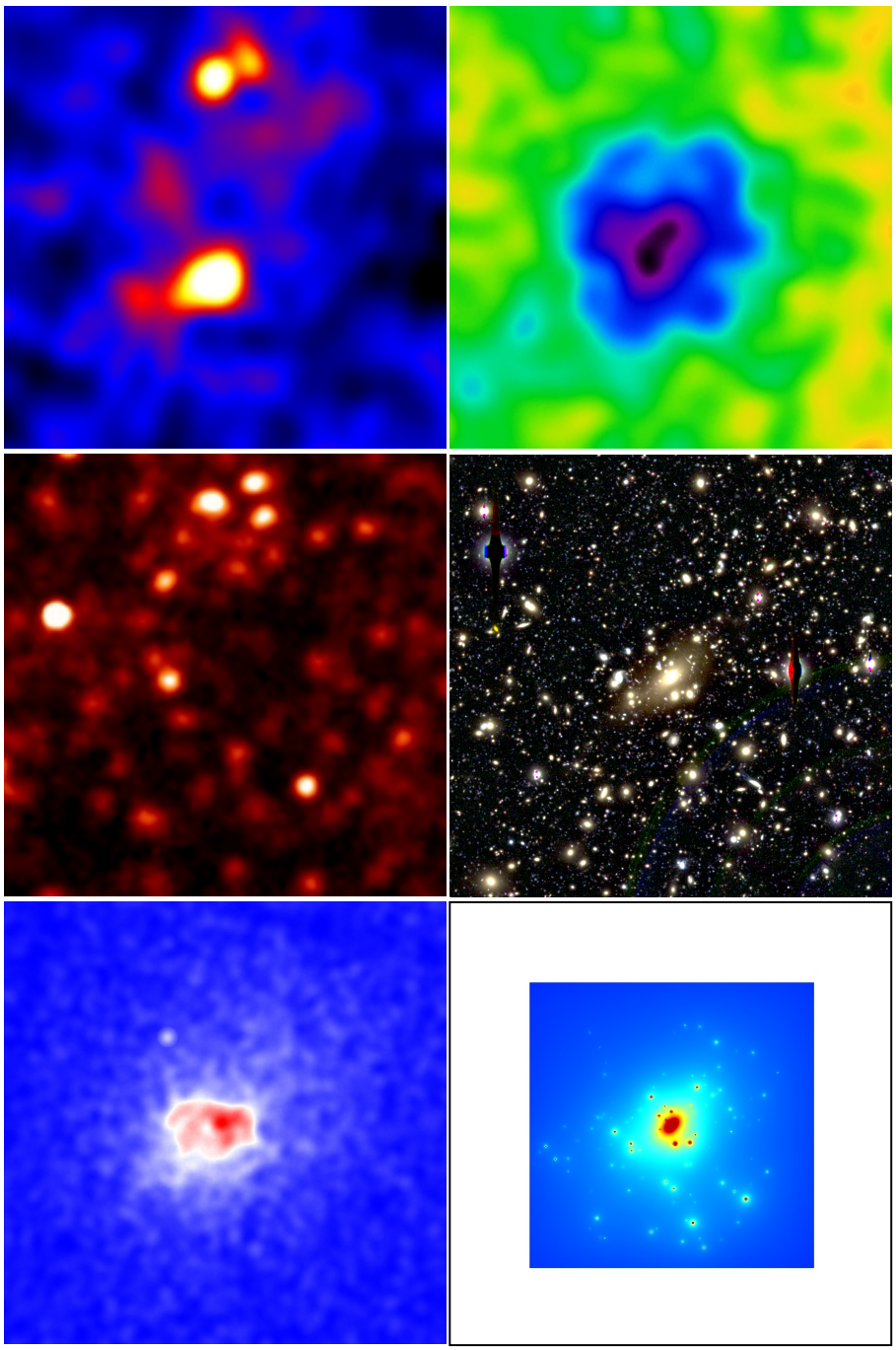

Figure 2.6: Multi-wavelength view of Abell 209, a massive merging cluster at z=0.206. The field of view of the image is 7 arcmin (∼1.4 Mpc). *Top left:* TGSS 150 MHz radio survey cut-out (Intema et al. 2017). We can see radio galaxies that appear as compact sources, as well as a giant radio halo corresponding to the diffuse emission (see also Venturi et al. 2007). *Top right:* BOLOCAM SZ image at 140 GHz tracing the pressure of the ICM (Sayers et al. 2013a). *Middle left:* Herschel 250 μm (PACS, Poglitsch et al. 2010) image showing the sub-millimetre view of Abell 209. *Middle right:* Subaru (Miyazaki et al. 2002) BVR composite image showing the optical component (see Umetsu et al. 2014, for the data reduction). *Bottom left:* Chandra X-ray photon count image mainly sensitive to the ICM gas density (ObsID3579). *Bottom right:* strong lensing projected mass model derived from CLASH data (Zitrin et al. 2015).

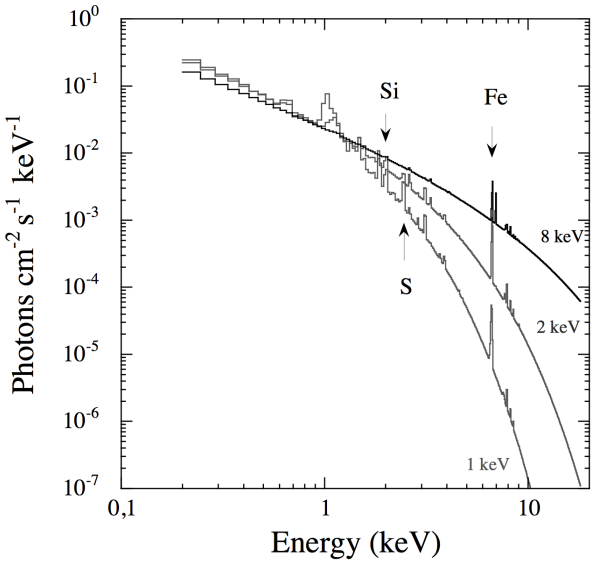

Figure 2.7: X-ray emission from a thin plasma with a metallicity $Z = 0.35 Z_{\odot}$, for different temperatures. The continuum corresponds to the spectrum of the bremsstrahlung emission, while the emission lines testify for the presence of heavy elements. Figure from Arnaud (2005).

left panel of Figure 2.6 presents the cluster radio emission at 150 MHz. The two compact peaks are likely to be associated to cluster radio galaxies (Venturi et al. 2007).

2.2.2 Intra cluster light

The Intra Cluster Light (ICL) is a diffuse stellar emission seen at the centres of groups and clusters of galaxies, which can span a few hundreds of kpc, but is not bound to galaxies. It is believed to originate mainly from stars stripped from galaxies via environmental processes (see Mihos 2016, for an introduction). Although there is no consensus about its formation yet, it is generally accepted that it progressively formed from $z \sim 1$ up to today, and sank to the bottom of the clusters potential well, getting smooth and mixed in the process. For this reason, it is difficult to distinguish the ICL from the emission of the outer envelope of the BCG. The ICL contains $\sim 20\%$ of the cluster total stellar mass and this fraction decreases with cluster mass and redshift (see e.g. Gonzalez et al. 2007; Morishita et al. 2017). As an example, we can see in the right panel of Figure 2.6 the presence of ICL surrounding the BCG of Abell 209 (see Annunziatella et al. 2016, for its characterisation).

2.2.3 Hot gas from the intra cluster medium

The ICM is composed of a ionised plasma gravitationally heated to temperatures of the order of $1 - 10$ keV ($\sim 10^{7-8}$ K), enriched in heavy elements produced by stars.

X-ray emission Because of its high temperature, the ICM emits at X-ray wavelengths via bremsstrahlung emission (also known as *free-free*), and because the metals are ionised, it produces emission lines (see Böhringer and Werner 2010, for a review). As shown in Figure 2.7, the ICM spectra presents a characteristic exponential cut-off at high energy, which depends on its temperature. X-ray spectroscopy thus allows us to derive the ICM temperature, and, if emission lines are detectable, its metallicity and the cluster redshift. The X-ray surface brightness, in units of erg s^{-1} cm^{-2} arcmin^{-2}, can be expressed as:

$$S_{\rm X} = \frac{1}{4\pi(1+z)^4} \int n_e^2 \Lambda(T_e, Z) dl, \tag{2.4}$$

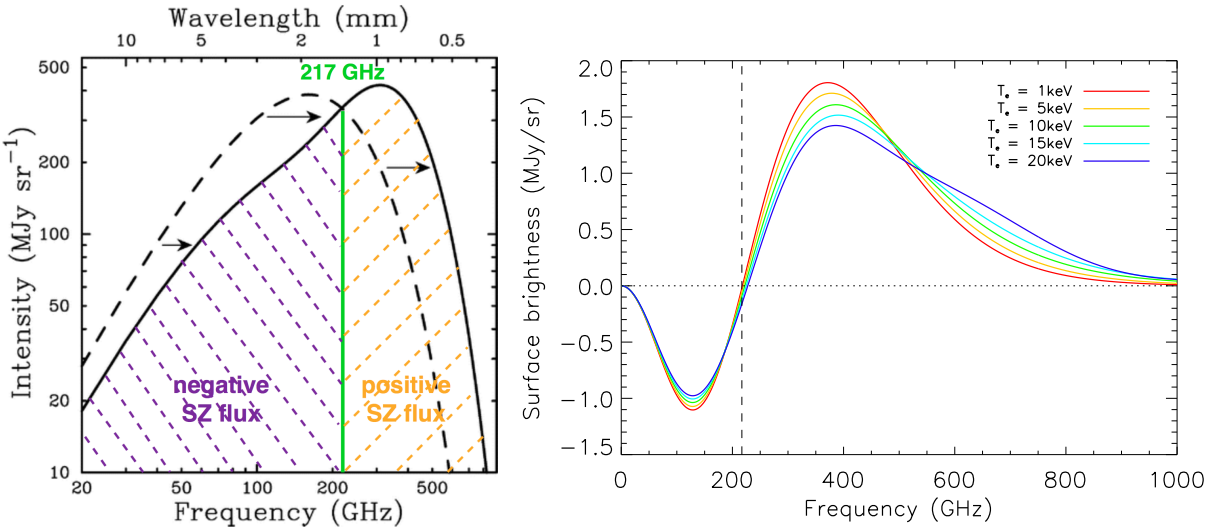

Figure 2.8: *Left:* illustration of the spectral distortion of the cosmic microwave background (CMB) spectrum induced by the SZ effect. The dashed line shows the original CMB spectrum and the solid line presents the CMB spectrum after distortion. Figure adapted from Carlstrom et al. (2002). *Right:* spectrum of the SZ effect, relative to the CMB black-body spectrum, corresponding to a Compton parameter $y = 10^{-3}$, as in the most extreme clusters in the Universe. The different coloured lines show the spectrum for different gas temperatures. Figure from Adam (2015).

where dl indicate the line of sight integration and $\Lambda(T_e, Z)$ is the cooling function. The latter depends on Z, the ICM metallicity and T_e, its temperature, such that $\Lambda(T_e, Z) \propto \sqrt{T_e}$. The typical electronic density of the ICM ranges from $n_e \sim 10^{-1}$ cm^{-3} in the cluster central regions, to $n_e \sim 10^{-5}$ cm^{-3} in the outskirts. We can remark that the X-ray surface brightness of an object is decreasing with its redshift and is proportional to the squared electronic density, and is thus not very sensitive to projection effects from extended structures along the line-of-sight. Thorough this thesis, we will study galaxy clusters detected via their X-ray emission.

The Sunyaev-Zel'dovich effect The ICM can also be detected thanks to the imprint it leaves in the CMB. Indeed, the photons from the CMB can interact with the hot electrons from the ICM via inverse Compton scattering, which causes their spectra to be modified (Weymann 1966; Sunyaev and Zeldovich 1970, 1972, 1980). This phenomena is known as the Sunyaev-Zel'dovich (SZ) effect. Different forms of the SZ effect can be observed, such as thermal, kinetic or polarised forms (see Birkinshaw 1999; Carlstrom et al. 2002; Kitayama 2014, for reviews). In the following, we will focus only on the thermal SZ effect, which is due to the ICM electronic pressure and is the most intense by about one order of magnitude in typical clusters, and we will refer to it as *the SZ effect*. The SZ effect induces a spectral distortion of the CMB photons, illustrated in the left panel of Figure 2.8: at frequencies lower/higher than 217 GHz, it translates into a decrement/increment with respect to the CMB surface brightness. The SZ spectrum, as a function of frequency, can be written as:

$$f(x, T_e) = \frac{x^4 e^x}{(e^x - 1)^2} \left(x \coth\left(\frac{x}{2}\right) - 4 \right) (1 + \delta_{\rm tSZ}(x, T_e)) \,, \tag{2.5}$$

with $x = \frac{h\nu}{k_{\rm B} T_{\rm CMB}}$ the adimensional frequency, h the Planck constant, $k_{\rm B}$ the Boltzmann constant, ν the observing frequency and $T_{\rm CMB}$ the CMB temperature. The $\delta_{\rm tSZ}(x, T_e)$ term represent the relativistic corrections, which become important when the ICM temperature exceed ~ 10 keV (see Itoh et al. 1998; Itoh and Nozawa 2004, for their derivations).

The brightness variation induced by the cluster ICM, with respect to that of the CMB I_0, is given by:

$$\frac{\Delta I_{\rm tSZ}}{I_0} = y\ f(x, T_e), \tag{2.6}$$

with y the Compton parameter, related to the electronic pressure integrated along the line of sight. It is computed as:

$$y = \frac{\sigma_{\rm T}}{m_e c^2} \int P_e dl \equiv \frac{\sigma_{\rm T}}{m_e c^2} \int n_e k_{\rm B} T_e dl, \tag{2.7}$$

where $\sigma_{\rm T}$ is the Thomson cross section and $m_e c^2$ the electron rest mass energy. An example of SZ spectra, for a fixed Compton parameter and different gas temperature, is shown in the right panel of Figure 2.8. We note that the SZ surface brightness is independent of redshift and directly proportional to the ICM pressure. In the third part of this thesis (part III), we will map and analyse the SZ effect in a distant cluster.

The example of the cluster Abell 209, observed at X-ray and millimetre wavelengths (140 GHz), is given in the bottom left and upper right panels of Figure 2.6, respectively. We can see the diffuse emission from the X-ray and SZ images, showing that the ICM density and pressure increase towards the centre, but are not very peaked in the case of this merging cluster. The offset between the SZ (tracing the pressure) and the X-ray (tracing the density) peaks is likely to be due to the merger, which results in a local compression, rising the ICM temperature and boosting the SZ signal locally. While both SZ and X-ray signal clearly present an extended emission, we note that the SZ signal is less peaked than the X-ray signal, as it depends linearly on the density, while the X-ray depends on the density square.

2.2.4 Relativistic electrons and magnetic fields in the intra cluster medium

Radio observations have revealed the presence of extended, cluster-scale, diffuse radio emission due to non-thermal processes in galaxy clusters (see e.g. Feretti et al. 2012; Ferrari et al. 2008, for a review). These sources emit synchrotron radiation and attest for the presence of relativistic electrons and magnetic fields in the ICM. They are usually classified as radio halos, radio relics and radio mini-haloes, depending on their positions, sizes, morphologies and polarisation properties. Radio halos and mini halos are believed to be related to turbulences in the ICM, while radio relics are attributed to ICM shocks induced by cluster mergers.

The upper left panel of Figure 2.6 presents the radio emission in A209. Apart from the two radio galaxies already mentioned, we notice the presence of a giant radio halo associated to the ICM (Venturi et al. 2007).

2.2.5 Dark matter

So far, there is no compelling evidence for dark matter direct observations. However, the total mass distribution of clusters, dominated by that of the dark matter, can be inferred from luminous tracers (as we will discuss in Section 2.3.2). Dark matter is believed to shape the potential well of galaxy clusters, in which baryons are falling. Based on observations at cosmological scales (e.g. Anderson et al. 2014; Planck Collaboration et al. 2018a), galaxy clusters (e.g. Clowe et al. 2006), and galaxies (e.g., Rubin et al. 1980), dark matter is expected to be massive, weakly interactive with ordinary matter, and cold. It might be made of weakly interacting massive particles (WIMP, see e.g. Jungman et al. 1996, for a review), which are, however, not part of the standard model of particle physics. As an example, the bottom right panel of Figure 2.6 shows a model for the total projected mass distribution of Abel 209 (and thus mainly tracing the dark matter), computed from the measurement of the strong gravitational lensing of background galaxies (Zitrin et al. 2015).

2.3 Building a cosmological cluster sample

Beyond the theoretical framework discussed in Chapter 1, the use of galaxy clusters as cosmological probes requires two key ingredients: the construction of a well controlled cluster sample and an estimation of the mass of the clusters (see Section 1.3). In this section, we review the current methods to build a sample based on the observables that are accessible from a survey, as introduced in Section 2.2. The different current methods to measure the mass of clusters are also discussed, both in the case of direct measurements from observables, and from scaling relations.

2.3.1 Detecting galaxy clusters

Cosmological analyses of clusters require both large samples of objects and precise modelling of their physics to robustly estimate their masses. Cluster detections are thus conducted either in survey mode, aiming at obtaining statistical samples over a large region of the sky, or in targeted mode, allowing for high quality observations of a few systems that serve as a reference. As presented in Section 2.2, galaxy clusters can be observed at different wavelengths, depending on the observable of interest.

In the optical and IR, clusters are usually detected as concentrations of galaxies in the plane of the sky and along the line of sight, by using galaxies' redshifts (see for instance the WaZP cluster finder algorithm in Chapter 8) or colours, making use of the fact that galaxies are redder in clusters than in the field. The different cluster finder algorithms may also use information about the form of the cluster galaxies luminosity function and/or density profile. In absence of spectroscopy, multi-band photometry allows us to estimate the redshift of galaxies via the computation of photometric redshifts (see Chapter 4 for more details). Therefore, in the optical and IR, clusters can be directly assigned a redshift.

Galaxies can also be used to map the total projected mass of structures. Indeed, massive objects induce distortions of the light of background galaxies, via gravitational lensing effect. While multiple images and arcs can be identified in the *strong lensing* regime, allowing us to obtain detailed mass models of the clusters cores, the statistical reconstruction of the distortions, in the *weak lensing* regime, allows us to build maps of the mass distribution on large scales, and potentially detect galaxy clusters (e.g., Gavazzi and Soucail 2007; Shan et al. 2012). Note that this technique is also possible using the CMB as the background image (e.g. Baxter et al. 2018).

One of the drawback of galaxy based cluster detection (except when spectroscopic redshifts are available for all member galaxies) is that it is sensitive to projection effects from un-virialised structures, as groups or filaments. Cluster galaxies can be detected at optical or IR wavelengths, depending on the clusters redshifts. Rest frame NIR observations are the most suitable for clusters as they are more sensitive to the stellar mass of galaxies than to the star formation. FIR and millimetre wavelengths can also be used to detect concentration of SMGs, which trace high redshift proto-clusters (e.g. Smolčić et al. 2017).

Optical and NIR observations can be achieved from ground based telescopes, while mid and FIR observations require satellites. Even in the optical and NIR the image quality largely increases with space based observations.

At X-ray wavelengths, clusters can be detected through the thermal emission of the ICM and appear as diffuse sources. In order not to be sensitive to the exponential cut-off in their spectra, detections are usually conducted in the soft X-ray band ($\sim 0.5 - 2$ keV). As detailed in Section 2.2.3, X-ray spectroscopy allows us to derive the clusters temperature, redshift and metallicity. However, it is expensive in terms of observing time and generally, only mean temperatures are available in surveys (at best). X-ray surveys are thus based on cluster imaging, for which cluster redshift estimations rely on follow-up in the optical or IR. The X-ray surface brightness drops

with redshift and distant clusters are more difficult to detect. Although X-ray cluster detections are not much affected by projection from un-virialised structures, they are sensitive to contamination by point-sources (essentially AGNs, see Chapters 7 and 8), which are more difficult to pinpoint when the angular size of the clusters is small and when their surface brightness is shallow. Since the earth atmosphere is opaque at X-ray photons, observations are conducted from satellites (see for instance the XMM-Newton telescope presented in Chapter 3).

At millimetre wavelengths, clusters can be detected via the SZ effect. Depending on the instruments and their technologies the observing frequency ranges from a few GHz to a few hundreds of GHz. SZ observations can be conducted in survey or targeted mode and from ground based telescopes or satellites. The SZ surface brightness does not depends on redshift, but as the apparent sizes of clusters decrease with redshift, the observations of distant objects are limited by the instruments angular resolution. The SZ signal is driven by hot virialised structures ($\propto T_e$), but unlike the X-ray surface brightness, it is linearly sensitive to the electron density, so that the SZ signal is intermediate between optical and X-ray observations in terms of sensitivity to projection effects. Similarly to X-ray, it can be contaminated by radio and infrared point sources.

At radio wavelengths, to date, less than a hundred of clusters have been detected through the synchrotron emission associated to the ICM. Although these obsevations are very useful for the characterisation of clusters, they are not yet mature for the blind detection of clusters from a survey. We note that a all new picture will be achieved from the Square Kilometre Array, which is expected to detect radio diffuse emission in a thousand of clusters (see the French SKA White Book, Acero et al. 2017).

2.3.2 Mass determination

Correctly estimating cluster masses is one of the main challenge of cluster cosmological analyses. The masses of clusters can be measured directly from spatially resolved observations, using some assumptions. However, these methods are used when high quality observations are available (usually in targeted mode), and for large samples with lower quality data, as it is the case in surveys, the mass is usually estimated using scaling relations. Under the assumption that clusters are self-similar objects, whose evolution is driven by gravitational collapse only, these relations can be predicted analytically or using simulations. However, this condition is often a crude approximation and scaling relations have to be calibrated using direct mass measurements. A perfect mass estimator should be easy to measure, unbiased and to present minimal scatter with respect to the true mass. In practice, the bias has to be characterised as well as possible and the scatter minimised. In the following, we present the methods to measure and estimate cluster masses via their different observables (see e.g. Biviano 2008; Allen et al. 2011, for reviews).

2.3.2.1 Direct mass measurements

Galaxy dynamics Cluster masses can be measured from the phase-space distribution of their member galaxies, under the assumption of dynamical equilibrium, using the Jeans equation (e.g. Binney and Tremaine 1987; Carlberg et al. 1997):

$$M_\sigma(r) = -\frac{r\sigma_{\rm r}^2(r)}{G}\left[\frac{d\,\ln(\sigma_{\rm r}^2)}{d\,\ln(r)} + \frac{d\,\ln(\nu)}{d\,\ln(r)} + 2\beta\right], \tag{2.8}$$

with G the gravitational constant, $\nu(r)$ the galaxy number density, $\sigma_{\rm r}^2(r)$ the 3-dimensional velocity dispersion and β a parameter accounting for velocity anisotropy. Under model assumption, these quantities can be estimated from the projected velocity dispersion and galaxy

number density. This method is sensitive to cluster triaxiality and the clusters dynamical state. Also, the velocity dispersion may vary depending on the galaxy population that is targeted.

Another way of using galaxies to measure masses is to use the *caustic* method (e.g. Rines and Diaferio 2006), which relies on the locus of galaxies in radius-redshift phase-space diagrams. This necessitate a high number of spectroscopic members but is more robust at large radii than the velocity dispersion method.

Lensing As mentioned in Section 2.3.1, gravitational lensing of background galaxies is sensitive to the total projected mass distribution (see Kneib and Natarajan 2011, for a review). The background galaxies present shear distortions that trace the gravitational field of the matter distribution of the lens. Depending on the geometry and the mass of the systems, we can distinguish too regimes: *weak lensing*, when the small distortions of background galaxies are measured statistically, and the *strong lensing*, when strong distortions and multiple images of individual galaxies are visible. Assuming a geometrical distribution for the matter, the lensing masses can be estimated from weak (up to large radii) or strong lensing (the core of clusters). Lensing methods do not rely on the dynamical equilibrium, but they are sensitive to projection effects and triaxiality because of the de-projection. Lensing cluster's masses are believed to be underestimated with an average bias of $5-10\%$ and present $\sim 10-25\%$ intrinsic scatter (see e.g. Sereno 2015).

Hydrostatic equilibrium Under the assumption of hydrostatic equilibrium (HSE), clusters' masses can be measured from their X-ray emission (see Ettori et al. 2013, for a review), or in combining with SZ observations, as:

$$M_{\rm HSE}(<r) = -\frac{r k_{\rm B} T(r)}{G \mu_{\rm gas} m_p}\left[\frac{d\ln(n)}{d\ln(r)} + \frac{d\ln(T)}{d\ln(r)}\right], \tag{2.9}$$

with $\mu_{\rm gas}$ the mean molecular weight, m_p the proton mass, $k_{\rm B}$ the Boltzmann constant and G the gravitational constant. Different methods with different model assumptions can be used to measure the mass from the projected density and temperature (or pressure) profiles. X-ray masses measurements are sensitive to the cluster dynamical state, non thermal pressure support and gas substructures. They are expected to be biased low by a factor $\sim$10-30% and are believed to be affected by an intrinsic scatter of $\sim 10\%$ (e.g. Piffaretti and Valdarnini 2008; Jeltema et al. 2008; Biffi et al. 2016).

2.3.2.2 Scaling relations

Since the global properties of galaxy clusters are related to their baryonic and dark matter content, they can be used to trace the total cluster mass via scaling relations. Numerous mass proxies have been derived at different wavelengths in the literature, and are use in cosmological studies from cluster surveys (e.g. Rozo et al. 2010; Böhringer et al. 2014; Planck Collaboration et al. 2014b).

In the optical and IR, the richness λ, i.e. an estimate of the number of cluster members, the projected velocity dispersion σ_v, the total stellar mass $M_\star$ and the luminosity $L_{\rm opt}$ can be used as proxy for the clusters masses (e.g. Rozo et al. 2009). In X-ray, one can use the ICM luminosity $L_{\rm X}$, its temperature $T_{\rm X}$, the gas mass $M_{\rm gas}$ or a combining of those, such as the product of the gas mass and temperature $Y_{\rm X}$ (e.g. Arnaud et al. 2005; Fabjan et al. 2011). These quantities show less scatter when the core of clusters is excluded. The SZ flux $Y_{\rm SZ}$, i.e. the integrated Compton parameter, is also a mass proxy that is related to the ICM and presents a low intrinsic scatter with respect to the total mass (Arnaud et al. 2010; Planck Collaboration et al. 2014b).

The scaling of the relations derived from the ICM can be obtained analytically, under the hypothesis of self-similarity (e.g. Kaiser 1986). They give:

$$\begin{aligned} L_{\rm bol} &\propto M^{4/3}E(z)^{7/3}, \\ T_{\rm mw} &\propto M^{2/3}E(z)^{2/3}, \\ M_{\rm gas} &\propto M, \\ Y_{\rm X} &\propto M^{5/3}E(z)^{2/3}, \\ Y_{\rm SZ} &\propto M^{5/3}E(z)^{2/3}, \end{aligned} \tag{2.10}$$

where the subscript $\rm bol$ and $\rm mw$ indicate that these relations apply to the bolometric luminosity and the gas mass weighted temperature, which may differ from direct X-ray measurements. In practice, the slopes of these relations, as calibrated from observations, may deviate significantly from the self-similar expectations. These relations are thus calibrated using, either, a sub-sample of objects for which direct mass measurements are available, or, by stacking the lensing signal and/or velocity dispersion in bins of observables. We note that the effects of the selection bias of the sample, such as the Malmquist bias, has to be taken into account to recover the scaling relation correctly (e.g. Pratt et al. 2009). Numerical hydrodynamic cosmological simulations can also be used to predict the expected scaling relations (e.g. Le Brun et al. 2017). The comparison between these expectations and observations are useful to constrain the complex physics of clusters that might be missed in simulations, and potential systematic effects affecting the observations.

2.3.3 Current and future cluster surveys

Cluster cosmology requires large samples of well characterised clusters, and well calibrated masses. Current and future cluster surveys should allow us to improve these requirements by increasing the number of clusters over an unprecedented range of masses and redshifts. Given the different systematics, advantages and drawbacks of the different probes of clusters, multi-wavelength studies are now becoming essential to improve cosmological constraints from clusters, as well as to better understand their formation and evolution from an astrophysical point of view. In this section, we give a non exhaustive overview of the main current and future surveys pertinent for cluster studies, which will likely help achieving these goals.

Current optical and NIR surveys include the Dark Energy Survey (DES, The Dark Energy Survey Collaboration 2005), and the Hyper Suprime-Cam Subaru Strategic Program Survey (HSC-SSP Survey, Aihara et al. 2018). DES is conducted with the DeCAM camera on the Blanco 4-meters telescope, covering 5000 square degrees in the $grizY$ bands, reaching a magnitude of $r \sim 24.3$. The HSC-SSP Survey is imaging 1400 square degrees in the $grizy$ bands, with a magnitude depth of $i \sim 26$, using the Hyper Suprime-Cam wide-field imaging camera on the 8.2m Subaru telescope. The Large Synoptic Survey Telescope (Ivezić et al. 2008; LSST Science Collaboration et al. 2009) will see light in the coming years. During 10 years, it will image ~ 18000 square degrees in the southern hemisphere in $ugrizY$ bands, reaching a magnitude $r \sim 27.5$ and unprecedented image quality. Around the same time the *Euclid* satellite (Laureijs et al. 2011), made of a 1.2 m telescope, will be launched. It will map ~ 15000 square degrees of the sky with a broad band optical filter, allowing for high image quality, and three NIR filters: YJH, reaching $H \sim 24$. These data will be complemented by NIR low resolution spectroscopy and ground based optical associated observations. *Euclid* and LSST will detect hundreds of thousands of clusters over an unprecedented range of masses and up to high redshift ($z \sim 2$ for *Euclid*, see Sartoris et al. 2016, Adam et al. in prep.). With a complementary strategy, the Javalambre-Physics of the Accelerated Universe Astrophysical Survey (J-PAS, Benitez et al. 2014) will map 8500 degrees in the northern hemisphere with 54 narrow band filters from UV to NIR, reaching a magnitude of $i \sim 22.5$. It will allow for the in depth characterisation of $z < 1$ clusters (Ascaso et al. 2016). All these surveys should be complemented by weak

lensing measurements, allowing for the internal mass calibration of the samples. They will push the detection limits to either low mass, high redshifts, or both. In addition to cluster detection from the galaxy spatial distribution, they will also potentially allow us to build large lensing mass selected samples, which will bring new insight into the selection effects at different wavelengths.

In the X-ray, the XXL survey (Pierre et al. 2016) will provide its final release and associated results within a few years. As it will be discussed in details in this thesis, XXL provides a unique way to probe clusters from their ICM gas content down to low masses and up to high redshifts. In the coming years, a nearly all sky survey will be provided by the eROSITA satellite (Merloni et al. 2012), which is planned for launched in 2019. eROSITA will allow for the detection of a hundred thousand of clusters up to $z \sim 1.5$, extending the XXL survey over a much larger area. Additionally, on longer time scales, other satellites, which are now in development, should provide a new window to the hot and energetic universe, such as Athena (Nandra et al. 2013).

At millimetre wavelengths, a new stage of cluster cosmology has been achieved thanks to the Planck satellite (Planck Collaboration et al. 2014b, 2016d). Now, current surveys, well suited for cluster detections using the SZ effect, include the Atacama Cosmology Telescope experiment (ACT, and its upgrade camera ACTpol and AdvAct, Marriage et al. 2011; Hasselfield et al. 2013; Hilton et al. 2018) and the South Pole Telescope (SPT, and its upgrade camera SPTpol and SPT3G, Staniszewski et al. 2009; Vanderlinde et al. 2010; Bleem et al. 2015). They cover respectively ~ 1000 and ~ 2500 square degrees on the southern hemisphere and detect hundreds of massive clusters up to $z \sim 1.5$. The CMB stage 4 collaboration, and associated experiments, may also lead to SZ cluster surveys (Abazajian et al. 2016). These surveys will be unique to provide SZ selected (nearly mass selected) samples down to low masses and up to high redshift. This should be not only be an excellent way to test cosmological models, but should also allow us to improve our understanding on cluster formation and evolution.

Finally, radio observations of galaxy clusters should enter a new era with the Square Kilometer Array (SKA, see e.g. Acero et al. 2017). SKA will open a completely new view on the non-thermal processes at play in the ICM. These observations will also be complemented by the Cherenkov Telescope Array (CTA, Cherenkov Telescope Array Consortium et al. 2017), which may allow us to probe the cosmic ray content of clusters in gamma ray, for the first time.

2.4 Summary

In this chapter, we discussed the observational properties of galaxies, focusing on the physical processes at play in clusters, and which affect the star formation history of galaxies. We then presented the components of clusters: the dark matter, the hot gas, and the galaxies, as well as their observational signatures from optical/IR, X-ray, SZ, or radio observations. Finally, we discussed the build-up of cosmological cluster samples. We focused on the detection of clusters from primary observable and the mass determination, which are key steps for any cosmological analysis with clusters. To conclude, we reviewed the current and future cluster surveys, which set the general context of this thesis.

Conventions used in this thesis

Notations

We use the notation log and ln for the common and natural logarithm respectively.

Cosmology

Throughout this work we have used the following cosmological parameters as our baseline: $H_0 = 70$ km s^{-1}Mpc^{-1}, $\Omega_m = 0.3$, $\Omega_\Lambda = 0.7$ and $\Omega_k = 0$.

Magnitude system

Throughout this thesis magnitudes are expressed in the AB system (Oke 1974). The conversion to flux spectral density is given by:

$$m_{AB} = -2.5 \log (f_\nu) + 8.90, \tag{2.11}$$

with f_ν the flux spectral density expressed in Jansky (Jy), and 1 Jy = 10^{-26} W Hz^{-1} m^{-2} = 10^{-23} erg s^{-1} Hz^{-1} cm^{-2}.

Reference galaxy evolution model

Throughout this thesis, we use a model of galaxy evolution as reference for the redshift evolution of the characteristic apparent magnitude m^*. This model was computed with LePhare (Ilbert et al. 2006; Coupon et al. 2009) using the elliptical galaxy SED template BURST_SC86_ZO.SED from the PEGASE2 library (Fioc and Rocca-Volmerange 1997), with a redshift of formation $z_f = 3$. We normalized the model using K^* values from Lin et al. (2006) corrected to AB system. This leads to a magnitude of $M_R^* = -21.36$ at $z = 0$, in the r' band.

Scaled radius

Throughout this thesis, we refer to the scale radius of an overdensity as R_Δ, and other quantities Q computed within this radius as Q_Δ. The radius R_Δ is defined as the radius of the sphere inside which the mean density is Δ times the critical density of the Universe at the cluster's redshift, $\rho_c(z)$. We generally use the typical values of $\Delta = 200$ or 500. The mass within R_Δ, written as M_Δ, is then equal to $4/3\pi\Delta\rho_c(z)R_{500}^3$, by definition.

Part II

Characterizing the optical properties of X-ray detected groups and clusters

Table of Contents

Objectives of this study

In this Part of the thesis we analyse the optical properties of a statistical sample of X-ray detected clusters from the XXL survey. Our aim is to optically characterise the systems detected in X-ray, over a wide range of mass and redshift, and to derive a reference parametrisation for cluster modelling and cluster detection.

We start by introducing the XXL survey and its optical counterpart, the CFHTLS survey, in Chapter 3. We also provide an illustration of the data we are using by presenting several typical clusters from our sample. We then investigate the quality of the photometric redshifts in the CFHTLS survey in Chapter 4. This allows us to pinpoint systematic effects and to define an unbiased way to select galaxies when studying the properties of clusters. We use this knowledge in Chapter 5 where we construct the luminosity functions of XXL clusters and we identify and quantify associated systematics. The analyses of the luminosity functions are performed in Chapter 6. We study the luminosity distribution of the brightest cluster galaxies and the satellites separately and we model their dependences with redshift and richness. In Chapter 7 we examine the activity of XXL cluster galaxies trough their AGN fraction and their colour. This brings valuable information about X-ray cluster contamination and cluster miscentring in the optical. Finally, in Chapter 8, we present the WaZP optical cluster finder and the matching statistics between the XXL and the WaZP cluster samples. This provides precious guidance on X-ray and optical cluster selection functions.

Chapter 3

Presentation of the XXL and the CFHTLS surveys

Contents

Abstract: In this Chapter we present the XXL survey, an X-ray cluster survey conducted with the XMM-Newton telescopes. We give an overview of the steps needed to build the cluster catalogue and we give the main characteristics of the cluster sample. We then present the properties of the Canada France Hawaii Telescope Legacy Survey (CFHTLS), which we used to study the optical counterparts of XXL clusters. Finally, we present the optical images and the X-ray emission of a selected sample of XXL clusters in order to give a flavour of the X-ray and optical properties of the entire XXL sample.

3.1 The XXL survey

3.1.1 Overview of the XXL survey

The XXL survey (Pierre et al. 2016, hereafter XXL Paper I) is an XMM-Newton (X-ray Multi-Mirror) project designed to provide a well defined sample of galaxy clusters out to redshift above unity, suitable for precision cosmology, and for the analysis of galaxy evolution and active galactic nuclei (see Pierre et al. 2011).

XMM-Newton is widely used in targeted mode and, thanks to its wide field of view, enables the build-up of large catalogues of clusters found serendipitously in individual pointings (see e.g. Watson et al. 2003). However, such samples suffers from non trivial selection biases and do not have a well defined selection function. Contigous surveys are thus better suited to detect clusters for cosmological purposes. Moreover, they allow to conduct both cluster number counts and cluster clustering analyses, which, as we saw in Chapter 1, are highly complementary. These considerations motivated the completion of a large XMM-Newton survey.

Figure 3.1: Artistic view of XMM-Newton. Image from ESA (https://www.cosmos.esa.int/web/xmm-newton/home).

Table 3.1: Main characteristics of the XMM-Newton EPIC instruments, taken at the centre of the pointings.

Band	EPIC MOS	EPIC pn
Field of view	$30'$	$30'$
Bandpass	$[0.15, 12]$ keV	$[0.15, 12]$ keV
Sensitivity (erg s^{-1} cm^{-2})	$\sim 10^{-14}$	$\sim 10^{-14}$
PSF (FWHM)	$5''$	$6''$
Spectral resolution	$\sim$ 70eV	$\sim$ 80eV
Time resolution	1,75 ms	0,03 ms

XXL spans 50 degrees, distributed in two contiguous fields, with a depth of $\sim$10ks. It thus occupy an intermediate and strategic position between shallow/wide and deep/narrow surveys. The scientific analysis of the XXL survey is still ongoing. The first data release occurred in 2016, the second one is expected for September 2018, and the third and last one should take place in 2019.

3.1.1.1 The telescopes

The XMM-Newton satellite was launched by the European Space Agency in December 1999 to orbits around the Earth and is still in operation. The satellite is composed of three X-ray telescopes mounted in parallel (see Figure 3.1) and an optical monitor. The X-ray instruments count three European Photon Imaging Cameras (EPIC) and two Reflection Grating Spectrometers (RGS). The main characteristics of the EPIC instruments (those used for XXL), which are composed of two MOS-CCD cameras and one pn-CCD camera, are given in Table 3.1. Due to its large effective collecting area, XMM-Newton reaches a high sensitivity. However, complex instrumental effects are affecting the observations[1]: for instance, the PSF and mirror effective area depend of the off-axis angle (vignetting effect), such that the sensitivity drops to $\sim 50\%$ at a $10'$ off axis. They are taken into account as described in Pacaud et al. (2006).

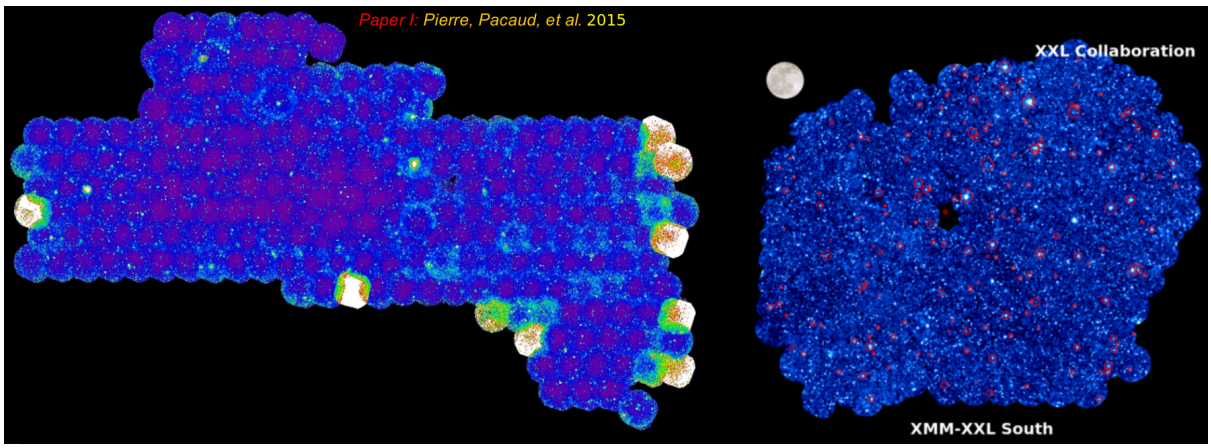

Figure 3.2: Count-rate maps of the XXL-N and XXL-S field. The XMM-Newton field of view is comparable to the size of the Moon ($30'$). Figure from Florian Pacaud (PNCG 2015).

3.1.1.2 XXL survey design

Although XMM-Newton was not designed as a survey instrument, its large field of view, good angular resolution and collecting area provide a unique opportunity to study the X-ray emission over large regions of the sky. The XXL survey was conducted with the EPIC imaging instruments and its observing strategy was to use the mosaic mode[1], which allows for nearby pointings to be scheduled consecutively with reduced instrument overheads. The area covered by the XXL survey is about 50 square degrees divided in two fields of 25 deg^2 each, XXL-North (XXL-N) and XXL-South (XXL-S) of respective centres R.A. = 2h30, Dec. = -4d30' and R.A. = 23h30, Dec. =-55d00 (see Figure 3.2). Those fields were partly chosen because they benefit from an already existing substantial XMM coverage (see XXL Paper I, for more details on the choice of the fields). The XXL observations were thus conducted to enlarge the existing coverage, keeping a separation of $20'$ between the different pointings (except in existing XXL-S pointings were the value was kept to $23'$). The final XXL survey sensitivity is about 10^{-15} erg s^{-1} cm^{-2} in the [0.5-2] keV band (3σ flux limit on point sources). The two XXL fields were also chosen because they benefit from an almost full imaging coverage in the optical, near and far infrared, millimetre and radio, making of XXL an exquisite multi-wavelength survey.

3.1.2 Image construction, source detection and classification

The image construction, source detection, and classification, are explained in details in Pacaud et al. (2006), XXL Paper I and Pacaud et al. (2016), hereafter XXL Paper II. In this section, we give an overview of this processing.

3.1.2.1 Data processing and image construction

The images corresponding to each pointing are produced from the raw observation files using the XMM-Newton Science Analysis Software for each EPIC detectors and energy bands, after filtering solar soft proton flares. The three EPIC images of each pointing are then co-added and wavelet filtering is applied on the resulting image to enhance the signal to noise ratio. Pointings with less than 3 ks of clean observation time or with a high background value (> 4.5 ct/s/pointing in the [0.5-2] keV band) are discarded (note that these are the "usable" limit values, which are slightly less constraining than the "nominal" XXL limits, i.e 7 ks of clean observing time, see XXL Paper I).

[1] See the XMM-Newton Users Handbook for details (http://xmm-tools.cosmos.esa.int/external/xmm_user_support/documentation/uhb/XMM_UHB.pdf)

3.1.2.2 Source detection

Each pointing is processed individually and the sources are detected within a $13'$ radius, using SExtractor (Bertin and Arnouts 1996). Although this software was designed for source detection in the optical, its utilisation is justified by the fact that the the pre-processing filtering removes most of the noise and produces a smoothed background. Cluster searches are performed in the [0.5-2] keV energy band, where the X-ray emissivity is nearly independent of the hot gas temperature.

3.1.2.3 Source characterisation and classification

The XXL cluster selection function is based on a source classification scheme that has been derived following the methodology developed for the XMM-LSS pilot survey and extensively tested on numerical simulations (see Pacaud et al. 2006). The source classification algorithm, XAminP06, determines a model that maximises the probability of generating the observed spatial photon distribution of each source detected by SExtractor. Two template models are tested: one corresponding to the PSF, to account for point like sources (e.g. AGN), and one spherically symmetric β model (with a fixed value of $\beta = 2/3$ Cavaliere and Fusco-Femiano 1976) for extended sources. The count rates, positions and core radii (for extended source only) are fitted for and the classification between extended and point sources is made by comparing the statistics assessing the reliability of the different models. The extended sources are further differentiated in two classes, referred to as C1 and C2, according to their fitted extension and its significance (see figure 5.B in Pacaud et al. 2006). XAminP06 has been tested with Monte-Carlo simulations, which showed that the C1 class is expected to be made of true clusters only, whereas the C2 class, allowing for lower detection level, shows 50% of contamination from point sources before visual inspection. The C2 clusters are thus confirmed a posteriori by, e.g., inspecting their counterparts in the optical.

A new detection and classification pipeline (XAminF18, see Faccioli et al. 2018), was recently developed and is in validation phase. The main improvements are that the detection is conducted on $68' \times 68'$ tiles composed of co-added pointings and that new source models are included, to distinguish clusters with central AGN and pairs of AGN. This detection pipeline, taking advantage of all the observations and accounting for cluster contamination from AGN, will be used for the final XXL data release.

3.1.3 Cluster catalogue construction

As we showed, clusters are detected and characterised with the XAminP06 pipeline, which returns their positions, corresponding to the centroid of their emission, and their classification as C1 or C2. However, further steps are needed in order to build a complete catalogue. Here we briefly present the spectroscopic confirmation process and the cluster parameters estimation methods used to construct the XXL 365 clusters catalogue (XXL-365-GC sample, Adami et al. 2018, hereafter XXL Paper XX).

3.1.3.1 Redshift determination

The moderate depth of the XXL survey does not allow us to derive spectroscopic redshifts from X-ray emission lines. Therefore the cluster redshifts have to be measured with optical data, when a clear galaxy concentration is visible within the X-ray extended emission. The redshifts confirmation of the XXL cluster candidates was presented in XXL Paper XX (see also Section 4.2.2 for more information on the spectroscopic catalogue), using as criteria to have at least three concordant redshifts or having the redshift of the BCG. The mean number of spectroscopic objects used for the validation was six per cluster and 62% of the clusters were confirmed with more than three objects. So far, 302 C1 and C2 clusters were assigned a spectroscopic redshift.

3.1.3.2 Estimation of cluster global properties

The parameters presented in the XXL-365-GC sample catalogue are estimated from direct measurements and from scaling relations (see Section 4 of XXL Paper XX). The two scaling relations used are: the mass-temperature (MT) relation from XXL Paper IV, computed from a sub-sample of 38 XXL clusters with weak lensing mass measurements and 58 additional clusters from the litterature (XXL+COSMOS+CCCP sample); and the luminosity-temperature (LT) relation from Giles et al. 2016 (hereafter XXL Paper III), computed from the 100 XXL brightest cluster sample (XXL Paper II, 100 BCS,). The MT relation is based on weak lensing masses and XXL temperatures, measured by fitting the [0.4-11] keV band spectra of the sources, extracted within 300 kpc (the largest radius within which a temperature could be derived for the entire 100 BCS). It is parametrised by:

$$log\,(M_{500,\mathrm{WL}}\,E(z)) = A_{\mathrm{MT}} + B_{\mathrm{MT}}\,log\,(T_{300\mathrm{kpc}}) \tag{3.1}$$

with $A_{\mathrm{MT}} = 13.57^{+0.09}_{-0.09}$ and $B_{\mathrm{MT}} = 1.67^{+0.14}_{-0.10}$. This relation is also used to estimate the scaled radius $R_{500,MT}$. The LT relation is based on the [0.5-2] keV band X-ray luminosities, measured within physical radii of 300 kpc and extrapolated to $R_{500,MT}$, by assuming that the emission of clusters follow a β model of parameters $r_c = 0.15 \times R_{500,MT}$ and $\beta = 2/3$. The LT relation is parametrised by:

$$\frac{L^{XXL}_{500,MT}}{3 \times 10^{43}\mathrm{erg.s^{-1}}} = E(z)^{\gamma_{\mathrm{LT}}}\,A_{\mathrm{LT}}\left(\frac{T_{300\mathrm{kpc}}}{3\mathrm{keV}}\right)^{B_{\mathrm{LT}}} \tag{3.2}$$

with $\gamma_{\mathrm{LT}} = 1.64 \pm 0.77$, $A_{\mathrm{LT}} = 0.71 \pm 0.11$ and $B_{\mathrm{LT}} = 2.63 \pm 0.15$. In addition, the gas masses $M_{gas,500kpc}$ are measured by extracting surface brightness profiles from the mosaic images of the XXL fields (and not individual pointings), and following the methodology of Eckert et al. 2015 (hereafter XXL Paper XIII) for their de-projection and conversion into gas densities.

Because of the faintness of some sources, it was not possible to obtain direct temperature estimates for all clusters. Parameter values are thus extrapolated from the $[0.5-2]$ keV X-ray count rates collected within a physical radius of 300 kpc, using scaling relations, and following an iterative procedure. First, the counts are converted into luminosities $L^{XXL}_{300kpc,scal}$, assuming certain values of the temperature $T_{300kpc,scal}$. Masses $M_{500,scal}$ and scaled radii $R_{500,scal}$ are then inferred from $T_{300kpc,scal}$ using the MT relation of Equation 3.1. The luminosities are then extrapolated to $R_{500,scal}$ using the same β profile modelling as described above. Finally, the luminosities $L^{XXL}_{500,scal}$ are used to infer a new estimation of $T_{300kpc,scal}$, using the relation of Equation 3.2. This procedure is repeated until the input and output values converge.

3.1.4 The XXL cluster sample

The XXL-365-GC sample associated to the second XXL data release is the last before the final release of the complete XXL cluster catalogue. It contains the complete subset of clusters for which the selection function is well determined, plus all X-ray clusters which are, to date, spectroscopically confirmed. Among the sample, 211 clusters are located in XXL-N and 154 in XXL-S. The sample contains all C1 clusters (207 objects) and the C2 clusters confirmed spectroscopically (119 systems). Thus, the C1 sample is complete (although 24 objects do not have a spectroscopic redshift confirmation yet), while the C2 sample is pure but not complete. Another class of cluster is defined, the C3 class, containing 39 spectroscopically confirmed clusters presenting X-ray emission that is too faint to be detected and classified by the XXL pipeline (their selection function is not defined).

In Figure 3.3, we show the mass versus redshift distribution of the C1 and C2 XXL clusters along with that of X-ray and SZ samples from the literature. We can see that XXL clusters span a wide redshift range, while being less massive in average than other X-ray or SZ selected samples.

Using a sub-sample of 178 C1 clusters with high signal to noise, Pacaud et al. (2018) found a dissension between the cosmological parameters extracted from the XXL cluster number counts

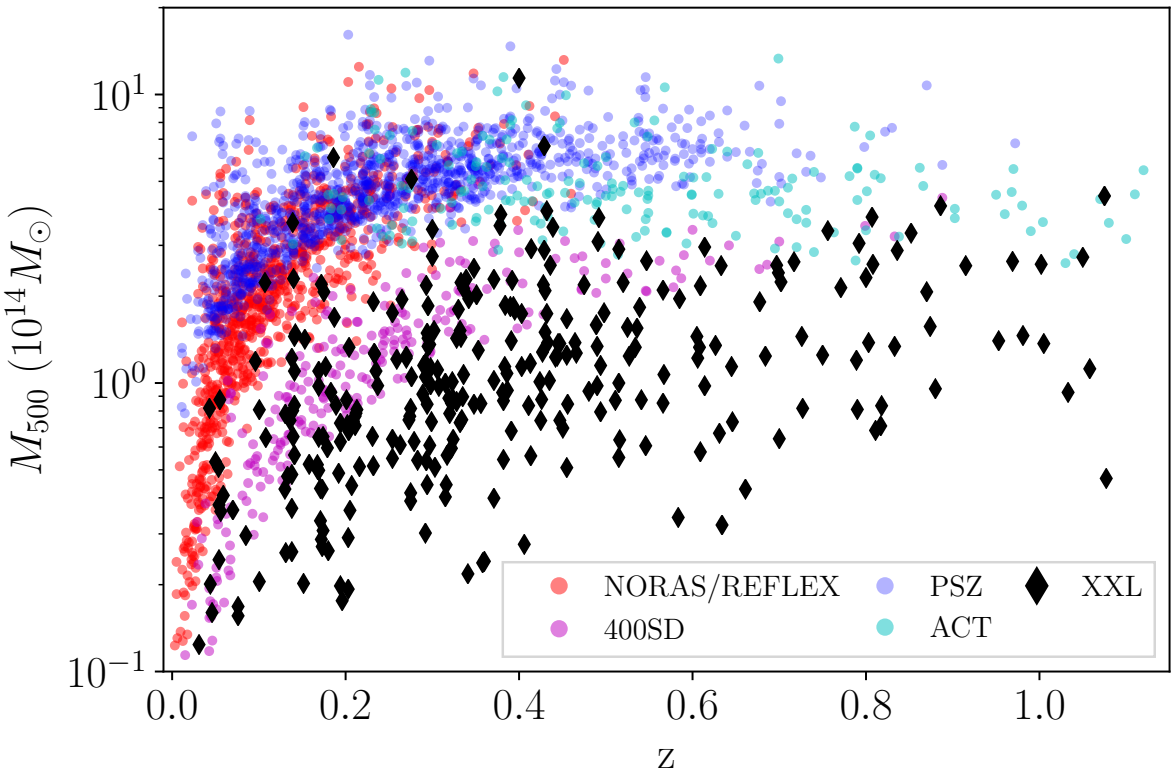

Figure 3.3: Mass – redshift distribution of the C1 and C2 XXL clusters with spectroscopic redshift measurements and comparison to other X-ray and SZ samples. The X-ray samples are extracted from the MCXC meta-catalogue (Piffaretti et al. 2011): clusters from the NORAS and REFLEX samples are shown in red and clusters from the the 400SD sample are shown in magenta. The two SZ samples are taken from the Planck SZ catalogue (Planck Collaboration et al. 2016b, blue points) and the ACT catalogue (Hilton et al. 2018, cyan points). The masses used are the ones provided in each catalogue. The XXL masses are computed from scaling relations. The maximum redshift is set to 1.15 and the minimum mass to 0.1×10^{14} $M_\odot$.

(dn/dz) and that of the Planck CMB (as already seen in XXL Paper II, using a smaller cluster sample), similar to that between the Planck CMB and the Planck SZ cluster sample parameters (Planck Collaboration et al. 2014b).

3.2 The CFHTLS survey as an optical counterpart of XXL-N

The XXL-N field corresponds to a region covered mostly in the optical and near infrared by the Canada France Hawaii Telescope Legacy Survey (CFHTLS, Gwyn 2012) and by the Hyper Suprime-Cam Subaru Strategic Program Survey (HSC-SSP survey, Aihara et al. 2018, still ongoing). In the south, the optical and near infrared observations comes from the Blanco Cosmology Survey (BCS, Desai et al. 2012) and the Dark Energy Survey (DES, The Dark Energy Survey Collaboration 2005, still ongoing). In this thesis we used data from the CFHTLS, which gives a good compromise between survey maturity and depth, to study the optical counterparts of XXL-N clusters.

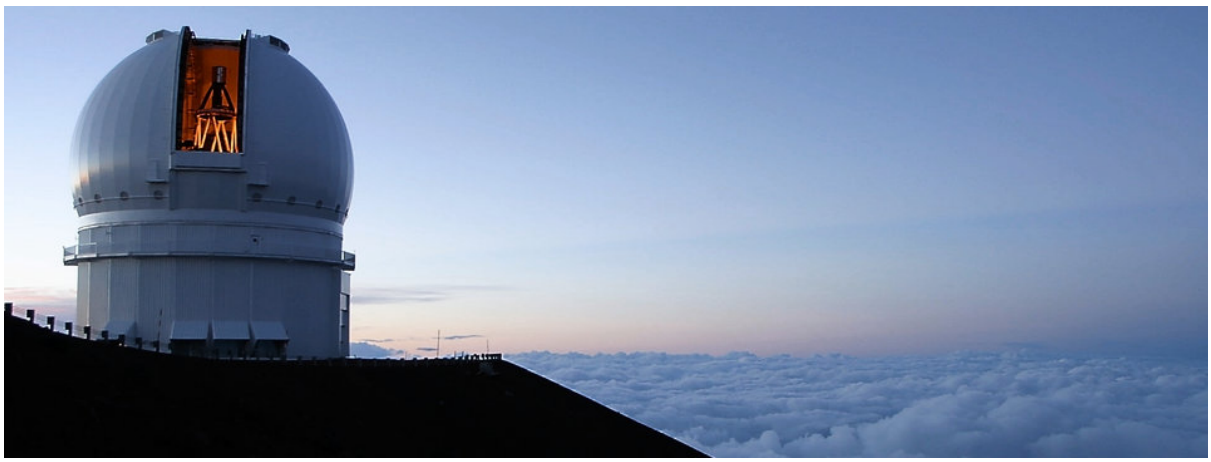

Figure 3.4: View of the Canada-France-Hawaii Telescope at the top of Mauna-Kea. Image from http://www.cfht.hawaii.edu/fr/.

Table 3.2: Mains characteristics of the photometry in the CFHTLS W1 field. The values are taken from the T007 release document (Hudelot et al. 2012, http://www.cfht.hawaii.edu/Science/CFHLS/T0007/CFHTLS_T0007-TechnicalDocumentation.pdf)

parameters	u^*	g'	r'	i'	z'
Seeing [″]	0.84 ± 0.11	0.77 ± 0.10	0.70 ± 0.07	0.65 ± 0.08	0.69 ± 0.13
80% compl. stellar	25.27 ± 0.21	25.52 ± 0.18	25.03 ± 0.16	24.73 ± 0.18	23.90 ± 0.26
80% compl. extended	24.45 ± 0.15	24.67 ± 0.14	24.00 ± 0.10	23.69 ± 0.13	22.91 ± 0.15
Mag. err. [mag]	0.05 ± 0.01	0.03 ± 0.01	0.03 ± 0.01	0.03 ± 0.01	0.04 ± 0.01

3.2.1 Overview of the CFHTLS

The CFHTLS is conducted with the optical and near infrared wide field imager MegaCam[2]. The camera is mounted at the prime focus of the Canada-France-Hawaii telescope, a 3.6m telescope situated at an altitude of 4200 m on top of Mauna Kea in Hawaii (see Figure 3.4). The CFHTLS is composed of two surveys of different depth and area: the Deep Survey, split in 4 regions of 1 deg^2 each, reaching a 80% completeness limit of $i' = 25.4$ in AB magnitude for point sources, and the Wide Survey, split in 4 regions of about 155 deg^2 in total, reaching a 80% completeness limit in AB of $i' = 24.8$ for point sources (see Hudelot et al. 2012, for more details). In this study, the data are taken from the W1 field of the Wide Survey, which covers about 64 deg^2 and overlaps most of the XXL-N survey. The main characteristic of the W1 field are presented in Table 3.2.

3.2.2 Photometric catalogue

The CFHTLS is conducted in five passbands: u^*, g', r', i' and z', from approximately 300 to 1000 nm (see Figure 3.5). The image stacking, calibration and catalogue extraction was performed by the Terapix data centre. We used the last version of the release, T007, which, compared to the previous releases, provides better image quality and flux measurement precision, due to improved flat-fielding and photometric calibration techniques (see Hudelot et al. 2012). The source detection is made by SExtractor (Bertin and Arnouts 1996) on composite $g'r'i'$ images and the flux of the sources is then measured in each band using the same aperture. This technique provides reliable fluxes as the aperture is constant in each band, but may however lead to miss distant objects that appear only in the z' band (see Szalay et al. 1999).

[2]See http://www.cfht.hawaii.edu/Instruments/Imaging/Megacam/.

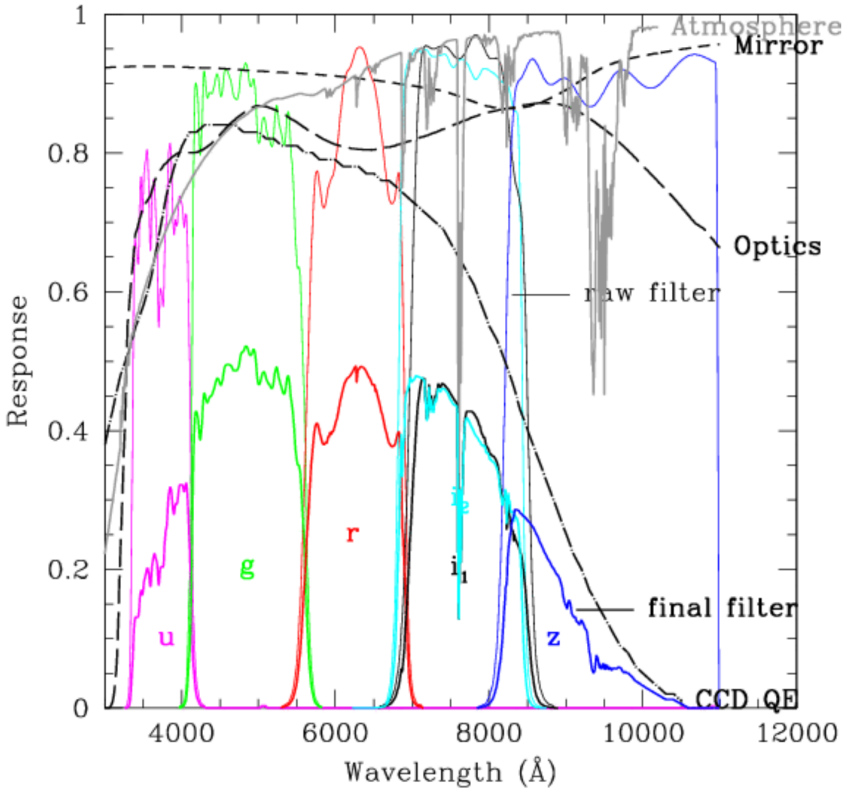

Figure 3.5: MegaCam $u^*g'r'i'z'$ filter set. The light-coloured lines show the final (thick) and raw (thin) response of the filters. The labeled black lines show the response of the primary mirror, the optics and the quantum efficiency of the CCDs. The Figure is taken from the Canadian Astronomy Data Centre website (http://www.cadc-ccda.hia-iha.nrc-cnrc.gc.ca/en/megapipe/docs/filtold.html).

The masking of bright stars and image defects over the W1 CFHTLS field was performed in a semi-automatic way (Benoist et al. in prep.). Standard polygons, with a cross shape designed to enclose stellar spikes, were created for all stars brighter than $i' = 16$. Polygons sizes are proportional to the star magnitude following an empirical relation validated by visual inspection. For the brightest stars and associated ghosts or for other types of defects (satellite trails, missing chips, field edges, etc.), polygons were designed by hand in order to optimise the effective area to cross-match X-ray and optical data. The final catalogue contains only unmasked objects and the magnitude used is `MAG-AUTO` (Kron 1980), which is well suited for galaxy studies.

3.3 Optical and X-ray view of XXL clusters

In this section, we present an optical and X-ray view of a selected sample of XXL clusters, in order to give a flavour of the X-ray and optical properties of the entire sample. The clusters were selected from the list of C1 and C2 clusters from the XXL-365-GC sample with spectroscopic redshift and falling in the CFHTLS W1 field (hereafter the XXL+W1 sample, see details in Section 5.2.1).

Figure 3.6 shows the optical MegaCam composite $g'r'i'$ images of XXL clusters with X-ray contours taken from the XXL database[3] and drawn from wavelet filtered X-ray images overlaid

[3] http://xmm-lss.in2p3.fr:8080/xxldb/login.jsp

Table 3.3: Main characteristics of the selected sample of XXL clusters shown in Figure 3.6. The redshifts are measured from optical spectroscopy, the masses are estimated from scaling relations, and the richnesses are computed in 0.5 Mpc (see Section 5.3.4.3 for definition).

name	z	class	$M_{500,scal}$	$\lambda_{0.5Mpc}$	comments
	–	–	$\times 10^{14}$ M$_\odot$	–	
XLSSC041	0.14	C1	1.5 ± 0.4	6 ± 3	
XLSSC091	0.19	C1	6.0 ± 2.0	45 ± 7	richest and second most massive cluster in our sample
XLSSC141	0.20	C2	0.2 ± 0.1	1 ± 1	very poor group
XLSSC098	0.30	C1	1.4 ± 0.4	11 ± 4	
XLSSC170	0.40	C2	1.1 ± 0.3	24 ± 5	
XLSSC006	0.43	C1	6.6 ± 2.4	36 ± 6	two BCGs
XLSSC083	0.43	C1	2.1 ± 0.6	26 ± 5	part of a super-cluster
XLSSC105	0.43	C1	4.0 ± 1.3	33 ± 6	two BCGs
XLSSC116	0.53	C2	1.3 ± 0.4	22 ± 5	
XLSSC188	0.57	C2	0.1 ± 0.2	1 ± 2	likely to be a missclassified point source [a]
XLSSC038	0.58	C2	0.3 ± 0.1	3 ± 3	very poor group
XLSSC029	1.05	C1	2.7 ± 1.2	17 ± 8	

[a] This appears to be the case for two C2 clusters in our sample. This object was assigned a spectroscopic redshift based on one galaxy only.

in magenta. We also indicate the brightest cluster galaxy (see Section 5.3.3.1 for their selection) and the spectroscopic members of each cluster as the yellow circle and cyan diamonds.

The properties of the cluster shown in Figure 3.6 are presented in Table 3.3. For comparison, we give the first, second and third quartiles of the redshift, mass and richness distributions of the full XXL+W1 sample: $z = [0.23, 0.34, 0.51]$, $M_{500,scal} = [0.7, 1.1, 1.5] \times 10^{14}$ M$_\odot$ and $\lambda_{0.5Mpc} = [7, 12, 19]$. As we can see from Figure 3.6, XXL systems display a large variety of properties, from very loose groups, hardly associated to any galaxy concentration, to rich clusters showing perturbed dynamical state, as can be inferred from their X-ray emission and member galaxies. This diversity, coupled to a large mass and redshift range, allows us to investigate clusters and cluster galaxies at different stages of their formation. This is highly valuable to study their physical properties and test their impact on the detection, selection function and mass characterisation of clusters.

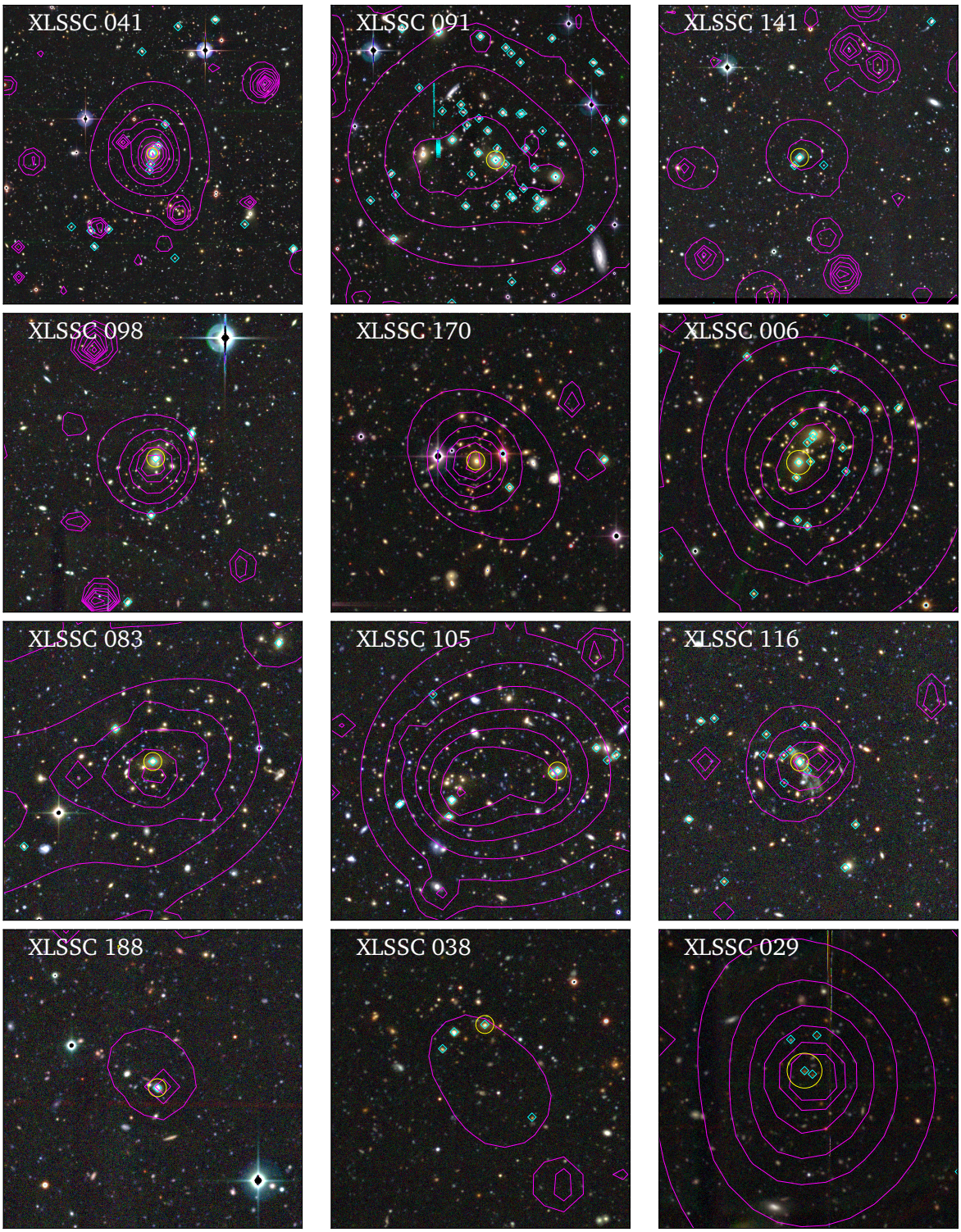

Figure 3.6: Gallery of a selected sample of XXL clusters, ordered by increasing redshift from upper left to bottom right. The corresponding properties are presented in Table 3.3. X-ray XXL contours drawn from wavelet filtered X-ray images are over-plotted in magenta on 0.5×0.5 Mpc^2 composite $g'r'i'$ MegaCam images from the CFHTLS survey. The cyan diamonds indicate galaxies with spectroscopic redshifts around the cluster spectroscopic redshift and the yellow circle indicate the brightest cluster galaxies (see Section 5.3.3.1 for their selection).

Chapter 4

Selecting galaxies using photometric redshifts in the CFHTLS-W1 field

Contents

Abstract: Photometric redshifts are now widely used for cosmological and astrophysical analyses. These applications require a strict control of any systematic effect in their estimation and utilisation. In this Chapter we present an unbiased method, in terms of redshift and magnitude, for selecting galaxies based on their photometric redshifts, latter used to study the galaxy population in clusters. This technique is applied to the CFHTLS-W1photometric sample and was used in Ricci et al. (2018) to investigate the luminosity function of clusters. We first introduce the different methods to derive photometric redshifts and the characteristics that drive their quality. We then present the data we use and our evaluation of the photometric redshift quality in the CFHTLS-W1 field, focusing on both redshift and magnitude dependences. Finally, we define and test the galaxy selection methods and conclude on the photometric redshifts limitations.

4.1 Introduction

Cosmological and astrophysical analyses using galaxies generally require information on their distances. Those can be derived from the galaxy spectrum, if spectroscopic observations are

available. However, if the current photometric galaxy surveys contains billions of objects, spectroscopic ones are more difficult to obtain, as the integration time required to obtain a reliable spectrum at a given depth is much higher than the one needed for an image. This motivated the utilisation of redshift measurements extracted from photometry, the so-called "photometric redshifts", when spectroscopy is unavailable or incomplete. The first idea of photometric redshift emerged from the observation of the link between galaxy colours, magnitude and distances (Baum 1962), using elliptical cluster galaxies. Since then, many developments regarding photometric redshift estimations have been carried out, but the methods are still mainly based on the detection of strong spectral features in the galaxy spectral energy distributions (SEDs), for instance the 4000Å break, the Lyman and Balmer dropouts or strong emission lines.

Photometric redshifts are widely used in cosmological analyses. They are a key ingredient of weak lensing tomography (see e.g. Ma et al. 2006), galaxy and cluster clustering (see e.g. Crocce et al. 2016; Sridhar et al. 2017), galaxy cluster detections and weak lensing cluster mass measurements (see e.g. Medezinski et al. 2018). In this thesis, the selection of galaxies using photometric redshifts will be essential for cluster galaxy luminosity function analysis (see Chapter 5) and cluster detection (see Chapter 8 and Appendix A). Therefore their quality has to be thoroughly assessed to control any associated systematic effects.

4.1.1 The different methods to derive photometric redshifts

Two main approaches are used to derive photometric redshifts: one based on SED template fitting and one that is empirical (see e.g. Walcher et al. 2011; Salvato et al. 2018, for reviews). Photometric redshift algorithms based on template fitting include, e.g., HyperZ (Bolzonella et al. 2000), BPZ (Benítez 2000) and ZEBRA (Feldmann et al. 2006); examples of empirical codes are ANNz (Collister and Lahav 2004), ArborZ (Gerdes et al. 2010), Random Forests (Carliles et al. 2010); and some others, such as EAZY (Brammer et al. 2008), GOODZ (Dahlen et al. 2010), or LePhare (Arnouts et al. 1999; Ilbert et al. 2006), use a combination between the two methods. Another approach, with different aims, is based on galaxy cross correlation. We present here those different techniques.

Empirical methods Empirical methods to derive photometric redshifts are based on the utilisation of a spectroscopic sample as a training set, to derive the relation between redshifts and photometric observables, such as magnitudes, colours, surface brightness or even light profiles (see e.g Wray and Gunn 2008). This requires that the training set is representative, in terms of redshift range, photometry, galaxy type and so on, of the population for which we want to measure the redshifts. The algorithms that are based on this empirical approach often use machine learning methodologies (such as "neural networks" or "regression trees") and some of them can return the redshift probability distribution functions (PDF_z).

Template fitting methods Another class of photometric redshift algorithm relies on the matching between the photometric properties of objects (essentially fluxes and/or color) with the properties extracted from a set of template SEDs (see Figure 4.1 for an illustration of SED reconstruction). The SEDs are derived either from real observations or from galaxy evolution models, and are shifted at different redshifts and convolved with the transmission curves of the filters used in the photometric surveys to build the final set of templates. This class of algorithms mainly uses a χ^2 minimisation and/or Bayesian inference and usually returns a best fit template and redshift, and often the PDF_z. These methods require the template set to be fairly representative of the galaxy diversity in the photometric sample, but to a lower extent than empirical methods. As they are sensitive to the photometric calibration and bandpass, they have the disadvantage of propagating any uncertainty in their measurements.

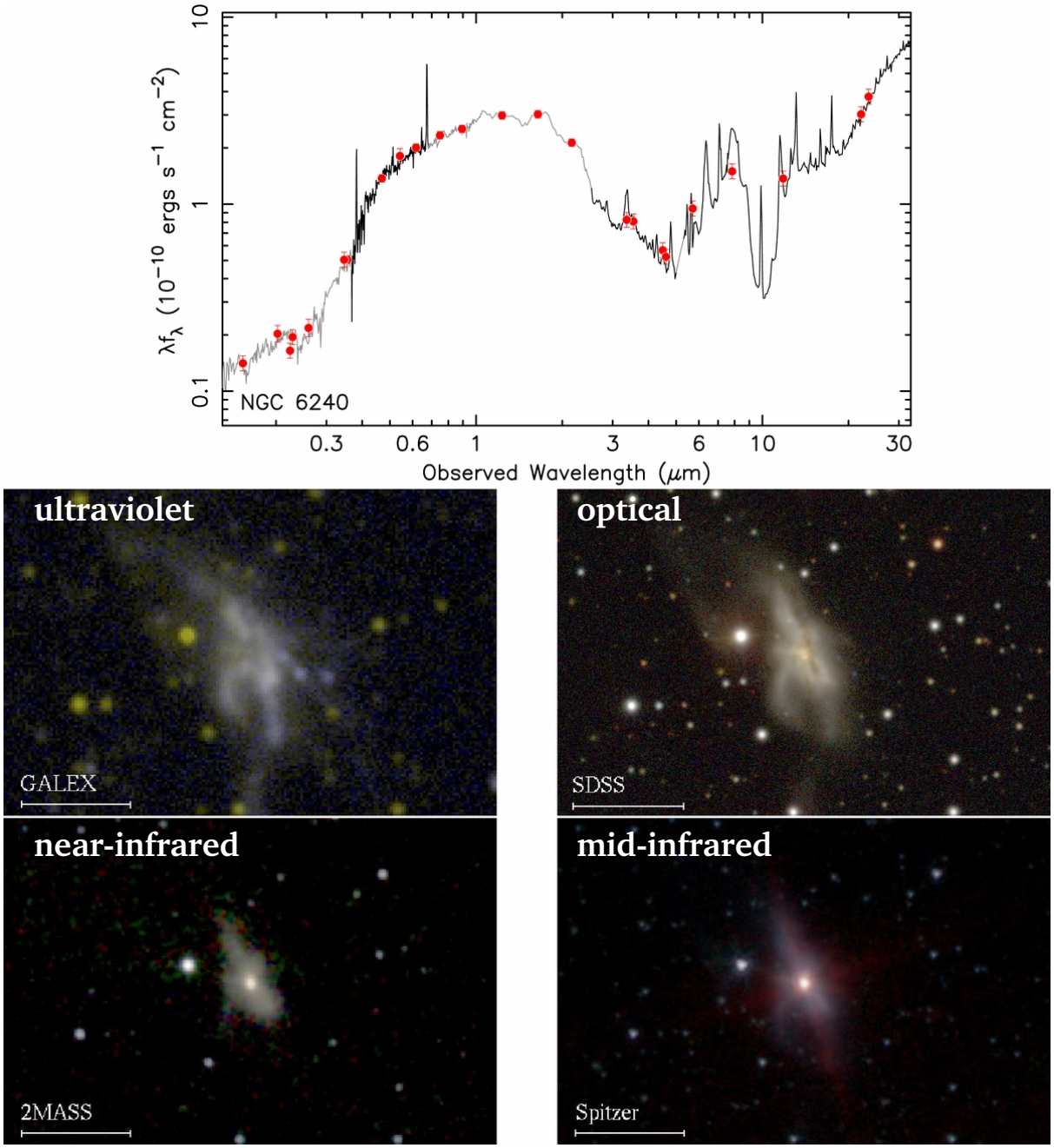

Figure 4.1: Illustration of SED fitting (figure from Brown et al. 2014): ultraviolet to mid-infrared SED of the galaxy NGC 6240 (*top panel*), along with some of the GALEX, SDSS, 2MASS, and Spitzer images that were used to constrain and verify the SED (*bottom panel*). The horizontal bar denotes an angular scale of 1′. In the top panel, the observed and model spectra are shown in black and grey, respectively, while the photometry used to constrain and verify the spectra is shown with red dots.

Hybrid methods The hybrid approach combines the advantages of empirical and template fitting based methods. Usually, the algorithms use template fitting techniques that are optimised using a spectroscopic training set. This can allow, for example, to calibrate the SED template set, remove photometric systematic offset or introduce priors on the redshift distribution. Hybrid algorithms generally perform better than the traditional one (see e.g., Ilbert et al. 2006, in the case of LePhare). Empirical and template fitting methods can also be combined to explore different regions of the parameter space of the same data set: e.g. the use of empirical methods where training sets can be obtained, and template fitting methods otherwise.

Cross correlation methods As the positions of galaxies are correlated with each other (galaxies are not randomly distributed), one can use the angular "cross-correlation" between galaxies to infer the redshift distribution of a photometric sample, from a spectroscopic reference sample. The idea of using the apparent clustering of objects on the sky was first developed by Seldner and Peebles (1979) and updated latter in the context of large cosmological surveys (see, e.g., Newman 2008; Ménard et al. 2013; Scottez et al. 2018). The main advantage of this method is that the reference sample does not have to be representative of the full photometric sample and can even be made of highly accurate photometric redshifts. However, these methods can only be used to derive the redshift distribution of a population of galaxies and are not adequate to select single objects.

4.1.2 Quality of the photometric redshifts

Photometric redshifts are hampered by larger uncertainties than spectroscopic ones and they are preferably used for the statistical studies of large samples. Here, we review some of the main aspects that affect their accuracy. The latter is assessed by measuring their dispersion and bias with respect to the true redshifts, and by evaluating the fraction of catastrophic failures, that is, objects for which the photometric redshift strongly deviates from the true value. All quantities have to be as low as possible.

Effect of the set of photometric bands As photometric redshift fitting techniques rely on strong spectral features in the SEDs, they heavily depend on the photometric band set that is used, in particular the number of filters and their wavelength coverage. In general, the more numerous and narrower the filters, the more accurate the photometric redshifts (see for instance Ilbert et al. 2009, for photometric redshifts derived from the 30 bands of the COSMOS survey, in which case photometric redshifts can be seen as redshifts from very low-resolution spectroscopy). The wavelength coverage of the filter set drives the redshift domain over which photometric redshifts can be accurately constrained (see e.g. Bolzonella et al. 2000; Ilbert et al. 2006, and Figure 4.2). For instance, because of the spectral features in the SEDs of galaxies, optical filters from ~ 450 to ~ 800 nm (e.g. g',r' and i') are able to measure photometric redshifts between approximately $0.2 < z < 1$, NIR is needed for the range $1 < z < 2.2$, and u band filters are required to increase the accuracy at $z < 0.2$, and if deep enough, to measure redshifts beyond $z \sim 3$. Different types of galaxy at different redshifts can have the same colour, which induces degeneracies in the colour/redshift distribution (Benítez 2000). Hence, the lack of data in a given wavelength regime can also affect the results in another redshift domain and lead to catastrophic failures in the photometric redshift identification. Disentangling between the different solutions requires to expand the wavelength coverage of the photometric set and/or to include priors in the algorithm.

Effect of the galaxy type Photometric redshift fitting measurements rely on the ability of an algorithm to detect strong spectral features in the SEDs of the objects. Therefore, photometric redshifts are easier to derive for galaxies which present a strong break in their continuum

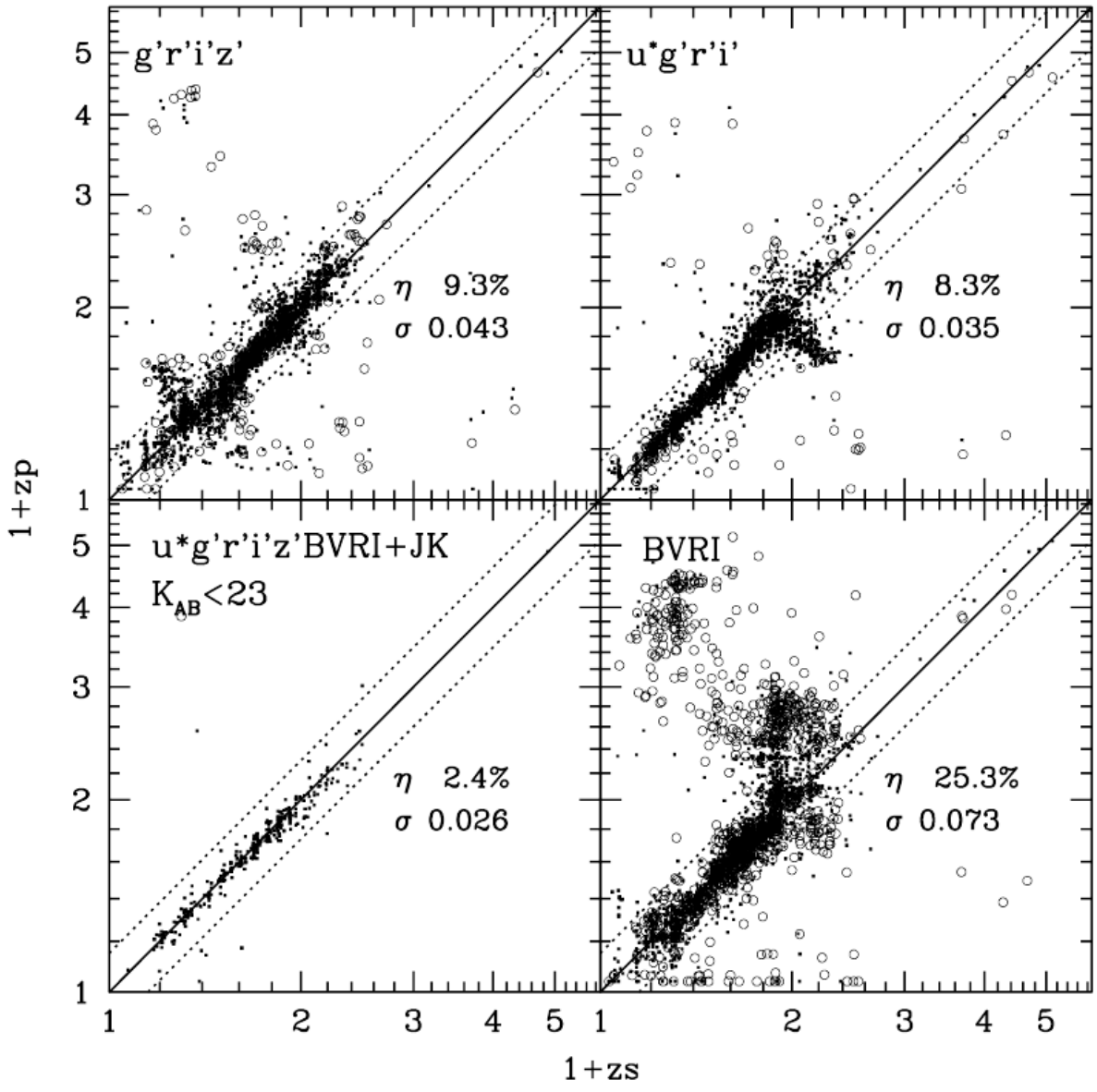

Figure 4.2: Illustration of the effect of the photometric band set (figure from Ilbert et al. 2006): Comparison between spectroscopic and photometric redshifts for different combinations of filters. *Top panels:* photometric redshifts computed without using the deep u^* (*left*) and z' (*right*) band. *Bottom left panel:* photometric redshifts for a near-infrared selected sample computed using B, V, R, I, u^* , g' ,r' , i', z' , J and K bands. *Bottom right panel:* photometric redshifts obtained using the B, V, R, I bands from the VVDS survey.

spectra. For instance, the photometric redshift dispersion is lower for elliptical galaxies (see e.g., Ilbert et al. 2006). In the case of empirical methods, galaxy populations that are not represented in the training sample will have wrong redshift estimates, the same applies for SED template based methods, as the template set has to be characteristic of the galaxy diversity in the photometric sample (see e.g. Benítez 2000). In general, template sets that are based on observed SEDs perform better than the ones derived from galaxy evolution model (see e.g., Yee 1998).

Effect of the signal to noise of the photometry The dispersion of the photometric redshifts obtained with template fitting methods is strongly sensitive to the photometric uncertainties (see e.g. Bolzonella et al. 2000; Ilbert et al. 2006). In the latter study, the authors found that the fraction of catastrophic errors was higher and the redshift accuracy lower for faint galaxies at all redshifts in the CFHTLS Deep Surveys. The same tendencies also apply to empirical methods, even when the photometry is not the only property that is being used (see e.g Wray and Gunn 2008). One has to note that this intrinsic signal to noise effect translates to a magnitude dependence of the photometric redshift quality, which depends on the photometry of each survey.

Effect of the redshift The accuracy of photometric redshifts is known to decrease with increasing redshift. For instance, Fernández-Soto et al. (1999) remarked that the photometric redshift dispersion, compared to spectroscopic ones, was increasing by a factor of $(1+z)$. Since then, the accuracy of the photometric redshifts is often expressed after normalising by this factor, although it is empirically rather than physically motivated. More generally, several factors impact the photometric redshift quality as a function of true redshift. Firstly, it depends on the galaxy spectral type and the photometric band set that is used: the accuracy may be degraded in regions that are subject to degeneracies, and improved when continuum features are better straddled by the photometric bands. Secondly, the photometric errors are generally large for high redshift objects because of low signal to noise and blending issues. Finally, the training and SED template sets are often based on observation of local galaxies, that may not be fully representative of the high redshift objects.

4.2 Catalogues construction

4.2.1 Photometric redshifts catalogue

The estimation of the photometric redshifts in the CFHTLS W1 survey was made using LePhare (see Ilbert et al. 2006; Coupon et al. 2009). LePhare is a `Fortran` code that computes photometric redshifts using SED fitting. An optimisation procedure, based on a spectroscopic training sample, is also performed. Firstly, the best fit SED templates of the training sample objects are determined, while keeping the redshift fixed to their spectroscopic values. Then, systematic offset between observed and predicted fluxes are corrected. The observed median rest frame SEDs of the training sample objects are constructed and compared to the theoretical SED, which are then optimised accordingly.

The training sample used for the photometric redshift determination of W1 field in the T007 CFHTLS release contained ~ 4600 galaxies from the VVDS Deep survey[1]. The set of SED templates used for the photometric redshifts computation was constructed using elliptical, spiral (SBc and Scd) and irregular galaxy templates from Coleman et al. (1980), and two star-forming galaxy templates from Kinney et al. (1996), given in the AVEROI_NEW LePhare SED package (as in Arnouts et al. 2007, see Figure 4.3). These six SEDs were then interpolated to produce a set of 62 templates. The SEDs were then redshifted onto a grid of interval $\Delta z = 0.04$ and

[1] http://cesam.oamp.fr/vvdsproject/vvds.htm

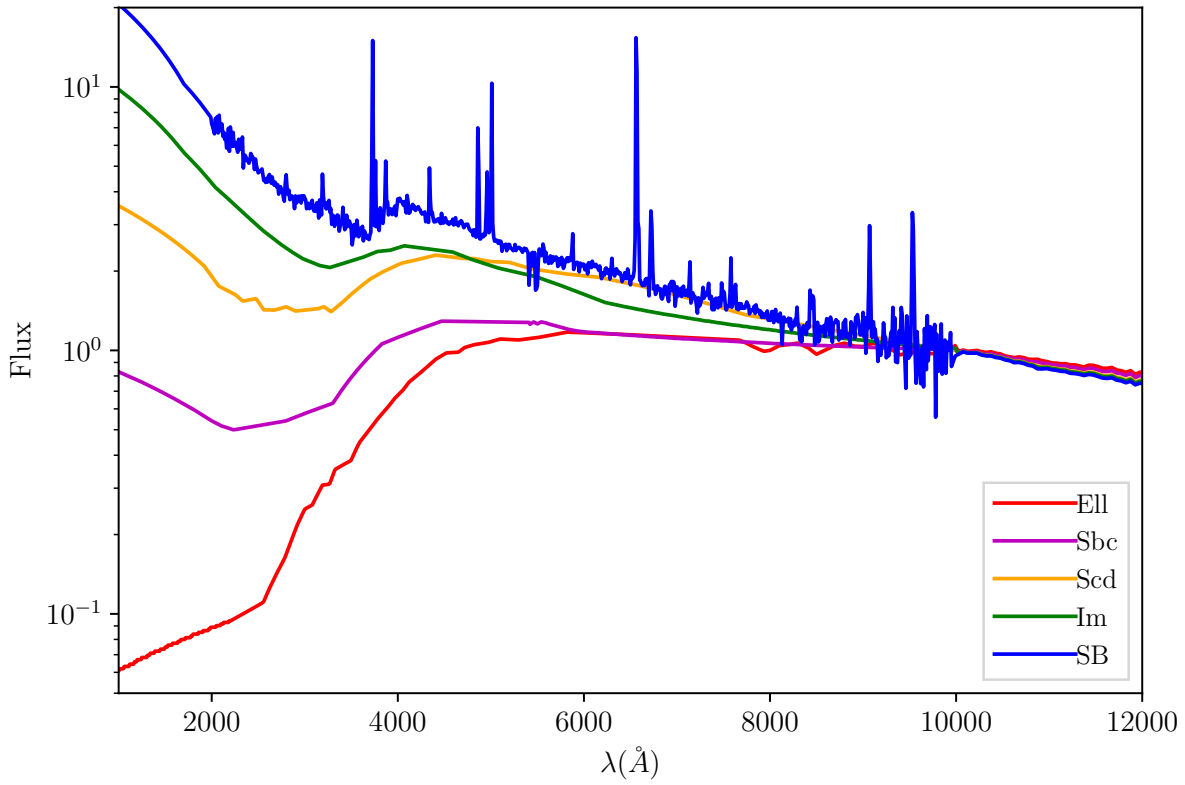

Figure 4.3: SED templates used for the photometric redshift computation with LEPHARE. The two starburst templates are similar in this wavelength range.

convolved with the filter transmission curves (including the instrument efficiency). The best fit photometric redshift and SED template were found by performing a χ^2 minimisation procedure. The same procedure was used to construct the PDF_z for the best fit SED template. A bayesian prior was applied to account for the degeneracy linked to the lack of NIR data.

The statistical choice to get discrete photometric redshift values from the PDF_z was to take its median value z_{PDF} instead of the mode of the distribution $z(\chi^2_{\rm min})$, because it limits the risk of preferred solutions in narrow redshift ranges, as suggested in the T007 photometric redshift release explanatory document[2].

A star/galaxy classification is also provided by using only a size criteria for bright objects and by adding best fit SED criteria for fainter objects. Wrong estimations lead to a contamination of about 1% of stars in W1 and an incompleteness of galaxies of about 2.6%, for objects with $i'_{AB} < 22.5$ (see Coupon et al. 2009).

Only the objects with photometric redshift computed with at least three photometric bands, a χ^2/dof value lower than 100, and a galactic type of SED, were included in the final catalogue. This catalogue was then cut at a magnitude of $i' = 24$.

4.2.2 Spectroscopic redshifts catalogue

The XXL spectroscopic data set used in this study is composed of several surveys and follow-ups conducted on the XXL-N field. It is described in details in XXL Paper XX and XXL Paper XXII (hereafter XXL Paper XXII), but a brief overview is given below.

A large ESO program has been performed for XXL spectroscopic follow-up and cluster redshift confirmation. Beside this program, several dedicated projects have been conducted by the

[2] http://cesam.lam.fr/cfhtls-zphots/files/cfhtls_wide_T007_v1.2_Oct2012.pdf

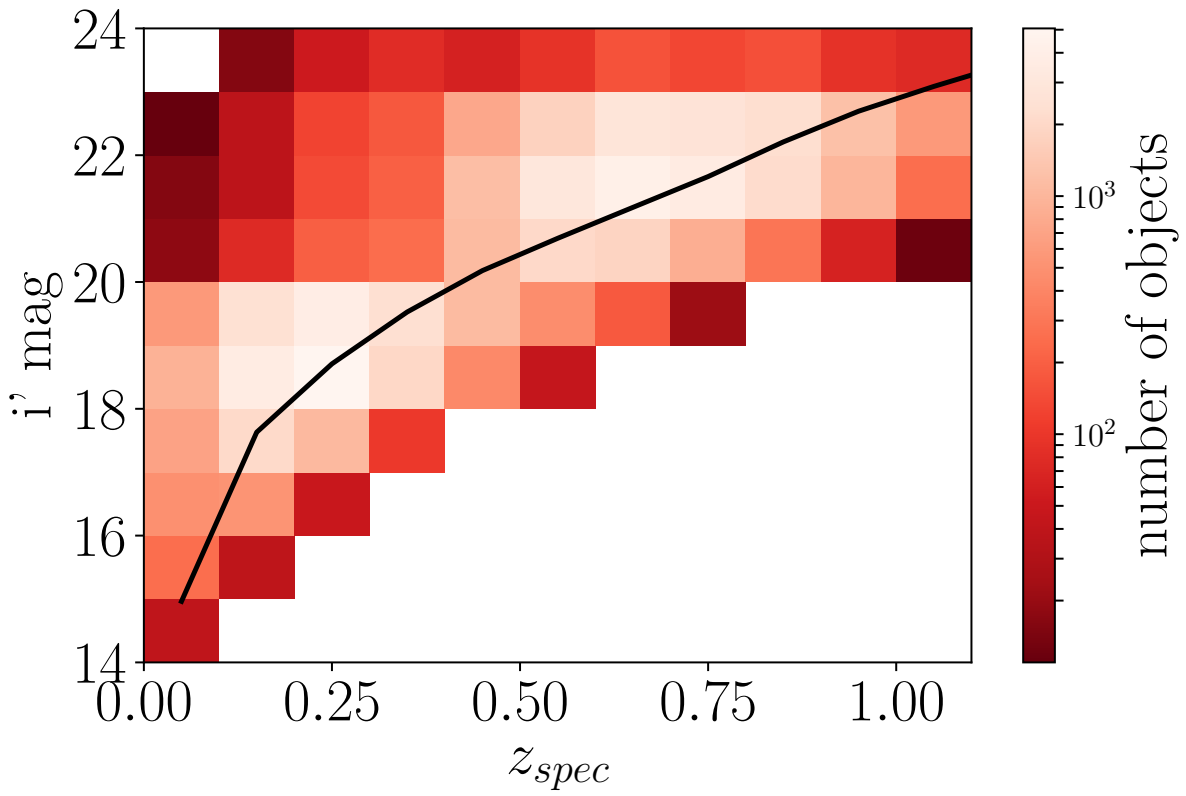

Figure 4.4: Number of objects with high quality spectroscopic measurements as a function of spectroscopic redshift and magnitude in the i' band. Only cells with more than 10 objects are represented. The black line represents a fiducial evolution model for m^*.

members of the XXL consortium. The two major surveys available in the XXL-N field are the VIMOS Public Extra-galactic Redshift Survey (VIPERS[3]) and the AAOmega GAMA survey[4]. They overlap 16 and 23.5 square degrees of XXL-N, respectively. Other sources come mainly from VVDS Deep and the SDSS DR10 surveys. All these surveys are photometrically selected ones and have different depths. VIPERS objects are selected using colour-colour diagrams to focus on galaxies between z = 0.5 and 1.2 with a limiting magnitude $I_{AB} = 22.5$. The other surveys have the following limiting magnitudes: $K_{AB} < 17.6$ for GAMA (Baldry et al. 2010), $I_{AB} = 24.75$ for VVDS Deep, and $g = 23$ for the SDSS-DR10 (York et al. 2000). All the spectroscopic data were taken from the CESAM[5] database.

Quality flags are available for the majority of surveys, albeit having different definitions, as indicated in Table 4.1. No quality flags are available for the spectra coming from SDSS, Subaru, Alpha compilation, and NED.

4.2.3 Spectro-photometric catalogue

The photometric and spectroscopic catalogues were matched according to their sky positions (right ascension and declination), allowing a maximal distance of one arc second. Multiple matches were treated by taking the nearest object. This procedure resulted in about 3% of the photometric objects having spectroscopic counterpart and a matched catalogue containing about 107500 objects.

[3] http://vipers.inaf.it/
[4] http://www.gama-survey.org/
[5] http://www.lam.fr/cesam/

Table 4.1: Definition of the spectroscopic redshift quality flags. They correspond to the last digit of the flag associated to each spectra (other digits indicate complementary information, e.g. if the source is an AGN or was found serendipitously).

Quality flag	Corresponding error probability
0	100%
1	50%
2	25%
3	5 %
4	1%
9	only one spectral line, equivalent to 25% of error probability

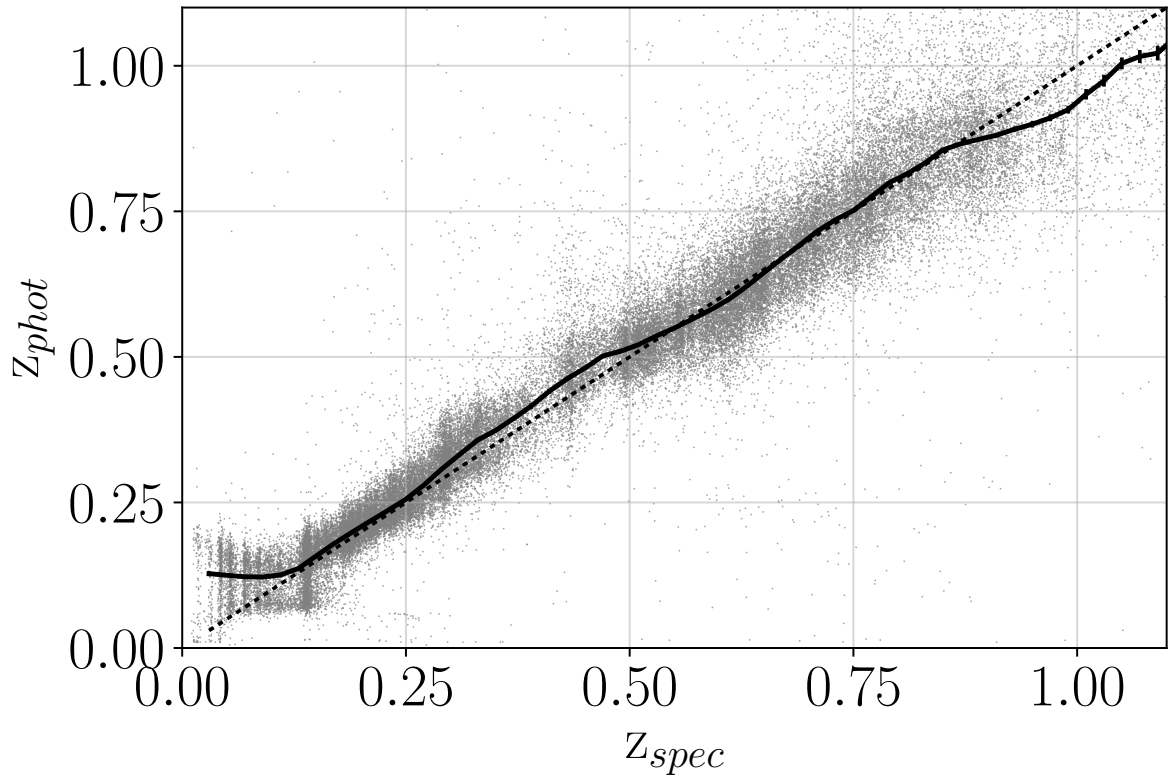

Figure 4.5: Relation between the photometric and spectroscopic redshifts, including all objects with a secure spectroscopic measurement. Each grey point represents a galaxy, the black line indicates the bias $b(z_{spec})$ and its error computed using equation 4.2 (only distinguishable at high redshift). The dotted dashed black lines indicates $z_{phot} = z_{spec}$ for visualisation purpose.

The resulting spectro-photometric sample is highly dominated by GAMA at $z < 0.5$ (28% of the catalog) and VIPERS at $z > 0.5$ (57% of the catalog). Other contributions come from VVDS (at 4%), SDSS (at 4%) and 24 other origins (with less than 2% of objects each).

The spectro-photometric catalogue presents 1% of objects with $z_{spec} < 0.003$. This is the highest recession velocity known for a star and is compatible with the 1% star contamination found by Coupon et al. (2009) in W1. Therefore, those objects can either have a wrong spectroscopic redshift or being stars that are missclassified as galaxies. We verified that they do not show any special trend in their photometric properties.

We homogenised the spectroscopic quality flags in order to have equivalent quality definitions. In the following analysis, we discarded objects with quality flags corresponding to more than 5% chances of having a false spectroscopic redshift, objects without quality information and objects with aberrant spectroscopic redshifts or flags (we kept objects with a quality flag of 3 and 4 in Table 4.1). The resulting high quality sub-sample includes 61% of the objects (65 183) from the spectro-photometric catalogue.

Figure 4.4 shows the number of objects in the high quality sub-sample of the spectro-photometric catalogue, as a function of redshift and magnitude in the i' band. The black line represents an evolution model for the characteristic magnitude m^* (see details in Chapter Conventions used in this thesis). Figure 4.5 shows the comparison of photometric to spectroscopic redshifts for all galaxies from the high quality sub-sample.

4.3 Measurement of the photometric redshift quality

The quality of the photometric redshifts obtained with LePhare in the W1 field of the CFHTLS survey has been assessed in e.g. Coupon et al. (2009) and the T007 photometric redshift release explanatory document[2]. Those studies showed that the dispersion of the photometric redshift was of the order of $\sigma = 0.04(1 + z)$ while the outliers fraction was $\sim 3\%$ for objects with $i'_{AB} < 22.5$, and that the accuracy was declining when considering fainter objects. They found that the bias was below 1% for objects verifying $i'_{AB} < 22.5$ and that the 68% confidence intervals extracted from the photometric redshift probability distribution function were correctly estimated in average. However, the spectroscopic catalogue used for calibration by Coupon et al. (2009) contained only 3356 galaxies and the one used in the T007 study only 8543. Those relatively small samples limited the investigation, in particular, the quality dependence on redshift and magnitude was not evaluated separately. Moreover, as the spectroscopic samples were used for the SED optimisation and the systematic offset correction, the accuracy derived may be overestimated.

As we now benefit, in the context of the XXL project, from a large associated spectroscopic catalogue that spans a wide range of redshifts, galaxy types, colours and magnitudes, we investigated the magnitude and redshift dependencies of the photometric redshift statistics. We used the spectrophotometric catalogue described in Section 4.2.3, selecting only secure spectroscopic redshifts (using the high quality sub-sample). As this sample contains much more objects than the training sample used for optimisation, we assumed that the derived quality would not be biased. In all the following analysis, the error on spectroscopic redshifts were considered as negligible, with respect to that on photometric redshifts.

4.3.1 Quality as a function of redshift

We started by analysing the quality of the photometric redshift as a function of redshift only and we tested different quality estimators. The statistics as a function of z_{spec} were computed in overlapping bins of $\Delta z = 0.04$ from $z = 0.01$ to $z = 1.31$. The least populated bin contains 51 objects.

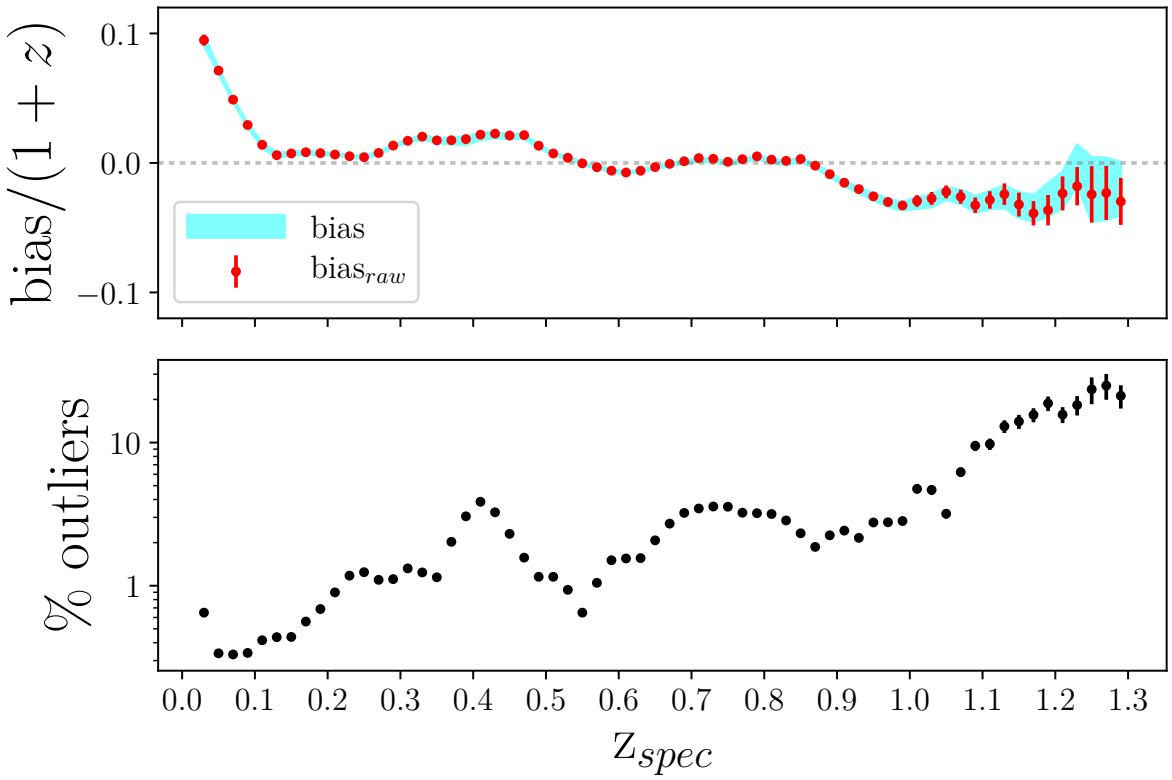

Figure 4.6: Quality of the photometric redshifts as a function of redshift. *Top:* bias of the $(z_{phot} - z_{spec})$ distribution, divided by a factor of $(1 + z)$. The red dots and error bars indicate the bias computed on the total distribution and the cyan shaded region highlights the bias computed after removing outliers. *Bottom:* fraction of outliers (or "catastrophic failures").

4.3.1.1 Bias

We quantified the bias, $b(z_{spec})$, as the median of the difference $(z_{phot} - z_{spec})$ and its error was computed assuming that this difference follows, at first order, a normal distribution:

$$b(z_{spec}) = \text{median}(z_{phot} - z_{spec}), \tag{4.1}$$

$$\Delta b(z_{spec}) = 1.253 \frac{\sigma_{(z_{phot} - z_{spec})}}{\sqrt{N}}, \tag{4.2}$$

with $\sigma_{(z_{phot} - z_{spec})}$ the standard deviation of the $(z_{phot} - z_{spec})$ distribution and N the number of object in the bin.

We then excluded the outliers (see equation 4.3, following Ilbert et al. 2006) and recomputed the bias, in order to investigate if they affect or not its measurement. The results are shown in the top panel of Figure 4.6. The red dots and error bars indicate the "raw" bias computed including all the objects, while the cyan shaded region shows the bias computed after rejecting the outliers. We can see that excluding or not the outliers before computing the median does not change the bias estimate in a significant way. We therefore used the "raw" bias estimate in the following analysis.

In the top panel of Figure 4.6 the bias is divided by $(1 + z)$ in order to be compared to the ones computed by Coupon et al. (2009) and the T007 study[2]. We included all the objects and not only the brightest ones, but we can see that the bias in much higher than 1%, especially at redshifts lower than ~ 0.1 where photometric redshifts are systematically overestimated, and at redshifts higher than ~ 0.9 where they are underestimated.

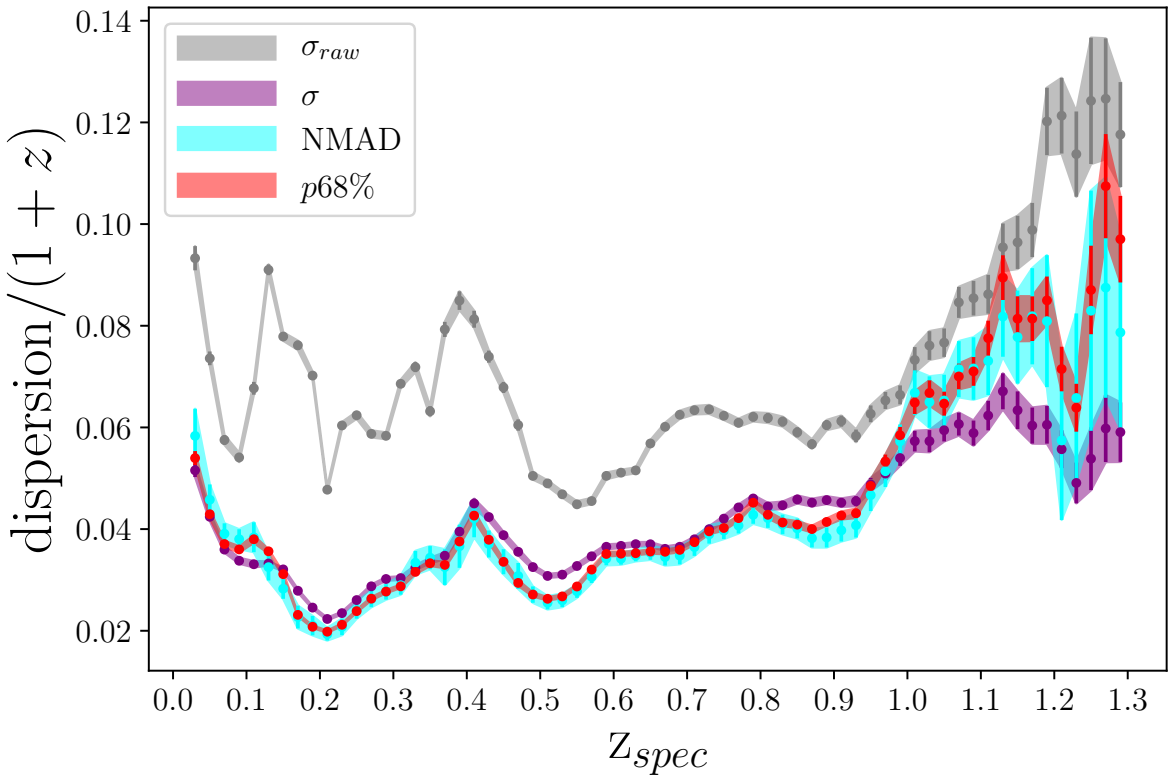

Figure 4.7: Dispersion of the photometric redshifts as a function of redshift, computed using different estimators, as indicated in the legend.

4.3.1.2 Catastrophic failure fraction

Following Ilbert et al. (2006) we defined catastrophic failures (or "outliers") as objects for which:

$$|z_{phot} - z_{spec} - b(z_{spec})| > 0.15(1 + z_{spec}). \tag{4.3}$$

The limit is arbitrary and we used 0.15 to be consistent with previous studies. We note that the bias was not accounted in the definition of Ilbert et al. (2006), however we account for it here as large bias values can artificially increase the catastrophic failure fraction. The error bars on the fraction of outliers was computed in the limit of large numbers of galaxies.

The fraction of catastrophic photometric redshift as a function of redshift is shown in the bottom panel of Figure 4.6. We can see that the fraction is not homogeneous and increases with redshift, with value comparable to the ones found by Coupon et al. (2009) and the T007 study[2].

4.3.1.3 Dispersion

In order to robustly quantify the dispersion in the $(z_{phot} - z_{spec})$ distribution, we implemented the following estimators:

- The standard deviation of the $(z_{phot} - z_{spec})$ distribution: σ_{raw},
- The standard deviation of the $(z_{phot} - z_{spec})$ distribution after rejection of the outliers: σ,
- The normal median absolute deviation (NMAD) of the $(z_{phot} - z_{spec} - b(z_{spec}))$ distribution, defined as:

$$NMAD = 1.48 \times \text{median}|z_{phot} - z_{spec} - b(z_{spec})| \tag{4.4}$$

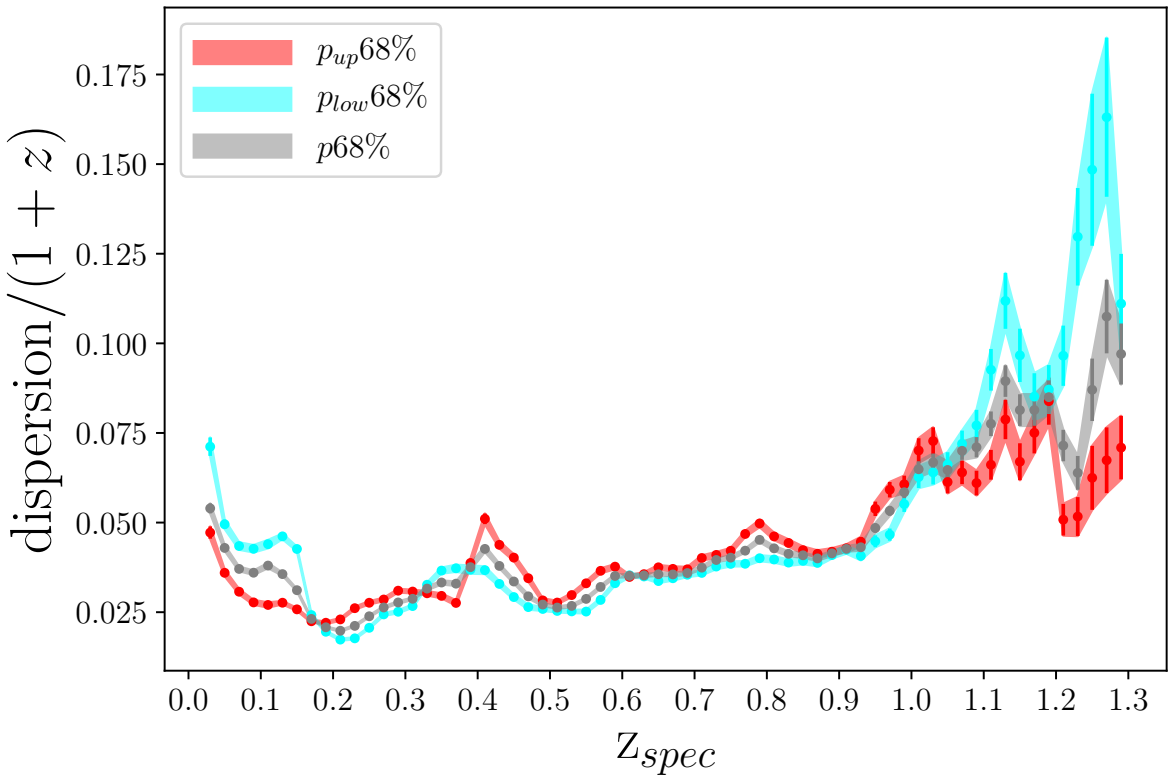

Figure 4.8: Dispersion of the photometric redshifts as a function of redshift. The red/cyan region shows the dispersion of the upper/lower tail of the distribution (points over/under the black line in Figure 4.5) and the grey region shows the dispersion for the entire distribution.

- The 68% percentile of the $|z_{phot} - z_{spec} - b(z_{spec})|$ distribution: $p68\%$
- The 68% percentiles of the upper and lower tails of the $(z_{phot} - z_{spec} - b(z_{spec}))$ distribution: $p_{up}68\%$ and $p_{low}68\%$.

The dispersion evaluated with the different estimators is shown as a function of redshift in Figures 4.7 and 4.8, normalised by $(1+z)$ for better comparison with the literature. We can see that the different estimators overly agree, except for the standard deviation σ_{raw} that is much higher due to the presence of outliers. The dispersion is increasing with redshift with a rate that is faster than $(1+z)$ and is also higher at $z < 0.1$. In the rest of the study we chose to use the percentile $p68\%$, which is equivalent to the NMAD in the present case, but does not assume any form for the $(z_{phot} - z_{spec} - b(z_{spec}))$ distribution.

As we can see in Figure 4.8, the $(z_{phot} - z_{spec} - b(z_{spec}))$ distribution is not perfectly symmetric, as $p_{up}68\% \neq p_{low}68\%$, but the differences are small above $z \sim 0.2$ and up to $z \sim 1$. When the number of objects is high enough to obtain robust statistics and when the $(z_{phot} - z_{spec} - b(z_{spec}))$ distribution shows asymmetric features, it is therefore more reliable to take into account both the upper and lower part of the distribution.

4.3.2 Quality as a function of redshift and magnitude

So far, we have investigated the dependence of the photometric redshifts accuracy as a function of redshift. However, the quality also depends on the signal to noise of the photometry and thus on the magnitude of the objects. Hence, when investigating the quality dependence as a function of redshift or magnitude only it is difficult to disentangle between these two effects. In the following we assess the quality of the photometric redshifts as a function of both redshift and

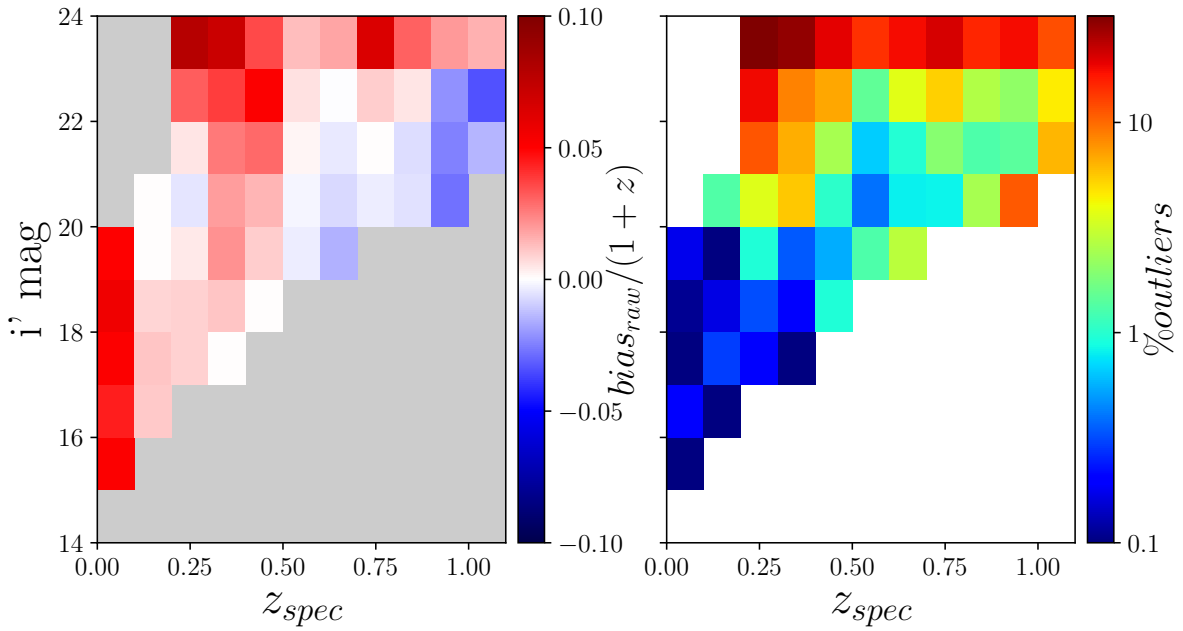

Figure 4.9: Quality of the photometric redshifts as a function of redshift and magnitude in the i' band. The estimator are only computed in cells containing more than 50 galaxies. *Left:* Bias of the $(z_{phot} - z_{spec})$ distribution, divided by a factor of $(1 + z)$. The colour-bar is clipped to $[-0.1, +0.1]$ for symmetry, but the bias is always below 10%. *Right:* fraction of outliers in percent. The null values have been set to 0.1 for visualisation purposes.

magnitude, using the estimators previously defined. To do so, we computed the bias, outliers fraction and dispersion in cells of size $\Delta(z, mag) = 0.1 \times 1$, if they contained at least 50 objects, in order to obtain robust measurements.

The bias and outliers fraction are shown as a function of both redshift and i' band magnitude in Figure 4.9. The associated errors are higher in low populated cells, following the pattern of Figure 4.4, and we have checked that they represent $\sim 10\%$ of the measurements at maximum. We can see that the bias, computed following Equation 4.1, is quite homogeneous as a function of magnitude below $i' \lesssim 23$ and high and positive for fainter objects. The bias evolution is compatible with the bias estimated as a function of redshift alone for $i' \lesssim 23$ (see Figure 4.6). This motivated us to use the bias computed as a function of redshift only in the outliers definition (following Equation 4.3). The outliers fraction increases both with magnitude and redshift in average, but is higher for faint objects at low redshift than for high redshift ones. The high ($\gtrsim 10\%$) outliers fraction for objects with $i' > 23$ explains the high bias seen in this region, and reinforce our choice to not use the bias computed as a function of both magnitude and redshift.

The dispersion, computed as the 68% percentile of the $|z_{phot} - z_{spec} - b(z_{spec})|$ distribution, is shown as a function of both redshift and i' band magnitude in Figure 4.10. We can see that the dispersion strongly increases at magnitudes $i' \gtrsim 23$. As for the outliers fraction, the dispersion is high for faint low redshift objects, even brighter than $i' \sim 23$. Apart from that, we can remark that the dispersion of bright objects mainly depends on redshift: it is higher for $z \lesssim 0.1$ objects (as also seen in Figure 4.5) and increases faster than $(1 + z)$ at higher redshifts.

Finally, we can conclude that the photometric redshift quality in W1 is a function of both the redshift and the magnitude. The quality is degraded for objects fainter than $i' \sim 23$ and faint objects at low redshifts ($i' \gtrsim 21$ and $z < 0.5$). Outside these regions the quality depends mainly on the redshift.

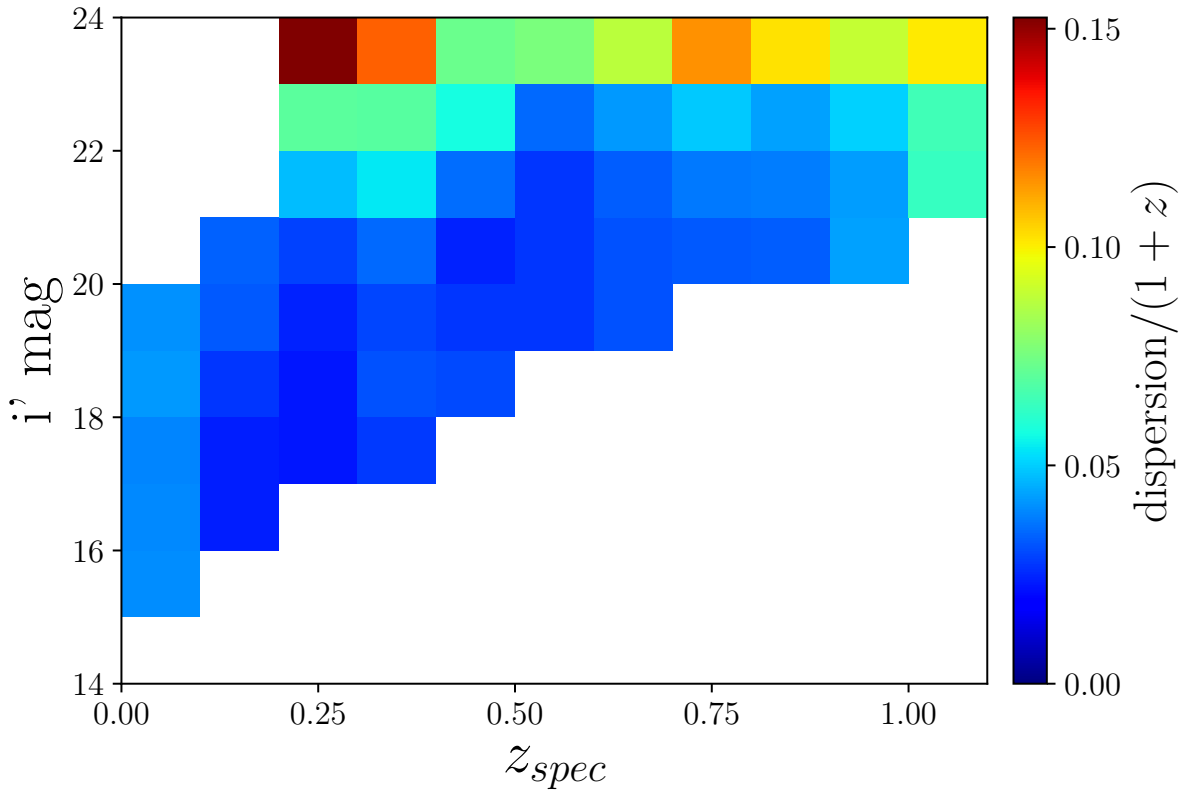

Figure 4.10: Dispersion of the photometric redshifts divided by a factor $(1+z)$, as a function of redshift and magnitude in the i' band. The estimator is the 68$^{\text{th}}$ percentile, $p_{68\%}$, and is only computed in cells containing more than 50 galaxies.

4.4 Methods to select galaxies using photometric redshifts

In the following chapters, we will study the statistical properties of galaxies in clusters (see Chapters 5, 6 and 7), and use galaxy overdensities to detect and characterise clusters (see Chapters 8, 9, 12). These analyses require to select galaxies likely to be at a given redshift z_{true}, either the one of the cluster or the one at which we want to map overdensities. In order to do so, one needs to build the probability distribution $P(z_{phot,gal}|z_{true})$, where $z_{phot,gal}$ are the galaxy photometric redshifts and z_{true} is the known spectroscopic redshift of the cluster. In the most general case this distribution depends on the galaxy magnitude, type and redshift (e.g. Ilbert et al. 2006). However, due to the large amount of spectroscopic data required to constrain these dependencies, the distribution is often averaged over magnitudes and types, and modeled by a Gaussian distribution with a standard deviation given as $\sigma_z = \sigma_0(1+z)$. If such a parametrisation is useful to describe the global performances of a photometric redshift algorithm, it may lead to inconsistencies in more detailed selections based on photometric redshifts. Indeed, the fraction of catastrophic failures and the dispersion both increase strongly with magnitude and redshift and are degraded for galaxies with starburst SEDs (see Section 4.3 and e.g. Ilbert et al. 2006). Moreover, the distribution $P(z_{phot,gal}|z_{true})$ is biased with respect to the mean and often shows non-Gaussian tails, which could lead to missing galaxies in their selection (source of incompleteness) if not accounted for. In this section, we thus develop and characterise different methods to select galaxies using photometric redshifts. Our main goal is to use them for the construction of galaxy cluster luminosity function (Chapter 5), for which an homogeneous selection is critical.

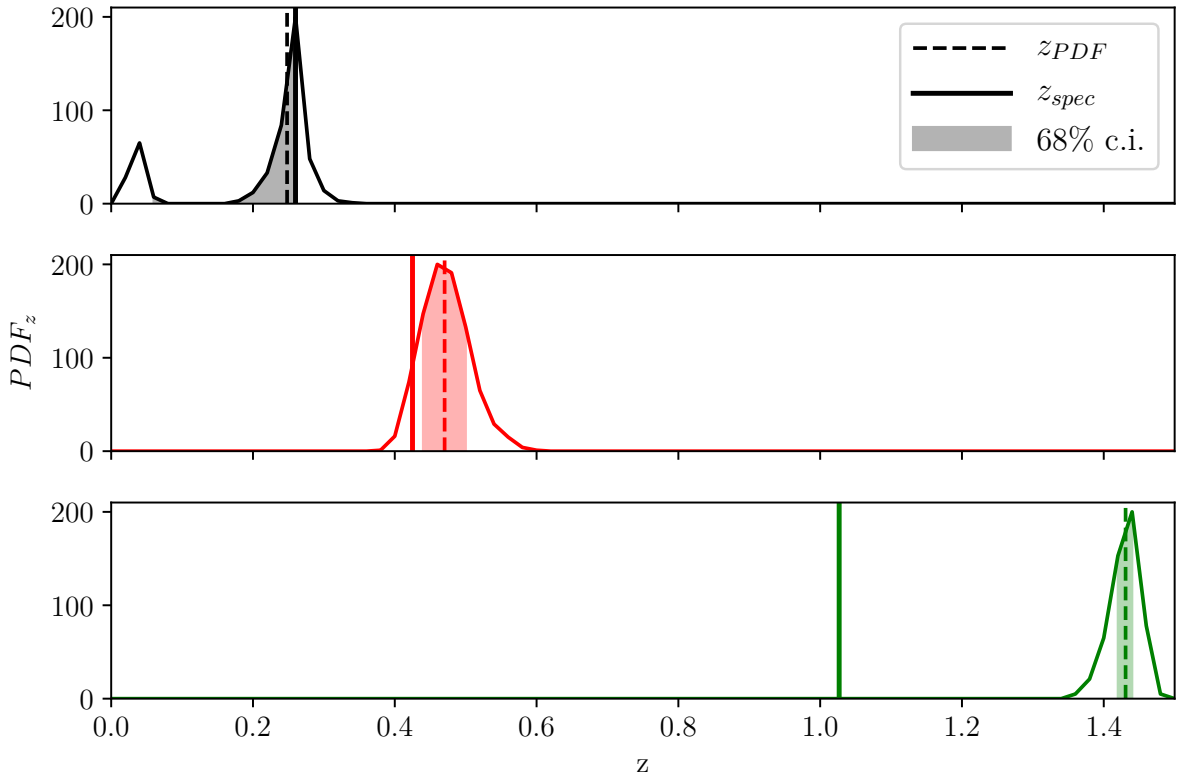

Figure 4.11: Three different cases of photometric redshift probability distribution functions (PDF_z), computed from the spectro-photometric catalogue. *Top:* The spectroscopic redshift value is within the 68% confidence interval around the median of the PDF_z, z_{PDF}. In this case we note that the distribution is bimodal due to redshift degeneracies. *Middle:* The spectroscopic redshift value is not within the 68% confidence interval around z_{PDF}, but would be included in the 95% c.i. *Bottom:* The spectroscopic redshift value is too far from the photometric redshift one, this case is considered as a catastrophic failure.

4.4.1 Construction of selection methods

Method 1: *ZPDF* A first approach to select galaxies likely to be at a given spectroscopic redshift, hereafter the *"ZPDF"* method, is based on individual photometric redshift probability distribution functions (PDF_z), provided for each object in the CFHTLS T0007 release. The lower and upper photometric redshift estimation values, z_{p-} and z_{p+} given in the catalogue, are computed to enclose 68% of the area around the median value, z_{PDF} (see Figure 4.11 for an illustration). On average, 68% of the true galaxy redshifts should be enclose within z_{p-} and z_{p+}. Therefore, the *ZPDF* method consists in selecting the galaxies verifying:

$$z_{p-} < z_{true} < z_{p+}. \tag{4.5}$$

We also investigated two other ways to perform the photometric redshift selection based on the $(z_{phot} - z_{spec})$ statistics, given the true spectroscopic redshift. The advantage of those methods is that, as they are directly computed from the $(z_{phot} - z_{spec})$ statistics, one can easily introduce a bias correction that appears to be non negligible in the present dataset (see Section 4.3).

Method 2: *cte* This method, hereafter the *"cte"* method, makes use of the Gaussian modeling of the $(z_{phot} - z_{spec})$ distribution with $\sigma_z = \sigma_0(1 + z)$. We used a constant dispersion of the distribution, $\sigma_0 = 0.04$ for $i' < 22.5$, and $\sigma_0 = 0.08$ for $i' > 22.5$, following the results of

the T007 photometric redshift release explanatory document[2], in order to take into account the degradation of the dispersion for faint objects. The selection of galaxies following the *cte* method is given by:

$$-\sigma_0(1+z_{true}) < z_{phot} - z_{true} - b(z_{true}) < +\sigma_0(1+z_{true}). \tag{4.6}$$

Method 3: *zfct* The third approach, hereafter the *"zfct"* method, also consists in modeling the $(z_{phot} - z_{spec})$ distribution with a Gaussian, but the dispersion is computed in consecutive spectroscopic redshift bins using the NMAD estimator. The corresponding galaxy selection criteria for the *zfct* method is given by:

$$-\sigma_{NMAD}(z_{true}) < z_{phot} - z_{true} - b(z_{true}) < +\sigma_{NMAD}(z_{true}). \tag{4.7}$$

4.4.2 Completeness of the selection methods

Having a well defined selection as a function of redshift and magnitude is essential for the construction of the galaxy cluster luminosity functions as it consists in counting galaxies per bins of magnitude (see Chapter 5). To characterise this selection, we defined the completeness, associated to a given method, as the ratio of the number of selected galaxies to the total number of galaxies, in a given redshift and magnitude bin:

$$\text{Completeness} = \frac{\text{number of selected galaxies around a given redshift}}{\text{total number of galaxies around a given redshift}}. \tag{4.8}$$

The ratio were computed using the spectro-photometric sample in cells of size $\Delta(z, mag) = 0.1 \times 1$, if they contained at least 50 objects. As the selections are performed at a 1σ level (of a Gaussian), the completeness is expected to be consistent with 68.2%. The completeness of each method, computed as a function of magnitude and redshift, is shown in Figure 4.12.

In the case of the *"ZPDF"* method (upper left panel of Figure 4.12), we can see that the selection leads to an inhomogeneous completeness, without a clear trend with redshift or magnitude. Except for some regions, the completeness is generally lower than 68%, showing that the confidence intervals coming from the PDF_z are usually underestimated. The lack of homogeneity observed in the completeness may be caused by the bias of the photometric redshifts with respect to the spectroscopic ones. In this case, using the 68% confidence limits around the median of the PDF_z leads to a photometric redshift window systematically shifted with respect to the spectroscopic value. Another reason is that uncertainties in the photometry or the inadequacy of the SED template set are not taken into account in the computation of the PDF_z.

The completeness map corresponding to the *"cte"* method is shown in the upper right panel of Figure 4.12. We can see that the completeness is still not uniform: it is higher than 68% for bright objects at low redshift and lower elsewhere, in particular at high redshift. This is due to the fact that the dispersion is not simply evolving as $(1+z)$ with redshift and as a step function with magnitude, unlike what is assumed for the *"cte"* method.

The completeness map corresponding to the *"zfct"* method is shown in the lower left panel of Figure 4.12. We can see that the completeness is still not homogeneous, but biased toward bright objects at every redshift. This is because the dispersion is accurate where the number of object is large, and the completeness pattern thus follows the redshift evolution of the median magnitude of the spectroscopic sample. This method accounts for the incompleteness due to redshift evolution of the dispersion but not that due to magnitude variation. This method is still not satisfying (in particular for luminosity function studies, see Chapter 5).

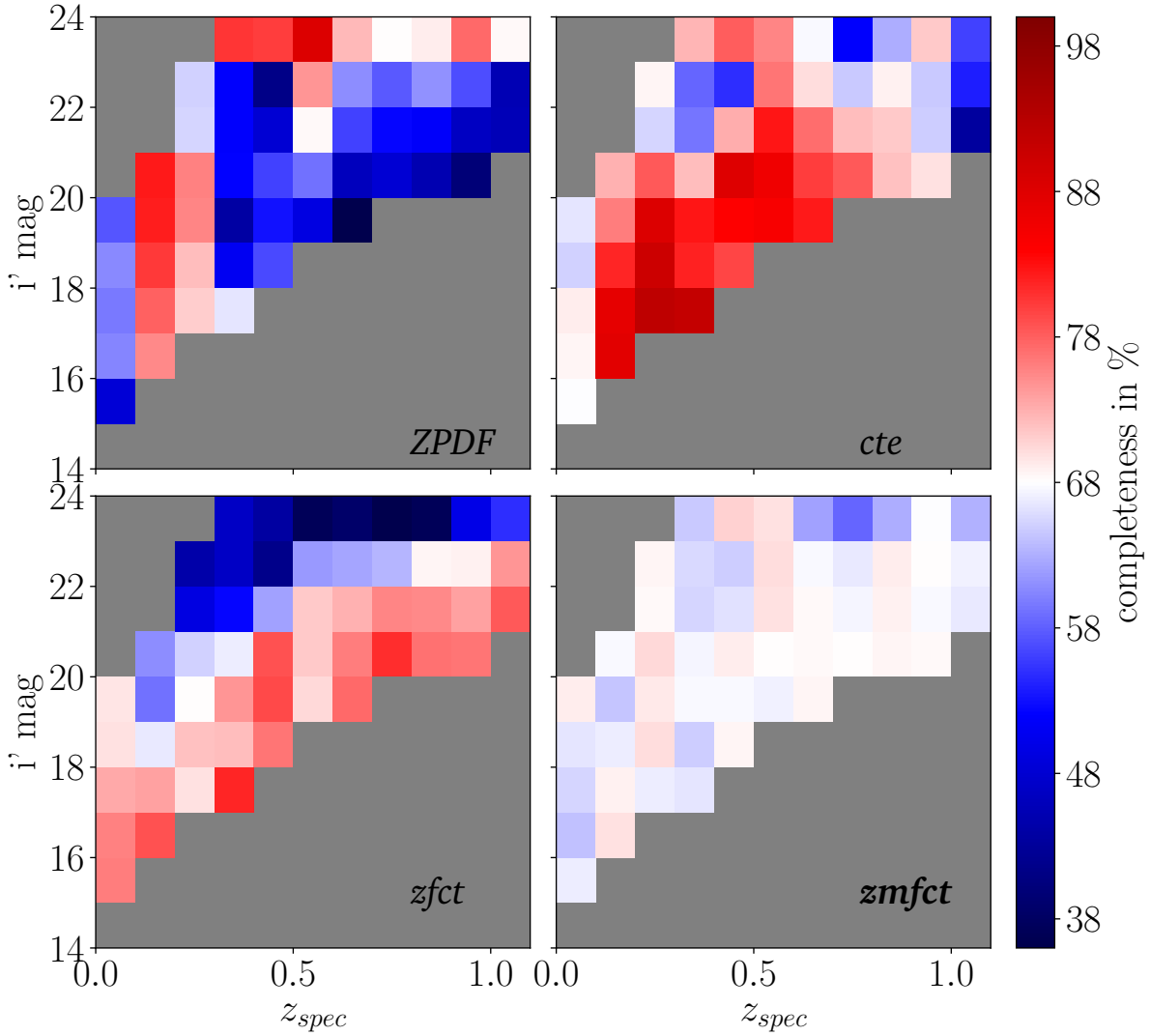

Figure 4.12: Completeness (fraction of objects for which the photometric redshift is inside a given slice around the true redshift) associated to different galaxy selection methods as a function of spectroscopic redshift and magnitude in the i' band, for selections at a 1σ (68%) level. In red/blue the selection methods lead to over/underestimate the number of objects. From top to bottom and left to right, the objects are selected using the PDZ errors (*ZPDF* method), constant dispersions corresponding to $\sigma_{1/(1+z)} = 0.04$ for $i' < 22.5$ and $\sigma_{1/(1+z)} = 0.08$ for $i' > 22.5$ (*cte* method), a dispersion computed as a function of z_{spec} (*zfct* method), and a dispersion computed as a (z_{spec}, i') function (*zmfct* method, used in the rest of the study, see Figure 4.13). The completeness is computed if there are at least 50 objects in the cell.

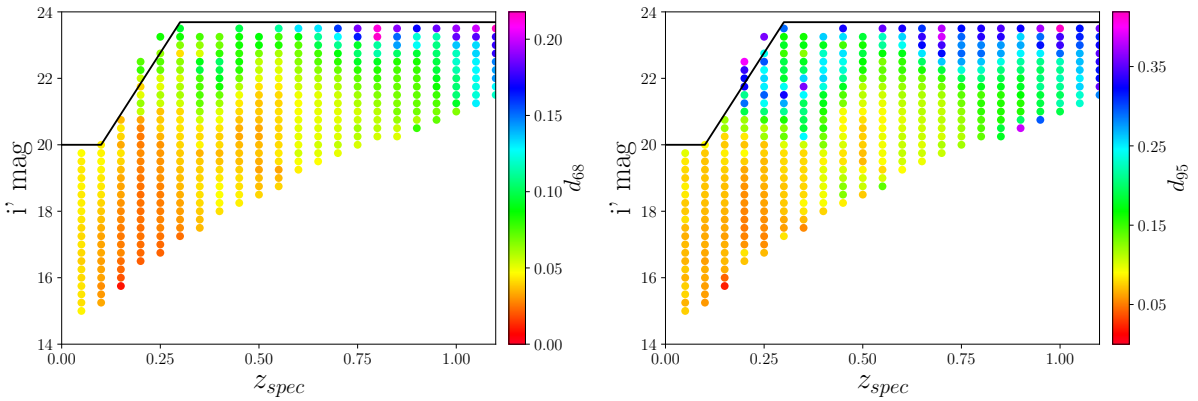

Figure 4.13: Photometric redshift dispersions d_{68} and d_{95}, computed as the 68% and 95% percentiles of $|z_{phot} - z_{true} - bias(z_{true})|$ in the (z, i') plane. The dots indicate the centres of the $\Delta(z, i'mag) = 0.1 \times 0.5$ cells used to compute the dispersion (if they contain at least 30 objects). The continuous black lines indicate the magnitude above which we cannot constrain the dispersion, this limit was used as limiting magnitude in Chapter 5.

4.4.3 Proposition of a new selection method

The construction of the galaxy cluster luminosity function (see Chapter 5) is sensitive to the completeness associated to the galaxy selection method. Indeed, any over-selection (completeness larger than 68.2%) or under-selection (completeness lower than 68.2%), as seen in Figure 4.12, will lead to biases in the estimation of the number of objects in a given magnitude bin. Thus, inhomogeneities in the completeness associated to a given selection method may lead to systematic effects affecting the shape of the luminosity function.

Method 4: *zmfct* Since the selection methods defined in Section 4.4.1 lead to inhomogeneities in the completeness, we designed a new selection (hereafter *"zmfct"*) dedicated to obtain the expected 68.2% completeness map. To do so, we computed the dispersion d_n using percentiles, as

$$d_n = P_n(|z_{phot} - z_{spec} - b(z_{spec})|), \tag{4.9}$$

with P_n the percentile of rank n. The dispersion d_n is calibrated in the (z_{spec}, i') plane thanks to the spectro-photometric sample, using running cells of size $\Delta(z, mag) = 0.1 \times 0.5$, with a minimum number of at least 30 objects per cell. In order to limit the influence of catastrophic failures, we filtered out the objects for which $|z_{phot} - z_{spec} - b(z_{spec})|$ is larger than 5 times the standard deviation of the global distribution. We then interpolated the data to obtain a function of (z_{spec}, i'). The resulting dispersion is shown in Figure 4.13 for d_{68} and d_{95}, corresponding to 68% and 95% of completeness, respectively. Unfortunately, we don't have enough spectroscopic data to constrain the dispersion for faint objects at low redshifts, as can be seen in Figures 4.4 and 4.13. This will limit our accessible magnitude limit in Chapter 5. Finally the galaxy selection associated to the *zmfct* method is defined as:

$$-d_{68}(z_{true}, i') < z_{phot} - z_{true} - b(z_{true}) < d_{68}(z_{true}, i') \tag{4.10}$$

The resulting completeness, computed as detailed in Section 4.4.2, is shown in the lower right panel of Figure 4.12. We can see that, thanks to this method, it is homogeneous and compatible with 68.2%. We therefore used this method to define the widths of the photometric slices in the rest of the Thesis.

4.5 Conclusions on the photometric redshifts and their limitations

In this Chapter, we have shown that the quality of the photometric redshifts obtained with LEPHARE in the W1 field of the CFHTLS survey depends both on the magnitude and true redshift of the objects. The photometric redshifts are biased with respect to the spectroscopic ones and the $(z_{phot} - z_{spec})$ distribution is not gaussian.

We have also shown that the usual methods to select galaxies likely to be at a given redshift using their photometric redshifts induce magnitude and redshift dependent incompleteness. Those effects have to be taken into account and avoided for all the studies that require homogeneous and defined completeness in redshift and magnitude, such as e.g. cluster detections, richness estimation or density profiles construction. Consequently, we developed a new galaxy selection method dedicated to obtain homogeneous completeness in the magnitude-redshift plane. When appropriate, one can think of checking the photometric redshift quality not as a function of redshift and magnitude but as a function of other properties such as e.g galaxy colours, type or environments.

In the future, larger spectroscopic samples are expected. They will allow us to investigate the photometric redshift quality using higher dimensions (e.g. as a function of redshift, magnitude and galaxy type). However, robust analysis using photometric redshift require the spectroscopic samples to be representative of the photometric data and thus limit the use of photometric redshift to the redshift-luminosity range covered by spectroscopy. This point apply to machine learning based photometric redshift algorithms since the photometric redshift are only representatives of the training sample used to derive them, but also to template fitting methods since the accuracy of the photometric redshift has to be measured and cannot be simply extrapolated.

In the case of the CFHTLS photometric redshift catalogue, we demonstrated that, on average, spectroscopic redshifts were included between the $16^{\rm th}$ and $84^{\rm th}$ percentiles of the photometric redshift PDF in less than 68% of the cases. This shows that the confidence intervals coming from the PDF are underestimated. Moreover, the photometric redshifts PDFs do not reflect the presence of bias between the photometric and spectroscopic redshifts. Therefore, the photometric redshift PDFs approach -albeit being very promising because it allows in principle to obtain and propagate uncertainties reflecting the signal to noise, redshift and SED of the source and possible multiple peaks- has to be used with caution and improved.

Chapter 5

Construction of the luminosity functions in XXL-N clusters

Contents

Abstract: Cluster galaxy luminosity functions, along with their density profiles, encode most of the observational properties of clusters in the optical. Despite their importance there is no consensus about their evolution with halo mass and redshift. As the XXL survey spans a wide range of cluster mass and redshift, it gives a unique opportunity to study the cluster luminosity functions without being biased by optical detection. In this Chapter, we develop the methodology used to determine the XXL clusters' luminosity functions that will be analysed in Chapter 6. After introducing the context, we describe the data and we present the method used to construct and parametrised the luminosity functions. We also determine the brightest cluster galaxy of XXL clusters and we define their richness. We then identify and quantify systematic effects and discuss their implications. This study is based on Ricci et al. (2018). This article and the associated BCG catalogue are part of the second XXL data release.

5.1 Introduction

The galaxy luminosity function (LF) and its evolution with redshift, galaxy type or environment, is one of the main tools to constrain models of galaxy formation and evolution. Knowledge about the LFs of galaxies in clusters is also important in cosmology, particularly in view of the future optical or near infrared (NIR) wide field surveys (e.g. *Euclid*, *LSST*). Indeed, the galaxy LFs of clusters, along with their density profiles, encode most of the observational properties of galaxy clusters in the optical. The LF and its evolution is therefore a key ingredient in cluster detection (see Chapter 8 and Appendix A and B). Moreover, in order to derive cosmological constraints from cluster counts, a precise and well calibrated cluster mass estimate, based on an observable, is required. The main mass proxies in the optical are the cluster richness (e.g. Rozo et al. 2009; Andreon and Hurn 2010) and optical-NIR luminosity (e.g. Lin et al. 2003; Mulroy et al. 2017; Ziparo et al. 2015, hereafter XXL Paper X), and these proxies often require the knowledge of the cluster's LFs, by e.g. counting galaxies brighter than a characteristic magnitude or by integrating the luminosity function. Thus, the LF of cluster galaxies is also a critical property that simulations need to reproduce, if they are later used to e.g. characterise cluster finder algorithms or calibrate galaxy cluster observables in the optical (see Appendix A and B for the validation of cluster luminosity functions in *Euclid* simulations).

In a pioneering study, based on the Press and Schechter (1974) work on the galaxy mass function, Schechter (1976) proposed an analytic expression to characterise the galaxy luminosity function, consisting of the product of a power law by a decreasing exponential function (see also Section 5.4). It is fully characterised by three parameters: the characteristic magnitude M^* corresponding to the « knee » of the function , the slope α of the power law dominating at faint luminosities and the normalisation density ϕ^*. In the last decades, extensive work has been devoted to evaluate galaxy luminosity functions in different environments, from field to clusters, in different redshift ranges, and with different selection for galaxies (colours and types). This resulted in a better theoretical modelling of galaxy and structure formation and evolution (see e.g. Menci et al. 2002; Mo et al. 2004).

Evolution of the LF with redshift is of particular interest as it is directly linked to the formation history of galaxies. It has been shown to be connected both to environment and to galaxy types. However, one of the main difficulties in the cluster LF determination from photometric surveys is the correct evaluation of the background contamination, which is more critical for faint galaxies. Many analyses focusing on early type galaxies used the red sequence (the locus formed by early type galaxies in the colour-magnitude plane, see Chapter 7) to optimise the LF determination. Most of them indicate that the fraction of passive galaxies in clusters changes with redshift, with a deficiency in low luminosity red galaxies for high redshift clusters with respect to low redshift ones (De Lucia et al. 2004, 2007; Stott et al. 2007; Gilbank et al. 2008; Lu et al. 2009; Rudnick et al. 2009), while some others disagree on this point (Andreon 2006, 2008; Crawford et al. 2009). This effect suggests that a large fraction of high redshift low mass galaxies are blue, and progressively migrate to the red sequence at lower redshift.

Improvements in the quality of the photometric redshifts over the last decade led to significant progress in the determination of the LF of the whole galaxy population in the optical rest-frame, and of the relative behaviour of the early type and late type galaxy components (Rudnick et al. 2009; Martinet et al. 2015; Sarron et al. 2018). Great insight at redshift $z > 1$ was provided by analysis in the NIR rest-frame, which traces well the stellar mass (Muzzin et al. 2008; Mancone et al. 2010).

Concerning the bright end of the LF, various analyses converge to the fact that the characteristic magnitude redshift evolution up to $z = 1$ can be described by the passive evolution of a population formed in a starburst at high redshift (De Propris et al. 1999, 2007, 2013; Lin et al. 2006). This has been confirmed up to higher redshifts by analyses in the NIR and IR (Strazzullo et al. 2006; Muzzin et al. 2008; Mancone et al. 2010, 2012). This last analysis also showed a flat faint end slope ($\alpha \sim -1$) with no significant redshift evolution and stressed that the evolu-

tion of α and M^* have to be considered jointly for any interpretation in terms of evolution, due to the strong degeneracy between these parameters.

The dependence of the galaxy luminosity function on cluster mass has also been investigated via observed mass proxies such as richness, velocity dispersion, or X-ray luminosities and temperatures. Here again, a full consensus has not yet been reached, with some studies showing differences in the LF in clusters with low/high mass proxies (Valotto et al. 1997; Croton et al. 2005; Hansen et al. 2005), while others show weak or no difference (De Propris et al. 2003; Alshino et al. 2010; Moretti et al. 2015; Lan et al. 2016).

Large cluster samples in X-rays or in the optical have recently become available, spanning wide redshift and cluster mass ranges. However, the study of the LF evolution in these samples is challenging because they are hampered by selection effects, leading to potential biases arising from the correlation between the cluster masses and their redshifts. So far, the approaches that have been used in order to disentangle between mass from redshift effects are either splitting the clusters and studying the LF in redshift and mass bins, as in Sarron et al. (2018), or using hierarchical Bayesian methods that simultaneously model redshift evolution and cluster mass dependence, as in Zhang (2017).

In the end, the evolution of the cluster galaxies LF with halo mass and redshift is still a matter of debate in the literature. The difficulty in comparing the results of the various analyses derives from the differences in sample selection, redshift and mass range, radius considered, method to select galaxies, and statistical analysis performed. This strongly motivates the determination of the LF for a statistical sample of clusters with an homogeneous selection and a firmly tested methodology, and taking into account the correlations between cluster mass and redshift.

5.2 Data description

5.2.1 The cluster sample

In this work, we used the list of all C1 and C2 clusters from the XXL-365-GC sample (see Table 5 in XXL Paper XX, and Section 3.1) overlapping with the W1 field of the CFHTLS (i.e. having a declination such as $Dec < -3.7$) and for which we have optical spectroscopic redshift confirmation, leading to a sample of 142 clusters from $z = 0.03$ to 1.06. Among these 142 clusters, 93 are classified as C1 and 49 as C2. We recall that their centre positions correspond to the centroids of their X-ray emission.

Due to the low X-ray photon number counts of several sources it was not possible to directly measure X-ray gas temperatures and luminosities for all clusters. Therefore, in order to allow for studies of the global properties of the full sample, we used cluster parameters extrapolated from scaling laws (see Section 3.1). Considering their good agreement with the parameters directly measured (see Figure 4 in XXL Paper XX), and the fact that we are interested in studying a global behaviour, we do not expect a major change in our results if we consider one or the other type of measurements.

For reference, Figure 5.1 shows the $[0.5-2]$ keV band luminosity within 300 kpc, $L^{XXL}_{300kpc,scal}$, as a function of redshift, for the clusters in our sample. The red dots indicate the C1 clusters and the blue square indicate the C2 clusters.

Throughout the study, the term 'cluster' refers to an extended X-ray source having undergone spectroscopic confirmation. However, some of them may remain undetected by optical cluster finders if they are too poor or if there is an offset between the gas and the galaxies (see Chapter 8). Also, no distinction is made between groups and clusters. Finally, in the case of multiple structures, each substructure or group is identified as an X-ray cluster.

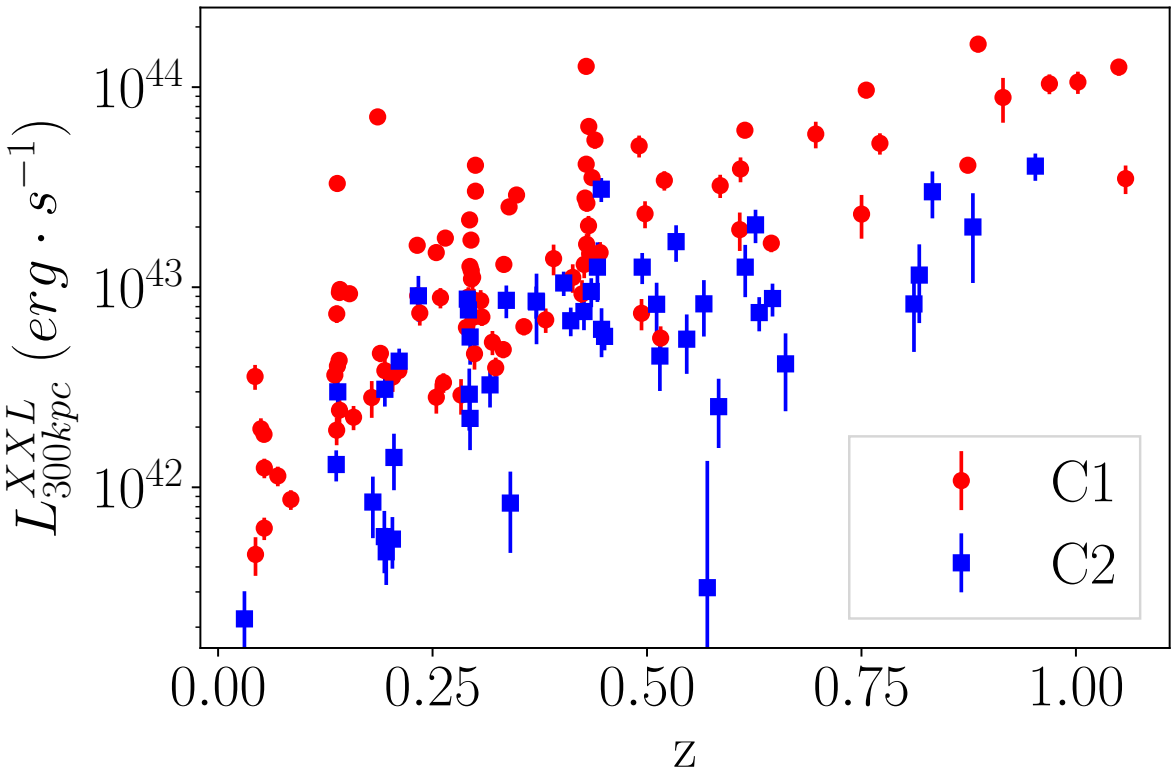

Figure 5.1: X-ray luminosity in the $[0.5 - 2]$ keV band computed in a 300 kpc aperture as a function of redshift for the cluster sample used in this study. Red points and blue squares represent clusters classified as C1 and C2, respectively.

5.2.2 Galaxy catalogues

Precise photometric redshifts, taking advantage of multi-wavelength photometry, are available in the XXL framework (see Fotopoulou et al. 2016, hereafter XXL Paper VI). The quality of these photometric redshifts is optimised for highest accuracy per galaxy, therefore they are computed using a combination of wide and deep photometric observations (e.g. using the UKIDSS[1] and VISTA[2] surveys), which however do not cover the full CFHTLS W1 area homogeneously. This strategy is not optimal for our statistical study, which requires homogeneous redshift quality across the whole field. We therefore used, instead, the photometric redshifts catalog associated with the CFHTLS W1 survey, which is computed with only five bands, but presents an homogeneous quality across the field (see Sections 3.2 and 4.2 for a detailed description).

5.3 Construction of the cluster galaxy luminosity functions

5.3.1 Luminosity function requirements

The first critical step in the computation of cluster galaxies LFs is to properly count the right number of galaxies belonging to the cluster, in a given range of luminosity. In an ideal case, one would like to identify which galaxies belong to the cluster. However, precise cluster membership assignments are often difficult to perform, especially without spectroscopy. Alternatively, one can select highly probable cluster members using e.g. photometric redshifts, and then statistically correct the field contamination by subtracting estimated counts from control background

[1] http://www.ukidss.org/
[2] www.vista.ac.uk/

fields. The second critical step is to define the range of cluster galaxy luminosities for which we will not suffer from incompleteness. The methodology used to address these two points is developed in the following section.

5.3.2 Selecting cluster galaxies

5.3.2.1 Selecting galaxies using photometric redshifts

As the number of available spectroscopic redshifts highly differs from cluster to cluster, we chose to use only photometric information to select member galaxies, in order to keep an homogeneous selection. We also chose to select photometric redshifts based on discrete values within some range around the cluster spectroscopic redshift. A similar treatment was then applied to control background fields.

We used the selection method *"zmfct"* defined in Section 4.4.3, which depends both on the cluster redshift and the galaxy magitudes. For each cluster with redshift z_{clus} we thus selected possible member galaxies by taking all the objects satisfying:

$$-d_{68}(z_{clus}, i') < z_{phot} - z_{clus} - b(z_{clus}) < d_{68}(z_{clus}, i'), \tag{5.1}$$

where $d_{68}(z_{clus}, i')$ is defined at the cluster redshift and changes according to the magnitude in the i' band of each object considered. We computed dispersions corresponding to 95% of completeness (d_{95}) in the same way as the 68% complete ones. Note that as we used percentiles and did not assume gaussianity, d_{95} is approximately, but not simply equal to $2 \times d_{68}$.

5.3.2.2 Defining the background fields

In order to take into account the contamination of the cluster galaxy counts by foreground and background galaxies, we chose to statistically subtract background galaxy counts for each cluster. The selection of local or global background fields to estimate the counts has been largely debated in the literature. Some differences may arise from the fact that, on one hand, selecting a region too close to the cluster can bias the counts because of correlated signal from filaments or enlarged cluster outskirts, and on the other hand, the clusters are embedded in the cosmic web and thus can lie on intrinsically high or low density regions compared to the whole field. Goto et al. (2002) and Popesso et al. (2005) showed that, in their rich cluster samples, the differences between the LF parameters obtained with the two methods were not significant. However, Lan et al. (2016) found that their global background estimate, computed using random fields of same aperture size than their cluster fields, tended to underestimate the background level, especially for low mass clusters. In this study we chose to use local background fields enclosed in annuli of 3 to 5 Mpc around the cluster centres (3 Mpc $\sim 2.5R_{500}$ for the more massive cluster in our sample).

In some cases, the presence of groups in the periphery of the clusters may lead to an overestimation of the counts in the background fields. For this purpose, we adopted a similar treatment to that of De Filippis et al. (2011) and we ran the WAZP cluster finder algorithm (Benoist et al. in prep., see Chapter 8) in a target mode on each cluster position and redshift, down to a magnitude of $i' = 24$, to detect structures that may contaminate the background (see Figure 5.2 for an illustration). These structures were masked in the following analysis.

By doing so, we do not take into account the possible projections along the cluster's line of sights and thus we may overestimate the galaxy counts in the cluster fields. However, the projected structures in cluster fields are less frequent than the structures in the background field, therefore not removing the structures in the background will bias the counts low. Castignani and Benoist (2016) found that their membership assignment was less biased when removing the structures in the background, and Rozo et al. (2015) found that, in their rich cluster sample, the correlated structures were contributing to approximatively 6% of the cluster's richnesses. As

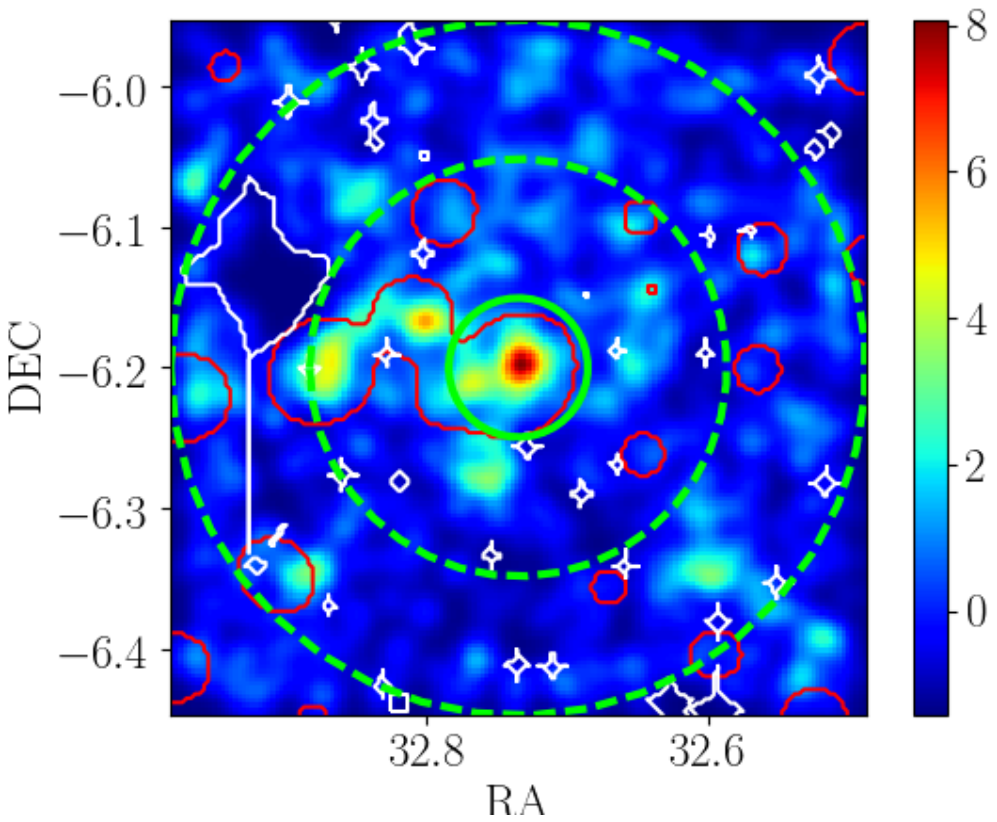

Figure 5.2: Example of a galaxy density map of a cluster in a 10×10 Mpc^2 field, constructed using gaussian kernel of width $\sigma = 0.1875$ Mpc. The colour-bar reflects the signal to background level, i.e the overdensity. Only galaxies with $m < m^* + 3$ (or $L > 0.06L^*$) are selected and the photometric redshift width depends on the galaxy magnitudes and is taken to ensure 68% completeness. The red contours indicate the structures detected by WAZP, and the white ones show the masked regions. The green inner circle shows 1 Mpc around the cluster X-ray centre and the dashed green lines delimitate the local background field from 3 to 5 Mpc. We can see that this cluster is part of a superstructure.

we are working with relatively low mass clusters, for which projections are expected to be rarer, we expect less than 6% contamination on our galaxy counts from possible correlated structures along the cluster's line of sights, and we therefore neglected this effect.

For each cluster, we also computed the effective local background area in Mpc^2, taking into account the photometric masks and the structure masks. We compared counts in the local background fields to those obtained using the whole W1 field of 68 deg^2, taking into account the photometric masks but not the structures. Figure 5.3 shows the distribution of the ratio of local to global background galaxy densities when structures are discarded and taken into account from the local background fields (respectively in blue and red) and using galaxies brighter than m^*+1 ($0.4L_*$). As one can see, before removing the structures, the galaxy densities in the local background fields are in good agreement with the densities in the global field ($\langle \Sigma_{local}/\Sigma_{global} \rangle \sim 1$). However, when the structures in the local fields are discarded, galaxy densities become in average smaller than in the field. Indeed, we estimated the density in the global field as the mean density, which is sensitive to the presence of structures. The shape of the distributions is in agreement with Coles and Jones (1991), who showed that the probability distribution of galaxy overdensities can be described by a log-normal function. Their widths denote the sample

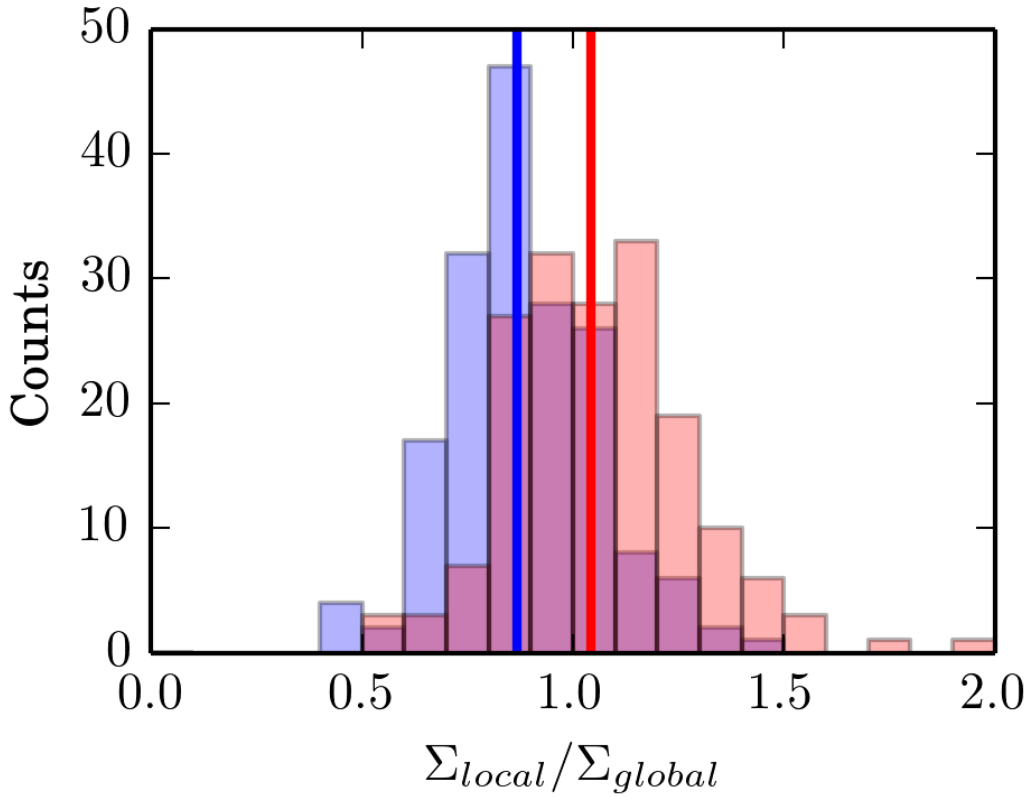

Figure 5.3: Histogram of the ratio between local and global background galaxy number densities for all the clusters in our sample. The global background refers to the whole CFHTLS W1 field whereas local backgrounds refer to annuli of 3 to 5 Mpc centred on the X-ray cluster positions. The distribution of the ratio, when structures are discarded/taken into account from the local background fields, is shown in blue/red. The solid lines indicate the median values of the ratios.

variance due to large scale structures: we can see that some clusters are located in intrinsically under-dense or over-dense regions.

5.3.2.3 Constructing galaxy density maps

In order to visualise the clusters' morphologies, and check for the presence of structures in the background, it is useful to map the galaxy density in the cluster fields. We thus constructed galaxy density maps by selecting the galaxies in a photometric redshift slice around the cluster redshift, satisfying Eq. 5.1. We then convolved the galaxy positions with a Gaussian kernel standard deviation of $\sigma = 187.5$ kpc ($1/16^{\rm th}$ of a Mpc). The maps M were converted in units of signal to background ratio (SBR) following:

$$M_{SBR} = \frac{M - \langle M_{10\times10Mpc^2}\rangle}{\sigma(M_{10\times10Mpc^2})} \tag{5.2}$$

where $\langle M_{10\times10Mpc^2}\rangle$ and $\sigma(M_{10\times10Mpc^2})$ are respectively the mean and the standard deviation of the pixel values of a 10×10 Mpc^2 density map centred on the cluster. We have checked that the mean and standard deviation were similar to that computed in the entire CFHTLS W1 field maps. An example of density map in a cluster field is shown in Figure 5.2. These galaxy density maps are also used in Chapters 8 and 9.

5.3.3 Definition of the luminosity range

5.3.3.1 Identification of the brightest cluster galaxy

The luminosity of the BCGs has been shown to differ from the extrapolation of the LF of the other cluster members at high luminosity (Schechter 1976) and many authors have chosen either to not include them in the calculation of the LF or to treat them differently (see e.g. Hansen et al. 2005; Wen and Han 2015). We therefore investigated the luminosity distribution of the BCGs separately and removed their contributions from the non BCG members LFs. By definition, no cluster galaxy can be brighter than the BCG, and thus, we used the BCGs magnitudes as the bright limits of our luminosity ranges.

We identified the BCG for each cluster as the brightest galaxy inside a projected radius of 400 kpc from the X-ray center, having either a spectroscopic redshift, z_{BCG}, such as $z_{BCG} = z_{clus} \pm 0.004 \cdot (1+z)$, with z_{clus} the mean cluster redshift, or no spectroscopic redshift but a photometric redshift satisfying Eq. 5.1. Visual inspection confirmed $134/142$ ($> 94\%$) BCGs selected with these criteria and allowed us to identify the 8 others. We present our BCGs sample in Appendix C.

Our BCG list was compared to the one of Lavoie et al. (2016), hereafter XXL Paper XV, as we have 40 clusters in common. We found different BCGs for $4/40$ clusters (10%). These discrepancies correspond to cases were several bright galaxies are present, which makes the identification of the BCG difficult. The absolute magnitudes of the BCGs as a function of redshift are shown by the red points in Figure 5.4.

5.3.3.2 Limiting magnitudes

The determination of the limiting magnitude is crucial for studies based on galaxy counts, such as the luminosity functions. Photometric surveys are flux limited and if this effect is not taken into account, it can produce a spurious decline of the luminosity function at faint magnitudes. We defined the completeness magnitude as the magnitude at which the completeness start to decrease. In general completeness values are computed during the survey calibration phase. In the case of the W1 field, the completeness magnitudes at 80% for extended sources, $mag_{80\%}$, are given by the CFHTLS-T0007 release explanatory document (Hudelot et al. 2012) and are $24.67 \pm 0.14, 24.00 \pm 0.10$ and 23.69 ± 0.13 in the g', r' and i' band respectively.

In this study, as we use photometric redshifts, we have to take into account another source of incompleteness, coming from the photometric redshift catalog construction. This is because not all the objects from the photometric catalog have a good photometric redshift estimation (computed in three bands or more, with a χ^2/dof value lower than 100 and a galactic type of SED). However, by computing the ratio of the magnitude distribution of the photometric and photometric redshift catalogues, we found that this incompleteness is less than 3% for every magnitude bin, and we neglected it in our analysis.

As the low redshift/faint magnitude parameter space region is not well covered by spectroscopic surveys, the dispersion of the photometric redshifts-spectroscopic redshifts relation in this region is not constrained, as can be seen from Figures 4.4 and 4.13. Therefore we defined the limiting magnitude to be $m_{lim} = 20$ at $z < 0.1$, then linearly growing between $0.1 < z < 0.3$, up to $mag_{80\%}$ at $z > 0.3$, as shown in Figure 4.13. According to our fiducial evolution model for m^*, this cut allows us to include galaxies with $m > m^* + 3$ (or $L < 0.06L^*$) up to $z = 0.6$.

We converted the limiting magnitudes $m_{lim}(z)$ in absolute magnitudes following

$$M_{lim}(z) = m_{lim}(z) - \mu(z) - \max\left[K_{corr}(z)\right], \tag{5.3}$$

with μ the distance modulus and K_{corr} the k-correction. The model taken for the k-correction is the one used by LePhare to compute the absolute magnitudes and depends on galaxy type. In order to be conservative we use the maximum value of the k-correction at each redshift,

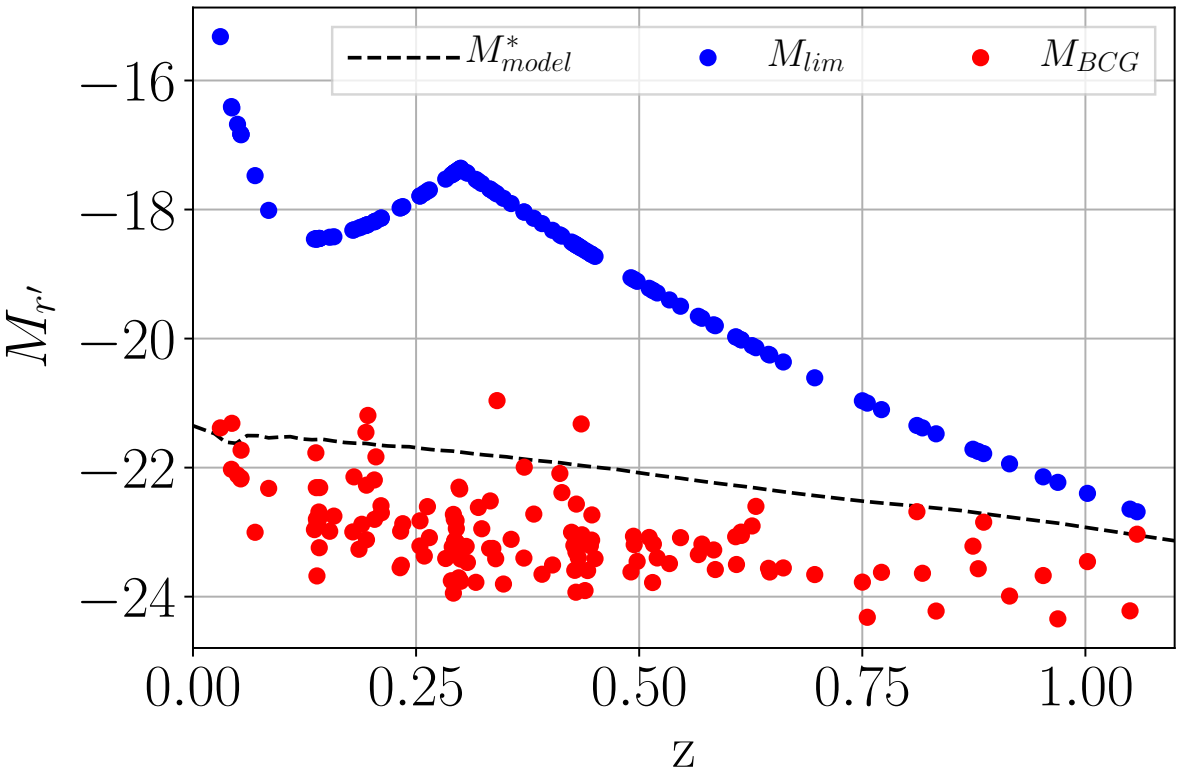

Figure 5.4: Redshift evolution of the luminosity range in which the LF is fitted. The red dots show the absolute magnitude of the BCGs of each cluster whereas the blue ones indicate the limiting magnitude we imposed. Our fiducial model for the evolution of M^* is indicated by the black dashed line for comparison.

corresponding to that obtained for elliptical galaxies. The limiting absolute magnitude for each cluster in our sample, as a function of redshift, is shown by the blue points in Figure 5.4. We can see that below $z = 0.67$ the accessible luminosity range is always larger than ~ 3 mag. The magnitude limit, $M_{lim}(z)$, is used in the following to define the magnitude range where to fit the luminosity functions.

5.3.4 Counting galaxies

As LePhare uses SED modeling to compute absolute magnitudes, in order to have the absolute magnitude at a wavelength λ_{rest} constrained by the observational data, we need to verify

$$\lambda_{u'} < (1+z)\lambda_{rest} < \lambda_{z'}, \tag{5.4}$$

with λ'_u and $\lambda_{z'}$ the wavelengths of the u' and z' filters and z the redshift of the considered object. This condition is satisfied up to high redshift for the bluest bands. However, redder bands are known to be more representative of the stellar mass because they are less affected by star formation. This is why we chose to use the rest frame r' band in this work. Given the condition of equation 5.4, the r' band is constrained up to $z \simeq 0.67$. We now count galaxies in absolute magnitude, within this limit.

5.3.4.1 Galaxy counts in absolute magnitude

We assumed that each cluster member is at the mean redshift of the cluster. We therefore used the value of the absolute magnitude provided by LePhare, computed with the photometric redshift estimation, and we corrected it by the redshift distance modulus offset.

After selecting the potential member galaxies for each cluster using their photometric redshifts and the method described in Section 4.4.3, we statistically removed the contribution from the background galaxies. To do so, we defined for each cluster field the probability $P_{out}(i')$ that a galaxy is not a cluster member, as

$$P_{out}(i') = \frac{\Sigma_{\rm background}(i')}{\Sigma_{\rm cluster\ field}(i')}, \tag{5.5}$$

with $\Sigma_{\rm cluster\ field}(i')$ the galaxy number density in the cluster fields and $\Sigma_{\rm background}(i')$ that of the background. Note that this probability is defined as a function of apparent magnitude in the band i' (the reference band of the survey). The associated probability density functions, as a function of continuous magnitude, were constructed by using the convolution with Gaussian kernel density estimator with a standard deviation of 0.5 mag.

We then assigned a random number uniformly distributed in [0,1], $U(0,1)$, to each potential member galaxy, to be compared to the probability $P_{out}(i')$ at the galaxy apparent magnitude. By doing so, we were able to subtract the galaxies associated to the background in a probabilistic way, by discarding the galaxies verifying $U(0,1) < P_{out}(i')$. Galaxy counts, $N_{\rm count}(M_R)$, were performed in each r-band absolute magnitude bin, to build the LFs. The counts were constructed inside projected R_{500} radii and in absolute magnitude bins of $\Delta M_R = 0.5$ mag. This procedure was repeated 100 times using Monte Carlo realisations ($N_{\rm MC} = 100$). The estimated counts were taken as the average values of the realisations, and the statistical error, $\Delta N_{\rm count}$, was taken as the standard deviation:

$$\bar{N}_{\rm count}(M_R) = \frac{1}{N_{\rm MC}} \sum_{j=1}^{N_{\rm MC}} \sum_{k} \Theta(U_{j,k}(0,1) - P_{out}(i')) \tag{5.6}$$

and

$$\Delta N_{\rm count}(M_R) = \sqrt{\frac{1}{N_{\rm MC}} \sum_{j=1}^{N_{\rm MC}} \left(\left[\sum_{k} \Theta(U_{j,k}(0,1) - P_{out}(i')) \right] - \bar{N}_{\rm count}(M_R) \right)^2}, \tag{5.7}$$

where k stands for the galaxies which belong to the considered magnitude bin and are at a projected distance smaller than R_{500}, and with $\Theta(x)$ the Heaviside step function, equal to 1 for $x > 1$ and 0 otherwise.

Finally, the number of galaxies per bin was normalised by the bin size and by the cluster area to obtain the galaxy surface density, $\phi(M_R)$, expressed in units of N_{gal} mag^{-1}Mpc^{-2}. The associated error in each bin was defined as the quadratic sum of the Poissonian and the statistical errors on the counts, normalised by the bin size and cluster area:

$$\phi(M_R) = \frac{\bar{N}_{\rm count}(M_R)}{\pi R_{500}^2 \Delta M_R} \tag{5.8}$$

and

$$\Delta\phi(M_R) = \frac{\sqrt{\Delta N_{\rm count}(M_R)^2 + \bar{N}_{\rm count}(M_R)}}{\pi R_{500}^2 \Delta M_R}. \tag{5.9}$$

In Figure 5.5, we present an example of a LF constructed in the case of an individual rich cluster. We can observe an increase in the number density of galaxies as a function of absolute magnitude up to $M_R \sim -16$. The LF reaches a knee at $M_R \sim -22$, corresponding to the characteristic magnitude. At faint magnitudes, we notice a drop in the LF, because the incompleteness limit has been reached, as discussed in Section 5.3.3.2. The best fit is provided in red (see Section 5.4 for more details about the procedure).

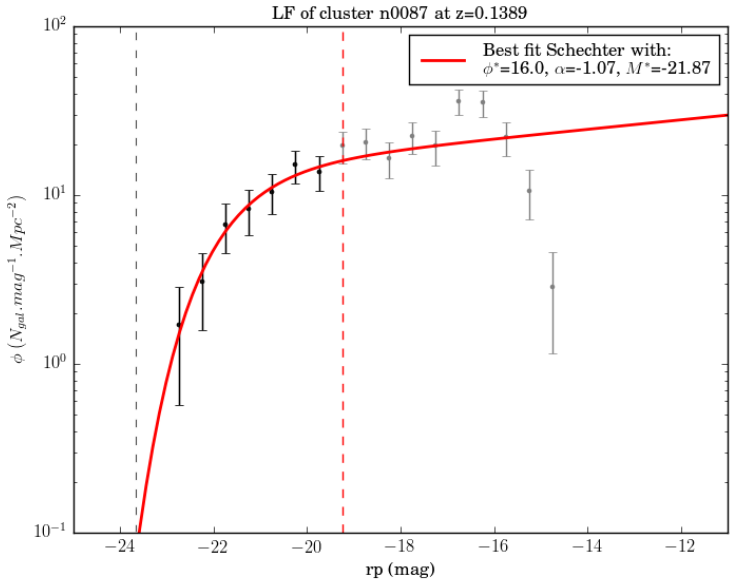

Figure 5.5: Illustration of the luminosity function of a rich cluster. The red dashed line corresponds to the magnitude limit and the grey dashed line to the magnitude of the BCG. The red solid line provides the best fit model of equation 5.15, obtained as discussed in Section 5.4. The grey points are affected by magnitude incompleteness and are discarded in the fit.

5.3.4.2 Composite luminosity functions

In order to investigate the dependence of the LF with cluster properties and enhance the signal to noise, we chose to create composite cluster luminosity functions (CLFs). The stacking procedure was made using the method described in Colless (1989) in order to obtain CLFs extending up to the faintest magnitude limits of our sample, and thus use all available data, as recommended by Popesso et al. (2005). We defined:

– The galaxy surface density in the $j^{\rm th}$ magnitude bin of the composite luminosity function as:

$$\phi_j = \frac{\phi_0}{n_j} \sum_i \frac{\phi_{ij}}{\phi_{i0}} \tag{5.10}$$

where ϕ_{ij} is the galaxy surface density, given by equation 5.8, in the $j^{\rm th}$ magnitude bin of the $i^{\rm th}$ cluster, n_j is the number of clusters contributing to the $j^{\rm th}$ magnitude bin, ϕ_{i0} is the normalisation of the $i^{\rm th}$ cluster and ϕ_0 is defined as the mean normalisation, $\phi_0 =< \phi_{i0} >_i$ (whereas in Colless 1989, $\phi_0 = \sum_i \phi_{i0}$). The normalisation ϕ_{i0} is defined as the sum of the galaxy surface densities in all the bins brighter than a limiting magnitude. This magnitude is tuned to be brighter than the limiting magnitudes of all the individual LFs in the stack. Possible clusters for which $\phi_{i0} = 0$ are not included in the CLF.

– The statistical error associated to ϕ_j as:

$$\delta\phi_j = \frac{\phi_0}{n_j} \left[\sum_i \left(\frac{\Delta\phi_{ij}}{\phi_{i0}} \right)^2 \right]^{1/2} \tag{5.11}$$

where $\Delta\phi_{ij}$ is given by equation 5.9, in the $j^{\rm th}$ magnitude bin of the $i^{\rm th}$ cluster.

Another source of errors comes from the intrinsic scatter between individual cluster LFs inside the CLF. To estimate this error we computed the CLF counts for 1000 resamplings of the stack using a bootstrap procedure. The final CLF counts were defined as the medians of the 1000 CLF realisation values and the standard deviations σ_j were used as the CLF intrinsic scatter per magnitude bin indicators.

The final errors in each magnitude bins of the CLF were taken as the quadratic sums of the statistical errors and the intrinsic scatter, $\sqrt{\delta\phi_j^2 + \sigma_j^2}$. In general, the statistical errors are dominant in the bright part of the CLFs and the intrinsic scatter are dominant in the faint part.

5.3.4.3 Definition of the clusters' richness

In the following analysis, we aim at investigating the LF dependences on clusters general properties. For this purpose we chose to use the richness, which is a quantity naturally connected to the LF and a cluster mass indicator. Indeed richness is a very promising mass-proxy (see e.g. Rozo et al. 2009; Andreon and Bergé 2012) and has the advantage of being directly derived from the same photometric galaxy catalog used for LF determination.

Precise membership assignment for our X-ray cluster sample is beyond the scope of this study, but we rather wish to quantify the galaxy excess at the positions of extended X-ray source detections. Therefore, richnesses λ_R were computed using the differences in galaxy density numbers between the cluster and background fields and their associated errors $\Delta\lambda_R$ were taken as Poissonian errors:

$$\lambda_R = \pi R^2 \cdot (\Sigma_{\text{cluster field}} - \Sigma_{\text{background}}) \tag{5.12}$$

and

$$\Delta\lambda_R = \pi R^2 \cdot \left(\frac{\Sigma_{\text{cluster field}}}{\sqrt{N_{\text{cluster field}}}} + \frac{\Sigma_{\text{background}}}{\sqrt{N_{\text{background}}}} \right) \tag{5.13}$$

with R the projected radius inside which the cluster field is defined, $\Sigma_{\text{cluster field}}$ and $\Sigma_{\text{background}}$ the cluster and background field galaxy number densities and $N_{\text{cluster field}}$ and $N_{\text{background}}$ the cluster and background field galaxy number counts.

To compute richnesses, we used the redshift and magnitude dependent photometric redshift dispersion defined in Section 4.4.3 and we only selected galaxies with $m < m^* + 1$ (or $L > 0.4L^*$), in order to be complete up to $z \sim 1$ and enhance the density contrast with respect to the field. Various aperture radii were explored, as a compromise is needed between large radii that will introduce interlopers and noise, and small radii that will be sensitive to X-ray-optical centring offset. Finally, we chose to use a constant physical radius to have a mass proxy independent from scaling laws, with a size of 0.5 Mpc, to be compared to the median R_{500} of our sample (~ 0.6 Mpc). In the rest of the study, the richness is denoted by $\lambda_{0.5Mpc}$.

5.4 Luminosity functions fitting procedure

5.4.1 Parametrisation by a Schechter function

In order to characterise the CLFs and to compare our measurements to other studies, we parametrised them by Schechter functions (Schechter 1976) of the form:

$$\phi(L)dL = \phi^* \left(\frac{L}{L^*}\right)^{\alpha} \exp\left(-\frac{L}{L^*}\right) \frac{dL}{L^*} \,, \tag{5.14}$$

and as $\frac{L}{L^*} = 10^{0.4(M^*-M)}$, the function can be expressed in terms of absolute magnitude as:

$$\phi(M)dM = 0.4\ln(10)\phi^* 10^{0.4(M^*-M)(\alpha+1)} e^{-10^{0.4(M^*-M)}} dM \tag{5.15}$$

with ϕ^* the characteristic number density, M^* (L^*, respectively) the characteristic absolute magnitude (luminosity, respectively) and α the faint-end slope.

Several authors (as Popesso et al. 2005) found that luminosity and stellar mass functions are best described by double Schechter functions, in order to model separately the behaviour of their bright and faint parts. However, we do not reach sufficiently faint magnitudes to need this double parametrisation and consider a single Schechter component sufficient to describe our data.

The contribution from the BCGs was removed and magnitude bins with less than 5 clusters contributing in average were not taken into account in the fit. Unless specified, the parameters ϕ^*, M^* and α were set free and constrained at the same time.

5.4.2 Computation of parameters probability density functions

In order to properly define the errors on our parameters, we chose to estimate their full probability density functions (PDFs). To do so, we computed the values of the likelihood of our model given the data, $\mathcal{L}$, on $\phi^* - \alpha - M^*$ 3D-grids, defined as

$$-2\ln\left(\mathcal{L}(\phi^*,\alpha,M^*)\right) \equiv \chi^2(\phi^*,\alpha,M^*) = \sum_j \frac{\left(\phi_j^{\rm data} - \phi_j^{\rm model}(\phi^*,\alpha,M^*)\right)^2}{\left(\delta\phi_j^{\rm data}\right)^2}, \tag{5.16}$$

and related to the χ^2, with $\phi_j^{\rm data}$ and $\delta\phi_j^{\rm data}$ constructed as described in Section 5.3.4.2, and $\phi_j^{\rm model}(\phi^*,\alpha,M^*)$ given by equation 5.15. Due to the "banana" shape of our posterior likelihood in the parameter space, we are sensitive to the so-called volume effect, which leads to the fact that depending on our statistical approach (marginalisation or profiling) to obtain the parameter's PDFs we will not get the same results. In our case, as we use a grid that does not sample finely the likelihood profiles we used marginalisation to obtain the PDF of the parameters. We thus marginalised over one parameter to compute the error contours around the other two, and marginalised over two parameters to obtain the PDF of the third one.

The size of the grids were chosen to encompass the 99% likelihood contours, and we verify that, if this criterion is satisfied, the choice of the size does not affect the results. Also, the size of the cells has to be small enough so that the numerical errors can be neglected.

In the rest of the study we chose to use the median of the PDF as our statistical estimator to get discrete values from the full likelihoods, as it is stable and not much sensitive to the grid sampling (we discuss the choice of statistical estimators in Section 5.5). The reported errors on the parameters are then the $16^{\rm th}$ and $84^{\rm th}$ percentiles. The grids were chosen to contain $101\times101\times101$ points and to be bound by $\phi^*=[0,125]$, $\alpha=[-3.5,3.5]$ and $M_R^*=[-32,-18]$ when binning in redshift and $\phi^*=[0,35]$, $\alpha=[-1.75,-0.25]$ and $M_R^*=[-32,-19]$ when binning in richness. Due to the low S/N and number of points of the CLF in the highest redshift bin (see Section 6.3), the parameters likelihood was sampled only up to 95%.

5.4.3 Construction of parametrised composite luminosity functions and derivation of integrated luminosities

The shapes of the parametrised composite cluster LFs were drawn by sampling the $\phi^* - \alpha - M^*$ space, according to the parameter likelihood values. We computed 1000 realisations of parameter set and derive a LF for each set. We then used the median of the resulting LFs as the parametrised baseline CLF profile, and we draw the 68% confidence intervals (c.i.) around it using percentiles.

Given the CLFs, the integrated luminosity L_R^{tot,M^*+3} was computed in the r' band and up to M_R^*+3, as

$$L_R^{tot,M^*+3} = \int_{L_{\rm min}}^{+\infty} \phi(L_R)dL_R, \tag{5.17}$$

where $L_{\rm min}=0.06L^*$ is the luminosity corresponding to M_R^*+3 and $\phi(L_R)$ is expressed as a function of luminosity, but was not normalised by the individual clusters area (πR_{500}^2) in

equation 5.8. In order to obtain the posterior PDF on the luminosity, the same approach as for the CLF was used. Equation 5.17 was computed for our 1000 LF realisations, and the median and percentiles were used to characterise the posterior likelihood. The integration was performed analytically using:

$$\frac{L_R^{tot,M^*+3}}{L_\odot} = \frac{L_R^{tot}}{L_\odot} \cdot \gamma\left(\alpha+2, 10^{-0.4(M_R^*-M_{\odot,R})}\right) \tag{5.18}$$

where:

$$\frac{L_R^{tot}}{L_\odot} = \phi^* \cdot 10^{-0.4(M_R^*-M_{\odot,R})} \cdot \Gamma(\alpha+2) \tag{5.19}$$

gives the luminosity integrated from zero to infinity. In this expression $L_\odot$ is the solar luminosity in the r' band and $M_{\odot,R}$ its associated absolute magnitude. $\gamma(s,x)$ denotes the incomplete gamma function and $\Gamma(x)$ denotes the gamma function. The value of $M_{\odot,R}$ in the CFHTLS r' filter was taken from Willmer (2018)[3].

5.5 Systematic effects in the luminosity function measurements

As discussed in Section 5.1, the luminosity function parameters found in the literature are varying from one study to another. There are different plausible explanations for this disparity, and in order to make physical interpretations, one as first to identify, characterise and reduce possible systematics. In this Section we analyse and discuss the implications of two main sources of systematic effects affecting the luminosity function measurements: one is related to the statistical choice used to obtain discrete LF parameter values and the other one related to the way galaxies are selected.

5.5.1 Origin of the systematic effects

5.5.1.1 Effects induced by the statistical estimators

We investigated different statistical choices to extract discrete parameters values from the likelihood and tested their stability. The statistical properties tested come from the full likelihood (the best fit and the value corresponding to the maximum likelihood), from the PDFs (the mode, median and mean) and from the Schechter fit of the median luminosity profile. The best fit value was obtained using the `Curve_fit` function from `Scipy.optimize` PYTHON library, which uses a Trust Region Reflective algorithm, whereas the value corresponding to the maximum likelihood was computed using the $\phi^* - \alpha - M^*$ 3D-grids, which is why those two values can differ.

Figure 5.6 illustrates the composite luminosity function fitting procedure for a sample of 121 clusters (general sample in Section 6.3). The 2D marginalised likelihoods of the Schechter fit parameters, and associated luminosity profile are shown in the four left panels whereas the PDF of the Schechter fit parameters after marginalisation are shown in the three right panels. The different statistical values are indicated in the 2D marginalised likelihoods (PDFs, respectively) by the following markers: black crosses (dotted black lines) for the best fit, black dots (black lines) for the maximum likelihood, blue points, red circles and green plus signs (blue, red and green lines) for the PDF mean, median and mode and black circles (dashed lines) for the Schechter fit of the median luminosity profile.

We can see that the shapes of the contours in the 2D likelihood function can be roughly approximated by ellipses while the PDFs can be roughly approximated by Gaussian functions. For this sample, the different statistical values are consistent with each other and hardly distinguishable on the figure.

[3] See also http://mips.as.arizona.edu/~cnaw/sun.html

Figure 5.7 illustrates again the composite luminosity function fitting procedure, but for a sample of 26 poor clusters (lowest richness sample in Section 6.3). For this sample, the statistical errors are larger and the magnitude range a bit smaller than for the larger sample, as can be seen in the luminosity profile plot. The "volume effect" is more pronounced. This causes the contours of the 2D marginalised likelihoods and the PDFs to be much broader, and the approximation by ellipses and Gaussian functions is no longer possible. For this sample, the different statistical values give different values.

This Section highlights the fact that even with the same data, it is possible to obtain very different parameter values, albeit being compatibles considering the errors, depending on the statistical choice to obtain discrete values. This is true in particular in the case of low signal to noise sample or sample with small magnitude range (e.g. at high redshift).

5.5.1.2 Effects induced by the different galaxy selections

Effects of photometric redshift selection methods As we discussed in Chapter 4, the usual photometric redshift selection methods lead to redshift and magnitude dependent completenesses. However, the impact of these redshift and magnitude dependent completenesses on the LFs shapes is not straightforward, because we are not measuring absolute counts, but an excess of galaxies with respect to a background field. In this section we thus investigate the influence of the different photometric redshift selection methods described in Chapter 4 on the shape of the luminosity functions.

In order to explore possible systematic effects induced by the photometric redshift selections, we computed the CLF (to enhance the signal) in redshift bins using the different methods. We then compared the parameters values for which each selection includes the same clusters.

Figure 5.8 shows the parameters evolution as a function of redshift, for CLFs constructed using different photometric redshift selection methods: using PDZ errors (*ZPDF*), constant dispersions corresponding to $\sigma_{1/(1+z)} = 0.04$ for $i' < 22.5$ and $\sigma_{1/(1+z)} = 0.08$ for $i' > 22.5$ (*cte*), a dispersion computed as a function of z (*zfct*) and a dispersion computed as a function of z and i' (*zmfct*). All the selections are made at the 1σ or 68% level. From top to bottom, we can see the evolution of the amplitude ϕ^*, the faint end slope α, and the characteristic magnitude M_R^*, for the different methods, as indicated in the legend. The vertical error bars indicate 68% c.i. and the the horizontal ones reflect the bin sizes.

We remark that the CLF profiles and their associated parameters overly agree, considering the error bars. However, as the different selection methods are applied on the same data, the differences we see between their CLFs are mainly due to systematic errors and not statistical ones. The relative fraction of the systematic error compared to the statistical one is non negligible, especially for ϕ^* and α. In some cases, systematic errors dominate.

The differences between the methods are due to the differences in their completenesses as a function of magnitude, in each redshift bin. The mean completeness value bias the amplitude ϕ^*, while the gradient as a function of magnitude leads to biases in the faint end slope α. The effect is stronger for the *zfct* method, which shows a higher amplitude, shallower faint end slope and fainter characteristic magnitude with respect to the *zmfct* method. When looking at the completeness maps of Figure 4.12, we remark that the *zfct* method shows indeed the strongest incompleteness gradient between the bright and faint magnitudes at each redshift.

We conclude that the selection methods having redshift and magnitude dependent completenesses can indeed bias the shape of the luminosity function. In our case, the systematic errors due to the selection methods are non negligible compared to the statistical errors.

Effects related to the selection width We defined our selection using photometric redshift dispersions at either 68 or 95% completeness. If we apply the same dispersion to both the cluster and background fields, we expect to obtain the same LF shape using one or the other definition, except for the normalization. Taking a higher dispersion value ensure a higher signal, but may

Table 5.1: Summary of the systematics affecting the faint end slope measurements. The systematics from different origins are estimated differently.

origin of the systematics	error sys.	error sys./error stat.
estimators stat.	$\sigma(\alpha_i)$	$\sigma(\alpha_i)/\Delta\alpha_{ref}$
	0.07	0.47
photo-z selections	$< \alpha_i - \alpha_{ref} >_z$	$< \frac{\lvert\alpha_i - \alpha_{ref}\rvert}{\Delta\alpha_{ref}} >_z$
$ZPDF$ method	0.06	0.68
cte method	0.07	0.61
$zfct$ method	0.17	1.25
selection width	$< \alpha_{95\%} - \alpha_{68\%} >_\lambda$	$< \frac{\lvert\alpha_{95\%} - \alpha_{68\%}\rvert}{\Delta\alpha_{68\%}} >_\lambda$
	-0.03	0.27

reduce the purity and introduce interlopers. We checked this possible effect by comparing the CLF computed using a dispersion at 68 or 95% in different richness bins. In order to compare, we only show richness bins for which each selection includes the same clusters.

Figure 5.9 shows the evolution of the CLF parameters with richness, for different photometric redshift selection widths: 68% in red and 95% in blue. From top to bottom, we can see the evolution of the amplitude ϕ^* normalized to 100%, the faint end slope α and the characteristic magnitude M_R^*. The vertical error bars indicate 68% c.i., whereas the horizontal ones reflect the bin sizes.

We remark that when we rescale the amplitude values by the level of completeness we used to compute them, we find that they agree very well ($\phi^*_{100\%} \equiv (1/0.68) \cdot \phi^*_{68\%} \equiv (1/0.95) \cdot \phi^*_{95\%}$), for all the richness bins . The values of the faint end slope α and characteristic magnitude M_R^* obtained with the two selections are in good agreements. We can also note that the error bars on the parameters are generally larger when computed with the dispersion at 68%.

Finally, we conclude that the level of completeness ensured by the photometric redshift selection does not affect considerably the shapes of the derived CLFs, except for the amplitude that increases proportionally with the completeness.

5.5.2 Quantification of the systematic effects affecting the CLF measurements

We have identified three different origins of systematics affecting the measurements of the luminosity function: the statistical estimators, the photometric redshift selection methods and the width of the photometric redshift slice. We chose to analyse the importances of those systematics by estimating the values of the systematic errors and ratios of systematic to statistical error for each origin. For the sake of conciseness we only focused on the measurement of the faint end slope α and we presented our values in Table 5.1.

The systematic error coming from the different statistical estimators i was estimated using the standard deviation $\sigma(\alpha_i)$ among the different values of the faint end slope α of the CLF containing the poorest clusters. The ratio of systematic to statistical error was estimated by dividing the standard deviation by the symmetrised statistical error of our reference value $\sigma(\alpha_i)/\Delta\alpha_{ref}$, with α_{ref} coming from the median of the PDF. In this case the systematic error value informs us about the spread among the statistical estimators and the ratio of systematic to statistical error tells us about the relative importance of this spread.

In the case of the systematics coming from the different galaxy selections, the differences between the values is not directly due to systematic errors because, even if the methods are applied on the same clusters, we do not select exactly the same galaxies (by definition). However,

the values are highly correlated and in the following analysis we make the assumption that the differences between them is mainly due to systematics.

The systematic errors coming from the different photometric redshift selection methods were estimated using as reference the values of α obtained with the *"zmfct"* selection method and by averaging over the redshift bins the deviation between the values of α from each method i with respect to the references: $\langle \alpha_i - \alpha_{ref} \rangle_z$. The ratios of systematic to statistical errors were estimated by dividing each absolute deviation by the symmetrised statistical error of our reference value and averaging over the redshift bins: $\langle \frac{|\alpha_i - \alpha_{ref}|}{\Delta\alpha_{ref}} \rangle_z$. In this case we see that the systematic error can be null if the values from one method are varying around the reference values and positive or negative in presence of bias, but the systematic error ratio will be null only if there is no differences in the measurements of α induced by one photometric redshift selection method.

Finally, the systematic errors coming from the width of the photometric redshift slice were estimated using as reference the values of α obtained with the dispersion at 68% and averaging the differences with the values obtained with the dispersion at 95% over the richness bins, using: $\langle \alpha_{95\%} - \alpha_{68\%} \rangle_\lambda$ and $\langle \frac{|\alpha_{95\%} - \alpha_{68\%}|}{\Delta\alpha_{68\%}} \rangle_\lambda$.

From Table 5.1 we can conclude that the different statistical estimators give results that have a standard deviation of $\sigma(\alpha_i) = 0.07$ which represents 47% of the statistical errors in the case of a CLF with low signal to noise. The three photometric redshift selection methods lead to faint end slope values that are biased high in average, in particular for the *"zfct"* method. The associated averaged systematic error ratio are higher than 60% and reaching 125% for the $zfct$ method. Finally, the averaged difference between the values obtained with the two dispersion widths is low. Its corresponds to 27% of the statistical error and is an upper limit since it also accounts partially for statistical uncertainties.

5.5.3 Importance of the systematics effects

Previously, we quantified and summarized the systematic effects affecting the faint end slope measurements. We found that the systematic error coming from the different statistical estimators was sub-dominant but non negligible in the case of a CLF with low signal to noise. The systematic and statistical error values are expected to decrease strongly with the signal to noise and the number of data points. Therefore the ratio of systematic to statistical error depends on the rate at which these quantities decrease.

The systematics induced by the different photometric redshift selection methods are biasing high the values of the faint end slope and are dominating the statistical errors in some cases. They are related to the redshift and magnitude dependent completeness studied at the 68% level in Chapter 4. If we increase the width of the selection, e.g. at the 95% level, the completenesses are closer to 100% and thus the variations are less important. On one hand, this means that selecting galaxies using a photometric redshift slice large enough will reduce the systematics coming from the different selection methods (albeit introducing other complications: e.g. reducing the purity). On the other hand, the variations of the completeness will be more important when larger magnitude ranges will be probed (e.g. with deeper photometry) and the systematics will dominate the error budget when the statistical errors will decrease (e.g. with a richer or larger cluster sample). Therefore, the systematics induced by the different photometric redshift selection methods need to be taken into account, in particular for studies using deeper photometry and/or larger cluster sample.

The systematics related to the width of the photometric redshift window were already studied by Crawford et al. (2009), who found that the faint end slope was becoming steeper when the window was increasing (and vice-versa) and suggested that this was due either to the fact that the photometric redshift errors were underestimated or to a contamination from field galaxies. However, they used a fixed window and did not take into account the magnitude

dependence of the photometric redshift errors. We thus stress that the effect they found is likely to be related to their photometric redshift dispersion modeling more than its size and that, as we have shown, the systematic is stronger when the dispersion width is small.

Finally, if the systematics coming from the width of the photometric redshift slice are negligible for our study, their precise origin has to be investigated in details if they become no longer subdominant.

5.6 Summary

In this Chapter we presented our methodology used to construct composite cluster luminosity functions and tested its robustness. We constructed LFs using a selection in photometric redshift around the cluster spectroscopic redshift, to reduce projection effects. The width of the photometric redshift selection has been carefully determined to avoid biasing the LF and depends on both the cluster redshift and the galaxy magnitudes. It was defined to obtain an homogeneous completeness in the redshift-magnitude plane (see Chapter 4). The purity was then enhanced by applying a precise background subtraction using fields in annulus from 3 to 5 Mpc around cluster centres. Maps of the galaxy density in the field of clusters were created for visual inspection. We identified BCGs and analysed completeness magnitude to define the luminosity range where to compute the clusters LFs. We then constructed composite luminosity functions and defined richnesses. We parametrised the LFs obtained by a Schechter function and estimated the parameters using 3-D likelihood grids. Finally, we identified, quantified and discussed the implications of two main sources of systematic effects affecting the luminosity function measurements: one related to the statistical choice used to obtain discrete LF parameters values and the other one related to the way galaxies are selected.

Our main findings are summarised in the following:

- In Section 5.5, we showed that, due to the complex shape of the Schechter parameters posterior likelihood, one can obtain different parameters values, and thus introduce systematics, using different statistical estimators. This is true in particular when the signal to noise of the data is low or when the magnitude range probed is small. This effect can be in part responsible for the large variety of values found in the literature.

- In Chapter 4, we have found that the usual method to select galaxies using photometric redshifts, defined by using external calibration or by integrating the PDF, lead to redshift and magnitude dependent completeness. In Section 5.5, we have shown that these non homogeneous completeness causes the resulting LFs shapes, in particular their amplitudes and faint end slopes, to be biased. Our selection in photometric redshift was defined to obtained an homogeneous completeness in the redshift-magnitude plane and allow us to construct unbiased LFs.

- In Section 5.5, we showed that the systematics introduced by the usual galaxy selection methods, using photometric redshifts, were expected to become even stronger when using deeper photometry. Those systematics may not only affect the LF determination, but also cluster detections, richness estimation or the construction of density profiles.

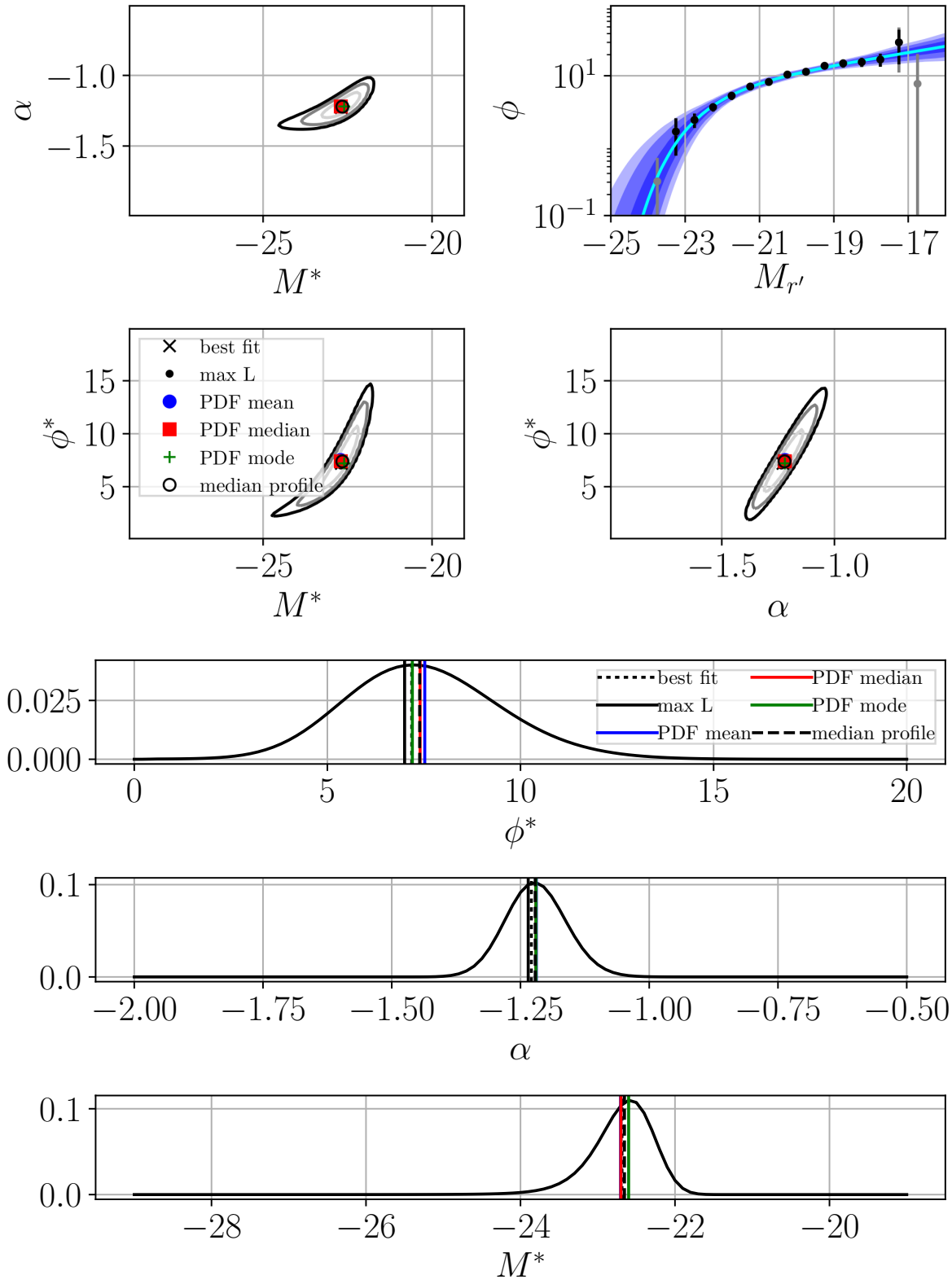

Figure 5.6: Illustration of the composite luminosity function fitting procedure for a sample of 121 clusters (general sample in Section 6.3). *Upper panels*: 2D marginalised likelihoods of the Schechter fit parameters, and associated luminosity profile. The contours show the 68, 95 and 99% levels and the different statistical values are indicated as in the legend. *Top left*: (α, M^*) marginalised over ϕ^*. *Top right*: posterior CLF shape, the data points are shown in black or grey if they are taken into account or not in the fit, the median profile is drawn in cyan and the blue shaded regions indicate the 68, 95 and 99% c.i. *Bottom left*: (ϕ^*, M^*) marginalised on α. *Bottom right*: (ϕ^*, α) marginalised on M^*. *Bottom panels*: Probability density functions of the Schechter fit parameters after marginalisation. The lines show the different statistical values, as indicated in the legend. In this sample, the different statistical estimators give indistinguishable values.

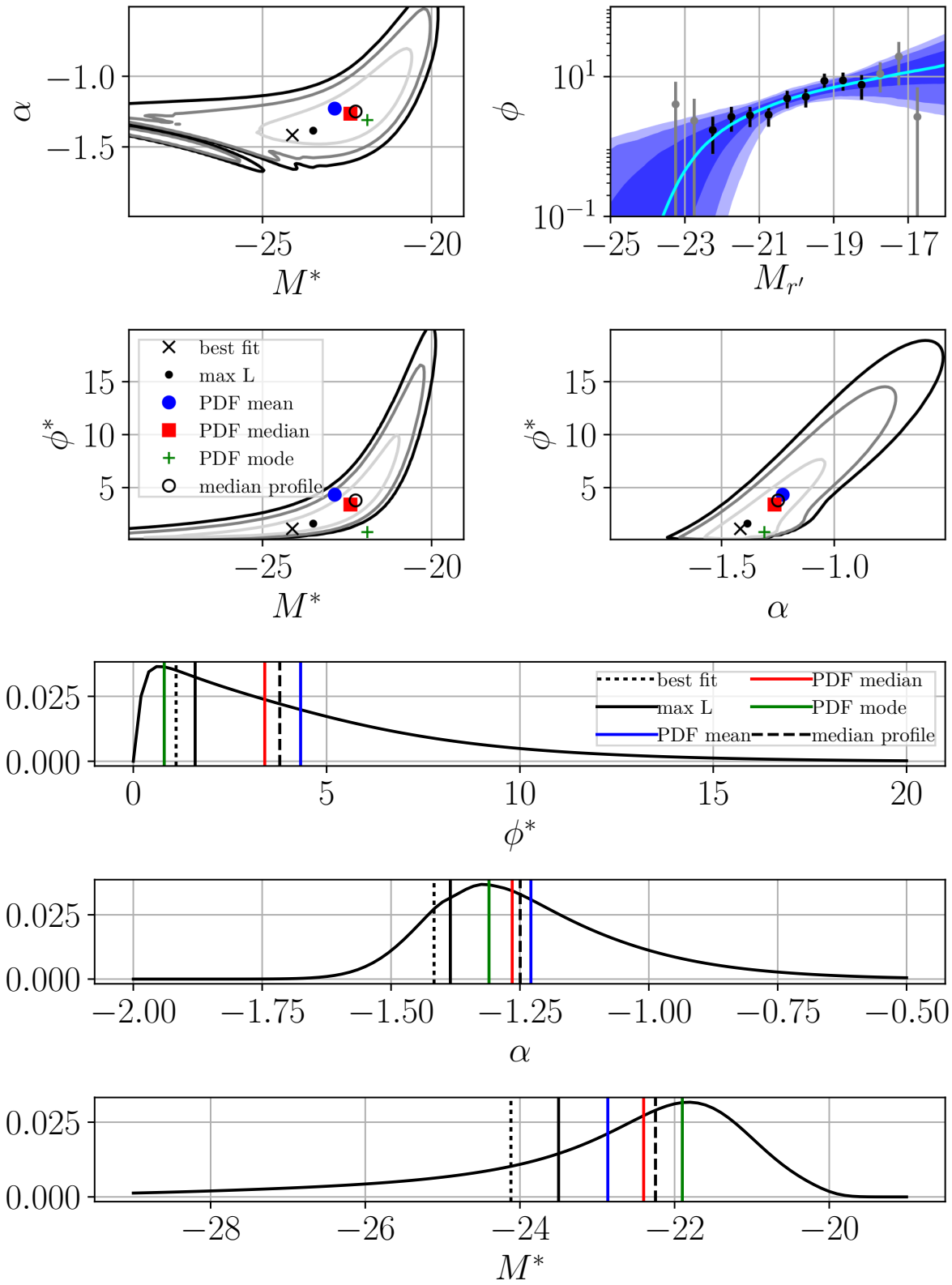

Figure 5.7: Illustration of the composite luminosity function fitting procedure as in Figure 5.6, but for a sample of 26 poor clusters (lowest richness sample in Section 6.3). In this sample, the different statistical estimators give distinguishable values.

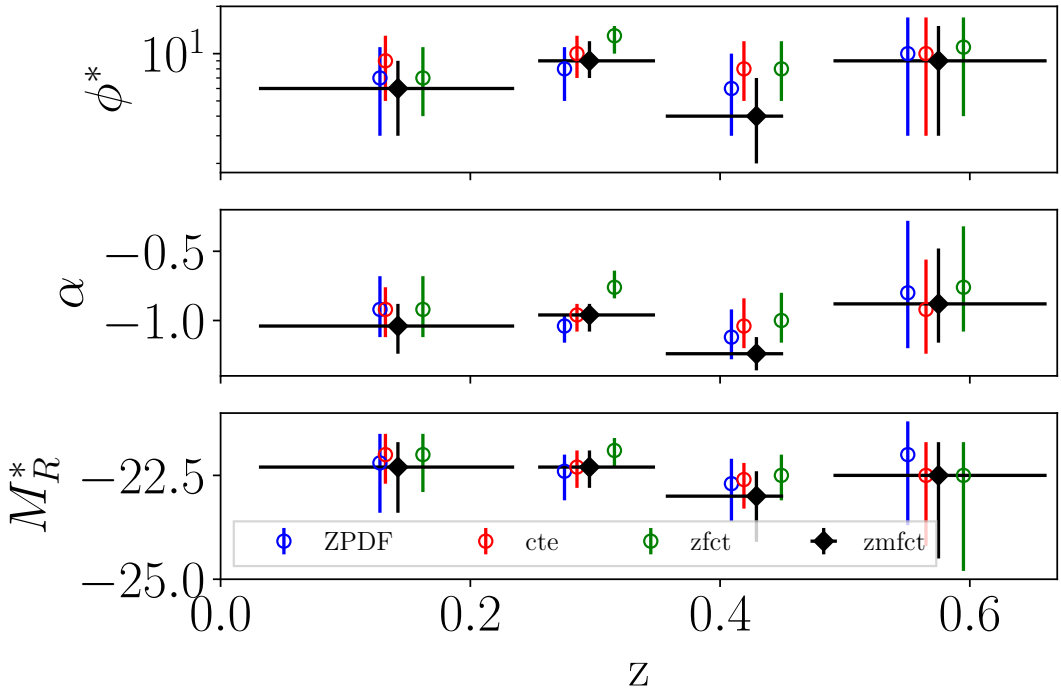

Figure 5.8: Evolution of the composite cluster luminosity function parameters with redshift, for different photometric redshift selection methods, as indicated in the legend. The vertical error bars indicate 68% c.i., whereas the horizontal ones reflect the bin sizes. The points have been slightly shifted in redshift for clarity.

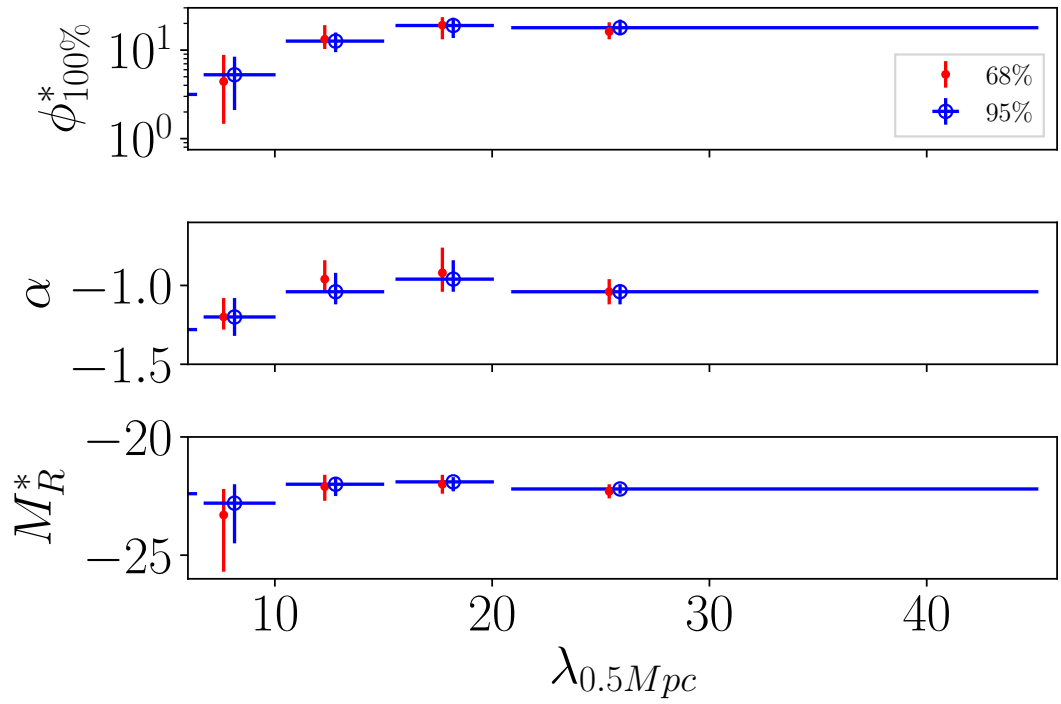

Figure 5.9: Evolution of the composite cluster luminosity functions parameters with richness, for two different dispersion widths, as indicated in the legend. The vertical error bars indicate 68% c.i., whereas the horizontal ones reflect the bin sizes. The points have been slightly shifted in richness for clarity.

Chapter 6

Analyses of the luminosity functions in XXL-N clusters

Contents

Abstract: In Chapter 5, we developed the methodology to construct the composite luminosity function (CLF) of XXL-N clusters. In this Chapter, we present their analyses. We first measure the CLF of the entire cluster sample and analyse the impact of poor clusters in our sample. Then, we study the luminosity of BCG and satellites galaxies and their dependence on cluster's redshift and richness. Finally, we discuss the implications of our results in terms of galaxy evolution and the cosmological utilisation of clusters. This study is based on Ricci et al. (2018).

Composite luminosity functions were computed for the entire cluster sample, with different selections, following the methodology described in Chapter 5. Galaxies were selected using photometric redshift dispersion ensuring 95% completeness ($d_{95\%}$, see equation 5.1 and Section 5.3.2) because the statistical errors are lower with the larger dispersion (see Section 5.5.1.2). The counts were made within projected radius R_{500}, in order to sample the same region for each cluster, and thus avoiding to mix radial dependences with other effects, (see e.g. Hansen et al. 2005; Popesso et al. 2006; Barkhouse et al. 2007). We restricted the study to the clusters with redshift $z < 0.67$, in order to have accurate estimations of the absolute magnitude in the rest frame r' band (see Section 5.3.4) and treated the other clusters separately. In the following sections we analyse the composite luminosity function of the general sample ($z < 0.67$) and investigate the dependence of the BCG and non-BCG luminosity distributions with both redshift and richness.

Table 6.1: Parameters of the composite luminosity functions for cluster selection as stated in the first column. The first block of columns indicates the bin information: number of objects, median redshift, richness, and mass $M_{500,scal}$ (in units of 10^{14} $M_\odot$). The second block indicates the results of the fit of the composite luminosity function: amplitude ϕ^* (in units of N_{gal} mag^{-1} Mpc^{-2}), faint end slope α, characteristic magnitude in the r' band M_R^*, and goodness of fit parameter Q. The third block indicates the results of the fit of the composite luminosity function when α is fixed to -1. The values are the median of the marginalised distribution and the errors correspond to 68% c.i. around the median (see Section 5.4). The goodness of fit parameters (see equation 6.2) are computed using the minimum χ^2 value in the grid (see Section 5.4).

selection	n	$\widetilde{z}$	$\widetilde{\lambda}$	$\widetilde{M_{500,scal}}$	ϕ^*	α	M_R^*	Q	$\phi^*_{\alpha fixed}$	$M^*_{R,\alpha fixed}$	$Q_{\alpha fixed}$
$z < 0.67$	121	0.30	11.9	1.00	8^{+2}_{-2}	$-1.22^{+0.06}_{-0.06}$	$-22.6^{+0.3}_{-0.4}$	0.99			
$z < 0.67$ & $\lambda > 6$	95	0.32	13.5	1.14	11^{+2}_{-2}	$-1.13^{+0.05}_{-0.05}$	$-22.4^{+0.2}_{-0.2}$	0.99			
$z < 0.67$ & $\lambda > 10$	71	0.37	17.1	1.27	14^{+2}_{-2}	$-1.06^{+0.05}_{-0.06}$	$-22.2^{+0.2}_{-0.2}$	0.97			
$\lambda > 6$ & $0.00 < z < 0.25$	26	0.14	9.9	0.75	10^{+4}_{-4}	$-0.98^{+0.14}_{-0.14}$	$-22.1^{+0.4}_{-0.6}$	0.99	$10.4^{+0.8}_{-0.8}$	$-22.1^{+0.3}_{-0.2}$	0.99
$\lambda > 6$ & $0.25 < z < 0.35$	28	0.30	13.5	1.15	15^{+3}_{-4}	$-1.05^{+0.07}_{-0.07}$	$-22.1^{+0.3}_{-0.3}$	0.95	$16^{+1.6}_{-0.8}$	$-21.9^{+0.1}_{-0.2}$	0.97
$\lambda > 6$ & $0.35 < z < 0.47$	24	0.43	18.1	1.37	13^{+4}_{-4}	$-1.05^{+0.14}_{-0.14}$	$-22.3^{+0.3}_{-0.4}$	0.97	$14.4^{+0.8}_{-1.6}$	$-22.3^{+0.2}_{-0.2}$	0.98
$\lambda > 6$ & $0.47 < z < 0.67$	17	0.55	15.5	1.14	14^{+9}_{-6}	$-0.91^{+0.28}_{-0.28}$	$-22.3^{+0.6}_{-0.8}$	0.98	$12.8^{+1.6}_{-1.6}$	$-22.4^{+0.3}_{-0.3}$	0.99
$\lambda > 6$ & $0.67 < z$	12	0.88	24.6	2.55	29^{+31}_{-16}	$-0.77^{+1.19}_{-0.91}$	$-21.8^{+0.7}_{-0.8}$	0.36	27.2^{+22}_{-13}	$-22.1^{+0.6}_{-0.6}$	0.60
$z < 0.67$ & $\lambda < 6$	26	0.27	4.4	0.64	3^{+4}_{-2}	$-1.27^{+0.18}_{-0.12}$	$-22.5^{+1.2}_{-2.2}$	0.92	9^{+2}_{-1}	$-21.2^{+0.5}_{-0.5}$	0.63
$z < 0.67$ & $6 < \lambda < 10$	24	0.21	7.6	0.71	5^{+3}_{-3}	$-1.23^{+0.14}_{-0.09}$	$-22.9^{+0.9}_{-2.1}$	0.98	10^{+1}_{-1}	$-21.7^{+0.2}_{-0.3}$	0.78
$z < 0.67$ & $10 < \lambda < 15$	28	0.31	12.3	1.01	11^{+3}_{-3}	$-1.05^{+0.11}_{-0.08}$	$-22.1^{+0.4}_{-0.4}$	0.86	$12^{+0.8}_{-1}$	$-22.0^{+0.2}_{-0.2}$	0.89
$z < 0.67$ & $15 < \lambda < 20$	21	0.33	17.7	1.21	18^{+5}_{-4}	$-0.96^{+0.12}_{-0.09}$	$-22.0^{+0.4}_{-0.3}$	0.96	16^{+1}_{-1}	$-22.1^{+0.2}_{-0.2}$	0.98
$z < 0.67$ & $20 < \lambda$	22	0.43	25.4	2.09	18^{+3}_{-3}	$-1.06^{+0.08}_{-0.06}$	$-22.3^{+0.3}_{-0.1}$	0.99	20^{+1}_{-1}	$-22.1^{+0.1}_{-0.1}$	0.99

6.1 Composite luminosity function of the general sample

6.1.1 Impact of poor clusters

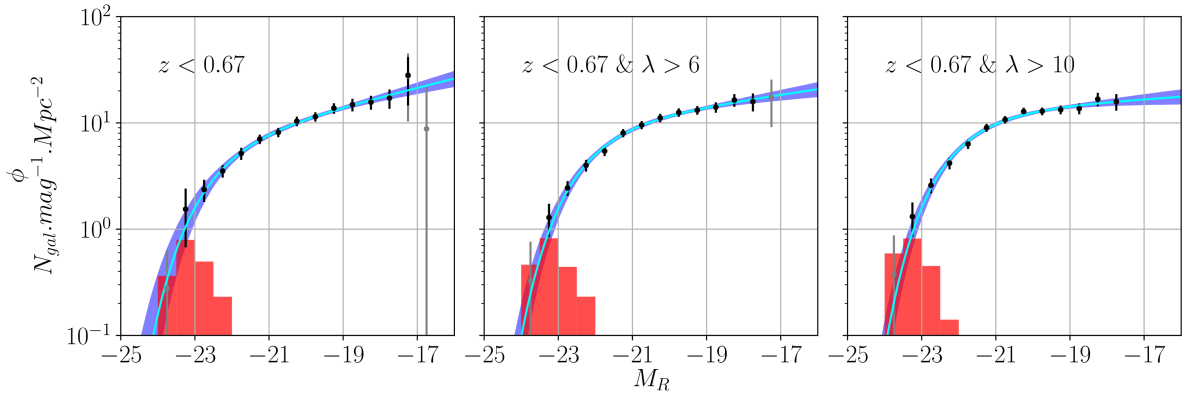

Figure 6.1: Composite luminosity functions including all clusters with a redshift lower than 0.67 (*left panel*), and those with a richness higher than 6 (*middle panel*) and higher than 10 (*right panel*). The black points represent the counts whereas the blue regions show the 68% c.i around the median parametrised composite luminosity functions, indicated by the cyan lines. The red normalised histograms show the magnitude distributions of the BCGs of all clusters included in each bin. The grey points show the counts when there is less than 5 clusters contributing, and are not taken into account in the fitting procedure.

The composite luminosity function including all clusters up to $z = 0.67$ is shown in the left panel of Figure 6.1. The black points represent the counts whereas the blue regions show the 68% confidence intervals around the median parametrised composite luminosity function,

Table 6.2: Schechter parameters M^* and α of field LF and CLFs retrieved in the literature

Reference	gal. type	radius	method	N_{clus}	sample	z	M^*	α
Blanton et al. (2001)	all	field	spec		SDSS	$z < 0.2$	-21.6 ± 0.03	-1.20 ± 0.03
Goto et al. (2002)	all	0.75 Mpc	phot	204	SDSS CE	$0.02 < z < 0.25$	-22.21 ± 0.05	-0.85 ± 0.03
Goto et al. (2002)	all	0.75 Mpc	spec	75	SDSS CE	$0.02 < z < 0.25$	-22.31 ± 0.13	-0.88 ± 0.07
Popesso et al. (2006)[a,b]	all	R_{500}	phot	69	RASS+SDSS	$< z >= 0.1$	-20.84 ± 0.13	-1.05 ± 0.07
Popesso et al. (2006)[a,c]	all	R_{500}	phot	69	RASS+SDSS	$< z >= 0.1$	-21.16 ± 0.26	-1.26 ± 0.12
Rudnick et al. (2009)	RS	0.75 Mpc	color	167	SDSS	$z < 0.06$	-21.21 ± 0.24	-0.78 ± 0.08
Rudnick et al. (2009)	RS	0.75 Mpc	color	16	EDisCS	$0.4 < z < 0.8$	$-21.51^{+0.23}_{-0.14}$	$-0.36^{+0.16}_{-0.08}$
Martinet et al. (2015)	RS	1 Mpc	photo-z+color	16	DAFT/FADA	$< z >= 0.58$	-22.4 ± 0.2	-0.80 ± 0.14
Martinet et al. (2015)	BC	1 Mpc	photo-z+color	6	DAFT/FADA	$< z >= 0.62$	-22.4 ± 0.5	-1.32 ± 0.36

[a] These values were obtain using $h_0 = 1$, we converted them to our cosmology in the Figure 6.2, [b] These values correspond to the bright part of a LF fitted using a double Schechter function (dS), [c] These values correspond to the bright part of a LF fitted using a Schechter plus an exponential functions (S+e).

indicated by the cyan line. The red normalised histogram shows the distribution of the BCGs. The grey points show the counts when there are less than 5 clusters contributing, and are not taken into account in the fitting procedure. The corresponding CLF parameters are presented in the first row of Table 6.1.

Within our magnitude range, we can see that, as expected, the composite luminosity function is well fitted by a single component Schechter function.

Selecting all clusters with $z < 0.67$ includes very poor clusters and we tested if this affects the CLF by applying richness cuts with $\lambda_{0.5Mpc} > 6$ and $\lambda_{0.5Mpc} > 10$. These limits correspond to the first and second richness bins discussed in the following Section. The resulting CLFs are shown in the middle and right panels of Figure 6.1 and their parameters are presented in Table 6.1. We can see that when the poorest clusters are discarded, the faint end slope becomes shallower, the characteristic magnitude fainter and the amplitude higher (following the degeneracy between the three parameters). The strong effect on the CLF caused by the poor clusters is driven by the fact that they are up-weighted by the Colless (1989) stacking method. Indeed, in Eq. 5.10 the individual LFs are weighted by the inverse of their normalisation: $1/\phi_{i0}$.

6.1.2 Comparison with the literature

In Figure 6.2, we compared our parameters values with the ones found in the literature and presented in Table 6.2, after accounting for the differences in the cosmological parameters used for the different studies. Unfortunately, the normalisation ϕ^* are often not mentioned or computed with different units and we thus restrained our comparison to the values of M^* and α, keeping in mind that the three parameters are degenerate. The M^* values from the literature were obtained in different red bands (R from VLT/FORS2 for Martinet et al. (2015) and r from SDSS for the others), but we checked that the corresponding differences in terms of absolute magnitudes were negligible.

We can remark that there is a disparity among CLF parameter's values, even when limited to the same galaxy population. The origin of the diversity may come from the different cluster samples and/or from the different methods to construct the CLF. We also have to keep in mind that the parameters are positively correlated, which can explain the tendency to have fainter M^* with shallower α. We can see that our M^* values are compatible within the errors with the values from Martinet et al. (2015), Goto et al. (2002) and partially with the value from Popesso et al. (2006) when fitted with a Schechter plus an exponential functions (S+e). Our faint end slope values are compatible with the field value from Blanton et al. (2001), the values from Popesso et al. (2006) and the value from Martinet et al. (2015) found for blue cloud galaxies. We note that our faint end slopes are steeper than the ones obtained with red sequence galaxies. Finally, considering the large scatter among the α and M^* reported in the literature, our values are comparable to the ones found by previous studies.

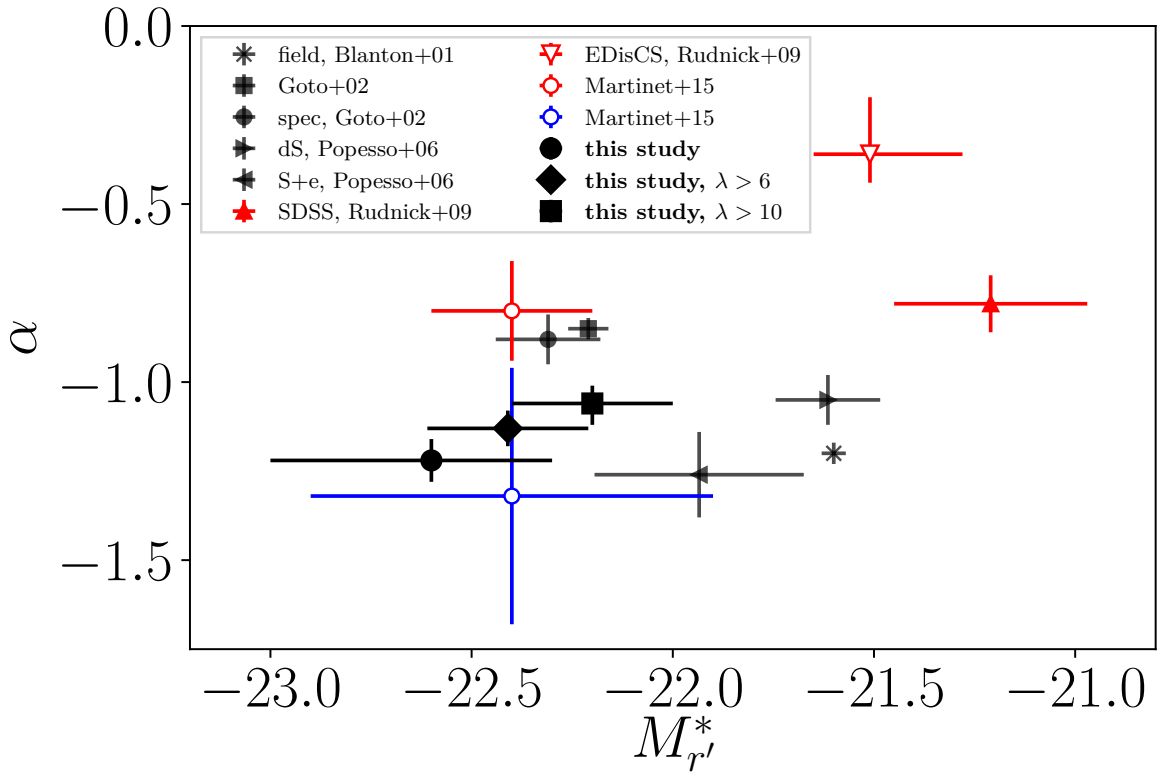

Figure 6.2: Comparison of our characteristic magnitude M^* and faint end slope α values obtained for the z<0.67 sample with different richness cuts (black circle, diamond and square), with those found in the literature. The asterisk indicates the field values from Blanton et al. (2001) whereas the other points indicate the values for composite luminosity functions from Goto et al. (2002), Popesso et al. (2006), Rudnick et al. (2009) and Martinet et al. (2015), including all galaxies (black), only the red sequence ones (red) or only the blue cloud ones (blue). The highest redshift samples are indicated by empty markers. Because of the good agreements between the bands used by the different studies, we did not apply any correction to transform one measurement into another. The values are corrected to our cosmology.

6.2 Redshift and richness dependence of the composite luminosity functions

6.2.1 Binning choice and fitting procedure of the parameters evolution

We studied the evolution of the CLF and BCG distributions with both redshift and richness by binning our cluster sample. Bins in richness were chosen in order to contain roughly the same number of objects, and bins in redshift were defined in order to have the median redshift increasing approximately by the same amount in each bin. The top panel of Figure 6.3 shows the richness as a function of redshift, with bins limits as well as median richness values indicated in each bin. The opposite is shown in the bottom panel. Further information on the bins can be found in Table 6.1. We applied a redshift cut at $z = 0.67$ when binning in richness and a richness cut at $\lambda_{0.5Mpc} = 6$ when binning in redshift, in order to remove possible contamination by ultra poor or miss-classified clusters. However, we found that our results are unchanged if we do not apply the richness cut, albeit being noisier.

As we aim to investigate the evolution of the CLF and BCG distributions parameters with redshift and richness separately, we need to consider the steep selection function of our X-ray cluster sample. Indeed, as can be seen in Figure 6.3, richness and redshift are not independent

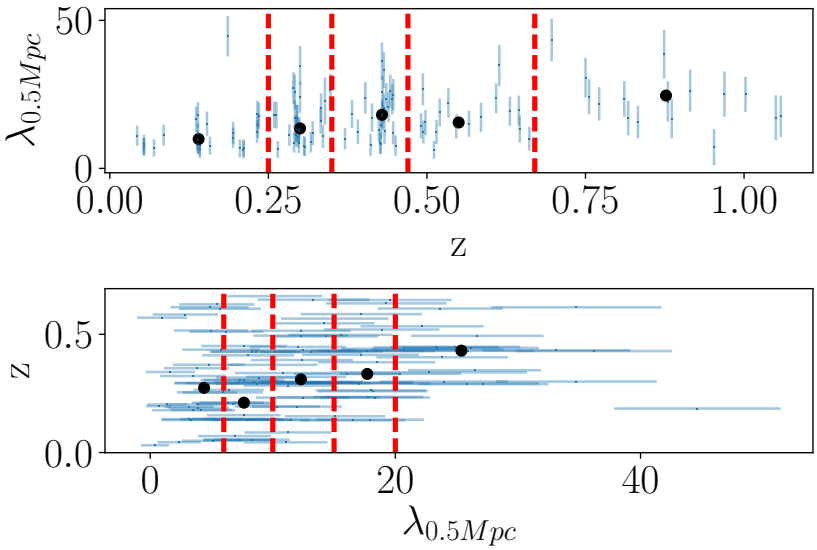

Figure 6.3: Illustration of the richness and redshift bins limits. Measurements for individual clusters are represented by the grey error bars. Bins delimitations are indicated by the red dashed lines. *Top:* richness in 0.5 Mpc as a function of redshift. The black dots indicate the median values of the richness in each redshift bin. *Bottom:* redshift as a function of the richness in 0.5 Mpc. The black dots indicates the median redshift value in each richness bin.

variables: we tend to detect richer clusters at high redshift and poorer at lower redshift. This is because of selection and volume effects affecting X-ray flux limited samples (see Giles et al. 2016, hereafter XXL Paper III, for details on selection effects in XXL). Therefore, to take into account those biases and disentangle between redshift and richness effects, we fitted the two parameter dependences conjointly. For this purpose we assumed the following evolution model:

$$Y = a \cdot \log(1 + \widetilde{z}) + b \cdot \log(\widetilde{\lambda}_{0.5Mpc}) + c \tag{6.1}$$

with Y standing for a parameter of the model describing the CLF or the BCG distribution computed in a given bin, $\widetilde{z}$ and $\widetilde{\lambda}_{0.5Mpc}$ being the median redshift and richness of the same bin, and a, b and c the evolution parameters. By doing so, we made the hypothesis that the median redshift and richness of a cluster sub-sample were the key parameters to describe the CLF and BCGs distribution in that sub-sample.

In order to constrain the evolution parameters a, b and c, we combined the values from the redshift and richness bins, and thus fitted 10 data points. We symmetrise the error bars and assumed $\Delta\log(\phi^*) = \Delta\phi^*/(\phi^* \cdot \ln(10))$, but we did not take into account the bin widths. Finally we fitted the model of Eq. 6.1 using the `Curve_fit` function from `Scipy.optimize` PYTHON library, which uses a Trust Region Reflective algorithm and returns the best fit evolution parameters and their covariance matrix.

Composite luminosity functions in increasing redshift and richness bins are shown in the top and bottom panel of Figure 6.4, respectively. The black points represent the counts whereas the blue regions show the 68% confidence intervals around the median parametrised composite luminosity function, indicated by the cyan line. The red normalised histogram shows the distribution of the BCGs. The grey points show the counts when there are less than 5 clusters contributing, and are not taken into account in the fitting procedure. The corresponding CLF parameters are presented in Table 6.1.

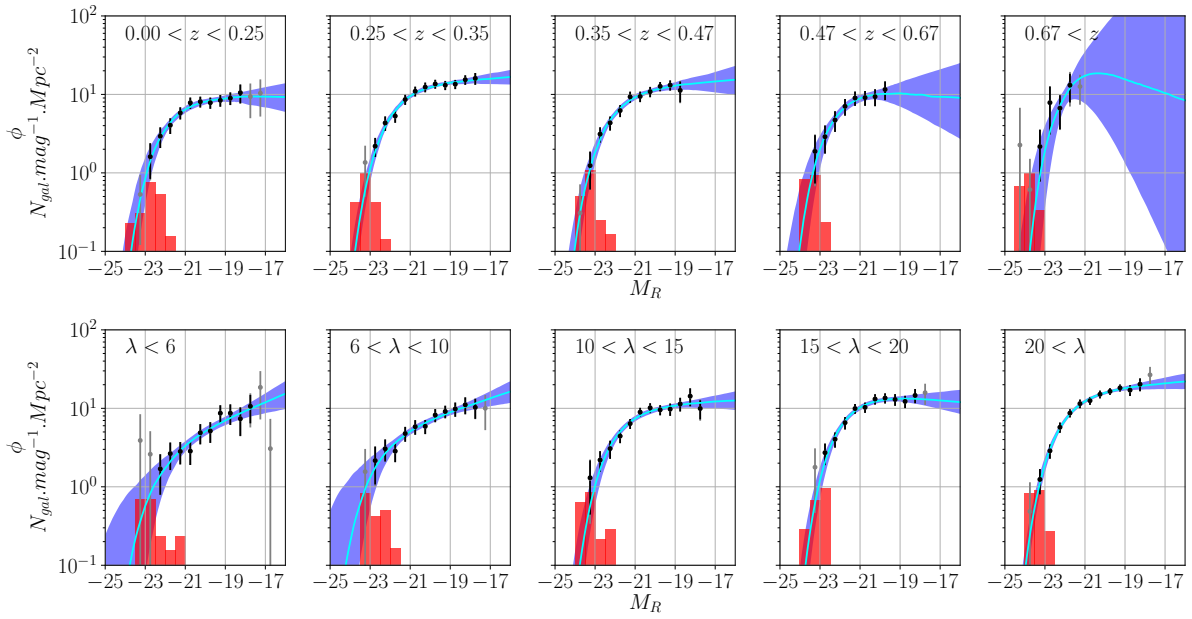

Figure 6.4: Composite cluster luminosity functions in increasing redshift bins (*top panel*) and increasing richness bins (*bottom panel*). The black points represent the counts whereas the blue regions show the 68% c.i around the median parametrised composite luminosity functions, indicated by the cyan lines. The red normalised histograms show the magnitude distributions of the BCGs of all clusters included in each bin. The grey points show the counts when there is less than 5 clusters contributing, and are not taken into account in the fitting procedure.

Table 6.3: Constraints on the evolution of the CLFs parameters (see model of Eq. 6.1) and associated goodness of fit parameters Q (see equation 6.2).

	a	b	c	Q
$\log(\phi^*)$	-0.4 ± 1.9	0.8 ± 0.4	0.3 ± 0.4	0.85
α	-1.3 ± 1.8	0.4 ± 0.3	-1.4 ± 0.2	0.87
M_R^*	-0.1 ± 4.9	-0.2 ± 1.2	-22 ± 1	0.98

6.2.2 Evolution of the non-BCGs luminosity distribution

6.2.2.1 CLF parameters' evolution

We studied the luminosity distribution of the non-BCG cluster members through their composite luminosity functions, shown by the black points and blue shaded regions in Figure 6.4.

The Schechter fits parameters from CLFs, computed in increasing bins of redshift (left) and richness (right), is shown in Figure 6.5, where we can see from top to bottom the evolution of the amplitude ϕ^*, the faint end slope α, and the characteristic magnitude M_R^*. The blue points show the CLF parameters obtained when the faint end slope is set free while the red points correspond to the case where it is fixed to $\alpha = -1$, as discussed below.

For each parameter we combined the two data sets and fitted the model from Eq. 6.1. The resulting best fit evolution parameters and their 1σ errors, along with the corresponding goodness of fit parameters Q are listed in Table 6.3. The goodness of fit is given by the probability to obtain, by random chance, a χ^2 value equal or greater than the one we obtained:

$$Q(\chi^2, n_{dof}) = 1 - \frac{1}{\Gamma(\frac{1}{2}n_{dof})} \int_0^{\chi^2} t^{\frac{1}{2}n_{dof}-1}\, e^{-t} dt, \tag{6.2}$$

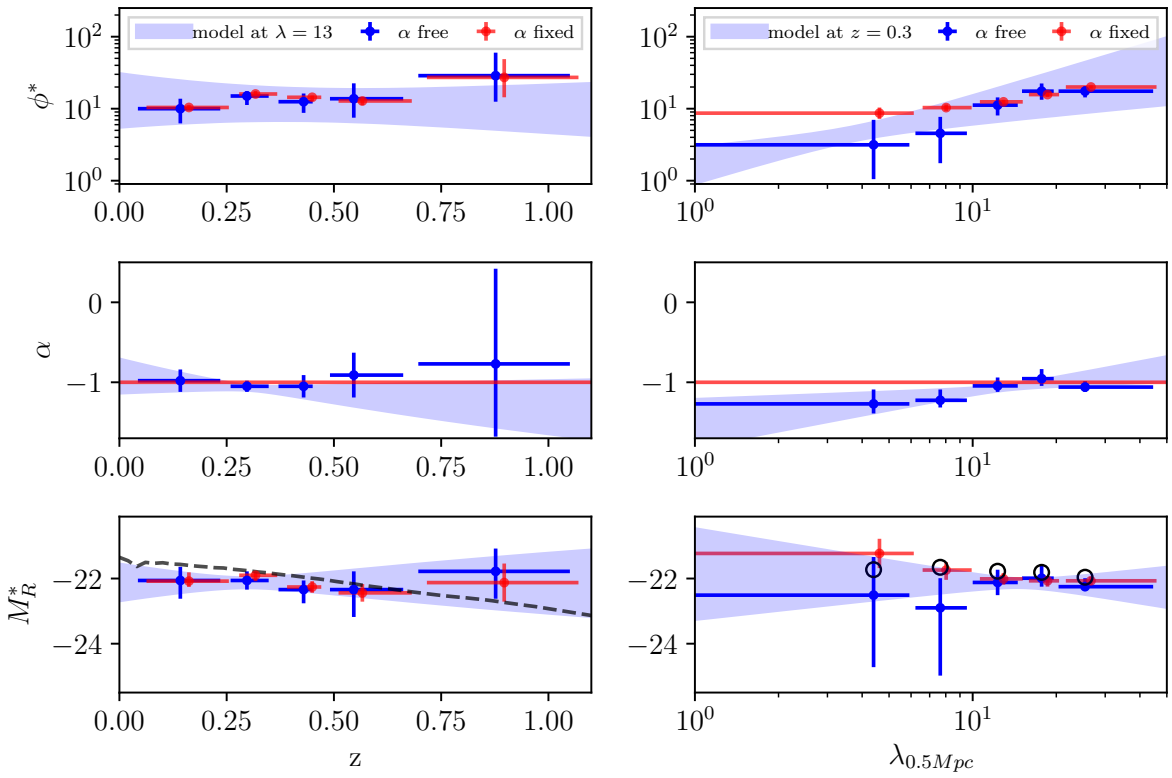

Figure 6.5: Parameters of the composite cluster luminosity functions computed in increasing bins of redshift (left) and richness (right). From top to bottom, the plots show: the normalisation ϕ^*, the faint end slope α, and the characteristic magnitude M_R^*. The vertical error bars indicate the 68% c.i, whereas the horizontal ones reflect the bin size. The blue/red points indicates the results when the faint end slope is free/fixed. The shaded blue regions show the evolution models that we constrained from Eq. 6.1, at fixed richness ($\lambda_{0.5Mpc}$ =13, left) and redshift (z=0.3, right). The dashed black line shows a fiducial model for the evolution of $M*$, the black circles indicate the model values at the median redshifts of the richness bins.

where Γ is the gamma function. It is defined with respect to a given χ^2 value and the number of degrees of freedom n_{dof}.

We represented the evolutionary models by the blue shaded regions in Figure 6.5, by fixing the richness or redshift at the sample median values ($z = 0.3$ and $\lambda_{0.5Mpc} = 13$). Those regions thus show the evolution we would expect if: the clusters were all at redshift $z = 0.3$ but had different richness (left), and the clusters all had the same richness $\lambda_{0.5Mpc} = 13$ but were at different redshifts (right).

We can see that the amplitude ϕ^* increases with richness (at 2σ) and a hint that the faint end slope α is getting shallower with richness (at 1.3σ). Our data are compatible with no redshift evolution for all the CLF parameters, and no richness evolution for the characteristic magnitude M_R^*.

Because the faint end slope values are compatible with no redshift evolution and the richness evolution has a low significance, we can fix the value of α to see if we obtain better constraints on the other two parameters, as it is often done in the literature. We thus fixed the faint end slope to a value of $\alpha = -1$ and repeated the same fitting procedure as before. The M^* and ϕ^* values we obtained are shown by the red data points and lines in Figure 6.5 and presented along with their associated goodness of fit parameters in Table 6.1. We can see that the values obtained with the faint end slopes fixed or free to vary are compatible in the redshift bins,

but not in the richness bins. The amplitude and characteristic magnitude values for the low richness bins are higher/fainter when the faint end slope is fixed. This is because of the richness evolution of the faint end slope, which is steeper than -1 in the low richness bins. When the faint end slope is fixed, the other two parameters are thus evolving so that the integrated luminosity is conserved. The errors on ϕ^* and M_R^* are reduced when α is fixed, however, the comparison of the goodness of fit parameters indicates that setting $\alpha = -1$ does not provide a good description of the CLF of poor clusters.

We compared our results to the fiducial M^* evolution model used through this study. It is shown by the black dashed line and the black open circles in Figure 6.5. We can see that the data are compatible in average with the fiducial evolution model –albeit not excluding a scenario without evolution– with an offset of $\sim$0.5 mag (the measured values of M^* being brighter). However, there is a mild tension at high redshift and at low richness, where our values of M^* are respectively too faint/bright compared to the fiducial model. If statistically meaningful, this would indicate that the characteristic luminosity of the overall galaxy population in the high redshift and low richness clusters in our sample are not very well represented by the passive evolution of an elliptical galaxy with a burst of star formation at a redshift of 3. We discuss this further in Section 6.4.

6.2.2.2 Are the CLFs representative of the individual LFs?

Along this study, we focused on the evolution of the composite luminosity functions, because of our relatively low mass (and thus low signal to noise) cluster sample. However, we showed in Section 6.1 that the stacking method we use (the method of Colless 1989) up-weights the poor clusters with respect to the rich ones. The CLF including all clusters with $z < 0.67$ is thus strongly affected by those poor clusters whereas they are not the more numerous. Therefore we study to what extent the CLFs are representative of the individual LFs and thus if we can generalise the findings about the CLF evolution to the behaviour of individual clusters.

We computed the LF parameters for each cluster in our sample, using the best fit statistical estimators (because it is easier to compute for low signal to noise LF, albeit being biased with respect to the median of the PDF, which was used for the CLFs, see Section 5.5). In each redshift and richness bins we compared the values of ϕ^*, α, and M_R^* coming from the CLF to the mean, median and weighted mean of the parameters from the individual LF in the same bins. We used the inverse of the squared parameters errors as weights (inverse variance weighting). We computed the error bars using for the mean: the standard deviation, for the median: 1.253 times the standard deviation, and for the weighted mean: the weighted standard deviation.

We found that the mean, median and weighted mean values of the faint end slope are compatible with the one from the CLF considering the errors, whereas only the mean and median were compatible with the CLF values for ϕ^* and M_R^*. When studying the LF and CLF with the faint end slope value fixed to -1, we found that the mean, median and weighted mean values of ϕ^* and M_R^* were compatible with the one from the CLF, considering the errors. In both cases, M_R^* values were systematically brighter/fainter with respect to the CLF values when using the mean/weighted mean. In general we found that the median values were closer to the parameter values from the CLFs.

We conclude that CLFs are representative of the median of the individual LFs and that the evolutions discussed in Section 6.2.2.1 can be generalised to the median behaviour of the clusters LFs.

6.2.2.3 Comparison with previous studies

In this Section we compare our finding about the CLF parameters to similar studies from the literature:

– Zhang (2017) studied the evolution of the red sequence LF parameters with mass and redshift in a sample of 100 X-ray detected clusters using hierarchical Bayesian method. Their data are compatible with no mass evolution of the faint end slope and characteristic magnitude and show hint that the faint end slope is getting shallower with redshift at a significance level of $\approx 1.9\sigma$.

– Sarron et al. (2018) studied the CLF evolution with mass and redshift in a large sample of mostly rich optically detected clusters in the CFHTLS-W1 field.

– Guglielmo et al. (2018), XXL Paper XXII, studied the stellar mass function in XXL-N clusters and in the field using a spectrophotometric catalog. They did not found any significant difference between the shape of the galaxy stellar mass function in the different environments and for galaxies located in clusters of different X-ray luminosities, above their stellar mass completeness limit.

– Moretti et al. (2015) studied the individual LFs of 72 WINGS nearby clusters and found that the M^* values (in the bright part of the LF) showed no correlation with mass proxies, using either X-ray luminosities or velocity dispersions.

– Lan et al. (2016) studied the CLF of a large sample of low redshift SDSS clusters, spanning a wide mass range. They found faint end slope values of $\alpha \approx -1$, and no evolution of M^* and α with mass inside R_{200}.

– Hansen et al. (2009) studied the CLF of a large sample of SDSS optically selected clusters (with detection based on the red sequence) in the redshift range $0.1 < z < 0.3$ and in a mass range comparable to ours. They found, that the CLF computed in R_{200} showed a faint end slope getting steeper and a characteristic magnitude getting brighter with richness, while ϕ^* (expressed in volume units) was decreasing. The same tendencies were found when only the red galaxies were selected.

– Alshino et al. (2010) studied the LF of 14 C1 clusters from XMM–LSS (that are part of our sample), looking for evolution with redshift and X-ray temperature. They found that, after removing the effects of redshift (correcting for the Malmquist effect), the temperature-stacked LFs did not exhibit any strong evidence for trends with X-ray temperature, while the faint end slope was becoming shallower with increasing redshift. They found faint end slope values much steeper than in our study, but did not constrain the characteristic magnitude of nearly a third of their systems. The values of their amplitudes are not available.

Our data are consistent with no richness dependence of the characteristic magnitude, which is coherent with the findings of Moretti et al. (2015) , Lan et al. (2016) and Alshino et al. (2010) but in apparent opposition with Hansen et al. (2009). We found a hint (at 1.15σ) for a positive evolution of the faint end slope with richness. Considering this low significance value, we are still compatible with the findings of Lan et al. (2016) and Alshino et al. (2010), but again in opposition with Hansen et al. (2009). The discrepancies of Hansen et al. (2009) with our study could be explained by the fact that the CLFs are computed in volume units and that the three parameters are degenerated. Another explanation for these differences may be attributed to the cluster detection: optically red sequence based versus X-ray detected clusters, the first method possibly selecting more evolved, red sequence dominated systems.

Comparison of our study with Zhang (2017) is not possible directly since we are not using the same galaxy population, but would suggest that the mild faint end slope evolution we see in our data is driven by an excess of faint blue cloud galaxies in poor clusters. Finally, our results are also in agreement with the study of Guglielmo et al. (2018), XXL Paper XXII, at least in the massive (bright) part they probe.

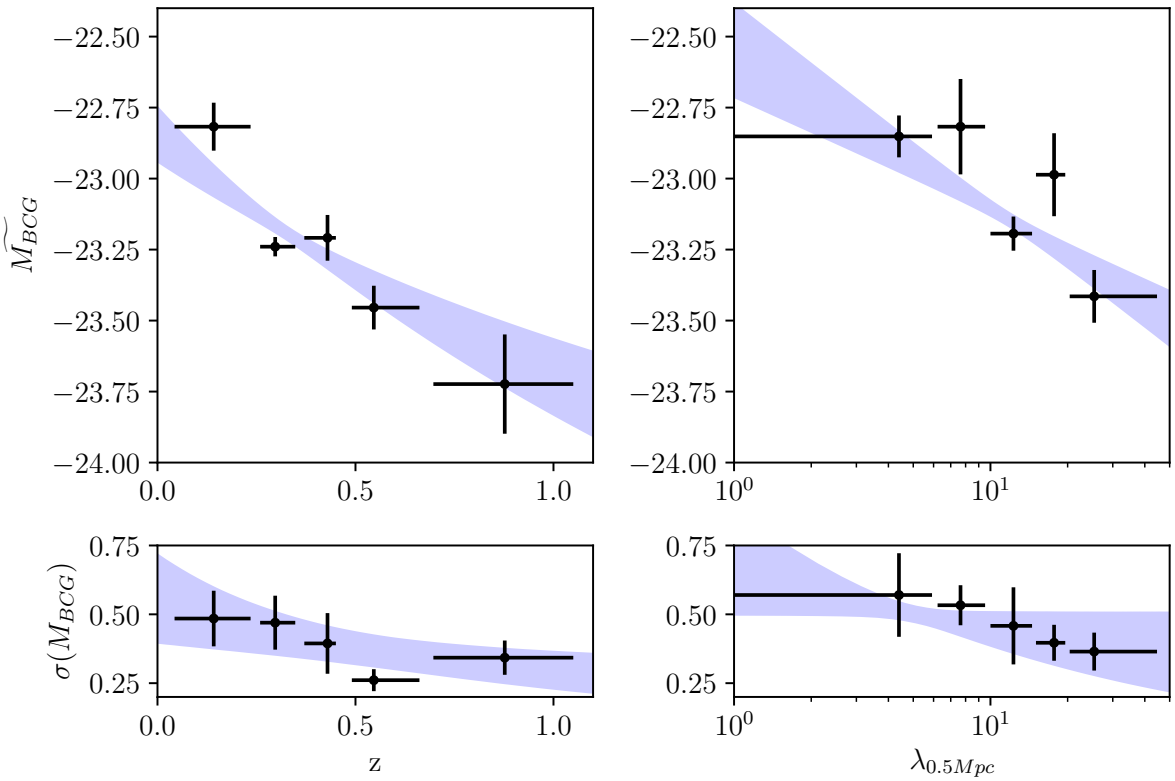

Figure 6.6: Parameters of the brightest cluster galaxies (BCGs) magnitude distributions, computed in increasing bins of redshift (left) and richness (right). *Top:* Median BCG magnitude. *Bottom:* symmetrised scatter of the BCGs distributions around the median values. The shaded blue regions show the evolution models we constrained from Eq. 6.1, at fixed richness ($\lambda_{0.5Mpc}$ =13, left) and redshift (z=0.3, right). The vertical error bars indicate 68% c.i. obtained from bootstrap, whereas the horizontal error bars reflect the bin sizes.

Our data are compatible with no redshift evolution of both the characteristic magnitude and the faint end slope. They are also compatible within the error bars with the values of Sarron et al. (2018) in their lowest mass bin. Our finding are in tension with those of Alshino et al. (2010), however we stress that since they did not constrain the characteristic magnitude of nearly a third of their systems, and did not provide the values of ϕ^*, the steep values of α they found and their redshift evolution could arise from the degeneracy between the LF parameters. Again, the comparison with Zhang (2017) would suggest that faint blue cloud galaxies balance the increasing deficit of faint red galaxies with redshift.

6.2.3 Evolution of the BCGs luminosity distribution

The brightest cluster galaxies and the central galaxies in general are known to follow a different distribution compared to the other galaxies, which is better represented by a Gaussian function (see e.g Hansen et al. 2005, 2009; De Filippis et al. 2011; Wen and Han 2015).

Here we investigated the BCGs luminosity distribution in our cluster sample and its evolution with richness and redshift. We first tested the gaussianity of the distributions and then studied their parameters' evolution with richness and redshift.

The distribution of the BCGs in each bin is represented by the red histograms in Figures 6.1 and 6.4. We can see that in some cases, the distributions seem quite irregular. We tested the null hypothesis that they follow Gaussian distributions using the D'Agostino and Pearson's test,

Table 6.4: Constraints on the evolution of the BCGs distributions (see model of Eq. 6.1) and associated goodness of fit Q (see equation 6.2).

	a	b	c	Q
$\widetilde{M_{BCG}}$	-2.8 ± 0.7	-0.6 ± 0.2	-22.2 ± 0.1	0.04
$log(\sigma(M_{BCG}))$	-0.9 ± 0.6	-0.2 ± 0.2	0.0 ± 0.2	0.52

based on skew and kurtosis information of the samples. According to this test, the distribution of the BCGs from all the clusters with a redshift $z < 0.67$ is very unlikely to be Gaussian (the p-value is 9×10^{-4}). In the case where we exclude poor clusters ($\lambda < 10$), we find that the distribution is compatible with a Gaussian (p-value=0.15). For the poorest clusters only ($z < 0.67$ & $\lambda < 6$), the p-value is relatively small (p-value=0.09), but still acceptable. We concluded that a Gaussian function is not a good approximation for the BCG distributions in our sample when poor clusters are included, but that it is satisfying for rich and poor clusters taken individually. In the following, we chose to use the median and the 16 and 84 percentiles to describe the distributions, rather than the mean and standard deviation.

The parameters of the BCGs distributions computed in increasing bins of redshift (left) and richness (right) are shown in Figure 6.6. The median BCG magnitude is shown in the top panels and the scatter of the BCG magnitude distributions is shown in the bottom ones. In both cases, the vertical error bars indicate the 68% c.i. and were computed using bootstrap, whereas the horizontal error bars reflect the bin sizes.

To evaluate the evolution of the BCG magnitude distributions and take into account the selection function effects, we again combined the two data sets and fitted the model from Eq. 6.1. The resulting best fit evolution parameters and their 1σ errors, along with their corresponding goodness of fit parameters are listed in Table 6.4. We represented those evolutionary models by the blue shaded regions in Figure 6.6, by fixing the richness or redshift at the sample median values ($z = 0.3$ and $\lambda_{0.5Mpc} = 13$). Those regions thus show the evolution we would expect if: the clusters were all at redshift $z = 0.3$ but had different richness (left), the clusters all had the same richness $\lambda_{0.5Mpc} = 13$ but were at different redshifts (right).

We can see that our data are compatible with the median BCG magnitude getting brighter with both redshift and richness (at respectively 4 and 3 σ) and a hint that the scatter of the distribution is decreasing with redshift (at 1.5 σ), while staying constant with richness. These evolutions are not consistent with pure passive evolution model and highlight the effect of environment on the BCG luminosities. The moderate values of the goodness of fit parameter may indicate that the redshift and mass (through richness) are not the only parameters describing the evolution of the BCGs luminosities. This is coherent with the study of XXL Paper XV, based on the XXL-100-GC sample, in which the authors found that the relation between clusters and BCGs masses depends on clusters dynamical state.

The scatter of the BCGs magnitude distributions $\sigma(M_{BCG})$ found is ~ 0.6 mag for poor and ~ 0.4 mag for rich clusters (equivalent to respectively $\sigma(\log L_{BCG}) \sim 0.25$ and $\sigma(\log L_{BCG}) \sim 0.15$) . Hansen et al. (2009) also studied the evolution with richness (and mass) of the BCGs median luminosity and scatter in their low redshift cluster sample. They found that the BCG luminosities increased with the richness (and mass) while the scatter of the distribution decreased. Their scatter values, $\sigma(\log L_{BCG}) \sim 0.23$ for the poorest and $\sigma(\log L_{BCG}) \sim 0.17$ for the richest clusters, are fully consistent with our findings. Wen and Han (2015) found a BCG magnitude scatter value of 0.36 mag in their study of a large sample of rich SDSS clusters, which is again consistent with what we obtained for our richest clusters.

We conclude that the BCG luminosities is an increasing function of both the redshift and richness, and that the diversity of BCG luminosity among clusters is decreasing predominantly with cluster redshift.

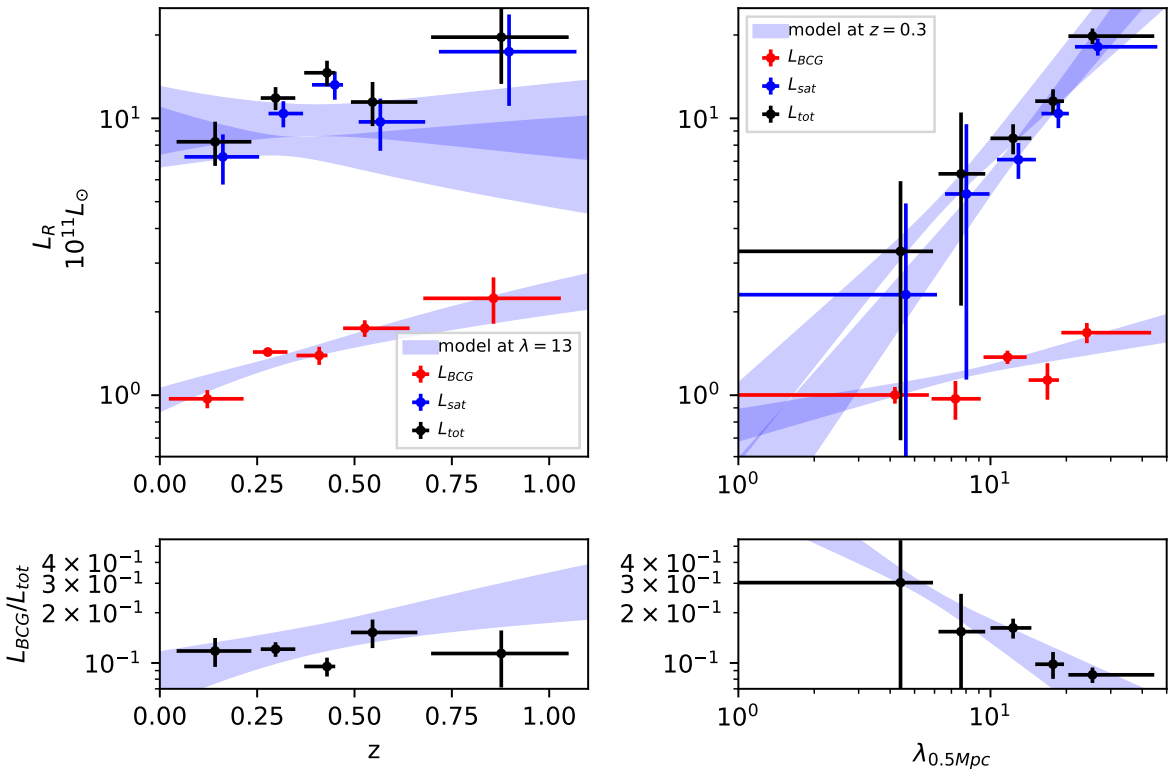

Figure 6.7: Composite cluster integrated luminosities computed in increasing bins of redshift (left) and richness (right). *Top:* BCG (red points), satellite (blue points) and total (BCG+satellite, black points) luminosities. *Bottom:* ratio of the BCG to total luminosity. The shaded blue regions show the evolution models we constrained from Eq. 6.1, at fixed richness ($\lambda_{0.5Mpc}$ =13, left) and redshift (z=0.3, right). The vertical error bars indicate 68% c.i., whereas the horizontal error bars reflect the bin sizes.

Table 6.5: Constraints on the evolution of the integrated luminosities (see model of Eq. 6.1) and associated goodness of fit Q.

	a	b	c	Q
$\log(L_{BCG})$	1.2 ± 0.3	0.21 ± 0.06	-0.25 ± 0.05	0.01
$\log(L_{sat})$	-0.3 ± 0.8	1.2 ± 0.2	-0.4 ± 0.1	0.46
$\log(L_{tot})$	-0.0 ± 0.7	1.0 ± 0.2	0.0 ± 0.2	0.57
$\log(L_{BCG}/L_{tot})$	1.6 ± 0.9	-0.9 ± 0.2	-0.1 ± 0.2	0.80

6.3 Evolution of the integrated luminosity with redshift and richness

In this section we analyse the evolution of the composite clusters integrated luminosity with redshift and richness. The luminosity of the satellite galaxies was computed by integrating the CLF up to $M_R^* + 3$, as detailed in Section 5.4.3.

The BCG luminosities were computed from the absolute magnitudes. The top panels of Figure 6.7 show the integrated luminosity as a function of redshift (left) and richness (right). The black, blue and red points represent the median and 68% c.i of the BCG, satellite and total (BCG+satellite) luminosities. The bottom panels show the ratio between the BCG and the total luminosity.

In order to disentangle the richness from the redshift effects we fitted the evolutions using the model of Eq. 6.1. The results are shown by the blue regions in Figure 6.7 and the evolution parameters are presented in Table 6.5. We can see that the satellite and total luminosities inside R_{500} increase with the richness (at respectively 6 and 5 σ) while they do not present significant evolution with redshift. Assuming a constant stellar mass to r-band luminosity ratio (as measured by Kauffmann et al. 2003, for bright galaxies) this result can be generalised to the cluster stellar mass evolution. As we showed in Section 6.3, the luminosity of the BCGs increases both with redshift and richness (at respectively 4 and 3.5 σ). The ratio of the BCG to total luminosity decreases with richness (at 4.5 σ) and possibly increases with redshift (at 1.8 σ). We note however that, as we use a spectroscopically confirmed sample we might witness a selection bias towards clusters with luminous BCGs, especially at high redshift where spectra are more difficult to obtain. We find that the BCG account for $\sim 30\%$ of the poor cluster luminosity while it represents less than 10% of the rich cluster luminosities. This result is compatible with the study of e.g. Lin et al. (2006), Hansen et al. (2009) and XXL Paper X and can be explained by a scenario in which BCGs grow in luminosity at a lower rate than the clusters.

6.4 Implications of the results

6.4.1 Implications for the use of clusters in cosmology

The luminosity function is an essential property of galaxies within clusters, in particular in the context of cluster detection. For instance, many cluster finder algorithms (in particular those based on the matched filter technique) use the cluster radial profile and luminosity function to construct their model (see e.g. Postman et al. 1996; Olsen et al. 2007; Bellagamba et al. 2018). A precise and unbiased determination of the luminosity function is therefore mandatory to optimise the cluster detection. Information about the cluster luminosity function can also be used to make predictions about cluster selection functions in optical surveys (see e.g. Sartoris et al. 2016, in the case of *Euclid*). In this Chapter we have parametrised the evolution of the composite luminosity function parameters with both redshift and richness, in a wide redshift range and for relatively low mass X-ray selected clusters. We have also found that the CLF evolution is a fair representation of the median behaviour of individual cluster LFs. Our study can therefore be used as a reference for analyses requiring knowledge of the optical cluster luminosity function evolution.

The LF can also be used to derive optical mass proxies such as the cluster richness or optical luminosity. This is done by integrating the LF to obtain the galaxy number density or the luminosity (as in e.g. Lin et al. 2003, and the present study) and/or by providing a characteristic galaxy luminosity used as a limit (as done in multiple studies, including the present one, using the values of Lin et al. 2006). Our results indicate an increase in the characteristic galaxy density with richness and no significant LF evolution with redshift. This is compatible with the redshift invariant mass-richness and mass-luminosity relations (at least below $z \sim 1$) found by e.g. Lin et al. (2006) and Andreon and Congdon (2014). The lack of redshift evolution of the integrated luminosity in the r' band while it scales almost linearly with the richness, is also encouraging for its utilisation as optical mass proxy. Under the assumption of a constant stellar mass to light ratio in the r-band up to $M_R \sim -19$ in cluster galaxies at $z < 1$, this results can be extrapolated to the evolution of the cluster stellar mass comprised in galaxies. The strong increase in the BCG median luminosity with redshift and richness compared to the CLF evolution also indicates that the BCG contributes more to the total luminosity budget of the poorest clusters (as also found by XXL Paper X) and the highest redshift clusters, as we find when investigating the BCG to total galaxy luminosity ratio.

We released the catalogue containing the BCGs positions, redshifts, and magnitudes for the 142 clusters in our sample. This is precious information as the BCG usually resides at the centre of the cluster potential well and is often used as a cluster centre indicator. The location of the

BCG with respect to, for instance, the X-ray centroid, can thus be used as a cluster dynamical state proxy (see Section 9.3.1).

6.4.2 Implications for galaxy evolution

The CLF (BCG excluded) in our cluster sample does not significantly evolve with redshift. The characteristic magnitude is still compatible with the passive evolution of an elliptical galaxy with a burst of star formation at a redshift of 3, at least up to $z \sim 0.7$. The fact that the measured characteristic magnitude at high redshift is fainter than expected by the model may be due to an enhancement of the star formation in the bright part of the LF, which would make the assumption of passive evolution inadequate. However, the tension is weak and may also be due to the fact that absolute magnitudes are not well constrained by the photometry at these redshifts (see Section 5.3.4). The lack of evolution is compatible with a scenario where the bright part of the LF inside R_{500} is already in place at $z \sim 1$ and does not significantly evolve afterwards. It is also consistent with the flattening of the cluster red sequence galaxies LF faint end with redshift (suggested by e.g. De Lucia et al. 2004, 2007; Stott et al. 2007; Gilbank et al. 2008; Lu et al. 2009; Rudnick et al. 2009), which would be compensated by the increase of the faint blue population. In this case, the number of faint galaxies would remains constant while the ratio of red and blue galaxies changes.

In opposition to what is found for typical cluster member galaxies, a clear evolution is seen in the median luminosity of the BCGs. We compared the median BCG magnitude to the passive evolution model and found an average offset of ~ 1.3 mag. However, if the passive evolution model (after applying the offset) fits the measured median BCG magnitudes relatively well, it is excluded by the evolution models that we constrained from Eq. 6.1. This indicates that the agreement between the BCG luminosity redshift evolution and pure passive evolution found in, e.g., XXL Paper XV, is only apparent, and when the selection biases are accounted for (when the richness dependence is fitted conjointly), the measured redshift evolution of the luminosity is weaker. In XXL Paper XV the authors found that the star formation of the $z < 0.5$ BCGs in the XXL-100-GC sample was comparable to that of similar mass, passive galaxies in the field. Thus, the weak luminosity evolution that we see in our sample, as compared to passive evolution, could be due to star formation happening either at $z > 0.5$ and/or in clusters that were not part of the XXL-100-GC sample (see Chapter 7 for a confirmation of this statement).

We found that the galaxy density at M^* increases with cluster richness, and a hint that the faint end slope is getting shallower. Our results thus require a scenario that reduces the number of faint galaxies while increasing the number of bright ones when a cluster grows in mass (gets richer), since the redshift evolution does not play a role. This could be explained by star formation occurring in faint poor cluster galaxies that act to enhance their luminosity. This would lead to a shallower faint end slope, if not enough faint galaxies are accreted, and an increase in intermediate ($\sim M^*$) galaxies. Another scenario that could be responsible for these results is the accretion of substructures with bright galaxies dominated LFs. Since we do not see any evidence of such objects in our sample, it indicates that if they exist, such substructures present X-ray emission below the XXL sensitivity.

Our results indicate that the BCG luminosity is increasing with cluster richness, as also found by e.g. Hansen et al. (2009). This is consistent with the hierarchical formation scenario, according to which BCGs grow by accretion of smaller galaxies and have masses that scale with the cluster total masses (see also XXL Paper XV, and reference therein).

6.5 Summary and conclusions

In this Chapter, we studied the optical LFs of a sample of 142 galaxy clusters detected in X-ray by the XXL survey and having spectroscopically confirmed redshifts. This unique survey allowed us

to study the LF of clusters spanning a wide range of redshifts and X-ray luminosities (and thus masses). We presented the general CLF of our sample, investigating the effects of poor clusters and comparing our values to previous studies. We then studied the evolution of the galaxy luminosity distributions with redshift and richness, analysing separately the non-BCG and BCG members. We fitted the dependences of the CLFs and BCG distributions parameters with redshift and richness conjointly, in order to disentangle between these two effects. Finally, we discuss the implications of our findings in terms of galaxy evolution and cosmological utilisation of clusters.

Our main findings are summarised in the following.

- In Section 6.1, we applied our method to construct CLF on our cluster sample (for clusters with z<0.67) and found that it was well fitted by a single component Schechter function. We studied the impact of poor clusters on this CLF and found that they steepen the faint end slope and brighten the characteristic magnitude, because they are up-weighted by the stacking method which we used (adapted from Colless 1989). Considering the large scatter among the α and M^* reported in the literature, our values are comparable with the ones found by previous studies.

- In Section 6.2.2, we studied the evolution of the CLF inside R_{500} with redshift and richness. We found that the amplitude ϕ^* was increasing with richness (at 2σ) and hint that the faint end slope α was getting shallower with richness (at 1.3σ). Our data are compatible with no redshift evolution for all the CLF parameters, and no richness evolution for the characteristic magnitude M^*_R. We verified that the CLFs were representatives of the median of the individual LFs, and that our findings could be thus generalised to the median behaviour of the cluster LFs. This indicates that the bright part of the LF in the inner region of clusters does not depends much on mass or redshift, except for its amplitude, in the redshift-mass range we probe (about $0 < z < 1$ and $10^{13}\mathrm{M}_\odot < M_{500} < 5 \cdot 10^{14}\mathrm{M}_\odot$). We also found a small tension between our data and fiducial evolution model for M^*, that we attributed to the contribution from poor clusters.

- In Section 6.2.3, we studied the evolution of the BCG distributions with redshift and richness. Our data are compatible with the median BCG magnitude getting brighter with both redshift and richness (at respectively 4 and 3 σ) and the scatter of the distribution decreasing with redshift (at 1.5 σ), while staying constant with richness. This means that BCGs are brighter in richer clusters, and that their luminosities decrease with cosmic time (because of the ageing of their stellar population), while their diversity increases. Those results are not consistent with passive evolution model and favour a hierarchical formation scenario.

- In Section 6.2.3, we studied the evolution of the composite cluster integrated luminosity inside R_{500} with redshift and richness, using only satellites or all galaxies. We found that in both cases it increases with richness (at respectively 6 and 5σ), while it is compatible with no redshift evolution. The ratio of BCG to total luminosity decreases with richness (at 4.5σ): it goes from $\sim 30\%$ for poor clusters to $< 10\%$ for richer ones. We find a hint that the luminosity ratio increases with redshift. However, this might be because of a selection bias caused by the spectroscopic redshift confirmation of the cluster sample.

Chapter 7

Measurement of the AGN activity and galaxy colours in XXL clusters

Contents

Abstract: Galaxy clusters are complex systems and their understanding is intertwined to that of galaxy evolution. Galaxies can be used to detect or characterise clusters in the optical, but can also be contaminants at other wavelengths. On the other side, dense environments play a key role in shaping galaxy stellar populations, morphologies and black hole activities. In this Chapter we investigate the cluster members activity through their AGN fraction and their colours and discuss implications for galaxy evolution and cluster detection. The first part of the Chapter is based on the analysis conducted in XXL Paper XXXV, for which I extracted cluster galaxy density profiles that were used to normalised AGN counts, a crucial step for their interpretation. The second part of the Chapter is based on a preliminary study.

7.1 Introduction

Galaxy clusters are dense environments where galaxies interact with the hot gas of the ICM through various process, which are believed to eventually quench the star formation and AGN activity, leading to what is currently seen in massive relaxed clusters: a predominantly passive galaxy population, with a lack of AGN activity compared to the field (except for the BCGs). Conversely, in intermediate density environments, such as galaxy groups or cluster outskirts, the interactions between galaxies are expected to be more frequent, and possibly trigger star formation and AGN activity (see e.g. Bai et al. 2010). However, a complete view of these phenomena as a function of redshift and for different environments is still missing.

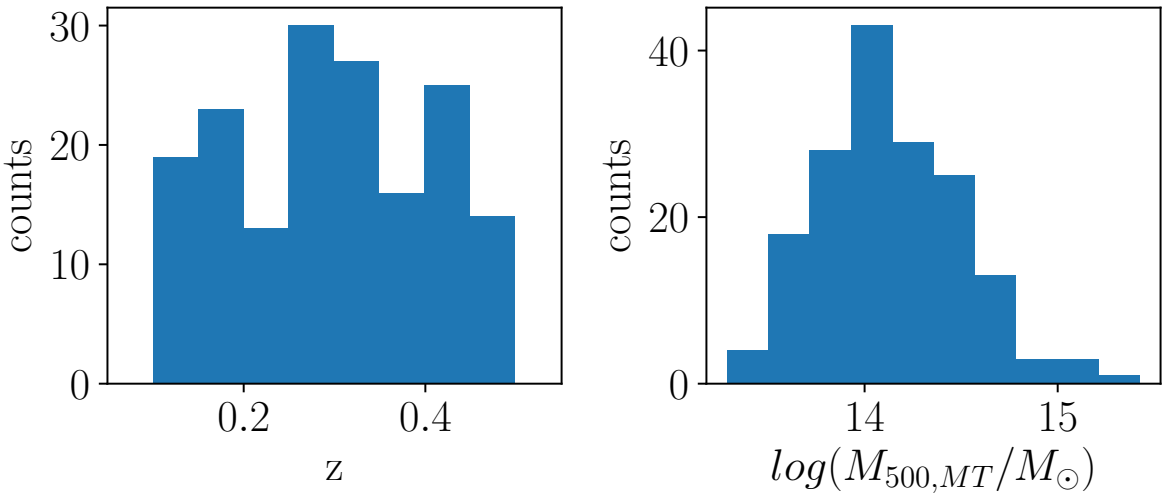

Figure 7.1: Redshift (right) and mass (left) distributions of the XXL cluster sample used in this study.

This is of particular importance to understand galaxy evolution, but also for cluster detection. Indeed, the passive (quenched) galaxies form a special locus in the galaxies colour-magnitude diagram, which depends mainly on the redshift, and is called the red sequence. This property is often used to detect galaxy clusters and estimate their photometric redshifts (see e.g., Koester et al. 2007; Rykoff et al. 2014; Oguri 2014). Moreover, the link between clusters and AGN activity is also important for X-ray cluster detections, which can be altered by the presence of point sources (see e.g. Clerc et al. 2014; Biffi et al. 2018). This is also the case for SZ cluster detections, which are affected by the contamination from radio galaxies, especially the central AGNs in cool-core clusters (Sayers et al. 2013b). AGNs can also affect the X-ray cluster temperature and luminosity measurements, especially at high redshift (see e.g. Branchesi et al. 2007).

7.2 Determining the fraction of X-ray AGNs in XXL cluster's galaxies

In this section, we present the study of the X-ray AGNs activity in XXL clusters performed in XXL Paper XXXV. We first introduce the data sample and methodology. Then, we show and discuss the results in terms of galaxy evolution and cluster detection.

7.2.1 Methodology

In the following we describe the methodology used to determine and analyse the fraction of X-ray AGNs in XXL clusters. We give details on the galaxy density profile computation and summarise the methodology followed in XXL Paper XXXV.

7.2.1.1 Data sample

For this analysis we used all spectroscopically confirmed C1 and C2 clusters from XXL-N and XXL-S in the redshift range $0.1 < z < 0.5$ and having direct temperature and luminosity measurements, resulting in a sample of 167 objects (121 C1 and 46 C2). The lower redshift limit ensures that clusters do not have a too large angular extension, and the upper limit that the X-ray AGN selection is complete. The redshift and mass distribution of the selected clusters is shown in Figure 7.1.

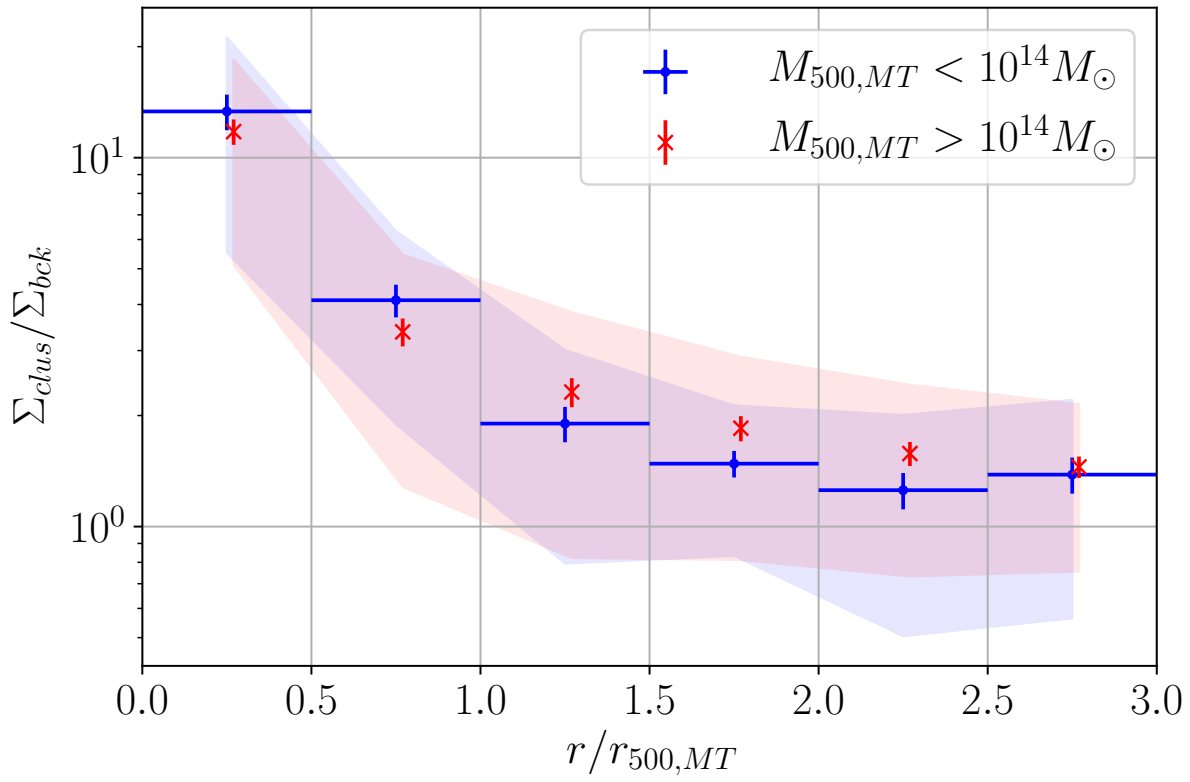

Figure 7.2: Optical overdensity (cluster to background galaxy density ratio) profiles of the $0.1 < z < 0.5$ XXL-N clusters. The blue/red points are the mean profiles for the clusters with masses below/above $M_{500,MT} = 10^{14}$ M$_\odot$. The error bars represent the error on the mean profile while the blue and red regions show the scatter among the clusters.

The X-ray AGN sample was extracted from the X-ray point source catalogue described in (Chiappetti et al. 2018, XXL Paper XXVII). Only AGNs with luminosities above $L_X[0.5 - 10 \text{ keV}] > 10^{42}$ erg s^{-1} were selected in order to have a complete catalogue in the considered redshift range.

7.2.1.2 Construction of the cluster galaxy density profiles

Any excess of X-ray AGNs in the area of galaxy clusters can be due to the obvious abundance of galaxies with respect to the field. Therefore, to reach a meaningful interpretation of the X-ray AGN density in clusters we need to take into account their galaxy density profiles.

For this calculation we have used the sample of XXL-N clusters selected as described above and that fall in the CFHTLS-W1 field, so that they have reliable photometric redshifts (see Chapter 4). The methodology used to define likely cluster members is the same as in Chapter 5: we selected galaxies with photometric redshifts in a certain window around the clusters spectroscopic redshifts, defined in order to obtain a homogeneous 68% membership completeness, accounting for the photometric redshifts bias (following Eq. 5.1). In order to have a homogeneous selection, we used galaxies having magnitude in the i' band such as: $m_i^* - 2 < m_i < m_i^* + 1$, with m^* the characteristic apparent magnitude of our fiducial model (see details in Chapter Conventions used in this thesis). The galaxy density were computed up to $3 \times R_{500,MT}$ in annuli of widths $0.5 \times R_{500,MT}$ around the X-ray centroid cluster positions and the background galaxy density was computed as the mean galaxy density in the entire CFHTLS-W1 field at the redshifts of the considered clusters. We expressed the densities in Mpc^{-2} and took into account the masked structures. Finally, we separated the clusters into low and high mass systems using

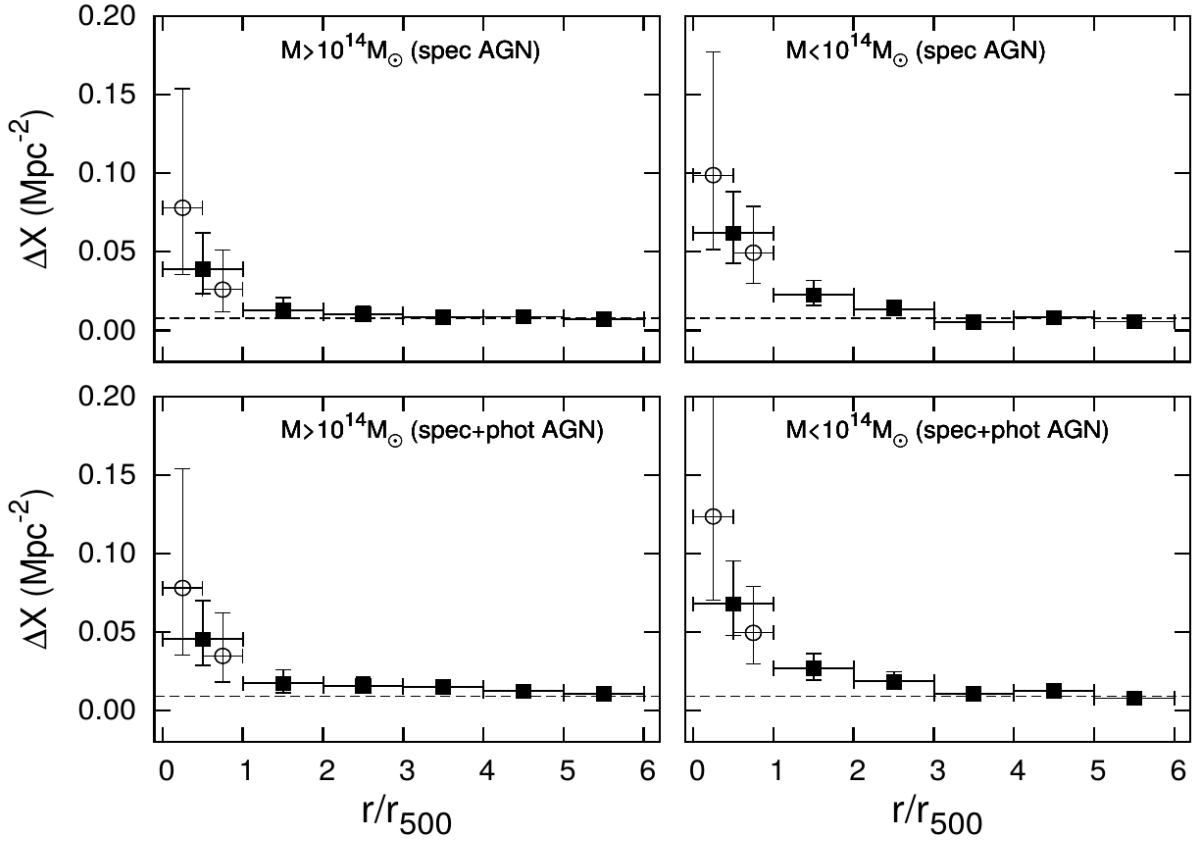

Figure 7.3: Stacked X-ray AGN density profiles around the $0.1 < z < 0.5$ XXL clusters. *Top panels:* spectroscopic sample only. *Bottom panels:* spectroscopic and photometric samples. The left/right panels are for systems with masses below/above $M_{500,MT} = 10^{14}$ M$_\odot$. The dashed lines represents the AGN field density. Figure from XXL Paper XXXV.

$M_{500,MT} = 10^{14}$ M$_\odot$ as the limit.

Figure 7.2 shows the mean optical over-density (cluster to background galaxy density ratio) profile of the XXL-N clusters sub-sample. The low/high mass clusters profile is shown in blue/red. We can see that, although the scatter among cluster is large, the two profiles are different in average: as expected (see e.g. Okabe and Smith 2016), the low mass clusters are more concentrated than the high mass ones.

7.2.1.3 X-ray AGNs density profiles in XXL clusters

The density of X-ray AGNs around clusters was computed by selecting objects with either a spectroscopic redshift within $\Delta u = 2000 \times (1+z)$ km/s of that of the cluster, or no spectroscopic information, but a concordant photometric redshift. We also applied a magnitude selection with criteria similar to that employed for the galaxies. Out of the resulting sources, ∼90% and ∼70% have a spectroscopic redshift in XXL-S and XXL-N, respectively. The profiles were constructed up to $6 \times R_{500,MT}$ in annuli of widths $1 \times R_{500,MT}$ around the X-ray centroid cluster positions. The first bin was split in two as the innermost AGNs may be missed or contaminated by the cluster emission. The background AGN density was computed using 100 mock catalogues matching the X-ray sensitivity of the survey and the number and redshift distributions of the cluster sample. This strategy was adopted in order to control selection effects.

Figure 7.3 shows the resulting X-ray AGN density profiles around the low and high mass clusters samples. The results obtained for all AGNs or only those with spectroscopic redshifts

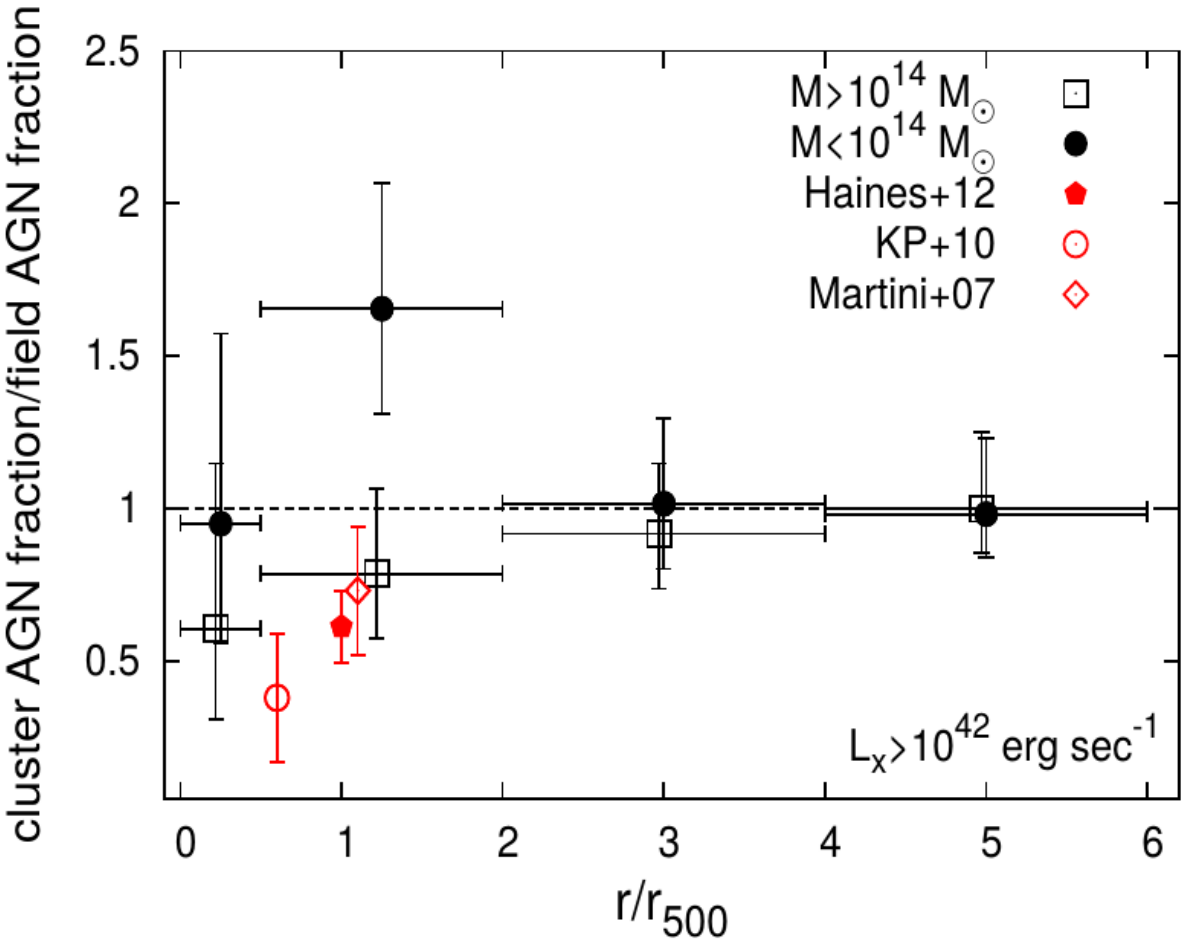

Figure 7.4: Overdensity of X-ray AGNs, with luminosities above $L_X[0.5-10\ \mathrm{keV}] > 10^{42}$ erg s^{-1}, in clusters as a function of scaled radius. The black square/circle are for the XXL clusters at $0.1 < z < 0.5$ with masses below/above $M_{500,MT} = 10^{14}$ $M_\odot$. Error bars indicate the 68% confidence limits for small number of events. Results from analyses of massive clusters by Martini et al. (2013), Koulouridis and Plionis (2010) and Haines et al. (2012) are shown by the red symbols. Figure from XXL Paper XXXV.

are shown separately. We can see that the two selections give equivalent results and only the spectroscopic sample is used in the following.

7.2.2 Results and discussions on the relation between cluster mass and AGN activity

The X-ray AGN over-density fraction around XXL clusters was computed by dividing the AGNs cluster to background density ratio by the galaxy cluster to background density ratio. This quantity thus reflects the fraction of bright galaxies hosting an X-ray AGN in clusters with respect to the field value. The resulting profiles, for the two cluster mass ranges, are shown by the black symbols in Figure 7.4. The results of similar analysis in massive clusters from Martini et al. (2013), with 8 clusters at $0.06 < z < 0.31$, Koulouridis and Plionis (2010), with 16 clusters at $0.07 < z < 0.28$, and Haines et al. (2012), with 26 clusters at $0.15 < z < 0.30$, are also shown for comparison.

We can see that the X-ray AGN fraction around massive XXL clusters is compatible with the one in the field and seems to steadily decrease towards the cluster centres. Its value at $r < 2 \times R_{500}$ is similar to that of massive clusters from the literature. Conversely, the X-ray

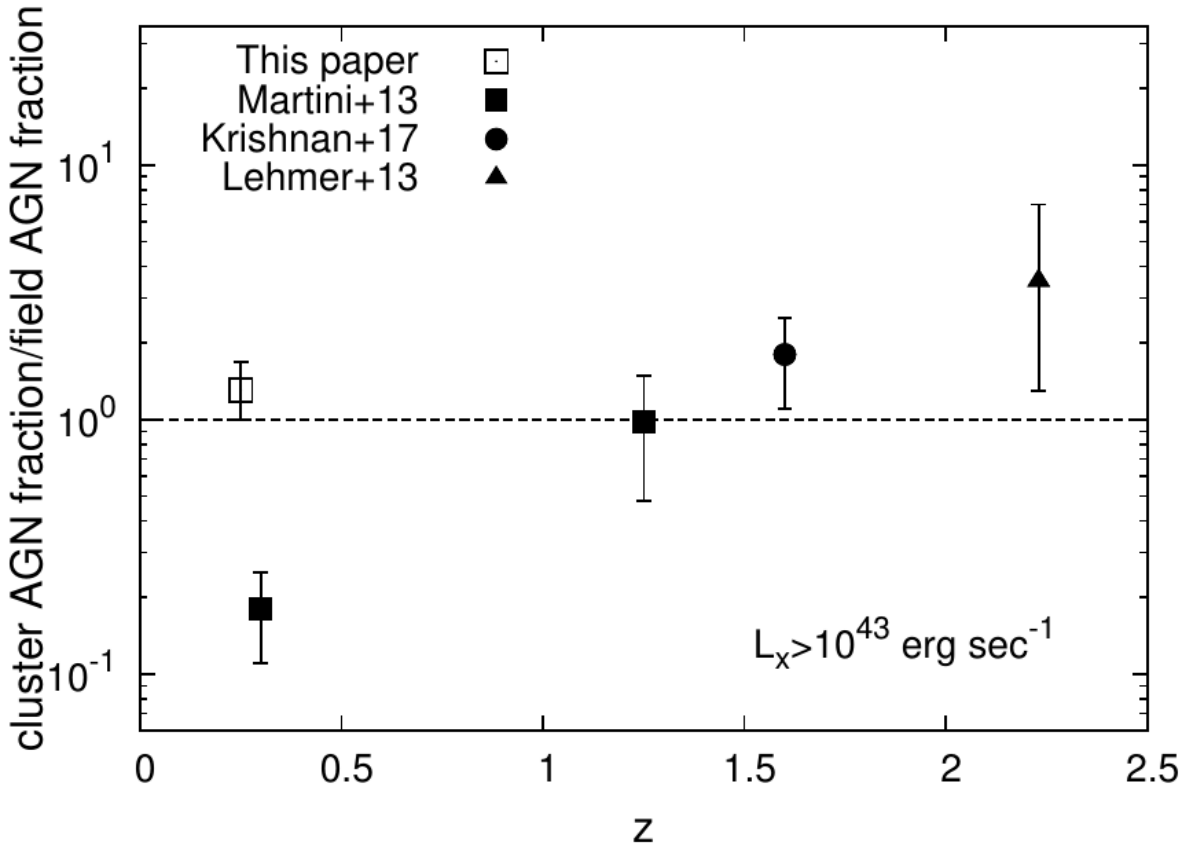

Figure 7.5: Over-density of X-ray AGNs with luminosities above $L_X[0.5-10\,\mathrm{keV}] > 10^{43}$ erg s^{-1} in clusters as a function of redshift. The XXL value is measured inside $2 \times R_{500}$ and compared to results from stacked samples (Martini et al. 2013) and individual clusters (Krishnan et al. 2017 and Lehmer et al. 2013). Figure from XXL Paper XXXV.

AGN fraction around low mass XXL clusters is enhanced with respect to field in the $0.5 \times R_{500} < r < 2 \times R_{500}$ bin, while being compatible with the field value at lower radius. The X-ray AGN excess in low-mass clusters was found to be produced by low-luminosity AGNs (with $L_X[0.5 - 10\ \mathrm{keV}] < 10^{43}$ erg s^{-1}). These findings are unchanged when using another mass estimation ($M_{500,scal}$) or a flux rather than a luminosity selection for the AGNs.

These results are consistent with that of Popesso and Biviano (2006), that found a anti-correlation between optically selected AGN fraction and velocity dispersion in nearby clusters. They are also coherent with other studies that found AGN enhancement in the clusters periphery (see e.g. Johnson et al. 2003; Lehmer et al. 2013; Koulouridis et al. 2014) and support the scenario of AGNs host galaxies being an in-falling population. The excess of X-ray AGN in the low mass clusters outskirts could be attributed to galaxy interactions (see e.g. Arnold et al. 2009; Ehlert et al. 2015), which are more likely in these intermediately dense environments. The decrease of AGN fraction towards the core of clusters in both the low and high mass clusters, and the hint that the AGN fraction in the first radius bin is lower in the high mass cluster sample, supports the ram pressure stripping scheme as induced by the ICM. Finally, this cluster mass - AGN activity anti-correlation shows that deeper gravitational potentials prevent AGN triggering in the outskirts and cause more effective ram pressure gas stripping, eventually leading to AGN suppression.

The value of the X-ray AGN fraction inside $r < 2 \times R_{500}$ of the XXL low mass cluster sample is compared to results from stacked samples (Martini et al. 2013) and individual proto-clusters (Krishnan et al. 2017 and Lehmer et al. 2013) in Figure 7.5. For a meaningful comparison only

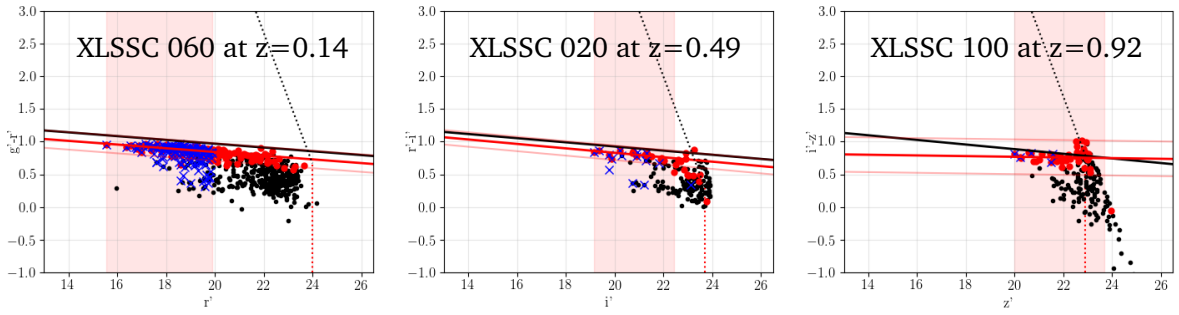

Figure 7.6: Colour magnitude diagrams of three example clusters at different redshifts. The black points indicate possible member galaxies inside a $2 \times R_{500}$ radius, the red points are possible members galaxies with elliptical SED and the blue crosses represent objects with spectroscopic redshifts around the cluster's redshift and inside $2 \times R_{500}$. The red lines show the red sequence fit and the black ones show the red sequence model from Kodama and Arimoto (1997). The pink shaded region indicate the magnitude range considered to fit the red sequence. The dotted lines indicate the 80% completeness magnitude and colours.

AGNs with $L_X[0.5-10 \text{ keV}] > 10^{43}$ erg s^{-1} are selected. The low redshift sample of (Martini et al. 2013) contains massive clusters while their higher redshift clusters have masses similar to that in the XXL high mass sample. The two proto-clusters have masses within the mass range of the XXL clusters low mass sample. We can see that the values of the AGN fraction at $z > 1$ is compatible with the one we found, while that obtained at a similar redshift, but for more massive clusters, is lower. This result highlight the necessity to take into account the mass dependence when investigating redshift evolution.

The galaxy density profiles in low and high mass clusters being comparable, considering the scatter, the enhanced AGNs fraction in low mass clusters cannot be attributed to a lower number of member galaxies. The number density of AGNs in low mass clusters is thus higher than in more massive ones (as can also be seen in Figure 7.3). This phenomena can impact the X-ray selection function of low mass clusters, which are, furthermore, shallower than their more massive counterparts.

7.3 Measuring the colour-magnitude relation of XXL-N cluster's galaxies

In addition to the AGN activity, the colours of galaxies provide precious insight into the star formation processes at play in clusters. In this section we focus on the star formation activity of XXL cluster's galaxies by studying their colour. In particular we characterise the properties of the cluster's red sequence and we investigate the colour of the BCGs.

7.3.1 Construction of colour-magnitude diagrams of the clusters and fit of the red sequence

To highlight the red sequence in the colour magnitude diagrams of the clusters, we used the colours and magnitude sets $g' - r'/r'$, $r' - i'/i'$ and $i' - z'/z'$ in order to bracket the 4000 Å break and minimise the magnitude uncertainties in the respective $z < 0.4$, $0.4 < z < 0.75$ and $0.75 < z < 1.1$ redshift ranges. We included the galaxies in a photometric redshift slice around the cluster spectroscopic redshift obeying Eq. 5.1 and located inside $2 \times R_{500}$ radii. We visually verified the selection by adding the objects having a spectroscopic redshift within $\Delta z = 0.006$. The colour magnitude diagrams of three example clusters are shown in Figure 7.6.

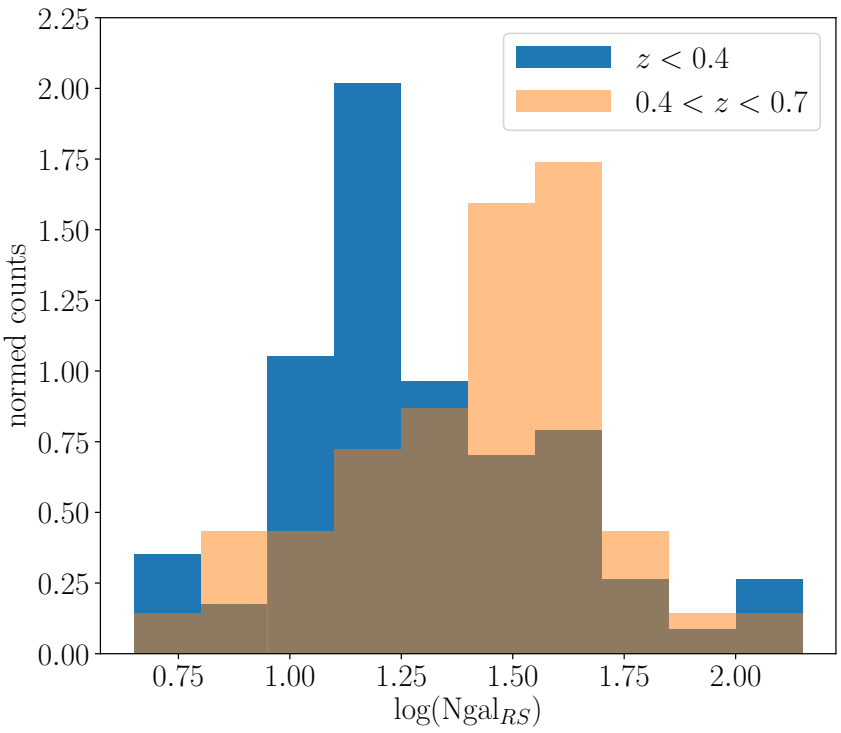

Figure 7.7: Distributions of the number of red sequence galaxies in the XXL cluster fields. The two histograms are normalised by their areas. Galaxies are selected within a radius of $2 \times R_{500}$ and have magnitudes brighter than m^*+2 and fainter than the BCG. In red and blue, histograms are for the $z < 0.4$ and $0.4 < z < 0.7$ samples and are computed using the $g' - r'$ and $r' - i'$ colours.

We found that the galaxies having an elliptical type of SED, according to LePhare (see Chapter 4 for details on the algorithm), and that are shown by the red points in Figure 7.6, trace well the red sequence, and we used them to fit its slope (Δ), zero point (ZP) and measure the scatter ($\sigma_{\rm col}$):

$$m_A - m_B = ZP + \Delta \times m_B, \tag{7.1}$$

with A and B the bands of interest. The fit was made by selecting the red sequence galaxies fainter than the BCG and brighter than $m^* + 2$ (see Chapter Conventions used in this thesis). This selection is complete up to $z = 0.7$ and the measurements at higher redshift are only qualitative. We applied an iterative σ-clipping on the red sequence normalised colour and took into account the photometric errors. The procedure was repeated for 1000 bootstrap sample realisations to estimate the errors on the parameter. For six clusters ($\sim 4\%$ of our sample) the red sequence could not be fitted because less than three galaxies were present.

Figure 7.7 shows the distribution of the number of red sequence galaxies within $2 \times R_{500}$ of the cluster centres, for the $z < 0.4$ and $0.4 < z < 0.7$ samples. The numbers are not corrected from background and foreground contamination, and thus, give an upper limit of the clusters red sequence richness. For 19 clusters ($\sim 15\%$ of the $z < 0.7$ sample) the number of red sequence galaxies is lower than ten.

7.3.2 Evolution of the red sequence slope, zero point and scatter

We computed the red sequence slope and zero point for all XXL clusters having enough galaxies. We also determined the red sequence scatter, as the standard deviation of the normalised red sequence colour. This measurement reflects the width of the photometric red sequence and not the intrinsic physical scatter. The redshift evolution of the red sequence colour (evaluated at

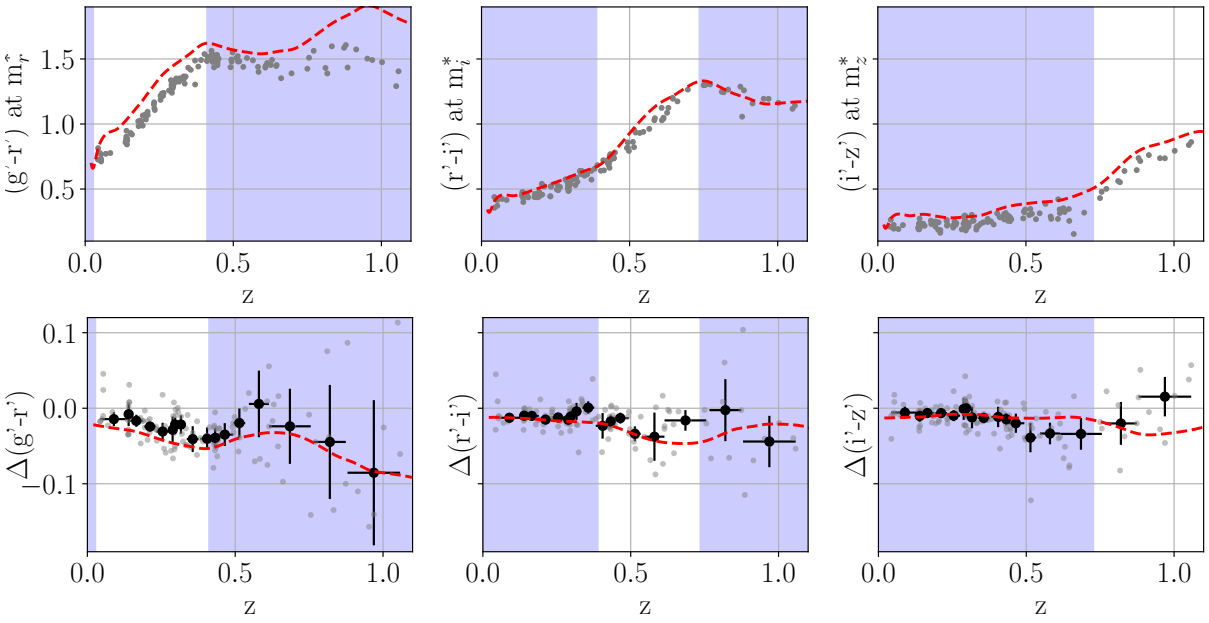

Figure 7.8: XXL clusters red sequence colours (top panel) and slopes (bottom panel) evolution with redshift and comparison to the model from Kodama and Arimoto (1997), given by the red dashed line. The red sequence colours are evaluated at the reference characteristic magnitudes m^* (see Chapter Conventions used in this thesis for more details on the model). The three columns are for different colours and magnitude sets and the white regions indicate the redshift range where each filter pair bracket the 4000 Å break. The grey points are for individual cluster measurements and the black points are for the median and standard deviation of the individual slopes per redshift bin.

m^*) and slope are shown in Figure 7.8. As the slope values have large statistical errors, we also computed the median values of the slopes in consecutive redshift bins. We compared our measurements to a red sequence model from Kodama and Arimoto (1997). This model is based on single stellar population modelling of galaxies with different metallicity and stipulate a burst of star formation at $z = 3$. It is computed in the CFHTLS bands and calibrated on the red sequence of the Coma cluster. The model colours and slopes are shown by the dashed red lines in Figure 7.8. We can see that the model reproduces well the evolution of the red sequence in the XXL clusters, although it is systematically offset. We thus used our data to re-calibrate the model, by computing the offsets for each colour and slope as the median of the differences between the data and the model. The redshift evolution of the red sequence zero points, slopes and scatter of individual clusters are shown in Figure 7.9. The re-calibrated model is indicated by the red lines. We can see that clusters have zero point and slope values compatible with the model, considering the error bars (the residuals are normally distributed). The red sequence scatter is relatively constant up to $z \sim 0.6$, with a median value $\sigma_{\rm col} \sim 0.06$ mag. These results show that the red sequence is also present in relatively low mass X-ray detected clusters, although it was not detectable in the poorest systems.

7.3.3 Colour of the brightest cluster galaxies

Many optical cluster finder algorithms use the BCG as cluster centre. For red sequence based cluster detection, the BCG is often selected among red galaxies (see e.g. Koester et al. 2007, for the MaxBCG and Oguri 2014 for the CAMIRA cluster finders). If a large fraction of BCGs have old stellar population (see e.g. Tal et al. 2014, for the evolution of central quenched fraction), some of them can show signs of star formation, which at low redshift, is often linked to the

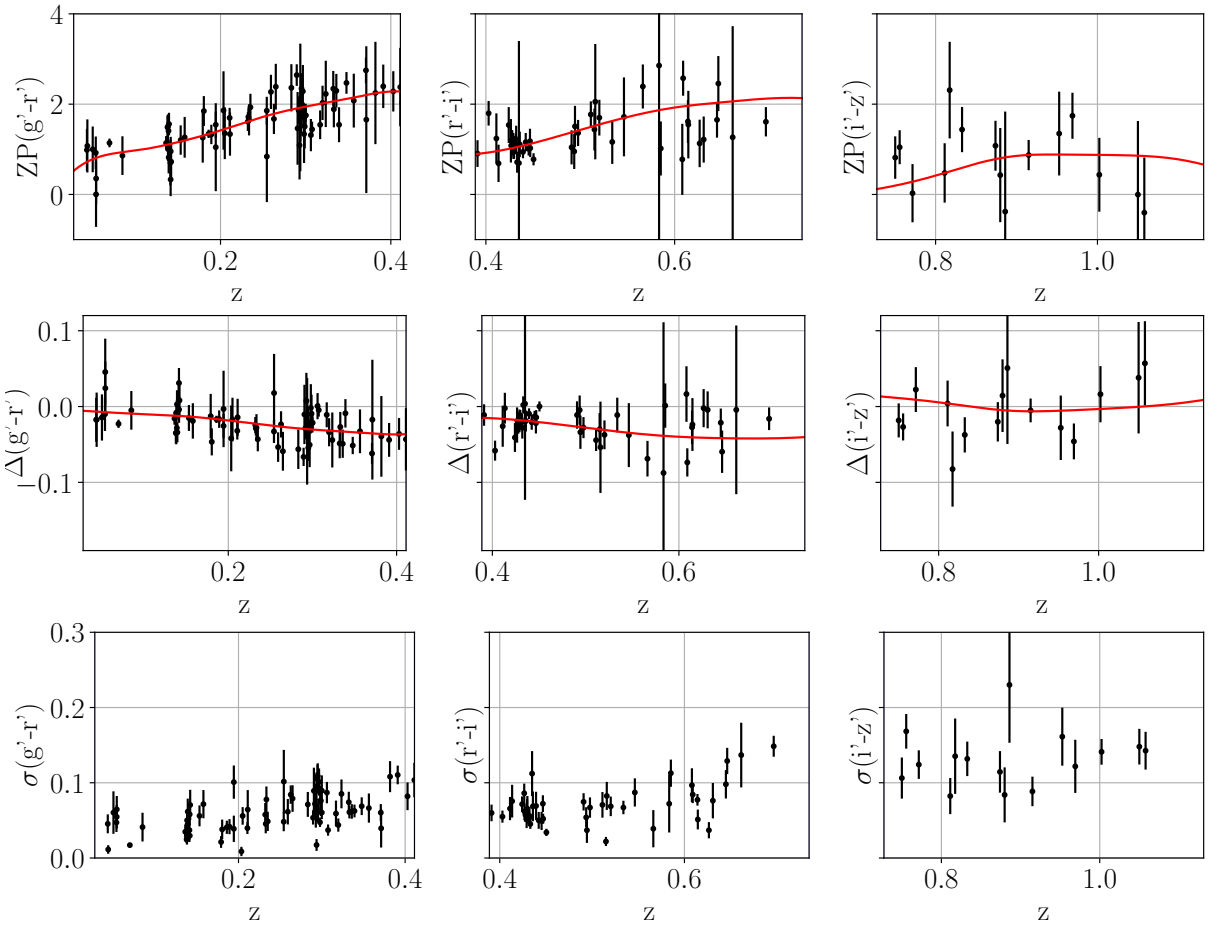

Figure 7.9: XXL clusters red sequence properties as a function of redshift. The top, middle, and bottom panels show the evolution of the red sequence zero points, slopes and scatter, respectively. The black points are for individual cluster measurements and the red lines show the model from Kodama and Arimoto (1997) after re-calibration.

ICM thermal state (see e.g. Fogarty et al. 2015, and Hicks et al. 2010). If the activity lasts long enough, such BCGs can have blue colours and may be missed by red sequence based cluster finders, leading to miscentering (see e.g. Sadibekova et al. 2014). In this context, X-ray or SZ cluster samples can be used to evaluate the effect of the BCG colour on optical centring.

We investigated the colour of the brightest cluster galaxies of the XXL clusters detected in Section 5.3.3.1 with respect to the re-calibrated colour model of the red sequence. Figure 7.10 shows the distribution of the colour difference between the BCG and the red sequence re-calibrated model for two redshift ranges. We can see that the major fraction of BCGs in the two samples have red colours: the median and scatter of the distribution are -0.03 ± 0.02 and $\sigma = 0.12$ at $z < 0.4$, and -0.01 ± 0.03 and $\sigma = 0.15$ at $0.4 < z < 0.7$. However, the distribution presents a tail corresponding to BCGs bluer than the red sequence.

The BCGs having a negative colour offset from the red sequence, by more than one standard deviation, are classified as blue. According to this criteria we found that the BCG colour is compatible with the red sequence colour model for 110/125 ($\sim 88\%$) clusters in our sample. However, 8/79 ($\sim 10\%$) have significantly bluer colours at $z < 0.4$ and 7/46 ($\sim 15\%$) at $0.4 < z < 0.7$. These fractions increase when we consider low mass objects: 13% (at $z < 0.4$) and 25% (at $0.4 < z < 0.7$) of the BCGs are bluer than the red sequence in clusters with $M_{500,scal} < 1 \times 10^{14}$ $M_{\odot}$. These results are compatible with the study of 14300 BCGs in the SDSS survey by Pipino et al. (2011), who found that the blue BCG fraction was lower in rich clusters and increasing with redshift, and that such galaxies were missed by the MaxBCG cluster finder.

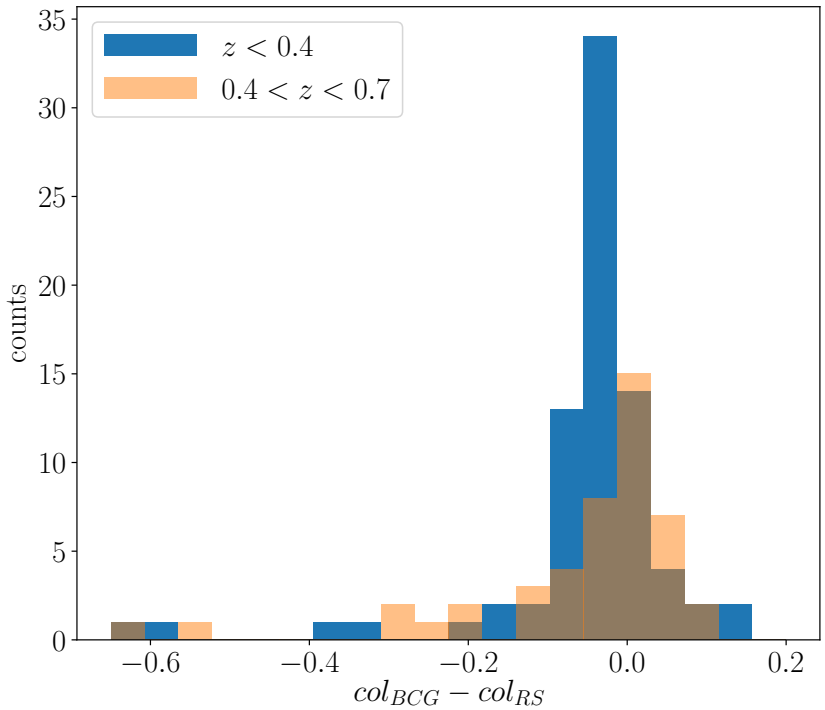

Figure 7.10: Distribution of the colour difference between the brightest cluster galaxies and the red sequence model. In red and blue, histograms are for the $z < 0.4$ and $0.4 < z < 0.7$ samples and are computed using the $g' - r'$ and $r' - i'$ colours.

The redshift dependence of the BCG star formation was also put in evidence by e.g. McDonald et al. (2016). They also found that the blue BCGs were preferentially found in disturbed clusters at $z \sim 0.6$ and in cool-core clusters at $z \sim 0$, and suggested that the star formation fuelling mechanism passed from galaxy-galaxy interactions to ICM cooling at lower redshift. The fact that XXL Paper XV found almost no sign of activity in the BCGs of the XXL bright cluster sample is expected if we consider the mass dependence of the blue BCG fraction (see also Section 6.4). Taken altogether, these results show that optical cluster finders that rely on the BCG for centring and only select red sequence galaxies may miscentre their detections. Moreover, the dependence of BCGs colour with cluster's masses, redshifts, dynamical or thermodynamic states may lead to centring bias towards a certain cluster population.

7.4 Conclusions

In this Chapter we studied the galaxy activity in clusters through their AGN fraction and colours, and we discussed its effect on cluster detection and characterisation. In the first part we presented the methodology used to derive the AGN fraction in XXL cluster's galaxies (XXL Paper XXXV), which requires to accurately measure the galaxy density profiles. We found that the cluster mass plays a key role in the AGN activity: the fraction of X-ray AGNs in massive ($M_{500,MT} > 1 \times 10^{14}$ M$_\odot$) XXL clusters is compatible with the field value and seems to decrease towards the centre while the AGN fraction in the outskirts of less massive systems ($M_{500,MT} < 1 \times 10^{14}$ M$_\odot$) is enhanced. The mean AGN fraction in the XXL clusters at $0.1 < z < 0.5$ is similar to that of clusters at higher redshift, but with similar masses. These results are coherent with a scenario in which AGN activity is enhanced by galaxy mergers and suppressed by ram pressure stripping by the hot ICM.

The enhanced X-ray AGN fraction found in low mass clusters with respect to higher mass ones is also important for cluster detection. Because of their shallowness and moderate angular

resolution, surveys such as XXL or eROSITA (Biffi et al. 2018) do not allow to fully disentangle the AGN and cluster emission, especially in faint and high redshift systems. However, the contamination can be measured via complementary observations at higher resolution (see e.g. Logan et al. 2018) or taken into account using realistic models of the AGN population (see e.g. Koulouridis et al. 2018a). Concerning the cluster detection, improvements can be achieved by accounting for more source models in the detection pipeline (see e.g. Faccioli et al. 2018).

In the second part, we constructed the colour-magnitude diagrams of XXL-N clusters and characterised the properties of their red sequence. We found that the red sequence is established in our relatively low mass X-ray detected sample, although it is not present in some poor clusters. We also found that the red sequence evolution is well described by the model from Kodama and Arimoto (1997) once re-calibrated on our data. We then studied the colour offset between the BCGs and the red sequence and found that $\sim 10\%$ of the BCGs were bluer at $z < 0.4$ and $\sim 15\%$ at $0.4 < z < 0.7$. Similarly to the AGN activity, we found that the fraction of star forming BCGs is higher in the low mass XXL clusters. These effects can lead to miscentring of cluster detections based solely on red sequence galaxies such as the ones from the MaxBCG or CAMIRA optical cluster finders. These analyses set the bases for further XXL cluster studies, such as the derivation of red galaxy luminosity functions or optical cluster sample comparison.

Chapter 8

Searching for the optical counterparts of XXL-N clusters with the WaZP cluster finder

Contents

Abstract: Cross-matching cluster catalogues detected in different wavelengths is of paramount importance for the validation of the cluster surveys selection functions. It is necessary for a meaningful interpretation of the cosmological constraints inferred from such cluster surveys. In this Chapter, we introduce the WAZP optical cluster finder algorithm and its application to the CFHTLS-W1 field. We then match WAZP to XXL detections and discuss the number of XXL clusters with or without optical association. This Chapter is based on an ongoing study (Benoist et al. in prep) to which I am contributing.

8.1 Introduction

Comparing cluster detected in surveys at different wavelengths informs us on the interplay between the gas and the galaxies in clusters (see e.g. Connelly et al. 2012), allows us to check survey and detection algorithm systematics (see e.g. Sadibekova et al. 2014), measure the surveys selection functions (see e.g. Rozo and Rykoff 2014), and to test the cosmological representativeness of the catalogues (see e.g. Rossetti et al. 2017). This is of paramount importance for the cosmological analysis of optical, X-ray or SZ cluster catalogues (see e.g. Rozo et al. 2010; Mantz et al. 2008; Planck Collaboration et al. 2014b).

Cluster selection is hampered with different systematics depending on the wavelength. For instance, X-ray detections are not very sensitive to projection effects from un-virialised structures, but may be contaminated by AGN, especially at high redshift (see Chapter 7). Conversely, optical detections are "inexpensive" in telescope time, but sensitive to projections of galaxy groups and filaments (see e.g. Rozo et al. 2015). Optical detections also provide cluster redshift estimates (see e.g. Ridl et al. 2017), which cannot be measured directly from shallow X-ray data and is not available from SZ observations. X-ray and SZ surveys are thus often followed-up with targeted optical spectroscopic observations and cross-matched with existing spectroscopic surveys (see e.g. Planck Collaboration et al. 2016c, for Planck, and XXL Paper XX for XXL clusters). Matching X-ray or SZ to optical cluster catalogues is a complementary approach to obtain redshift estimations. Firstly, it allows us to obtain photometric redshifts for a large number of systems. Secondly, it can provide targets for spectroscopic follow-up, preventing the spectroscopic redshift estimations, which rely on galaxies that are not members of an optical structure.

Comparisons between optical (or infrared) and X-ray cluster detections have been performed with various samples (see e.g. Donahue et al. 2002; Gilbank et al. 2004; Barkhouse et al. 2006; Connelly et al. 2012; Rozo and Rykoff 2014; Sadibekova et al. 2014; Willis et al. 2018). Cross matching X-ray emission, a projected signal by nature, with a concentration of galaxies, is a complex task, especially when no X-ray spectroscopy is available to obtain a redshift (see e.g. Connelly et al. 2012; Sadibekova et al. 2014). The matching can be obvious when a prominent galaxy (the BCG), dominating a clump of fainter ones, coincides with the X-ray centre. However, a number of cases can be ambiguous, due to offsets between the X-ray centre and the closest bright galaxy, or simply due to the lack of clear counterparts. Such cases occur more frequently when considering relatively low-luminosity or poor clusters (see e.g. Connelly et al. 2012; Rozo and Rykoff 2014). In this Chapter, we use the WAZP optical cluster finder algorithm (Benoist et al in prep.). This code participated to the Euclid cluster finder challenge, which compared and evaluated the performance of the detection codes in the *Euclid* context (Adam et al. in prep., see Appendix A). Here, we apply WAZP on the CFHTLS W1 field, to search for optical counterparts to the XXL clusters. The opposite exercise will be addressed in a future study.

8.2 The WAZP cluster finder

The Wavelet Z-Photometric WAZP cluster finder is an optical cluster finder based on the identification of galaxy over-densities in sky coordinates and photometric redshift space. An illustration of its operation is shown in Figure 8.1. The WAZP algorithm procedure can be described by the following step sequence.

Step 1: Choice of the limiting magnitude for the detections and catalogue cut We first select a reference band (e.g. the i-band here) and apply a cut at magnitudes $m = m^*(z_{spec}) + \delta m$, where m^* is the characteristic magnitude of the luminosity function and δm sets a faint cut used to estimate redshift independent richnesses. The evolution of m^* is taken from the model described in Conventions used in this thesis. We note that it is justified by the consistency between the evolution of the model and that of the median XXL-N clusters luminosity function characteristic magnitudes (see Chapter 6). The choice of δm leads to a redshift completeness limit z_{lim} for cluster detection when $m^*(z_{lim}) + \delta m$ reaches the limiting magnitude of the survey. In the present study $\delta m = 2$ was chosen, leading to $z_{lim} = 0.8$.

Step 2: Slicing of the galaxy catalogue in photometric redshift The slicing procedure along the z_{phot} axis depends on the chosen treatment of the photometric redshifts. In the present study we use an external spectroscopic redshift (z_{spec}) catalogue to model the $(z_{phot} - z_{spec})$ distribution, as a function of z_{spec} (see Chapter 4 for the details). These statistics were computed using only galaxies brighter than $m^* + 2$, which justify the modelling as a function of redshift

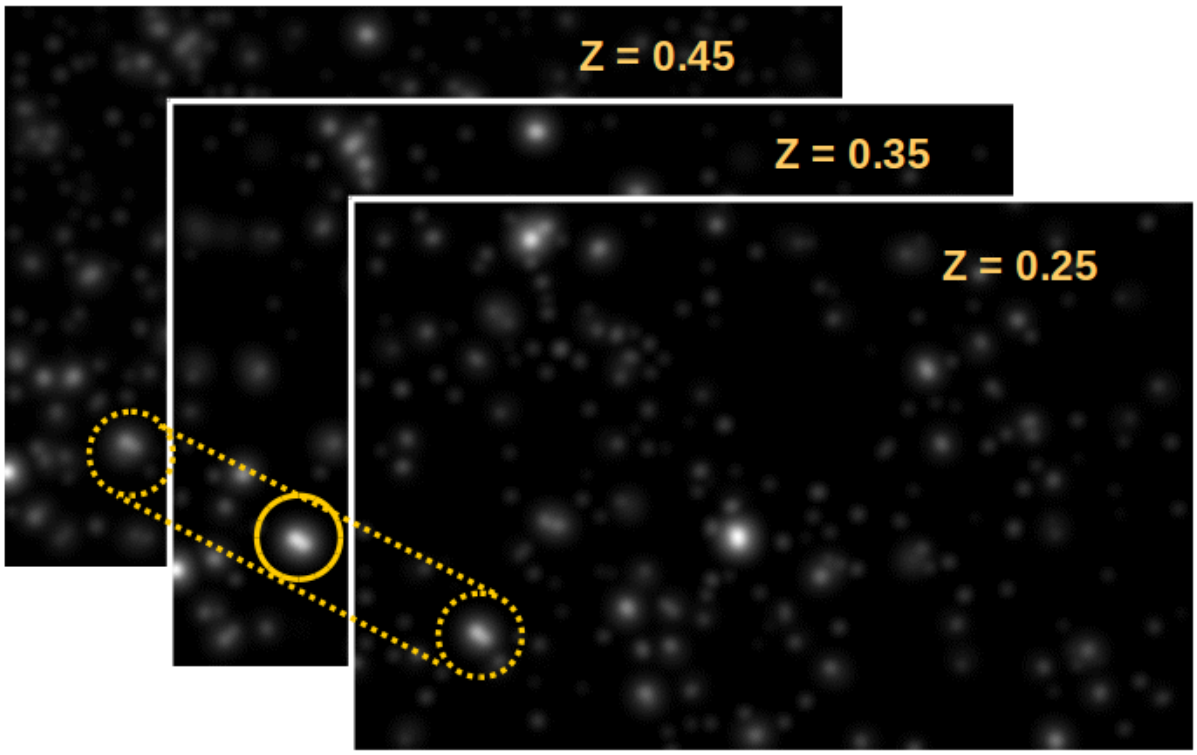

Figure 8.1: Illustrative view of the WAZP cluster finder detection process. A cluster is identified in galaxy density maps in consecutive redshift slices.

only (and not magnitude, as done in previous Chapters). The width of the photometric redshift slices correspond to the scatter of the $(z_{phot} - z_{spec})$ distribution. It is computed using the $5^{\rm th}$ and $95^{\rm th}$ percentile and the distance between two consecutive slices correspond to the $68^{\rm th}$ percentile.

Step 3: Wavelet filtering of each slice to generate a continuous density field of the significant structures For each slice of photometric redshift, the galaxy catalogue, cut at $m^* + 2$, is pixelated on a grid of pixel size equal to $1/16^{\rm th}$ of a Mpc. The resulting images are filtered using the wavelet task MR FILTER from the multi-resolution package MR1 (Starck et al. 1998). This task incorporates a statistically rigorous treatment of the Poisson noise, which enables to keep significant structures in an appropriate scale range. Here, structures with scales from ~ 300 kpc to ~ 1 Mpc are selected. A 3σ iterative multi-resolution thresholding with a B-spline wavelet transform is then applied.

Step 4: Detection of the density peaks The smooth density maps obtained in Step 3 are segmented and peaks are extracted in each object domain. In the case of several peaks in one domain, they can be merged or preserve their identity depending on the distance between a peak and the closest saddle point. Pixels of a domain are then distributed to peaks by proximity. A radius R_w, enclosing the significant over-density, is computed for each structure.

Step 5: Computation of the significance for each peak The peaks significance is measured with respect to local background density of galaxies. The significance is computed in a radius $R_s = 300$ kpc and the local background density Σ_{loc} is estimated in annulus of 3 to 5 Mpc around the mode of the peak. To estimate the variance of the local galaxy density, the whole slice is pixelated with pixel areas equal to 16π Mpc^2. Any pixel intersecting a bad region or an edge is removed. Standard counts-in-cells technique (see e.g. Bouchet et al. 1993; Efstathiou

1995) is then applied to estimate the standard deviation $\sigma(\Sigma_{glob})$ of the counts. The significance is then defined as:

$$SNR = \frac{\Sigma_s - \Sigma_{loc}}{\sigma(\Sigma_{glob})}, \tag{8.1}$$

where Σ_s is the galaxy density in the slice in a radius of 300 kpc around the structure peak. The maximum radius at which the significance is higher than one, R_{SNR}, is used as a cluster size proxy.

Step 6: Association of the peaks found along the line of sight when combining successive slices As slices overlap, one can expect that clusters can be detected in several consecutive slices. To build the final list of clusters, peaks of consecutive slices are associated and only the slice in which the system has maximum significance is kept. Note that two clusters can be identified on the same line of sight if their distance in redshift is larger than $6\sigma dz$.

Step 7: Computation of a refined redshift A reconstructed photometric redshift PDF can be assigned to each galaxy using Gaussian modelling and the scatter of the $(z_{phot} - z_{spec})$ distribution. At the position of each peak, a photometric redshift PDF is computed by summing the contribution from the PDF of all galaxies within R_w and ± 4 photometric redshift slices. The mode of summed PDFs defines the cluster photometric redshift.

Step 8: Galaxy probability membership assignment and centre definition Based on the structure centre, redshift and radius R_{SNR} defined above, membership probabilities (P_{mem}) are computed following the prescription given in Castignani and Benoist (2016). If the brightest member falls at a distance less than $d = 50$ kpc of the structure centre, its position is adopted as the cluster centre, which is otherwise unchanged.

Step 9: Computation of the richness In this study the richness is computed as the sum of the galaxy membership probabilities:

$$N_{gal} = \sum P_{mem}, \tag{8.2}$$

Note that given this definition, the richness can be less than 1.

8.3 Application to the CFHTLS-W1 field

8.3.1 Detection signal to noise and richness

We applied the WAZP cluster finder on the CFTLS-W1 field and identified the sources with a detection SNR greater than two, by using local density background estimation. The left panel of Figure 8.2 shows the value of the local background density used to compute the detection SNR as a function of redshift (note that it is similar to that obtained in Chapter 5). We can see that the local density increases up to $z \sim 0.8$ and slightly decreases afterwards. This is due to the scatter and bias of the photometric redshift/spectroscopic redshift distribution (see Chapter 4). Thus, the SNR depends on the cluster intrinsic richness but also on its redshift: for the same cluster the SNR will be lower at high redshift. This is also shown in the right panel of Figure 8.2, which presents the richness computed in a fixed physical radius $R = 300$ kpc as a function of SNR for different redshift cut. We can see that the zero point of the richness/SNR relation increases with redshift.

The cluster catalogue contains contains 7645 objects, 44% of which have a detection $SNR > 3$, and respectively 19% and 8% have $SNR > 4$ and $SNR > 5$. The redshift distribution of the detected clusters with different SNR cut is shown in the left panel of Figure 8.3. The redshift range goes from $z_{min} = 0.12$ to $z_{max} = 0.98$. This is explained by the high bias of the CFHTLS

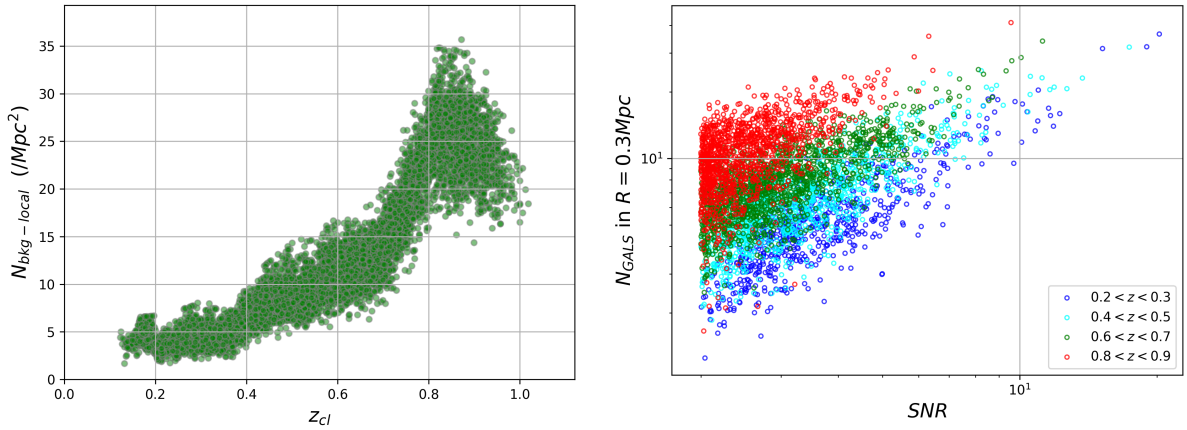

Figure 8.2: *Left:* local galaxy density used to determine the detection SNR as a function of redshift. *Right:* relation between the richness in 300 kpc and the detection SNR for clusters at different redshifts.

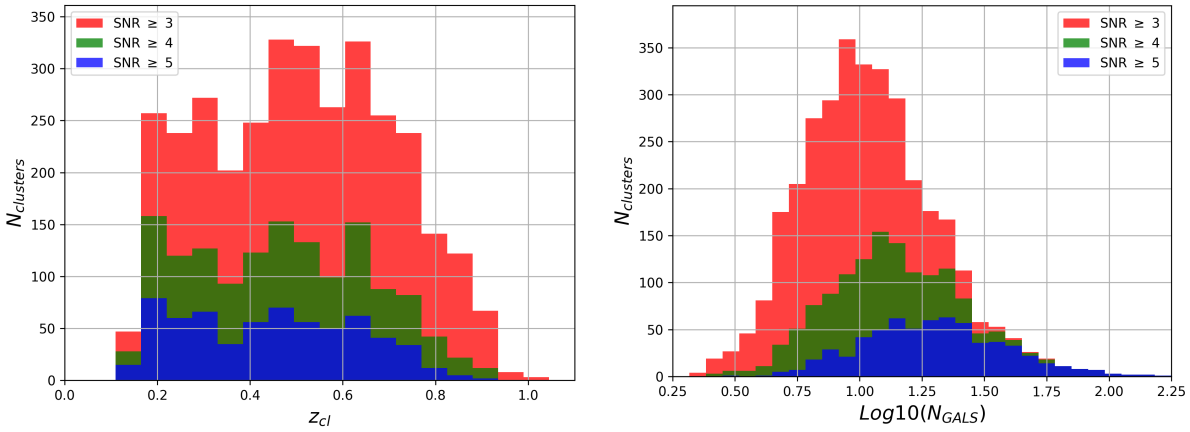

Figure 8.3: Redshift (left) and richness (right) distribution of the WAZP clusters for different cut in detection SNR.

photometric redshifts below $z \sim 0.1$ and their low quality at $z > 0.8$ (see Chapter 4). The right panel of Figure 8.3 shows the richness distribution for different SNR cut. As expected, we can see that the median richness increases with the SNR. The spatial density of systems with $SNR > 5$ and $N_{gals} > 10$ is ~ 8 cluster/deg^2, this value drops to ~ 5 cluster/deg^2 for $N_{gals} > 20$.

8.3.2 Redshift recovery

In order to assess the quality of the cluster redshift recovery, we matched the cluster members with the spectroscopic dataset described in Chapter 4. We then selected the WAZP clusters containing at least five members with spectroscopic redshifts falling in the same radial velocity window of ± 1000 km.s^{-1}. This criterion leads to a sub-sample of 400 clusters, for which we estimated their mean spectroscopic redshift using the bi-weight estimator. The relation between the photometric and spectroscopic redshift for this cluster sub-sample is shown in Figure 8.4. We recognise the presence of bias and scatter following that of the galaxy distribution (see Chapter 4), but with lower amplitude. This is expected as the scatter in cluster redshifts relative to galaxies is expected to be lower by $\sim \sqrt{N_{gals}}$. The mean richness of the cluster sub-sample being $N_{gals} \sim 10$ we expect to have $\sigma_{z_{clus}} \sim \sigma_{z_{gal}}/3$, which is compatible with the measured

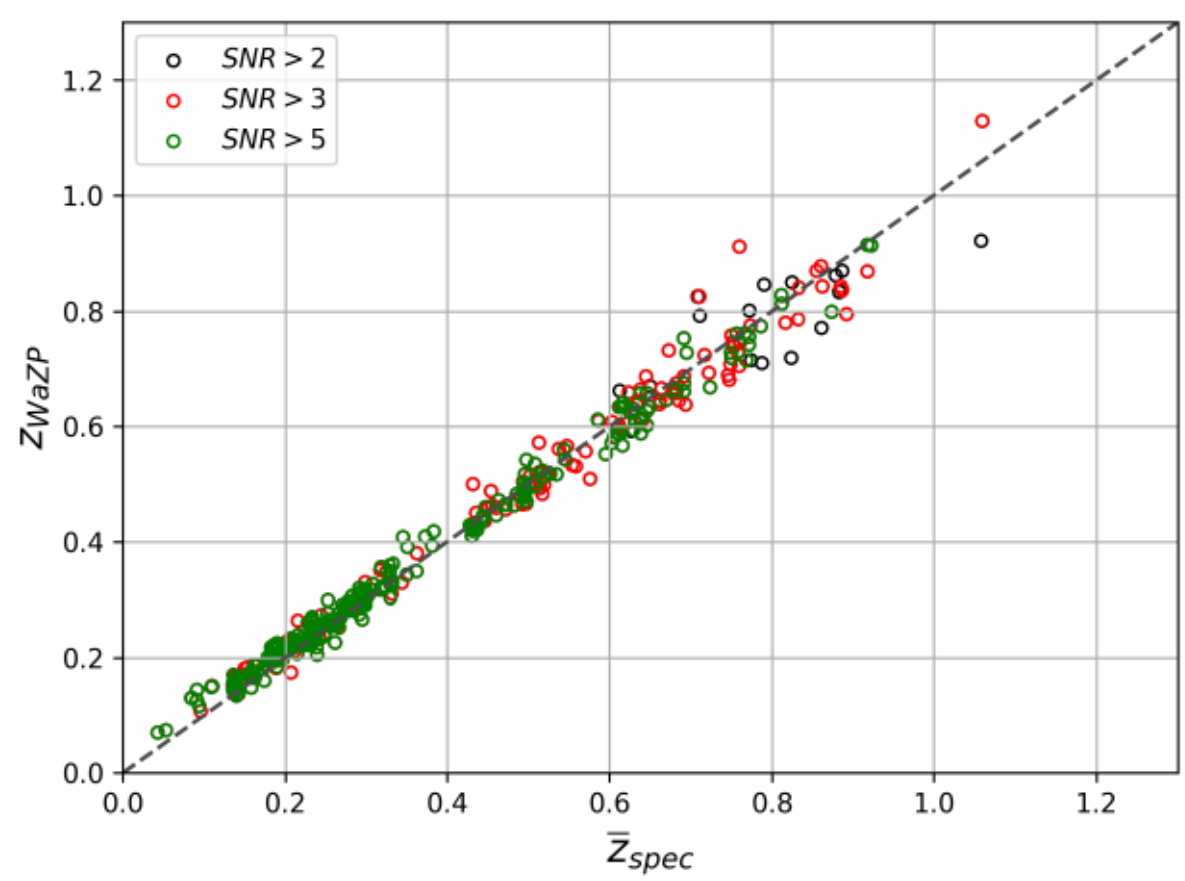

Figure 8.4: WAZP cluster photometric redshift/spectroscopic redshift relation for a sub-sample of 400 clusters containing at least 5 members with coherent spectroscopic redshift. The different colours are for different SNR cut.

value.

8.3.3 Impact of the photometric redshift quality in cluster detection

We evaluated the effect of the photometric redshifts quality on the detected clusters redshift distribution using a mock galaxy catalogue (Aardvark mock, Busha et al. 2013). The mock catalogue has a size of ~ 20 deg^2 and contains galaxies up to $z \sim 3$ with simulated CFHTLS photometry. This catalogue contains "true" spectroscopic redshifts from which we simulated associated photometric redshifts with three different degrees of realism:

1. using a Gaussian modelling with a standard deviation equal to $0.03 \times (1 + z_{true})$
2. using a modelling that reproduces the scatter of the CFHTLS photometric redshifts
3. using a modelling that reproduces the scatter and bias of the CFHTLS photometric redshifts.

We then ran WAZP on the three versions of the mock catalogue, using a magnitude cut at $m^* + 1$ for the detection. Figure 8.5 shows the photometric redshift distributions of the cluster detected in the three versions of the catalogue, with increasing degree of photometric redshifts realism from left to right. We can see that, in the case photometric redshifts are computed as (1) the number of detection increases with the photometric redshift up to $z \sim 0.7$ and reaches a plateau afterwards. When photometric redshifts are computed as (2), the number of detected clusters

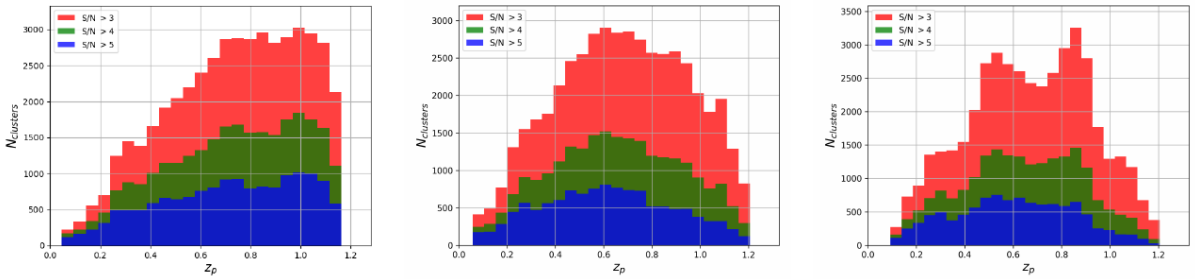

Figure 8.5: Photometric redshifts distribution of the clusters detected by WAZP in the three version of the Aardvark galaxy mock. The colours indicate the different cuts in SNR (blue, green, red for $SNR > 5$, 4 and 3, respectively). In the left panel photometric redshifts are Gaussian with a dispersion that increases as $(1 + z)$. In the central panel, the scatter of the photometric redshifts reproduces the scatter measured in the CFHTLS, in particular with an increase that is faster than $(1 + z)$. In the right panel, same as the central panel with, in addition the same bias in the photometric redshift as the one measured in the CFHTLS.

increases faster than in the previous case up to $z \sim 0.6$ and decreases afterwards, such as only a few clusters are detected at $z \sim 1.2$. In the case of photometric redshifts computed as (3), the redshift distribution of the detected clusters is more complex: their number increases up to $z \sim 0.5$ where it reaches a peak; a second peak is present at $z \sim 0.9$ and the number decreases afterwards; the shape of the distribution is different depending on the SNR cut. We found that the last distribution reproduce fairly well that of the clusters detected in the CFHTLS W1 field with a magnitude cut at $m^* + 1$. This analysis highlight the importance of the photometric redshift quality in cluster detection and characterisation.

8.4 Matching WAZP and XXL cluster detections

In this section, we associate XXL to WAZP detections, going from X-ray to the optical. We first describe the matching procedure, and then, we present the global matching statistics. Finally, we discussed the possible reasons explaining X-ray detections with no optical counterpart.

8.4.1 Input catalogues

The XXL-WAZP cluster association procedure is based on the 365-GC XXL cluster sample (see Section 3.1.4) and the WAZP catalogue described in Section 8.3 and cut at a minimum SNR of 2. To perform the matching, the two catalogues are first filtered in order to keep only the systems included in the common XXL-CFHTLS footprint, which is shown in Figure 8.6. The footprint's area is about $\sim$ 20 deg^2 and does not include masked photometric regions and "bad" XXM pointings, i.e. with low exposure or high background. The filtered XXL and WAZP catalogues contains 181 and 2648 detections, respectively.

8.4.2 Matching procedure

In this study we chose to perform a blind angular association between the X-ray and optical detections. This allows not to be biased by the optical identification performed during the XXL spectroscopic redshift assignment procedure, and to verify its estimation in the case when only a few galaxies were used (see Section 3.1.3.1). Following the study of Sadibekova et al. (2014), we first used a maximum matching distance of $d_{max} = 1'$ between the X-ray centroids and the optical centres. At low redshift we found that this limit was too small to account for typical

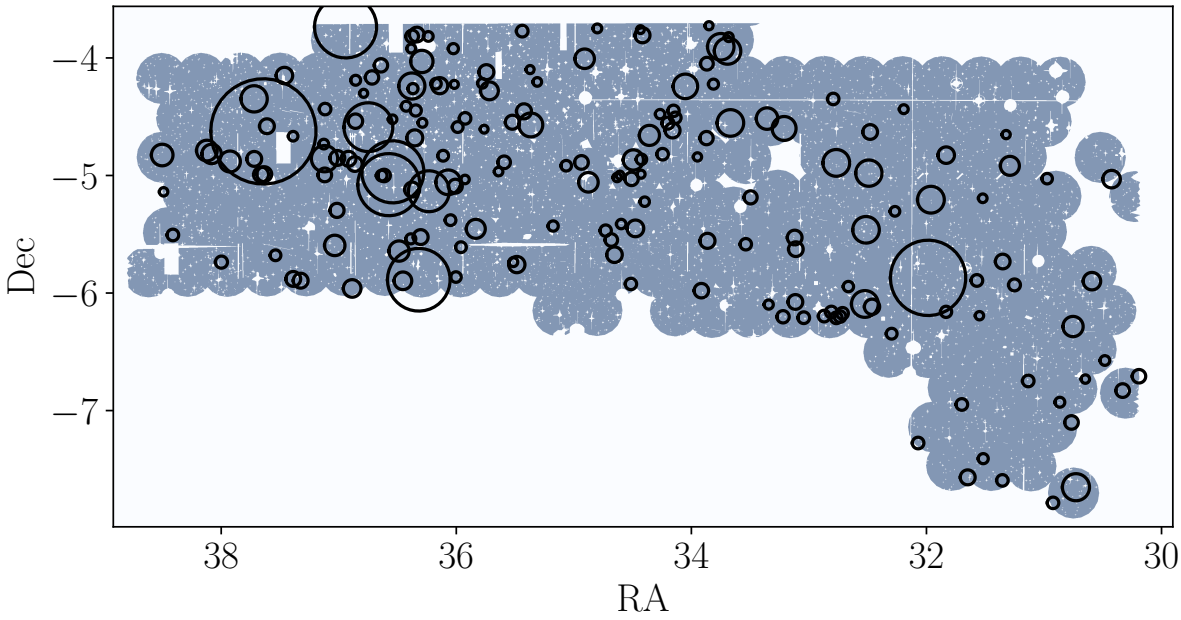

Figure 8.6: Spatial footprint common to the XXL and CFHTLS W1 surveys. The disks correspond to the XMM pointings whereas the holes and lines correspond to missing optical data due to bright stars or other defects. The black circle indicate 1 Mpc around the XXL clusters considered for the matching procedure.

optical-X-ray offsets. We thus adapted the angular criterion and used:

$$d_{max}(z) = \left\{ \begin{array}{ll} 270 \text{ kpc } (1' \text{ at } z = 0.3) & \text{for } z < 0.3 \\ 1' & \text{for } z > 0.3 \end{array} \right\} \tag{8.3}$$

with the physical size based on the WAZP redshift. Multiple matches were treated by taking the nearest object.

8.4.3 Global X-ray to optical matching statistics

We present here the global statistics of the matching procedure described in the previous section. We focus on the number of XXL clusters associated to an optical detection, as given in Table 8.1. We evaluated the errors on the matched systems fractions assuming binomial distributions and using Wilson score intervals.

8.4.3.1 Angular match

When performing a blind angular match, we find that 87^{+3}_{-3} % of the C1 and C2 XXL clusters that were assigned a spectroscopic redshift are matched with an optical detection. This fraction is higher when considering only C1 or the more massive half ($M_{500,scal} > 1.7 \times 10^{14}$ $M_{\odot}$) of the C1 and C2 clusters. We find that 91^{+4}_{-6}% of C3 clusters with a spectroscopic redshift have an optical association. Even if C3 clusters are very faint in X-ray, this high number is not surprising since they are not a direct output of the XXL detection pipeline and several of them are optical clusters from the literature (see XXL Paper XX). Finally 40^{+21}_{-18}% (2 out of 5) of the C1 clusters that were not assigned a spectroscopic redshift are matched to an optical detection. The photometric redshift associated to these clusters is compatible with that found by WAZP. The fact that the 3 other clusters are unmatched must be related to the difficulty in finding associated concentration of galaxies allowing a spectroscopic redshift. This could be a sign that

Table 8.1: Matching statistics between the XXL clusters and optical associations. The first block corresponds to C1 and C2 clusters with spectroscopic redshifts. Col1: type of clusters considered; col2: number of clusters in the input XXL catalogue; col3: number of angularly matched clusters; col4: fraction of angularly matched clusters; col5: number of angularly matched clusters with $z_{WaZP} = z_{XXL} \pm 0.15(1 + z_{XXL})$; col6: fraction of angularly matched clusters with $z_{WaZP} = z_{XXL} \pm 0.15(1 + z_{XXL})$. The errors correspond to 68% confidence intervals and are computed assuming binomial distributions and using the Wilson score interval.

type	#	$\#_{m,ang}$	$\%_{m,ang}$	$\#_{m,ang+z}$	$\%_{m,ang+z}$
C1 + C2	141	123	87^{+3}_{-3}	115	82^{+3}_{-3}
C1	92	86	93^{+2}_{-3}	82	89^{+3}_{-4}
C2	49	37	76^{+6}_{-7}	33	67^{+6}_{-7}
$M_{500,scal} < 1.7 \times 10^{14}$ M$_\odot$	70	58	83^{+4}_{-5}	50	71^{+5}_{-6}
$M_{500,scal} > 1.7 \times 10^{14}$ M$_\odot$	71	65	92^{+3}_{-4}	65	92^{+3}_{-4}
$z < 0.34$	71	68	96^{+2}_{-3}	60	85^{+4}_{-5}
$z > 0.34$	70	55	79^{+5}_{-5}	55	79^{+5}_{-5}
C3	35	32	91^{+4}_{-6}	29	83^{+5}_{-7}
C1 (no z_{spec})	5	2	40^{+21}_{-18}	-	-

the 3 unmatched clusters are at high redshifts, higher than that probed by the CFHTLS (i.e. at $z \gtrsim 1$).

8.4.3.2 Redshift criterion

As we showed, WAZP recovers well the photometric redshifts of the clusters and the majority of XXL clusters in our sample has been assigned a spectroscopic redshift. We measured the number of matched clusters for which the two estimates are concordant by imposed a criterion such as:

$$z_{WaZP} = z_{XXL} \pm 0.15(1 + z_{XXL}), \tag{8.4}$$

with z_{WaZP} the photometric redshift of the WAZP detection and z_{XXL} the spectroscopic redshift of the XXL detection. We found discrepant redshifts in 11 of the angularly matched systems: 3 C3 clusters, 4 C2 clusters and 4 C1 clusters. These C1 and C2 clusters have masses below $M_{500,scal} = 10^{14}$ M$_\odot$ and the 4 C2 clusters have been assigned a spectroscopic redshift based on 5 galaxies or less. All these clusters have redshifts $z_{XXL} \leq 0.3$, which supports the fact that wrong associations are caused by projection effects. The statistics are presented in the right part of Table 8.1. We can see that the difference in the fraction of C1 and C2 clusters with optical associations in a redshift window is compatible with that between the less and more massive half of the sample. When splitting the C1+C2 sample at its median redshift we observe that low redshift clusters have a higher matching fraction. However, when the redshift criterion is applied, the difference decreases and the two values are compatible.

8.4.4 Discussion about the XXL clusters unmatched in the optical

There are 18 C1+C2 XXL clusters with an optical spectroscopic redshift confirmation that are not associated to any WAZP detection. If we discard the systems that are matched, but do not have compatible redshift estimates, this number increases to 26. We investigated the possible reasons for these unmatched detections in the following.

The unmatched systems can be caused by an intrinsic lack of clustered galaxies around the X-ray emission or by possible failures of the optical and X-ray detection pipelines. In order to distinguish between these cases we ran the WAZP cluster finder in a "target" mode at the position and redshift of the XXL clusters. We thus obtained an optical SNR and richness $N_{\mathrm{gals,\ target}}$

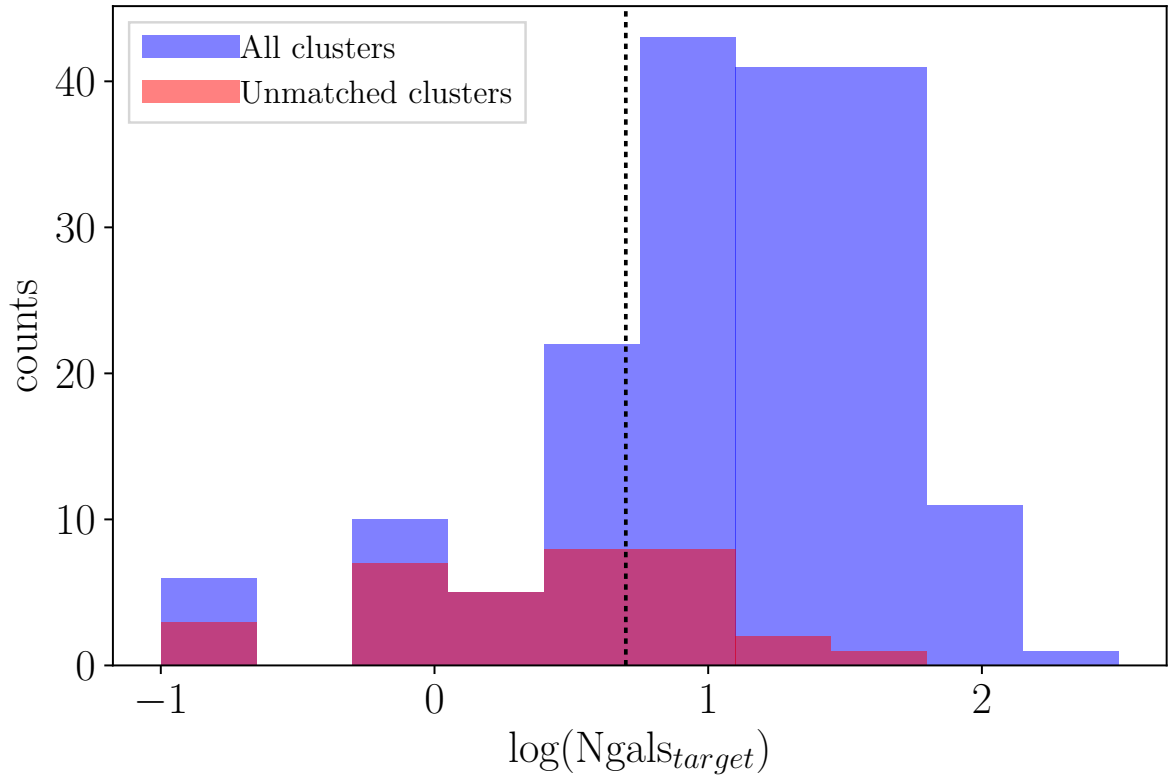

Figure 8.7: Distribution of the optical richness of the XXL clusters, computed in a target mode. The blue histogram is for the entire XXL sample and the red histogram is for clusters that are not matched to optical detection at a concordant redshift. The dotted line indicates $N_{\rm gals,\ target} = 5$. Un-matched systems poorer and richer than this arbitrary limit are discussed in the text. The minimum richness was set to 0.1 for visualisation purpose.

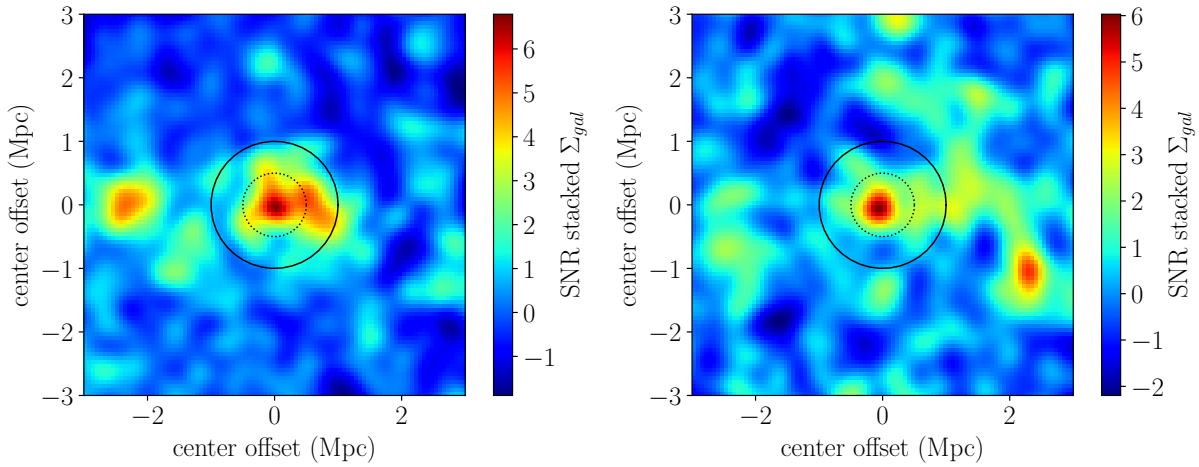

Figure 8.8: Stacked galaxy density maps of the unmatched C1+C2 clusters with optical spectroscopic redshift measurements, stacked at their X-ray centroid positions. The left and right panels are for clusters with richness above and below $N_{\rm gals,\ target} = 5$, respectively. Galaxies are selected in a photometric redshift slice around the XXL cluster spectroscopic redshift (see Section 5.3.2.3 for details) and up to $m^* + 2$. The maps unit are expressed in signal-to-background levels. The dotted and solid circles indicate 0.5 and 1 Mpc, respectively.

for each XXL clusters, similarly to the analysis performed in Chapter 5. The resulting richness distribution for the XXL clusters is shown in Figure 8.7. The systems unmatched to an optical structure at a concordant redshift are over-plotted in red. The clusters with $N_{\rm gals,\ target} < 1$ that appears to be matched correspond to cases where there is a large offset between the optical and X-ray detection. In the following we analysed the unmatched systems with richness above and below $N_{\rm gals,\ target} > 5$.

We find that 6/26 clusters correspond to optical detection with $N_{\rm gals,\ target} > 5$. We thus investigated why they are not matched blindly. We noticed that:

- 2 are part of a superstructure;
- 2 have a large optical to X-ray offset and are likely to be merging clusters (one of them is XLSSC102, studied in details in Chapter 12);
- 1 corresponds to a loose group,
- 1 is near an optical mask.

The fact that these clusters are not angularly matched is therefore understandable. In the left panel of Figure 8.8, we show the stack of the optical density maps of these clusters (see Section 5.3.2.3 for details on their computation). The galaxy selection is similar to that operated by WaZP and the centres are defined by the X-ray centroid positions. As expected from their richness, we can detect the averaged optical signal of these clusters, centred on the X-ray centroid positions. We see, however, that the stacked emission is not highly peaked, compatible with the fact that the majority of those systems are mergers or parts of superstructure with asymmetric distributions, which translates in a blurring during the stacking.

We then focused on the 20 XXL clusters for which the optical richness computed in target mode is below $N_{\rm gals,\ target} < 5$. We find that:

- 13 of them have very low masses ($M_{500,scal} < 0.5 \times 10^{14}$ M$_\odot$). Under this mass limit, only 33^{+11}_{-09} % of the C1+C2 clusters with determined redshifts are matched to an optical counterpart. This could be caused by the scatter between the richness and the intrinsic X-ray surface brightness.
- 4 clusters have a high redshift. The poor quality of the CFHTLS photometric redshifts at $z > 0.85$ could thus explain that only 45^{+15}_{-14} % of C1+C2 clusters with determined redshifts are matched above that limit.
- 8 systems have at least one X-ray point source located within 500 kpc of their centroid. They could be either miss-classified point sources or contaminated clusters with an enhanced X-ray surface brightness compared to their richness.

All the 20 XXL clusters without significant optical detections can be explained by one or several reasons discussed above. In the right panel of Figure 8.8, we show the stacked optical density map of these clusters. A peaked emission, centred around the X-ray centroid positions, is clearly detectable on the stacked optical density map. The shape of the emission is roughly circular, but its extent is small: the signal-to-background level becomes lower than two at ~ 300 kpc from the centre. This could explain why those systems are not matched in the optical. We note, however, that the stacked density map can be dominated by a few clusters, and the fact that optical signal is detectable in average does not mean that all individual clusters present optical signal.

8.5 Conclusions

In this Chapter, we used the WAZP optical cluster finder algorithm to search for the optical counterparts of XXL-N clusters. We first presented WAZP and its application to the CFHTLS-W1field. We used simulated catalogues to investigate the effect of the photometric redshift quality on the detected clusters redshift distribution. We then performed a blind association between the WAZP and XXL catalogues and measured the fraction of matched systems, imposing or not an a posteriori redshift criterion. We found that 82^{+3}_{-3}% of XXL clusters have an optical counterpart at a concordant redshift. The fraction is higher for C1 and more massive clusters. We then studied the unmatched systems and found that a large fraction of them have low masses. We evaluated that some of them could be miss-classified X-ray point sources or contaminated clusters. An optical signal is detectable in the stacked density maps of the unmatched clusters, signifying that at least some of them present bright galaxies clustered around the X-ray centroid positions. We also found that 3 out of 5 C1 clusters without spectroscopic redshift estimation do not have a counterparts in the CFHTLS. If those are true clusters, this could be a sign that they are at high redshift ($z > 1$).

This analysis is still ongoing and several aspects are under investigation. Firstly, the matching procedure was applied to the WAZP clusters to search for X-ray counterparts. We will thus investigate the matching statistics and the reasons for the optical clusters without X-ray counterparts. An analysis of the relation between richness and X-ray temperature will also be conducted, to evaluate if the scatter can be responsible for the low mass unmatched systems. A study of the relation between the X-ray and optical morphologies will help us to understand how they impact the detections. Finally, we will achieve an optical characterisation of the C1 and C2 clusters at same mass, to investigate if they display different properties.

When completed, this study will shed light on optical and X-ray cluster selection functions, down to low mass and up to high redshift, and bring valuable information for future surveys such as eROSITA, *Euclid*, or LSST.

Summary, perspectives and conclusion

In this part, we have explored the optical properties of galaxy clusters detected in X-ray by the XXL survey. We have shown that XXL clusters span a wide redshift range, while being less massive in average than the ones from other X-ray or SZ selected samples (Chapter 3). We constructed robust cluster composite luminosity functions (CLF) in Chapter 5 and we showed that the CLF of the XXL cluster sample is comparable to that of other X-ray or optical samples (Chapter 6). We also find that the majority of XXL clusters present a red sequence in their colour magnitude diagrams (Chapter 7). Taken altogether, the results of Chapters 6 and 7 show that the properties of cluster galaxies depend on the cluster mass. For instance, there is a higher luminosity segregation between BCG and regular members in poor clusters. Also, the fraction of AGN and blue BCGs is higher in low mass systems. These effects might affect X-ray cluster detection and optical cluster centring. The galaxy density and integrated luminosity, computed within the scale radius, increases with richness, but is compatible with no redshift evolution. This strengthen the fact that they can be used as cluster mass proxies. In Chapter 8, we matched the XXL cluster sample to that obtained in the optical with the WaZP cluster finder. A high fraction of systems are detected in both wavelengths. The majority of the remaining cases have low masses.

We inspected the quality of the photometric redshifts in the CFHTLS survey using a large associated spectroscopic redshift catalogue (Chapter 4). We showed that the photometric redshifts dispersion increases with both redshift and magnitude and that ignoring this effect leads to systematics in the luminosity function measurements (Chapter 5). We also found that the photometric redshifts are biased and that their dispersion increases with redshift faster than the usual factor of $(1 + z)$. In Chapter 8, we showed that it directly impacts optical cluster detections. Lastly, we find that the photometric redshift probability density functions provided in the CFHTLS catalogue are inaccurate and we warned against the utilisation of photometric redshifts in parameter space regions that are not covered by spectroscopy.

This work could be pursued with a larger sample of clusters. This would allow us to model the evolution of cluster galaxies luminosity, colour and density as a function of redshift, mass and distance from the cluster centre. This would constitute the ultimate optical characterisation of XXL clusters. The same methodology could be applied to optical, SZ, or even weak lensing (in a near future) selected samples to test their cosmological representativity. However, this would first require investigating the quality of the photometric redshift with colour. Another interesting perspective is to compare the cluster richness and integrated optical luminosities to X-ray mass proxies and calibrate them with weak lensing masses. The effect of the cluster dynamical state on these scaling relations could also be explored by using, for instance, the offset between the BCG and the X-ray centroid as a proxy (see Section 9.3.1 for an application).

The analyses conducted in this part of the thesis highlight the strong connexion between galaxy and cluster evolution. The physics of galaxies is a particularly interesting topic in itself, but galaxies can also be seen as a nuisance for the use of clusters as cosmological probes. Therefore, clusters and galaxies have to be studied conjointly to better understand and take into account their intricacy.

Part III

Unveiling the internal structure of distant clusters with the Sunyaev-Zel'dovich effect

Table of Contents

Objectives of this study

In part II, we used a large sample of XXL X-ray detected clusters and we statistically characterised their optical properties. Here, we chose a complementary approach: studying a few clusters in details, in order to understand their physical properties in depth. To do so, we proposed to observe three XXL galaxy clusters with NIKA2, a high resolution camera operating at millimetre wavelengths, in order to map their Sunyaev-Zel'dovich (SZ) signal. Our main motivation is to conduct a multi-wavelength characterisation of the clusters, in a mass and redshift regime that is barely explored to date, but which will be extensively probed by future large X-ray and optical/NIR missions, and which is becoming accessible to ground based SZ surveys.

This part is based on the preparation of a NIKA2 observing proposal, of which I am principal investigator (PI), the process of data acquisition at the telescope, to which I participated during one week of observing campaign, and the preliminary analysis and results that I obtained. The analyses were conducted in collaboration with Rémi Adam, who is the co-PI of the proposal and a core member of the NIKA2 collaboration. We took advantage of data reduction and analysis softwares developed in the NIKA2 collaboration. The methodology and the results presented in this part will be included in a future article (Ricci et al. in prep.).

The structure of this part is defined as follows: we describe the project motivations and the preparatory analyses in Chapter 9; we present the instruments and the procedures from the data acquisition at the telescope to the data reduction and map-making in Chapter 10; in Chapter 11 we develop the tools to conduct a preliminary extraction and analyses of the sub-millimetre galaxies present in our field; finally, in Chapter 12, we present the preliminary analysis of the morphology, the characterisation of the radial physical properties, and the global properties of the cluster XLSSC102.

Chapter 9

Preparation of the NIKA2 follow-up: towards the Sunyaev-Zel'dovich mapping of $z \sim 1$ XXL clusters

Contents

Abstract: In this Chapter we describe the preparation of a project aiming at mapping the thermal SZ emission of three relatively low mass, high redshift XXL clusters with the high angular resolution NIKA2 camera. We present our motivations and the target selection process. We investigate the morphologies and dynamical states of the selected clusters using optical and X-ray data. We also simulate the expected SZ surface brightness maps and profiles in order to define the observing time needed to achieve our goals. This follow-up project, of which I am principal investigator, was proposed to the IRAM committee in September 2017.

9.1 Project motivations

As we showed in Part II, the depth of XXL allows us to detect clusters with relatively low masses[1] at high redshift, and thus represents an excellent pathfinder to future X-ray and optical/NIR

[1]High mass for XXL, but low mass for SZ surveys such as the ones performed with the Atacama Cosmology Telescope (ACT, Hilton et al. 2018) or the South Pole Telescope (SPT, Bleem et al. 2015). See Figure 3.3.

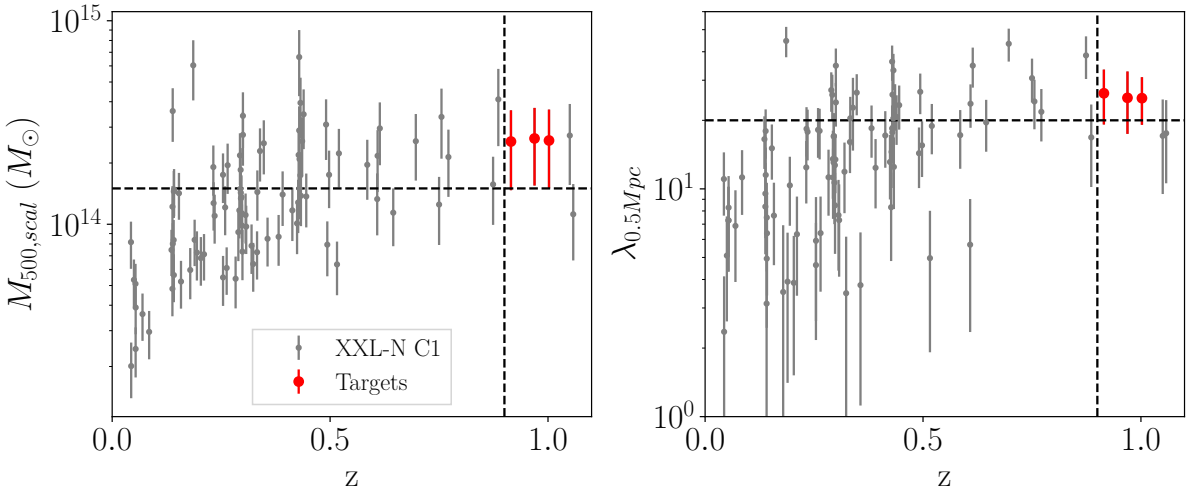

Figure 9.1: Targets selection among the XXL-N C1 clusters falling in the CFHTLS-W1 field. *Left:* mass as a function of redshift. *Right:* richness computed in 0.5 Mpc as a function of redshift. Our targets are shown in red. The dashed lines show the selection limits we imposed.

missions. Due to their shallow potential wells, low mass clusters are more affected by gas stripping, shocks heating or turbulences that are caused by merging events as well as AGN feedback. Therefore, deviations from self-similar scaling relations are expected to be enhanced in this regime, in particular at high redshift, where those effects are more efficient (see e.g. Le Brun et al. 2017). Thanks to XXL, it is now possible to investigate the impact of such potential non-gravitational processes in clusters, up to $z \sim 1$. Understanding in depth the physical properties of low mass/high redshift clusters is also crucial to calibrate numerical simulations that are later used when comparing cosmological models to observations (see, e.g., the impact of baryonic processes on the halo mass function, Bocquet et al. 2016).

Despite its importance, this region of the mass-redshift plane is still unexplored using high resolution SZ observations, due to the lack of dedicated instruments, while such data would provide unique insight into the physical properties of these objects. Indeed, provided that sufficiently deep and resolved observations are available, the thermal SZ effect (hereafter referred to as "SZ effect") is very useful to study the dynamical states of clusters, since merging events cause overpressure in the ICM (see e.g. Pointecouteau et al. 1999; Komatsu et al. 2001). Moreover, the integrated SZ flux, Y, directly probes the overall thermal energy of clusters, and has been shown to closely track the clusters' total masses (see e.g. Planck Collaboration et al. 2014b), with a low intrinsic scatter. Finally, the SZ surface brightness is independent of redshift. Consequently, resolved SZ observations, combined with optical/NIR and X-ray, offer a unique opportunity to study in depth the physics of distant clusters.

We thus proposed to follow-up a sample of high redshift XXL clusters, in SZ, with the New IRAM KIDs Array 2 high angular resolution camera (NIKA2, NIKA2 Collaboration et al. 2018, see also Chapter 10 for more details on the instruments). Our goal is to study the internal structure of a sample of XXL clusters with resolved SZ observations and combined them to X-ray and optical data to achieve a multi-wavelength characterisation.

9.2 Targets selection

9.2.1 Selection of cluster candidates

Given its high angular resolution ($< 20''$, see Chapter 10), NIKA2 observations give the opportunity to study high redshift clusters in detail. We therefore chose to select only clusters with

Table 9.1: Names, coordinates and redshifts of the selected clusters.

ID (—)	R.A. (degree)	Dec. (degree)	z (—)
XLSSC102	31.322	−4.652	0.969
XLSSC100	31.549	−6.193	0.915
XLSSC072	33.850	−3.726	1.002

$z > 0.9$, as they are the most relevant for our purpose. We chose our targets among the C1 clusters from XXL-N[2], which all have spectroscopically confirmed redshifts.

We want to study the typical low mass systems (compared to e.g. SZ selected sample) selected by XXL. However, the masses of our targets have to be high enough to ensure their detection in a reasonable amount of observing time with NIKA2. We thus selected clusters with mass $M_{500} > 1.5 \times 10^{14} M_{\odot}$. We verified that this criterion was satisfied with different mass estimates: $M_{500}^{\rm scal}$ (see Section 5.2 and XXL Paper XX); $M_{500}^{f_{\rm gas}}$ (XXL internal release), estimated from the mass-gas fraction relation from Eckert et al. (2015), hereafter XXL Paper XIII; and $M_{500}^{Y_{\rm X}}$, estimated from the analogous of the SZ flux, $Y_{\rm X,500}$ (see Section 9.2.2), and the mass-$Y_{\rm X}$ relation from Planck Collaboration et al. (2014b) as given in equation 9.2, assuming an hydrostatic mass bias of $b_{\rm HSE} = 0.2$.

Finally, we need to select systems rich enough to be able to compare their gas morphology to their galaxy distribution. We thus imposed a minimum richness, $\lambda_{0.5Mpc} > 20$, as computed in Chapter 5.

Our selection resulted in a sample of three candidate clusters, whose properties are presented in Tables 9.1 and 9.2. Figure 9.1 shows the limits imposed for the selection and the location of the targets in the mass-redshift and the richness-redshift planes.

9.2.2 Sunyaev-Zel'dovich flux prediction from XXL and Planck data

Before proposing observations, it is necessary to have an estimate of the total flux that we expect. This is done under different assumptions, using XXL and Planck data.

Estimation from XXL We estimated the total integrated SZ flux of our cluster candidates using $Y_{\rm X,500}$, computed as the product of the gas mass and the gas temperature:

$$Y_{\rm X,500} = T_{\rm X} \cdot M_{\rm gas,500}, \tag{9.1}$$

where we use $T_{\rm X} \equiv T_{300\ \rm kpc}$. We then apply the scaling relations and assumes the universal pressure profile from Arnaud et al. (2010), to convert $Y_{X,500}$ to the total SZ flux,

$$D_A(z)^2 Y_{\rm tot} = 1.796 \times (0.924 \pm 0.004) \cdot Y_{\rm X,500} \cdot C_{\rm XSZ}, \tag{9.2}$$

and related to the mass as

$$E^{-2/3}(z) \left[\frac{Y_{\rm X,500}}{2 \times 10^{14}\ {\rm M}_{\odot}\ {\rm keV}}\right] = 10^{0.376 \pm 0.018} \left[\frac{(1-b_{\rm HSE}) M_{500}^{Y_{\rm X}}}{6 \times 10^{14}\ {\rm M}_{\odot}}\right]^{1.78 \pm 0.06}. \tag{9.3}$$

The factor 1.796 allows us to convert the SZ flux within R_{500} to the total SZ flux, under our assumption about the shape of the pressure profile, and $C_{\rm XSZ} = 1.416 \times 10^{-19}$ Mpc^2 M$_{\odot}^{-1}$ keV^{-1}. Note that as the temperature is computed within 300 kpc and includes the central region, it can be biased low if a cluster is a cool-core, and lead to an underestimated mass, $M_{500}^{Y_{\rm X}}$, and

[2]The XXL-S clusters are not observable from the IRAM 30m telescope.

Table 9.2: Properties of the selected clusters, see text for the description of each parameter.

ID (—)	$\lambda_{0.5Mpc}$ (—)	$R_{500}^{\rm scal}$ (kpc)	$M_{500}^{\rm scal}$ (10^{14} M$_\odot$)	$M_{500}^{f_{\rm gas}}$ (10^{14} M$_\odot$)	$M_{500}^{Y_{\rm X}}$ (10^{14} M$_\odot$)	$T_{300\ {\rm kpc}}$ (keV)	$Y_{X,500}$ (10^{14}keV M$_\odot$)	$D_A(z)^2 Y_{\rm tot}^{Y_{\rm X}}$ (kpc^2)	$D_A(z)^2 Y_{\rm tot}^{\rm Planck}$ (kpc^2)
XLSSC102	25 ± 8	688 ± 94	2.6 ± 1.1	$4.4^{+1.6}_{-1.0}$	2.9 ± 0.5	$3.9^{+0.8}_{-0.9}$	1.27 ± 0.39	30 ± 9	40 ± 57
XLSSC100	26 ± 7	694 ± 98	2.5 ± 1.1	$3.7^{+1.3}_{-0.8}$	3.2 ± 0.3	$5.6^{+0.5}_{-0.6}$	1.48 ± 0.26	35 ± 6	66 ± 64
XLSSC072	25 ± 6	674 ± 94	2.6 ± 1.1	$3.9^{+1.3}_{-0.9}$	1.8 ± 0.3	$2.0^{+0.4}_{-0.3}$	0.56 ± 0.15	13 ± 4	24 ± 65

integrated Compton parameter. Additionally, we stress that $M_{\rm gas,500}$ is computed within a given R_{500}. This already assumes a given mass M_{500}, which is not necessarily self-consistent with the mass that we obtain from our $Y_{\rm X,500}$ estimate. While it should be necessary to iterate about the scaling relation of (Arnaud et al. 2010) to refine our estimates of $Y_{\rm X,500}$ and $M_{500}^{Y_{\rm X}}$, this already provides a useful first estimate given our aims, especially since the value of R_{500} used to derive $M_{\rm gas,500}$ is close to the one we obtain with $Y_{\rm X,500}$.

Estimation from Planck Because of the large beam of Planck ($10'$ for the Compton parameter map, Planck Collaboration et al. 2016f), our targets are not detected in the Planck SZ catalog (Planck Collaboration et al. 2016b) at such masses and redshifts. Nevertheless, we also checked that the Planck SZ fluxes were compatible with the X-ray expectations. This was done by extracting the total SZ flux at the XXL coordinates in the Planck Compton parameter map (Planck Collaboration et al. 2016f; Hurier et al. 2013), by fitting 2D Gaussians of FWHM equal to the map resolution. The flux error was estimated by repeating the measurements at random positions around the cluster. This procedure assumes that our targets are point sources with respect to the $10'$ Planck beam, and provide an estimate of the total SZ flux, $Y_{\rm tot}$.

The Compton parameter values estimated from X-ray, $D_A(z)^2 Y_{\rm tot}^{Y_{\rm X}}$, and measured in the Planck map, $D_A(z)^2 Y_{\rm tot}^{\rm Planck}$, are presented in Table 9.2. We can see that they are compatible, considering the large uncertainties in the Planck based measurements.

Comparison to ACT masses Two of our targets, XLSSC102 and XLSSC072, were detected independently by the ACT survey in SZ, as published after the completion of our observation proposal (Hilton et al. 2018). The masses (referred to as M_{500c}^{Cal} in their study) are derived assuming a universal pressure profile and the scaling relation from Arnaud et al. (2010), and recalibrated using weak-lensing measurements from Sereno (2015). The ACT masses are $4.6^{+1.1}_{-1.0} \times 10^{14} M_\odot$ and $3.6^{+0.9}_{-0.8} \times 10^{14} M_\odot$ for XLSSC102 and XLSSC072, respectively. They are in overall agreement with our estimates (see Table 9.2).

9.2.3 AGN contamination

Radio sources can contaminate the SZ signal (see e.g. Zhou and Wu 2004; Massardi and De Zotti 2004; Sayers et al. 2013b, and Chapter 7). Therefore, we have checked in the NVSS and FIRST radio catalogues that no radio sources will contaminate our data within the clusters targeted regions. Also, Chandra X-ray snapshot observations have been recently obtained for XLSSC072 (Logan et al. 2018) revealing that the corresponding cluster field is clear of AGN contamination in X-rays.

9.3 Targets characterisation and simulations

9.3.1 Estimation of the morphology from optical and X-ray data

We investigated the morphology and dynamical state of our targeted clusters using optical and X-ray indicators to better address their expected properties.

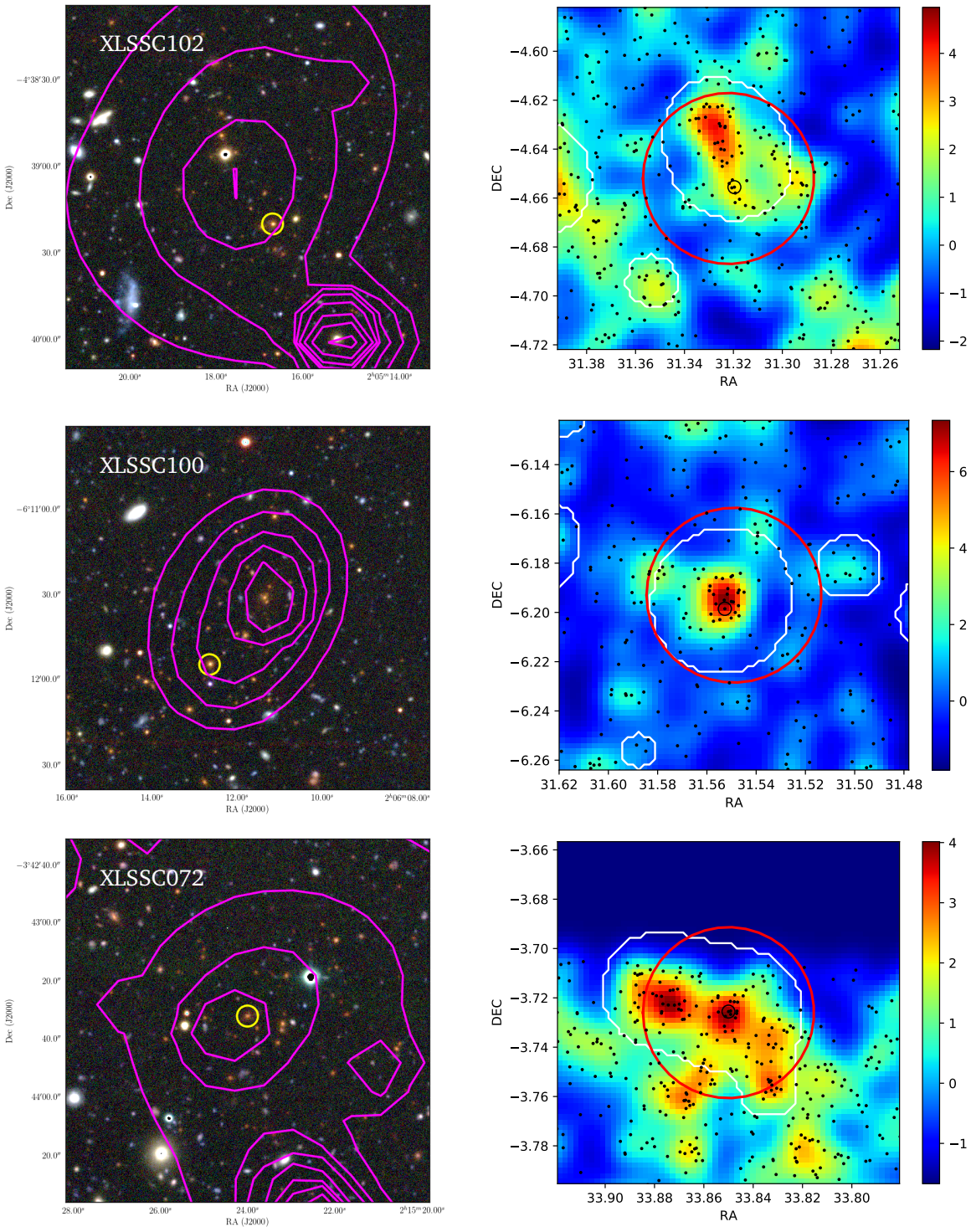

Figure 9.2: Optical and X-ray view of our targets. *Left panels:* 1×1 Mpc^2 ($\sim 2'$ across) optical Megacam $g'r'i'$ images centred on the X-ray peak. Yellow circles indicate the brightest cluster galaxies, whereas the pink contours indicate filtered X-ray emission. *Right panels:* 4×4 Mpc^2 optical density maps in units of background subtracted SNR. The white contours indicate the structures detected by the WAZP cluster finder, the red circles show the X-ray centre with 1 Mpc radius, the black dots represent galaxies selected in magnitude and photometric redshift, and the black circles indicate the BCGs. The north part of the field of XLSSC072 is outside the CFHTLS-W1 field.

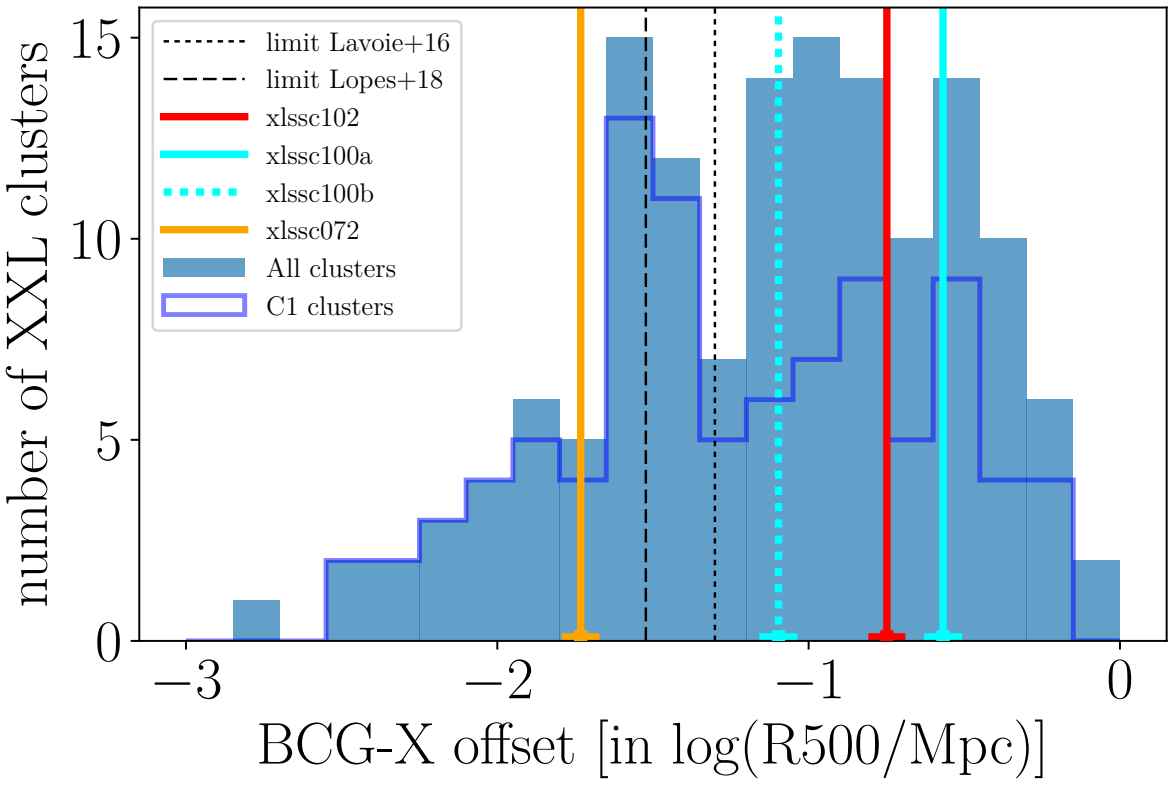

Figure 9.3: Distribution of the BCG-X-ray centroid offset, in units of R_{500} (using $R_{500}^{\rm scal}$). The blue filled histogram shows the distribution including all the sample of XXL-N clusters described in Section 5.2. The dark blue line shows the distribution when only the C1 clusters are included. The colour lines show the offset measured in our three targeted clusters, as indicated in the legend. Two BCGs are detected in XLSSC100. The limits chosen by XXL Paper XV and Lopes et al. (2018) to distinguish between relaxed or disturbed clusters are shown by the black dotted and dashed lines.

9.3.1.1 X-ray morphology

The left panel of Figure 9.2 shows X-ray photon count contours drawn from wavelet filtered X-ray images, over-plotted on the composite $gr'i'$ CFHTLS 1×1 Mpc^2 images of our targeted clusters. The concentrated contours at the bottom of XLSSC102 and XLSSC072 images are due to X-ray point sources. We can see that XLSSC100 presents a more compact X-ray morphology than the other two, with an apparent offset between the centre of the detection and the peak of the emission, which could indicate a perturbed dynamical state. XLSSC102 presents a slightly elongated morphology, while XLSSC072 appears to be more regular.

9.3.1.2 BCG offset from X-ray centroid

The offset between the BCG and the X-ray centroid is known to be a dynamical state indicator (see e.g. Hudson et al. 2010; Zhang et al. 2017; Katayama et al. 2003). As the gas density and the BCG trace the cluster potential well, their offset should be small in relaxed clusters (see e.g. Lin and Mohr 2004). We computed the BCG-X-ray centroid offsets of our targets in units of R_{500} using the positions of the BCGs detected as explained in Chapter 5 and Ricci et al. (2018). We used the value of $0.05\times R_{500}$ to classify between relaxed and disturbed clusters. This limit was chosen in XXL Paper XV in order not to be biased by the X-ray centroid positional uncertainty due to the XMM PSF. Figure 9.3 shows the BCG-X-ray centroid offset distribution for the sample of XXL-N used in Chapter 5 and the value of the offset for our targeted clusters. We can see

that XLSSC102 and XLSSC100 are classified as perturbed clusters, while XLSSC072 appears as a relaxed cluster, according to this criterion.

By comparing our BCG sample to the one of XXL Paper XV we found that we have a different result for XLSSC100: they selected the bright galaxy that coincides with the X-ray peak. This difference is due to the slightly different selection criteria we imposed (e.g. brightest galaxy in the z' band in XXL Paper XV and in the i' band in Ricci et al. 2018) but shows that two bright galaxies are present in XLSSC100. The BCG multiplicity can be due to the presence of a sub-group and is a sign of disturbed dynamical state. As can be seen in Figure 9.3, using one or the other BCG does not change the classification of XLSSC100. Our conclusions are unchanged if we use the limiting value of $0.03\times R_{500}$ used by Lopes et al. (2018) and if we use another estimation of R_{500} ($R_{500,MT}$ instead of $R_{500,scal}$, see Section 5.2 and XXL Paper XX for details).

9.3.1.3 Optical morphology

We investigated the optical morphology of our targets by using galaxy density maps constructed as explained in Section 5.3.2.3. In order to enhance the cluster signal we only selected galaxies having apparent magnitude in the i' band fainter than the cluster BCG and brighter than m^*+1, with m^* our reference characteristic magnitude (see Conventions used in this thesis).

The 4×4 Mpc^2 density maps of our targets are shown in the right panel of Figure 9.2. We can see that the three clusters have different optical morphologies: XLSSC102 is elongated and offsetted toward the north with respect to the X-ray centroid and seems to be disturbed, XLSSC100 is compact and regular, and XLSSC102 appears to be bimodal, with the two main structures separated by $\sim 0.7Mpc$. The morphology seen in the density maps computed with Gaussian kernel is similar to that found by the WaZP cluster finder (white contours in Figure 9.2), at larger scale and using a wavelet filtering method.

9.3.2 Simulation of the expected maps

In order to test what we can expect from our observations in terms of mapping quality, we used the eight simulated clusters from the RHAPSODY-G simulation (Hahn et al. 2017), selected at $z = 1$ and having masses similar to that of our targets. We used this sample to construct mock SZ surface brightness maps at 150 GHz, applying the NIKA2 beam and bandpass (as done for NIKA in Adam et al. 2018). We then evaluated the signal to noise by assuming a noise rms corresponding to 0.10 mJy/beam. As we will see, this is appropriate given our purposes and this is what will set the requested observing time.

For illustration, the left panel of Figure 9.4 shows the dark matter density of three RHAPSODY-G clusters, selected to roughly match the optical morphology of our targets. The corresponding mock NIKA2 maps, smoothed at a resolution of $22''$ FWHM and with expected signal to noise level contours, are shown in the right panel. These three clusters have masses slightly lower than the expected values for our targets, and thus represent a lower limit on the amplitude of the signal that we expect. As can be seen in Figure 9.4, with a noise rms corresponding to 0.10 mJy/beam, it will be possible to study the gas morphology and detect sub-structures in such clusters. Another example of mock NIKA2 map, corresponding to a more massive cluster, is shown in Figure 9.5 and we can see that in this case, we expect a signal to noise reaching 12 at the peak, at a resolution of $22''$. As our targets are similar to the RHAPSODY-G clusters we expect that the proposed NIKA2 observations will allow us to detect sub-structures and to study the gas morphology within a large fraction of R_{500}. In Appendix D, we present the dark matter and the 150 GHz SZ surface brightness maps of the complete RHAPSODY-G sample.

9.3.3 Simulation of the expected profiles

In order to evaluate the feasibility of our project in terms of radial analysis, we simulated the NIKA2 SZ surface brightness profiles and the associated SNR profiles of our targets. We first used

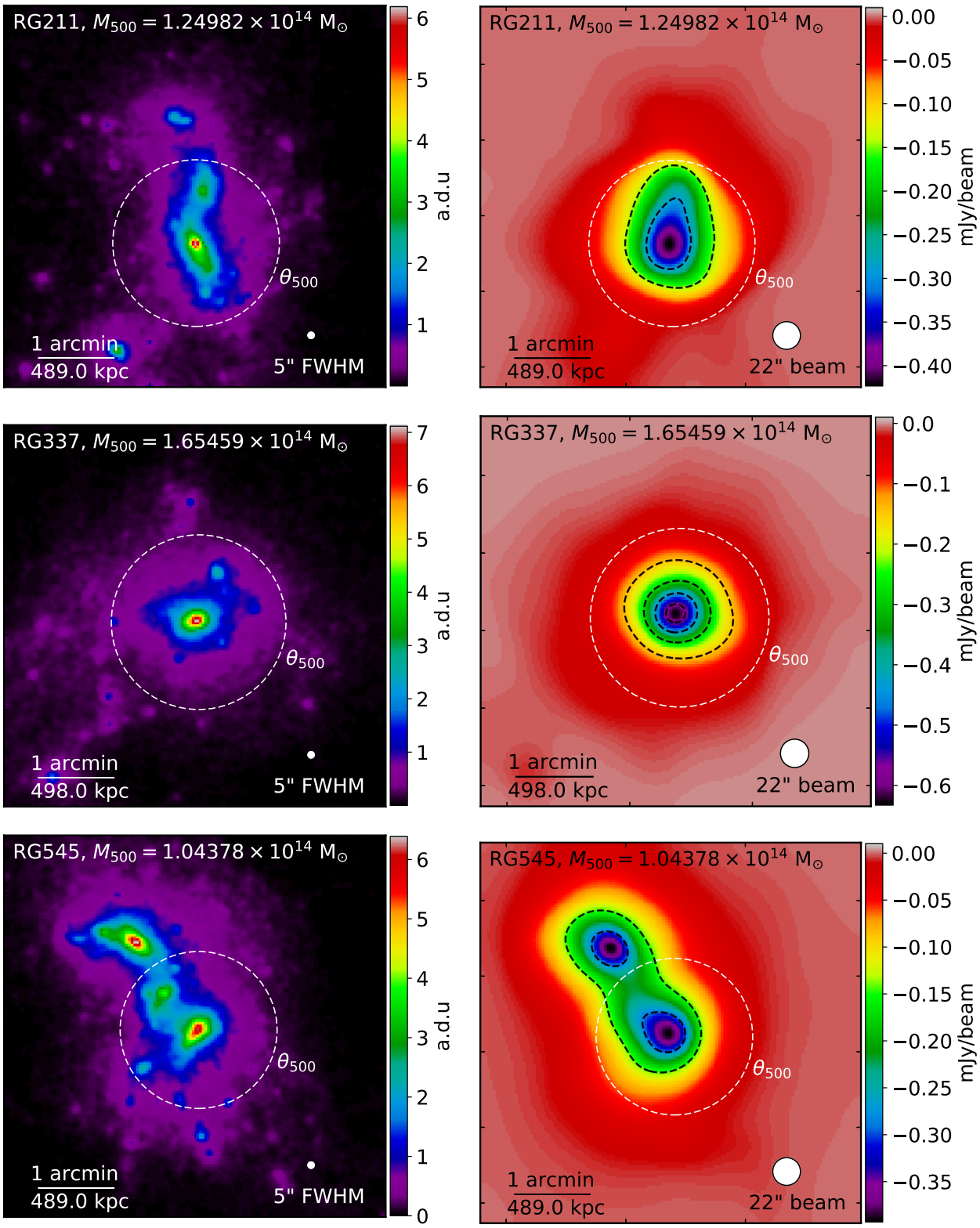

Figure 9.4: Examples of RHAPSODY-G simulated clusters. They are selected at $z = 1$ and present the same kind of morphologies as our targets, but with slightly lower masses. *Left:* dark matter particle density, smoothed at a resolution of $5''$ FWHM, for visual purpose. *Right:* SZ surface brightness images at 150 GHz, taking into account the NIKA2 beam and bandpass, smoothed at a resolution of $22''$ FWHM. The black dashed contours indicate expected signal to noise level, with 2σ steps. The dashed white circles indicates θ_{500}.

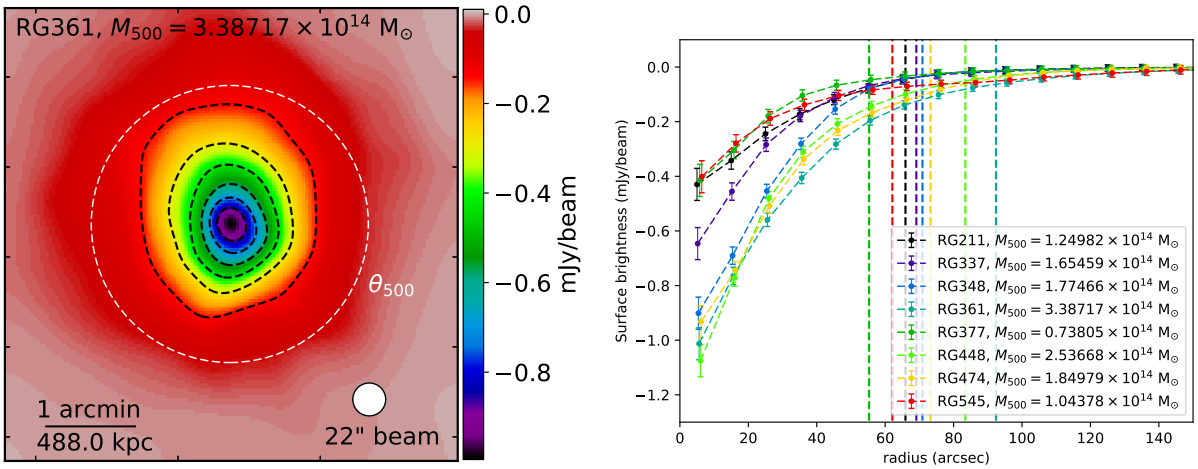

Figure 9.5: *Left:* 150 GHz SZ surface brightness image of a RHAPSODY-G simulated cluster, as in Figure 9.4, selected at $z = 1$ and with a mass similar to our targets. *Right:* SZ surface brightness profiles of eight simulated clusters selected at $z = 1$ and with a mass range ($0.7 \times 10^{14}\mathrm{M}_\odot < M_{500} < 3.5 \times 10^{14}\mathrm{M}_\odot$). The vertical lines provide the values of θ_{500}. The error bars provide the expected uncertainties given the noise rms that we assume.

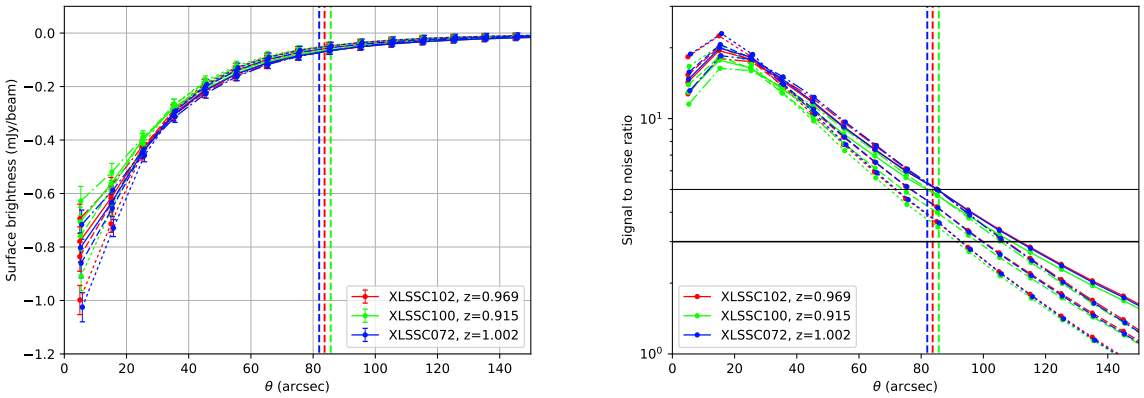

Figure 9.6: Surface brightness profile expectations at 150 GHz. For a given cluster, the different lines correspond to different pressure profile parameters (solid: Planck nearby clusters profile (Planck Collaboration et al. 2013), dashed: REXCESS Universal profile, dotted: REXCESS cool-core clusters profile, and dotted-dashed: REXCESS morphologically disturbed clusters profile (Arnaud et al. 2010). *Left panel:* Surface brightness profiles. *Right panel:* expected signal to noise ratios. The vertical dashed lines correspond to θ_{500} and the horizontal lines correspond to 3σ and 5σ thresholds.

their expected masses and redshifts to compute their expected pressure distribution, assuming a universal pressure profile (UPP, Arnaud et al. 2010) with the parameters measured on Planck nearby clusters (Planck Collaboration et al. 2013) and on REXCESS (X-ray) nearby clusters (Arnaud et al. 2010), given different dynamical states. This pressure profiles were then used to predict the 150 GHz surface brightness profiles seen by NIKA2, accounting for the angular and spectral transmission of the instrument, as well as the noise rms that we aim to reach. This was done following the procedure that will be presented in Section 12.2.

The different surface brightness and SNR profiles, obtained for each cluster using the masses $M_{500}^{\rm scal}$ and assuming a noise of 0.10 mJy/beam, are shown in Figure 9.6. The bins are 10 arcseconds wide, and could be adapted, at some loss in resolution, to improve the signal to noise. We can see that, for this set of noise rms and bin size, we are able to distinguish between the different models (e.g. morphologically disturbed or cool-core) and we reach a signal to noise value around four at R_{500}. By using lower mass estimates, we reach a minimum signal to noise value of about three at R_{500}. The surface brightness profiles corresponding to the eight RHAPSODY-G simulated clusters are shown in the right panel of Figure 9.5 for comparison. As we can see in Figure 9.5, we expect similar profiles in the case of RHAPSODY-G clusters, albeit with a large scatter, given the differences in mass among the sources.

9.4 Scientific objectives and proposed observations

9.4.1 Objectives

As we have showed in the previous sections, our observations will allow us to extract information from the clusters images, radial profiles and global properties. In the following we describe our objectives at these three levels. We will see in Chapter 12 that our preliminary results allow us to fulfil these goals in large part for one cluster.

9.4.1.1 Imaging

The SZ maps will give us a unique access to the gas morphology, thanks to the redshift independence of the SZ surface brightness and its linear sensitivity to the gas density. We will identify substructures and possible local compressions or shocks in the ICM, as in Adam et al. (2018). We will compare the gas and the galaxy distributions to study the interplay between these two matter tracers. The peak offsets between the SZ, X-ray and optical, using the density map peaks or the BCGs, will also provide complementary dynamical states indicator and help understand the assembly history of our targets.

9.4.1.2 Radial profiles

We will measure the SZ surface brightness profile and use it to extract the ICM pressure profile. This will allow us to search for deviations from standard evolution (see e.g. Adam et al. 2015). By combining the pressure obtained from NIKA2 with the X-ray density obtained from XMM, we will fully characterise the thermodynamic profiles of the clusters by extracting the temperature, entropy, gas fraction and hydrostatic masses ($\sim$20% precision expected, Adam et al. 2015).

9.4.1.3 Global properties

We will obtain the SZ flux $Y_{\rm SZ}$ from NIKA2 and compare it with its X-ray analogue $Y_{\rm X}$ known from XXL (see Section 9.2.2). We will also obtain the hydrostatic masses by integrating the profiles. These quantities will allow us to investigate the scaling relations at high redshift and relatively low mass, in terms of calibration and deviations from standard evolution. As our three targets have similar redshifts and masses, but different morphologies and dynamical state, we

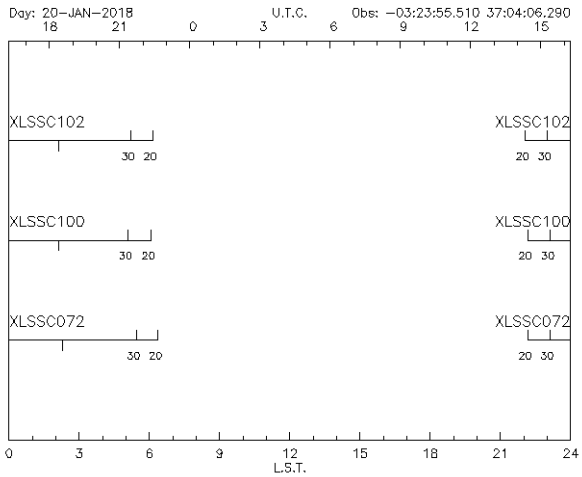

Figure 9.7: Visibility of our three targets on the 20$^{\text{th}}$ of January 2018. The bottom axis indicates the local sideral time (LST) and the upper axis indicates the universal time coordinated (UTC). Below an elevation of 20 degrees, the quality of the observations with NIKA2 is highly degraded and we considered this value as the visibility limit.

will be able to test the stability of the scaling relations with the different physical properties of the clusters.

9.4.2 Observing time estimation

For SZ observations, the NIKA2 150 GHz band is the most important and we focused on this channel to estimate the observing time needed. Based on figure 9.4 and 9.6 we can see that we need a detection greater than 2σ within one arc-minute diameter in 2D and out to two arc-minutes radius in 1D to fulfil our goals. As we showed, this can be achieved with a noise rms of 0.10 mJy/beam.

Assuming average winter condition with 4 mm of precipitable water vapour, a mean elevation of 40 degrees and using the IRAM time estimator[3] with the NIKA2 instrument performances (NIKA2 Collaboration et al. 2018), we estimated that we need a total time of 12h per cluster to reach the desired noise rms.

In summary, we need 36 hours in total in order to fulfil the goals of our project. As shown in Figure 9.7, our sources are visible six hours per day in average and our project will thus require six days of observations.

9.5 Conclusions

This Chapter treats about the preparation of the observational follow-up of three XXL clusters in SZ with the NIKA2 camera, project of which I am principal investigator. We first presented our motivations and we then described how we selected our targets. We used optical and X-ray data to investigate the morphologies and dynamical states of our selected clusters and find that they are diverse. We used the RHAPSODY-G cosmological hydrodynamical cluster simulations, with masses and redshifts similar to our targets, to predict the expected signal to noise ratio of our SZ surface brightness maps. We also simulated surface brightness profile using different models of pressure profiles. Finally, we used our findings to estimate the observing time needed to fulfil our goals.

[3] http://www.iram.es/IRAMES/mainWiki/Continuum/TimeEstimatorScript_winter

Chapter 10

Observing with NIKA2 at the IRAM 30 meter telescope

Contents

Abstract: The NIKA2 observing proposal detailed in Chapter 9 was accepted and rated "A" by the IRAM programme committee. Due to a revision of the NIKA2 reference sensitivity by IRAM, we have been allocated 81 hours of observing time instead of the 36 hours requested. Three observing pools were scheduled in January, February and March 2018 and I participated to the last one. Due to bad weather conditions and competition at the telescope, we only obtained 10 hours of observations so far, which we spend on XLSSC102. The observations are re-scheduled for October 2018. In this chapter we present the IRAM 30 meter telescope and the NIKA2 instrument. We describe our observation strategy and the course of a typical observing session. Finally, we introduce the data reduction process and present the resulting maps and associated products.

10.1 Presentation of the instrument

10.1.1 The IRAM 30 meter telescope

The IRAM 30 metre telescope (Baars et al. 1987) is a classic single dish parabolic antenna (see Figure 10.1) located at an altitude of 2850m on Pico Veleta, in the Spanish Sierra Nevada (at 45km of Granada). It is composed of a 30m paraboloidal main mirror and a 2m secondary mirror placed on an azimuthal mounting and is one of the most sensitive (sub-)millimetre telescope in the world. The receptor instruments are placed at the focus, in the Nasmyth cabin,

Figure 10.1: View of the IRAM 30m telescope on Pico Veleta in the Spanish Sierra Nevada. Credits: http://www.iram.es.

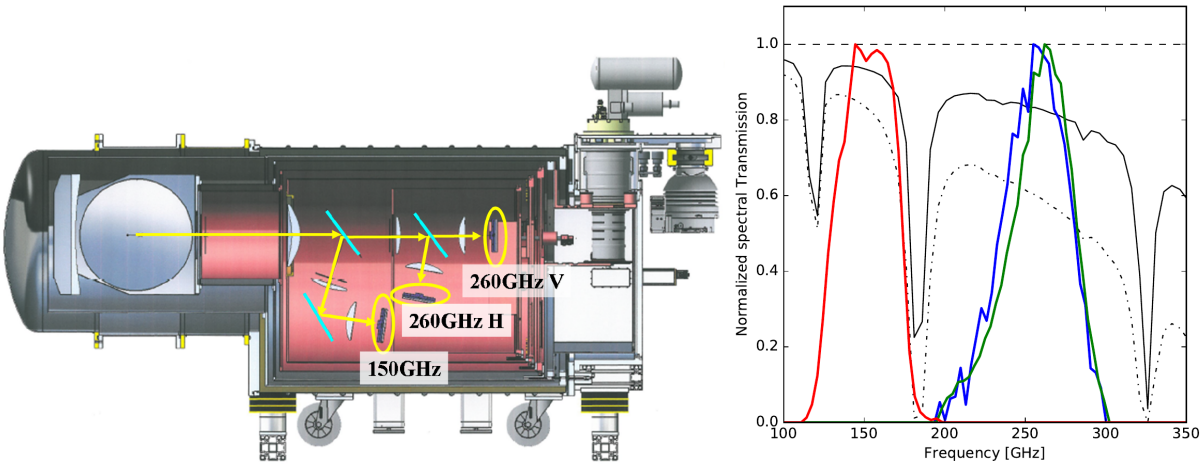

Figure 10.2: *Left:* scheme of the NIKA2 instrument. The optical path and the positions of the three detector matrices are indicated in yellow. *Right:* NIKA2 bandpass. The red, blue and green curves are for the A2, A1 (H) and A3 (V) matrix respectively. The black lines show the atmospheric transmissions for very good conditions (solid) and average conditions (dash-dotted). Images taken from NIKA2 Collaboration et al. (2018).

and are composed, to date, of two heterodyne receivers: EMIR (Carter et al. 2012) and HERA (Schuster et al. 2004); and one continuum camera, NIKA2.

10.1.2 The NIKA2 camera

The NIKA2[1] (New IRAM KID Array 2, NIKA2 Collaboration et al. 2018) camera is a broad-band continuum photometric instrument operating at millimetre wavelengths. It was installed at the 30m telescope in 2015, replacing its pathfinder, the NIKA camera (Monfardini et al.

[1] http://ipag.osug.fr/nika2/Welcome.html

2011; Catalano et al. 2014). NIKA2 is a dual-band camera, which allows us to observe the sky simultaneously at 150 and 260 GHz and to measure the linear polarisation at 260 GHz, when operated in a polarimetric mode. In the following, we present an overview of the NIKA2 main components.

10.1.2.1 The cryostat

The NIKA2 detectors are contained in a cryostat of about 2.3 meters for a mass of 1.3 tons. It is composed of four cryogenic stages, the last one reaching a minimal temperature of around 150 mK and containing the focal plane arrays and the last portion of the optics. A scheme of the cryostat is shown in the left part of Figure 10.2.

10.1.2.2 Optical path

The optical path from the telescope optics to the detector matrices is composed of several mirrors, lenses and filters. The light beam is split between the 150 and 260 GHz channels by a dichroic. Further away, a grid polariser is splitting the 260 GHz beam into two linear polarisations. Finally, the signal reaches the three detector matrices: A1 and A3 at 260 GHz, which allow us to measure the polarisation, and A2 at 150 GHz. A schematic view of the optical path in the cryostat is shown in the left part of Figure 10.2. The NIKA2 band transmissions are defined by the different elements of the optical path and are shown in the right panel of Figure 10.2.

10.1.2.3 The KIDs detectors

NIKA2 uses kinetic inductance detectors (KIDs, Day et al. 2003), which are supra-conducting RLC resonators, each having its proper resonance frequency. The 150 GHz matrix (A2) is composed of 616 KIDs detectors of 2.8 mm^2, while the two 260 GHz arrays (A1 and A3) contain 1140 KIDs of 2 mm^2 each, providing a field of view of 6.5 arc-minutes diameter.

The operating principle of the KIDs is that incident photons, with an energy above a given threshold, induce a shift in the resonance frequency of the detectors, by an amount δf_0 that is proportional to the absorbed optical power. Dedicated electronics are used to read the resonance frequencies of each detector (up to 400 KIDs can be sampled simultaneously by each readout boards, Bourrion et al. 2016). However, the shift in resonance frequency for each KID is not measured directly and it has to be reconstructed from the outputs of the electronics (see Calvo et al. 2013, and section 10.2.3.1 for more details).

10.2 Observations at the telescope

10.2.1 Definition of the scanning strategy

In practice, NIKA2 is designed to be sensitive to the time variation of the signal rather than the source absolute emission. Therefore, in order to measure an astrophysical signal with NIKA2 we have to modulate it in time. The solution is to integrate while spatially scanning the astrophysical source, in a way that maximises the changes of optical power seen by each KID. Another reason for this spatial modulation is that, as all the detectors do not observe the same astrophysical signal at the same moment, the part of the signal that is identical for all detectors is coming from the atmosphere and can thus be identified and subtracted. Also, because the signal at low time frequencies is more affected by the slowly varying atmospheric noise, it is better to modulate the source with high frequency to differentiate it from the atmosphere (Adam 2015). This means that the scanning direction should be perpendicular to the source elongation axis, if any. Thereby, the scanning strategy depends on the type of source we want to observe. Before

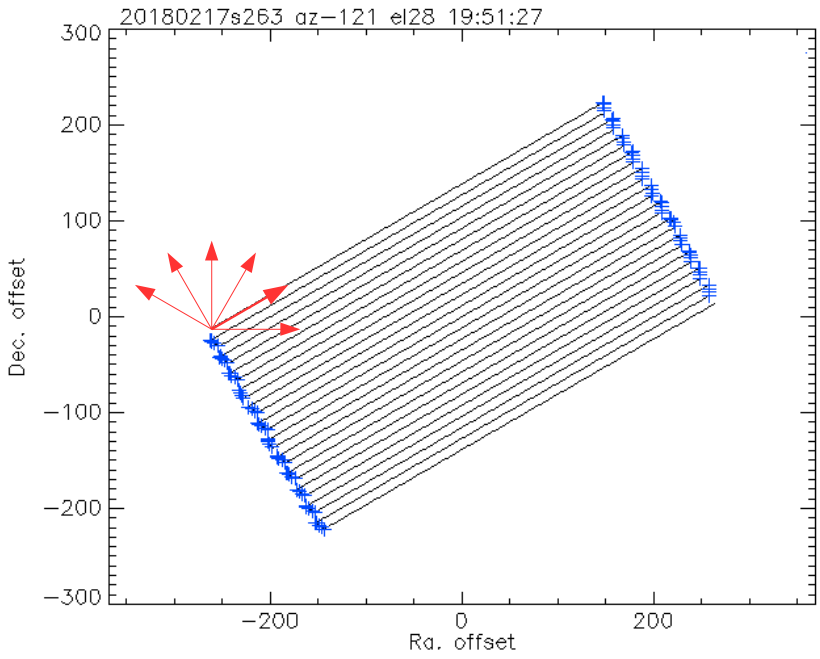

Figure 10.3: Illustration of our scanning strategy: position on the sky seen by the centre of the detector matrix during one scan, expressed in RA and Dec offsets with respect to our target centre, in arc seconds. The size of each scan is 8×4 arc-minutes. The red arrows indicate the six orientations we chose for our scans. As an example, the scan shown is orientated with a 30 degree angle with respect to the right ascension axis. This figure was produce using the NIKA2 reduction pipeline.

the beginning of the observing run one must define the scanning strategy to observe its target and write the corresponding scripts to be integrated by the telescope.

Our choice of scanning strategy is illustrated in Figure 10.3. We chose to use the "On The Fly "(OTF) type of scanning procedure, which consists in a series of parallel sub-scans forming straight lines on the sky, and we took the RA-Dec coordinate system as reference[2]. As our targets are a priori azimuthally symmetric, at first order, we chose to use rectangular scans, orientated along six different directions, to avoid residual stripping patterns in the maps (see Section 10.3.2). The scanning speed was chosen in order to maximise the signal modulating frequency, while avoiding to have too much acceleration variation between each sub-scan, since they lead to the loss of data. The compromise was found for a scanning speed of 40 arcsec.s^{-1}, which results in five minutes duration scans. We verified that the scan duration was long enough to minimise the number of overheads between each scan and small enough so that the KIDs resonances are unlikely to be lost by the acquisition during a scan (see Section 10.2.3.1 for further details). In order to reach our requested observing time per source (27 hours), and accounting for the 50% calibration overhead, the series of six scans should be repeated 36 times.

10.2.2 Observing weather conditions

The quality of millimetre observations strongly depends on the weather conditions, in particular the humidity and the wind velocity. The atmosphere absorbs a fraction of the signal, but also generate thermal emission, which induces noise fluctuations, mainly due to turbulences of the water vapour. The amount of atmosphere is quantified by the opacity, τ, which should be as low as possible (the maximal opacity to observe faint sources under correct conditions is $\tau \sim 0.3$

[2]Scans can also be defined in other coordinate systems, such as in Azimuth-Elevation.

at 225 GHz). The good stability of the atmosphere is essential in order to better subtract the atmosphere contribution from the data. Usually, the observing conditions are best at night, because of better stability, and during winter, because of lower temperatures and less humidity. Finally, other problems related to the weather conditions can affect the telescope and forbid the observations, such as the presence of ice on the primary mirror structure. See Adam (2015) for further details concerning the impact of atmospheric conditions on the observations.

10.2.3 Presentation of a typical observation session

In the following, we briefly introduce the different procedures related to the camera and the telescope that need to be achieved during an observation session before observing the astrophysical source of interest.

10.2.3.1 Calibration procedures related to the camera

Frequency scan As we discussed in Section 10.1, the primary signal from NIKA2 is related to the KIDs resonating frequencies. In a first step, the resonating frequencies are measured by injecting and modulating an exciting frequency on each transmission line (Bourrion et al. 2016). This 'frequency scan" procedure last for a couple of minutes. As the atmosphere variations can be responsible of significant frequency drifts, and thus the loss of some resonances, the procedure is repeated about one time per day or more, depending on the weather conditions.

Once this procedure is done, the approximate positions of the resonating frequencies $(f_0)_k$ and the corresponding excitation frequencies are known and can be measured more precisely using a frequency comb. This "frequency tuning" procedure last $\sim$ 2s and is repeated before each scan (Catalano et al. 2014; NIKA2 Collaboration et al. 2018). During the on source integration, the resonating frequency shifts are measured with respect to the $(f_0)_k$ values evaluated by the tuning procedure (Calvo et al. 2013).

Skydip Because of the atmospheric absorption, the amplitude of the astrophysical signal is reduced by a factor $\exp\left(-\tau/\sin(\delta)\right)$, where τ is the zenith opacity and δ the source declination. Therefore, in order to correct the data from this attenuation, we need to precisely measure the opacity for each scan. As the position of the KIDs resonating frequencies depend on the opacity, via the optical load induced by the atmosphere, they can be used to internally derive its value, once the exact relation between the two quantities is calibrated. The relation is measured by performing resonating frequencies tuning at different elevations, and thus different optical load (Catalano et al. 2014). This "skydip" procedure is repeated several time during each observing run. It has to be carried out on stable weather conditions in order to neglect the weather induced opacity variations while it is being done.

Beam map The absolute calibration of each detector is done by observing a bright source of known flux, usually Uranus (NIKA2 Collaboration et al. 2018). This kind of observation is called "beam map" and allows us: 1) to attribute to each resonating frequency the position of the corresponding KID in the focal plane; 2) to characterise the beam for each detector and measure the effective beam; 3) to determine the calibration between each KID resonance frequencies and the absorbed flux. This procedure lasts for about half an hour and is repeated once per day. A high number of beam maps allow us to test the stability of the calibration (see Section 10.3).

10.2.3.2 Procedures linked to the telescope

We present here the procedures to adjust the telescope pointing and focus. They are usually done every two hours and repeated iteratively until convergence. Further details about these

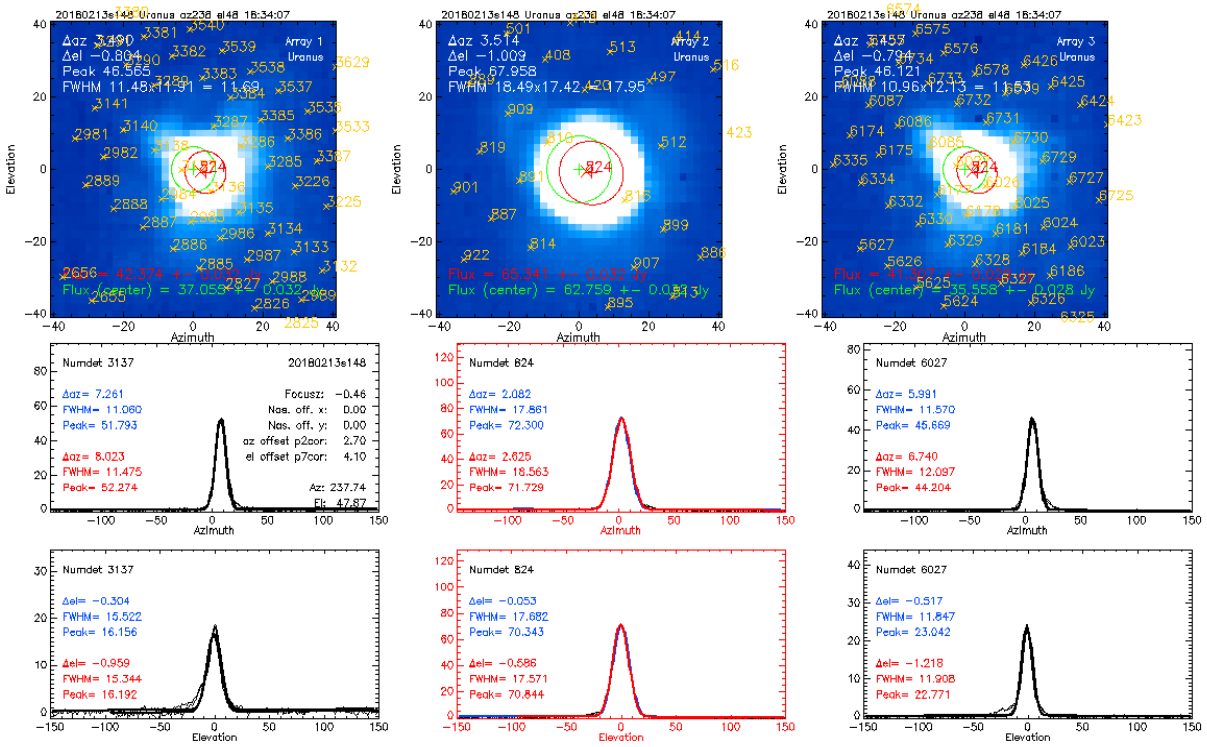

Figure 10.4: Pointing adjustment procedure using Uranus observations. The different columns are for the three matrices. The top row shows the reconstructed maps of Uranus. The yellow crosses and numbers indicate the centre of the detectors that are seeing the source. The centres of the green circles show the expected source position, while the centres of the red ones show the measured source position. The differences between the two positions inform on the pointing correction that is needed. The two bottom rows show the flux variation seen by the reference detector while scanning as a function of the azimuth (middle row) and elevation (bottom row). The flux evolution as a function of azimuth and elevation are then fitted by Gaussian functions, whose centres indicate the pointing correction to apply to the telescope. This figure has been produced using the NIKA2 reduction pipeline.

procedures can be found in (Adam 2015).

Pointing adjustment The telescope uses a pointing model based on the positions of known quasars. However, the pointing needs to be regularly verified and potentially corrected because of the small variations that can be induced by mechanical stress on the telescope. The usual pointing adjustment procedure is made by rapidly scanning a bright known source in azimuth and elevation (with a cross shape). The reconstructed source maps and the flux variation seen by the reference detectors during a sub-scan are then used to infer the pointing correction to apply (see Figure 10.4).

Focus adjustment Because of the tiny mirror deformations induced by temperature variations, the secondary mirror position needs to be re-adjusted so that the KIDs matrices positions remain in the telescope focal plane. This focus correction procedure is made by taking five images of a bright source, while varying the position of the secondary mirror of the telescope on the optical path. The source flux and FWHM are then measured for each image and KID matrix. For each matrix, the evolution of the measured flux (respectively FWHM) with the focus offset is fitted by a parabola, whose maximum (respectively minimum) indicates the optimal focus correction to apply (see Figure 10.5, for an example). Due to the differences in optical paths,

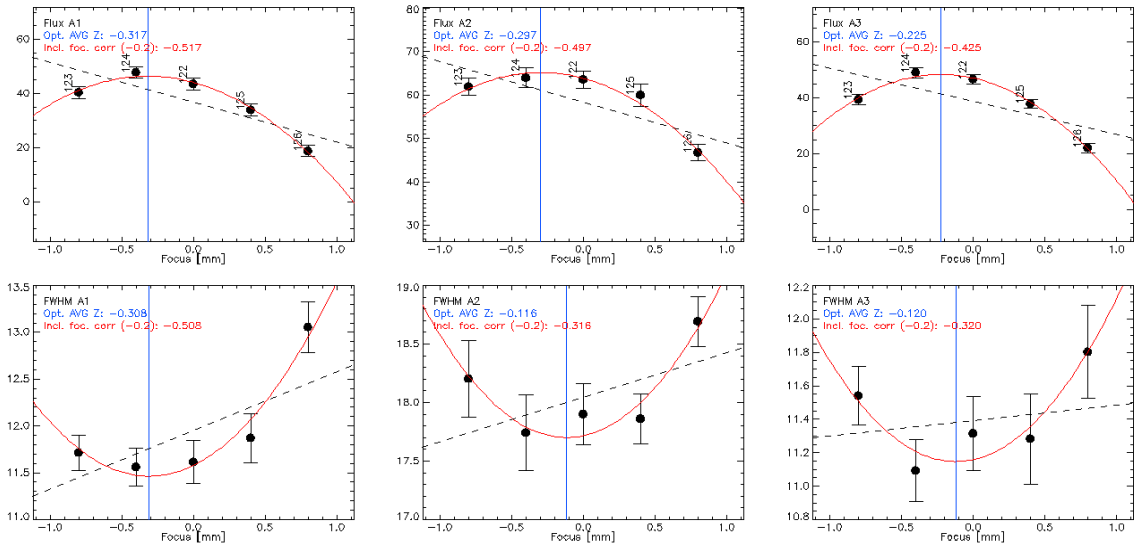

Figure 10.5: Focus adjustment procedure. The top/bottom row shows the source flux/FWHM for different focus values. The different columns correspond to the three matrices, respectively A1, A2 and A3. This figure has been produced using the NIKA2 reduction software.

the optimal focus can be slightly different for each matrix. However, this effect is negligible for NIKA2.

10.2.3.3 On source integration

After all the procedures described above are completed, the integration on the source can start. Time ordered data (TOD) containing the pointing information and the signal from the KIDs readout electronics, as a function of time, are then recorded individually for each scan. The sampling frequency is set to 23.8418 Hz and thus each sample corresponds to an integration time of $\sim$ 0.04 s. Depending on the weather stability and the scanning duration, the observations can be interspersed by pointing and focus adjustment procedures to ensure the obtention of well calibrated data.

10.3 Off-line data reduction

In this section we present the data reduction procedure used to convert the TODs into astrophysical maps. We first present the calibration that we applied and then the different steps needed to produce the final maps.

10.3.1 Absolute calibration

10.3.1.1 Description of the different calibration steps

Focal plane reconstruction The first step of the calibration is the determination of the KID position in the focal plane and their attribution to each resonating frequency. This is done by the NIKA2 collaboration using the beam map procedure, as explained in 10.2.3.1.

The opacity The opacity is measured thanks to the Skydip procedure, explained in 10.2.3.1. The attenuation correction factor, $\exp(\tau/\sin(\delta))$, is then applied to the TOD for each scan and each detector. This is done automatically in the NIKA2 reduction pipeline.

Table 10.1: Summary of the main characteristics of the NIKA2 instrument. The plain values are taken from NIKA2 Collaboration et al. (2018) and give the reference NIKA2 performances. The bold values correspond to the calibration that we measured on Uranus scans and thus reflect the effective performances at the time of our observations. Note that the model absolute calibration uncertainty is estimated to be 5%.

Channel	260 GHz (1.15mm)			150 GHz (2.0mm)
Arrays	A1	A3	A1&3	A2
FoV diameter (arcmin)	6.5	6.5	6.5	6.5
FWHM (arcsec)	11.3 ± 0.2	11.2 ± 0.2	11.2 ± 0.1	17.7 ± 0.1
	12.1±0.4	**12.0±0.6**		**18.0±0.3**
rms calibration error (%)	4.5	6.6		5
	7	**8**		**4**
σ pointing error			<3	
	2.2	**2.2**		**2.3**

The flux The conversion of the TOD KID resonance frequencies into flux is computed by the NIKA2 collaboration, using the beam map. The flux of Uranus is known with 5% uncertainty, given the brightness model used by the NIKA2 collaboration[3].

The effective beam The beam maps also allow us to estimate the effective beam patterns. As shown in Figure 10.6, the total NIKA2 beam present complex structures that extends further than the main beam 2D Gaussian approximation. The beam efficiency, computed as the ratio of the main beam power and the beam power integrated up to a radius of 250 arc-seconds is of the order of 60% at 260 GHz and 75% at 150 GHz (see NIKA2 Collaboration et al. 2018). The exact shape of the beam is used to convert the surface brightness of extended sources expressed in Jansky per beam into physical units (e.g. Jansky per steradians, or unit of Compton parameter).

The bandpass The spectral characterisation of the NIKA2 bandpass has been achieved in laboratory (see NIKA2 Collaboration et al. 2018). As the flux calibration is made using Uranus observations, it has to be corrected from the differences between the source SED and Uranus SED. For point sources this lead to colour correction coefficients (see Section 11.2.2.3). For SZ sources, the calibration between surface brightness and Compton parameter is done by integrating the SZ spectra on the NIKA2 bandpass and taking into account the effective beam. In our analysis we obtain -10.7 Jy per beam, per unit of Compton parameter, using the tools developed in the NIKA2 collaboration (Adam 2015).

10.3.1.2 Measurement of the absolute calibration and the effective beam

At the time of our analysis, the calibration file corresponding to the February 2018 observing run (when most of our data were collected) was not ready. We therefore chose to use an anterior version of the calibration. We verified its quality of the calibration, under the observing conditions of the February run, using Uranus scans taken around the same time as our target cluster, and thus reflecting the effective performances at that time. For each scan we measured the source flux and the size of the beam for each matrix, as shown in Figure 10.7. In these conditions, the performance that we measure are slightly degraded, but still close to expectations when using an up to date calibration (NIKA2 Collaboration et al. 2018). We estimated the error on the calibration to be less than 10% and the pointing offset less than 3%, as presented in

[3]Moreno, R., 2010, Neptune and Uranus planetary brightness temperature tabulation. Tech. rep., ESA Herschel Science Center, https://www.cosmos.esa.int/web/herschel/calibrator-models

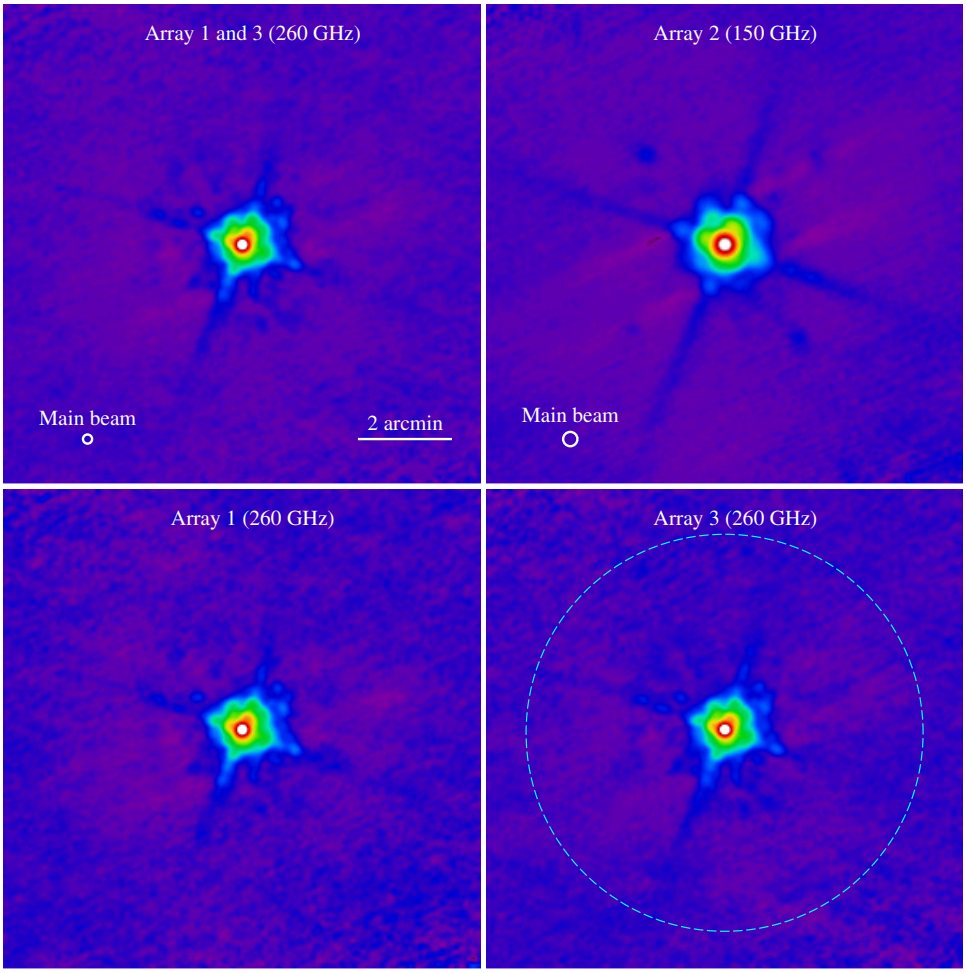

Figure 10.6: Measured beam patterns. The $10' \times 10'$ beam map is shown for the combined A1 and A3 matrices and each individual matrix, as indicated in the legend. The small white circles indicate the main beam for the two bands, which correspond to the central Gaussian approximation of the effective beam. The cyan dotted circle indicates the $250''$ radius used to compute the beam efficiency. The colour scale is in logarithmic units, showing the beam patterns with amplitudes down to $\sim 10^{-3}$ at 260 GHz and $\sim 10^{-4}$ at 150 GHz, with respect to the main beam normalisation.

Table 10.1. We also measured the effective beam for each matrix, as shown in Figure 10.6. We found that given our preliminary calibration, the effective FWHMs were slightly larger than the reference values (see Table 10.1) and we used our measured values in the rest of our analysis.

10.3.2 Map-making procedure

10.3.2.1 Reduction pipeline per scan

Here we briefly present the main steps needed to process the TOD corresponding to each scan (see Adam et al. 2014; Catalano et al. 2014; Adam et al. 2015, for details). Firstly, the TOD, the telescope information and the calibration files are loaded; secondly, the conversion between the KIDs resonance frequency and flux, including the opacity correction, is applied; thirdly, invalids detectors and cosmic rays impacts are detected and flagged; then, the atmospheric and the electronic noises are decorrelated and the low frequency noise residuals may be subtracted using low order polynomial fitting; finally, the reduced TOD are projected onto pixelated maps.

The reduction procedure can be tuned depending on the astrophysical signal we want to

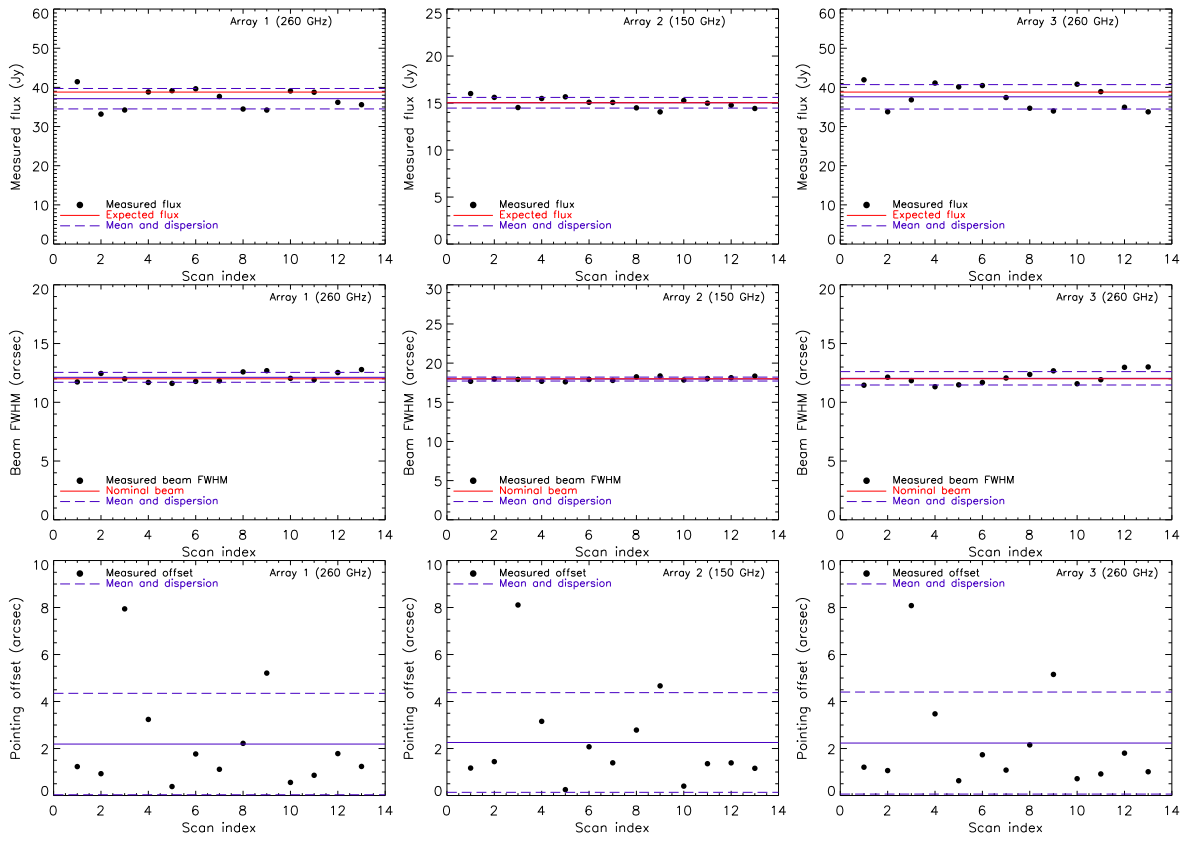

Figure 10.7: Measurement of the calibration stability using different scans of Uranus. *Top:* flux calibration. *Middle:* beam FWHM. *Bottom:* pointing offset. The scans are ordered in time and are taken around the same time as our astrophysical observations. The three columns are for the matrices A1, A2 and A3. The black points show the measurements, the blue lines show the mean values and the standard deviations, and the red lines show the fiducial values. In all cases the statistical errors are negligible with respect to the systematic ones. The corresponding values are given in Table 10.1.

probe. For instance, for bright sources and/or extended emission, a mask can be applied in the region were the signal is dominant, in order to minimise filtering effects on the signal happening during the decorrelation process (Adam et al. 2015). Also, the choice of subtracting or not low frequency noise residuals is determined by the shape of the source, since this procedure can alter extended emission. The resulting signal to noise depends on the target signal and the reduction method, and the tuning of the reduction parameters consists in finding the best compromise between the removal of the correlated noise, and the filtering of astrophysical signal on large scales.

For each scan we obtain the corresponding surface brightness map, constructed as the weighted mean of the TOD samples falling in each map pixel, and a number of hit map giving the number of samples falling in each pixel. The weights are given by the inverse variance of the detectors timelines.

10.3.2.2 Flagging of low quality scans

Some scans might have been undertaken under bad weather conditions or at low elevation and present too high level of noise, or excessive residual noise correlated structures. Including those scans in the final maps may increase the noise and therefore, the quality of each scan has to be evaluated so that they can be excluded from our analysis. To do so, we used a combination of empirical and automatic criteria. Firstly, 150 and 260 GHz surface brightness maps were

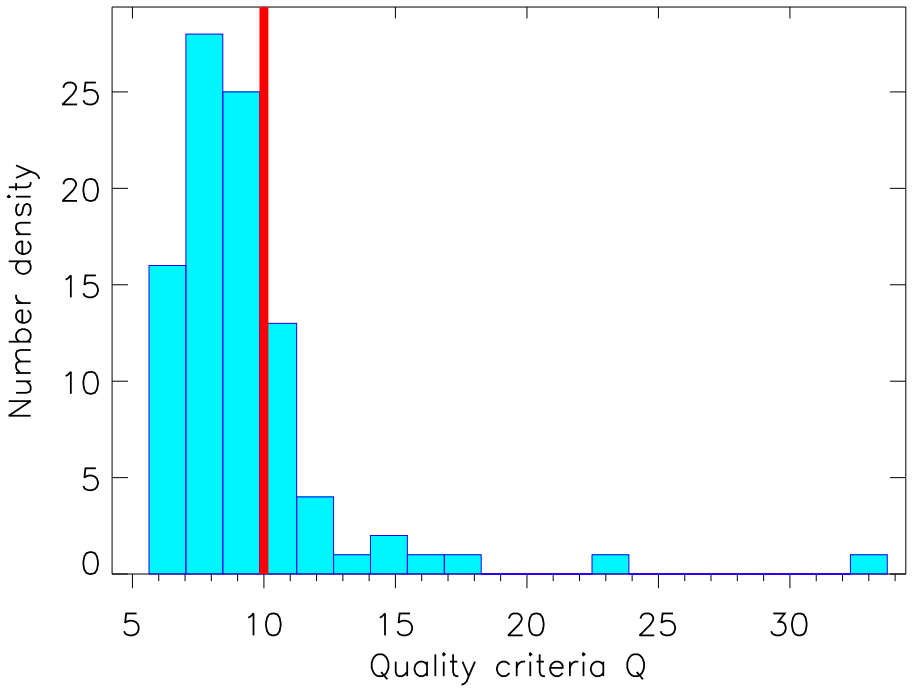

Figure 10.8: Histogram of the quality parameter Q measured in the scans of the 150 GHz band. The red line shows the arbitrary limit we imposed for the rejection.

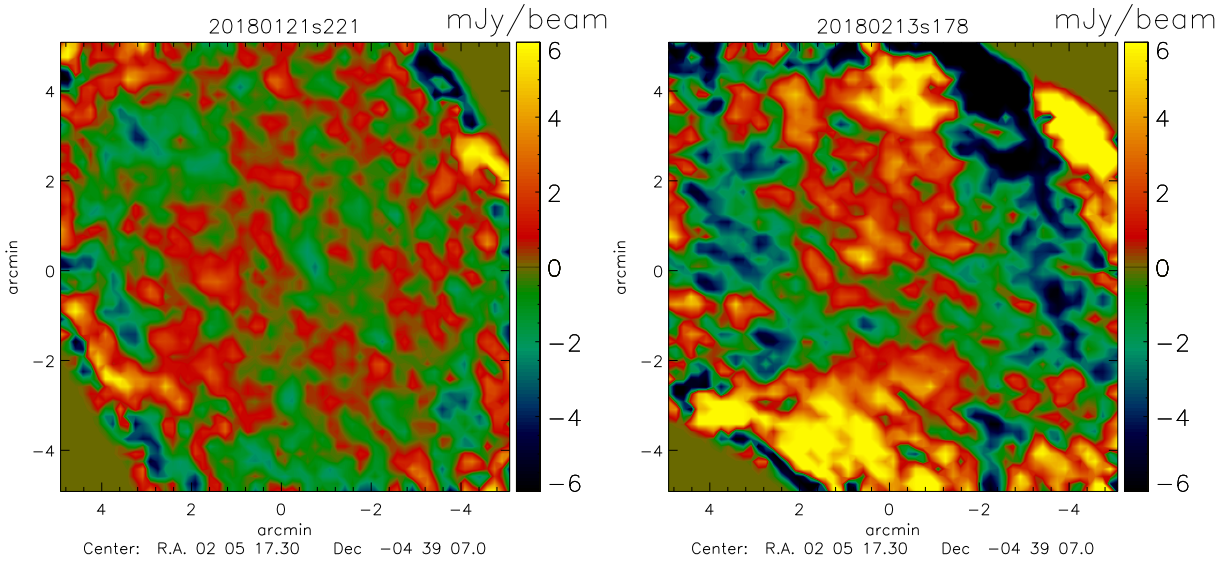

Figure 10.9: Example of a "good" scan (left) and a "bad" scan (right) in the 150 GHz (2 mm) band. The present "bad" scan was taken with an elevation < 20 deg. All the "bad" scans were rejected from the final combined maps.

created by co-adding all the scans (see Section 10.3.2.3). We then defined a quality parameter $Q_{\rm scan}$ for each scan, as the ratio between the standard deviation of the co-added scan map $M_{\rm co-added}$, and the standard deviation of the individual scan maps $M_{\rm scan}$:

$$Q_{\rm scan} \equiv \frac{\sigma\left(M_{\rm scan}\right)}{\sigma\left(M_{\rm co-added}\right)} = \sqrt{\frac{< M_{\rm scan}^2 > - < M_{\rm scan} >^2}{< M_{\rm co-added}^2 > - < M_{\rm co-added} >^2}}, \tag{10.1}$$

where "scan" is the scan index. Given this definition, we flag all the scans verifying $Q_{\rm scan} > 10$ as they correspond to outliers in the distribution of quality criteria, as can be seen in Figure 10.8. Independently, we visually inspected each scan and we flagged the ones presenting obvious artefacts. Finally, we rejected the scans that did not pass the two criteria. Examples of "good" and "bad" scans are shown in Figure 10.9. We can see that the noise is quite homogeneous in the "good" scan whereas is its higher and presents correlated structures in the "bad" one.

10.3.2.3 Maps combination

We combined the surface brightness maps $M_{\rm scan}$ from the different scans, at each pixel coordinate (x, y), by applying a weighted mean:

$$M_{\rm tot}(x,y) = \frac{\sum_{\rm scan} W_{\rm scan}(x,y) M_{\rm scan}(x,y)}{\sum_{\rm scan} W_{\rm scan}(x,y)}, \tag{10.2}$$

with the weights $W_{\rm scan}(x, y)$ constructed for each scan as its number of hit map $N_{\rm scan}^{\rm hit}(x, y)$ divided by the variance of its homogenised surface brightness map, once the source is masked:

$$W_{\rm scan}(x,y) = \frac{N_{\rm scan}^{\rm hit}(x,y)}{V_{\rm Off-source}\left[M_{\rm scan}(x,y)\sqrt{N_{\rm scan}^{\rm hit}(x,y)}\right]}. \tag{10.3}$$

Considering only off-source pixels allows us not to bias high the variance of each scan map in the presence of strong emission, and the noise normalisation by the number of hit allows us to account for noise inhomogeneity. We defined the noise rms map associated to $M_{\rm tot}(x, y)$ as:

$$\mathrm{rms}_{\rm tot}(x,y) = \sqrt{\frac{1}{\sum_{\rm scan} W_{\rm scan}(x,y)}}. \tag{10.4}$$

Finally, the total number of hit is the sum of the number of hit per scan, in each map pixel:

$$N_{\rm tot}^{\rm hit}(x,y) = \sum_{\rm scan} N_{\rm scan}^{\rm hit}(x,y). \tag{10.5}$$

For each matrix we thus obtain three types of maps, as shown in Figure 10.10. We can remark that the number of hits per pixel decreases strongly in the outskirts of the map leading to an increase of the noise. We chose to construct maps with a size of 10×10 arc-minutes, as going further will not be useful because of the noise increases toward the edges. The maps contain 301×301 pixels, with a size of 2 arc-second per pixel.

In order to test our source detection and analysis algorithms we also constructed noise realisation maps, by using a jackknife resampling method. We thus defined the noise surface brightness map $JK_{\rm tot}(x, y)$ and the associated rms map, $\mathrm{rms}_{JK_{\rm tot}}(x, y)$, by multiplying half of the scans by -1 and following equations 10.2 and 10.4.

10.3.2.4 Additional products

In addition to the output maps, several data products are necessary to make a proper use of the data when extracting astrophysical information (see Chapters 11 and 12). The angular and

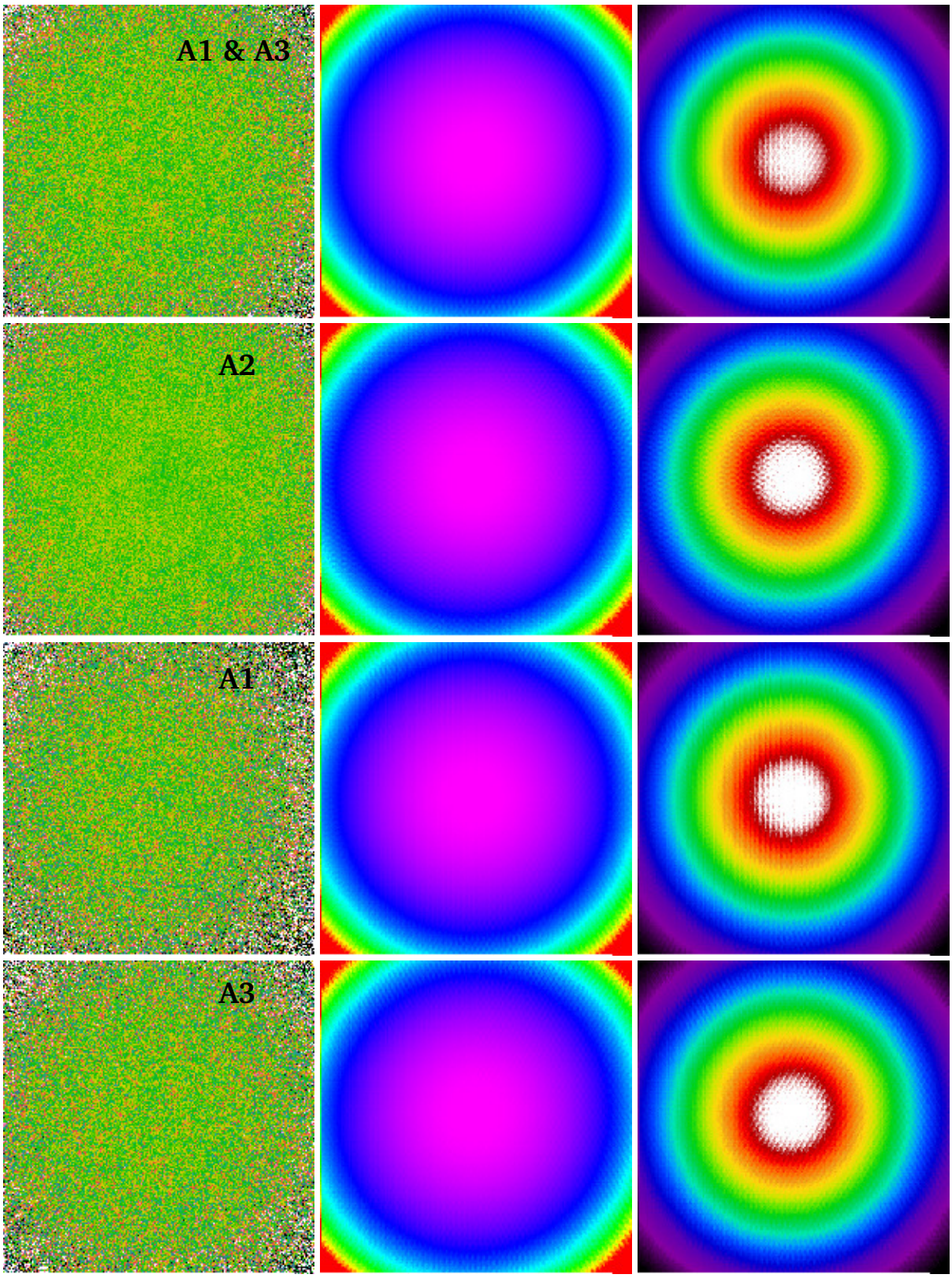

Figure 10.10: Maps resulting from the data reduction of XLSSC102 observations. The first column contains the surface brightness maps in Jy/beam. The second column contains the maps of the rms per pixel and the last column contains the maps of the number of hit per pixel. The first line is for the combined 1mm matrices, the second is for the 2mm matrix (A2), the third and fourth are for the two 1mm matrices (A1 and A3). The same colour-bar is used for the three 1mm surface brightness maps.

spectral responses of the observations are already available via the beam pattern (see Figure 10.6) and the spectral transmissions have been measured in the laboratory (see Figure 10.2). However, the filtering induced by the data processing and the noise statistical properties have to be estimated a posteriori. Indeed, they depend on the observing conditions and the scientific goals via the set of parameter used when reducing the raw data.

Transfer function The data reduction transfer function is computed using the tools developed in the NIKA2 collaboration, as described in Adam et al. (2015). In brief, a known simulated input signal is injected in the NIKA2 raw data, which are then processed trough the reduction pipeline. The same processing is applied on the raw data without adding any extra signal. Then, the difference between the two output maps is used to provide a noise-free estimate of the filtered signal. Finally, the transfer function is computed as a function of angular scale by taking the ratio of the Fourier transforms of the filtered signal and that of the original input signal. This transfer function is used in the following chapters to account for the filtering in our data.

Noise covariance matrix The noise covariance matrix encodes the amount of residual noise correlations. It is computed using the tools developed in the NIKA2 collaboration, as described in Adam et al. (2016). In brief, the jackknife maps are used to estimate the power spectrum of the noise. The latter is used to generate noise Monte Carlo simulations that contain the same correlation properties as the data. These noise realisations n_i are then used to compute the covariance matrix as $C = \frac{1}{N_{\rm MC}} \sum_{i=1}^{N_{\rm MC}} n_i n_i^T$.

10.4 Conclusions and final products

In this chapter, we presented the IRAM 30 metre telescope and the NIKA2 camera, the course of a typical observing session, and the data reduction process. It is important to understand these steps in order to correctly analyse and interpret the data. The main final products of the data reduction are surface brightness and associated rms maps expressed in Jansky per beam, in the 150 and 260 GHz bands. We adapted the data reduction process to construct two types of maps: one dedicated to point sources analysis and the other one dedicated to the extended cluster emission. These four maps are shown in Figure 10.11 for the cluster XLSSC102. We can remark the presence of point sources with positive emission in the two bands and negative signal coming from the SZ effect from the cluster in the 150 GHz band. These two types of signal will be studied in Chapters 11 and 12, respectively.

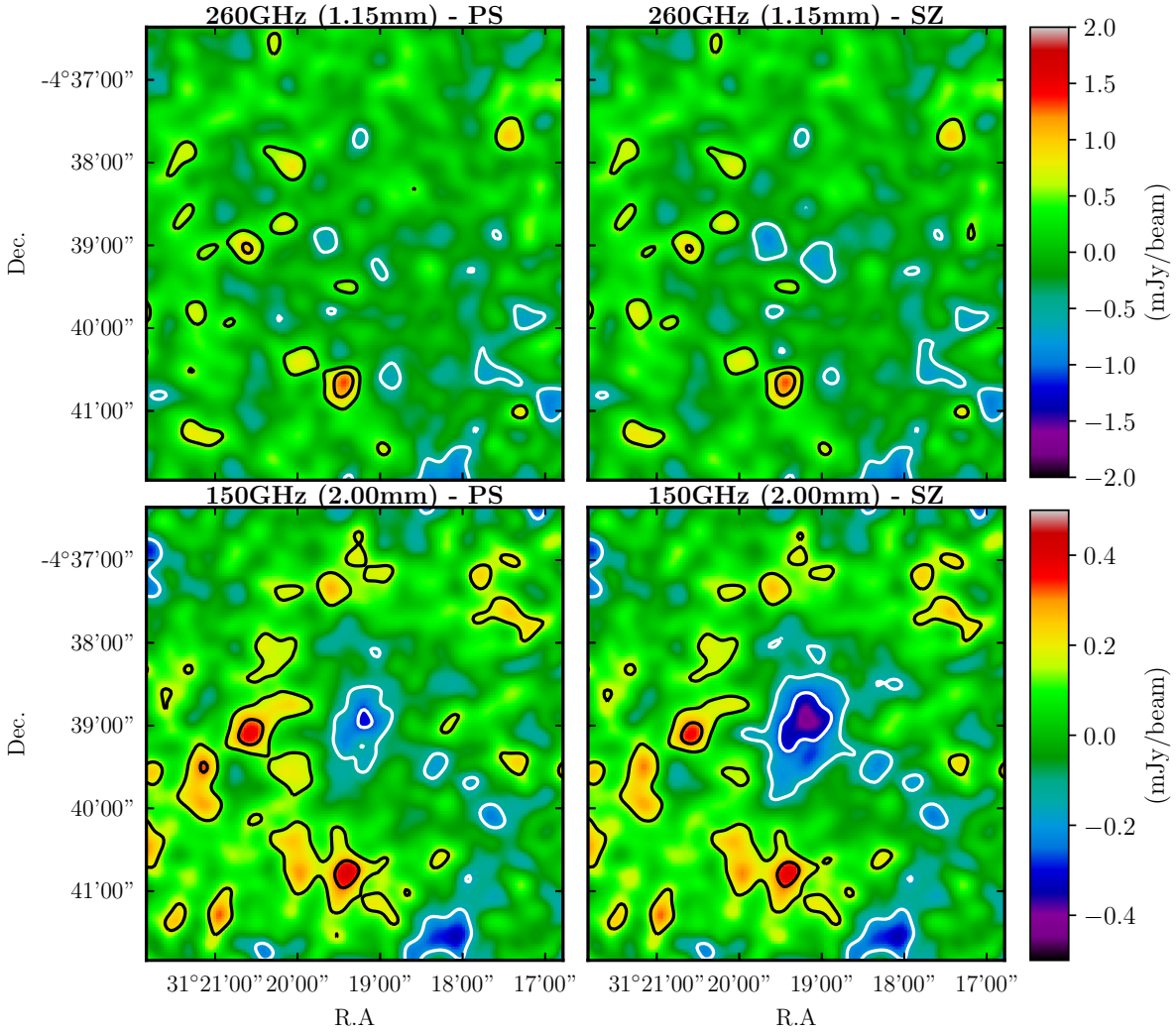

Figure 10.11: Final maps at 260 GHz (top) and 150 GHz (bottom) obtained with two different data reductions. *Left:* maps reduced to highlight the point sources. *Right:* maps reduced to highlight the extended SZ signal. The maps have sizes of $5' \times 5'$ and are smoothed at a resolution of FWHM $= 10''$. Signal to noise levels are shown in white and black, with respective contours at SNR $= [-2, -4]$ and $[2, 4]$.

Chapter 11

Detection and preliminary analysis of the sub-millimetre galaxies in the field of XLSSC102

Contents

Abstract: As already revealed with NIKA, NIKA2 observations of cluster fields may contain several high redshift dusty star forming galaxies. Those galaxies are of strong interest to constrain the cosmic star formation history. However, deriving their exact properties and precise position and redshift usually requires associated observations at other wavelength or follow-up with different instruments[1]. In this chapter we construct a catalogue of sub-millimetre sources detected in a cluster field with NIKA2 bands only. We precisely quantify the purity of the sample and search for counterparts at other wavelengths. Finally we compare our sources to sub-millimetre evolution models and define a preliminary sample of interesting sources to follow-up with complementary instruments.

11.1 Introduction

One of the main topic of modern cosmology is the mapping of the cosmic star formation history (SFH). Rapid progress on the understanding of galaxy formation and evolution has been achieved in the last decades, thanks to multi-wavelength observations. This led to the actual picture of a star-formation rate density peaking at $z \sim 2$ and declining exponentially at later times (see Madau and Dickinson 2014, for a review). It has been shown that at redshifts $z < 3$

[1] As an example, I participated to proposals aiming at following up bright NIKA distant lensed galaxy candidates with the EMIR and NOEMA IRAM instruments.

the cosmic star formation is dominated by dusty star forming galaxies (see e.e. Burgarella et al. 2013), which constitute the building blocks of proto-clusters (see e.g. Strazzullo et al. 2018) and are believed to be the progenitor of the massive early-type galaxies seen in the local Universe (see e.g. Simpson et al. 2014). Such galaxies have been recently detected at redshift as high as $z = 6.64$ (Riechers et al. 2013) and could contribute significantly to the cosmic star formation at those epochs.

Interstellar dust absorbs the UV light of young stellar populations and re-emit it in the far infrared (FIR), such that dusty star forming galaxies can be detected at sub-millimetre and millimetre wavelengths. So far, a few thousands of such "sub-millimetre galaxies" (SMGs) have been detected (see Blain et al. 2002; Casey et al. 2014, for reviews on their properties). Cluster fields have been used to search for high redshift SMGs, as clusters can act as strong gravitational lenses, allowing for the detection of sources fainter than the ones detected in blank fields (see e.g. Knudsen et al. 2006; Egami et al. 2010; Aguirre et al. 2018). Also, Béthermin et al. (2015) showed that, due to the evolution of the surveys detection limits with redshift and the FIR luminosity function, the median redshift of SMGs was increasing with the wavelength of the detection band. Because of these two effects, high redshift SMGs are likely to be found in NIKA2 clusters field observations (as was already shown with NIKA, see, e.g., Adam et al. 2017).

Finally, SMGs can contaminate the cluster extended SZ emission (see e.g. Adam et al. 2016). It is thus important to detect them and correctly model their emission in order to subtract their contribution and not bias SZ flux and morphology estimates.

11.2 Point sources detection and flux measurements

In this Section we describe the point source detection pipeline we constructed. The procedure is applied on the two NIKA2 bands[2], which have been reduced with a procedure dedicated to highlight point like sources emission, as explained in Chapter 10.

11.2.1 Map filtering and signal to noise estimation

11.2.1.1 Map filtering

In order to enhance the signal to noise ratio from the point sources it is necessary to smooth the NIKA2 surface brightness maps and filter the signal on large scale, as it is dominated by correlated noise or diffuse SZ signal. We thus applied a Difference of Gaussian (hereafter "DoG") filter, which consists in computing the difference between a map convolved with a Gaussian kernel of FWHM θ_1 (G_{θ_1}) and one convolved with a Gaussian kernel of FWHM θ_2 (G_{θ_2}):

$$M_{DoG} = G_{\theta_1} * M - G_{\theta_2} * M, \tag{11.1}$$

with M the input map and M_{DoG} the resulting filtered map (which is homogeneous to M and has no residual background level).

To be efficient, the filter should suppress the power on scales smaller than the beam size, because there is no signal at these scales and only noise, and suppress power at scale corresponding to extended signal or residual correlated noise. The optimal choice of kernel sizes thus depends on the data reduction and the properties of the noise affecting each map. We set $\theta_1 = 12''$ at 1 mm and $\theta_1 = 18''$ at 2 mm, to match the beam size, and we empirically tuned the value of θ_2, finding that $75''$ was a good size for the two bands.

[2]Note that throughout this Chapter, we refer to the 260 GHz and 150 GHz NIKA2 bands as "1 mm" and "2 mm". In practice, the true NIKA2 bandpass are used for any analysis.

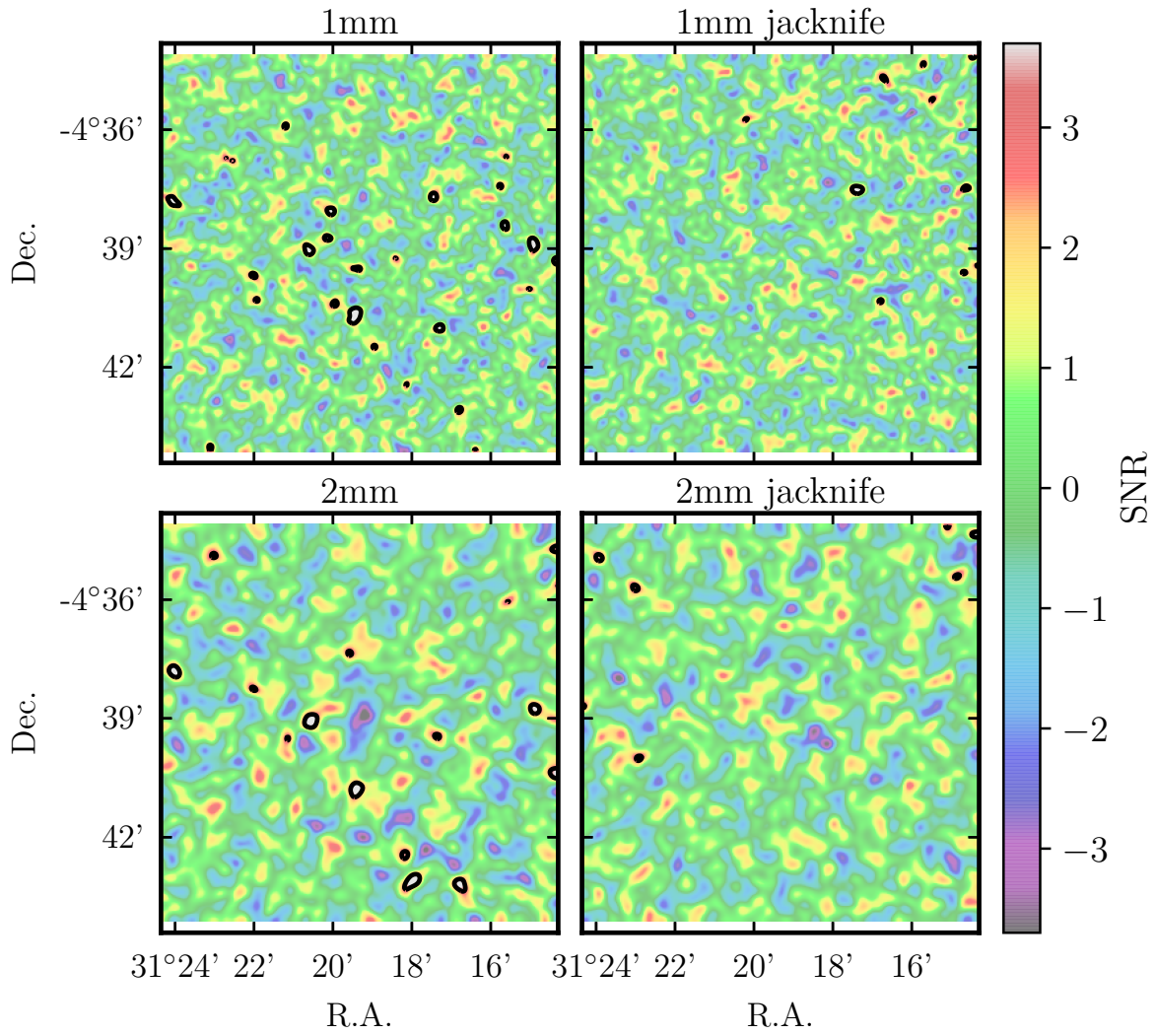

Figure 11.1: Maps filtered to highlight the point sources. *Top left:* field map at 1 mm. *Top right:* jackknife realisation at 1 mm. *Bottom left:* field map at 2 mm. *Bottom right:* jackknife realisation at 2 mm. All the maps are in units of signal to noise. The colour-bar is clipped to [-3.7,3.7]. The black contours indicate regions above SNR=3.

11.2.1.2 Signal to noise ratio estimation

As we showed in Chapter 10, the noise rms is not spatially homogeneous. For instance, it is much higher in the outskirts of the maps (see Figure 10.10). Thus, the source detection needs to be performed in the signal-to-noise maps rather than in the surface brightness maps.

In the case of the DoG filtered maps, the signal-to-noise ratio is computed for each pixel as the ratio between the filtered surface brightness maps and the rms maps. The rms maps corresponding to the "raw" (unfiltered) surface brightness maps are a product of the data reduction (see Chapter 10). Given the definition of the filter in equation 11.1, the rms of the filtered maps is proportional to the rms of the raw maps and the normalisation between the two depends on the noise angular power spectrum. We thus have:

$$SNR(M_{DoG}) = \frac{M_{DoG}}{Coeff \times \mathrm{rms}_M} \tag{11.2}$$

with $SNR(M_{DoG})$ the SNR map associated to the filtered surface brightness map M_{DoG}, $Coeff$ a constant coefficient and rms_M the rms map associated to the raw map M.

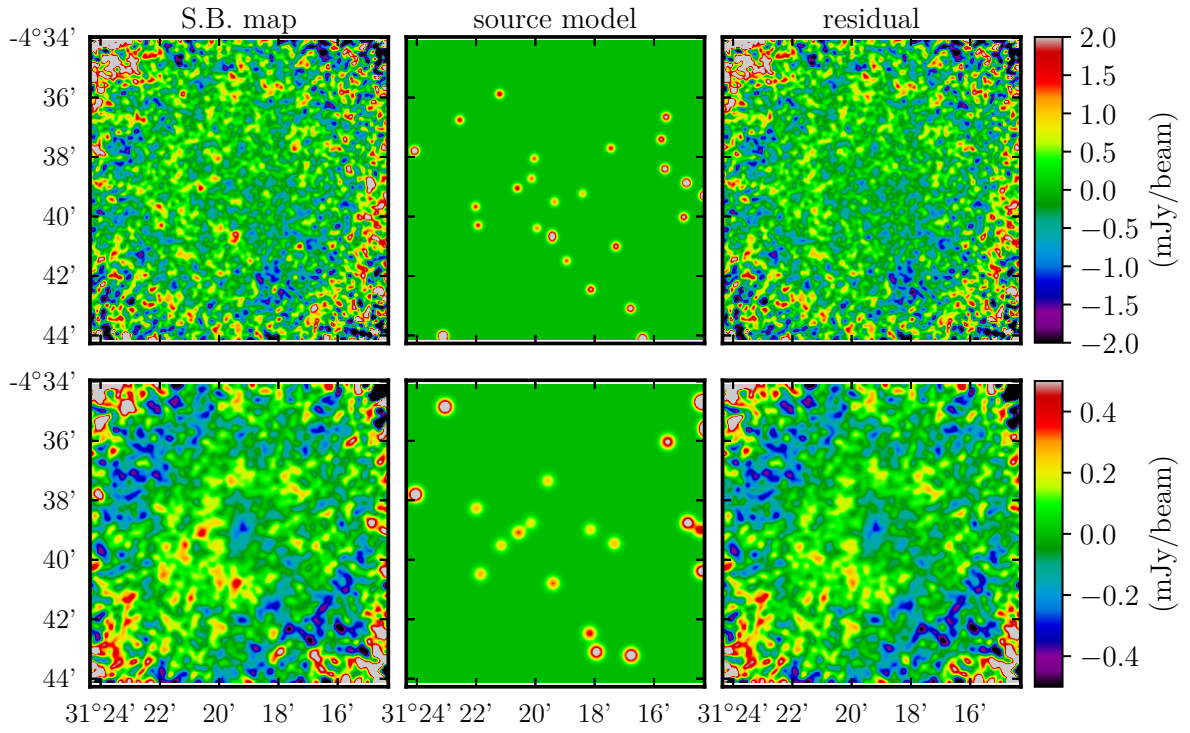

Figure 11.2: Comparison of the point source models, constructed with a limiting signal to noise $\mathrm{SNR}_{cut} = 3$, and the data. *Left:* input surface brightness maps. *Middle:* point source models. *Right:* residuals between the two. The top row contains the 1 mm maps and the bottom row contains the 2 mm ones. The maps have been smoothed to $9''$ and $13.5''$ for display purpose and the colour-bar is clipped to $[-2, +2]$ mJy and $[-0.5, +0.5]$ mJy, for the 1 and 2 mm maps, respectively.

As the noise is spatially correlated, the coefficients can not be computed analytically and we used the jackknife maps to estimate them. By construction, the signal to noise map corresponding to a filtered jackknife map has a standard deviation equal to unity, thus we have:

$$\sigma\left[SNR(JK_{DoG})\right] = \sigma\left[\frac{JK_{DoG}}{Coeff \times \mathrm{rms}_{JK}}\right] = 1 \tag{11.3}$$

with JK_{DoG} the filtered jackknife map. As $\mathrm{rms}_{JK} = \mathrm{rms}_{M}$, by construction, we have:

$$Coeff = \sigma\left(\frac{JK_{DoG}}{\mathrm{rms}_{M}}\right). \tag{11.4}$$

The filtered maps at 1 and 2 mm, expressed in units of signal to noise, along with the corresponding jackknife maps, are shown in Figure 11.1. The black contours indicate regions with a signal to noise level greater than three. We can see that, as expected in presence of point sources, much more regions satisfy this criteria in the signal maps than in the jackknife ones.

11.2.2 Point source detection and catalogue construction

As the maps in the two NIKA2 bands have different noise properties and resolution, we chose to conduct the source detection in each band independently. The source candidate positions and flux are estimated in one band (at 1 or 2 mm) and their fluxes in the other band are measured in a second time, by forcing the position at the one of the primary band. We thus obtain one source catalogue for each band. The source detection procedure is iterative and described in the following.

11.2.2.1 Point source fitting

As the sources are not resolved, their emissions can be approximated by Gaussian functions of FWHM equal to the effective beam FWHM:

$$F_{\rm PS}(x,y) = A \cdot \exp\left(-\frac{(x-x_0)^2+(y-y_0)^2}{2\sigma^2_{\rm beam}}\right) + Z_0, \tag{11.5}$$

where A is the source amplitude (i.e. its flux), x_0 et y_0 its position, $\sigma_{\rm beam}$ the beam standard deviation and Z_0 a background level.

The Gaussian functions are fitted to the raw surface brightness maps using `MPFIT`, an `IDL` robust non-linear least squares curve fitting method, where each pixel is weighted by its inverse variance. The fit is performed within a circular region of radius equal to three times the effective beam FWHM, centred on a given position. In case the exact position of the source is not known, it can be evaluated within a squared box of size equal to the effective beam FWHM.

11.2.2.2 Measurements of source positions and amplitudes

The source detection procedure is iterative and done in each band individually as follows.

1. The surface brightness map is filtered and converted into SNR map using Equation 11.2.
2. The source model of Equation 11.5 is fitted at the position of the pixel with the highest SNR, whose value indicate the SNR level in the filtered detection map. The resulting position, amplitude and amplitude error are recorded.
3. The fitted source model is subtracted from the raw surface brightness map.
4. The process is repeated, until the maximum of the SNR of the filtered map reaches a limiting value.

Additionally, for each source detected in a band "A", the amplitude in the band "B" is measured by forcing the fit at the position of the source in the band "A" ("A" and "B" being the 1 and 2 mm bands).

11.2.2.3 Flux corrections

The amplitudes of the fitted sources and their errors are converted into fluxes by applying different correction coefficients, such as:

$$F_\nu = \frac{A_\nu \times C_{col}}{C_{filt}} \tag{11.6}$$

$$\Delta F_\nu = \frac{\Delta(A) \times C_{corr} \times C_{col}}{C_{filt}} \tag{11.7}$$

with:

- C_{filt} the correction coefficient arising from the filtering of the signal due to the data reduction (see Section 10.3.2.4),
- C_{col} a colour coefficient coming from the differences between the SEDs of the detected source and the source used for the calibration (usually Uranus),
- C_{corr} the noise correction coefficient linked to the fact that, as the noise is correlated, the error on the amplitude is underestimated by the fitting procedure (equation 11.5).

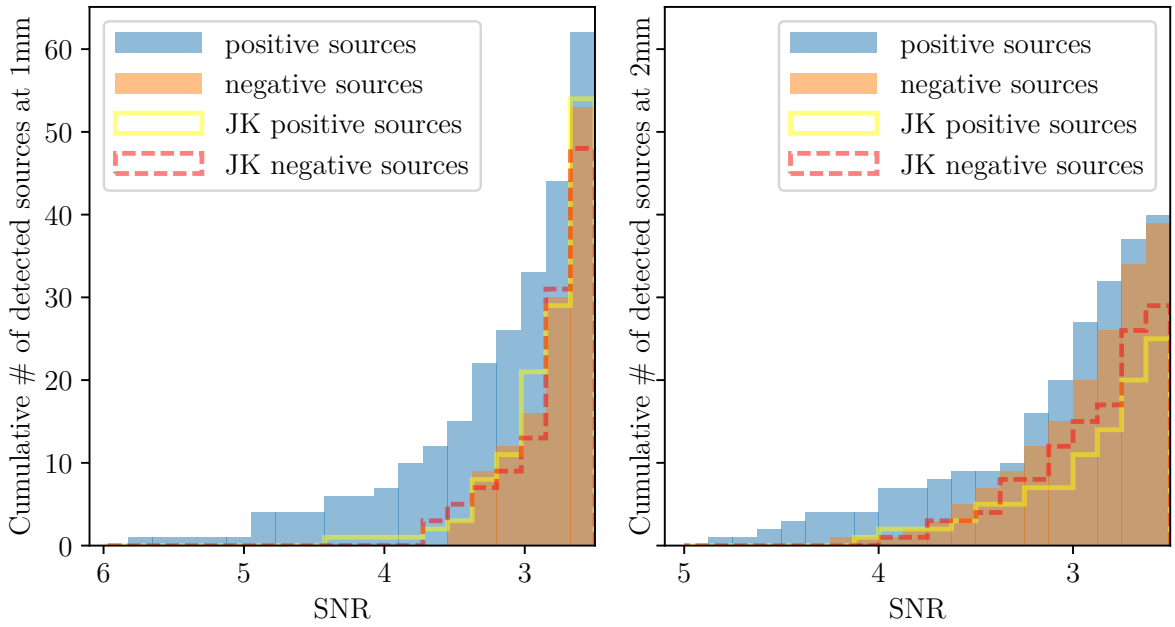

Figure 11.3: Cumulative number of detected sources as a function of the detection signal to noise, at 1 mm (left) and 2 mm (right). The blue histograms show sources from our detection catalogues while the other histograms show three independent measurements of the number of "fake" sources.

We estimated $C_{filt} = 0.98$ by convolving a simulated point source map to the transfer function (see Section 10.3.2.4). Using NIKA as a reference we found that the colour correction was negligible and use $C_{col} = 1$ (see for instance the Table associated to the NIKA release[3]). Finally, by injecting fake sources in the jackknife maps and measuring the standard deviation of their amplitudes, we estimated C_{corr}=1.53 at 1 mm and C_{corr}=1.48 at 2 mm, corresponding to a boost of the errors on point sources of about 50% due to noise correlations.

11.2.2.4 Outputs of the detection pipeline

Thanks to our procedure, we obtain two catalogues of sources, detected in the 1 and 2 mm bands. Each of them contain the SNR values associated to the detection filter of Equation 11.1, the sources positions, and the fluxes with their errors in both bands (the one used for the detection, but also the complementary band). For a given surface brightness map, the properties of the catalogue depend mainly on the choice of kernel sizes for the DoG filter and the limiting SNR (SNR$_{cut}$) adopted. Besides the source catalogues, we also constructed for each band a source model image, shown in Figure 11.2, which can be used to remove the contribution of point like sources when studying SZ extended signal in Chapter 12.

11.3 Catalogues properties

11.3.1 Purity of the detections and source numbers counts

11.3.1.1 Estimation of the number of "fake" sources

Some detections can be attributed to the noise fluctuations in our filtered maps and not to true astrophysical sources. As the true point sources have positive fluxes, they are only found in the

[3] http://lpsc.in2p3.fr/NIKA2LPSZ/nika2sz.release.php

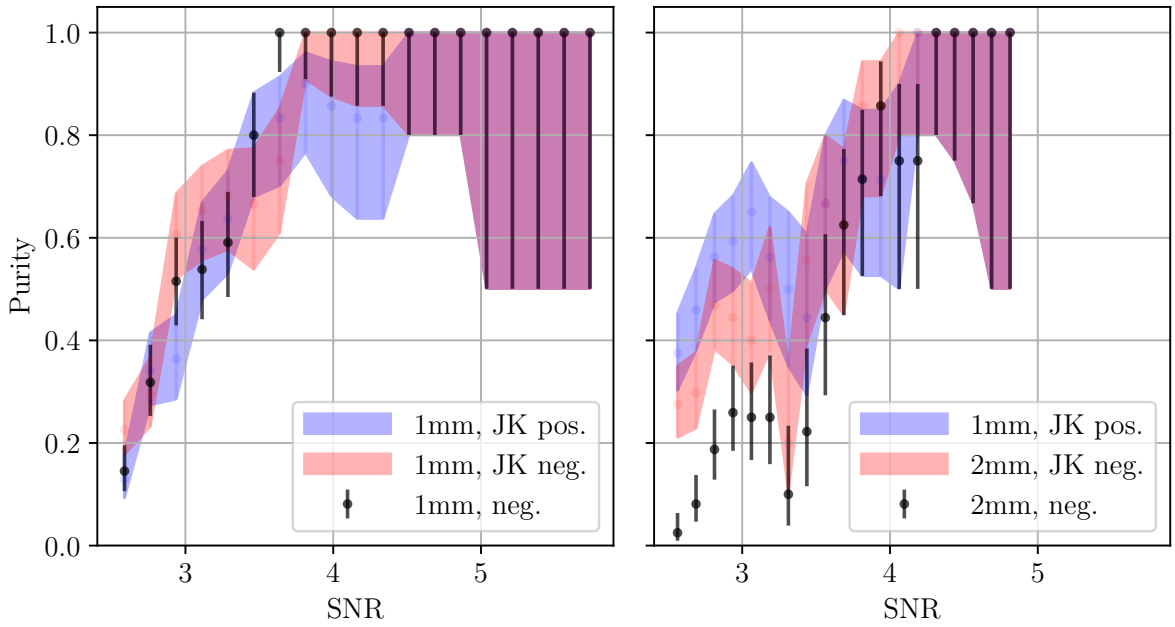

Figure 11.4: Purity of the source catalogues as a function of the detection signal to noise, at 1 mm (left) and 2 mm (right). The black points and error-bars show the purity estimated by taking as "fake" sources the ones detected in the negative part of the signal maps. The blue and red regions show the purity estimated by taking as "fake" sources the ones detected in the positive and negative parts of the jackknife maps. The errors are computed assuming binomial distributions and using Wilson score intervals.

positive part of the signal maps. Any negative point source in the surface brightness maps or in the jackknife maps are expected to be due to noise. In order to evaluate the purity of our catalogue we therefore counted the number of "fake" detected sources in each band by applying our detection pipeline to the negative part of the filtered signal maps and the positive and negative parts of the jackknife maps. These three estimations give independent measurements of the number of "fake" sources in our catalogue. The number of sources in our catalogues is shown as a function of the detection signal to noise and compared to the number of "fake" sources in Figure 11.3. We can see that the fraction of "fake" detections increases when the SNR cut is decreasing. These quantities are used in Section 11.3.1.2 for catalogue purity estimates.

11.3.1.2 Definition of the purity

We defined the purity $P(SNR_{cut})$ of our catalogues as:

$$P(SNR_{cut}) = 1 - \frac{N_{fake}}{N_s}, \tag{11.8}$$

with N_{fake} the estimated number of "fake" sources and N_s the number of detected sources. The uncertainty on the purity is computed assuming binomial distributions and using Wilson score intervals (Wilson 1927). The purity depends on the SNR cut (SNR_{cut}) imposed for the detection. We have three independent measurements of the purity, corresponding to the different estimation of N_{fake}. Those are shown as a function of the SNR cut for the 1 and 2 mm catalogues in Figure 11.4. We can see that the two purity estimation computed using the jackknife maps (red and blue regions in Figure 11.4) are compatibles. The purity of the 1 mm catalogue estimated using the negative part of the signal map overly agree with the other estimations, considering the error bars. However, we see a systematic trend for the purity of the 2 mm catalogue: the

Table 11.1: Statistics of the 1 and 2 mm point source catalogues. Column 1 indicates the cut in signal to noise used for the detections, columns 2 and 3 (respectively 4 and 5) present the number of detected sources at 1 mm (respectively 2 mm) and the associated catalogue purity. The purity has been computed using the mean number of "fake" sources estimated from the jackknife maps.

SNR cut (SNR_{cut})	# of 1 mm sources	purity at 1 mm	# of 2 mm sources	purity at 2 mm
4.5	4	$1.0^{+0.0}_{-0.2}$	2	$1.0^{+0.0}_{-0.3}$
4.0	6	$0.9^{+0.1}_{-0.2}$	4	$0.9^{+0.1}_{-0.2}$
3.5	12	$0.75^{+0.10}_{-0.15}$	9	$0.7^{+0.1}_{-0.2}$
3.0	26	$0.6^{+0.1}_{-0.1}$	20	$0.5^{+0.1}_{-0.1}$

one estimated using the negative part of the signal map starts to decrease at $SNR_{cut} \sim 3.7$ with respect to the ones estimated with the jackknife map. This is due to the contribution from the cluster SZ signal, which is negative. Indeed, it has not been entirely removed by our filter and it boosts the number of "fake" point source detection. We concluded that for the 2 mm band estimating the point source detection contamination on the same map as the astrophysical signal may artificially decrease the estimated purity.

11.3.1.3 Statistics of the source number counts

The catalogues properties at 1 mm and 2 mm are summarised in Table 11.1 for four different SNR cut. We can see that for these SNR cut the purity is similar in the two bands, considering its uncertainty. This allows a fair comparison of the number of sources in the two bands and we can remark that more sources are detected at 1 mm than at 2 mm. In order to ensure a purity around 90% we chose to cut our source catalogues at $SNR_{cut} = 4.0$ for the two bands.

11.3.2 Association of the 1 and 2 mm catalogues and flux boost correction

11.3.2.1 Matching statistics

We matched the catalogues of sources detected at 1 and 2 mm by associating the objects above a given detection SNR, within a search radius of $18''$, corresponding to the effective beam FWHM at 2 mm. In order to check if the associations can be attributed to random chance, it is necessary to test the same procedure using a randomised catalogues with the same statistical properties as the detection catalogue. As a preliminary analysis we use the fake sources catalogues, constructed using the jackknife maps, as random catalogues. They only contain the contribution from noise, and thus, provide an upper limit on the purity induced by accidental matches. However, given the low number density of sources, we expect that this provides a good first estimates of the purity in the low SNR regime, where noise dominates. The results are summarised in Figure 11.5, where colours show the number of matched sources and written numbers indicate the estimated purity of the match.

11.3.2.2 Flux and colour bias

Using a sample of matched sources with $SNR_{cut,1mm}$=3.5 and $SNR_{cut,2mm}$=2.5, which is expected to provide a high purity (see Figure 11.5), we compared the fluxes obtained by fixing or not the position of the source (see Figure 11.6). We can see that the fluxes measured at fixed positions are systematically underestimated with respect to the fluxes measured when the position are free to vary. This is expected because as the detections coordinates are computed at the peak signal to noise of our filtered map, the noise fluctuations will lead to a boost in the point source amplitude at the position we are fitting for its flux (see Casey et al. 2014, for discussions

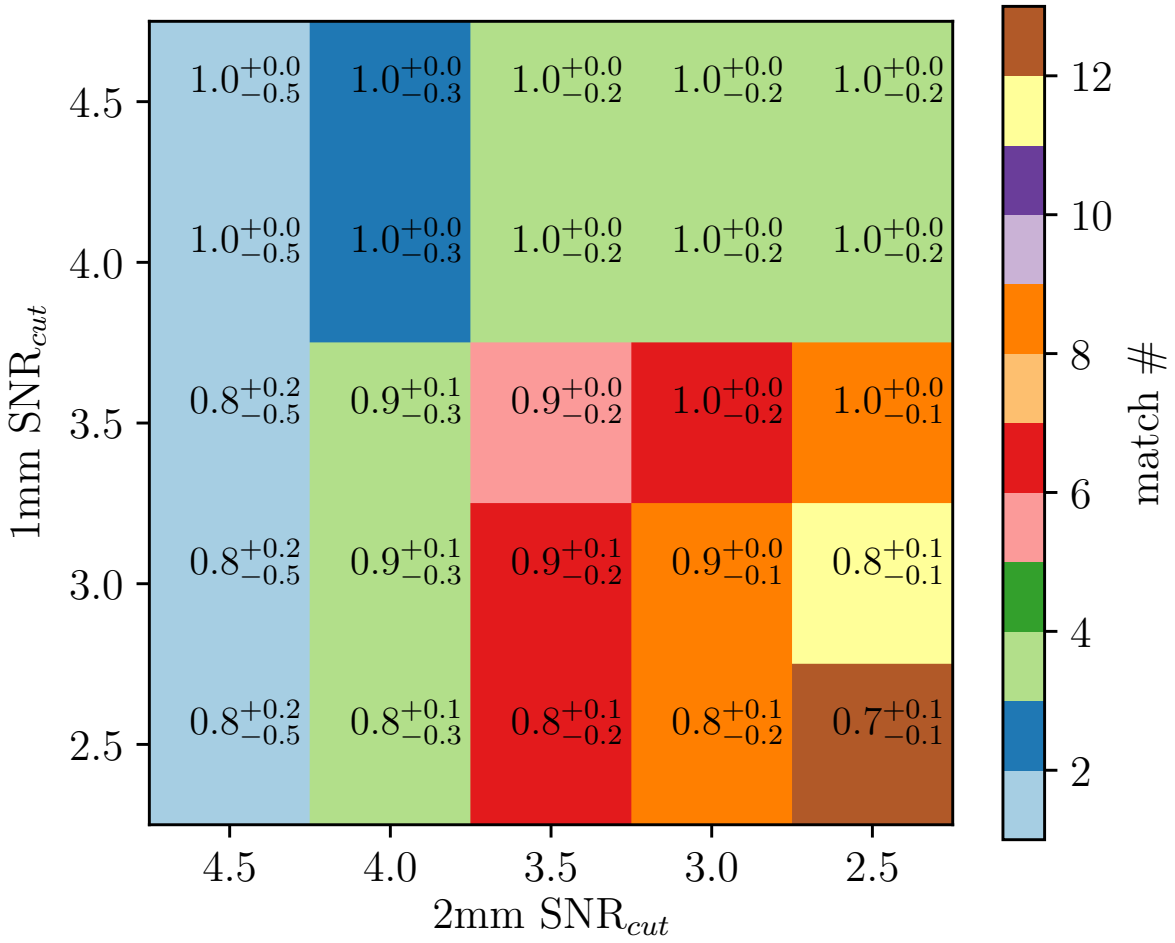

Figure 11.5: Matching statistics as a function of the cut in detection signal to noise in each band. Colours show the number of matched sources and written numbers indicate the estimated purity of the match. The purity has been computed using the mean number of match between "fake" sources from the jackknife maps.

about the sources of boost of the fluxes). For each band, we defined the relative bias b_{flux} as :

$$b_{flux} = median\left(\frac{F_f - F_m}{F_m}\right) \tag{11.9}$$

with F_m the flux measured with the position free to vary and F_f the flux measured at the fixed position. We found that the fluxes were significantly biased, with $b_{flux} = -0.14 \pm 0.05$ at 1 mm and $b_{flux} = -0.15 \pm 0.04$ at 2 mm. We then studied how these biases affect the estimated source colours, as defined as

$$R = \frac{F_{2mm}}{F_{1mm}}. \tag{11.10}$$

The uncertainties on the colour are computed using Monte Carlo realisation, by sampling the 1 mm and the 2 mm fluxes within their Gaussian error bars. The percentiles of the resulting colour PDF provides the confidence interval. We compared the ratio of the fluxes measured independently in the two bands (R_{ind}) with the ratio of the flux measured at the position of the detection in the two primary bands ($R_{f,1mm}$ with respect to the 1 mm positions and $R_{f,2mm}$ with respect to the 2 mm positions). We thus have three colour estimates and we defined the

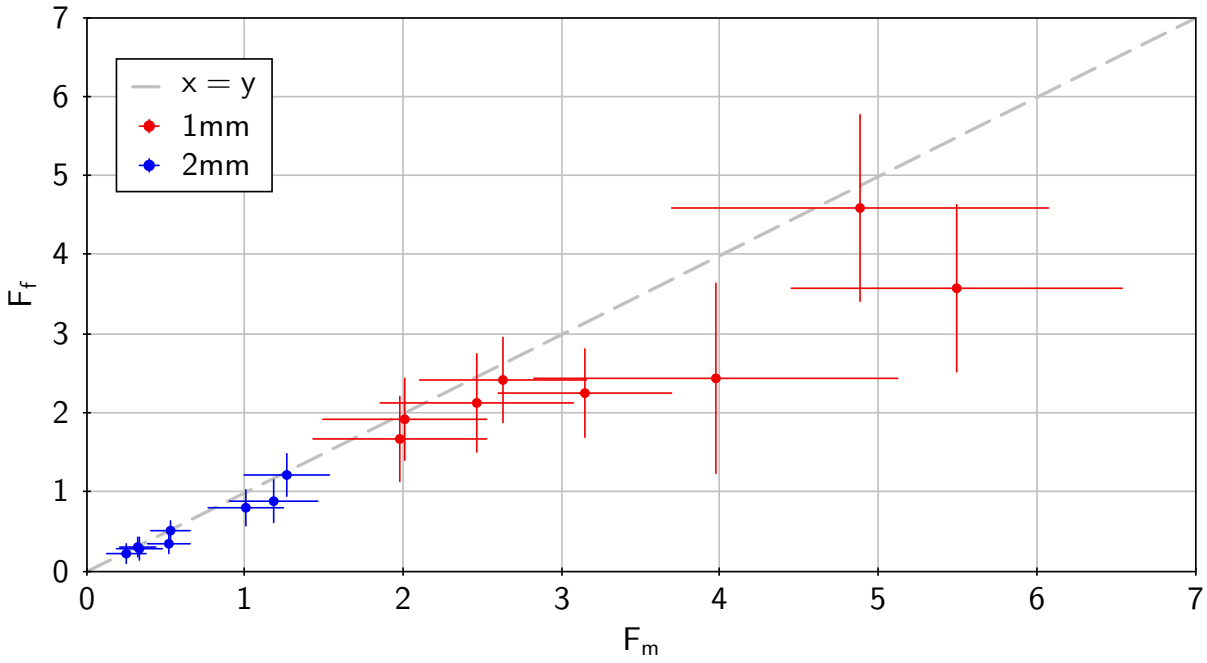

Figure 11.6: Comparison of the fluxes measured in the band used for the detection (F_m) and the fluxes measured in the associated band (F_f). The red/blue points are for the 1/2 mm fluxes. The dashed line indicate $F_f = F_m$ relation, for visualisation purposes.

relative colour biases for each band as:

$$b_{col} = median\left(\frac{R_f - R_{ind}}{R_{ind}}\right) \tag{11.11}$$

with $R_f = R_{f,1mm}$ or $R_{f,2mm}$. For the 2 over 1 mm flux colour we found $b_{col} = -0.15 \pm 0.04$ when the detection is done in the 1 mm band and $b_{col} = 0.18 \pm 0.09$ when the detection is done in the 2 mm band. This results will be used in Section 11.5 when investigating the properties of our sources.

11.4 Seeking for counterparts at other wavelengths

We investigated the counterparts of our sources in multi-wavelength observations, from radio to X-ray, as shown in Figure 11.7. The data include images from FIRST at 21 cm, WISE at 22, 12, 4.6 and 3.4 μm, Megacam at ~ 0.7 μm (in the i' band) and XMM in X-ray.

Despite the good sensitivity of FIRST, no significant emission is seen at the location of our sources [4]. Assuming galaxies with standard radio sources spectral indices (typically $\sim -0.7 \pm 0.2$, see Witzel et al. 1979), it indicates that the point source we detect are not radio sources, and we assume instead that they are dusty SMGs with rising spectral index. Although it has been found that a large fraction of SMGs presents X-ray emission due to the presence of AGNs (see e.g. Johnson et al. 2013), no significant point source are seen in the XMM image. No significant counterparts are seen in the WISE bands, which indicates, considering their fluxes, that our sources are likely to be at $z > 1$. This can also be seen in Figure 11.8, where we show SMG spectral energy distributions from da Cunha et al. (2015) at different redshifts, along with the flux limits from WISE and the NIKA2 flux of our sources. These SEDs are constructed based on a sample of SMGs detected with ALMA and may not be completely representative of the population we are probing here, thus the comparison can only be qualitative. However, we

[4] We note that the sources also do not have counteparts at 325 and 610 MHz, as seen in recently obtained GMRT data (Horellou et al. 2018), which are much more sensitive than FIRST.

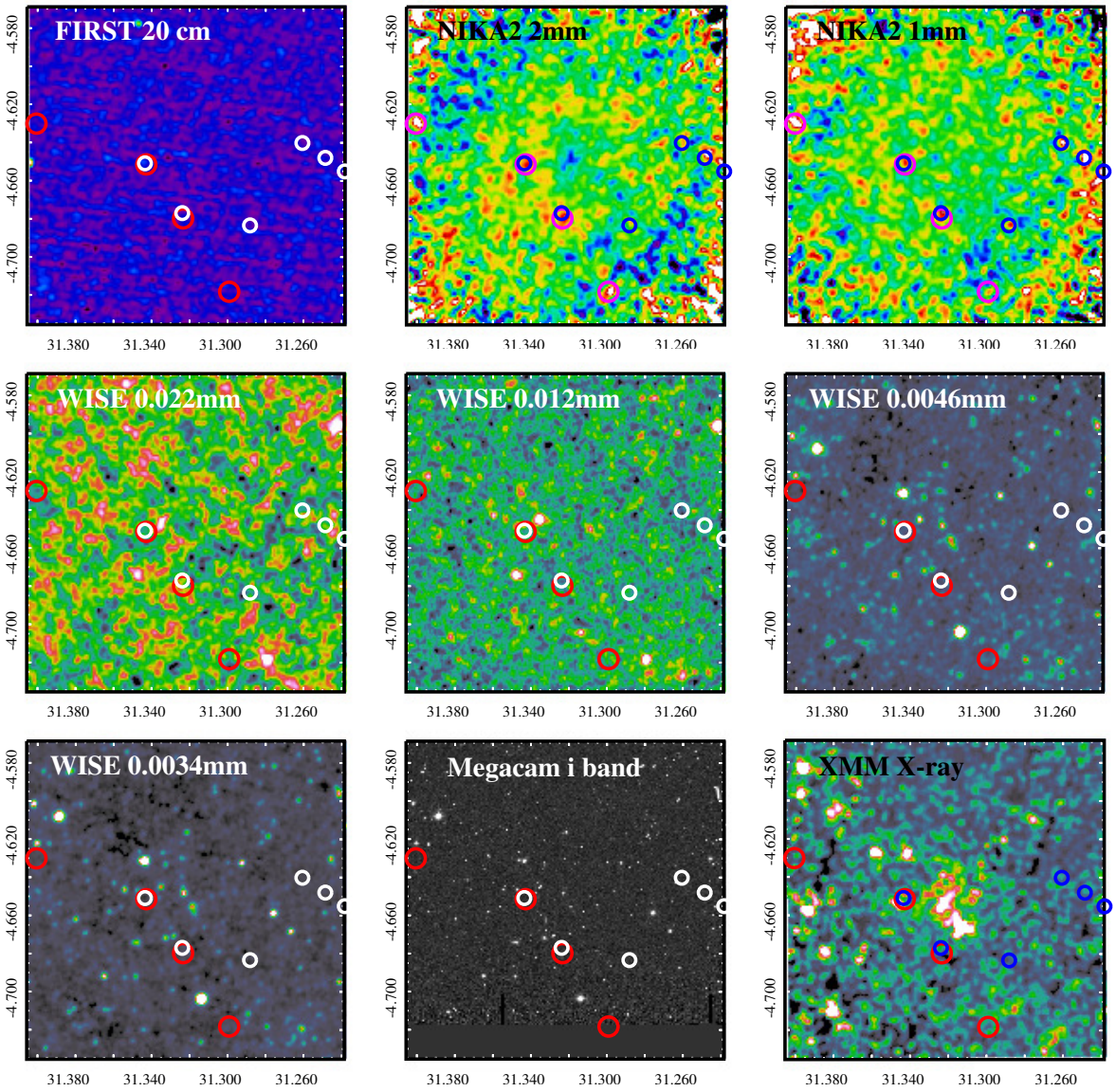

Figure 11.7: Multi-wavelength view of the XLSSC102 field from radio to X-ray. The observation wavelength is decreasing from top left to bottom right. The white (and dark blue) circles show the sources detected with SNR>4 in the 1 mm NIKA2 band and the red (and magenta) circles indicate the sources detected with SNR>4 in the 2 mm NIKA2 band. The sizes of the circles reflect the beam FWHM in the detection band.

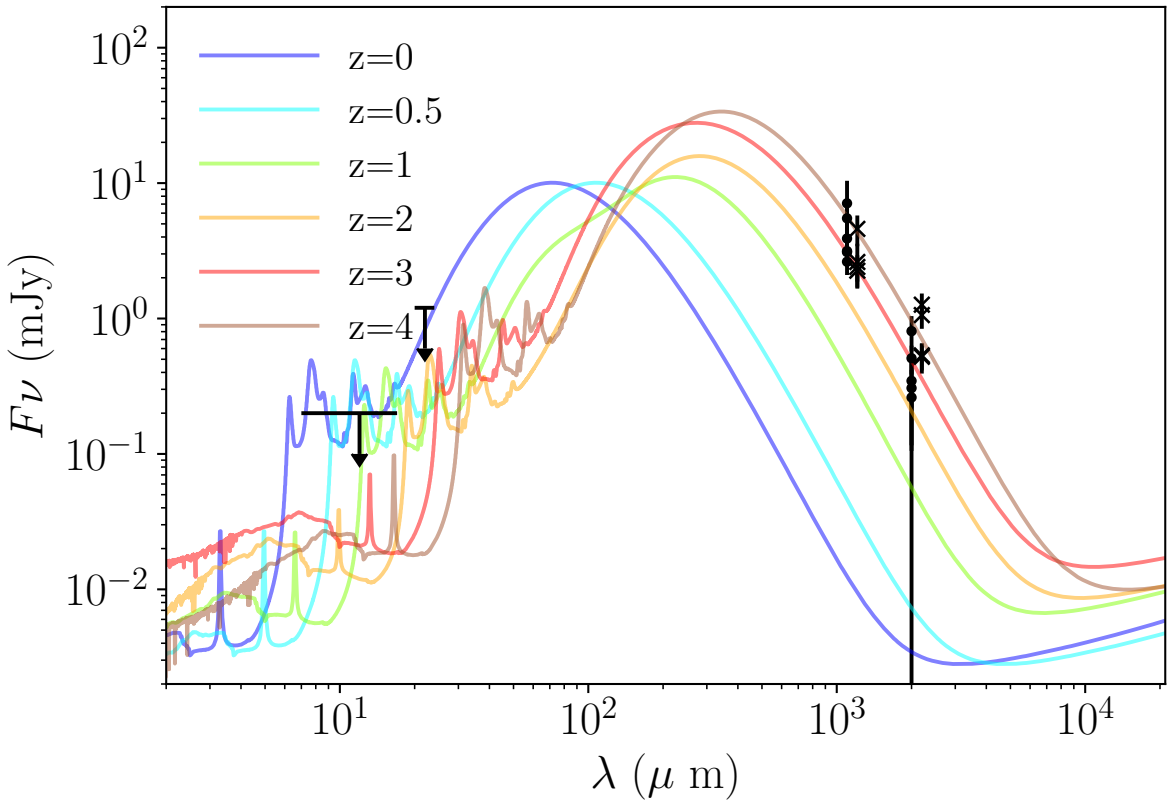

Figure 11.8: SMG spectral energy distributions from da Cunha et al. (2015). The SEDs at $z = 0$ and $z = 0.5$ are for optically faint sources and the other SEDs are computed for each redshift. The two black arrows indicate the maximum sensitivity of the WISE-3 and WISE-4 bands (values taken from Casey et al. 2014). The black points indicate the fluxes of the SNR>4 sample detected in the NIKA2 1 mm band and the crosses (slightly shifted for clarity) indicate the fluxes of the SNR>4 sample detected in the NIKA2 2 mm band .

can see that it is unlikely that SMGs at $z < 1$ have fluxes as high as the ones we measured with NIKA2 and do not appear in WISE bands. Finally, considering the large beam sizes, several galaxies are seen in the optical image at the source positions. The majority are faint and they do not present any special feature. Taken all together, these comparisons confirm that our sources are dusty star forming galaxies, likely to be at redshift $z > 1$.

SMGs can present strong Lyman Alpha ($Ly\alpha$) emission: Chapman et al. (2005) found that nearly $\sim 50\%$ of the $z > 1.47$ SMGs in their sample were $Ly\alpha$ emitters. We thus matched our source catalogues with a sample of spectroscopically confirmed Lyman Alpha emitting galaxies at redshift $z \sim 4.5$ from Wang et al. (2009). We found one possible association between a source detected with a SNR of 3.43 in the NIKA2 1 mm band and a $Ly\alpha$ galaxy at $z = 4.436$; and one other possible association between a source detected with a SNR of 3.19 in the NIKA2 2 mm band and a $Ly\alpha$ galaxy at $z = 4.431$. If confirmed, with more precise position or redshift measurements, these associations would bring interesting informations about the dust properties of those sources and allow their stellar populations and star formation history to be measured precisely (see e.g. Finkelstein et al. 2009; Yajima et al. 2012).

11.5 Comparison to sub-millimetre galaxies evolution models

As no observations of our cluster field exist at sub-millimetre wavelengths we cannot estimate the photometric redshifts of our sources. Thereby, we chose to use the millimetre colour as a

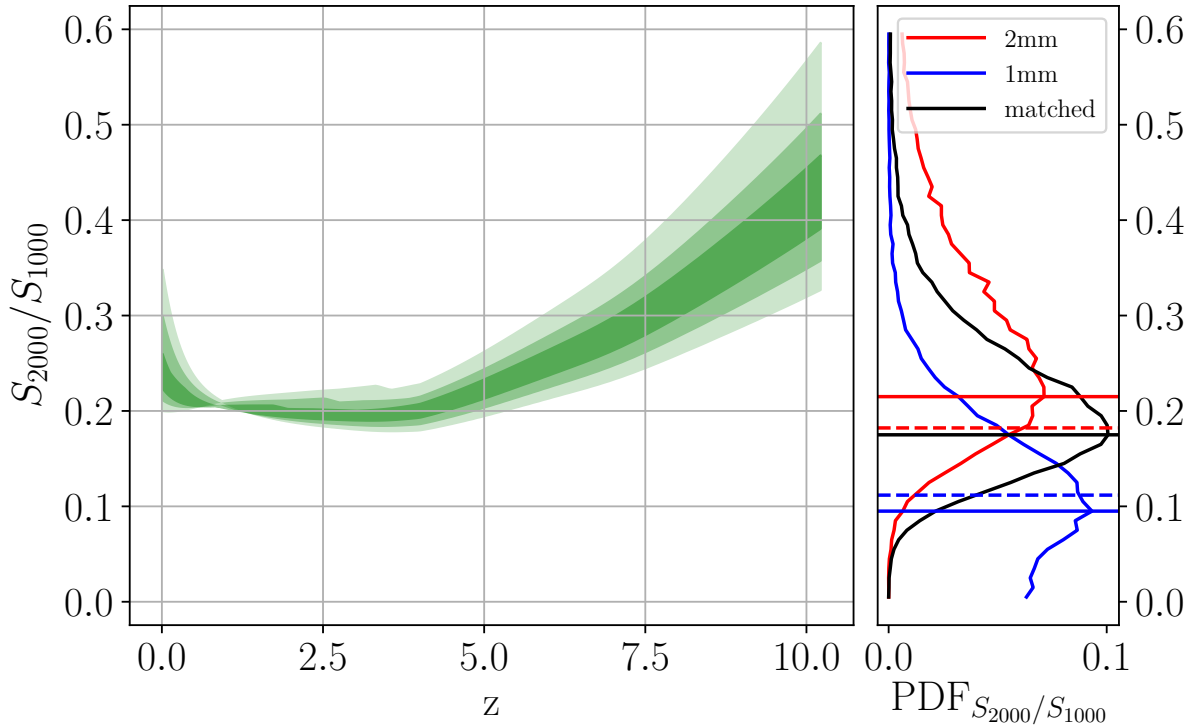

Figure 11.9: *Left:* SMG colour evolution with redshift from the model of Béthermin et al. (2012), evaluated in the NIKA2 bandpass. The model is computed for main sequence galaxies and is marginalised over the dust temperature. The green shaded areas indicate the 68, 95 and 99% c.i. around the median relation. *Right:* probability distribution function of our point sources colours (the x and y axis are inverted). The sources are primary detected with SNR_{cut}>4 in the 1 mm band (blue) and 2 mm band (red). The black curve is for the colour from a matched sample. The horizontal solid lines indicate the colour at the maximum of the PDFs and the dashed lines show the same values corrected from the colour bias.

redshift indicator. In the left part of Figure 11.9 we show a model for the evolution of main sequence SMGs colours with redshift, computed using the SMGs models of Béthermin et al. (2012). We can see that the colour is relatively flat up to $z \sim 4$ and is getting redder at higher redshifts. This is because at $z < 4$, the dust SED remains in the Rayleigh-Jeans limit at the frequencies covered by NIKA2, while at $z \gtrsim 4$, the peak of the dust SED approaches the NIKA2 bands and NIKA2 becomes sensitive to the slope of the spectrum, and thus the peak position and the redshift (see Figure 11.8). A red colour could therefore indicate a high redshift galaxy candidate. We compared in the right part of Figure 11.9 the colour probability distribution functions of the sources detected with SNR>4 in the 1 mm and 2 mm bands (blue and red curves). We also show the colour PDF of a matched sample (black curve), constructed as the combination of the matched sample with $\mathrm{SNR}_{cut,1mm}$=4.0 and $\mathrm{SNR}_{cut,2mm}$=2.5 and the matched sample with $\mathrm{SNR}_{cut,1mm}$=4.0 and $\mathrm{SNR}_{cut,2mm}$=2.5. The colours corresponding to the maximum probabilities are indicated by the solid lines, while the dashed lines indicate the same values corrected from the flux bias computed from Eq.11.11. We can see that, while the bias corrected colour of the 2 mm sample agree with the colour of the matched sample, the bias corrected colour of the 1 mm sample is significantly lower. This could indicate a redshift selection effect with wavelength such as discussed in Béthermin et al. (2015).

Finally, we searched for the reddest sources in our sample with reliable colour measurements (having a colour $R > 0.2$ with a 95% confidence). We found one source satisfying this criteria: the source detected with the highest SNR in the 2 mm band. Figure 11.10 shows the colour

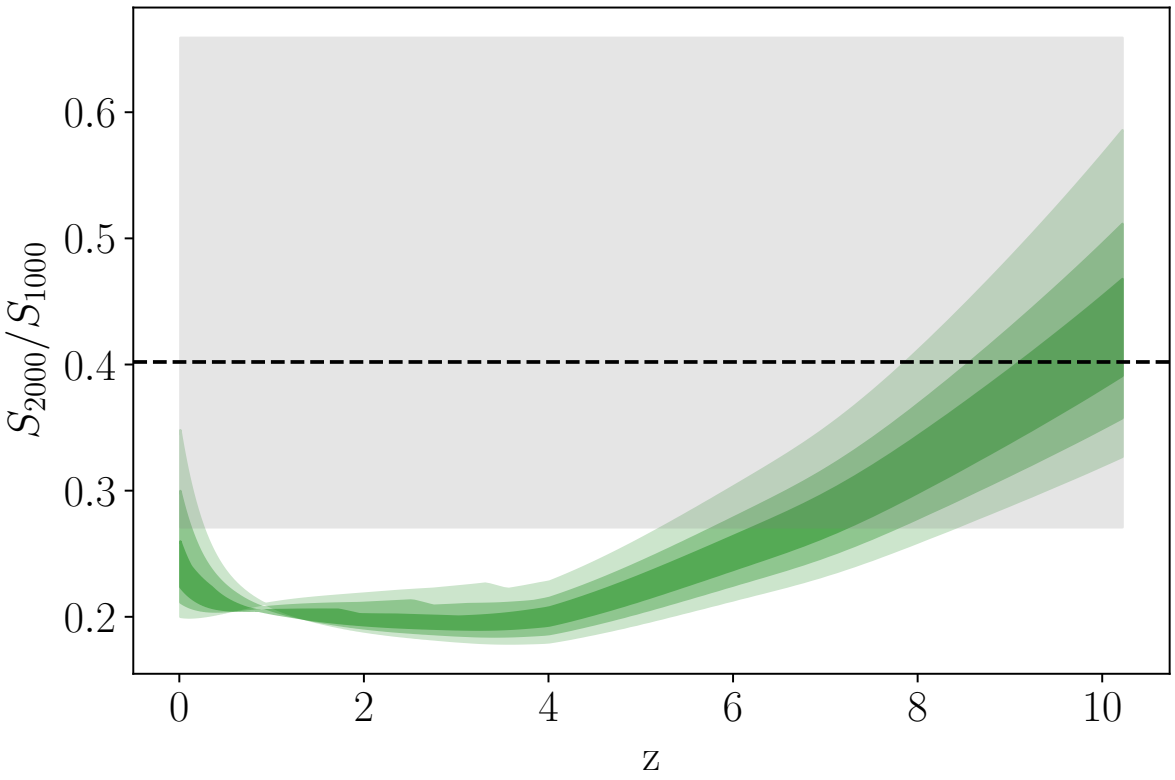

Figure 11.10: SMG colour evolution with redshift from the model of Béthermin et al. (2012), as in Figure 11.9. The horizontal dashed line indicate the colour of our best high redshift SMG candidate and the grey area indicate the $16^{\rm th}$ and $84^{\rm th}$ percentiles.

measurements of this source, with the 68% c.i., compared to the evolution model. As the very low redshift region is excluded because of the lack of counterparts seen in the WISE images, the colour we observe indicate that this source could be at $z > 5$. However, the error bars are large and lower redshifts are allowed at 95% confidence level. This source is thus a high redshift candidate and more data are needed to reduce the colour uncertainty and improve the constraint on its redshift. This object could also be an outlier at lower redshift, but even in that case, its red colour makes it an interesting object to study.

11.6 Conclusions

In this chapter, we developed a pipeline dedicated to the blind detection of point sources in the NIKA2 maps. We constructed two catalogues of sources detected in the field of XLSSC102 (in each band) and quantitatively assessed their purity using noise realisation ("jackknife") maps. Comparison to associated multi-wavelength data indicate that those point sources are dusty star forming galaxies, likely to be at redshift above unity. Unfortunately, no ancillary data exist of our cluster field at sub-millimetre wavelengths, which prevents us to determine the photometric redshifts of our sources. Nevertheless, we compared the colour of our sources to evolution models of main sequence SMGs, and found hint that the population detected in the 1 mm band is at lower redshift than the one detected in the 2 mm band.

We present the sample of our most interesting sources in Table 11.2. All sources detected with with SNR>4 plus the two sources possibly matched with $Ly\alpha$ emitting galaxies at $z \sim 4.5$. Our high purity sample (SNR>4) contains 6 independent sources detected at 1 or 2 mm. The source detected with the highest SNR in the 2 mm band does not present any associated

Table 11.2: Catalogue of our most interesting point sources. Top block: sources with SNR>4 detected in the 1 mm band, middle block: sources with SNR>4 detected in the 2 mm band, bottom block: sources possibly associated with $Ly\alpha$ emitters (Wang et al. 2009). The flux values with bold font are the ones measured in the band used for the detection.

ID	SNR	RA	Dec	flux 1 mm	flux 2 mm	comments
XLSSC-PS1-1	5.77	31.3239	-4.6770	**3.1 ± 0.6**	0.3 ± 0.1	matched with XLSSC-PS2-3
XLSSC-PS1-2	4.89	31.2486	-4.6479	**5.5 ± 1.0**	0.8 ± 0.2	matched with a 2 mm source with SNR=3.92
XLSSC-PS1-3	4.85	31.2383	-4.6551	**7.1 ± 3.3**	-0.2 ± 0.4	
XLSSC-PS1-4	4.81	31.3435	-4.6509	**2.6 ± 0.5**	0.5 ± 0.1	matched with XLSSC-PS2-2
XLSSC-PS1-5	4.41	31.2607	-4.6402	**3.9 ± 0.8**	0.3 ± 0.2	
XLSSC-PS1-6	4.41	31.2882	-4.6834	**3.1 ± 0.7**	0.3 ± 0.2	
XLSSC-PS2-1	4.84	31.2991	-4.7182	2.6 ± 1.0	**1.1 ± 0.2**	high z candidate shown in Fig. 11.10
XLSSC-PS2-2	4.50	31.3428	-4.6515	2.4 ± 0.5	**0.5 ± 0.1**	matched with XLSSC-PS1-4
XLSSC-PS2-3	4.47	31.3234	-4.6798	2.3 ± 0.6	**0.5 ± 0.1**	matched with XLSSC-PS1-1 and another 1 mm source with SNR=3.36
XLSSC-PS2-4	4.33	31.4006	-4.6301	4.6 ± 1.2	**1.3 ± 0.3**	matched with a 1 mm source with SNR=3.90
XLSSC-PS1-A	3.43	31.3669	-4.6612	**2.3 ± 0.7**	0.0 ± 0.1	matched with J020527.7-043944[a] at $z = 4.436$
XLSSC-PS2-A	3.19	31.2401	-4.6500	-1.9 ± 1.3	**0.7 ± 0.3**	matched with J020457.3-043847[a] at $z = 4.431$

[a] from Wang et al. (2009)

counterpart detected with SNR>2.5 in the 1 mm band and is the reddest galaxy we detect, it is thus a good high redshift SMG candidate (Figure 11.10).

More data will allow us to reduce the flux and colour uncertainties and make rough estimation of the sources redshifts. However, due to the large size of the beam, follow-up observations will be necessary to confirm the associations with $Ly\alpha$ emitters. Finally we note that Spitzer and Herschel SPIRE data are available for our second target (XLSSC 072), which will make the characterisation of the SMGs possibly present in the field easier.

Chapter 12

Preliminary analysis of the galaxy cluster XLSSC102

Contents

Abstract: The characterization of the morphologies of cluster, mass profiles and gas thermodynamics can be achieved through a multi-wavelength approach. This permits a better understanding of the formation of clusters and allows for a more realistic modelling of their physics. Finally, the global properties of clusters can be compared to scaling relations to search for deviations or systematics, as a function of their mass and/or redshift and/or dynamical state. In this Chapter we conduct the preliminary analysis of the cluster XLSSC102 at z=0.97, by combining SZ, X-ray and optical data. First, we investigate the morphology of the cluster; then we determine the radial profiles of the intra cluster medium properties and finally, we compare our findings to the "universal" pressure profiles and scaling laws.

12.1 Morphology of the intra cluster medium

Scaling relations and mass measurements are often obtained assuming spherical symmetry and using the hydrostatic equilibrium assumption. However, the mass distribution in clusters is

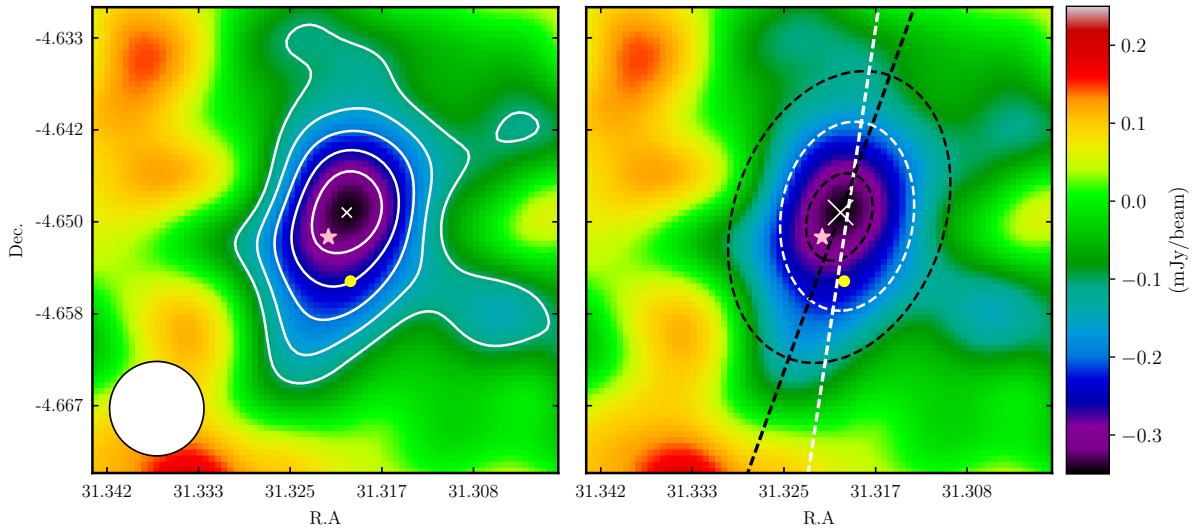

Figure 12.1: Surface brightness map of the cluster SZ signal. The map has a size of $2.5' \times 2.5'$ and has been smoothed to a resolution of $25''$. The effective resolution is shown in white in the bottom left corner. The white cross indicates the position of the SZ peak, the pink star shows the position of the X-ray centroid and the yellow circle indicates the BCG location. *Left:* the contours indicate the signal to noise levels of $SNR = [-2, -3, -4, -5, -6]$. *Right:* The contours show the 2D Gaussian functions fitted to respectively the total (black) and inner part (white) of the cluster. The dotted lines indicate the directions of the major axes.

known to often be triaxial, reflecting their formation via accretion and the merger of substructures (see e.g. Limousin et al. 2013, for a review and Despali et al. 2017, 2014 for results using simulations), and a large fraction of systems are found to be unrelaxed, especially at high redshifts (see e.g. Mann and Ebeling 2012). Moreover, cluster geometry and dynamical state can also affect cluster detection (see e.g. Rossetti et al. 2016, for a study of the different fractions of relaxed cluster in X-ray and SZ selected samples). Characterising the morphology and dynamical state of clusters is therefore mandatory to understand how their detection and mass measurements affect cluster based cosmological constraints. Furthermore, the cluster triaxiality can also be used to test cosmological models (see e.g. Sereno et al. 2018).

In this section we investigate the ICM morphology of XLSSC102, from NIKA2 data alone on one hand, and by combining SZ, X-ray and optical informations on the other hand. We subtracted the contribution from point sources detected with a SNR>2.5 in Chapter 11 using the point source model. However, we note that no strong point source appears to contaminate the cluster emission. In the rest of the chapter we only focus on the 150 GHz band because it is the one in which the SZ signal is well detected[1].

12.1.1 Sunyaev-Zel'dovich imaging

In Figure 12.1, we present a $2.5' \times 2.5'$ SZ surface brightness map of XLSSC102. We smoothed the map at a resolution of 25 arc-seconds using Gaussian filtering and we added signal to noise contour levels estimated using the methodology explained in Section 11.2. We can see that the ICM SZ signal of XLSSC102 is elongated along the North-West-South-East axis.

As shown in the right panel of Figure 12.1 we find that the cluster emission is well fitted by a 2D Gaussian of ellipticity $\epsilon = 0.3$, defined as $1 - \frac{\sigma_b}{\sigma_a}$, with σ_a and σ_b the standard deviations of

[1]Given the noise rms achieved so far, we do not expect any significant SZ signal to be visible in the 260 GHz band.

the major and minor axes, respectively. Consistent result is found considering the global cluster region or only the inner region (in which SNR < -4).

The ellipticity of the SZ signal alone can not be used to distinguish between relaxed and disturbed dynamical state, or simply effects of triaxiality (see e.g. Cialone et al. 2018). However, taken with the morphological indicators presented in Section 9.3.1 it could indicate a perturbed morphology due to a merging event in the same direction as the major axis. The similar shape found in the inner and global region could also be a sign of recent merger (see e.g. Despali et al. 2014, 2017, for studies of dark matter simulated haloes).

Interestingly, the major axis of the global ellipse passes through the SZ peak and the X-ray centroid while the major axis of the inner ellipse passes through the SZ peak and the BCG. However, a more quantitative analysis will require using noise realisations, needed in order to evaluate the significance of this effect.

12.1.2 Searching for substructures and compressions in the intra cluster medium

Over the last few years, detailed characterisation of the ICM structure has been achieved in X-ray using dedicated filtering techniques (see e.g. Sanders et al. 2016). More recently, we applied such methods to NIKA resolved distant cluster SZ images (Adam et al. 2018). We employed the same procedure in the following, in order to investigate the ICM pressure sub-structures in XLSSC102. We used the eight RHAPSODY-G simulated clusters at $z = 1$ to interpret our findings. Due to the preliminary nature of our analyses and the presumption that RHAPSODY-G absolute SZ flux are overestimated (see Section 12.3) we conducted a relative (rather than absolute) comparison, by rescaling the RHAPSODY-G clusters surface brightness amplitude to the one of XLSSC102, after convolving the maps to a common resolution of $30''$. By doing so, we ensure that the RHAPSODY-G bulk SZ signal on large scales matches the one seen in our data

12.1.2.1 Pressure peaks

In order to search for sub-structures in the ICM pressure we applied a difference of Gaussian functions (DoG, similarly to the one used for point sources ; see Section 11.2 for definition) filter on the surface brightness maps of XLSSC102 and the eight rescaled RHAPSODY-G simulated clusters. We choose to use Gaussian kernels of FWHM $\theta_1 = 15''$ and $\theta_2 = 60''$, because its allows us to select the signal at scales where NIKA2 is the most sensitive. Additionally, it corresponds to scales of a few hundreds kpc, where merger induced substructures are expected to show up (see e.g. Khatri and Gaspari 2016). We estimated the signal to noise levels following the procedure described in Section 11.2. We estimated the signal to noise that would be expected for the observations of the RHAPSODY-G clusters using the noise level seen in our observations.

The resulting filtered maps are shown in Figure 12.2. The map corresponding to XLSSC102 is in the top left panel and we can see that we detect substructures corresponding to the cluster emission and reaching a signal to noise level SNR > 4. The main peak in the spatial pressure distribution coincides with the SZ surface brightness maximum. We also remark the presence of a secondary peak towards the south east. We will see in the following that this extension roughly coincide with the X-ray emission peak (see Figure 12.4).

When comparing the pressure peak significance with that found in the RHAPSODY-G clusters, we find that it is comparable with clusters such as RG211, which also matches well the optical morphology of XLSSC102 (see Section 9.3) or RG474, which shows a flat and elongated morphology. More spherical and relaxed RHAPSODY-G clusters do not match the signal we observe. In Appendix D, we present the dark matter and SZ surface brightness maps of the complete RHAPSODY-G sample.

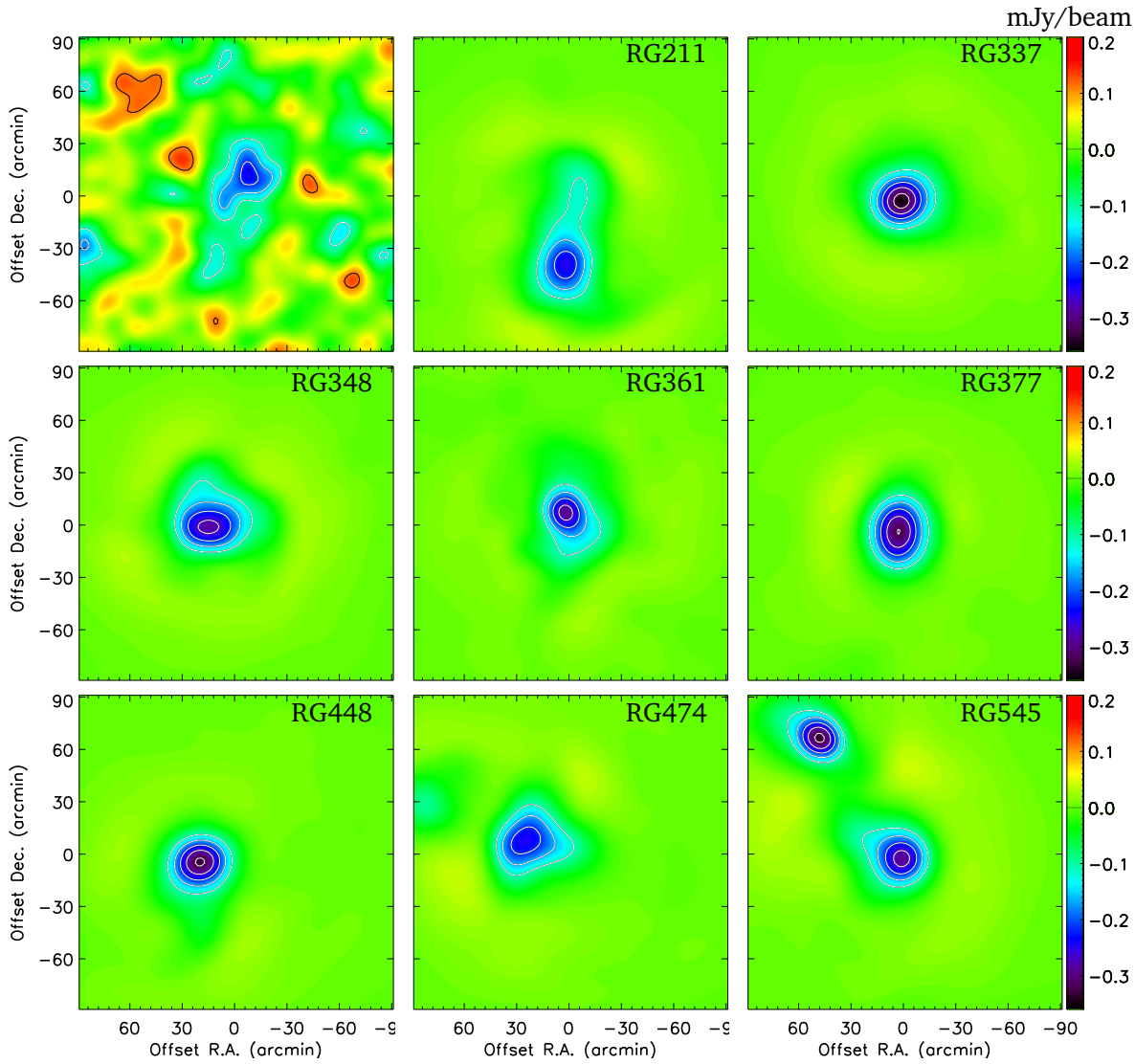

Figure 12.2: Maps filtered with the DoG method to highlight substructures in the pressure. *Top left panel:* map of XLSSC102. *Top middle to bottom right:* RHAPSODY-G simulated clusters at z=1, rescaled to match the SZ amplitude seen in the XLSSC102 observations. The black (respectively white) contours show the signal to noise levels starting at $\sigma = 2$ (respectively -2) and increasing (respectively decreasing) per one sigma step.

Despite relatively low signal to noise, the presence of two pressure peaks and the similarity with RG211 and RG474, which are both merging systems, indicates that XLSSC102 is likely to present substructures that are related to a merging event.

12.1.2.2 Local compression regions

Strong gradient in the SZ surface brightness are related to shocks and mergers induced compressions, or might indicate local peaks of pressure in the core of compact clusters (Adam et al. 2018). In order to search for such features, we applied a Gaussian gradient magnitude (GGM) filter on the surface brightness maps of XLSSC102 and the eight rescaled RHAPSODY-G simulated clusters. The GGM filter is defined following Adam et al. (2018) as:

$$M_{\rm GGM} = \sqrt{(\mathcal{D} * [G_{\theta_0} * M])^2 + (\mathcal{D}^{\rm T} * [G_{\theta_0} * M])^2}, \tag{12.1}$$

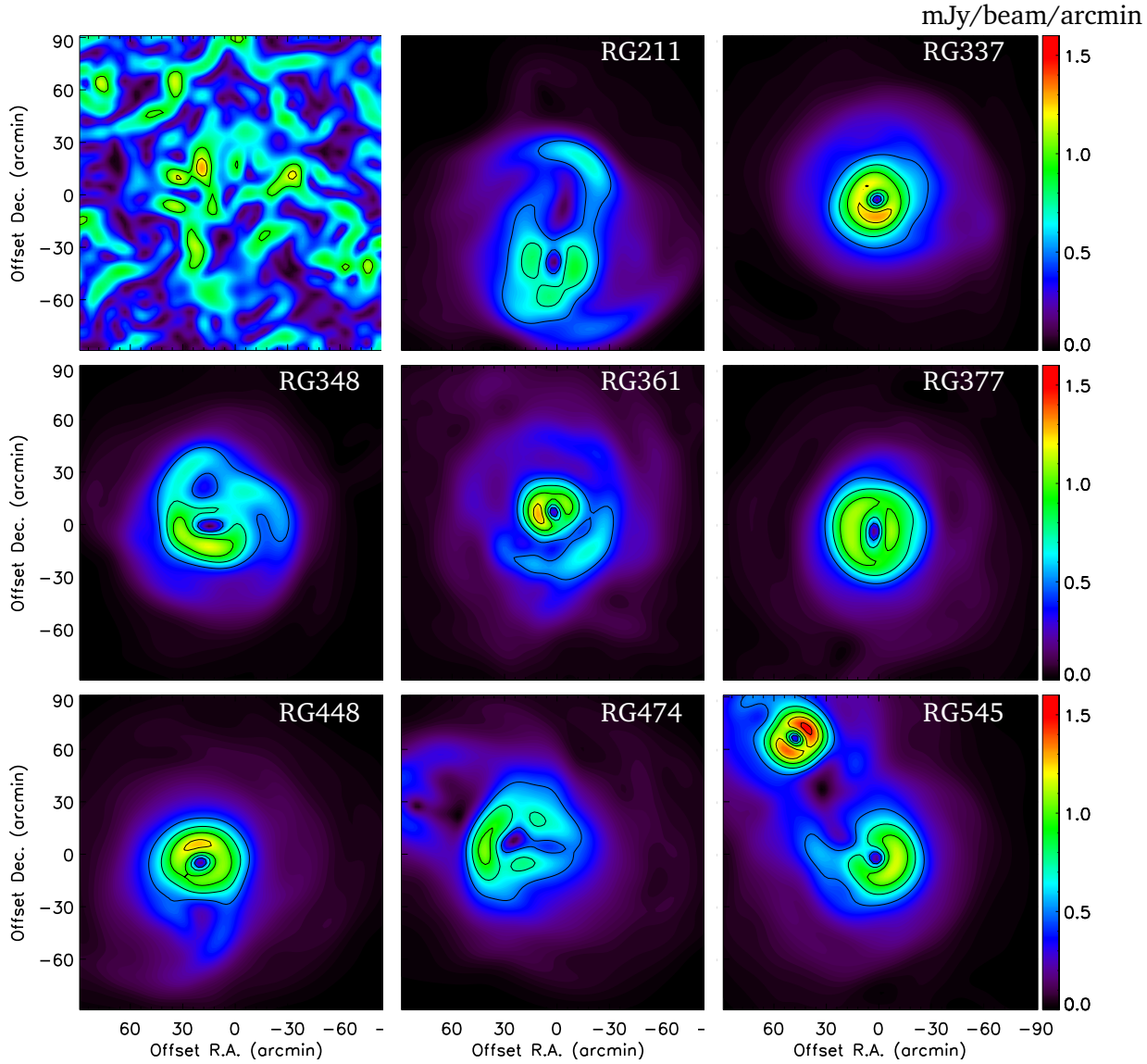

Figure 12.3: Maps filtered with the GGM method to highlight ICM compressions or shocks. *Top left panel:* map of XLSSC102. *Top middle to bottom right:* RHAPSODY-G simulated clusters at $z = 1$, rescaled (in surface brightness) to match the SZ amplitude seen in the XLSSC102 observations. The contours show the signal to noise levels starting at $\sigma = 2$ and increasing per one sigma step.

where $M_{\rm GGM}$ gives the magnitude of the gradient, $G_{\theta_0} * M$ is the input surface brightness map convolve with a Gaussian kernel of FWHM θ_0 and $\mathcal{D}$ is the convolution kernel defined as:

$$\mathcal{D} = \frac{1}{8\Delta\theta} \begin{bmatrix} -1 & 0 & 1 \\ -2 & 0 & 2 \\ -1 & 0 & 1 \end{bmatrix}. \tag{12.2}$$

The signal arising from gradients in SZ surface brightness are expected to be stronger on small scales, in particular if they are related to shocks (i.e. discontinuities in the pressure) (Adam et al. 2018). Thus, we used $\theta_0 = 15''$ as it allows us to search for gradient at the smallest scale allowed by the NIKA2 beam.

The GGM filter is not linear and the noise of the filtered maps $N_{\rm GGM}$ depends on the surface brightness signal S_{true} itself (see Adam et al. 2018, for more details). When the signal to noise level per pixel is high, S_{true} can be approximated by the observed signal $\hat{S}$. The noise

of the filtered map is then estimated using Monte Carlo signal plus noise realisations and by computing, for each realisation i:

$$N^{(i)}_{\rm GGM} = \left(\hat{S} + N^{(i)}\right)_{\rm GGM} - \hat{S}_{\rm GGM}, \tag{12.3}$$

with $N^{(i)}$ the noise affecting the surface brightness map and the index GGM indicating the application of the filter. The signal to noise associated to the filtered map can then be defined as:

$$\mathrm{SNR}_{\rm GGM} = \frac{\hat{S}_{\rm GGM} - \mu_{\rm GGM}}{\sigma_{\rm GGM}}, \tag{12.4}$$

with $\mu_{\rm GGM}$ and $\sigma_{\rm GGM}$ the mean and standard deviation of the noise realisations $N^{(i)}_{\rm GGM}$ per pixel. In our case, however, the SNR of the surface brightness map is low (< 10, per beam, at an effective resolution of $22''$) and $\hat{S}_{\rm GGM}$ is dominated by noise over nearly all the field of view. We thus used $\hat{S}_{GGM}$ directly as an estimation of $N_{\rm GGM}$. The values of $\mu_{\rm GGM}$ and $\sigma_{\rm GGM}$ were computed directly on the $\hat{S}_{GGM}$ map, by taking into account the noise inhomogeneities (as in Section 11.2.1.2). The cluster signal may affect a few pixels (see Figure 12.3), but we have checked that it does not significantly affect the signal to noise estimate. We estimated the corresponding signal to noise as one would expect for the RHAPSODY-G cluster observations using the noise level $\sigma_{\rm GGM}$ computed in our observations, but the mean of the noise $\mu_{\rm GGM}$ was set to zero as the simulations are noise free.

The resulting GGM filtered maps are shown in Figure 12.3. The map corresponding to XLSSC102 is in the top left panel and we can see that the regions with the highest significance reach a maximum signal to noise of 3, which does not allows us to identify any specific feature. We can conclude that they are nearly compatible with noise fluctuations. If we compare our observations with the RHAPSODY-G clusters, we can see that, at this signal to noise, the detectable gradients are mainly caused by peaked emission from compact cores rather than merger induced compressions or shocks. Again, our observations are in agreements with the type of structures seen in clusters with flat surface brightness, such as RG211 or RG474.

We conclude that we need more observations to be able to identify any local compression or shocks in the ICM of XLSSC102.

12.1.3 Comparison to optical and X-ray morphologies

In order to better interpret the cluster morphology and dynamical state, it is important to use different estimators at different wavelengths. We thus combined SZ, X-ray and optical data to achieve a complete characterisation of our cluster.

12.1.3.1 Offset between the different tracers

A multi-wavelength view of XLSSC102 is shown in Figure 12.4. The left panel shows the background subtracted X-ray image[2] of our cluster, smoothed at a resolution of $20''$. The bright (saturated) emission corresponds to an AGN. Arbitrarily linearly spaced contours extracted from this map are shown in black in the middle and left panels. The middle panel shows the SZ surface brightness map, smoothed at a resolution of $20''$. The contours extracted from this map are over-plotted in black and white in the left and right panel respectively. The right panel shows the optical density map presented in Section 9.3.1. The associated contours indicate the background subtracted density contrast at 2, 3 and 4σ and are represented in white in the left and middle panels. The X-ray centroid is indicated by the small cross and the BCG by the red circle.

The first thing we can remark is that the main peak of the optical density is highly offset from the BCG ($d \sim 1.55'/740$ kpc), the X-ray centroid ($d \sim 1.3'/620$ kpc), the X-ray peak

[2]Provided to the XXL consortium by D. Eckert.

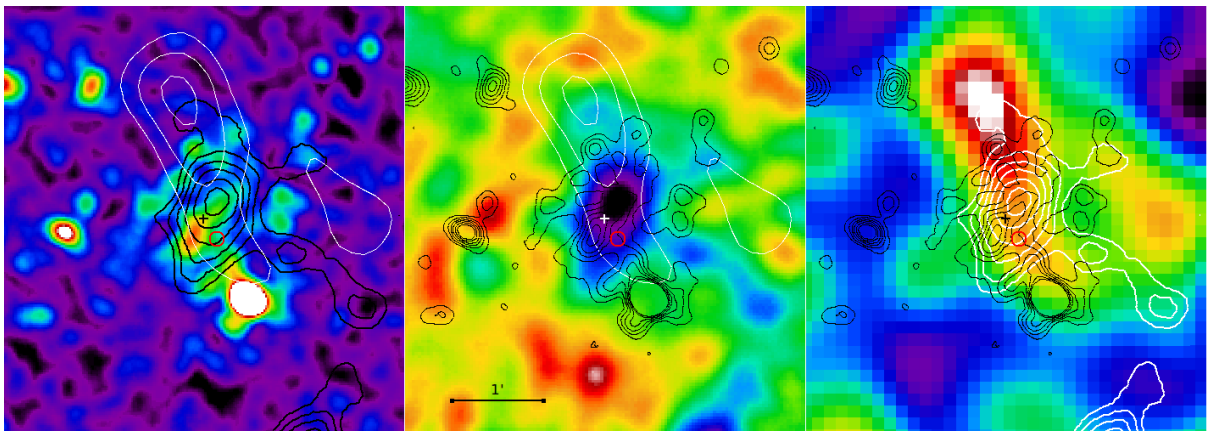

Figure 12.4: Multi-wavelength view of XLSSC102. *Left:* X-ray XMM-Newton background subtracted image with optical density contours overlaid in white and SZ contours in black. *Middle:* NIKA2 SZ image at 150 GHz with X-ray contours in black and optical density contours in white. *Right:* optical density map with X-ray contours in black and optical contours in white. The X-ray and SZ images are smoothed with a FWHM of $20''$. The X-ray contours are arbitrarily linearly spaced. The SZ contours are linearly spaced, with respect to the surface brightness map, and match well the signal to noise levels from $\sigma = -2$ to -7, at the centre of the field (but not on the edges as the noise increases in this region). The optical density contours show the background subtracted signal to noise levels of $\sigma = 2$, 3 and 4. The small cross indicates the X-ray centroid and the red circle indicates the BCG.

($d \sim 1.6'/760$ kpc), and the SZ peak ($d \sim 1.25'/600$ kpc). At smaller scales, we see that the SZ and X-ray peaks are also offset from one another ($d \sim 0.5'/240$ kpc), which means that the peak of the gas pressure does not coincide with the gas density peak, indicating the presence of an overpressure region and a local boost in the gas temperature. The offset between the X-ray and SZ peak has been investigated in hydrodynamical simulations by Zhang et al. (2014). Based on their finding we evaluated that the probability to have an offset of ~ 240 kpc or larger at $z = 1$ a for cluster with masses higher than $M = 1.4 \times 10^{14}$ $M_\odot$ is around 0.2, and thus not uncommon. As found in Section 9.3.1 the BCG is offset from the X-ray centroid, but it is also offset from the X-ray peak ($d \sim 0.3/140$ kpc) and the SZ peak ($d \sim 0.4/190$ kpc). For a high redshift comparison, Mantz et al. (2018) found in their $z = 1.99$ galaxy cluster an offset of $\sim 35''$ (~ 300 kpc at their redshift) between the SZ peak and the X-ray peak (which coincide with the BCG) albeit with lower resolution SZ data. Finally we remark that at large scale, the optical and X-ray morphologies are elongated along the same NE-SW axis, while the X-ray emission in the inner part and the SZ signal seem to follow a NW-SE axis. We also note that, if alignment of the BCG and cluster major axes are observed in clusters up to high redshift (see e.g. West et al. 2017), we do not observe this in our cluster.

Deeper analyses, accounting for the angular resolution and the noise properties on both X-ray and SZ images, are needed to precisely estimate the uncertainties on the offset measurements. Nevertheless, multiple indicators point towards a perturbed cluster in a merging phase.

12.1.3.2 Merging scenario

In order to understand how XLSCC102 can present such high offset values between its different component we over-plotted in Figure 12.5 the SZ, X-ray and optical density contours on composite (R, I, Z) Hyper Suprime-Cam (HSC) Subaru optical image of our cluster constructed to highlight cluster members [3]. While the offsets between the BCG, X-ray peak and SZ peak

[3]The fits files were taken from the HSC public database, http://hsc.mtk.nao.ac.jp/ssp/data-release/, and used for visualisation purposes instead of the CFHTLS because of deeper images.

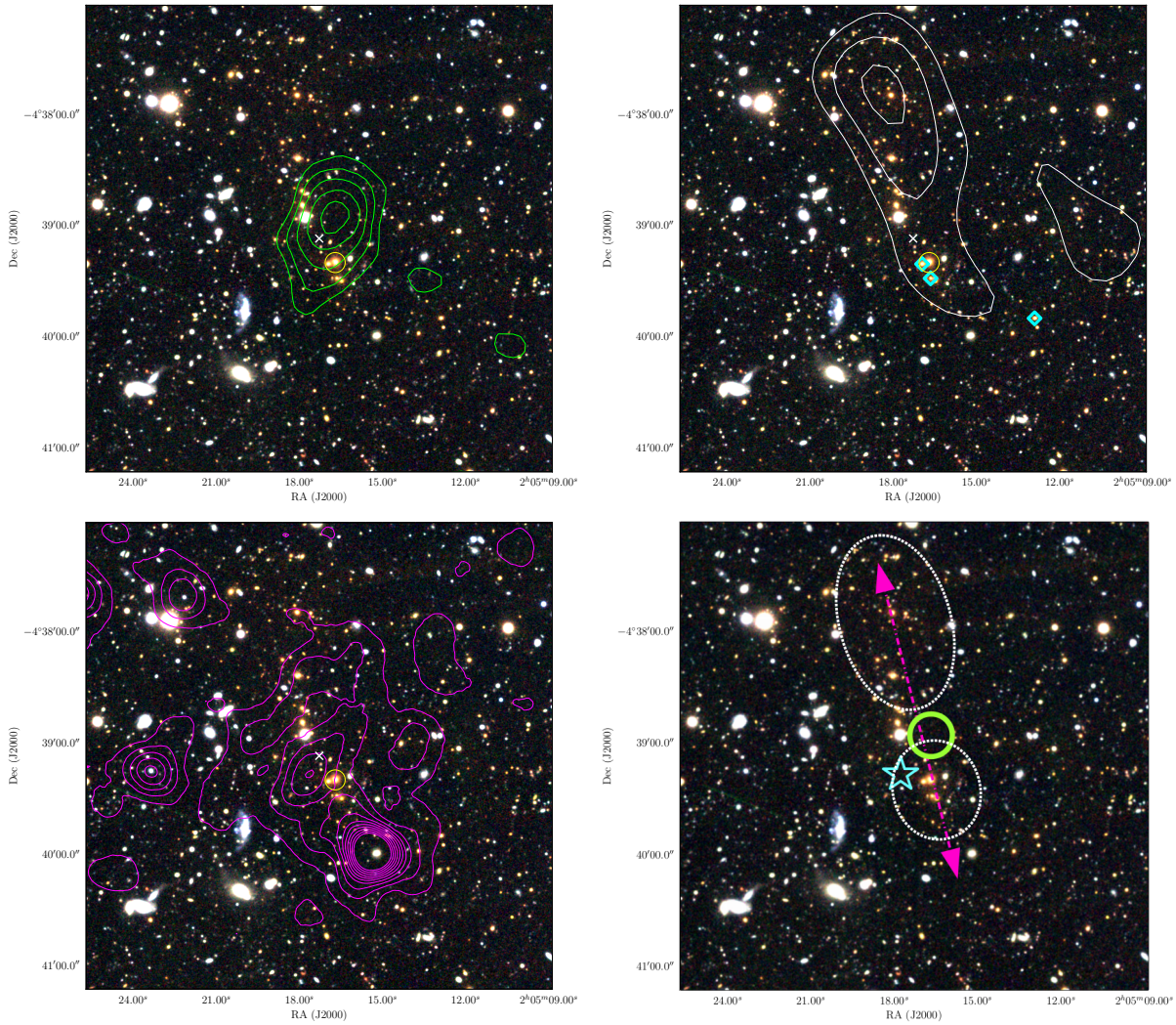

Figure 12.5: Composite HSC optical image (R, I, Z), with SZ (upper left), optical density (upper right) and X-ray (bottom left) contours over-plotted. The SZ contours represent the signal to noise levels, from $\sigma = -3$ to -7. The optical density contours show the background subtracted signal to noise levels of $\sigma = 2$, 3 and 4. The X-ray contours are arbitrarily linearly spaced. The yellow circle indicate the BCG and the white cross show the X-ray centroid. The cyan diamonds indicate galaxies with spectroscopic redshifts around the cluster redshift. The bottom right panel illustrates a merger scenario. The merger axis is shown by the pink arrow, the green circle indicates an over-pressure region, the blue star highlights the gas density and the white ellipses the galaxy groups.

can be understood in the context of a merger, the location of the optical density peak and the fact that it does not coincide with gas emission is more puzzling. We can see that a bright galaxy, possibly a local BCG can be seen at the location of the optical density peak. According to Kolmogorov-Smirnov tests, we can not reject the hypothesis that the galaxies belonging to the northern and southern groups have similar photometric redshift and i' band magnitude distributions. A plausible explanation, illustrated in the bottom right panel of Figure 12.5, is that a group of galaxies passed through the main cluster (located near the X-ray centroid), causing overpressure and disturbances in the gas emission and shifting the optical density peak to the North. The group of galaxies may have been stripped of its gas during this process, which would explain the X-ray and SZ signal elongation toward the North. The enhanced galaxy density in the group, with respect to the main cluster, could be due to the projection of the merger axis along the line of sight. However, in absence of enough spectroscopic members and without lensing measurements, such scenario remains speculative. The merging scenario would indicate that the cluster is in a post-merger state after a collision with a smaller unit. In a future study, comparison with multi-wavelength observations and simulations of merging clusters (see e.g. Maurogordato et al. 2011; Golovich et al. 2017, and "The merging cluster collaboration" web page [4]) could help us reconstruct more precisely the merging event.

12.2 Three dimensional radial profiles of the intra cluster medium properties

Characterising the physics of the ICM allows us to better understand cluster formation processes and is thus crucial for their correct modelling (see e.g. Kravtsov and Borgani 2012). Moreover, it enables to determine the cluster's thermal state (e.g. cool-core or non-cool-core), which is known to impact scaling relations used in cosmological studies (see e.g. O'Hara et al. 2006), and to measure the total mass under the hydrostatic equilibrium hypothesis. The modelling of the pressure profile is also important for the detection of clusters using unresolved SZ observations (as from matched-filtering technics, see, e.g., Melin et al. 2006; Hasselfield et al. 2013), or when deriving cosmological constraints from diffuse SZ signal over large regions of the sky (e.g., Planck Collaboration et al. 2016f).

In the following, we used and adapted the `IDL` package `ICMtools`, constructed for the NIKA2 collaboration in Adam (2015), in order to combine SZ and X-ray data and derive the ICM radial profiles. In this section, we present the methodology adopted and the preliminary results obtained on XLSSC102.

12.2.1 Physical description of the intra cluster medium

The SZ surface brightness $S_{\rm SZ}$ is related to the ICM pressure via:

$$S_{\rm SZ}(\nu) = \frac{\sigma_{\rm T}}{m_e c^2} \int f(\nu)(1+\delta(T_e))\, P_e\, d\ell, \tag{12.5}$$

where $\sigma_{\rm T}$ is the Thomson cross section, $m_e c^2$ the electron rest mass energy, $f(\nu)$ the SZ frequency spectrum, T_e the gas temperature, and $\delta(T_e)$ give relativistic corrections (Itoh et al. 1998), which are important for $T_e > 10$ keV, but are expected to be negligible in our case. The X-ray surface brightness $S_{\rm X}$ is related to the gas density n_e through:

$$S_{\rm X} = \frac{1}{4\pi(1+z)^4} \int n_e^2 \Lambda(T_e, Z) d\ell, \tag{12.6}$$

where $\Lambda(T_e, Z)$ is the cooling function, which depends on temperature and the ICM metallicity Z, and is roughly proportional to $\sqrt{T_e}$.

[4] http://www.mergingclustercollaboration.org/

By combining the pressure P_e obtained from SZ observations with the gas density n_e obtained from X-ray observations, and under the assumption of spherical symmetry, it is possible to derive the 3-D radial profiles of other thermodynamic quantities (see, e.g., Mroczkowski et al. 2009; Adam et al. 2015; Ruppin et al. 2018). For instance, the temperature is given by:

$$k_{\rm B}\, T_e(r) = P_e(r)/n_e(r), \tag{12.7}$$

under the ideal gas assumption, with $k_{\rm B}$ the Boltzmann constant. It is connected to the depth of the cluster potential well, but also to its dynamical and thermal states, providing precious information. The entropy K, which records the thermal history of the cluster, can be defined as (see Voit 2005):

$$K(r) = \frac{P_e(r)}{n_e(r)^{5/3}}. \tag{12.8}$$

The SZ flux, which is proportional to the cluster total thermal energy, is given by the cylindrically integrated Compton parameter, expressed as a function of the pressure as:

$$Y_{\rm cyl}(R) = 2\pi \int_0^R \left(\frac{\sigma_{\rm T}}{m_e c^2} \int P_e d\ell \right) r dr, \tag{12.9}$$

or by the spherically integrated Compton parameter:

$$Y_{\rm sph}(R) = 4\pi \frac{\sigma_{\rm T}}{m_e c^2} \int_0^R P_e(r) r^2 dr. \tag{12.10}$$

Note that the two definitions are equal when $R \to \infty$.

The matter distribution can also be constrained, as the gas mass profile is given by:

$$M_{\rm gas}(R) = 4\pi \int_0^R \mu_e m_p n_e(r) r^2 dr, \tag{12.11}$$

with $\mu_e = 1.15$ the mean molecular weight per electron and m_p the mass of the proton. The total hydrostatic mass can be computed as:

$$M_{\rm HSE}(r) = \frac{-r^2}{G \mu_{\rm gas} m_p n_e(r)} \frac{dP_e(r)}{dr}, \tag{12.12}$$

with $\mu_{\rm gas} = 0.61$ the mean molecular weight per gas particle, computed from primordial abundances from Anders and Grevesse (1989), and G the gravitational constant. Hydrostatic masses are known to be biased low with respect to true masses because of the contribution of non thermal pressure support and bulk motions in the gas (see Ettori et al. 2013, for a review). The total true mass is then related to the hydrostatic mass via the hydrostatic bias $b_{\rm HSE}$ as:

$$M_{\rm HSE}(r) = (1 - b_{\rm HSE}) M_{\rm tot}(r), \tag{12.13}$$

where $b_{\rm HSE}$ may also depend on the radius, the mass scale or other cluster properties, but little is know about the hydrostatic bias to date. By combining Eq. 12.11 and 12.12 we can also define the gas fraction profile as:

$$f_{\rm gas}(r) = \frac{M_{\rm gas}(r)}{M_{\rm tot}(r)}, \tag{12.14}$$

which provides a probe of the relative spatial distribution of dark matter and gas in clusters. Finally, the overdensity contrast at distance R can be calculated as:

$$\Delta(R) = \frac{3 M_{\rm tot}(R)}{4\pi R^3 \rho_c(z)}. \tag{12.15}$$

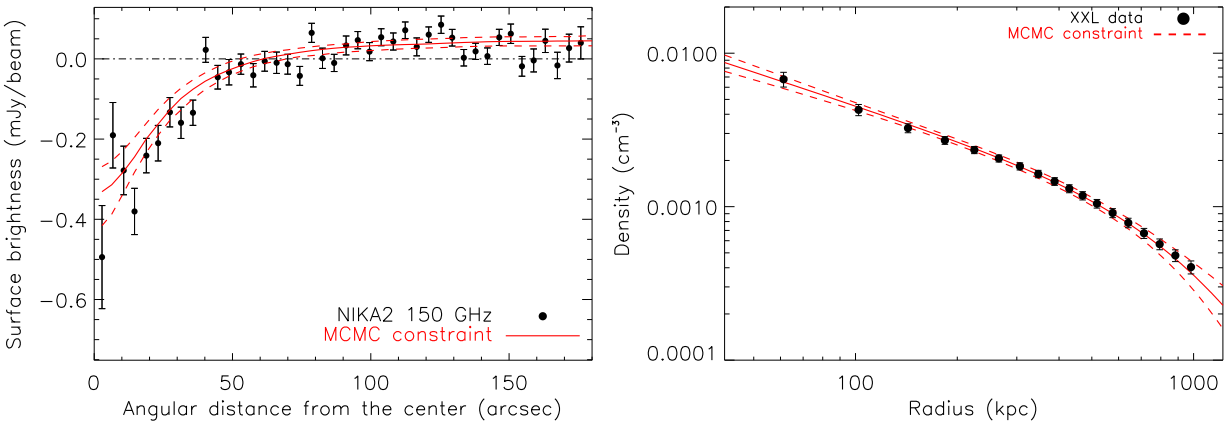

Figure 12.6: SZ and X-ray input data for the combined analysis. *Left:* SZ surface brightness profile, centred on the X-ray centroid position. The black points show the inverse variance weighted mean surface brightness in each annulus. *Right:* X-ray density profile, centred on the X-ray centroid position. The error bars indicate the 68% c.i., but we note that they only represent the diagonal of the covariance matrix as errors are correlated. The red lines indicate the median profile constraints and the dashed lines the 68% c.i. computed with the MCMC fitting procedure.

12.2.2 Input data

The following data were used in order to derive the ICM physical profiles.

NIKA2 surface brightness map We used the NIKA2 150 GHz surface brightness map, re-projected in $4'' \times 4''$ pixel and a $5'$ field of view in order to lighten the numerical computation. The associated noise covariance matrix and the transfer function of the data reduction were computed as described in Section 10.3.2.4 and are also taken into account in the analysis. The map is treated as a 1D vector and as we consider a spherical model, it conveys the same information as the surface brightness profile presented in the left panel of Figure 12.6.

XMM X-ray density profile The X-ray density profile of XLSSC102 used in this preliminary analysis was obtained[5] following a new methodology (Eckert et al. in prep), which is an evolution of the multiscale forward-fitting de-projection method presented in XXL Paper XIII. It is built from the soft band [0.5–2 keV] XXL mosaic image and takes into account the complex XXL effective exposure. Point sources from the XXL catalogue (Chiappetti et al. 2018) are identified and masked within 30 arc-second regions. The profile is represented on the right panel of Figure 12.6. The data points are correlated and we thus take their covariance matrix into account in the fitting procedure.

Planck total SZ flux We used the value of the total SZ flux $Y_{\rm tot}^{Planck}$ measured in the Planck map (see Section 9.2.2) as an extra constraint. However, we note that, considering its large uncertainty and the small angular extent of the source, this data point does not add much information compared to NIKA2 alone.

12.2.3 Methodology

In the following we present the parametric modelling of the pressure and density profile and we give an overview of the fitting algorithm.

[5] It was computed and provided by D. Eckert.

12.2.3.1 Modelling

Pressure profile model We modelled the pressure profile by a generalised Navarro Frenk and White model (gNFW, Nagai et al. 2007a), since it allows us to describe the profile from the core to the outskirts. It is given by:

$$P_e(r) = \frac{P_0}{\left(\frac{r}{r_p}\right)^c \left(1 + \left(\frac{r}{r_p}\right)^a\right)^{\frac{b-c}{a}}}, \tag{12.16}$$

with P_0 a normalisation constant, $r_p = R_\Delta/c_\Delta$ the characteristic radius expressed with c_Δ describing the gas concentration, and a, b and c the parameters describing the slope of the profile at radii $r \sim r_p$, $r \gg r_p$ and $r \ll r_p$, respectively.

Density profile model We model the electron density profile by a *simplified Vikhlinin Model* (SVM Vikhlinin et al. 2006), given by:

$$n_e(r) = n_{e0} \left[1 + \left(\frac{r}{r_c}\right)^2\right]^{-3\beta/2+\alpha/4} \left(\frac{r}{r_c}\right)^{-\alpha/2} \left[1 + \left(\frac{r}{r_s}\right)^\gamma\right]^{-\epsilon/2\gamma}. \tag{12.17}$$

In this expression, n_{e0} is the normalisation ; the first term in bracket corresponds to a β-model with characteristic core radius r_c and outer slope β ; the second term allows for modification of the inner slope according to the parameter α ; and the last term allows for a change of slope near the radius r_s, given by the parameter ϵ, with a transition region width controlled by γ. We aim at an accurate description of our data with a minimal set of parameters. After testing different sets of parameters, and given the error bars on the measured profile, we found that the second term, i.e. the parameter α, was necessary to model the core of XLSSC102. On the other hand, we found that adding the last term was unnecessary and we set $\epsilon = 0$. The parameters r_s and γ were set to 1 kpc and 3, respectively, but their values are irrelevant for $\epsilon = 0$.

12.2.3.2 Description of the MCMC fitting algorithm

The fitting algorithm package, `ICMtools`, is described in details in Adam (2015) and we briefly summarise its operating principle in the following. The approach consists in sampling the parameter space of equations 12.16 and 12.17 using a Markov chain Monte Carlo algorithm and evaluating at each step the likelihood of the pressure and density profiles models, given the data.

NIKA2 SZ surface brightness model The expected SZ surface brightness, as would be observed by NIKA2, is computed by integrating the pressure along the line of sight, accounting for the NIKA2 instrumental response. The surface brightness at projected radius R is given by:

$$S_{\rm SZ}(R) = \frac{2\sigma_{\rm T}}{m_e c^2} \int_R^{R_{\rm max}} C_{\rm Jy/beam/}{}_y \times P_e(r) \frac{r}{\sqrt{r^2 - R^2}} dr, \tag{12.18}$$

where $R_{\rm max}$ is the maximum radius for the integration, chosen to be large enough to not loose any signal (typically $5R_{500}$), and $C_{\rm Jy/beam/}{}_y$ the calibration coefficient factor between surface brightness and Compton parameter described in Section 10.3. The instrumental transfer function including the beam and the filtering due to the data reduction (see Section 11.2.2.3) is applied to the surface brightness model. We finally obtain a model that can be directly compared to the NIKA2 data.

X-ray density profile The X-ray density profile was processed upstream so that we directly compare it to the model and no further processing is required.

Table 12.1: Prior on the model parameters.

	Pressure profile				
Parameter	P_0	r_p	a	b	c
Unit	keV cm^{-3}	kpc	–	–	–
Value	[0,+∞]	[50,+∞]	1.33 ± 0.3325	4.13 ± 1.0325	0.31 ± 0.0775
Prior type	Flat	Flat	Gaussian	Gaussian	Gaussian
Prior origin	Physical	Numerical	Planck UPP $\pm$ 25% standard deviation		

	Density profile						
Parameter	$n_{e,0}$	r_c	β	α	r_s	γ	ϵ
Unit	cm^{-3}	kpc	–	–	kpc	–	–
Value	[0,+∞]	[0,2000]	[0,5]	[0,+∞]	1	3	0
Prior type	Flat	Flat	Flat	Flat	Fixed	Fixed	Fixed
Prior origin	Physical	Model	Model	Model	Model	Vikhlinin et al. (2006)	Model

	Nuisance parameters	
Parameter	$Z_0^{\rm SZ}$	$Z_0^{\rm X}$
Unit	mJy/beam	cm^{-3}
Value	[$-\infty$,+∞]	0
Prior type	Flat	Flat
Prior origin	Data related	

Planck total SZ flux Given a pressure profile, we compute the total integrated Compton parameter following equation 12.9. This quantity can be directly compared to the total flux as measured from Planck data.

Physical and nuisance parameters The fitted variables are the five parameters of the gNFW model, the four free parameters remaining of the SVM model plus a set of nuisance parameters: in our case the zero level of the NIKA2 surface brightness map $Z_0^{\rm SZ}$ (see Table 12.1). The residual zero level in the density profile, $Z_0^{\rm X}$, is set to 0 since the X-ray background have been subtracted in the data we have in hand, and possible residuals are accounted for in the error bars.

Likelihood function In a Bayesian formalism, the probability density function of the parameters, given the data D and the priors $\pi(\vec{\theta})$ associated to the parameters, is computed as:

$$P(\vec{\theta}|D) \propto \mathcal{L}(\vec{\theta}|D) \times \pi(\vec{\theta}), \tag{12.19}$$

with $\mathcal{L}(\vec{\theta}|D)$ the likelihood of the model computed for the set parameter $\vec{\theta}$.

The parameter space can be described by $\vec{\theta} = \{\theta^{(1)}, \theta^{(2)}, ..., \theta^{(10)}\}$ with $\theta^{(i)}$ a model or nuisance parameter, and the data by $D = \{D^{NIKA2}, D^{XMM}, D^{Planck}\}$ having the dimension $n = N_{\rm pix} + N_{\rm bin} + 1$ (number of pixel of the NIKA2 SZ map, number of bin in the X-ray density profile and one for the Planck integrated flux). The likelihood associated to the model $M(\vec{\theta})$ can thus be expressed by:

$$\begin{aligned} \mathcal{L}(\vec{\theta}|D) &= \mathcal{L}(\vec{\theta}|D^{NIKA2}) \times \mathcal{L}(\vec{\theta}|D^{XMM}) \times \mathcal{L}(\vec{\theta}|D^{Planck}) \\ &= \frac{1}{\sqrt{(2\pi)^n |det(C)|}} \exp\left(-\frac{1}{2}\sum_{ij}\left(D - M(\vec{\theta})\right)_i C_{ij}^{-1}\left(D - M(\vec{\theta})\right)_j\right) \end{aligned} \tag{12.20}$$

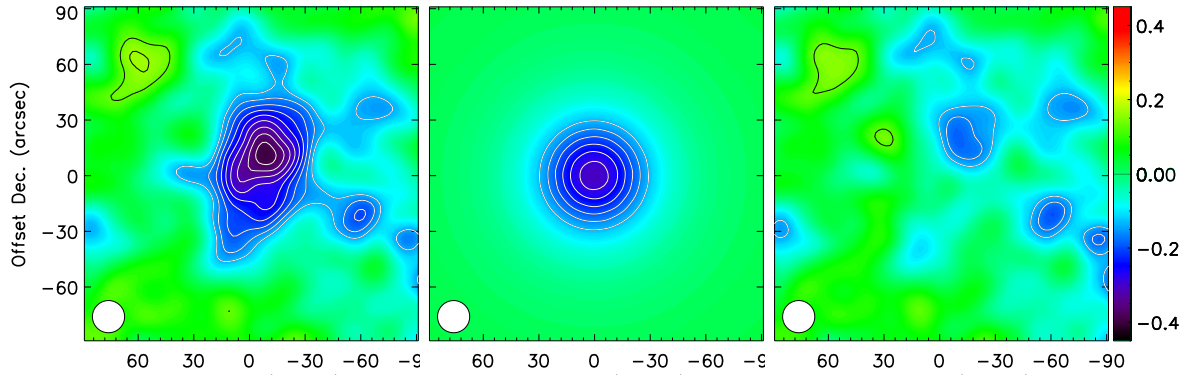

Figure 12.7: Comparison between the NIKA2 data and the best-fit model. *Left:* input SZ map. *Middle:* model map. *Right:* residual.

with $C_{ij} =< (D - M(\vec{\theta}))_i (D - M(\vec{\theta}))_j >$ the noise covariance matrix. The latter is constructed by assuming no correlation between the different data sets and is thus block diagonal, each block being the covariance matrix of each dataset.

Priors The priors chosen for the parameters are presented in Table 12.1. They arise both from physical and numerical considerations. We also added a prior on the combination of parameters to force $dM/dr \geqslant 0$, i.e. ensuring the mass profile to increase with the radius.

Chain evolution and MCMC fitting constraints Finally, the fitting algorithm uses a Metropolis–Hastings method of MCMC sampling to constrain the parameters. Once the chains converge and the burn-in is removed, we obtain the PDF sampling in the 11 dimensions parameter space. The PDF of one parameter can then be obtained by marginalising over the other ten.

In Figure 12.6, we provide the MCMC models together with the data, in the case of the NIKA2 SZ surface brightness profile and the X-ray density profile. We can see that the model provides a good description of the data at all radial scales. In the case of NIKA2, we also provide the comparison between the model and the data at the map level in Figure 12.7. We can see that overall the model provides a good description of the data. Nonetheless, as the morphology of the cluster is elongated and the model centred on the X-ray centroid, which does not agree with the SZ centre (see Section 12.1.3), residuals are visible at the level of $> 3\sigma$ on the map. In particular, the north-west region of the cluster present a significant excess. This agrees with XLSSC102 having a disturbed morphology and is consistent with the merger scenario proposed in Section 12.1.3.2.

12.2.4 Thermodynamic and mass radial profiles characterisation

With the MCMC chains in hand, we construct the thermodynamic and mass profiles using the relations presented in Section 12.2.1. To do so, we compute the median and the 68% confidence intervals of the derived quantities, at each radius using all the MCMC sample.

The thermodynamic and mass profiles of XLSSC102 are shown by the blue regions in Figure 12.8. We provide: the pressure, the density, the temperature, the entropy, the SZ flux, the gas mass, the hydrostatic mass and the gas fraction profiles. The gas fraction is computed for different value of the hydrostatic mass bias: $b_{\rm HSE} = 0$, 0.2 and 0.4. We present the profiles up to ~ 1 Mpc, which corresponds to the maximum radius at which the X-ray signal is detected ($\sim 2'$). We note that we expect $R_{500} \sim 0.7$ Mpc from scaling law measurements (see Table 9.2), which roughly correspond to $R_{200} \sim 1$ Mpc. We thus probe the thermodynamic and mass profiles of XLSSC102 up to $\sim R_{200}$. We can see that we obtain tight constraints, considering the

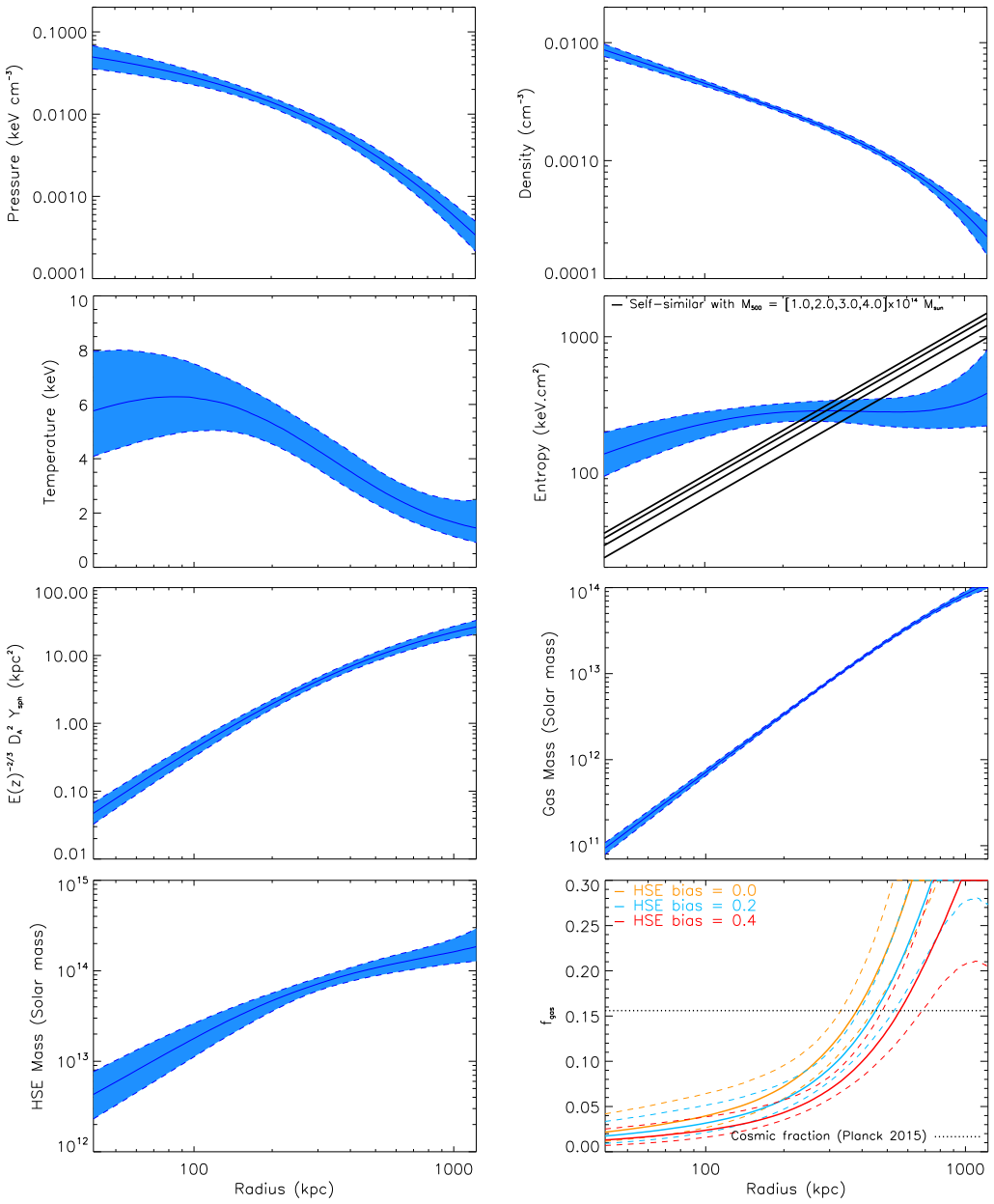

Figure 12.8: Radial physical profiles of XLSSC102. From left to right and top to bottom: pressure, density, temperature, entropy, SZ flux, gas mass, hydrostatic mass and gas fraction profiles. The blue shaded regions shows 68% c.i. around the median profiles. Self similar entropy expectations from Voit (2005) are indicated for different masses. The gas fraction is computed assuming $b_{\rm HSE} = 0$ (yellow), 0.2 (cyan) and 0.4 (red). The value of the cosmic gas fraction is shown by the dotted line, computed as $\frac{\Omega_b}{\Omega_m}$ under the assumption that all the baryons are in the hot gas phase, with baryonic and matter density taken from Planck Collaboration et al. (2016e).

moderate depth of the XXL and NIKA2 data (as we only obtain ∼1/3 of the observing time we requested for on this cluster).

As expected, we find that the pressure is decreasing with radius. The constraint is tighter at intermediate scales, where NIKA2 is the most sensitive. Indeed, on small and large scales, the beam and the transfer function filter out the signal. Additionally, the noise correlations and the uncertainties in the zero level boost the error bars on large scales. The pressure distribution

will be discussed in details in the following Sections of this Chapter.

Similarly, the density profile is best constrained at intermediate scales. We notice that the profile is more peaked than a simple β-model. On large scales, we notice that the profile remains relatively flat up to the outskirts, being nearly consistent with a single power law at all scales.

The temperature profile reaches about 6 keV in the cluster centre ($r < 150$ kpc), and drops by a factor of ~ 4 towards the outskirts. This steep decrease is larger than expectations from studies of more nearby cluster samples (typically a temperature drop by a factor of $2.5 - 3$ at R_{200} with respect to the inner regions, see Eckert et al. 2013b; Reiprich et al. 2013). The temperature profile we measure is consistent with that of a morphologically disturbed cluster, but not with that of a cool-core. We note that our temperature profile is compatible with the XMM cluster temperature measured within 300 kpc (see Table 9.2).

The entropy profile of XLSCC102 is very flat. We can see an excess of entropy in the inner region, with respect to the pure gravitational collapse expectation (shown for different masses by the black lines, see Voit 2005), which is expected for disturbed clusters (e.g. Pratt et al. 2010). More surprisingly, we observe that the entropy is lower than the pure gravitational collapse expectation beyond 400 kpc. This can be seen in unrelaxed clusters (see e.g. Eckert et al. 2013b; Tchernin et al. 2016) due to gas density inhomogeneities that may affect the density measurement, as the X-ray emissivity is sensitive the density squared.

The spherically integrated Compton parameter smoothly increases with radius. Following the constraints on the pressure, it presents larger uncertainties at intermediate scales. This profile will be used in Section 12.3 when studying scaling relations.

Similarly, the gas mass increases with radius, and is nearly consistent with a power law.

The hydrostatic mass profile is relatively steep in the centre and flattens at $r \sim 400$ kpc. The profile reaches about 2×10^{14} $M_\odot$ at 1 Mpc, indicating that the hydrostatic mass we measure is significantly lower than what we expect from our various mass estimations (see Section 9.2).

Finally, the gas fraction increases with the distance from the centre. Surprisingly, it becomes larger than the cosmic gas fraction at $r \gtrsim 400$ kpc. We note that a high hydrostatic bias would diminish the gas fraction, but an excessively large values would be necessary to avoid exceeding the cosmic fraction. However, this behaviour is also seen in non-relaxed clusters (see e.g. Eckert et al. 2013a) and could be attributed to gas inhomogeneities biasing high the density measurement.

All the recovered physical radial profiles of XLSSC102 are in agreement with the cluster being unrelaxed. Additionally, based on the definitions of Section 12.2.1, several quantities indicate that the pressure is too low compared to the X-ray density - or the other way around - when reaching radii larger than 400 kpc (see e.g. Eq 12.8, 12.12 and 12.11). As discussed above, several physical reasons could be invoked, and in particular the presence of gas inhomogeneities, which can bias high the recovered density, and are common in merging systems. However, as our NIKA2 analysis is preliminary (for instance the map calibration is not final) it is important to first verify the consistency of our measurements.

12.2.5 Comparison of the NIKA2 surface brightness profile to ACT expectations

The thermodynamic characterisation of XLSSC102 points towards a deficit of pressure or an excess of density at $r \gtrsim 400$ kpc. We took advantage of the ACT detection of XLSSC102, also in the SZ (see Section 9.2), in order to test if this effect could be due to a mis-calibration or uncontrolled systematics in the NIKA2 data. The resolution of ACT does not allow us to measure the cluster surface brightness profiles and the detection and mass estimation is based on a match filter that uses the Arnaud et al. (2010) UPP. Therefore, we used their estimated mass to reconstruct surface brightness profiles of XLSSC102 and compared them to the data obtained with NIKA2. The result is shown in Figure 12.9: the black points shows NIKA2 measurements and the pink, red and blue lines show different form of surface brightness profiles (drawn from different pressure profiles, but with the same mass normalisation, see Arnaud et al. 2010)

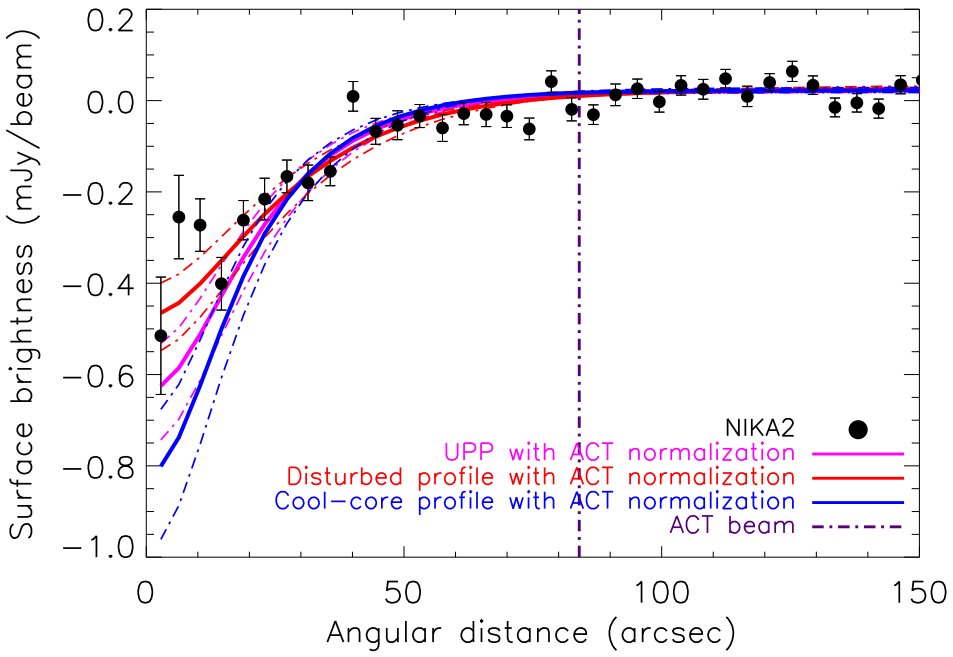

Figure 12.9: Comparison of the NIKA2 surface brightness profile (black points) to that predicted from the ACT detection (Hilton et al. 2018). The pink, red and blue lines show surface brightness profiles drawn from pressure profile models from Planck and REXCESS (cool-core and morphologically disturbed) evaluated at the cluster redshift and considering the mass estimated by ACT. The dash-dotted line indicate the ACT beam, showing that ACT cannot distinguish between the different scenarii.

evaluated at the redshift and ACT mass of our cluster. We can see that the profile used for the ACT detection predicts a higher inner flux than what we measure, but a lower signal on large scales, and that NIKA2 measurement is in better agreement with a disturbed cluster profile. This results indicate that the NIKA2 data are coherent with ACT, for a disturbed cluster profile, at a mass $M_{\rm HSE} = 3.1^{+0.5}_{-0.4} \times 10^{14}$ M$_\odot$ (Hilton et al. 2018), and that a pressure deficit in the outskirts is unlikely. The more plausible explanation to explain the thermodynamic properties of XLSSC102 is thus that the behaviour of the profiles is due to an excess of gas density at $r \gtrsim 400$ kpc.

12.2.6 Evidence for gas inhomogeneities?

The low temperature profile, the flat entropy that goes below pure gravitational collapse expectation at $r > 400$ kpc, while the gas fraction exceeds the cosmic value and the lower than expected hydrostatic mass of XLSSC102, all suggest the presence of gas inhomogeneities or clumps (see e.g. Nagai and Lau 2011; Ettori et al. 2013; Eckert et al. 2013b, 2015). This is expected in the case of merging clusters and in the clusters outskirts (see e.g. Reiprich et al. 2013; Eckert et al. 2012) for which and where X-ray masses are known to suffer from biases (see e.g. Nagai et al. 2007b; Piffaretti and Valdarnini 2008; Burns et al. 2010).

Gas clumpiness caused by substructures bias high the X-ray density, which in turns, bias the thermodynamic and mass profiles. As we showed and as can be seen from Figure 12.4, the X-ray morphology is elongated towards the north. However, we note that the bias due to asymmetric morphology alone is expected to be low and mainly affects the cluster core (see e.g. Piffaretti et al. 2003). On the other side, considering the post-merger scenario, the presence of a substructure in the northern sector is likely. As shown by Tchernin et al. (2016), the correct interpretation of the thermodynamic and mass measurements would necessitate to mask the

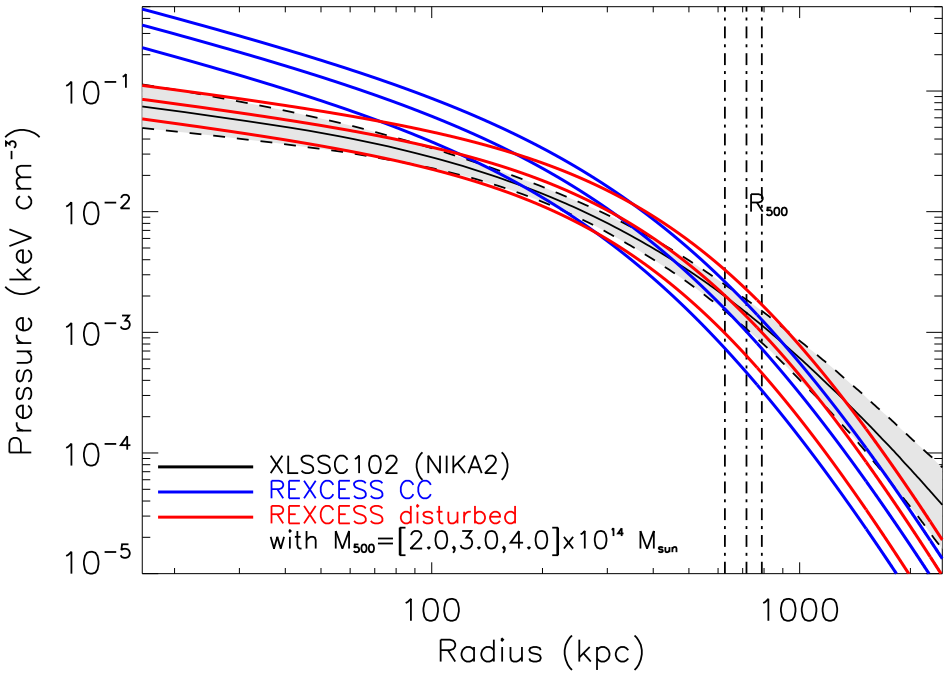

Figure 12.10: Comparison of the NIKA2 pressure profile of XLSSC102 to that of the REXCESS (Arnaud et al. 2010) cool-core (blue) and disturbed (red) cluster samples. The REXCESS profiles are evaluated at z=0.97 and at different masses, increasing from bottom to top, as indicated in the legend. The dashed lines indicate the corresponding values of R_{500}.

substructure in the X-ray analysis.

Unfortunately, in the present study (and as would also be the case with future mission such as eROSITA) the shallowness of the X-ray data does not allow us to efficiently detect and mask the substructures. One solution that will be explored in a future study is to split the cluster into northern and southern regions (see e.g. Ruppin et al. 2018, for an application in SZ) and compare the profiles and integrated quantities in the two parts. This could also allow us to constrain the clumpiness factor profile in the northern region.

12.3 Global properties and comparison to standard evolution expectations

In this section we compare the pressure profiles of XLSSC102 to the universal pressure profile as calibrated using local clusters, to search for deviations in the mass and redshift regime we are probing. We also discuss the mass estimation and compare integrated quantities to scaling relations from the literature.

12.3.1 Pressure profile comparison

The form of the cluster pressure profile measured from X-ray data was found to be "universal" by Arnaud et al. (2010) in their sample of 33 low redshift clusters and up to R_{500}, once rescaled by mass and redshift according to the standard the self-similar model. Nonetheless, the exact form of the profile depends on the thermal state of the clusters (cool-core or morphologically disturbed), but not its integration (which is related to the mass). Latter, Planck Collaboration et al. (2013) extended this result up to $3 \times R_{500}$ using SZ observations of 62 local clusters. Since then, some studies have been focused in measuring the pressure up to the cluster outskirts (see e.g. Eckert et al. 2017) and up to high redshifts (see e.g. McDonald et al. 2014; Adam

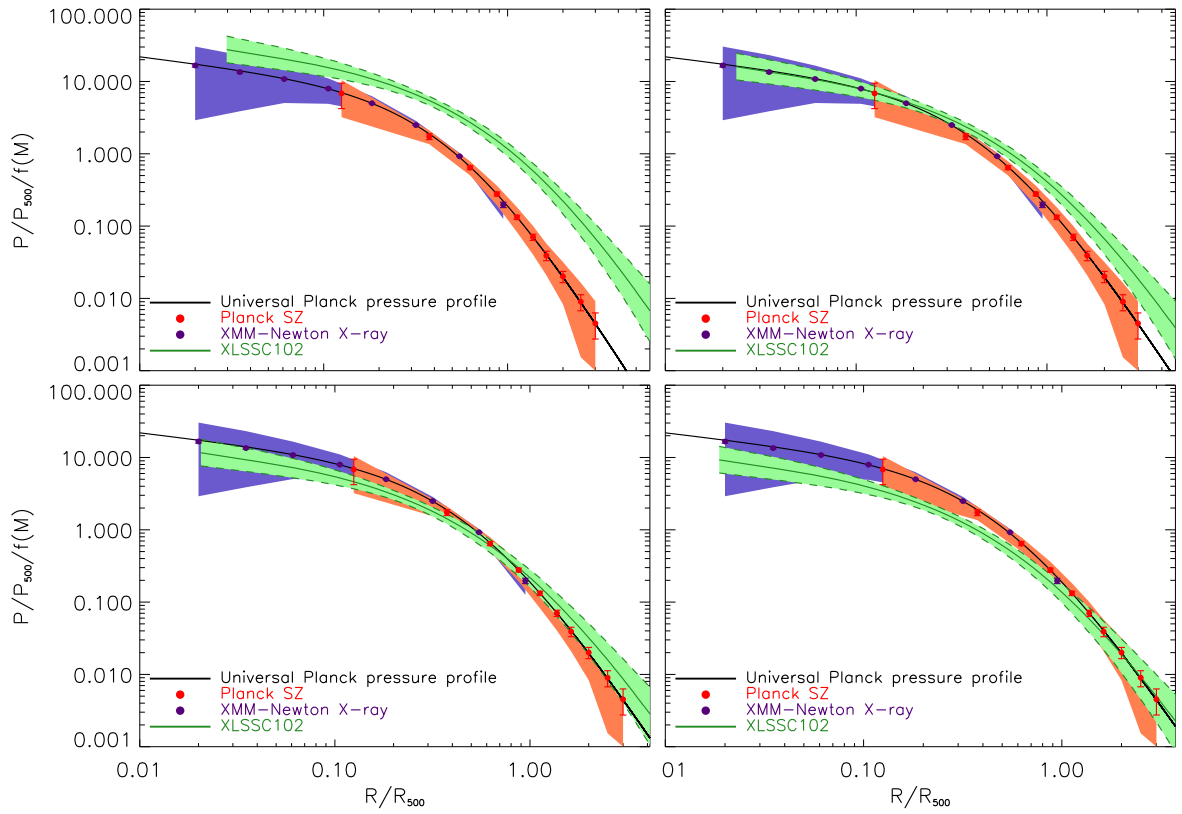

Figure 12.11: Comparison of the NIKA2 pressure profile of XLSSC102 (in green) to that from Planck Collaboration et al. (2013). The error bars on the Planck and XMM profiles show the uncertainties and the shaded region show the intrinsic scatter. The four panels are for different mass estimates: $M_{500} = (1, 2, 3 \text{ and } 4) \times 10^{14}$ $M_\odot$ from left to right and top to bottom. Following the methodology used in Planck Collaboration et al. (2013) and for a meaningful comparison, P_{500} is computed from scaling laws.

et al. 2015; Bourdin et al. 2017; Ghirardini et al. 2017). SZ observations probe directly the pressure in a redshift independent manner when resolved observations are available. They are particularly useful for distant cluster, and are now being possible thanks to the advance of resolved SZ instruments such as NIKA2 or MUSTANG2 (NIKA2 Collaboration et al. 2018; Dicker et al. 2014). Despite recent progress, the universality of the pressure profile in high redshift clusters, down to low masses and up to large radii is barely tested to date. It is thus of paramount importance to test the pressure profiles of high redshift clusters, considering their strong cosmological constraining power and the fact that they are largely probed by unresolved SZ surveys such as SPT (Bleem et al. 2015) or ACT (Hilton et al. 2018), whose detection pipelines relies on the form of the pressure profile.

Pressure profile and cluster dynamical state We compared our pressure profile to that of the REXCESS sample of local clusters from Arnaud et al. (2010) in Figure 12.10. The profiles from the cool-core (blue lines) and disturbed (red lines) REXCESS samples are evaluated at $z = 0.97$ for different masses. The scatter among the profiles is not shown here and is of the order of 80% at $0.03 \times R_{500}$ and less than 30% beyond $0.2 \times R_{500}$ for the full REXCESS sample (see Arnaud et al. 2010). We can see that the XLSSC102 pressure profile is compatible with the ones of low redshift and higher mass disturbed clusters. The compatibility is best for a mass $M_{500} = 3 \times 10^{14}$ $M_\odot$, which is consistent with our estimations from scaling laws (see Section 12.3.2). A pressure excess is seen in XLSSC102 at $r \gtrsim R_{500}$, a region where the Arnaud et al. (2010) profiles are

Table 12.2: Mass values measured from the combination of SZ+X-ray data (top row) and SZ data plus Planck Collaboration et al. (2014b) scaling law (bottom row), for different values of bias parameter b. The mass values correspond to the median of the distribution and the uncertainties to the 68% confidence intervals around the median.

	$b_{\rm HSE} = 0.0$	$b_{\rm HSE} = 0.2$	$b_{\rm HSE} = 0.4$
M_{500} from SZ+X-ray data	$1.1^{+0.3}_{-0.2} \times 10^{14} M_\odot$	$1.5^{+0.5}_{-0.3} \times 10^{14} M_\odot$	$2.1^{+0.7}_{-0.5} \times 10^{14} M_\odot$
M_{500} from SZ data + scaling law	$2.6^{+0.5}_{-0.4} \times 10^{14} M_\odot$	$3.5^{+0.7}_{-0.6} \times 10^{14} M_\odot$	$5.0^{+1.0}_{-0.8} \times 10^{14} M_\odot$

not constrained by the data, but by simulations. This was also found by Planck Collaboration et al. (2013) and interpreted as a sign of substructure accretion by Reiprich et al. (2013). In our case, this could be caused by the merger event. However, the differences are small and could only be the result of intrinsic scatter and noise. These results show again that XLSSC102 is a disturbed cluster and reinforce the universality of the pressure profile at a mass lower than the average mass of the REXCESS sample and at $z \sim 1$.

Comparison to the Planck universal pressure profile We also compared our pressure profile to the universal pressure profile from Planck Collaboration et al. (2013) using a different approach. To do so we normalise the profile of XLSSC102 by the characteristic pressure P_{500}, which is related to the mass by a scaling relation, given by

$$P_{500} = 1.65 \times 10^{-3} E^{8/3}(z) \left(\frac{M_{500}}{3 \times 10^{14} h_{70}^{-1} \mathrm{M}_\odot} \right)^{2/3} h_{70}^2 \text{ keV cm}^{-3}, \tag{12.21}$$

in the self-similar case based on pure gravitational collapse (Nagai et al. 2007a; Arnaud et al. 2010). We also account for the small mass dependence, $f(M)$, found in Arnaud et al. (2010):

$$f(M_{500}) = \left(\frac{M_{500}}{3 \times 10^{14} h_{70}^{-1} M_\odot} \right)^{0.12}. \tag{12.22}$$

Our scaled pressure profile is then given by $P_e(r)/P_{500}/f(M_{500})$.

The results are shown in Figure 12.11. Our profile is shown in green while the one from Planck Collaboration et al. (2013) is shown in purple for the part constrained with X-ray data and in orange for the part constrained with Planck SZ data. The error bars indicate uncertainties while the shaded region indicate the scatter among the sample. The four panels are for different masses: $M_{500} = (1, 2, 3 \text{ and } 4) \times 10^{14}$ M$_\odot$, from left to right and top to bottom. We can see that our profile is compatible (at 95% at least) with that of Planck Collaboration et al. (2013) for $M_{500} = [2, 3, 4] \times 10^{14}$ M$_\odot$. Again, the best agreement is obtained for $M_{500} = 3 \times 10^{14}$ M$_\odot$. In coherence with our previous findings we remark that our profile is flatter than the mean profile from Planck Collaboration et al. (2013) in the inner part and shallower at $r \sim R_{500}$. This results show again the lack of significant deviation from standard evolution of the pressure profile once rescaled to proper quantities, in such merger at high redshift and relatively low mass. It also strengthen the incompatibility of the low mass measurement obtained directly with combined SZ+X-ray data.

12.3.2 Mass estimation

We measured the mass of XLSSC102 directly from the combined SZ+X-ray analysis under the assumptions of our pressure and density models (see Section 12.2.3.1), which assume spherical symmetry, and the hydrostatic equilibrium. The hydrostatic mass bias (see equation 12.13) is generally found to be $b_{\rm HSE} \sim 0.2$ (baseline value in Planck Collaboration et al. 2014b, see

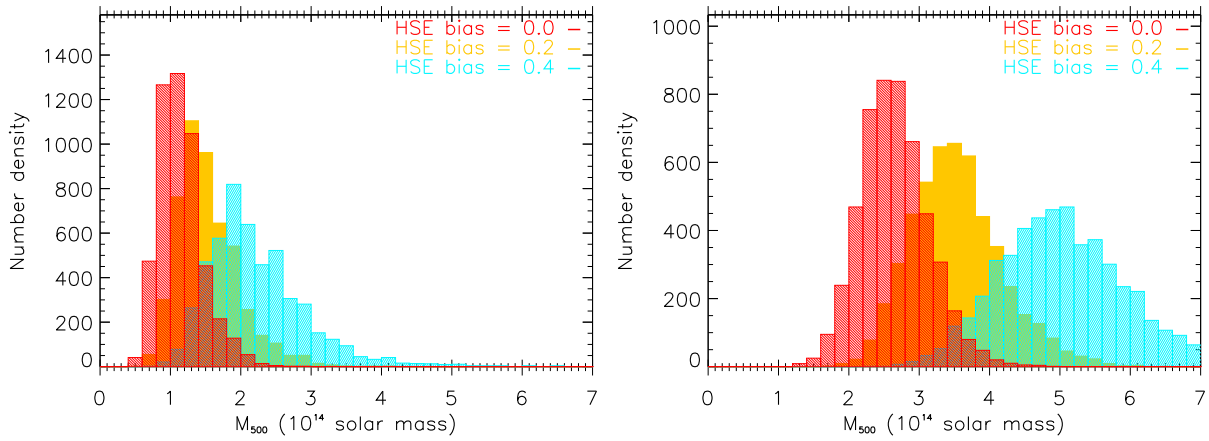

Figure 12.12: M_{500} mass distributions of XLSSC102 for different assumption of the hydrostatic bias ($b_{\rm HSE} = 0$, 0.2 and 0.4). *Left:* mass measured from the joint SZ+X-ray analysis. *Right:* mass inferred from our Compton parameter profile and the Planck scaling law (Planck Collaboration et al. 2014b).

references therein). However, there is no consensus about its dependence with cluster mass, redshift, dynamical state and its radial variation. The scatter among literature values is high (see e.g. Penna-Lima et al. 2017): some authors find a bias consistent with $b_{\rm HSE} \sim 0$ (Melin and Bartlett 2015), while others argue for a bias value as high as $b_{\rm HSE} \sim 0.3$ (von der Linden et al. 2014), close to the $b_{\rm HSE} \sim 0.4$ value needed to reconcile CMB and cluster counts cosmological constraints (Planck Collaboration et al. 2014b). The discrepancies may come from the different cluster samples, but also from the intrinsic difficulty to access to the unbiased true mass, either from weak lensing measurements, that are also hampered with systematics, or to accurately reproduce the complexity of the cluster physics in numerical simulations. As we are dealing with a post-merger cluster at $z \sim 1$, a variety of cluster for which little is known, we tested different values of the bias parameter: $b_{\rm HSE}$ = 0, 0.2 and 0.4. We stress that as we are measuring the mass from a profile, we can not simply divide M_{500} by $(1 - b_{\rm HSE})$, as the bias also impact the value of R_{500}. We thus have to take it into account both in the mass and over-density profiles (see equations 12.13 and 12.15).

The M_{500} mass distribution measured from the SZ+Xray analysis for different hydrostatic bias values is shown in the left panel of Figure 12.12. We can see that the median mass increases with the bias, as expected, but the dispersion also increases. This is because the value of R_{500} increases with $b_{\rm HSE}$ and the mass uncertainties get larger with the radius (see Figure 12.8). The median mass values and the 68% c.i. are presented in Table 12.2. Theses values are significantly lower, by a factor of about 2, than that expected from scaling relations and the ACT detection (see Section 9.2). The mass obtained with $b_{\rm HSE} = 0.2$ is compatible with the mass estimated from XXL weak lensing scaling law $M_{500,\rm scal}$ considering the error bars. The mass obtained with $b_{\rm HSE} = 0.4$ is also compatible with that obtained from the $Y_{\rm X}$ proxy: $M_{500,Y_{\rm X}}$. However, these agreements would necessitate the measured masses to be higher and that from scaling laws to be lower. This is not surprising since we have showed that gas clumps are likely to bias low our measurements, as discussed in Section 12.2.6.

For comparison, we also estimated the mass of XLSSC102 from our measured integrated Compton parameter profile (see Figure 12.8) and the Planck scaling relation between $Y_{\rm SZ,500} \equiv Y_{\rm sph}(R_{500})$ and M_{500} (Planck Collaboration et al. 2014b):

$$E^{-2/3}(z)\left[\frac{D_A^2 Y_{\rm SZ,500}}{10^{-4}\ {\rm Mpc}^2}\right] = 10^{-0.19}\left[\frac{(1-b_{\rm HSE})M_{500}^{Y_{\rm SZ}}}{6\times10^{14}\ {\rm M}_\odot}\right]^{1.79}. \quad (12.23)$$

Since $Y_{\rm SZ,500}$ itself depends on R_{500}, which is computed from M_{500}, the SZ derived mass is

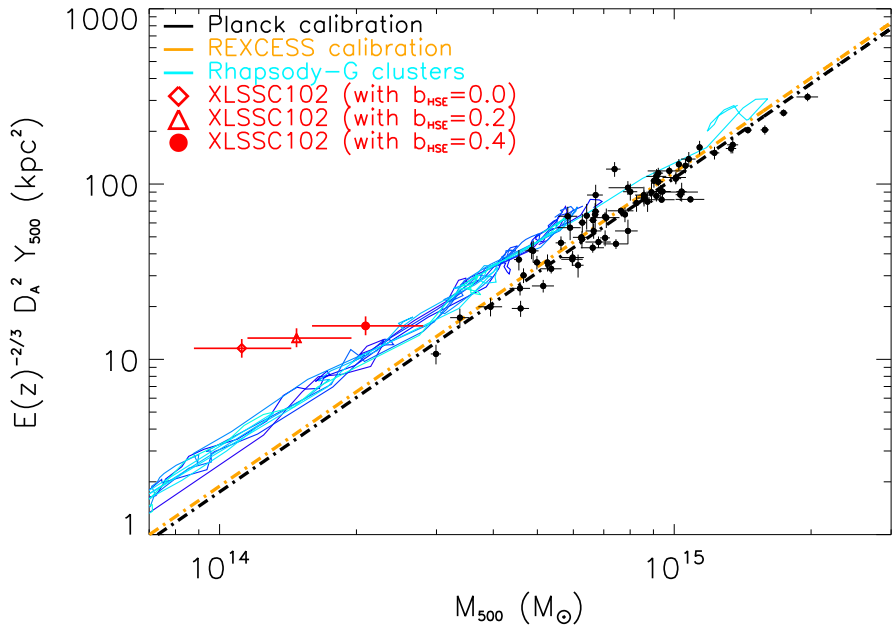

Figure 12.13: Scaling relation between the spherically integrated Compton parameter Y_{500} and the mass M_{500} from Planck Collaboration et al. (2014b). The three red markers indicate the values from the combined SZ+X-ray analysis of XLSSC102 assuming different values of hydrostatic bias ($b_{\rm HSE} = 0, 0.2$ and 0.4). The black data points and dotted lines show the Planck clusters and their calibration. The yellow dotted line show the calibration from the REXCESS sample (Arnaud et al. 2010). The blue lines indicate the evolution of the RHAPSODY-G clusters (Hahn et al. 2017).

computed by iterating about the scaling relation until convergence. Note that the intrinsic scatter of $\sigma_{\log Y} = 0.075$ (Planck Collaboration et al. 2014b) is taken into account account by including this dispersion among the $Y_{\rm sph}(R)$ profiles given by each MCMC step. The resulting mass distributions are shown in the right panel of Figure 12.12 for different hydrostatic bias parameters. The median and the 68% c.i. of the distributions are presented in Table 12.2. We can see that according to these measurements a mass value below $2 \times 10^{14} M_\odot$ is unlikely and we obtain masses in better agreement with our predictions from other scaling relations (see Table 9.2).

12.3.3 Location of XLSSC102 on scaling relations

We now compare the integrated quantities M_{500} and Y_{500} as measured via the SZ+X-ray combination to scaling relations from the literature and nearby cluster samples. Figure 12.13 shows the scaling relation used by Planck Collaboration et al. (2014b) for the mass calibration of their local cluster sample. The black points show their individual measurements and the black dotted line shows the calibration adopted. The calibration from the REXCESS sample is also shown in yellow. The blue lines show the relation measured in the RHAPSODY-G simulated cluster sample Hahn et al. (2017). The three red symbols show the measurements made in XLSSC102, for the three hydrostatic mass bias parameters. We can see that, as expected from Figure 12.12, our measurements are offset from the scaling law and a large bias parameter in needed to reconcile the two. More surprisingly, we remark that the RHAPSODY-G clusters are systematically biased with respect to the Planck clusters. As noted by Hahn et al. (2017), a null bias value is needed to agree with Planck, while the baseline bias is 0.2.

In Figure 12.14 we adopted another method and compared our XLSSC102 measurements (the three red symbols) to the scaling relations extracted from simulations by Le Brun et al.

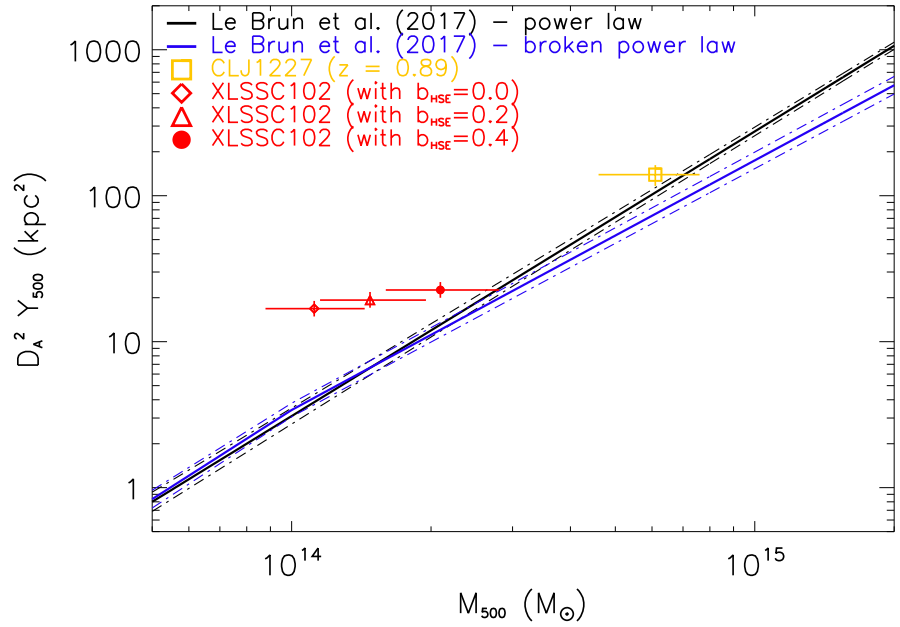

Figure 12.14: Scaling relation between the spherically integrated Compton parameter Y_{500} and the mass M_{500} from Le Brun et al. (2017), taken at $z = 0.97$. The three red markers indicate the values from the combined SZ+X-ray analysis of XLSSC102 assuming different values of hydrostatic bias ($b_{\rm HSE} = 0, 0.2$ and 0.4). The yellow point shows the value for a cluster at $z = 0.89$ from Adam et al. (2015). The blue and black lines show the relations estimated at $z = 0.97$ from simulations, using two kind of parametrisation and their associated intrinsic scatter.

(2017) and evaluated at $z = 0.97$. Two parametrisation are shown: a single power law (black line) or a broken power law (blue). For comparison, we represented the value corresponding to a massive cluster at z=0.89 measured by Adam et al. (2015) using a similar analysis. We can see that our measurements are again offset from the relation, which shows that the differences we observe are not due to a non-standard redshift evolution, or a least that the latter is not expected in the simulation used in Le Brun et al. (2017).

As mentioned in Section 12.2, in a future study we will split the cluster in two regions and re-do the analysis. This will allow us to compare the mass measurements in the different regions and quantify the effect of gas substructures on mass measurements of high redshift clusters with shallow X-ray data. In a future analysis we will also evaluate how the cluster mass derived from $Y_{\rm X}$ through scaling laws is affected by the presence of substructures. This could be used as a reference for future studies of distant eROSITA clusters.

12.4 Conclusion

In this chapter we completed a preliminary analysis of the galaxy cluster XLSSC102 at z=0.97. We first analysed its ICM morphology, using SZ data alone. We find that the cluster is elongated with an ellipticity of ~ 0.3. We detect substructures in the pressure at a 4σ level. We do not see evidence of pressure gradients, which shows that our cluster does not present a compact core. However the signal to noise of our data is to low for the moment to detect merger induced compressions or shocks in the ICM.

We then conducted a multi-wavelength comparison using X-ray, SZ and optical data which revealed that the different tracers (the SZ peak, the X-ray peak, the X-ray centroid, the optical density peak and the BCG) are offset from each other. We see the presence of a gasless galaxy

group in the northern region, orientated along the optical, X-ray and SZ signal elongation axes and the BCG. We interpret this as a sign of a post-merger phase: the northern group must have passed through the main cluster and have been stripped from its gas in the process.

We then combined SZ+X-ray data to compute the thermodynamic and mass profiles of XLSSC102. We obtain tight constraints up to $r \sim R_{200}$. However, we find that the temperature profile is steep, while the entropy profile is flat and below self-similar expectation at $r \sim 0.5 \times R_{500}$. The gas fraction increases with radius and gets larger than the cosmic fraction at $r \sim 0.5 \times R_{500}$. The hydrostatic mass is also lower than expected from scaling relation. We interpret these findings as the effect of gas inhomogeneities caused by the northern structure that is likely related to the merger event.

We find that the form of the pressure profile of XLSSC102 is compatible with that of disturbed clusters at low redshifts, and does not show significant deviations from standard evolution expectations. This is remarkable given the high redshift and relatively low mass of this dynamically complex system. This strengthen the robustness detection and mass estimations based on low resolution SZ surveys. Finally, we derived the total cluster mass from the SZ+X-ray data combination and from SZ data and scaling relations. We find a significant discrepancy between the two, which agrees with our measured hydrostatic mass being biased low because of the gas density substructure. This is also seen when directly comparing to scaling relations calibrated at low redshifts or from that of simulations at high redshifts. This effect has to be taken into account when directly measuring the mass using shallow X-ray data (e.g. from the future eROSITA mission).

Perspectives and future work

This part of the thesis was dedicated to the observational project aiming at following-up 3 high redshift XXL clusters with NIKA2, a high angular resolution millimetre camera. This project was accepted and is still ongoing. So far, we obtained $\sim 1/8^{\rm th}$ of the total granted time, which we spent on the cluster XLSSC102 at $z = 0.97$.

In Chapter 9, we presented our motivations, the selection, and the optical and X-ray characterisation of our targets. In Chapter 10, we presented the NIKA2 instruments and the course of a typical observing session at the telescope. We validated the data calibration process and described the data reduction. In Chapter 11, we focused on the detection and characterisation of point sources (dusty star forming galaxies) in our cluster field. We developed a detection pipeline and used it to construct a high purity sample of interesting sources. Finally, in Chapter 12 we analysed the SZ emission of XLSSC102. We characterised its morphology through a multi-wavelength approach, that revealed a complex, presumably post-merger system with disturbed dynamical state. We derived its thermodynamic and mass three-dimensional radial profiles by combining X-ray and SZ data. Those showed signs of bias due to gas inhomogeneities in the cluster. We then derived the cluster mass and compared it to scaling relations calibrated with low redshift cluster samples. We also compared our data to the universal pressure profile, showing that the internal structure of our cluster was consistent with that of a disturbed cluster at lower redshift and higher mass, once normalised to scaled quantities. These results are encouraging in the context of cluster mass measurement, at low mass and high redshifts, as derived from the integrated Compton parameter in unresolved SZ surveys.

These analyses are preliminary and some refinement would be necessary at the data processing stage. For instance, the calibration files we used are not the "official" ones since they were not available at the time of writing the thesis manuscript. This will thus be updated once we obtain all the requested observing time on XLSSC102. The first, obvious, perspective is to reproduce our analysis with more data, allowing us to obtain a better signal to noise for XLSSC102, and to explore our two other targets. In particular, this will allow us to measure the flux of the point sources more accurately and to refine their colour based redshift estimation. For the cluster signal, this will be critical for the detection of substructures and compressions or shocks. Some elaboration is also needed to access more precisely the reliability of our results (e.g. the offset between the SZ and X-ray peaks) using simulated SZ and X-ray maps. This could also be measured in simulations such as RHAPSODY-G to access the probability of such configuration. Another perspective is to study the effect of the merging event on the cluster thermodynamic and mass profiles, and integrated quantities. This could be achieved by splitting the cluster in two regions. We could also benefit from the perturbed dynamical state to study the effect of centring on the different profiles. These analyses will be included in a future article (Ricci et al in prep.). Then, they will be extended to the other two clusters. The differences among our sources, in terms of dynamical state, will help us to understand how this can affect the clusters locations in the mass–observable scaling relations, in the mass and redshift regime we are probing. Concerning optical data, some improvement could be achieved using a galaxy catalogue containing UV and near infrared K-band photometry (Moutard et al. 2016). This would reduce the photometric uncertainties at high redshift and allow us to select galaxies based on their stellar mass rather than luminosity. The comparison of the optical density maps to numerical

simulations would then be easier. This catalogue also provides star formation rates, which could be used to study if the cluster dynamical state impact the star formation in the member galaxies. Finally, the pipeline developed for the point source detection and characterisation could be used to select interesting sources in other cluster fields observed with NIKA2.

Closing remarks and perspectives

> Que vivront ces théories nouvelles? Sans doute ce que vivent toutes les théories: l'espace d'un matin. [...] Ainsi en est-il des théories, elles sont, fatalement, remplacées un jour ou l'autre par d'autres théories plus complètes, plus voisines de cette absolue Vérité vers laquelle nous courrons sans cesse, comme la gazelle altérée court aux palmiers qui abritent la source d'eau claire. Mais elles laissent du moins, comme trace de leur existence, les découvertes qu'elles ont contribué à faire.
>
> Alphonse Berget, Le Ciel

I spent the three years of my Ph.D. in the Laboratoire Lagrange of the Observatoire de la Côte d'Azur. This time was shared between research, which is presented in this thesis document, and teaching activities at the Université Nice Sophia Antipolis. The main subject of my studies is the analyses of galaxy clusters towards their utilisation as probes to constrain cosmological models. In the following, I review my implications in the collaborations in which I have been involved, and the research axes I developed, before giving the perspectives of my work.

Implication in the XXL and Euclid collaborations

During my thesis, I studied the properties of galaxy clusters for the purpose of their utilization as cosmological probes. In particular, I built tools to characterise them from optical/IR and multi-wavelength (X, SZ) approaches. I applied this methodology to statistical samples as well as individual clusters, down to low mass and up to high redshift, and obtained important results in a cosmological context. I am deeply involved in the XXL consortium, where I took a leadership position in the optical and SZ analyses of X-ray clusters:

- using CFHTLS data, I led the analysis of the galaxy luminosity functions of a statistical sample of XXL-N clusters, which resulted in the article Ricci et al. (2018) and the catalogue of BCG properties that will be included in the second XXL data release. I contributed to the article Koulouridis et al. (2018b), also part of the release, in which I applied the tools constructed for the luminosity functions analyses, and to the article presenting the 365 XXL cluster sample (XXL Paper XX). Lastly, I am involved in the study of optical clusters detected in the common XXL and CFHTLS footprint with the WaZP cluster finder (Benoist et al. in prep.). The goal is to compare and characterise X-ray and optical systems and to draw conclusions about possible systematics in the surveys and detection pipelines. This work constitute the second part of my thesis (Part II).
- I took the opportunity to conduct a follow-up of three distant XXL clusters in SZ with the NIKA2 camera. This project was highly rated and granted with 81 hours of observing time. I spent one week at the telescope and participated to the observations and data reduction. Although the project is still ongoing and only one cluster is partially observed so far, I was able to push the exploitation of the data to fulfil nearly all the goals defined in the proposal. These results will be included in a forthcoming article (Ricci et al. in prep.). Moreover, I developed a pipeline to blindly extract and characterise dusty star forming galaxies found serendipitously in our cluster field. This work constitute the third part of my thesis (Part III).

Because of my expertise in photometric redshifts and galaxy luminosity functions I also contributed to the preparation of the *Euclid* mission, via the validation of clusters' and galaxies' properties in simulations (Adam et al. in prep., De Lucia et al. internal Euclid report). This work is presented in the appendices of my thesis (Appendices A and B).

Research axes and outcomes

Throughout this thesis I developed several research axes. I summarised them and give their main outcomes in the following.

Multi-wavelength cluster analyses In Part II, I conducted joint optical+X-ray analyses. I used the optical data from the CFHTLS to study the counterparts of XXL clusters (see Chapter 3). I constructed and analysed the luminosity functions and colour magnitude diagrams of their member galaxies, finding that, overall, they are compatible with that observed in other cluster samples (see Chapters 5, 6 and 7). A combined X-ray and optical approach was also used to study their AGN activity (see Chapter 7), allowing for a meaningful interpretation of the X-ray AGN counts and revealing the role played by the mass of cluster. Finally, it enabled the comparison of optical and X-ray clusters, detected in the common XXL+CFHTLS footprint, with the XAmin and WaZP algorithms (see Chapter 8). This showed that the majority of XXL clusters are detected independently in the optical. In Part III, I developed SZ+X-ray+optical analyses. I led a project aiming at mapping the SZ signal of three XXL clusters, and used optical and X-ray data, together with numerical simulations, to select the targets and predict their SZ flux (see Chapter 9). This multi-wavelength approach was essential to characterise the morphology of the galaxy cluster XLSSC102, finding that it was disturbed and likely to be in a post-merger state. Lastly, X-ray and SZ data were fitted jointly to derive the mass and thermodynamic radial profiles of the intra cluster medium (see Chapter 12). In conclusion, this approach allowed me to better characterise clusters and to draw conclusions about their appearance at different wavelengths. This is crucial in the context of cluster cosmology as it permits to tackle the systematics effects associated to each survey, test the detection pipelines, selection functions, and cosmological representativeness of the samples, and compare mass proxies.

Studies of galaxy clusters at low mass In this thesis, I worked on the properties of galaxy clusters detected in the XXL survey. As I showed in Chapter 3, this survey allows us to detect clusters in the mass range $M_{500} \sim 10^{13} - 10^{15}$ $M_{\odot}$, with a median mass of $M_{500} \sim 1 \times 10^{14}$ $M_{\odot}$. It thus covers lower masses compared to other catalogues, and that, up to high redshift. This is of particular importance because such clusters will constitute the bulk of the detections of future surveys such as *Euclid* and LSST, but also because they offer unique ways to tackle systematics in mass estimation, as they are more affected by ICM and galaxies physics. This is also likely the case for high redshift clusters, which are the progenitors of local massive systems and have great cosmological constraining power. Due to their shallow potential wells, low mass clusters are more affected by merging events and AGN feedback and are expected to deviate from equilibrium further than their high mass counterparts. Moreover their member galaxies are believed to host more star formation. These lead to bias and uncertainties in their detection and mass measurements. XXL gave us the opportunity to test these effects in a statistical sample of clusters and up to high redshift. I found that low mass X-ray clusters host a higher number of faint galaxies and that their integrated optical luminosity, and hence their stellar mass, is lower than in more massive clusters. Their BCG is also less luminous, but contribute more to the total optical luminosity budget (see Chapter 6). In opposition to what is found in more massive systems, the fraction of AGN in low mass cluster members is similar to that in the field and even enhanced in the outskirts (see Chapter 7). This has to be taken into account when interpreting X-ray cluster samples because AGN contaminate the detection and characterisation of extended sources. When investigating the colours of cluster member galaxies I found that a red sequence was not always detectable in the poorest clusters. This can affect the selection function of certain cluster finders as this feature is often used to detect clusters or estimate their redshift. I also found that low mass clusters present a larger fraction of blue BCGs. This is an issue for optical cluster finder based on red sequence galaxies that use the BCG as cluster

centre. When matching XXL to optical cluster sample I showed that a large fraction of low mass X-ray systems are not associated to any optical detection. Finally, the distant cluster XLSSC102 for which I obtained SZ observations and which is studied in details in Chapter 12, is in the high mass tail of the XXL sample. However, its mass is quite low compared to the usual clusters studied at its redshift. More details on its properties are given in the following.

High redshift clusters The XXL survey allows us to detect clusters up to high redshift (z$\sim$1 and higher, see Chapter 3). In Part II, the optical data we used prevented us to put high constraints on their properties. In part III, I proposed to use the SZ signal, which does not suffer from redshift dimming, to probe the inner structure of three XXL clusters at $z \sim 1$ (see Chapter 9). As explained above, I have found that the cluster XLSSC102, at z=0.97, shows signs of merging events. This causes inhomogeneities in the gas that bias measurements based on X-ray data. This is likely to be the case for a large fraction of high redshift clusters. However, I showed that the form of the pressure profile of XLSSC102 obtained from SZ data is compatible with that of disturbed clusters at low redshifts, and does not show significant deviation from standard evolution expectations.

Relation between galaxy and cluster evolution Cluster evolution is intertwined to that of galaxy, and they have to be studied alongside. This is obvious in the optical and infrared where member galaxies are used to trace the cluster mass. This is why I studied their luminosity and their colours, an paid a special attention to their dependence with cluster mass and richness (see Chapters 6 and 7). However, it is also the case in X-ray, as shown in Chapter 7, and at millimetre wavelengths, since AGN suffer environmental effects but also induce energetic feedback in the ICM, and can contaminate cluster emission. Moreover, the bright red sequence galaxies studied in XXL clusters likely find their progenitors in the dusty star forming galaxies detected and characterised in Chapter 11. Better characterizing those galaxies may thus help to detect clusters in their early stage of formation.

Test of the optical and SZ properties that drives cluster detection The galaxy luminosity functions of clusters, along with their density profiles, encode most of the observational properties of galaxy clusters in the optical. In this context I constructed and analysed the luminosity function of XXL clusters, finding that its form was compatible with a Schechter function, and I identified their BCGs (see Chapter 5 and 6). I measured and modelled the evolution of the luminosity function parameters with both redshift and richness, distinguishing between these two effects. I found that the bright part of the luminosity function in the inner region of clusters does not significantly evolve with redshift and little with richness, apart for its amplitude. The integrated luminosities does not depend on redshift but scales with richness and can be used as a mass proxy. In Chapter 7, I constructed optical density profile, that can be used in a future study. I also investigated the colour magnitude diagrams of clusters, in order to derive the properties of their red sequence. I found that those could be well fitted by a single stellar population evolution model, once calibrated. In SZ, the clusters can be described by their pressure profile, which is believed to be nearly universal. I tested this assumption in the highly perturbed, distant, intermediate mass cluster XLSSC102. The observations of the remaining two clusters will allow to investigate its stability under different dynamical state. These type of optical and SZ analyses are crucial to improve the detection and representativeness of clusters.

Statistical and individual cluster analyses In this thesis, I adopted two complementary approach: the statistical study of a large cluster sample and the in depth characterisation of one system. Studying relatively low mass clusters is challenging because of their faint signal and low galaxy number. Thus it requires to enhance their signal to noise ratio using stacking procedures (see Chapters 5 and 7). Large samples also permit to test the relations between properties (see

Chapter 6) and establish statistics (see Chapter 8). It is important to develop these methods as future surveys will provide large samples of cluster to analyse. However, studying a few clusters in details is also fundamental, to test the assumptions used in statistical studies and to pinpoint any bias in the mass measurements (see Chapter 12).

Identification and quantification of systematic effects Systematic effects and biases are the main obstacle for the use of clusters as cosmological probes. In this thesis, I evaluated the quality of the CFHTLS photometric redshifts using new estimators. I have shown that it directly impacts the detection of clusters (see Chapter 8). I identified and quantified systematics related to their misuse (see Chapter 4), and shown that it affects the luminosity functions measurements (see Chapter 5). Concerning the latter, I have demonstrated that the statistical estimators and the stacking method were also introducing systematics and biases.

Future prospect

In the coming years, galaxy cluster cosmology will likely enter a golden era, with the advance of high quality multi-wavelength surveys, allowing the build-up of large, well controlled cluster samples. In the optical and near infrared, the *Euclid* and LSST surveys will set a new milestone in cluster cosmology, as hundreds of thousands of clusters are expected to be detected, covering a wide mass range and spanning the last three quarters of the Universe history. Different cosmological probes will be extracted from those surveys, allowing their direct comparison and combination. Cluster detection will rely on our knowledge of the average distribution, luminosity and colours of member galaxies, up to high redshift. The cluster selection function will be estimated from simulations and comparison to X-ray and SZ catalogues. Mass measurements will be obtained using weak lensing analyses, for individual clusters when possible or through a stacking analysis as a function of richness. These measures will be tested and completed with a multi-wavelength approach, taking advantage of missions such as eROSITA in X-ray or SPT-Pol and ACT-Pol in SZ. The advent of SKA and CTA will revolutionise our understanding of non thermal processes in clusters. If their connection to the cluster dynamical state is confirmed, this will allow us to determine sample of perturbed clusters and deeply understand their impact on scaling laws. In this multi-wavelength context, the near future of cluster cosmology is very promising.

Appendix

Appendix A

Characterisation of the mock catalogue used to select the Euclid cluster finder algorithms

Cluster finders algorithms were applied on a mock catalogue in the *Euclid Cluster Finder Challenge 4* (CFC4). This was done in order to select the algorithms to be implemented in the *Euclid* pipeline, and it required the in depth characterisation of the simulation for interpreting the results. I provided the analysis pipeline for the photometric redshifts quality assessment and contributed to the characterisation of the cluster luminosity functions. Thank to this work, I have co-signed the paper presenting the *Euclid* cluster detection performances (Adam et al. in prep.). In this Appendix, I present the analyses of the mock photometric redshifts and cluster luminosity functions.

A.1 Context

The Euclid CFC4 made use of a main simulation mock, based on Merson et al. (2013) and modified in Ascaso et al. (2015, 2017), in order to test the behaviour of the detection algorithm on Euclid representative data. This mock was provided with photometric redshifts, $z_{\rm phot}$, and their probability distribution function. It was limited to H-band magnitudes brighter than $H_{\rm AB} = 24$ to mimic the Euclid Wide survey. In order to calibrate the photometric redshifts, a 20 square degrees region including both photometric and spectroscopic redshifts was also provided. The mock was constructed to be representative of expected Euclid data. However, it was originally designed for large scale galaxy clustering studies, and not for galaxy cluster studies.

A.2 Quality of the mock photometric redshifts

The precision on the photometric redshift estimates can have a strong impact on the cluster finder performances. Indeed, clusters appear as over density not only in projected space, but also in redshift space, information that is used by the detection algorithms via the photometric redshifts (see Chapter 8 for the WAZP cluster finder). We thus characterise the photometric redshift properties as discussed below.

We follow the methodology described in Chapter 4 and for each bin in redshift, we computed the difference $(z_{\rm phot} - z_{\rm spec})$, and use the resulting distributions to extract the bias, the catastrophic failure fraction and the dispersion. We first investigated the dependence of the photometric redshift quality as a function of true spectroscopic redshift ($z_{\rm spec}$) and magnitude in the Euclid NISP H band ($m_{\rm H}$). The bias, computed as in Eq. 4.1, and the dispersion, computed by integrating the distributions up to 68.2% confidence level on the positive and negative

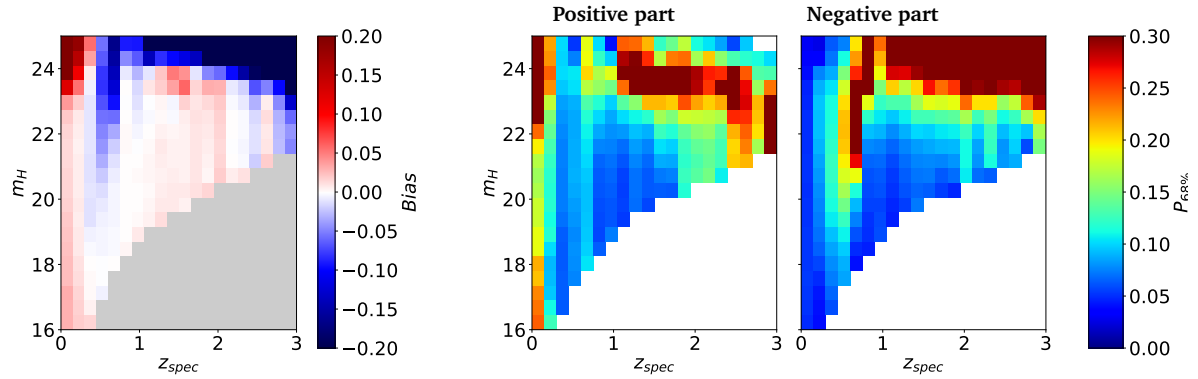

Figure A.1: Mock photometric redshifts bias (left) and dispersion (right) as a function of redshift and magnitude, computed as detailled in Chapter 4.

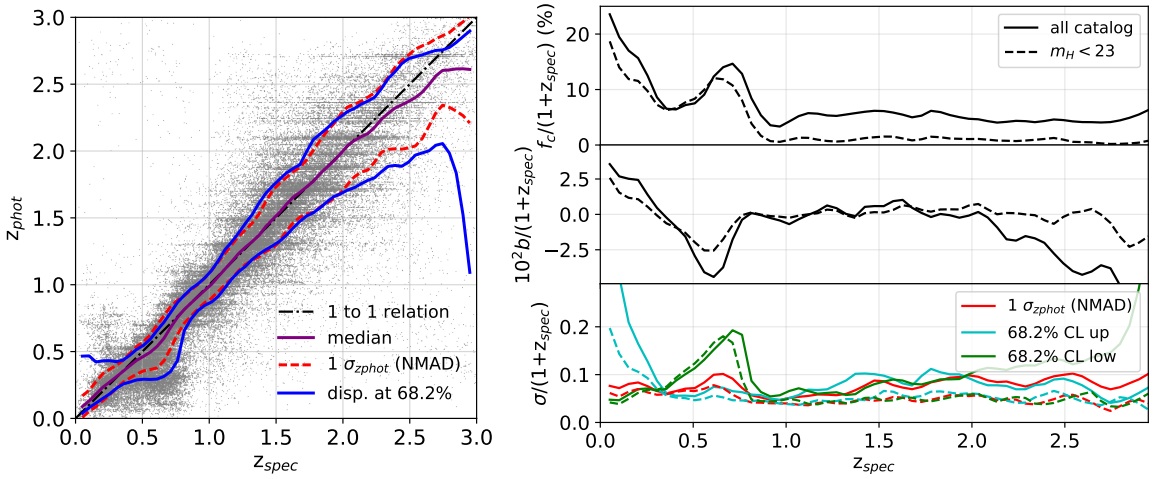

Figure A.2: Mock photometric redshifts quality evaluation. *Left:* Comparison between the photometric redshift, z_{phot}, and the true spectroscopic redshifts, z_{spec}. The bias is shown by the purple solid line, the NMAD is shown as the red dashed line, and the dispersion computed as percentiles is shown by the blue solid line. The black dashed-doted line provides the one-to-one relation for visualisation purpose. *Right:* Redshift evolution of the catastrophic outlier fraction (f_c, upper panel), the bias (b, middle panel), and different estimates of the dispersions (σ, lower panel) as a function of z_{spec}. The solid lines correspond to the full catalogue, while the dashed lines correspond to the catalogue cut at $m_H = 23$. See Chapter 4 for the definitions of the estimators. These Figures are extracted from Adam et al. (in prep.).

parts of the distribution (see Section 4.3.1.3), are shown in Figure A.1. We can see that below $m_{\rm H} = 23$, the magnitude dependence remains fairly homogeneous. In a second time, we thus computed the statistics of the photometric redshifts as a function of redshift only, treating separately the objects brighter and fainter $m_{\rm H} = 23$ to highlight the effects of contamination from low signal to noise objects.

The left panel of Figure A.2 shows the comparison between the true spectroscopic redshift $z_{\rm spec}$ and the photometric redshifts $z_{\rm phot}$, for a sub-sample of 10^5 galaxies galaxies extracted within the mock by random sampling. The bias of the distribution is shown in purple, and the dispersions computed with the NMAD estimator (see Eq. 4.4) and the upper and lower 68% percentiles are shown in red and blue, respectively. The right panel of Figure A.2 provides the redshift evolution of the catastrophic fraction (see Eq. 4.3), the bias, and the different estimates of the dispersion for the mock, both in the case of the full catalogue and after removing objects with $m_{\rm H} > 23$. We measure the overall mean photometric uncertainty to be $\frac{\sigma_{z_{\rm phot}}}{1+z_{\rm spec}} = 0.050$. The dispersion increases by a factor of ~ 2, and becomes very asymmetric, at redshift around $z \sim 0.5-0.6$. It is also rising by a similar amount at redshift below 0.2 and above 2.5 for the full catalogue, but remains relatively flat for the high signal to noise catalogue ($m_{\rm H} < 23$). The bias becomes large where the photometric uncertainties are large, even for the $m_{\rm H} < 23$ catalogue. The fraction of catastrophic redshift is small at redshifts above 0.8 ($\lesssim 0.05$ even for the full catalogue, and ~ 0.01 for the high signal to noise catalogue). However, it becomes large at lower redshifts, reaching up to 20% for the full catalogue and 15% for the $m_{\rm H} < 23$ catalogue.

Based on the photometric redshift properties of the catalogue, we expect cluster finders detections properties to be altered in the redshift range in which the catastrophic fraction is large ($z \sim 0.5-0.6$, and $z \lesssim 0.2$). This is even more true in the regime of low number of cluster member galaxies, i.e. at lower masses. This might show up as an increased number of false detections, or larger uncertainties in the redshift recovery of the clusters, depending on how the photometric redshifts are modelled by the finders. The bias can also affect the matching performed to associate the detections to the true clusters. On the contrary, at redshift larger than 0.8, the cluster finders are expected to behave well, even if the larger photometric errors and the lower number of galaxies, being reduced by redshift dimming, are expected to affect the completeness.

A.3 Mock cluster luminosity functions

Several cluster finders use assumptions about the shape and the redshift evolution of the luminosity function, based on real data. Thus, their performance may be affected if the mock luminosity function differs from the model.

To investigate the luminosity of galaxy clusters within the simulations, we follow a slightly different approach from the one presented in Chapter 5, since here, the cluster membership of each galaxy is known from the simulation. We simply count the number of cluster galaxies in bins of apparent magnitude (in the Euclid NISP H band), within a projected radius of R_{200} and per Mpc^2. This is done after selecting clusters within bins of mass and redshifts. The luminosity functions are then fitted by a Schechter function (see Eq 5.15 and Section 5.4 for more details).

We fit for the parameters ϕ^*, m^*, and α. A simple Schechter function is not able to describe the mock luminosity function in the faint part, where a more sophisticated modelling would be necessary. Therefore, we first focus on the bright part of the luminosity function studying the evolution of the parameter m^*. To do so, we perform the fit of equation 5.15 in the magnitude range limited to $m_{\rm min} + 3$, where $m_{\rm min}$ is the magnitude of the brightest galaxy in the bin we consider, to ensure good modelling of the mock LF in this regime. We check that our best-fit is not sensitive to this magnitude limit. The faint end properties of the luminosity function is addressed as a function of redshift for both mocks in a model independent way.

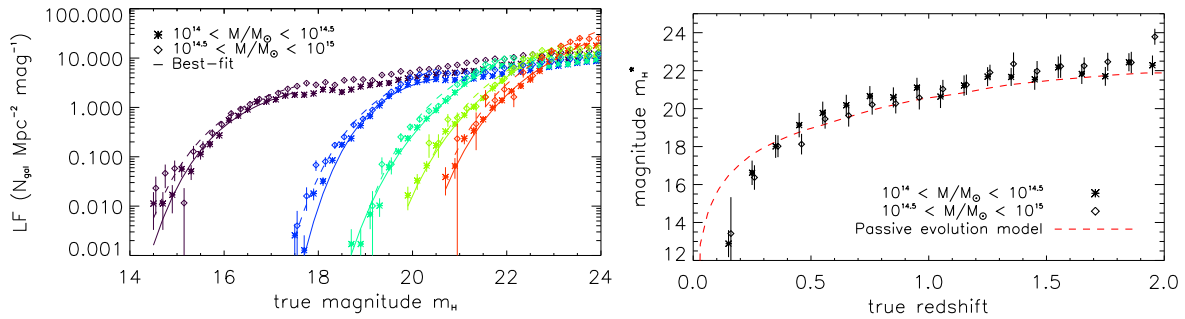

Figure A.3: *Left:* stacked LF of cluster galaxies in different redshift bins of width $\Delta z = 0.1$ and centred on $z = 0.15$ (purple), 0.55 (blue), 0.95 (cyan), 1.35 (green) and 1.75 (red). The star and diamond symbols and the dotted and dashed lines correspond to the mass bin $10^{14} < M_{DH}/\mathrm{M}_\odot < 10^{14.5}$ and $10^{14.5} < M_{DH}/\mathrm{M}_\odot < 10^{15}$, respectively. *Right:* redshift evolution of m^*_H in the two mass bins. The error bars provide the standard deviation of the posterior distribution of m^*_H, but we stress that the distributions are generally non Gaussian and non symmetric (see Chapter 5). The red line show our fiducial evolution model for the characteristic magnitude m^*_H (see Conventions used in this thesis). These Figures are extracted from Adam et al. (in prep.).

The left panel of figure A.3 provides the cluster galaxies luminosity function in two bins of mass (10^{14} $\mathrm{M}_\odot < M < 10^{14.5}$ $\mathrm{M}_\odot$ and $10^{14.5}$ $\mathrm{M}_\odot < M < 10^{15}$ $\mathrm{M}_\odot$) and 5 redshift bins (out of the twenty that are computed, from 0 to 2). We can observe that the mock luminosity functions are well described by the Schechter function in the bright regime, but that the faint part may require more sophisticated modelling. The right panel of figure A.3 compares the evolution of the best fit m^* parameter to our fiducial passive evolution model (see Chapter Conventions used in this thesis). While the shape of the evolution is relatively well described by the model at redshift larger than 0.5, independently of the considered mass bin, the amplitude of m^* is larger by about 0.75 magnitude for the mock. At lower redshifts, the evolution is stronger with redshift and the mock m^* values are lower than the model. This can thus affect cluster detections and richness estimations for algorithms that rely on a model of a luminosity function evolution (such as the WaZP cluster finder, see Chapter 8).

In addition to the luminosity function itself, we have checked the luminosity differences between the BCG and the central galaxies, i.e. the one coincident with the dark matter halo centre, in the mocks. The BCG is coincident with the central galaxy in about 70% of the clusters. This number increases with mass, reaching nearly 100% for the most massive clusters. When the BCG is not the central galaxy, the distance from the BCG to the cluster centre (either defined as the central galaxy or the barycentre), is about $0.45R_{200}$, decreasing by a few percent as mass increases. However, the distribution extent up to about nearly $2R_{200}$ in the low mass clusters. Even when it is not the BCG, the central galaxy is among the brightest members and the magnitude difference with the BCG does not exceed $\Delta m_\mathrm{H} \sim 2$, and even $\Delta m_\mathrm{H} \sim 0.5$ at high mass. The differences between the BCG and the central galaxy can affect the cluster finders in case they rely on the BCG, in particular to identify the cluster centre.

A.4 Conclusions

The characterisation of the properties of the simulation used for the CFC4 has been essential for the interpretation of the results. With the work presented in this appendix, we contributed to the determination of the photometric redshift quality and the cluster galaxy luminosity function, which are essential for cluster detection in the optical (see Chapter 8). The photometric redshift characterisation allowed us to identify redshifts at which cluster finders may be affected by biases and outliers. The luminosity function were shown to be marginally consistent with

standard evolution expectations, especially at low redshift, possibly affecting cluster finders that rely on a galaxy evolution model. This work was included in a forthcoming Euclid publication (Adam et al. in prep.).

Appendix B

Validation of the properties of clusters in the Euclid Flagship simulation

The scientific preparation of the *Euclid* mission relies on simulated ("mock") galaxy catalogues. They need to be representative of the future data, in order to develop performant analysis softwares, and identify and minimise potential associated systematic effects in cosmological analyses. In this Appendix we present the analysis of cluster galaxies properties in the Flagship Euclid galaxy mock, which is the largest simulated galaxy catalogue to date and is currently in a verification phase[1]. The validation of the cluster properties in Flagship is essential because this simulation will later be used in cluster cosmological analysis (e.g. to test cluster finder algorithms and determine their cluster selection functions). The main results from the analysis shown here were included in an internal *Euclid* report, dedicated to improve the reliability of the simulation[2]. Here, we focus on the investigation of the properties of BCGs and the cluster galaxies luminosity function.

B.1 The Euclid Flagship galaxy catalogue

The Euclid Flagship[3] mock is the largest simulated galaxy catalogue to date. It aims at matching the complexity of real data, to test and develop the data processing necessary for *Euclid*. It was built from the Flagship N-body simulation halo catalogue (generated using the Rockstar halo finder, Behroozi et al. 2013b). The galaxy light-cone catalogue contains 2.6×10^{12} galaxies over 5000 deg^2 and extends up to $z = 2.3$, with a cut at magnitude $m_H < 26$ in the Euclid NISP band. The galaxies in the Flagship mock are assigned to haloes and flagged as centrals or satellites using Halo Occupation Distribution (HOD, Zheng et al. 2005) prescription. Their luminosity is assigned using halo abundance matching, constrained by observation of local luminosity functions from Blanton et al. (2003) and Blanton et al. (2005). The magnitude evolutionary corrections are applied following evolutionary spectral synthesis model from the PEGASE library (Fioc and Rocca-Volmerange 1997).

B.2 Methodology and results

The analyses were conducted with the version `v1.3.3_s` of the Flagship simulation, which was downloaded from the CosmoHub platform[4] (Carretero et al. 2017). We selected all galaxies

[1] Science Performance Validation 3 (2019-2010).
[2] This report was prepared by G. De Lucia, using results from several analysis.
[3] https://www.euclid-ec.org/?page_id=4133
[4] https://cosmohub.pic.es/home

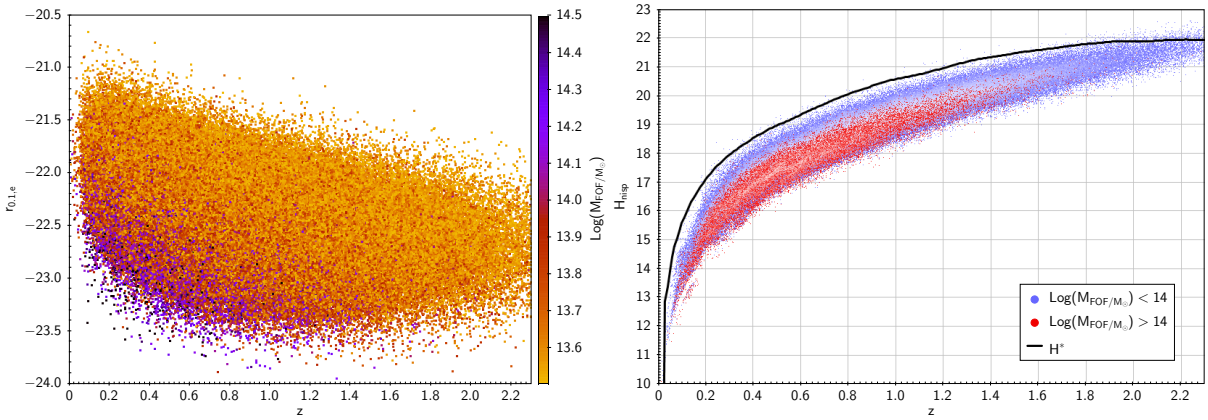

Figure B.1: Redshift evolution of the central galaxies magnitudes. *Left:* absolute magnitudes computed in the SDSS r-band redshifted to $z = 0.1$ and including evolution. The colour-bar indicates the mass and is clipped to a maximum value $\log(M_{FoF}/\mathrm{M}_\odot) = 14.5$. *Right:* apparent magnitude in the Euclid NISP H band. The blue and red points indicate the central galaxies magnitude in low and high mass haloes. The black line show our fiducial evolution model for the characteristic magnitude m^*_H (see Conventions used in this thesis).

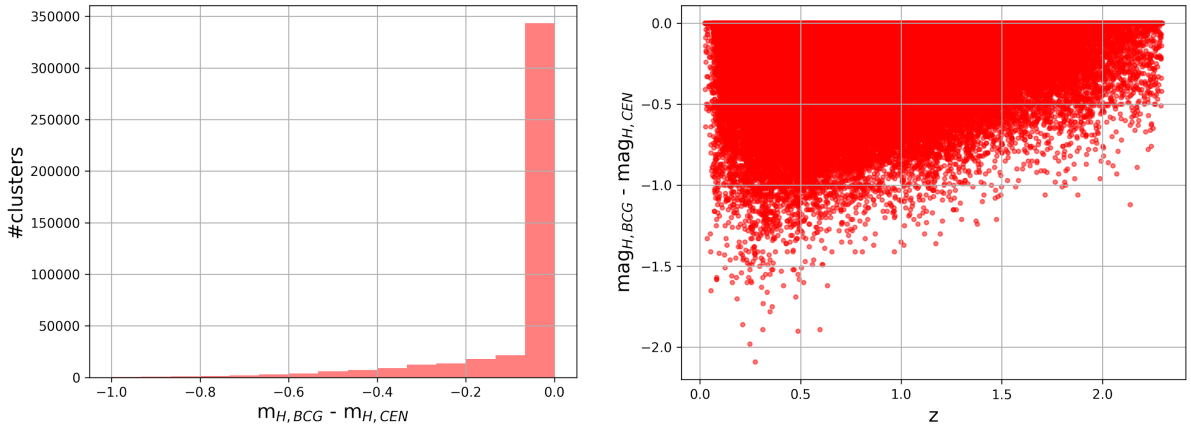

Figure B.2: Magnitude offset between the BCGs and the central galaxies. *Left:* magnitude offset distribution. *Right:* magnitude offset as a function of redshift.

inside haloes of masses $M_{FoF} > 10^{13.5} M_\odot$ (`halo_lm` entry, with FoF standing for Friends-of-Friends) from the entire simulation, leading to a catalogue of $\sim 4.9 \times 10^7$ galaxies and $\sim 4.4 \times 10^5$ haloes [5].

B.2.1 Properties of the central galaxies

In simulations, the cluster centres are generally given by the position of the most massive galaxies, called "central" in the HOD framework. However, as we have shown in Chapters 7 and 8, optical cluster finders often use the brightest cluster galaxy (BCG) as the detection centre. It is therefore important to study the properties of the central galaxies in the Flagship mock catalogue, and evaluate if they can be detected as BCGs.

Figure B.1 shows the magnitude of the central galaxies as a function of redshift. The absolute magnitude in the SDSS r-band, redshifted to $z = 0.1$ and including evolution ($r_{0.1}, e$, `abs_mag_r01_evolved` entry), is used in the left panel, while the apparent Euclid NISP H

[5] Exact numbers: 49223866 galaxies and 444116 haloes.

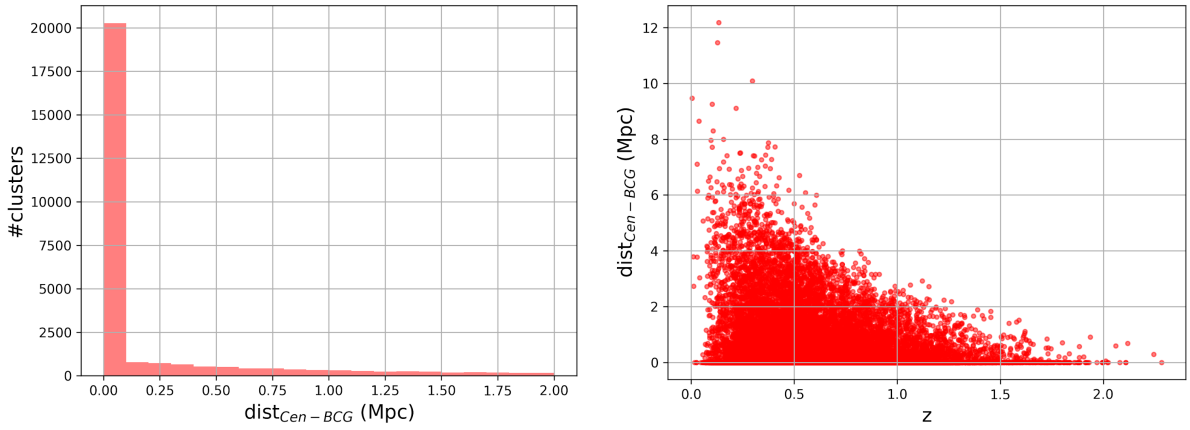

Figure B.3: Distance between the BCGs and the central galaxies. *Left:* distance distribution. *Right:* distance as a function of redshift.

band magnitude (`euclid_nisp_h` entry) is used in the right panel. We can see that the luminosity of the central galaxies is increasing with redshift and is higher in high mass haloes, as expected and observed for the BCGs of the XXL cluster sample in Chapter 6. The shape of the evolution overall agree with our fiducial evolution model for the characteristic magnitude.

Figure B.2 shows the magnitude offset between the central and the brightest galaxy in the Euclid NISP H band of each halo. The left panel shows the distribution of the offset and the right panel shows its evolution with redshift. We can see that the BCGs coincide with the central galaxy in the majority of the haloes. However, a small fraction of central galaxies are fainter than the BCGs, with an average magnitude offset value that decreases with redshift. In these cases, an optical cluster finder might miscentre the haloes. In Figure B.3 we show the distance between the BCG and the central galaxy (and thus the cluster centre). The left panel shows the distribution of the distance offset and the right panel shows its evolution with redshift. In the cases where the central galaxy is not the BCG, the distance offset can be as high as 12 Mpc and is decreasing with redshift in average. Such large numbers, albeit occurring only in a very few cases, are likely to be due to the membership attribution of galaxies to clusters, using a friends-of-friends algorithm.

B.2.2 Characterisation of the luminosity functions of galaxies inside haloes

Being another key aspect of cluster detections, we tested the representativeness of the cluster luminosity functions in the Flagship catalogue. We constructed composite luminosity functions (CLFs) in bin of masses and redshift. We used the masses M_{200}[6] and their corresponding radius R_{200}.

Figure B.4 shows the CLFs computed in the Euclid NISP H band for different bins of masses and redshift. The black points are for the satellite galaxies and the red histograms for the central ones. Figure B.4 shows the same CLFs shifted by the value of the model characteristic magnitude m^*_H.

We can see the presence of an upturn at faint luminosities ($\sim m^*_H + 3$), corresponding to the double Schechter form of parametrisation observed in low redshift clusters (see, e.g., Popesso et al. 2005). Once the passive evolution is taken into account, we do not see any evolution of the LF shape with redshift. No dependence on mass is seen, which is unexpected, in particular for the amplitude of the CLF (see Chapter 6 and e.g. Lan et al. 2016). The magnitude distributions of the central galaxies is Gaussian, as expected (see Chapter 6).

[6]Provided by G. De Lucia.

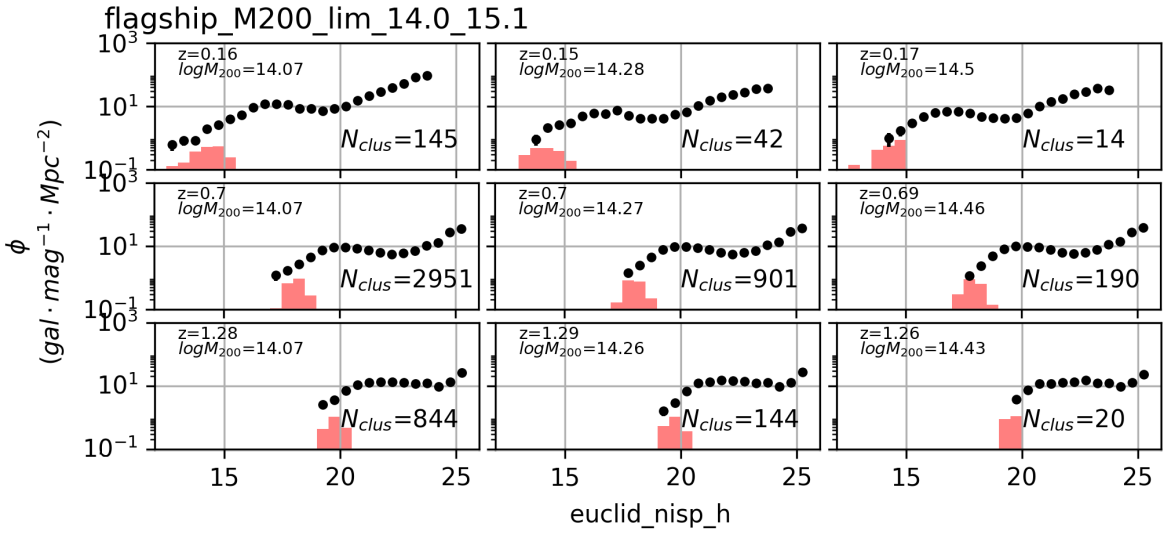

Figure B.4: Composite luminosity functions in the Euclid NISP H band for haloes in different bins of redshift (increasing from top to bottom) and mass (increasing from left to right). The red histograms show the distribution of the central galaxies magnitude.

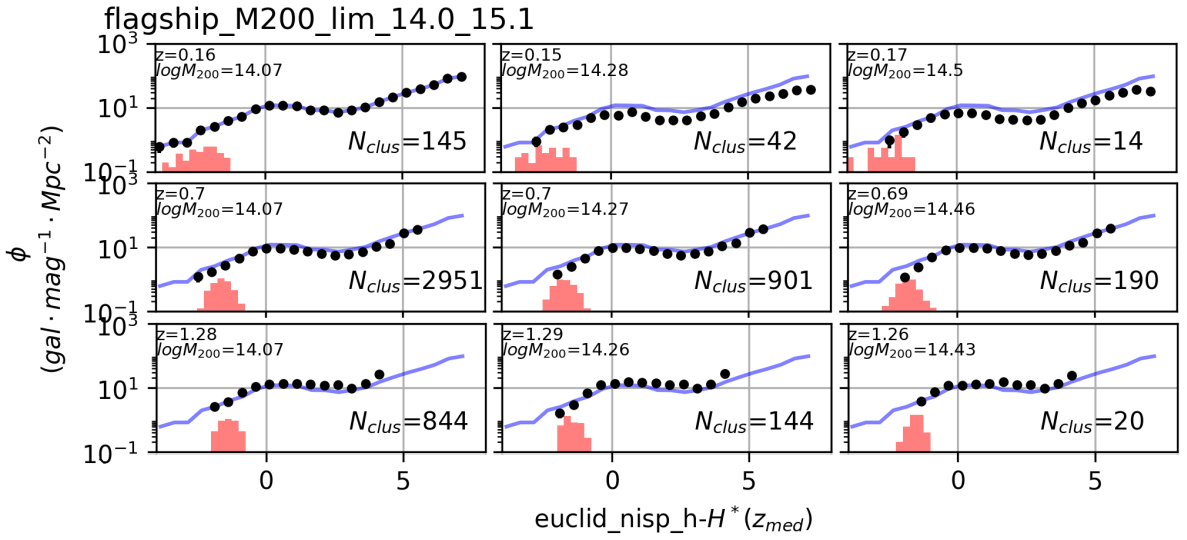

Figure B.5: Composite luminosity functions in the Euclid NISP H band shifted by the value of a model characteristic magnitude m^*_H, for haloes in different bins of redshift (increasing from top to bottom) and mass (increasing from left to right). The red histograms show the distribution of the central galaxies magnitude. The blue curve indicate the shape of the composite luminosity function at low mass and low redshift.

B.3 Conclusions

An exhaustive set of tests of the properties of galaxies in clusters was performed to validate the Flagship simulation. In this thesis, we focused on the properties of BCGs and the cluster galaxies luminosity function. We observed several unexpected features that are related to the membership attribution of galaxies and the redshift evolution of their properties. They are related to the recipes used to generate the galaxy properties in the simulation. These findings were included in a report sent to the cosmological simulations scientific working group, in order to generate new simulations more compliant with the expected data properties.

Appendix C

BCG catalogue of the XXL-N clusters

Table C.1: Properties of the BCGs in the XXL-N cluster sample, ordered by increasing redshift. Column 1 indicates the XXL cluster's name, Cols. 2, 3 and 4 indicate the position and redshift of the X-ray cluster center, Col. 5 indicates the XXL classification of the cluster, Col. 6 indicates the apparent magnitude of the BCG in the i' band, Cols. 7, 8 and 9 indicate the position and redshift of the BCG. When no spectroscopic redshift is available for the BCG, we used instead the photometric redshift (*phot.*). The table is available at the XXL Master Catalogue browser (http://cosmosdb.iasf-milano.inaf.it/XXL) and at the Centre de Données astronomiques de Strasburg (CDS, http://vizier.u-strasbg.fr/viz-bin/VizieR-3?-source=IX/52/xxlnbcg&-out.add=_r).

Name	R.A.	dec.	z	class	$i'_{mag,BCG}$	R.A.$_{BCG}$	dec.$_{BCG}$	z$_{BCG}$
XLSSC 147	37.641	-4.625	0.0307	2	13.932	37.6410	-4.6247	0.0298
XLSSC 115	32.681	-6.588	0.0431	1	14.048	32.6799	-6.5797	0.0429
XLSSC 171	31.986	-5.871	0.0436	1	14.787	31.9868	-5.8699	0.0433
XLSSC 113	30.561	-7.009	0.0499	1	14.291	30.5610	-7.0082	0.0510
XLSSC 054	36.319	-5.887	0.0535	1	14.415	36.3185	-5.8869	0.0534
XLSSC 011	36.540	-4.969	0.0538	1	14.441	36.5403	-4.9682	0.0500
XLSSC 191	36.574	-5.078	0.0539	1	14.786	36.5727	-5.0787	0.0546
XLSSC 190	36.748	-4.589	0.0696	1	14.153	36.7457	-4.5908	0.0700
XLSSC 021	36.233	-5.134	0.0848	1	15.330	36.2339	-5.1332	0.0845
XLSSC 196	30.728	-7.652	0.1361	1	15.786	30.7270	-7.6508	0.1376
XLSSC 162	32.524	-6.093	0.1377	2	16.995	32.5234	-6.0961	0.1378
XLSSC 095	31.962	-5.206	0.1382	1	16.471	31.9625	-5.2063	*phot.*
XLSSC 201	32.767	-4.893	0.1383	1	15.981	32.7621	-4.8938	0.1379
XLSSC 060	33.668	-4.553	0.1389	1	15.114	33.6713	-4.5673	0.1392
XLSSC 112	32.514	-5.462	0.1391	1	15.940	32.5093	-5.4678	0.1381
XLSSC 138	33.750	-3.905	0.1395	2	15.967	33.7658	-3.8969	0.1375
XLSSC 090	37.121	-4.857	0.1411	1	16.164	37.1222	-4.8565	0.1417
XLSSC 087	37.720	-4.348	0.1414	1	16.060	37.7208	-4.3478	0.1409
XLSSC 176	32.490	-4.980	0.1415	1	15.609	32.4941	-4.9824	*phot.*
XLSSC 041	36.378	-4.239	0.1420	1	16.547	36.3782	-4.2385	0.1430
XLSSC 057	34.051	-4.242	0.1532	1	16.068	34.0506	-4.2394	0.1534
XLSSC 166	33.211	-4.600	0.1579	1	16.349	33.2122	-4.5977	0.1572
XLSSC 154	38.502	-4.826	0.1791	1	16.445	38.5017	-4.8272	0.1801
XLSSC 165	33.356	-4.516	0.1804	2	17.295	33.3565	-4.5150	0.1817
XLSSC 091	37.926	-4.881	0.1860	1	16.283	37.9216	-4.8826	0.1852
XLSSC 151	38.122	-4.788	0.1892	1	16.702	38.1435	-4.7609	0.1889

Table C.1: continued.

Name	RA	Dec	z	class	$i'_{mag,BCG}$	RA_{BCG}	Dec_{BCG}	z_{BCG}
XLSSC 079	34.494	-4.868	0.1938	2	18.190	34.5074	-4.8504	0.1924
XLSSC 178	30.753	-6.285	0.1944	2	17.362	30.7566	-6.2801	*phot.*
XLSSC 123	36.487	-5.643	0.1944	1	16.537	36.4870	-5.6428	0.1947
XLSSC 141	34.357	-4.659	0.1960	2	18.481	34.3596	-4.6598	0.1950
XLSSC 193	34.876	-5.058	0.2032	2	17.571	34.8743	-5.0555	0.2035
XLSSC 189	34.908	-4.007	0.2035	1	16.975	34.9241	-4.0093	0.2042
XLSSC 152	38.082	-4.817	0.2050	2	17.945	38.0648	-4.8100	0.2042
XLSSC 075	35.834	-5.454	0.2107	1	17.242	35.8342	-5.4542	0.2111
XLSSC 177	31.290	-4.918	0.2111	2	17.151	31.2905	-4.9184	0.2114
XLSSC 055	36.454	-5.896	0.2321	1	16.562	36.4554	-5.8962	0.2329
XLSSC 103	36.886	-5.961	0.2327	1	17.154	36.8867	-5.9645	0.2319
XLSSC 114	30.425	-5.031	0.2335	2	16.605	30.4207	-5.0302	0.2332
XLSSC 174	30.592	-5.899	0.2351	1	17.259	30.5905	-5.9031	0.2352
XLSSC 108	31.832	-4.827	0.2543	1	17.114	31.8336	-4.8252	0.2546
XLSSC 146	37.462	-4.150	0.2544	1	17.532	37.4514	-4.1316	0.2549
XLSSC 061	35.485	-5.758	0.2592	1	17.061	35.4849	-5.7588	0.2592
XLSSC 044	36.141	-4.236	0.2627	1	17.805	36.1385	-4.2387	0.2621
XLSSC 025	36.353	-4.680	0.2649	1	17.408	36.3530	-4.6792	0.2643
XLSSC 163	32.463	-6.117	0.2832	1	17.224	32.4663	-6.1199	0.2835
XLSSC 180	33.863	-5.556	0.2895	1	16.942	33.8730	-5.5486	*phot.*
XLSSC 137	34.416	-3.807	0.2905	2	17.476	34.3994	-3.8017	0.2915
XLSSC 150	37.661	-4.992	0.2918	1	16.804	37.6616	-4.9910	0.2919
XLSSC 149	37.634	-4.989	0.2918	2	18.004	37.6333	-4.9895	0.2910
XLSSC 202	34.160	-4.617	0.2920	2	18.821	34.1503	-4.6394	0.2940
XLSSC 175	31.649	-7.568	0.2928	2	17.911	31.6483	-7.5699	0.2924
XLSSC 022	36.917	-4.858	0.2932	1	17.656	36.9181	-4.8586	0.2940
XLSSC 104	37.324	-5.895	0.2936	1	17.532	37.3287	-5.8872	0.2912
XLSSC 140	36.303	-5.524	0.2937	2	17.611	36.3025	-5.5227	0.2939
XLSSC 148	37.719	-4.859	0.2938	2	17.580	37.7228	-4.8583	0.2939
XLSSC 168	37.387	-5.880	0.2948	1	17.953	37.3690	-5.8890	0.2951
XLSSC 088	37.611	-4.581	0.2951	1	17.800	37.6156	-4.5636	0.2950
XLSSC 027	37.012	-4.851	0.2954	1	17.648	37.0186	-4.8499	0.2941
XLSSC 098	33.115	-6.076	0.2967	1	17.575	33.1144	-6.0750	0.2965
XLSSC 117	33.121	-5.528	0.2978	1	17.057	33.1212	-5.5292	0.2985
XLSSC 167	32.479	-4.630	0.2981	1	18.447	32.4694	-4.6325	0.2994
XLSSC 008	36.336	-3.801	0.2989	1	18.445	36.3374	-3.7969	0.2973
XLSSC 111	33.111	-5.627	0.3000	1	17.033	33.1124	-5.6265	0.2999
XLSSC 106	31.351	-5.732	0.3000	1	17.372	31.3676	-5.7324	0.2972
XLSSC 161	33.915	-5.980	0.3061	1	17.649	33.9145	-5.9802	0.3082
XLSSC 013	36.858	-4.538	0.3075	1	17.386	36.8585	-4.5372	0.3100
XLSSC 121	37.015	-5.297	0.3170	2	17.218	37.0212	-5.2950	0.3163
XLSSC 040	35.523	-4.547	0.3198	1	18.366	35.5190	-4.5501	0.3188
XLSSC 018	36.008	-5.091	0.3236	1	18.023	36.0090	-5.0907	0.3238
XLSSC 058	34.935	-4.889	0.3324	1	17.815	34.9229	-4.8752	0.3328
XLSSC 200	30.331	-6.830	0.3331	1	18.550	30.3364	-6.8313	*phot.*
XLSSC 156	30.766	-7.101	0.3360	2	17.900	30.7695	-7.1092	0.3326
XLSSC 199	30.192	-6.708	0.3392	1	17.708	30.1922	-6.7083	0.3387
XLSSC 192	34.509	-5.029	0.3407	2	20.234	34.5105	-5.0291	*phot.*

Table C.1: continued.

Name	RA	Dec	z	class	$i'_{mag,BCG}$	RA_{BCG}	Dec_{BCG}	z_{BCG}
XLSSC 056	33.871	-4.682	0.3479	1	17.383	33.8676	-4.6781	0.3469
XLSSC 198	33.496	-5.186	0.3565	1	18.191	33.4950	-5.1862	0.3540
XLSSC 135	33.868	-4.049	0.3708	2	18.016	33.8691	-4.0453	0.3709
XLSSC 181	36.376	-3.817	0.3712	2	19.436	36.3830	-3.8239	0.3720
XLSSC 067	34.681	-5.549	0.3819	1	18.782	34.6907	-5.5485	0.3839
XLSSC 099	33.220	-6.202	0.3911	1	17.834	33.2195	-6.2032	0.3911
XLSSC 170	37.998	-5.737	0.4029	2	18.086	37.9988	-5.7367	0.4027
XLSSC 194	34.200	-4.555	0.4111	2	19.581	34.2025	-4.5553	0.4132
XLSSC 173	31.251	-5.931	0.4134	1	19.288	31.2516	-5.9301	0.4134
XLSSC 086	32.809	-6.162	0.4242	1	18.691	32.8087	-6.1660	0.4236
XLSSC 172	31.571	-5.893	0.4265	2	18.821	31.5694	-5.8893	0.4272
XLSSC 082	32.714	-6.173	0.4268	1	18.532	32.7140	-6.1788	0.4240
XLSSC 085	32.870	-6.196	0.4278	1	18.211	32.8698	-6.1963	0.4289
XLSSC 093	31.699	-6.948	0.4291	1	18.518	31.6987	-6.9499	0.4328
XLSSC 006	35.439	-3.772	0.4291	1	17.882	35.4406	-3.7720	0.4331
XLSSC 084	32.767	-6.211	0.4296	1	19.286	32.7621	-6.2130	*phot.*
XLSSC 083	32.735	-6.200	0.4299	1	18.601	32.7350	-6.1984	0.4303
XLSSC 092	32.071	-7.276	0.4318	1	18.492	32.0840	-7.2774	0.4272
XLSSC 105	38.411	-5.506	0.4321	1	18.751	38.3983	-5.5060	0.4299
XLSSC 155	31.134	-6.748	0.4331	1	18.722	31.1359	-6.7479	0.4328
XLSSC 065	34.245	-4.819	0.4350	2	20.672	34.2428	-4.8156	0.4340
XLSSC 107	31.354	-7.594	0.4359	1	18.772	31.3541	-7.5945	0.4338
XLSSC 197	30.923	-7.785	0.4393	1	17.978	30.9245	-7.7850	0.4401
XLSSC 158	32.793	-4.349	0.4422	2	18.343	32.7938	-4.3448	0.4433
XLSSC 110	33.537	-5.585	0.4453	1	18.760	33.5339	-5.5927	0.4453
XLSSC 187	34.136	-4.509	0.4467	2	18.823	34.1328	-4.5075	0.4469
XLSSC 144	34.152	-4.450	0.4470	2	19.259	34.1508	-4.4515	0.4475
XLSSC 142	34.729	-5.469	0.4505	2	18.538	34.7355	-5.4721	0.4532
XLSSC 109	32.296	-6.346	0.4908	1	18.567	32.2967	-6.3453	0.4873
XLSSC 049	35.988	-4.588	0.4936	1	19.179	35.9897	-4.5861	0.4954
XLSSC 020	36.635	-5.001	0.4944	2	19.148	36.6369	-5.0086	0.4976
XLSSC 169	37.538	-5.679	0.4977	1	18.918	37.5396	-5.6759	0.4991
XLSSC 183	35.065	-4.917	0.5112	2	19.459	35.0590	-4.9243	0.5112
XLSSC 186	36.003	-5.864	0.5150	2	18.645	35.9999	-5.8632	0.5147
XLSSC 124	34.425	-4.863	0.5159	1	19.088	34.4196	-4.8622	0.5190
XLSSC 096	30.973	-5.027	0.5202	1	19.019	30.9709	-5.0279	0.5203
XLSSC 116	32.664	-5.945	0.5339	2	19.066	32.6653	-5.9437	0.5349
XLSSC 130	35.176	-5.430	0.5463	2	19.306	35.1759	-5.4319	0.5509
XLSSC 185	36.387	-5.539	0.5663	2	19.403	36.3888	-5.5346	0.5661
XLSSC 188	33.812	-4.223	0.5703	2	19.648	33.8113	-4.2242	0.5703
XLSSC 038	36.856	-4.190	0.5835	2	19.500	36.8554	-4.1823	0.5855
XLSSC 157	30.865	-6.929	0.5853	1	19.180	30.8644	-6.9385	0.5847
XLSSC 179	30.482	-6.574	0.6081	1	19.767	30.4914	-6.5648	0.6091
XLSSC 089	37.127	-4.733	0.6090	1	19.615	37.1302	-4.7309	*phot.*
XLSSC 001	36.238	-3.817	0.6141	1	19.830	36.2388	-3.8147	0.6171
XLSSC 159	32.268	-5.305	0.6145	2	19.894	32.2621	-5.2992	0.6142
XLSSC 145	37.388	-4.666	0.6265	2	20.157	37.3878	-4.6632	0.6256
XLSSC 030	35.778	-4.216	0.6308	2	20.428	35.7905	-4.2103	0.6330

Table C.1: continued.

Name	RA	Dec	z	class	$i'_{mag,BCG}$	RA_{BCG}	Dec_{BCG}	z_{BCG}
XLSSC 059	34.397	-5.223	0.6449	1	19.729	34.4049	-5.2248	0.6470
XLSSC 080	34.597	-5.413	0.6463	2	19.670	34.5980	-5.4168	0.6457
XLSSC 195	34.266	-4.478	0.6615	2	19.537	34.2700	-4.4795	0.6582
XLSSC 097	33.342	-6.098	0.6967	1	19.811	33.3427	-6.0990	0.6952
XLSSC 076	33.682	-3.823	0.7501	1	19.884	33.6821	-3.8226	0.7473
XLSSC 101	32.193	-4.436	0.7556	1	19.254	32.1958	-4.4311	0.7533
XLSSC 002	36.384	-3.920	0.7715	1	20.246	36.3853	-3.9193	0.7716
XLSSC 184	35.311	-4.204	0.8112	2	21.155	35.3142	-4.2083	0.8125
XLSSC 160	31.521	-5.194	0.8174	2	20.522	31.5202	-5.1925	0.8175
XLSSC 071	35.640	-4.967	0.8327	2	20.172	35.6420	-4.9655	0.8320
XLSSC 064	34.632	-5.017	0.8740	1	21.257	34.6336	-5.0165	0.8740
XLSSC 153	38.490	-5.139	0.8799	2	20.951	38.4890	-5.1398	0.8794
XLSSC 094	30.648	-6.732	0.8860	1	21.233	30.6545	-6.7418	0.8855
XLSSC 100	31.549	-6.193	0.9150	1	20.796	31.5527	-6.1985	0.9202
XLSSC 078	33.948	-4.842	0.9527	2	21.125	33.9482	-4.8376	0.9531
XLSSC 102	31.322	-4.652	0.9691	1	20.821	31.3196	-4.6556	*phot.*
XLSSC 072	33.850	-3.726	1.0023	1	21.438	33.8500	-3.7256	*phot.*
XLSSC 029	36.017	-4.225	1.0500	1	21.766	36.0174	-4.2240	1.0500
XLSSC 005	36.788	-4.301	1.0579	1	22.120	36.7872	-4.2988	1.0574
XLSSC 203	34.428	-4.989	1.0770	2	22.199	34.4248	-4.9999	*phot.*

Appendix D

Dark matter and Sunyaev-Zel'dovich maps of the RHAPSODY-G clusters

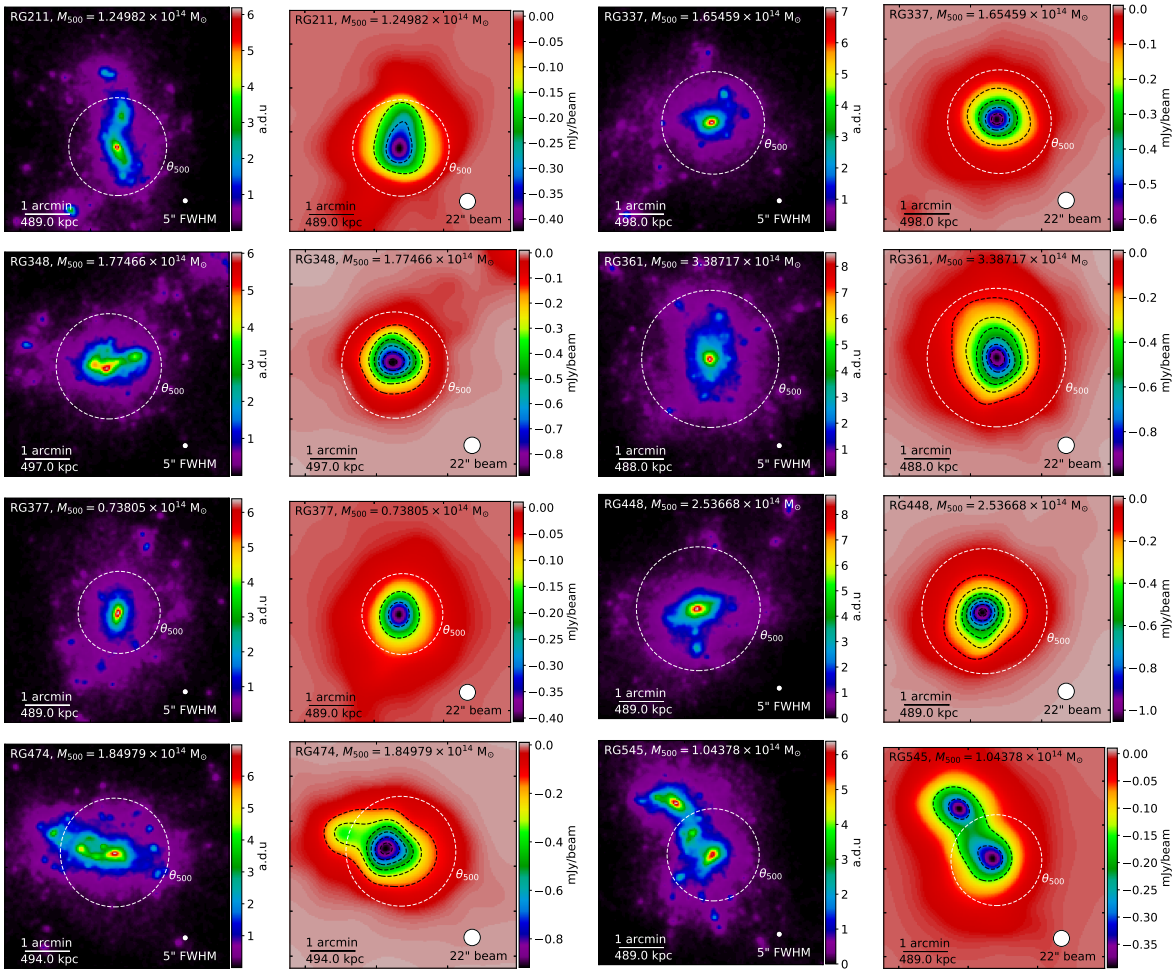

Figure D.1: RHAPSODY-G simulated clusters (Hahn et al. 2017) selected at $z = 1$. 1^{st} *and* 3^{rd} *columns:* dark matter particle density, smoothed at a resolution of $5''$ FWHM. 2^{nd} *and* 4^{th} *column:* NIKA2 SZ simulated surface brightness images at 150 GHz, taking into account the beam and bandpass, smoothed at an effective resolution of $22''$ FWHM. The dashed white circles indicates θ_{500}.

Appendix E

List of publications

I present in the following the list of proposals and publications which I led, or to which I contributed, during the course of my PhD.

E.1 Referred publications

Published articles:

- **M. Ricci**, C. Benoist, S. Maurogordato et al., A&A, 620:A13. 2018
  The XXL survey XXVIII: Galaxy luminosity functions of the XXL-N clusters
- E. Koulouridis, **M. Ricci**, P. Giles et al., A&A, 620:A20. 2018
  The XXL survey XXXV: The role of cluster mass in AGN activity
- C. Adami, P. Giles, E. Koulouridis, [...], **M. Ricci** et al., A&A, 620:A5. 2018
  The XXL Survey XX: The 365 cluster catalogue
- R. Adam, O. Hahn, F. Ruppin , [...], **M. Ricci** et al., A&A, 614:A118. 2018
  Sub-structure and merger detection in resolved NIKA Sunyaev-Zel'dovich images of distant clusters

Published proceeding:

- M. Pierre et al., Astronomische Nachrichten, 338, 334–341 2017
  The XXL survey: first results and future
  Proceeding of the XMM Next Decade Workshop held at ESAC, 9-11 May 2016

Articles in preparation:

- M. Ricci et al.,
  Sunyaev-Zel'dovich imaging of XLSSC102 at $z \sim 1$: multi-wavelength analysis and implication for the pressure profile
- R. Adam et al., (submitted to the Euclid collaboration)
  Euclid: Detection of galaxy clusters in the wide survey - performance and algorithm selection
- C. Benoist et al.,
  The XXL survey : Comparison of X-ray and optically selected clusters in the XXL survey

E.2 Other publications

Observing proposals:

As Principal Investigator:

– ***Sunyaev-Zel'dovich follow-up of XXL galaxy clusters at z∼1 with NIKA2*** Sept 2017
PIs: M. Ricci and R. Adam - IRAM 30m telescope, NIKA2 instrument - A Rated, 81 hours awarded

As Co-Investigator:

– ***CO redshift search for bright NIKA distant lensed galaxy candidates*** Sept 2016
PIs: R. Adam and A. Beelen - IRAM 30m telescope, EMIR instrument - A Rated, 21.3 hours awarded

– ***NOEMA follow-up of NIKA high redshift lensed galaxy candidates*** Sept 2016
PIs: R. Adam and A. Beelen - IRAM NOEMA - B Rated

Collaboration report:

– G. de Lucia et al., Euclid internal report 2017
Flagship Validation activities

Press releases:

– ***Redessiner l'Univers en rayons X***
XXL press release from the Lagrange laboratory
https://www.oca.eu/fr/evenements/2085-redessiner-univers-en-rayonsx

– ***Tracing the Universe: X-ray survey supports standard cosmological model***
XXL press release from ESA
http://sci.esa.int/xmm-newton/60686-tracing-the-universe-x-ray-survey-supports-standard-cosmological-model/

Bibliography

Abazajian, K. N., Adshead, P., Ahmed, Z., et al. (2016). CMB-S4 Science Book, First Edition. *ArXiv e-prints*. (Cited on page 38.)

Abbott, B. P., Abbott, R., Abbott, T. D., et al. (2016). Tests of general relativity with gw150914. *Phys. Rev. Lett.*, 116:221101. (Cited on page 12.)

Abbott, B. P., Abbott, R., Abbott, T. D., et al. (2017). Gw170817: Observation of gravitational waves from a binary neutron star inspiral. *Phys. Rev. Lett.*, 119:161101. (Cited on page 8.)

Abbott, B. P., Abbott, R., Abbott, T. D., et al. (2017). A gravitational-wave standard siren measurement of the Hubble constant. Nature, 551:85–88. (Cited on page 12.)

Acero, F., Acquaviva, J.-T., Adam, R., et al. (2017). French SKA White Book - The French Community towards the Square Kilometre Array. *ArXiv e-prints*. (Cited on pages 35 and 38.)

Adam, R. (2015). *Observation of galaxy clusters via the Sunyaev-Zel'dovich effect and the polarization of the cosmic microwave background*. Theses, Université Grenoble Alpes. (Cited on pages 32, 151, 153, 154, 156, 187, and 190.)

Adam, R., Bartalucci, I., Pratt, G. W., et al. (2017). Mapping the kinetic Sunyaev-Zel'dovich effect toward MACS J0717.5+3745 with NIKA. A&A, 598:A115. (Cited on pages 20 and 165.)

Adam, R., Comis, B., Bartalucci, I., et al. (2016). High angular resolution Sunyaev-Zel'dovich observations of MACS J1423.8+2404 with NIKA: Multiwavelength analysis. A&A, 586:A122. (Cited on pages 162 and 165.)

Adam, R., Comis, B., Macías-Pérez, J.-F., et al. (2015). Pressure distribution of the high-redshift cluster of galaxies CL J1226.9+3332 with NIKA. A&A, 576:A12. (Cited on pages 147, 157, 158, 162, 188, 196, and 201.)

Adam, R., Comis, B., Macías-Pérez, J. F., et al. (2014). First observation of the thermal Sunyaev-Zel'dovich effect with kinetic inductance detectors. A&A, 569:A66. (Cited on page 157.)

Adam, R., Hahn, O., Ruppin, F., et al. (2018). Substructure and merger detection in resolved NIKA Sunyaev-Zel'dovich images of distant clusters. A&A, 614:A118. (Cited on pages 144, 147, 181, 182, and 183.)

Adami, C., Giles, P., Koulouridis, E., et al. (2018). The XXL Survey. XX. The 365 cluster catalogue. A&A, 620:A5. (Cited on pages 47, 48, 60, 76, 123, 129, 140, 144, and 206.)

Aguirre, P., Lindner, R. R., Baker, A. J., et al. (2018). The LABOCA/ACT Survey of Clusters at All Redshifts: Multiwavelength Analysis of Background Submillimeter Galaxies. ApJ, 855(1):26. (Cited on page 165.)

Aihara, H., Arimoto, N., Armstrong, R., et al. (2018). The Hyper Suprime-Cam SSP Survey: Overview and survey design. PASJ, 70:S4. (Cited on pages 37 and 49.)

Albrecht, A., Bernstein, G., Cahn, R., et al. (2006). Report of the Dark Energy Task Force. *ArXiv Astrophysics e-prints*. (Cited on page 18.)

Allen, S. W., Evrard, A. E., and Mantz, A. B. (2011). Cosmological Parameters from Observations of Galaxy Clusters. *Annual Review of Astronomy and Astrophysics*, 49:409–470. (Cited on pages 18 and 35.)

Allen, S. W., Rapetti, D. A., Schmidt, R. W., et al. (2008). Improved constraints on dark energy from Chandra X-ray observations of the largest relaxed galaxy clusters. MNRAS, 383:879–896. (Cited on page 20.)

Alpher, R. A., Bethe, H., and Gamow, G. (1948). The Origin of Chemical Elements. *Physical Review*, 73:803–804. (Cited on page 8.)

Alshino, A., Khosroshahi, H., Ponman, T., et al. (2010). Luminosity functions of XMM–LSS C1 galaxy clusters. MNRAS, 401(2):941–962. (Cited on pages 76, 103, and 104.)

Anders, E. and Grevesse, N. (1989). Abundances of the elements - Meteoritic and solar. Geochim. Cosmochim. Acta, 53:197–214. (Cited on page 188.)

Anderson, L., Aubourg, É., Bailey, S., et al. (2014). The clustering of galaxies in the SDSS-III Baryon Oscillation Spectroscopic Survey: baryon acoustic oscillations in the Data Releases 10 and 11 Galaxy samples. MNRAS, 441:24–62. (Cited on page 33.)

Andreon, S. (2006). The build-up of the red sequence in the galaxy cluster MS1054-0321 at z = 0.831. MNRAS, 369:969–975. (Cited on page 75.)

Andreon, S. (2008). The history of mass assembly of faint red galaxies in 28 galaxy clusters since z = 1.3. MNRAS, 386:1045–1052. (Cited on page 75.)

Andreon, S. and Bergé, J. (2012). Richness-mass relation self-calibration for galaxy clusters. A&A, 547:A117. (Cited on page 85.)

Andreon, S. and Congdon, P. (2014). The insignificant evolution of the richness-mass relation of galaxy clusters. A&A, 568:A23. (Cited on page 107.)

Andreon, S. and Hurn, M. A. (2010). The scaling relation between richness and mass of galaxy clusters: a bayesian approach. MNRAS, 404:1922–1937. (Cited on page 75.)

Angulo, R. E., Springel, V., White, S. D. M., et al. (2012). Scaling relations for galaxy clusters in the Millennium-XXL simulation. MNRAS, 426:2046–2062. (Cited on page 18.)

Annunziatella, M., Mercurio, A., Biviano, A., et al. (2016). CLASH-VLT: Environment-driven evolution of galaxies in the z = 0.209 cluster Abell 209. A&A, 585:A160. (Cited on page 31.)

Aragon-Calvo, M. A., Neyrinck, M. C., and Silk, J. (2016). How Cosmic Web Detachment Drives Galaxy Quenching. *ArXiv e-prints*. (Cited on page 26.)

Arnaud, M. (2005). X-ray observations of clusters of galaxies. In Melchiorri, F. and Rephaeli, Y., editors, *Background Microwave Radiation and Intracluster Cosmology*, volume 2005937974, page 77. (Cited on page 31.)

Arnaud, M., Pointecouteau, E., and Pratt, G. W. (2005). The structural and scaling properties of nearby galaxy clusters. II. The M-T relation. A&A, 441:893–903. (Cited on page 36.)

Arnaud, M., Pratt, G. W., Piffaretti, R., et al. (2010). The universal galaxy cluster pressure profile from a representative sample of nearby systems (REXCESS) and the Y_{SZ} - M_{500} relation. A&A, 517:A92. (Cited on pages 36, 140, 141, 146, 147, 194, 196, 197, 198, and 200.)

Arnold, T. J., Martini, P., Mulchaey, J. S., Berti, A., and Jeltema, T. E. (2009). Active Galactic Nuclei in Groups and Clusters of Galaxies: Detection and Host Morphology. ApJ, 707:1691–1706. (Cited on page 115.)

Arnouts, S., Cristiani, S., Moscardini, L., et al. (1999). Measuring and modelling the redshift evolution of clustering: the Hubble Deep Field North. MNRAS, 310:540–556. (Cited on page 55.)

Arnouts, S., Walcher, C. J., Le Fèvre, O., et al. (2007). The SWIRE-VVDS-CFHTLS surveys: stellar mass assembly over the last 10 Gyr. Evidence for a major build up of the red sequence between $z = 2$ and $z = 1$. A&A, 476(1):137–150. (Cited on page 59.)

Ascaso, B., Benítez, N., Dupke, R., et al. (2016). An accurate cluster selection function for the J-PAS narrow-band wide-field survey. *Monthly Notices of the Royal Astronomical Society*, 456:4291–4304. (Cited on page 37.)

Ascaso, B., Mei, S., Bartlett, J. G., and Benítez, N. (2017). Apples to apples A^2 - II. Cluster selection functions for next-generation surveys. MNRAS, 464:2270–2280. (Cited on page 211.)

Ascaso, B., Mei, S., and Benítez, N. (2015). Apples to apples A^2 - I. Realistic galaxy simulated catalogues and photometric redshift predictions for next-generation surveys. MNRAS, 453:2515–2532. (Cited on page 211.)

Baars, J. W. M., Hooghoudt, B. G., Mezger, P. G., and de Jonge, M. J. (1987). The IRAM 30-m millimeter radio telescope on Pico Veleta, Spain. A&A, 175:319–326. (Cited on page 149.)

Bacon, D. J., Refregier, A. R., and Ellis, R. S. (2000). Detection of weak gravitational lensing by large-scale structure. MNRAS, 318:625–640. (Cited on page 12.)

Bahcall, N. A. and Fan, X. (1998). A Lightweight Universe? *Proceedings of the National Academy of Science*, 95:5956–5959. (Cited on page 8.)

Bai, L., Rasmussen, J., Mulchaey, J. S., et al. (2010). The First Mid-infrared View of the Star-forming Properties of Nearby Galaxy Groups. ApJ, 713:637–650. (Cited on page 110.)

Baldry, I. K., Glazebrook, K., Brinkmann, J., et al. (2004). Quantifying the Bimodal Color-Magnitude Distribution of Galaxies. ApJ, 600:681–694. (Cited on page 25.)

Baldry, I. K., Robotham, A. S. G., Hill, D. T., et al. (2010). Galaxy And Mass Assembly (GAMA): the input catalogue and star-galaxy separation. MNRAS, 404:86–100. (Cited on page 61.)

Barkhouse, W. A., Green, P. J., Vikhlinin, A., et al. (2006). ChaMP serendipitous gonlaxy cluster survey. ApJ, 645(2):955. (Cited on page 123.)

Barkhouse, W. A., Yee, H. K. C., and López-Cruz, O. (2007). The Luminosity Function of Low-Redshift Abell Galaxy Clusters. ApJ, 671:1471–1496. (Cited on page 95.)

Baron, D., Netzer, H., Prochaska, J. X., et al. (2018). Direct evidence of AGN-feedback: a post starburst galaxy stripped of its gas by AGN-driven winds. MNRAS. (Cited on page 27.)

Bartelmann, M. and Maturi, M. (2017). Weak gravitational lensing. *Scholarpedia*, 12:32440. (Cited on page 12.)

Baum, W. A. (1962). Photoelectric Magnitudes and Red-Shifts. In McVittie, G. C., editor, *Problems of Extra-Galactic Research*, volume 15 of *IAU Symposium*, page 390. (Cited on page 55.)

Baxter, E. J., Raghunathan, S., Crawford, T. M., et al. (2018). A measurement of CMB cluster lensing with SPT and DES year 1 data. MNRAS, 476:2674–2688. (Cited on page 34.)

Behroozi, P. S., Wechsler, R. H., and Conroy, C. (2013a). The average star formation histories of galaxies in dark matter halos from $z = 0$-8. ApJ, 770(1):57. (Cited on page 17.)

Behroozi, P. S., Wechsler, R. H., and Wu, H.-Y. (2013b). The rockstar phase-space temporal halo finder and the velocity offsets of cluster cores. ApJ, 762(2):109. (Cited on page 216.)

Bell, E. F., Wolf, C., Meisenheimer, K., et al. (2004). Nearly 5000 Distant Early-Type Galaxies in COMBO-17: A Red Sequence and Its Evolution since z∼1. ApJ, 608:752–767. (Cited on page 25.)

Bellagamba, F., Roncarelli, M., Maturi, M., and Moscardini, L. (2018). AMICO: optimized detection of galaxy clusters in photometric surveys. MNRAS, 473:5221–5236. (Cited on page 107.)

Benitez, N., Dupke, R., Moles, M., et al. (2014). J-PAS: The Javalambre-Physics of the Accelerated Universe Astrophysical Survey. *ArXiv e-prints*. (Cited on page 37.)

Benson, A. J. (2010). Galaxy formation theory. *Physics Reports*, 495(2):33–86. (Cited on page 17.)

Benítez, N. (2000). Bayesian Photometric Redshift Estimation. ApJ, 536:571–583. (Cited on pages 55, 57, and 59.)

Bernardeau, F., Colombi, S., Gaztañaga, E., and Scoccimarro, R. (2002). Large-scale structure of the Universe and cosmological perturbation theory. Phys. Rep., 367:1–248. (Cited on page 14.)

Bertin, E. and Arnouts, S. (1996). SExtractor: Software for source extraction. A&AS, 117:393–404. (Cited on pages 47 and 50.)

Bhattacharya, S. and Kosowsky, A. (2007). Cosmological Constraints from Galaxy Cluster Velocity Statistics. ApJ, 659:L83–L86. (Cited on page 20.)

Bhattacharya, S. and Kosowsky, A. (2008). Dark energy constraints from galaxy cluster peculiar velocities. Phys. Rev. D, 77(8):083004. (Cited on page 20.)

Biffi, V., Borgani, S., Murante, G., et al. (2016). On the Nature of Hydrostatic Equilibrium in Galaxy Clusters. ApJ, 827:112. (Cited on pages 21 and 36.)

Biffi, V., Dolag, K., and Merloni, A. (2018). AGN X-ray emission in galaxy clusters: contamination to the ICM X-ray luminosity. *ArXiv e-prints*. (Cited on pages 111 and 121.)

Binney, J. and Tremaine, S. (1987). *Galactic dynamics*. Princeton, NJ, Princeton University Press, 1987, 747 p. (Cited on page 35.)

Birkinshaw, M. (1999). The Sunyaev-Zel'dovich effect. Phys. Rep., 310:97–195. (Cited on page 32.)

Biviano, A. (2000). From Messier to Abell: 200 Years of Science with Galaxy Clusters. In *Constructing the Universe with Clusters of Galaxies*. (Cited on page 29.)

Biviano, A. (2008). Galaxy systems in the optical and infrared. *ArXiv e-prints*. (Cited on pages 28, 29, and 35.)

Blain, A. W. (1997). Gravitational lensing by clusters of galaxies in the millimetre/submillimetre waveband. MNRAS, 290:553–565. (Cited on page 29.)

Blain, A. W., Smail, I., Ivison, R. J., Kneib, J. P., and Frayer, D. T. (2002). Submillimeter galaxies. *Physics Reports*, 369(2):111–176. (Cited on page 165.)

Blanton, M. R., Dalcanton, J., Eisenstein, D., et al. (2001). The Luminosity Function of Galaxies in SDSS Commissioning Data. ApJ, 121:2358–2380. (Cited on pages 97 and 98.)

Blanton, M. R., Hogg, D. W., Bahcall, N. A., et al. (2003). The Galaxy Luminosity Function and Luminosity Density at Redshift z = 0.1. ApJ, 592:819–838. (Cited on pages 25 and 216.)

Blanton, M. R., Lupton, R. H., Schlegel, D. J., et al. (2005). The Properties and Luminosity Function of Extremely Low Luminosity Galaxies. ApJ, 631:208–230. (Cited on page 216.)

Bleem, L. E., Stalder, B., de Haan, T., et al. (2015). Galaxy Clusters Discovered via the Sunyaev-Zel'dovich Effect in the 2500-Square-Degree SPT-SZ Survey. ApJS, 216:27. (Cited on pages 38, 138, and 197.)

Bocquet, S., Saro, A., Dolag, K., and Mohr, J. J. (2016). Halo mass function: baryon impact, fitting formulae, and implications for cluster cosmology. MNRAS, 456:2361–2373. (Cited on page 139.)

Böhringer, H., Chon, G., and Collins, C. A. (2014). The extended ROSAT-ESO Flux Limited X-ray Galaxy Cluster Survey (REFLEX II). IV. X-ray luminosity function and first constraints on cosmological parameters. A&A, 570:A31. (Cited on page 36.)

Böhringer, H. and Werner, N. (2010). X-ray spectroscopy of galaxy clusters: studying astrophysical processes in the largest celestial laboratories. A&A Rev., 18:127–196. (Cited on page 31.)

Bolzonella, M., Miralles, J.-M., and Pelló, R. (2000). Photometric redshifts based on standard SED fitting procedures. A&A, 363:476–492. (Cited on pages 55, 57, and 59.)

Bouchet, F. R., Strauss, M. A., Davis, M., et al. (1993). Moments of the Counts Distribution in the 1.2 Jansky IRAS Galaxy Redshift Survey. ApJ, 417:36. (Cited on page 124.)

Bouillot, V. R., Alimi, J.-M., Corasaniti, P.-S., and Rasera, Y. (2015). Probing dark energy models with extreme pairwise velocities of galaxy clusters from the DEUS-FUR simulations. MNRAS, 450:145–159. (Cited on page 20.)

Bourdin, H., Mazzotta, P., Kozmanyan, A., Jones, C., and Vikhlinin, A. (2017). Pressure profiles of distant galaxy clusters in the planck catalogue. ApJ, 843(1):72. (Cited on page 197.)

Bourrion, O., Benoit, A., Bouly, J. L., et al. (2016). NIKEL_AMC: readout electronics for the NIKA2 experiment. *Journal of Instrumentation*, 11:P11001. (Cited on pages 151 and 153.)

Brammer, G. B., van Dokkum, P. G., and Coppi, P. (2008). EAZY: A Fast, Public Photometric Redshift Code. ApJ, 686(2):1503–1513. (Cited on page 55.)

Branchesi, M., Gioia, I. M., Fanti, C., and Fanti, R. (2007). High redshift X-ray galaxy clusters. I. The impact of point sources on the cluster properties. A&A, 472:727–737. (Cited on page 111.)

Brinchmann, J., Charlot, S., White, S. D. M., et al. (2004). The physical properties of star-forming galaxies in the low-redshift Universe. MNRAS, 351:1151–1179. (Cited on page 26.)

Brodwin, M., Stanford, S. A., Gonzalez, A. H., et al. (2013). The Era of Star Formation in Galaxy Clusters. ApJ, 779:138. (Cited on page 29.)

Brown, M. J. I., Moustakas, J., Smith, J.-D. T., et al. (2014). An Atlas of Galaxy Spectral Energy Distributions from the Ultraviolet to the Mid-infrared. ApJ*Supplement Series*, 212:18. (Cited on page 56.)

Bullock, J. S. and Boylan-Kolchin, M. (2017). Small-Scale Challenges to the ΛCDM Paradigm. ARA&A, 55:343–387. (Cited on page 13.)

Burgarella, D., Buat, V., Gruppioni, C., et al. (2013). Herschel PEP/HerMES: the redshift evolution ($0 < z < 4$) of dust attenuation and of the total (UV+IR) star formation rate density. A&A, 554:A70. (Cited on page 165.)

Burns, J. O., Skillman, S. W., and O'Shea, B. W. (2010). Galaxy Clusters at the Edge: Temperature, Entropy, and Gas Dynamics Near the Virial Radius. ApJ, 721:1105–1112. (Cited on page 195.)

Busha, M. T., Wechsler, R. H., Becker, M. R., Erickson, B., and Evrard, A. E. (2013). Catalog Production for the DES Blind Cosmology Challenge. In *American Astronomical Society Meeting Abstracts #221*, volume 221 of *American Astronomical Society Meeting Abstracts*, page 341.07. (Cited on page 127.)

Butcher, H. and Oemler, Jr., A. (1978). The evolution of galaxies in clusters. I - ISIT photometry of C1 0024+1654 and 3C 295. ApJ, 219:18–30. (Cited on page 29.)

Béthermin, M., Daddi, E., Magdis, G., et al. (2012). A Unified Empirical Model for Infrared Galaxy Counts Based on the Observed Physical Evolution of Distant Galaxies. ApJ*Letters*, 757:L23. (Cited on pages 176 and 177.)

Béthermin, M., De Breuck, C., Sargent, M., and Daddi, E. (2015). The influence of wavelength, flux, and lensing selection effects on the redshift distribution of dusty, star-forming galaxies. A&A, 576:L9. (Cited on pages 165 and 176.)

Calvo, M., Roesch, M., Désert, F.-X., et al. (2013). Improved mm-wave photometry for kinetic inductance detectors. A&A, 551:L12. (Cited on pages 151 and 153.)

Carlberg, R. G., Yee, H. K. C., and Ellingson, E. (1997). The Average Mass and Light Profiles of Galaxy Clusters. ApJ, 478:462–475. (Cited on page 35.)

Carliles, S., Budavári, T., Heinis, S., Priebe, C., and Szalay, A. S. (2010). Random Forests For Photometric Redshifts. ApJ, 712(1):511–515. (Cited on page 55.)

Carlstrom, J. E., Holder, G. P., and Reese, E. D. (2002). Cosmology with the Sunyaev-Zel'dovich Effect. ARA&A, 40:643–680. (Cited on page 32.)

Carniani, S., Marconi, A., Maiolino, R., et al. (2016). Fast outflows and star formation quenching in quasar host galaxies. A&A, 591:A28. (Cited on page 27.)

Carretero, J. et al. (2017). CosmoHub and SciPIC: Massive cosmological data analysis, distribution and generation using a Big Data platform. *PoS*, EPS-HEP2017:488. (Cited on page 216.)

Carter, M., Lazareff, B., Maier, D., et al. (2012). The EMIR multi-band mm-wave receiver for the IRAM 30-m telescope. A&A, 538:A89. (Cited on page 150.)

Casey, C. M., Narayanan, D., and Cooray, A. (2014). Dusty star-forming galaxies at high redshift. *Physics Reports*, 541(2):45–161. (Cited on pages 165, 171, and 175.)

Castignani, G. and Benoist, C. (2016). A new method to assign galaxy cluster membership using photometric redshifts. A&A, 595:A111. (Cited on pages 78 and 125.)

Catalano, A., Calvo, M., Ponthieu, N., et al. (2014). Performance and calibration of the NIKA camera at the IRAM 30 m telescope. A&A, 569:A9. (Cited on pages 151, 153, and 157.)

Cavaliere, A. and Fusco-Femiano, R. (1976). X-rays from hot plasma in clusters of galaxies. A&A, 49:137–144. (Cited on page 47.)

Chapman, S. C., Blain, A. W., Smail, I., and Ivison, R. J. (2005). A Redshift Survey of the Submillimeter Galaxy Population. ApJ, 622:772–796. (Cited on page 175.)

Cherenkov Telescope Array Consortium, T., :, Acharya, B. S., et al. (2017). Science with the Cherenkov Telescope Array. *ArXiv e-prints*. (Cited on page 38.)

Chiappetti, L., Fotopoulou, S., Lidman, C., et al. (2018). The XXL Survey: XXVII. The 3XLSS point source catalogue. A&A, 620:A12. (Cited on pages 112 and 189.)

Cialone, G., De Petris, M., Sembolini, F., et al. (2018). Morphological estimators on Sunyaev-Zel'dovich maps of MUSIC clusters of galaxies. MNRAS, 477:139–152. (Cited on page 181.)

Cicone, C., Maiolino, R., Sturm, E., et al. (2014). Massive molecular outflows and evidence for AGN feedback from CO observations. A&A, 562:A21. (Cited on page 27.)

Clerc, N., Adami, C., Lieu, M., et al. (2014). The XMM-LSS survey: the Class 1 cluster sample over the extended 11 deg^2 and its spatial distribution. MNRAS, 444:2723–2753. (Cited on page 111.)

Clowe, D., Bradač, M., Gonzalez, A. H., et al. (2006). A Direct Empirical Proof of the Existence of Dark Matter. ApJ, 648:L109–L113. (Cited on pages 20 and 33.)

Coleman, G. D., Wu, C.-C., and Weedman, D. W. (1980). Colors and magnitudes predicted for high redshift galaxies. ApJS, 43:393–416. (Cited on page 59.)

Coles, P. and Jones, B. (1991). A lognormal model for the cosmological mass distribution. MNRAS, 248:1–13. (Cited on page 79.)

Colless, M. (1989). The dynamics of rich clusters. II - Luminosity functions. MNRAS, 237:799–826. (Cited on pages 84, 97, 102, and 109.)

Collister, A. A. and Lahav, O. (2004). ANNz: Estimating Photometric Redshifts Using Artificial Neural Networks. *Publications of the Astronomical Society of the Pacific*, 116:345–351. (Cited on page 55.)

Connelly, J. L., Wilman, D. J., Finoguenov, A., et al. (2012). Exploring the Diversity of Groups at 0.1<z<0.8 with X-Ray and Optically Selected Samples. ApJ, 756:139. (Cited on pages 122 and 123.)

Conselice, C. J. (2014). The Evolution of Galaxy Structure Over Cosmic Time. ARA&A, 52:291–337. (Cited on page 24.)

Cooper, M. C., Newman, J. A., Coil, A. L., et al. (2007). The DEEP2 galaxy redshift survey: evolution of the colour-density relation at $0.4 < z < 1.35$. MNRAS, 376:1445–1459. (Cited on page 25.)

Coupon, J., Ilbert, O., Kilbinger, M., et al. (2009). Photometric redshifts for the CFHTLS T0004 deep and wide fields. A&A, 500:981–998. (Cited on pages 39, 59, 60, 63, 64, and 65.)

Crawford, S. M., Bershady, M. A., and Hoessel, J. G. (2009). The red-sequence luminosity function in massive intermediate-redshift galaxy clusters. ApJ, 690:1158–1180. (Cited on pages 75 and 90.)

Crocce, M., Carretero, J., Bauer, A. H., et al. (2016). Galaxy clustering, photometric redshifts and diagnosis of systematics in the DES Science Verification data. MNRAS, 455:4301–4324. (Cited on page 55.)

Croton, D. J., Farrar, G. R., Norberg, P., et al. (2005). The 2df Galaxy Redshift Survey: luminosity functions by density environment and galaxy type. MNRAS, 356:1155–1167. (Cited on page 76.)

Curtis, H. D. (1917). Novae in the Spiral Nebulae and the Island Universe Theory. PASP, 29:206–207. (Cited on page 7.)

da Cunha, E., Charlot, S., and Elbaz, D. (2008). A simple model to interpret the ultraviolet, optical and infrared emission from galaxies. *Monthly Notices of the Royal Astronomical Society*, 388:1595–1617. (Cited on page 23.)

da Cunha, E., Walter, F., Smail, I. R., et al. (2015). An ALMA Survey of Sub-millimeter Galaxies in the Extended Chandra Deep Field South: Physical Properties Derived from Ultraviolet-to-radio Modeling. ApJ, 806:110. (Cited on pages 173 and 175.)

Dahlen, T., Mobasher, B., Dickinson, M., et al. (2010). A Detailed Study of Photometric Redshifts for GOODS-South Galaxies. ApJ, 724:425–447. (Cited on page 55.)

Darvish, B., Mobasher, B., Sobral, D., et al. (2016). The Effects of the Local Environment and Stellar Mass on Galaxy Quenching to z∼3. ApJ, 825:113. (Cited on page 27.)

Day, P. K., LeDuc, H. G., Mazin, B. A., Vayonakis, A., and Zmuidzinas, J. (2003). A broadband superconducting detector suitable for use in large arrays. Nature, 425:817–821. (Cited on page 151.)

De Bernardis, F., Aiola, S., Vavagiakis, E. M., et al. (2017). Detection of the pairwise kinematic Sunyaev-Zel'dovich effect with BOSS DR11 and the Atacama Cosmology Telescope. J. Cosmology Astropart. Phys., 3:008. (Cited on page 20.)

De Bernardis, P., Ade, P. A. R., Bock, J. J., et al. (2000). A flat Universe from high-resolution maps of the cosmic microwave background radiation. Nature, 404:955–959. (Cited on pages 8 and 12.)

De Filippis, E., Paolillo, M., Longo, G., et al. (2011). The Luminosity Function of the NoSOCS Galaxy Cluster Sample. MNRAS, 414(3):2771–2784. arXiv: 1102.5310. (Cited on pages 78 and 104.)

De Lucia, G. (2007). How 'Heredity' and 'Environment' Shape Galaxy Properties. In Metcalfe, N. and Shanks, T., editors, *Cosmic Frontiers*, volume 379 of *Astronomical Society of the Pacific Conference Series*, page 257. (Cited on page 27.)

De Lucia, G., Poggianti, B. M., Aragón-Salamanca, A., et al. (2004). The Buildup of the Red Sequence in Galaxy Clusters since z ∼ 0.8. ApJ, 610:L77–L80. (Cited on pages 75 and 108.)

De Lucia, G., Poggianti, B. M., Aragón-Salamanca, A., et al. (2007). The build-up of the colour-magnitude relation in galaxy clusters since z ∼ 0.8. MNRAS, 374:809–822. (Cited on pages 75 and 108.)

De Lucia, G., Weinmann, S., Poggianti, B. M., Aragón-Salamanca, A., and Zaritsky, D. (2012). The environmental history of group and cluster galaxies in a λ cold dark matter universe. MNRAS, 423:1277–1292. (Cited on page 27.)

De Propris, R., Colless, M., Driver, S. P., et al. (2003). The 2df Galaxy Redshift Survey: the luminosity function of cluster galaxies. MNRAS, 342:725–737. (Cited on page 76.)

De Propris, R., Phillipps, S., and Bremer, M. N. (2013). Deep luminosity functions and colour-magnitude relations for cluster galaxies at $0.2 < z < 0.6$. MNRAS, 434:3469–3486. (Cited on page 75.)

De Propris, R., Stanford, S. A., Eisenhardt, P. R., Dickinson, M., and Elston, R. (1999). The K-Band Luminosity Function in Galaxy Clusters to $Z \sim 1$. ApJ, 118:719–729. (Cited on page 75.)

De Propris, R., Stanford, S. A., Eisenhardt, P. R., Holden, B. P., and Rosati, P. (2007). The Rest-Frame K-Band Luminosity Function of Galaxies in Clusters to $z = 1.3$. ApJ, 133:2209–2215. (Cited on page 75.)

Dekel, A. and Birnboim, Y. (2006). Galaxy bimodality due to cold flows and shock heating. *Mon Not R Astron Soc*, 368(1):2–20. (Cited on page 17.)

Desai, S., Armstrong, R., Mohr, J. J., et al. (2012). The blanco cosmology survey: Data acquisition, processing, calibration, quality diagnostics, and data release. ApJ, 757(1):83. (Cited on page 49.)

Despali, G., Giocoli, C., Bonamigo, M., Limousin, M., and Tormen, G. (2017). A look into the inside of haloes: a characterization of the halo shape as a function of overdensity in the Planck cosmology. MNRAS, 466:181–193. (Cited on pages 180 and 181.)

Despali, G., Giocoli, C., and Tormen, G. (2014). Some like it triaxial: the universality of dark matter halo shapes and their evolution along the cosmic time. MNRAS, 443:3208–3217. (Cited on pages 180 and 181.)

Dicke, R. H., Peebles, P. J. E., Roll, P. G., and Wilkinson, D. T. (1965). Cosmic Black-Body Radiation. ApJ, 142:414–419. (Cited on page 8.)

Dicker, S. R., Ade, P. A. R., Aguirre, J., et al. (2014). MUSTANG 2: A Large Focal Plane Array for the 100 m Green Bank Telescope. *Journal of Low Temperature Physics*, 176:808–814. (Cited on page 197.)

Donahue, M., Scharf, C. A., Mack, J., et al. (2002). Distant cluster hunting. ii. a comparison of x-ray and optical cluster detection techniques and catalogs from the rosat optical x-ray survey. ApJ, 569(2):689. (Cited on page 123.)

Eckert, D., Ettori, S., Coupon, J., et al. (2015). The XXL Survey. XIII. Baryon content of the bright cluster sample. A&A. (Cited on pages 21, 48, 140, and 189.)

Eckert, D., Ettori, S., Molendi, S., Vazza, F., and Paltani, S. (2013a). The X-ray/SZ view of the virial region. II. Gas mass fraction. A&A, 551:A23. (Cited on page 194.)

Eckert, D., Ettori, S., Pointecouteau, E., et al. (2017). The XMM cluster outskirts project (X-COP). *Astronomische Nachrichten*, 338(2-3):293–298. (Cited on page 196.)

Eckert, D., Molendi, S., Vazza, F., Ettori, S., and Paltani, S. (2013b). The X-ray/SZ view of the virial region. I. Thermodynamic properties. A&A, 551:A22. (Cited on pages 194 and 195.)

Eckert, D., Roncarelli, M., Ettori, S., et al. (2015). Gas clumping in galaxy clusters. MNRAS, 447:2198–2208. (Cited on page 195.)

Eckert, D., Vazza, F., Ettori, S., et al. (2012). The gas distribution in the outer regions of galaxy clusters. A&A, 541:A57. (Cited on page 195.)

Efstathiou, G. (1995). Counts-in-cells comparisons of redshift surveys. MNRAS, 276:1425–1434. (Cited on page 124.)

Egami, E., Rex, M., Rawle, T. D., et al. (2010). The Herschel Lensing Survey (HLS): Overview. A&A, 518:L12. (Cited on pages 29 and 165.)

Ehlert, S., Allen, S. W., Brandt, W. N., et al. (2015). X-ray bright active galactic nuclei in massive galaxy clusters - III. New insights into the triggering mechanisms of cluster AGN. MNRAS, 446:2709–2729. (Cited on page 115.)

Einasto, J. (2011). Dark Matter. *Baltic Astronomy*, 20:231–240. (Cited on page 8.)

Einstein, A. (1917). Kosmologische Betrachtungen zur allgemeinen Relativitatstheorie. *Sitzungsberichte der Königlich Preußischen Akademie der Wissenschaften (Berlin), Seite 142-152.* (Cited on page 7.)

Eisenstein, D. J., Zehavi, I., Hogg, D. W., et al. (2005). Detection of the Baryon Acoustic Peak in the Large-Scale Correlation Function of SDSS Luminous Red Galaxies. ApJ, 633:560–574. (Cited on page 12.)

Erb, D. K. (2015). Feedback in low-mass galaxies in the early Universe. Nature, 523:169–176. (Cited on page 17.)

Ettori, S., Donnarumma, A., Pointecouteau, E., et al. (2013). Mass Profiles of Galaxy Clusters from X-ray Analysis. Space Sci. Rev., 177:119–154. (Cited on pages 36, 188, and 195.)

Ettori, S., Morandi, A., Tozzi, P., et al. (2009). The cluster gas mass fraction as a cosmological probe: a revised study. A&A, 501:61–73. (Cited on page 20.)

Fabjan, D., Borgani, S., Rasia, E., et al. (2011). X-ray mass proxies from hydrodynamic simulations of galaxy clusters - I. MNRAS, 416:801–816. (Cited on page 36.)

Faccioli, L., Pacaud, F., Sauvageot, J. L., et al. (2018). The XXL Survey. XXIV. The final detection pipeline. A&A, 620:A9. (Cited on pages 47 and 121.)

Feldmann, R., Carollo, C. M., Porciani, C., et al. (2006). The Zurich Extragalactic Bayesian Redshift Analyzer and its first application: COSMOS. MNRAS, 372:565–577. (Cited on page 55.)

Feretti, L., Giovannini, G., Govoni, F., and Murgia, M. (2012). Clusters of galaxies: observational properties of the diffuse radio emission. A&A Rev., 20:54. (Cited on page 33.)

Fernández-Soto, A., Lanzetta, K. M., and Yahil, A. (1999). A New Catalog of Photometric Redshifts in the Hubble Deep Field*. *ApJ*, 513(1):34. (Cited on page 59.)

Ferrari, C., Govoni, F., Schindler, S., Bykov, A. M., and Rephaeli, Y. (2008). Observations of Extended Radio Emission in Clusters. Space Sci. Rev., 134:93–118. (Cited on page 33.)

Finkelstein, S. L., Rhoads, J. E., Malhotra, S., and Grogin, N. (2009). Lyman Alpha Galaxies: Primitive, Dusty, or Evolved? ApJ, 691:465–481. (Cited on page 175.)

Fioc, M. and Rocca-Volmerange, B. (1997). PEGASE: a UV to NIR spectral evolution model of galaxies. Application to the calibration of bright galaxy counts. A&A, 326:950–962. (Cited on pages 39 and 216.)

Fixsen, D. J. (2009). The Temperature of the Cosmic Microwave Background. ApJ, 707:916–920. (Cited on page 11.)

Fogarty, K., Postman, M., Connor, T., Donahue, M., and Moustakas, J. (2015). Star formation activity in clash brightest cluster galaxies. ApJ, 813(2):117. (Cited on page 119.)

Fotopoulou, S., Pacaud, F., Paltani, S., et al. (2016). The XXL Survey - VI. The 1000 brightest X-ray point sources. A&A, 592:A5. (XXL Paper VI). (Cited on page 77.)

Freedman, W. L., Madore, B. F., Gibson, B. K., et al. (2001). Final Results from the Hubble Space Telescope Key Project to Measure the Hubble Constant. ApJ, 553:47–72. (Cited on page 8.)

Friedmann, A. (1922). Über die Krümmung des Raumes. *Zeitschrift fur Physik*, 10:377–386. (Cited on pages 8 and 9.)

Friedmann, A. (1924). Über die Möglichkeit einer Welt mit konstanter negativer Krümmung des Raumes. *Zeitschrift fur Physik*, 21:326–332. (Cited on page 9.)

Gavazzi, R. and Soucail, G. (2007). Weak lensing survey of galaxy clusters in the CFHTLS Deep. A&A, 462:459–471. (Cited on page 34.)

Gerdes, D. W., Sypniewski, A. J., McKay, T. A., et al. (2010). ArborZ: Photometric Redshifts Using Boosted Decision Trees. ApJ, 715:823–832. (Cited on page 55.)

Ghirardini, V., Ettori, S., Amodeo, S., Capasso, R., and Sereno, M. (2017). On the evolution of the entropy and pressure profiles in X-ray luminous galaxy clusters at z>0.4. A&A, 604:A100. (Cited on page 197.)

Gilbank, D. G., Baldry, I. K., Balogh, M. L., Glazebrook, K., and Bower, R. G. (2010). The local star formation rate density: assessing calibrations using [OII], H and UV luminosities. MNRAS, 405:2594–2614. (Cited on page 26.)

Gilbank, D. G., Bower, R. G., Castander, F. J., and Ziegler, B. L. (2004). Exploring the selection of galaxy clusters and groups: an optical survey for X-ray dark clusters. MNRAS, 348:551–580. (Cited on page 123.)

Gilbank, D. G., Yee, H. K. C., Ellingson, E., et al. (2008). The Red-Sequence Luminosity Function in Galaxy Clusters since z $\sim$ 1. ApJ, 673:742–751. (Cited on pages 75 and 108.)

Giles, P. A., Maughan, B. J., Pacaud, F., et al. (2016). The XXL Survey. III. Luminosity-temperature relation of the bright cluster sample. A&A, 592:A3. (XXL Paper III). (Cited on pages 48 and 99.)

Golovich, N., Dawson, W. A., Wittman, D. M., et al. (2017). Merging Cluster Collaboration: Optical and Spectroscopic Survey of a Radio-Selected Sample of Twenty Nine Merging Galaxy Clusters. *ArXiv e-prints*. (Cited on page 187.)

Gonzalez, A. H., Zaritsky, D., and Zabludoff, A. I. (2007). A census of baryons in galaxy clusters and groups. ApJ, 666(1):147. (Cited on page 31.)

Goto, T., Okamura, S., Mckay, T. A., et al. (2002). Composite Luminosity Functions Based on the Sloan Digital Sky Survey "Cut and Enhance" Galaxy Cluster Catalog. PASJ, 54(4):515–525. (Cited on pages 78, 97, and 98.)

Gott, III, J. R., Gunn, J. E., Schramm, D. N., and Tinsley, B. M. (1974). An unbound universe. ApJ, 194:543–553. (Cited on page 18.)

Guglielmo, V., Poggianti, B. M., Vulcani, B., et al. (2018). The XXL Survey: XXII. The XXL-North spectrophotometric sample and galaxy stellar mass function in X-ray detected groups and clusters. A&A, 620:A7. (Cited on pages 60 and 103.)

Guth, A. H. (1981). Inflationary universe: A possible solution to the horizon and flatness problems. Phys. Rev. D, 23:347–356. (Cited on page 8.)

Gwyn, S. D. J. (2012). The Canada-France-Hawaii Telescope Legacy Survey: Stacked Images and Catalogs. AJ, 143:38. (Cited on page 49.)

Haehnelt, M. G. and Tegmark, M. (1996). Using the Kinematic Sunyaev-Zeldovich effect to determine the peculiar velocities of clusters of galaxies. MNRAS, 279:545. (Cited on page 20.)

Hahn, O., Martizzi, D., Wu, H.-Y., et al. (2017). Rhapsody-G simulations - I. The cool cores, hot gas and stellar content of massive galaxy clusters. MNRAS, 470:166–186. (Cited on pages 144, 200, and 225.)

Haines, C. P., Pereira, M. J., Sanderson, A. J. R., et al. (2012). LoCuSS: A Dynamical Analysis of X-Ray Active Galactic Nuclei in Local Clusters. ApJ, 754:97. (Cited on page 114.)

Hand, N., Addison, G. E., Aubourg, E., et al. (2012). Evidence of Galaxy Cluster Motions with the Kinematic Sunyaev-Zel'dovich Effect. *Physical Review Letters*, 109(4):041101. (Cited on page 20.)

Hansen, S. M., McKay, T. A., Wechsler, R. H., et al. (2005). Measurement of Galaxy Cluster Sizes, Radial Profiles, and Luminosity Functions from SDSS Photometric Data. ApJ, 633:122–137. (Cited on pages 76, 81, 95, and 104.)

Hansen, S. M., Sheldon, E. S., Wechsler, R. H., and Koester, B. P. (2009). The Galaxy Content of SDSS Clusters and Groups. ApJ, 699:1333–1353. (Cited on pages 103, 104, 105, 107, and 108.)

Hasselfield, M., Hilton, M., Marriage, T. A., et al. (2013). The Atacama Cosmology Telescope: Sunyaev-Zel'dovich selected galaxy clusters at 148 GHz from three seasons of data. J. Cosmology Astropart. Phys., 7:008. (Cited on pages 38 and 187.)

Hicks, A. K., Mushotzky, R., and Donahue, M. (2010). Detecting Star Formation in Brightest Cluster Galaxies with GALEX. ApJ, 719:1844–1858. (Cited on page 119.)

Hildebrandt, H., Viola, M., Heymans, C., et al. (2017). KiDS-450: cosmological parameter constraints from tomographic weak gravitational lensing. MNRAS, 465:1454–1498. (Cited on page 21.)

Hilton, M., Hasselfield, M., Sifón, C., et al. (2018). The Atacama Cosmology Telescope: The Two-season ACTPol Sunyaev-Zel'dovich Effect Selected Cluster Catalog. ApJS, 235:20. (Cited on pages 38, 49, 138, 141, 195, and 197.)

Hoessel, J. G., Gunn, J. E., and Thuan, T. X. (1980). The photometric properties of brightest cluster galaxies. I - Absolute magnitudes in 116 nearby Abell clusters. ApJ, 241:486–492. (Cited on page 18.)

Hogg, D. W. (1999). Distance measures in cosmology. *ArXiv Astrophysics e-prints*. (Cited on page 8.)

Hogg, D. W., Baldry, I. K., Blanton, M. R., and Eisenstein, D. J. (2002). The K correction. *ArXiv Astrophysics e-prints*. (Cited on page 24.)

Horellou, C., Intema, H. T., Smolčić, V., et al. (2018). The XXL Survey: XXXIV. Double irony in XXL-North. A tale of two radio galaxies in a supercluster at z = 0.14. A&A, 620:A19. (Cited on page 173.)

Hubble, E. P. (1925). Cepheids in Spiral Nebulae. *Popular Astronomy*, 33. (Cited on page 7.)

Hubble, E. P. (1926). Extragalactic nebulae. ApJ, 64. (Cited on page 8.)

Hudelot, P., Cuillandre, J.-C., Withington, K., et al. (2012). VizieR Online Data Catalog: The CFHTLS Survey (T0007 release) (Hudelot+ 2012). *VizieR Online Data Catalog*, 2317. (Cited on pages 50 and 81.)

Hudson, D. S., Mittal, R., Reiprich, T. H., et al. (2010). What is a cool-core cluster? a detailed analysis of the cores of the X-ray flux-limited HIFLUGCS cluster sample. A&A, 513:A37. (Cited on page 143.)

Hurier, G., Macías-Pérez, J. F., and Hildebrandt, S. (2013). MILCA, a modified internal linear combination algorithm to extract astrophysical emissions from multifrequency sky maps. A&A, 558:A118. (Cited on page 141.)

Huterer, D., Kirkby, D., Bean, R., et al. (2015). Growth of cosmic structure: Probing dark energy beyond expansion. *Astroparticle Physics*, 63:23–41. (Cited on page 18.)

Ilbert, O., Arnouts, S., McCracken, H. J., et al. (2006). Accurate photometric redshifts for the CFHT Legacy Survey calibrated using the VIMOS VLT Deep Survey. A&A, 457(3):841–856. arXiv: astro-ph/0603217. (Cited on pages 39, 55, 57, 58, 59, 64, 65, and 68.)

Ilbert, O., Capak, P., Salvato, M., et al. (2009). Cosmos Photometric Redshifts with 30-Bands for 2-deg2. ApJ, 690:1236–1249. (Cited on page 57.)

Intema, H. T., Jagannathan, P., Mooley, K. P., and Frail, D. A. (2017). The GMRT 150 MHz all-sky radio survey. First alternative data release TGSS ADR1. A&A, 598:A78. (Cited on page 30.)

Itoh, N., Kohyama, Y., and Nozawa, S. (1998). Relativistic Corrections to the Sunyaev-Zeldovich Effect for Clusters of Galaxies. ApJ, 502:7–15. (Cited on pages 32 and 187.)

Itoh, N. and Nozawa, S. (2004). Relativistic corrections to the Sunyaev-Zeldovich effect for extremely hot clusters of galaxies. A&A, 417:827–832. (Cited on page 32.)

Ivezić, Ž., Kahn, S. M., Tyson, J. A., et al. (2008). LSST: from Science Drivers to Reference Design and Anticipated Data Products. *ArXiv e-prints*. (Cited on page 37.)

Jeltema, T. E., Hallman, E. J., Burns, J. O., and Motl, P. M. (2008). Cluster Structure in Cosmological Simulations. I. Correlation to Observables, Mass Estimates, and Evolution. ApJ, 681:167–186. (Cited on page 36.)

Johnson, O., Best, P. N., and Almaini, O. (2003). The content of active galactic nuclei in the z= 0.83 cluster MS 1054-0321. MNRAS, 343:924–932. (Cited on page 115.)

Johnson, S. P., Wilson, G. W., Wang, Q. D., et al. (2013). X-ray detections of submillimetre galaxies: active galactic nuclei versus starburst contribution. MNRAS, 431(1):662–682. (Cited on page 173.)

Jungman, G., Kamionkowski, M., and Griest, K. (1996). Supersymmetric dark matter. Phys. Rep., 267:195–373. (Cited on page 33.)

Kahlhoefer, F., Schmidt-Hoberg, K., Frandsen, M. T., and Sarkar, S. (2014). Colliding clusters and dark matter self-interactions. MNRAS, 437:2865–2881. (Cited on page 20.)

Kaiser, N. (1986). Evolution and clustering of rich clusters. MNRAS, 222:323–345. (Cited on page 37.)

Kaiser, N. (1987). Clustering in real space and in redshift space. MNRAS, 227:1–21. (Cited on page 20.)

Kaiser, N., Wilson, G., and Luppino, G. A. (2000). Large-Scale Cosmic Shear Measurements. *ArXiv Astrophysics e-prints*. (Cited on page 12.)

Katayama, H., Hayashida, K., Takahara, F., and Fujita, Y. (2003). Properties of the Brightest Cluster Galaxy and Its Host Cluster. ApJ, 585:687–693. (Cited on page 143.)

Kauffmann, G., Heckman, T. M., White, S. D. M., et al. (2003). Stellar masses and star formation histories for 10^5 galaxies from the Sloan Digital Sky Survey. MNRAS, 341:33–53. (Cited on pages 25 and 107.)

Khatri, R. and Gaspari, M. (2016). Thermal SZ fluctuations in the ICM: probing turbulence and thermodynamics in Coma cluster with Planck. MNRAS, 463:655–669. (Cited on page 181.)

Kilbinger, M. (2015). Cosmology with cosmic shear observations: a review. *Reports on Progress in Physics*, 78(8):086901. (Cited on page 12.)

Kinney, A. L., Calzetti, D., Bohlin, R. C., et al. (1996). Template Ultraviolet to Near-Infrared Spectra of Star-forming Galaxies and Their Application to K-Corrections. ApJ, 467:38. (Cited on page 59.)

Kitayama, T. (2014). Cosmological and astrophysical implications of the Sunyaev-Zel'dovich effect. *Progress of Theoretical and Experimental Physics*, 2014(6):06B111. (Cited on page 32.)

Kneib, J.-P. and Natarajan, P. (2011). Cluster lenses. A&A Rev., 19:47. (Cited on page 36.)

Knudsen, K. K., Barnard, V. E., Werf, V. D., et al. (2006). An ultradeep submillimetre map: beneath the SCUBA confusion limit with lensing and robust source extraction. *Mon Not R Astron Soc*, 368(1):487–496. (Cited on page 165.)

Kodama, T. and Arimoto, N. (1997). Origin of the colour-magnitude relation of elliptical galaxies. A&A, 320:41–53. (Cited on pages 116, 118, 119, and 121.)

Koester, B. P., McKay, T. A., Annis, J., et al. (2007). MaxBCG: A Red-Sequence Galaxy Cluster Finder. ApJ, 660:221–238. (Cited on pages 111 and 118.)

Komatsu, E., Matsuo, H., Kitayama, T., et al. (2001). Substructures Revealed by the Sunyaev-Zel'dovich Effect at 150 GHz in a High-Resolution Map of RX J1347-1145. PASJ, 53:57–62. (Cited on page 139.)

Kormendy, J. and Bender, R. (2012). A Revised Parallel-sequence Morphological Classification of Galaxies: Structure and Formation of S0 and Spheroidal Galaxies. ApJS, 198:2. (Cited on page 29.)

Koulouridis, E., Faccioli, L., Le Brun, A. M. C., et al. (2018a). The XXL Survey. XIX. A realistic population of simulated X-ray AGN: Comparison of models with observations. A&A, 620:A4. (Cited on page 121.)

Koulouridis, E. and Plionis, M. (2010). Luminous X-ray Active Galactic Nuclei in Clusters of Galaxies. ApJ, 714:L181–L184. (Cited on page 114.)

Koulouridis, E., Plionis, M., Melnyk, O., et al. (2014). X-ray AGN in the XMM-LSS galaxy clusters: no evidence of AGN suppression. A&A, 567:A83. (Cited on page 115.)

Koulouridis, E., Ricci, M., Giles, P., et al. (2018b). The XXL Survey. XXXV. The role of cluster mass in AGN activity. A&A, 620:A20. (Cited on pages 110, 111, 113, 114, 115, 120, and 206.)

Kravtsov, A. V., Berlind, A. A., Wechsler, R. H., et al. (2004). The Dark Side of the Halo Occupation Distribution. ApJ, 609:35–49. (Cited on page 26.)

Kravtsov, A. V. and Borgani, S. (2012). Formation of galaxy clusters. *Annual Review of* A&A, 50(1):353–409. (Cited on page 187.)

Kravtsov, A. V., Vikhlinin, A. A., and Meshcheryakov, A. V. (2018). Stellar Mass-Halo Mass Relation and Star Formation Efficiency in High-Mass Halos. *Astronomy Letters*, 44:8–34. (Cited on page 17.)

Krishnan, C., Hatch, N. A., Almaini, O., et al. (2017). Enhancement of AGN in a protocluster at z = 1.6. MNRAS, 470:2170–2178. (Cited on page 115.)

Kron, R. G. (1980). Photometry of a complete sample of faint galaxies. ApJS, 43:305–325. (Cited on page 51.)

Lan, T.-W., Ménard, B., and Mo, H. (2016). The galaxy luminosity function in groups and clusters: the faint-end upturn and the connection to the field luminosity function. MNRAS, 459:3998–4019. (Cited on pages 76, 78, 103, and 218.)

Lange, A. E., Ade, P. A., Bock, J. J., et al. (2001). Cosmological parameters from the first results of Boomerang. Phys. Rev. D, 63(4):042001. (Cited on page 8.)

Laureijs, R., Amiaux, J., Arduini, S., et al. (2011). Euclid Definition Study Report. *ArXiv e-prints*. (Cited on page 37.)

Lavoie, S., Willis, J. P., Démoclès, J., et al. (2016). The XXL survey XV: evidence for dry merger driven BCG growth in XXL-100-GC X-ray clusters. MNRAS, 462:4141–4156. (XXL Paper XV). (Cited on pages 81, 105, 108, 120, 143, and 144.)

Le Brun, A. M. C., McCarthy, I. G., Schaye, J., and Ponman, T. J. (2017). The scatter and evolution of the global hot gas properties of simulated galaxy cluster populations. MNRAS, 466:4442–4469. (Cited on pages 37, 139, 200, and 201.)

Leavitt, H. S. and Pickering, E. C. (1912). Periods of 25 Variable Stars in the Small Magellanic Cloud. *Harvard College Observatory Circular*, 173:1–3. (Cited on page 12.)

Lehmer, B. D., Lucy, A. B., Alexander, D. M., et al. (2013). Concurrent Supermassive Black Hole and Galaxy Growth: Linking Environment and Nuclear Activity in z = 2.23 Hα Emitters. ApJ, 765:87. (Cited on page 115.)

Lemaître, G. (1927). Un Univers homogène de masse constante et de rayon croissant rendant compte de la vitesse radiale des nébuleuses extra-galactiques. *Annales de la Société Scientifique de Bruxelles*, 47:49–59. (Cited on page 8.)

Lemaitre, G. (1931). L'Expansion de l'Espace. *Publications du Laboratoire d'Astronomie et de Geodesie de l'Universite de Louvain, vol. 8, pp.101-120*, 8:101–120. (Cited on page 8.)

Lemaître, G. (1931). The Beginning of the World from the Point of View of Quantum Theory. Nature, 127:706. (Cited on page 8.)

Lewis, A. and Challinor, A. (2006). Weak gravitational lensing of the CMB. Phys. Rep., 429:1–65. (Cited on page 12.)

Lieu, M., Smith, G. P., Giles, P., et al. (2015). The XXL Survey. IV. Mass-temperature relation of the bright cluster sample. A&A. (Cited on page 48.)

Limousin, M., Morandi, A., Sereno, M., et al. (2013). The three-dimensional shapes of galaxy clusters. *Space Science Reviews*, 177(1):155–194. (Cited on page 180.)

Lin, Y.-T. and Mohr, J. J. (2004). K-band properties of galaxy clusters and groups: Brightest cluster galaxies and intracluster light. ApJ, 617(2):879. (Cited on page 143.)

Lin, Y.-T., Mohr, J. J., Gonzalez, A. H., and Stanford, S. A. (2006). Evolution of the K-Band Galaxy Cluster Luminosity Function and Scaling Relations. ApJ, 650:L99–L102. (Cited on pages 39, 75, and 107.)

Lin, Y.-T., Mohr, J. J., and Stanford, S. A. (2003). Near-infrared properties of galaxy clusters: Luminosity as a binding mass predictor and the state of cluster baryons. ApJ, 591:749–763. (Cited on pages 75 and 107.)

Linde, A. D. (1982). A new inflationary universe scenario: A possible solution of the horizon, flatness, homogeneity, isotropy and primordial monopole problems. *Physics Letters B*, 108:389–393. (Cited on page 8.)

Logan, C. H. A., Maughan, B. J., Bremer, M. N., et al. (2018). The XXL Survey: XXXIII. Chandra Constraints on the AGN Contamination of z > 1 XXL Galaxy Clusters. A&A, 620:A18. (Cited on pages 121 and 141.)

Lopes, P. A. A., Trevisan, M., Laganá, T. F., et al. (2018). Optical Substructure and BCG Offsets of Sunyaev-Zel'dovich and X-ray Selected Galaxy Clusters. MNRAS. arXiv: 1805.09631. (Cited on pages 143 and 144.)

LSST Science Collaboration, Abell, P. A., Allison, J., et al. (2009). LSST Science Book, Version 2.0. *ArXiv e-prints*. (Cited on page 37.)

Lu, T., Gilbank, D. G., Balogh, M. L., and Bognat, A. (2009). Recent arrival of faint cluster galaxies on the red sequence: luminosity functions from 119 deg2 of CFHTLS. MNRAS, 399(4):1858–1876. (Cited on pages 75 and 108.)

Ma, Z., Hu, W., and Huterer, D. (2006). Effects of photometric redshift uncertainties on weak-lensing tomography. ApJ, 636(1):21. (Cited on page 55.)

Madau, P. and Dickinson, M. (2014). Cosmic Star-Formation History. ARA&A, 52:415–486. (Cited on pages 24, 25, and 164.)

Majumdar, S. and Mohr, J. J. (2004). Self-Calibration in Cluster Studies of Dark Energy: Combining the Cluster Redshift Distribution, the Power Spectrum, and Mass Measurements. ApJ, 613:41–50. (Cited on page 20.)

Mana, A., Giannantonio, T., Weller, J., et al. (2013). Combining clustering and abundances of galaxy clusters to test cosmology and primordial non-Gaussianity. MNRAS, 434:684–695. (Cited on page 20.)

Mancone, C. L., Baker, T., Gonzalez, A. H., et al. (2012). The faint end of the cluster-galaxy luminosity function at high redshift. ApJ, 761(2):141. (Cited on page 75.)

Mancone, C. L., Gonzalez, A. H., Brodwin, M., et al. (2010). The Formation of Massive Cluster Galaxies. ApJ, 720:284–298. (Cited on page 75.)

Mann, A. W. and Ebeling, H. (2012). X-ray–optical classification of cluster mergers and the evolution of the cluster merger fraction. MNRAS, 420(3):2120–2138. (Cited on page 180.)

Mantz, A., Allen, S. W., Ebeling, H., and Rapetti, D. (2008). New constraints on dark energy from the observed growth of the most X-ray luminous galaxy clusters. MNRAS, 387:1179–1192. (Cited on page 122.)

Mantz, A. B., Abdulla, Z., Allen, S. W., et al. (2018). The XXL Survey. XVII. X-ray and Sunyaev-Zel'dovich properties of the redshift 2.0 galaxy cluster XLSSC 122. A&A, 620:A2. (Cited on page 185.)

Mantz, A. B., Allen, S. W., Morris, R. G., et al. (2014). Cosmology and astrophysics from relaxed galaxy clusters - II. Cosmological constraints. MNRAS, 440:2077–2098. (Cited on page 20.)

Markevitch, M., Gonzalez, A. H., Clowe, D., et al. (2004). Direct Constraints on the Dark Matter Self-Interaction Cross Section from the Merging Galaxy Cluster 1E 0657-56. ApJ, 606:819–824. (Cited on page 20.)

Marriage, T. A., Acquaviva, V., Ade, P. A. R., et al. (2011). The Atacama Cosmology Telescope: Sunyaev-Zel'dovich-Selected Galaxy Clusters at 148 GHz in the 2008 Survey. ApJ, 737:61. (Cited on page 38.)

Martinet, N., Durret, F., Guennou, L., et al. (2015). The evolution of the cluster optical galaxy luminosity function between z = 0.4 and 0.9 in the DAFT/FADA survey. A&A, 575. (Cited on pages 75, 97, and 98.)

Martini, P., Miller, E. D., Brodwin, M., et al. (2013). The Cluster and Field Galaxy Active Galactic Nucleus Fraction at z = 1-1.5: Evidence for a Reversal of the Local Anticorrelation between Environment and AGN Fraction. ApJ, 768:1. (Cited on pages 114, 115, and 116.)

Marulli, F., Veropalumbo, A., Sereno, M., et al. (2018). The XXL Survey. XVI. The clustering of X-ray selected galaxy clusters at z 0.3. A&A, 620:A1. (Cited on page 20.)

Massardi, M. and De Zotti, G. (2004). Radio source contamination of the Sunyaev-Zeldovich effect in galaxy clusters. A&A, 424:409–414. (Cited on page 141.)

Maurogordato, S., Sauvageot, J. L., Bourdin, H., et al. (2011). Merging history of three bimodal clusters. A&A, 525:A79. (Cited on page 187.)

McDonald, M., Benson, B. A., Vikhlinin, A., et al. (2014). The Redshift Evolution of the Mean Temperature, Pressure, and Entropy Profiles in 80 SPT-Selected Galaxy Clusters. ApJ, 794:67. (Cited on page 196.)

McDonald, M., Stalder, B., Bayliss, M., et al. (2016). Star-forming brightest cluster galaxies at 0.25 < z < 1.25: A transitioning fuel supply. ApJ, 817(2):86. (Cited on page 120.)

Medezinski, E., Oguri, M., Nishizawa, A. J., et al. (2018). Source selection for cluster weak lensing measurements in the hyper suprime-cam survey. *Publications of the Astronomical Society of Japan*, 70(2):30. (Cited on page 55.)

Melin, J.-B. and Bartlett, J. G. (2015). Measuring cluster masses with CMB lensing: a statistical approach. A&A, 578:A21. (Cited on page 199.)

Melin, J.-B., Bartlett, J. G., and Delabrouille, J. (2006). Catalog extraction in SZ cluster surveys: a matched filter approach. A&A, 459:341–352. (Cited on page 187.)

Ménard, B., Scranton, R., Schmidt, S., et al. (2013). Clustering-based redshift estimation: method and application to data. *ArXiv e-prints*. (Cited on page 57.)

Menci, N., Cavaliere, A., Fontana, A., Giallongo, E., and Poli, F. (2002). Binary Aggregations in Hierarchical Galaxy Formation: The Evolution of the Galaxy Luminosity Function. ApJ, 575:18–32. (Cited on page 75.)

Merloni, A., Predehl, P., Becker, W., et al. (2012). eROSITA Science Book: Mapping the Structure of the Energetic Universe. *ArXiv e-prints*. (Cited on page 38.)

Merson, A. I., Baugh, C. M., Helly, J. C., et al. (2013). Lightcone mock catalogues from semi-analytic models of galaxy formation - I. Construction and application to the BzK colour selection. MNRAS, 429:556–578. (Cited on page 211.)

Mihos, J. C. (2016). Intragroup and Intracluster Light. In Bragaglia, A., Arnaboldi, M., Rejkuba, M., and Romano, D., editors, *The General Assembly of Galaxy Halos: Structure, Origin and Evolution*, volume 317 of *IAU Symposium*, pages 27–34. (Cited on page 31.)

Miyazaki, S., Komiyama, Y., Sekiguchi, M., et al. (2002). Subaru Prime Focus Camera – Suprime-Cam. PASJ, 54:833–853. (Cited on page 30.)

Mo, H., van den Bosch, F. C., and White, S. (2010). *Galaxy Formation and Evolution*. Cambridge University Press, 2010. (Cited on pages 17, 22, 23, and 28.)

Mo, H. J., Yang, X., van den Bosch, F. C., and Jing, Y. P. (2004). The dependence of the galaxy luminosity function on large-scale environment. MNRAS, 349:205–212. (Cited on page 75.)

Monfardini, A., Benoit, A., Bideaud, A., et al. (2011). A Dual-band Millimeter-wave Kinetic Inductance Camera for the IRAM 30 m Telescope. *ApJS*, 194(2):24. (Cited on page 150.)

Moretti, A., Bettoni, D., Poggianti, B. M., et al. (2015). Galaxy luminosity functions in WINGS clusters. A&A, 581. (Cited on pages 76 and 103.)

Morishita, T., Abramson, L. E., Treu, T., et al. (2017). Characterizing Intracluster Light in the Hubble Frontier Fields. ApJ, 846:139. (Cited on page 31.)

Moscardini, L., Matarrese, S., and Mo, H. J. (2001). Constraining cosmological parameters with the clustering properties of galaxy clusters in optical and X-ray bands. MNRAS, 327:422–434. (Cited on page 20.)

Moutard, T., Arnouts, S., Ilbert, O., et al. (2016). The VIPERS Multi-Lambda Survey. I. UV and near-IR observations, multi- colour catalogues, and photometric redshifts. A&A, 590:A102. (Cited on page 203.)

Mroczkowski, T., Bonamente, M., Carlstrom, J. E., et al. (2009). Application of a Self-Similar Pressure Profile to Sunyaev-Zel'Dovich Effect Data from Galaxy Clusters. ApJ, 694:1034–1044. (Cited on page 188.)

Mroczkowski, T., Dicker, S., Sayers, J., et al. (2012). A Multi-wavelength Study of the Sunyaev-Zel'dovich Effect in the Triple-merger Cluster MACS J0717.5+3745 with MUSTANG and Bolocam. ApJ, 761:47. (Cited on page 20.)

Mulroy, S. L., McGee, S. L., Gillman, S., et al. (2017). Galaxy cluster luminosities and colours, and their dependence on cluster mass and merger state. MNRAS, 472(3):3246–3255. arXiv: 1708.05971. (Cited on page 75.)

Murray, S. G., Power, C., and Robotham, A. S. G. (2013). HMFcalc: An online tool for calculating dark matter halo mass functions. *Astronomy and Computing*, 3:23–34. (Cited on pages 17 and 18.)

Muzzin, A., Wilson, G., Lacy, M., Yee, H. K. C., and Stanford, S. A. (2008). The Evolution of Dusty Star Formation and Stellar Mass Assembly in Clusters: Results from the IRAC 3.6, 4.5, 5.8, and 8.0 μm Cluster Luminosity Functions. ApJ, 686:966–994. (Cited on page 75.)

Nagai, D., Kravtsov, A. V., and Vikhlinin, A. (2007a). Effects of Galaxy Formation on Thermodynamics of the Intracluster Medium. ApJ, 668:1–14. (Cited on pages 190 and 198.)

Nagai, D. and Lau, E. T. (2011). Gas Clumping in the Outskirts of ΛCDM Clusters. ApJ, 731:L10. (Cited on page 195.)

Nagai, D., Vikhlinin, A., and Kravtsov, A. V. (2007b). Testing X-Ray Measurements of Galaxy Clusters with Cosmological Simulations. ApJ, 655:98–108. (Cited on page 195.)

Nandra, K., Barret, D., Barcons, X., et al. (2013). The Hot and Energetic Universe: A White Paper presenting the science theme motivating the Athena+ mission. *ArXiv e-prints*. (Cited on page 38.)

Naselsky, P. D., Novikov, D. I., and Novikov, I. D. (2006). *The Physics of the Cosmic Microwave Background*. Cambridge Astrophysics. Cambridge University Press. (Cited on page 8.)

Newman, J. A. (2008). Calibrating Redshift Distributions beyond Spectroscopic Limits with Cross-Correlations. ApJ, 684:88–101. (Cited on page 57.)

NIKA2 Collaboration, Adam, R., Adane, A., et al. (2018). The NIKA2 large-field-of-view millimetre continuum camera for the 30 m IRAM telescope. A&A, 609:A115. (Cited on pages 139, 148, 150, 153, 156, and 197.)

Noeske, K. G., Weiner, B. J., Faber, S. M., et al. (2007). Star Formation in AEGIS Field Galaxies since z=1.1: The Dominance of Gradually Declining Star Formation, and the Main Sequence of Star-forming Galaxies. ApJ, 660:L43–L46. (Cited on page 26.)

Oguri, M. (2014). A cluster finding algorithm based on the multiband identification of red sequence galaxies. MNRAS, 444:147–161. (Cited on pages 111 and 118.)

O'Hara, T. B., Mohr, J. J., Bialek, J. J., and Evrard, A. E. (2006). Effects of Mergers and Core Structure on the Bulk Properties of Nearby Galaxy Clusters. ApJ, 639:64–80. (Cited on page 187.)

Okabe, N. and Smith, G. P. (2016). LoCuSS: weak-lensing mass calibration of galaxy clusters. MNRAS, 461:3794–3821. (Cited on page 113.)

Oke, J. B. (1974). Absolute Spectral Energy Distributions for White Dwarfs. ApJS, 27:21. (Cited on page 39.)

Olsen, L. F., Benoist, C., Cappi, A., et al. (2007). Galaxy clusters in the CFHTLS. First matched filter candidate catalogue of the Deep fields. A&A, 461:81–93. (Cited on page 107.)

Opik, E. (1922). An estimate of the distance of the Andromeda Nebula. ApJ, 55. (Cited on page 7.)

Pacaud, F., Clerc, N., Giles, P. A., et al. (2016). The XXL Survey. II. The bright cluster sample: catalogue and luminosity function. A&A, 592:A2. (XXL Paper II). (Cited on pages 21, 46, 48, and 49.)

Pacaud, F., Pierre, M., Melin, J. B., et al. (2018). The XXL Survey. XXV. Cosmological analysis of the C1 cluster number counts. A&A, 620:A10. (Cited on page 48.)

Pacaud, F., Pierre, M., Refregier, A., et al. (2006). The XMM Large Scale Structure survey: The X-ray pipeline and survey selection function. MNRAS, 372(2):578–590. arXiv: astro-ph/0607177. (Cited on pages 45, 46, and 47.)

Peng, Y.-j., Lilly, S. J., Kovač, K., et al. (2010). Mass and Environment as Drivers of Galaxy Evolution in SDSS and zCOSMOS and the Origin of the Schechter Function. ApJ, 721:193–221. (Cited on pages 25 and 26.)

Peng, Y.-j., Lilly, S. J., Renzini, A., and Carollo, M. (2012). Mass and Environment as Drivers of Galaxy Evolution. II. The Quenching of Satellite Galaxies as the Origin of Environmental Effects. ApJ, 757:4. (Cited on pages 25 and 26.)

Penna-Lima, M., Bartlett, J. G., Rozo, E., et al. (2017). Calibrating the Planck cluster mass scale with CLASH. A&A, 604:A89. (Cited on page 199.)

Penzias, A. A. and Wilson, R. W. (1965). A Measurement of Excess Antenna Temperature at 4080 Mc/s. ApJ, 142:419–421. (Cited on page 8.)

Perlmutter, S., Aldering, G., Goldhaber, G., et al. (1999). Measurements of Ω and Λ from 42 High-Redshift Supernovae. ApJ, 517:565–586. (Cited on page 8.)

Peter, A. H. G., Moody, C. E., and Kamionkowski, M. (2010). Dark-matter decays and self-gravitating halos. Phys. Rev. D, 81(10):103501. (Cited on page 20.)

Pierre, M., Pacaud, F., Adami, C., et al. (2016). The XXL Survey. I. Scientific motivations - XMM-Newton observing plan - Follow-up observations and simulation programme. A&A, 592:A1. (XXL Paper I). (Cited on pages 38, 44, and 46.)

Pierre, M., Pacaud, F., Juin, J. B., et al. (2011). Precision cosmology with a wide area XMM cluster survey. MNRAS, 414(2):1732–1746. arXiv: 1009.3182. (Cited on page 44.)

Piffaretti, R., Arnaud, M., Pratt, G. W., Pointecouteau, E., and Melin, J.-B. (2011). The MCXC: a meta-catalogue of x-ray detected clusters of galaxies. A&A, 534:A109. (Cited on page 49.)

Piffaretti, R., Jetzer, P., and Schindler, S. (2003). Aspherical galaxy clusters: Effects on cluster masses and gas mass fractions. A&A, 398:41–48. (Cited on page 195.)

Piffaretti, R. and Valdarnini, R. (2008). Total mass biases in X-ray galaxy clusters. A&A, 491:71–87. (Cited on pages 36 and 195.)

Pipino, A., Szabo, T., Pierpaoli, E., MacKenzie, S. M., and Dong, F. (2011). The properties of brightest cluster galaxies in the sloan digital sky survey data release 6 adaptive matched filter cluster catalogue. MNRAS, 417(4):2817–2830. (Cited on page 119.)

Pizzuti, L., Sartoris, B., Borgani, S., et al. (2016). CLASH-VLT: testing the nature of gravity with galaxy cluster mass profiles. J. Cosmology Astropart. Phys., 4:023. (Cited on page 20.)

Planck Collaboration, Adam, R., Ade, P. A. R., et al. (2016a). Planck 2015 results. IX. Diffuse component separation: CMB maps. A&A, 594:A9. (Cited on page 15.)

Planck Collaboration, Ade, P. A. R., Aghanim, N., et al. (2014a). Planck 2013 results. XVI. Cosmological parameters. A&A, 571:A16. (Cited on page 18.)

Planck Collaboration, Ade, P. A. R., Aghanim, N., et al. (2014b). Planck 2013 results. XX. Cosmology from Sunyaev-Zeldovich cluster counts. A&A, 571:A20. (Cited on pages 21, 36, 38, 49, 122, 139, 140, 198, 199, and 200.)

Planck Collaboration, Ade, P. A. R., Aghanim, N., et al. (2013). Planck intermediate results. V. Pressure profiles of galaxy clusters from the Sunyaev-Zeldovich effect. A&A, 550:A131. (Cited on pages 146, 147, 196, 197, and 198.)

Planck Collaboration, Ade, P. A. R., Aghanim, N., et al. (2016b). Planck 2015 results. XXVII. The second Planck catalogue of Sunyaev- Zeldovich sources. A&A, 594:A27. (Cited on pages 49 and 141.)

Planck Collaboration, Ade, P. A. R., Aghanim, N., et al. (2016c). Planck intermediate results. XXXVI. Optical identification and redshifts of Planck SZ sources with telescopes at the Canary Islands observatories. A&A, 586:A139. (Cited on page 123.)

Planck Collaboration, Ade, P. A. R., Aghanim, N., et al. (2016d). Planck 2015 results. XXIV. Cosmology from Sunyaev-Zeldovich cluster counts. A&A, 594:A24. (Cited on pages 21 and 38.)

Planck Collaboration, Ade, P. A. R., Aghanim, N., et al. (2016e). Planck 2015 results. XIII. Cosmological parameters. A&A, 594:A13. (Cited on page 193.)

Planck Collaboration, Aghanim, N., Akrami, Y., et al. (2018a). Planck 2018 results. VI. Cosmological parameters. *ArXiv e-prints*. (Cited on pages 11, 14, and 33.)

Planck Collaboration, Aghanim, N., Arnaud, M., et al. (2016f). Planck 2015 results. XXII. A map of the thermal Sunyaev-Zeldovich effect. A&A, 594:A22. (Cited on pages 141 and 187.)

Planck Collaboration, Akrami, Y., Arroja, F., et al. (2018b). Planck 2018 results. I. Overview and the cosmological legacy of Planck. *ArXiv e-prints*. (Cited on page 13.)

Poggianti, B. M. (1997). K and evolutionary corrections from UV to IR. *Astronomy and Astrophysics Supplement Series*, 122:399–407. (Cited on page 24.)

Poglitsch, A., Waelkens, C., Geis, N., et al. (2010). The Photodetector Array Camera and Spectrometer (PACS) on the Herschel Space Observatory. A&A, 518:L2. (Cited on page 30.)

Pointecouteau, E., Giard, M., Benoit, A., et al. (1999). A Sunyaev-Zeldovich Map of the Massive Core in the Luminous X-Ray Cluster RX J1347-1145. ApJ, 519:L115–L118. (Cited on page 139.)

Popesso, P. and Biviano, A. (2006). The AGN fraction-velocity dispersion relation in clusters of galaxies. A&A, 460:L23–L26. (Cited on page 115.)

Popesso, P., Biviano, A., Böhringer, H., and Romaniello, M. (2006). RASS-SDSS Galaxy cluster survey. IV. A ubiquitous dwarf galaxy population in clusters. A&A, 445:29–42. (Cited on pages 95, 97, and 98.)

Popesso, P., Böhringer, H., Romaniello, M., and Voges, W. (2005). RASS-SDSS galaxy cluster survey. II. A unified picture of the cluster luminosity function. A&A, 433:415–429. (Cited on pages 78, 84, 86, and 218.)

Postman, M., Lubin, L. M., Gunn, J. E., et al. (1996). The Palomar Distant Clusters Survey. I. The Cluster Catalog. AJ, 111:615. (Cited on page 107.)

Pratt, G. W., Arnaud, M., Piffaretti, R., et al. (2010). Gas entropy in a representative sample of nearby X-ray galaxy clusters (REXCESS): relationship to gas mass fraction. A&A, 511:A85. (Cited on page 194.)

Pratt, G. W., Croston, J. H., Arnaud, M., and Böhringer, H. (2009). Galaxy cluster X-ray luminosity scaling relations from a representative local sample (REXCESS). A&A, 498:361–378. (Cited on page 37.)

Press, W. H. and Schechter, P. (1974). Formation of Galaxies and Clusters of Galaxies by Self-Similar Gravitational Condensation. ApJ, 187:425–438. (Cited on pages 17 and 75.)

Reiprich, T. H., Basu, K., Ettori, S., et al. (2013). Outskirts of galaxy clusters. *Space Science Reviews*, 177(1):195–245. (Cited on pages 194, 195, and 198.)

Ricci, M., Benoist, C., Maurogordato, S., et al. (2018). The XXL Survey. XXVIII. Galaxy luminosity functions of the XXL-N clusters. A&A, 620:A13. (Cited on pages 54, 74, 95, 143, 144, and 206.)

Ridl, J., Clerc, N., Sadibekova, T., et al. (2017). Cosmology with XMM galaxy clusters: the X-CLASS/GROND catalogue and photometric redshifts. MNRAS, 468:662–684. (Cited on page 123.)

Riechers, D. A., Bradford, C. M., Clements, D. L., et al. (2013). A dust-obscured massive maximum-starburst galaxy at a redshift of 6.34. *Nature*, 496(7445):329–333. (Cited on page 165.)

Riess, A. G., Casertano, S., Yuan, W., et al. (2018). Milky Way Cepheid Standards for Measuring Cosmic Distances and Application to Gaia DR2: Implications for the Hubble Constant. ApJ, 861:126. (Cited on pages 12 and 21.)

Riess, A. G., Filippenko, A. V., Challis, P., et al. (1998). Observational Evidence from Supernovae for an Accelerating Universe and a Cosmological Constant. AJ, 116:1009–1038. (Cited on page 8.)

Rines, K. and Diaferio, A. (2006). CIRS: Cluster Infall Regions in the Sloan Digital Sky Survey. I. Infall Patterns and Mass Profiles. AJ, 132:1275–1297. (Cited on page 36.)

Rossetti, M., Gastaldello, F., Eckert, D., et al. (2017). The cool-core state of Planck SZ-selected clusters versus X-ray-selected samples: evidence for cool-core bias. MNRAS, 468:1917–1930. (Cited on page 122.)

Rossetti, M., Gastaldello, F., Ferioli, G., et al. (2016). Measuring the dynamical state of Planck SZ-selected clusters: X-ray peak - BCG offset. MNRAS, 457:4515–4524. (Cited on page 180.)

Rozo, E. and Rykoff, E. S. (2014). redMaPPer II: X-Ray and SZ Performance Benchmarks for the SDSS Catalog. ApJ, 783:80. (Cited on pages 122 and 123.)

Rozo, E., Rykoff, E. S., Becker, M., Reddick, R. M., and Wechsler, R. H. (2015). redMaPPer - IV. Photometric membership identification of red cluster galaxies with 1 per cent precision. MNRAS, 453:38–52. (Cited on pages 78 and 123.)

Rozo, E., Rykoff, E. S., Koester, B. P., et al. (2009). Improvement of the Richness Estimates of maxBCG Clusters. ApJ, 703:601–613. (Cited on pages 36, 75, and 85.)

Rozo, E., Wechsler, R. H., Rykoff, E. S., et al. (2010). Cosmological constraints from the sloan digital sky survey maxbcg cluster catalog. ApJ, 708(1):645. (Cited on pages 36 and 122.)

Rubin, V. C., Ford, Jr., W. K., and Thonnard, N. (1980). Rotational properties of 21 SC galaxies with a large range of luminosities and radii, from NGC 4605 /R = 4kpc/ to UGC 2885 /R = 122 kpc/. ApJ, 238:471–487. (Cited on page 33.)

Rudnick, G., von der Linden, A., Pelló, R., et al. (2009). The Rest-frame Optical Luminosity Function of Cluster Galaxies at z < 0.8 and the Assembly of the Cluster Red Sequence. ApJ, 700:1559–1588. (Cited on pages 75, 97, 98, and 108.)

Ruppin, F., Mayet, F., Pratt, G. W., et al. (2018). First Sunyaev-Zel'dovich mapping with the NIKA2 camera: Implication of cluster substructures for the pressure profile and mass estimate. A&A, 615:A112. (Cited on pages 188 and 196.)

Rykoff, E. S., Rozo, E., Busha, M. T., et al. (2014). redMaPPer. I. Algorithm and SDSS DR8 Catalog. ApJ, 785:104. (Cited on page 111.)

Sadibekova, T., Pierre, M., Clerc, N., et al. (2014). The X-CLASS-redMaPPer galaxy cluster comparison. I. Identification procedures. A&A, 571:A87. (Cited on pages 119, 122, 123, and 128.)

Salim, S., Rich, R. M., Charlot, S., et al. (2007). UV Star Formation Rates in the Local Universe. ApJS, 173:267–292. (Cited on page 26.)

Salvato, M., Ilbert, O., and Hoyle, B. (2018). The many flavours of photometric redshifts. *Nature Astronomy*. (Cited on page 55.)

Sánchez, E., Alonso, D., Sánchez, F. J., García-Bellido, J., and Sevilla, I. (2013). Precise measurement of the radial baryon acoustic oscillation scales in galaxy redshift surveys. MNRAS, 434:2008–2019. (Cited on page 12.)

Sanders, J. S., Fabian, A. C., Taylor, G. B., et al. (2016). A very deep Chandra view of metals, sloshing and feedback in the Centaurus cluster of galaxies. MNRAS, 457:82–109. (Cited on page 181.)

Sarron, F., Martinet, N., Durret, F., and Adami, C. (2018). Evolution of the cluster optical galaxy luminosity function in the CFHTLS: breaking the degeneracy between mass and redshift. A&A, 613:A67. (Cited on pages 75, 76, 103, and 104.)

Sartoris, B., Biviano, A., Fedeli, C., et al. (2016). Next generation cosmology: constraints from the Euclid galaxy cluster survey. MNRAS, 459:1764–1780. (Cited on pages 20, 37, and 107.)

Sartoris, B., Biviano, A., Rosati, P., et al. (2014). CLASH-VLT: Constraints on the Dark Matter Equation of State from Accurate Measurements of Galaxy Cluster Mass Profiles. ApJ, 783:L11. (Cited on page 20.)

Sayers, J., Czakon, N. G., Mantz, A., et al. (2013a). Sunyaev-Zel'dovich-measured Pressure Profiles from the Bolocam X-Ray/SZ Galaxy Cluster Sample. ApJ, 768:177. (Cited on page 30.)

Sayers, J., Mroczkowski, T., Czakon, N. G., et al. (2013b). The Contribution of Radio Galaxy Contamination to Measurements of the Sunyaev-Zel'dovich Decrement in Massive Galaxy Clusters at 140 GHz with Bolocam. ApJ, 764:152. (Cited on pages 111 and 141.)

Sayers, J., Mroczkowski, T., Zemcov, M., et al. (2013c). A Measurement of the Kinetic Sunyaev-Zel'dovich Signal Toward MACS J0717.5+3745. ApJ, 778:52. (Cited on page 20.)

Schechter, P. (1976). An analytic expression for the luminosity function for galaxies. ApJ, 203:297–306. (Cited on pages 75, 81, and 85.)

Schuster, K.-F., Boucher, C., Brunswig, W., et al. (2004). A 230 GHz heterodyne receiver array for the IRAM 30 m telescope. A&A, 423(3):1171–1177. (Cited on page 150.)

Scottez, V., Benoit-Lévy, A., Coupon, J., Ilbert, O., and Mellier, Y. (2018). Testing the accuracy of clustering redshifts with simulations. MNRAS, 474:3921–3930. (Cited on page 57.)

Seldner, M. and Peebles, P. J. E. (1979). Statistical analysis of catalogs of extragalactic objects. XI - Evidence of correlation of QSOs and Lick galaxy counts. ApJ, 227:30–36. (Cited on page 57.)

Sereno, M. (2015). CoMaLit - III. Literature catalogues of weak lensing clusters of galaxies (LC^2). MNRAS, 450:3665–3674. (Cited on pages 36 and 141.)

Sereno, M., Umetsu, K., Ettori, S., et al. (2018). CLUMP-3D: Testing ΛCDM with Galaxy Cluster Shapes. ApJ, 860:L4. (Cited on page 180.)

Serra, A. L. and Domínguez Romero, M. J. L. (2011). Measuring the dark matter equation of state. MNRAS, 415:L74–L77. (Cited on page 20.)

Shan, H., Kneib, J.-P., Tao, C., et al. (2012). Weak Lensing Measurement of Galaxy Clusters in the CFHTLS-Wide Survey. ApJ, 748:56. (Cited on page 34.)

Simpson, J. M., Swinbank, A. M., Smail, I., et al. (2014). An ALMA Survey of Submillimeter Galaxies in the Extended Chandra Deep Field South: The Redshift Distribution and Evolution of Submillimeter Galaxies. *ApJ*, 788(2):125. (Cited on page 165.)

Slipher, V. M. (1913). The radial velocity of the Andromeda Nebula. *Lowell Observatory Bulletin*, 2:56–57. (Cited on page 7.)

Smail, I., Ivison, R. J., and Blain, A. W. (1997). A Deep Sub-millimeter Survey of Lensing Clusters: A New Window on Galaxy Formation and Evolution. ApJ, 490:L5–L8. (Cited on page 29.)

Smith, S. (1936). The Mass of the Virgo Cluster. ApJ, 83:23. (Cited on page 18.)

Smolčić, V., Miettinen, O., Tomičić, N., et al. (2017). (Sub)millimetre interferometric imaging of a sample of COSMOS/AzTEC submillimetre galaxies. III. Environments. A&A, 597:A4. (Cited on page 34.)

Spergel, D. N. and Steinhardt, P. J. (2000). Observational Evidence for Self-Interacting Cold Dark Matter. *Physical Review Letters*, 84:3760–3763. (Cited on page 20.)

Spergel, D. N., Verde, L., Peiris, H. V., et al. (2003). First-Year Wilkinson Microwave Anisotropy Probe (WMAP) Observations: Determination of Cosmological Parameters. ApJS, 148:175–194. (Cited on page 8.)

Springel, V. and Farrar, G. R. (2007). The speed of the 'bullet' in the merging galaxy cluster 1E0657-56. MNRAS, 380:911–925. (Cited on page 20.)

Sridhar, S., Maurogordato, S., Benoist, C., Cappi, A., and Marulli, F. (2017). Evolution of the real-space correlation function from next generation cluster surveys. Recovering the real-space correlation function from photometric redshifts. A&A, 600:A32. (Cited on page 55.)

Staniszewski, Z., Ade, P. A. R., Aird, K. A., et al. (2009). Galaxy Clusters Discovered with a Sunyaev-Zel'dovich Effect Survey. ApJ, 701:32–41. (Cited on page 38.)

Starck, J.-L., Murtagh, F. D., and Bijaoui, A. (1998). *Image Processing and Data Analysis*. (Cited on page 124.)

Starobinsky, A. A. (1980). A new type of isotropic cosmological models without singularity. *Physics Letters B*, 91:99–102. (Cited on page 8.)

Stott, J. P., Smail, I., Edge, A. C., et al. (2007). An Increase in the Faint Red Galaxy Population in Massive Clusters since z ∼ 0.5. ApJ, 661:95–101. (Cited on pages 75 and 108.)

Strateva, I., Ivezić, Ž., Knapp, G. R., et al. (2001). Color Separation of Galaxy Types in the Sloan Digital Sky Survey Imaging Data. AJ, 122:1861–1874. (Cited on page 25.)

Strazzullo, V., Coogan, R. T., Daddi, E., et al. (2018). Deciphering the Activity and Quiescence of High-redshift Cluster Environments: ALMA Observations of Cl J1449+0856 at z=2. ApJ, 862:64. (Cited on page 165.)

Strazzullo, V., Rosati, P., Stanford, S. A., et al. (2006). The near-infrared luminosity function of cluster galaxies beyond redshift one. A&A, 450:909–923. (Cited on page 75.)

Stromberg, G. (1925). Analysis of radial velocities of globular clusters and non-galactic nebulae. ApJ, 61. (Cited on page 8.)

Sun, M., Donahue, M., and Voit, G. M. (2007). Hα Tail, Intracluster H II Regions, and Star Formation: ESO 137-001 in Abell 3627. ApJ, 671:190–202. (Cited on page 28.)

Sun, M., Jones, C., Forman, W., et al. (2006). A 70 Kiloparsec X-Ray Tail in the Cluster A3627. ApJ, 637:L81–L84. (Cited on page 28.)

Sunyaev, R. A. and Zeldovich, I. B. (1980). The velocity of clusters of galaxies relative to the microwave background - The possibility of its measurement. MNRAS, 190:413–420. (Cited on page 32.)

Sunyaev, R. A. and Zeldovich, Y. B. (1970). Small-Scale Fluctuations of Relic Radiation. Ap&SS, 7:3–19. (Cited on page 32.)

Sunyaev, R. A. and Zeldovich, Y. B. (1972). The Observations of Relic Radiation as a Test of the Nature of X-Ray Radiation from the Clusters of Galaxies. *Comments on Astrophysics and Space Physics*, 4:173. (Cited on page 32.)

Szalay, A. S., Connolly, A. J., and Szokoly, G. P. (1999). Simultaneous Multicolor Detection of Faint Galaxies in the Hubble Deep Field. ApJ, 117:68–74. (Cited on page 50.)

Tal, T., Dekel, A., Oesch, P., et al. (2014). Observations of Environmental Quenching in Groups in the 11 GYR since z = 2.5: Different Quenching for Central and Satellite Galaxies. ApJ, 789:164. (Cited on page 118.)

Tchernin, C., Eckert, D., Ettori, S., et al. (2016). The XMM Cluster Outskirts Project (X-COP): Physical conditions of Abell 2142 up to the virial radius. A&A, 595:A42. (Cited on pages 194 and 195.)

The Dark Energy Survey Collaboration (2005). The Dark Energy Survey. *ArXiv Astrophysics e-prints*. (Cited on pages 37 and 49.)

The IceCube collaboration, Fermi-LAT, Magic, et al. (2018). Multimessenger observations of a flaring blazar coincident with high-energy neutrino IceCube-170922a. *Science*, 361(6398):eaat1378. (Cited on page 8.)

Umetsu, K., Medezinski, E., Nonino, M., et al. (2014). CLASH: Weak-lensing Shear-and-magnification Analysis of 20 Galaxy Clusters. ApJ, 795:163. (Cited on page 30.)

Umetsu, K., Zitrin, A., Gruen, D., et al. (2016). CLASH: Joint Analysis of Strong-lensing, Weak-lensing Shear, and Magnification Data for 20 Galaxy Clusters. ApJ, 821:116. (Cited on page 29.)

Valotto, C. A., Nicotra, M. A., Muriel, H., and Lambas, D. G. (1997). The Luminosity Function of Galaxies in Clusters. ApJ, 479:90–96. (Cited on page 76.)

Van Waerbeke, L., Mellier, Y., Erben, T., et al. (2000). Detection of correlated galaxy ellipticities from CFHT data: first evidence for gravitational lensing by large-scale structures. A&A, 358:30–44. (Cited on page 12.)

Vanderlinde, K., Crawford, T. M., de Haan, T., et al. (2010). Galaxy Clusters Selected with the Sunyaev-Zel'dovich Effect from 2008 South Pole Telescope Observations. ApJ, 722:1180–1196. (Cited on page 38.)

Venturi, T., Giacintucci, S., Brunetti, G., et al. (2007). GMRT radio halo survey in galaxy clusters at z = 0.2-0.4. I. The REFLEX sub-sample. A&A, 463:937–947. (Cited on pages 30, 31, and 33.)

Veropalumbo, A., Marulli, F., Moscardini, L., Moresco, M., and Cimatti, A. (2014). An improved measurement of baryon acoustic oscillations from the correlation function of galaxy clusters at z $\sim$ 0.3. MNRAS, 442:3275–3283. (Cited on page 20.)

Veropalumbo, A., Marulli, F., Moscardini, L., Moresco, M., and Cimatti, A. (2016). Measuring the distance-redshift relation with the baryon acoustic oscillations of galaxy clusters. MNRAS, 458:1909–1920. (Cited on page 20.)

Vikhlinin, A., Kravtsov, A., Forman, W., et al. (2006). Chandra Sample of Nearby Relaxed Galaxy Clusters: Mass, Gas Fraction, and Mass-Temperature Relation. ApJ, 640:691–709. (Cited on pages 190 and 191.)

Voit, G. M. (2005). Tracing cosmic evolution with clusters of galaxies. *Reviews of Modern Physics*, 77:207–258. (Cited on pages 17, 188, 193, and 194.)

von der Linden, A., Mantz, A., Allen, S. W., et al. (2014). Robust weak-lensing mass calibration of Planck galaxy clusters. MNRAS, 443:1973–1978. (Cited on page 199.)

Walcher, C. J., Groves, B., Budavari, T., and Dale, D. (2011). Fitting the integrated Spectral Energy Distributions of Galaxies. *Astrophysics and Space Science*, 331(1):1–51. arXiv: 1008.0395. (Cited on page 55.)

Wang, J.-X., Malhotra, S., Rhoads, J. E., Zhang, H.-T., and Finkelstein, S. L. (2009). Lyα-Emitting Galaxies at Redshift z$\sim$ 4.5 in the LALA Cetus Field. ApJ, 706:762–771. (Cited on pages 175 and 178.)

Watson, M. G., Pye, J. P., Denby, M., et al. (2003). The XMM-Newton serendipitous source catalogue. *Astronomische Nachrichten*, 324:89–92. (Cited on page 44.)

Way, M. J. (2013). Dismantling Hubble's Legacy? In Way, M. J. and Hunter, D., editors, *Origins of the Expanding Universe: 1912-1932*, volume 471 of *Astronomical Society of the Pacific Conference Series*, page 97. (Cited on page 8.)

Weinberg, D. H., Mortonson, M. J., Eisenstein, D. J., et al. (2013). Observational probes of cosmic acceleration. Phys. Rep., 530:87–255. (Cited on pages 11, 13, and 18.)

Weinberg, S. (1972). *Gravitation and Cosmology: Principles and Applications of the General Theory of Relativity*. ISBN 0-471-92567-5. Wiley-VCH , July 1972. (Cited on page 8.)

Wen, Z. L. and Han, J. L. (2015). Dependence of the bright end of composite galaxy luminosity functions on cluster dynamical states. MNRAS, 448(1):2–8. (Cited on pages 81, 104, and 105.)

West, M. J., de Propris, R., Bremer, M. N., and Phillipps, S. (2017). Ten billion years of brightest cluster galaxy alignments. *Nature Astronomy*, 1:0157. (Cited on page 185.)

Wetzel, A. R., Tinker, J. L., and Conroy, C. (2012). Galaxy evolution in groups and clusters: star formation rates, red sequence fractions and the persistent bimodality. MNRAS, 424:232–243. (Cited on pages 26, 27, and 29.)

Weymann, R. (1966). The Energy Spectrum of Radiation in the Expanding Universe. ApJ, 145:560. (Cited on page 32.)

White, S. D. M., Navarro, J. F., Evrard, A. E., and Frenk, C. S. (1993). The baryon content of galaxy clusters: a challenge to cosmological orthodoxy. Nature, 366:429–433. (Cited on page 20.)

Willis, J. P., Ramos-Ceja, M. E., Muzzin, A., et al. (2018). X-ray versus infrared selection of distant galaxy clusters: a case study using the XMM-LSS and SpARCS cluster samples. MNRAS, 477:5517–5535. (Cited on page 123.)

Willmer, C. N. A. (2018). The absolute magnitude of the sun in several filters. ApJ*Supplement Series*, 236(2):47. (Cited on page 87.)

Willmer, C. N. A., Faber, S. M., Koo, D. C., et al. (2006). The Deep Evolutionary Exploratory Probe 2 Galaxy Redshift Survey: The Galaxy Luminosity Function to z∼1. ApJ, 647:853–873. (Cited on page 25.)

Wilson, E. B. (1927). Probable Inference, the Law of Succession, and Statistical Inference. *Journal of the American Statistical Association*, 22(158):209–212. (Cited on page 170.)

Wilson, G. W., Hughes, D. H., Aretxaga, I., et al. (2008). A bright, dust-obscured, millimetre-selected galaxy beyond the Bullet Cluster (1E0657-56). MNRAS, 390:1061–1070. (Cited on page 29.)

Wittman, D. M., Tyson, J. A., Kirkman, D., Dell'Antonio, I., and Bernstein, G. (2000). Detection of weak gravitational lensing distortions of distant galaxies by cosmic dark matter at large scales. Nature, 405:143–148. (Cited on page 12.)

Witzel, A., Schmidt, J., Pauliny-Toth, I. I. K., and Nauber, U. (1979). 21 CM flux density measurements of sources from the NRAO-MPIfR 6 CM surveys. AJ, 84:942–945. (Cited on page 173.)

Woo, J., Dekel, A., Faber, S. M., et al. (2013). Dependence of galaxy quenching on halo mass and distance from its centre. MNRAS, 428:3306–3326. (Cited on pages 26 and 27.)

Wray, J. J. and Gunn, J. E. (2008). A New Technique for Galaxy Photometric Redshifts in the Sloan Digital Sky Survey. ApJ, 678:144–153. (Cited on pages 55 and 59.)

Yajima, H., Umemura, M., and Mori, M. (2012). Sub-millimetre brightness of early star-forming galaxies. MNRAS, 420:3381–3388. (Cited on page 175.)

Yee, H. K. C. (1998). Photometric Redshift Techniques: Reliability and Applications. *ArXiv Astrophysics e-prints*, pages arXiv:astro–ph/9809347. (Cited on page 59.)

York, D. G., Adelman, J., Anderson, Jr., J. E., et al. (2000). The Sloan Digital Sky Survey: Technical Summary. ApJ, 120:1579–1587. (Cited on page 61.)

Yunes, N. and Siemens, X. (2013). Gravitational-wave tests of general relativity with ground-based detectors and pulsar-timing arrays. *Living Reviews in Relativity*, 16(1):9. (Cited on page 12.)

Zhang, C., Yu, Q., and Lu, Y. (2014). Offsets between the X-Ray and the Sunyaev-Zel'dovich-effect Peaks in Merging Galaxy Clusters and their Cosmological Implications. ApJ, 796:138. (Cited on page 185.)

Zhang, Y. e. a. (2017). Galaxies in x-ray selected clusters and groups in dark energy survey data II: Hierarchical bayesian modeling of red-sequence galaxy luminosity function. arxiv:1710.05908. (Cited on pages 76, 102, 103, and 104.)

Zhang, Y.-Y., Reiprich, T. H., Schneider, P., et al. (2017). HIFLUGCS: X-ray luminosity-dynamical mass relation and its implications for mass calibrations with the SPIDERS and 4MOST surveys. A&A, 599:A138. (Cited on page 143.)

Zheng, Z., Berlind, A. A., Weinberg, D. H., et al. (2005). Theoretical Models of the Halo Occupation Distribution: Separating Central and Satellite Galaxies. ApJ, 633:791–809. (Cited on page 216.)

Zhou, W. and Wu, X.-P. (2004). Contamination of Cluster Radio Sources in the Measurement of the Thermal Sunyaev-Zel'dovich Angular Power Spectrum. ApJ, 600:501–507. (Cited on page 141.)

Ziparo, F., Smith, G. P., Mulroy, S. L., et al. (2015). The XXL Survey. X. K-band luminosity - weak-lensing mass relation for groups and clusters of galaxies. A&A. (XXL Paper X). (Cited on pages 75 and 107.)

Zitrin, A., Fabris, A., Merten, J., et al. (2015). Hubble Space Telescope Combined Strong and Weak Lensing Analysis of the CLASH Sample: Mass and Magnification Models and Systematic Uncertainties. ApJ, 801:44. (Cited on pages 30 and 33.)

Zwicky, F. (1933). Die Rotverschiebung von extragalaktischen Nebeln. *Helvetica Physica Acta*, 6:110–127. (Cited on pages 8 and 18.)